ISBN 1-56677-221-4

Editors

Gottesfeld
Fuller

PROTON CONDUCTING MEMBRANE FUEL CELLS II

PV 98-27

ISBN 1-
56677-
221-4

PROTON CONDUCTING MEMBRANE FUEL CELLS II

The Electrochemical Society
Founded in Philadelphia 1902
Incorporated 1930

Edited by

S. Gottesfeld
T. F. Fuller

PROCEEDINGS OF THE SECOND INTERNATIONAL
SYMPOSIUM ON

PROTON CONDUCTING MEMBRANE FUEL CELLS II

Editors

S. Gottesfeld
Los Alamos National Laboratory
Los Alamos, New Mexico

T. F. Fuller
International Fuel Cells
South Windsor, Connecticut

*ENERGY TECHNOLOGY, PHYSICAL ELECTROCHEMISTRY,
AND BATTERY DIVISIONS*

Proceedings Volume 98-27

THE ELECTROCHEMICAL SOCIETY, INC.,
10 South Main St., Pennington, NJ 08534-2896, USA

Published by:

The Electrochemical Society, Inc.
10 South Main Street
Pennington, New Jersey 08534-2896, USA

Telephone (609) 737-1902
Fax (609) 737-2743
e-mail: ecs@electrochem.org
Web site: http://www.electrochem.org

ISBN 1-56677-221-4

Printed in the United States of America

Preface

This is the 2nd ECS volume covering a symposium devoted to Proton Conducting Membrane Fuel Cells. Since the 1st symposium in the fall of 1995, this field of electrochemical science and technology has seen a dramatic increase in activity. Research, development, and engineering investments, driven primarily by the automotive industries need to develop leaner and greener vehicles, have risen from tens of millions to billions of dollars.

Although polymer electrolyte fuel-cell technology has already reached what can be described as the initial industrial phase, many and significant challenges remain. The R&D activities of electrochemists and electrochemical engineers described in this volume give a good account of these challenges: (1) the thorough understanding of processes and materials properties in the operating polymer electrolyte fuel cell, (2) advancements in materials used to manufacture cell components and stack, and (3) configurations to improve the performance and reliability of cells and cell-stacks and to lower their cost. In the hands of an increasing number of electrochemists and electrochemical engineers, such requirements are translated into the following: (1) improvements of electrocatalysis at the anode in the presence of fuel impurities; (2) examination of air cathode operation on non-noble metal catalysts; (3) innovative water management schemes and theoretical studies of proton transport through ionomeric membranes; (4) specific metal corrosion issues related to use of low-cost metal hardware for the polymer electrolyte fuel cell; and (5) the variety of scientific & technical issues associated with the advanced concept of direct methanol fuel cells.

The number of papers presented in this symposium is twice that presented in the first symposium in Chicago just three years ago, reflecting the increase in activity worldwide. The Symposium was clearly an international event and included valuable discussions that took place in an overflowing room. We are glad to be able to offer this volume to the international community of electrochemists, electrochemical engineers, and fuel cell technologists as an account of central activities in this intensive area of R&D in electrochemical science & technology.

S. Gottesfeld

T. F. Fuller

Table of Contents

PEM Cathodes

Membranes

CO Tolerance and Fuel Impurities

Direct Methanol Fuel Cells

Cell Stack and System Optimization

FACTS ABOUT THE ELECTROCHEMICAL SOCIETY, INC.

The Electrochemical Society, Inc., is an international, nonprofit, scientific, educational organization founded for the advancement of the theory and practice of electrochemistry, electrothermics, electronics, and allied subjects. The Society was founded in Philadelphia in 1902 and incorporated in 1930. There are currently over 7,000 scientists and engineers from more than 70 countries who hold individual membership; the Society is also supported by more than 100 corporations through Contributing Memberships.

The Technical activities of the Society are carried on by Divisions and Groups. Local Sections of the Society have been organized in a number of cities and regions. Major international meetings of the Society are held in the Spring and Fall of each year. At these meetings, the Divisions and Groups hold general sessions and sponsor symposia on specialized subjects.

The Society has an active publications program which includes the following:

Journal of The Electrochemical Society - The *Journal* is a monthly publication containing technical papers covering basic research and technology of interest in the areas of concern to the Society. Papers submitted for publication are subjected to careful evaluation and review by authorities in the field before acceptance, and high standards are maintained for the technical content of the *Journal.*

Electrochemical and Solid-State Letters - *Letters* is the Society's rapid-publication, electronic journal. Papers are published as available at http://www3.electrochem.org/letters.html. This peer-reviewed journal covers the leading edge in research and development in all fields of interest to ECS. It is a joint publication of the ECS and the IEEE Electron Devices Society.

Interface - *Interface* is a quarterly publication containing news, reviews, advertisements, and articles on technical matters of interest to Society Members in a lively, casual format. Also featured in each issue are special pages dedicated to serving the interests of the Society and allowing better communication among Divisions, Groups, and Local Sections.

Meeting Abstracts *(formerly Extended Abstracts)* - Meeting Abstracts of the technical papers presented at the Spring and Fall Meetings of the Society are published in serialized softbound volumes.

Proceedings Series - Papers presented in symposia at Society and Topical Meetings are published as serialized Proceedings Volumes. These provide up-to-date views of specialized topics and frequently offer comprehensive treatment of rapidly developing areas.

Monograph Volumes - The Society sponsors the publication of hardbound Monograph Volumes, which provide authoritative accounts of specific topics in electrochemistry, solid-state science, and related disciplines.

For more information on these and other Society activities, visit the ECS Web site:

http://www.electrochem.org

Proton_Conducting_Membrane_Fuel_Cells_II, PV 1998-27, 1-9 (1998)
DOI: 10.1149/199827.0001PV © The Electrochemical Society

CARBON CLOTH GAS DIFFUSION BACKINGS FOR HIGH PERFORMANCE PEFC CATHODES

B. Mueller, T. Zawodzinski, J. Bauman,
F. Uribe and S. Gottesfeld

Electronic Materials and Devices Group
Los Alamos National Laboratory
Los Alamos, NM 87545

E. De Castro and M. De Marinis
E-TEK, Inc.,
6 Mercer Road, Natick, MA 01760-2415

ABSTRACT

We report results comparing the performance of polymer electrolyte fuel cells (PEFCs) using a series of variously structured carbon cloth gas diffusion backings on the cathode side of the PEFC. Backing performance is considered in light of measurements of gas permeation rate through the (dry) backing samples. Comparisons are made of backing effects in both 5 and 50 cm^2 cells, operated with a series of oxygen partial pressures in the cathode feedstream. In tests with 50 cm^2 cells, backings which exhibited 3-5 fold higher gas permeation rates (in dry state) than the standard ELAT, enabled an increase of maximum PEFC power density by about 20%.

INTRODUCTION

The gas diffusion backing is a critical component in achieving high performance in polymer electrolyte fuel cells (PEFCs). The requirements of an ideal gas diffusion backing are several, including diffusing the gaseous reactant effectively across to the catalyst layer and assisting in water management by allowing passage of water into or out of the electrode without flooding with liquid water. LANL has previously characterized gas diffusion backings by their effective porosity and tortuosity in an operating cell, estimated via modeling the steady state or ac response of the cell (1,2). It was suggested that backing layer thickness could play an important role in cathode performance (2). This work and that of others on air cathode diagnostics has contributed to the recent development of advanced backing layers by several fuel cell component manufacturers.

For porous and/or fibrous gas filtration media, resistance to flow is often used as a characteristic measure for quality control and performance. This measurement is standardized and sufficiently widely performed that a commercially produced instrument is employed, called a "Gurley" device. The Gurley number is the time it takes to move a fixed volume of air at a fixed pressure difference through a fixed area of sample, and thus indicates the resistance to gas flow. As effective backing permeability is an important parameter for optimized cell operation, the Gurley number is expected to correlate with backing performance in the PEFC.

An additional effect of the gas diffusion backing on PEFC performance is related to its role in helping maintain proper water balance. Water balance in the fuel cell entails delicate balance of hydrophobic and hydrophilic character within the backing layer. Such balance depends, in turn, on cell operating parameters such as current density (which determines how much water is generated within the cell), humidification conditions and the flow rate of gases into the cell.

Here we describe work attempting to correlate fuel cell performance with a series of backing materials with intrinsic properties of the backings including the thickness , disposition of applied hydrophobic and hydrophilic layers and the resistance to flow of the dry backing layer. This paper describes results obtained with a series of E-TEK backings with hydrophobic layers of varying thickness applied on only one side of a carbon cloth, termed here 'single-sided' backing layers, and compares such results to those obtained with more typical, 'double-sided' backings.

EXPERIMENTAL

Fuel cell MEA fabrication and testing on single cells was carried out as described elsewhere (3). For experiments in which the oxygen partial pressure in the cathode feedstream was varied, O_2 and N_2 were mixed in appropriate combinations using calibrated computer controlled mass flow controllers (MKS Inc.). Cathode flow rates were kept constant at a multiple of the stoichiometric flow rate for 1 A cm^{-2}. For 5 cm^2 cells, the multiple was typically 5 while for 50 cm^2 cells, 1.5 times stoichiometric flow was used.

A series of experimental backings were created and compared to the commercially available ELAT™ and single-sided ELAT backings. Figure 1 illustrates schematically the arrangement between the carbon cloth web and microporous layers applied to the web. Table 1 summarizes the key differences between the backings tested. The style designation is an arbitrary manufacturing number. All backings were fabricated using E-TEK's proprietary "Version 2" methodology (for example, a backing designation of 2.11 indicates a version 2, style 11 backing). Except for the standard ELAT, all the carbon black microporous coatings are applied on one side of the carbon cloth web only, i.e., all are 'single sided' backings. The thickness of each backing layer is determined by nine measurements across the entire (100 cm^2) sample. A representative thickness of each sample is the average of these nine measurements.

Table 1 Backings used in this Study

Backing Style	Description	Thickness, +/- mils	Number of Samples
2.20	Uniform thin hydrophobic microporous layer	17.0+/-0.6	4
2.11	Composite of very thin hydrophobic and hydrophilic microporous layers	15.6+/-.2	4
2.22 ("single sided ELAT)	Standard composite of thin hydrophobic and hydrophilic microporous layers	16.2+/-0.7	5
2.33	Thick composite of hydrophobic and hydrophilic microporous layers	18.8+/-1.0	4
Standard ELAT	Coatings on both sides of web	19.4 +/-0.6	6

To determine the 'Gurley' number of the various backings, an apparatus for measuring resistance to flow was constructed at E-TEK, employing two water-filled "U" tubes, one 80 and the other 40cm long, a nitrogen flow meter (0-20LPM), and a back-pressure valve (See Figure 2). Samples of electrode backing (5 x 5 cm) were cut and fitted into a manifold with gaskets, such that the uncoated side of the backing is oriented towards the nitrogen inlet. Prior to evaluation of a backing sample, the system inherent resistance to gas flow of the system is evaluated by measuring back pressure in the U-tubes over a range of flow rates. This system resistance to flow is used as a correction in the subsequent measurement of backing gas flow characteristics.

In order to first establish an appropriate operating range, five samples of single-sided ELAT ("style 22") were subjected to a series of output flow rates by progressively increasing the flow and noting output flow and input and output pressures. The output flow was varied from 1 to 12 LPM. Pressure differentials, corrected for the system resistance to flow , were calculated and the output flow rate in LPM divided by the differential pressure (in units of cm of H_2O) and normalized to the exposed backing area of 25cm^2. The resulting value is the characteristic "Gurley number" for resistance to flow. A plot of output flow rate versus the measured backing resistance to flow is shown in Figure 3. An output range of 2-4 LPM yields consistent results and an output flow of 3.6 LPM was thus selected for subsequent comparative measurements.

RESULTS AND DISCUSSION

In Figure 4, PEFC polarization curves are shown to illustrate the range of variation of cell performance with different cathode feeds (1) for cells of 5 cm^2 active area utilizing a standard, 'double sided' E-TEK cathode backing. Figure 5 shows results for all cathode backings tested in operation on neat O_2 and on 13.5 % O_2 in N_2. These tests are based on the approach taken in reference 1 (Figure 15) which shows simultaneous fits of a cathode model to data obtained for similar gas compositions. However, in the experiments shown in Figure 5, very little difference in performance is observed between the various backing layer tested at the given cathode gas composition. (The data shown in fact illustrates the excellent reproducibility achievable in preparation of a series of such cells). These results suggest that there is little difference in the effective tortuosity and porosity of these backings under cell operation conditions.

A summary of measured resistances to flow for the five styles of backing layers employed is given in Figure 6 in the form of a bar chart. One would anticipate that the resistance to flow should increase as the backing thickness increases. This trend is generally followed by the data. With the exception of backing 2.33, the thicker single-sided structure, which has a slightly lower apparent flow resistance than the thinner backing 2.22. We attribute the lower resistance to flow for the 2.33 backing to higher effective porosity. Backings 2.20 and 2.11 are substantially more open to flow than the single-sided ELAT (type 2.22). Apparently, for the 5 cm^2 cells tested (Figure 5), that employed backing layers of such different dry gas permeabilities (Figure 6), oxygen permeability was determined by factors other than the dry permeability, most probably transport through a water layer within the backing or through a water -soaked cathode catalyst layer (such 5 cm^2 cells are typically water-soaked on the cathode side at high cell current density).

Similar tests of the different backing layers in larger cells resulted in some discrimination amongst various backing types. A series of polarization curves obtained for 50 cm^2 cells with different backings operating on oxygen, air and 13.5% O_2 in N_2 are shown in Figures 7-10. (Polarization curves were repeated on air between runs with other oxygen percentages, to ensure that differences observed were not reflecting any degradation of cell performance). Direct comparison of neat oxygen and 13.5% oxygen polarization curves is made in Figure 10. Clearly, the results here indicate that some advantages accrue to structures with thinner microporous layers. A difference in these tests relative to those of the 5 cm^2 cells, is, most probably, lower average level of water along the cathode side of the cell which allows to better show the advantage of higher dry permeability. The results indicate that backings 2.33 and 'double-sided' ELAT exhibit limiting current behavior at ca. 20% lower current densities than for the other cases. We expect that such differences in limiting current amongst such backings could be even higher when the stoichiometric flow of air is somewhat more realistic: we employed a stoichiometric flow of 1.5 x 1 A cm^{-2} in the tests with the 50 cm^2 cell, thus "forcing" a limiting current density of somewhat over 1 A cm^{-2} with any backing material because of the strong oxygen utilization demanded. In fact, Figure 10 shows that the advantage of more permeable backing layers is observed mainly in the region of a limiting current dictated by high oxygen utilization, highlighting the special advantage of such higher backing permeabilities in operation on highly diluted feed streams.

Backing 2.20, the uniformly hydrophobic backing exhibits slightly lower performance relative to 2.11 and 2.22 at lower current densities, but has similar higher performance at high current density. This result likely indicates that it is relatively difficult to humidify the cell effectively through the hydrophobic backing at lower current densities but, once water is more copiously produced at high current densities, the hydrophobic layer is more effective in maintaining parts of the backing water-free. Note also the smaller difference between the air and the 13.5% O_2 in N_2 performance observed with 2.20 (Figure 8), compared to that observed for other backings (Figures 7 and 9). This could indicate that less hindrance of oxygen diffusion occurs because of the more hydrophobic nature of microporous layer.

CONCLUSION

The dry permeability of the backing layer, as described by the "Gurley number", provides some indication on the relative performance level expected in the operating PEFC at high current densities. However, complete characterization of the backings must also take into account effective handling of liquid water. In tests with 50 cm^2 cells, backings which exhibited 3-5 fold higher gas permeation rates (in dry state) than the standard ELAT enabled an increase of maximum PEFC power density by about 20%. In general, backings with thin microporous layers on one side of the carbon cloth material exhibited better performance under higher current densities, corresponding to higher water generation and oxygen utilization rates.

ACKNOWLEDGMENT

We gratefully acknowledge the support of the US DOE Office of Advanced Automotive Technology for this work.

REFERENCES

1. T. E. Springer, M. S. Wilson and S. Gottesfeld, *J. Electrochem. Soc.*, **140**, 3513 (1993).
2. T. E. Springer, T. A. Zawodzinski, M. S. Wilson and S. Gottesfeld, *J. Electrochem. Soc.*, **143**, 587 (1996).
3. T. Zawodzinski, T. Springer, J. Bauman, T. Rockward, F. Uribe and S. Gottesfeld, *this volume.*

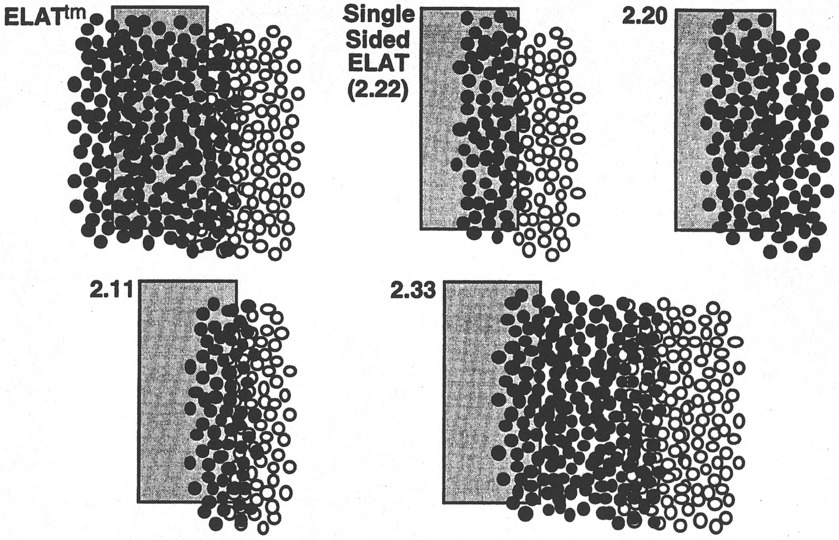

Figure 1: Schematic of backing types used in this work.

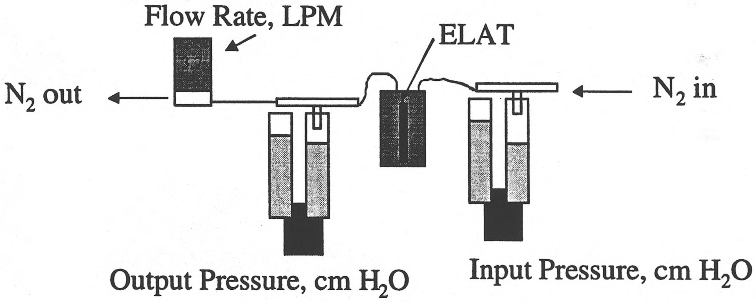

Figure 2: Apparatus for measuring resistance to flow.

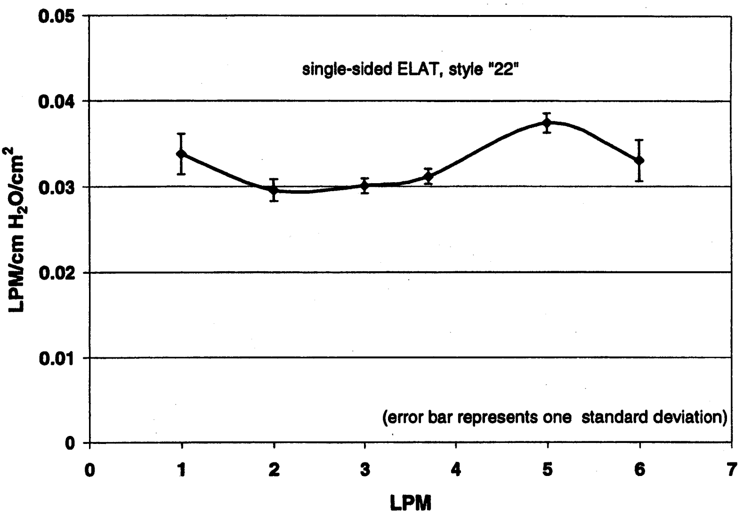

Figure 3: Raw data from flow resistance measurement, backing 2.22.

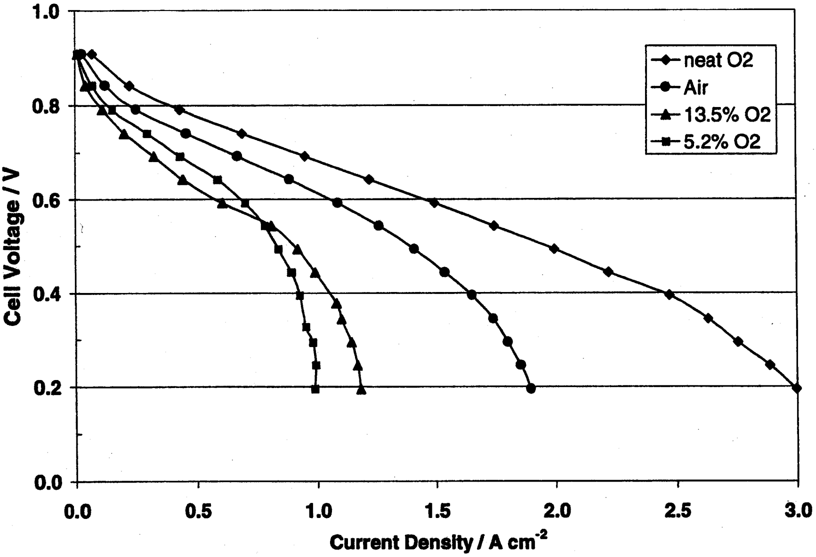

Figure 4: PEFC polarization curves for a 5 cm^2 cell using standard double-sided ELAT backing. Test conditions: 5 cm^2 cell, Pt loading: 0.15-0.2 mg cm^{-2} for anode and cathode; T_{cell} = 80°C, anode and cathode back pressure = 30 psig; 5 stoich anode and cathode flow rate.

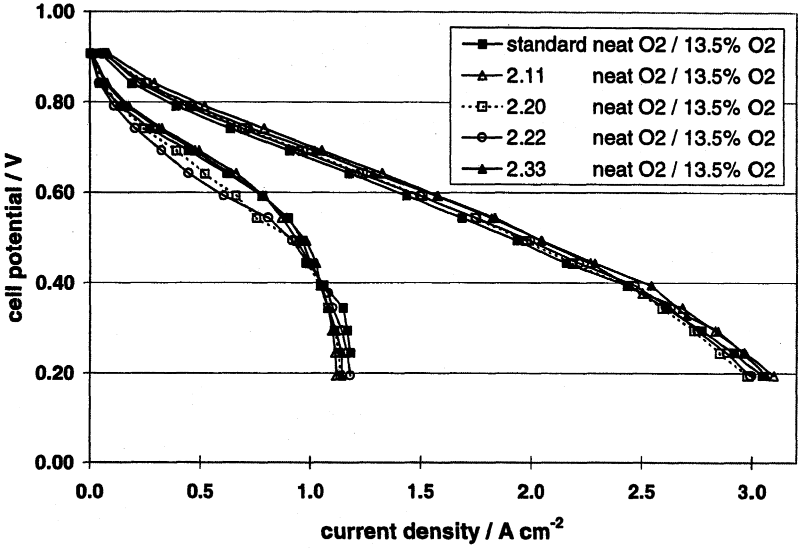

Figure 5: Comparison of fuel cell performance for a series of gas diffusion backings. Test conditions: 5 cm^2 cell, Pt loadings 0.15-0.2 mg cm^{-2} for anode and cathode of all cells; T_{cell}= 80°C, anode and cathode backpressure = 30 psig; 5 stoich anode and cathode flow rate.

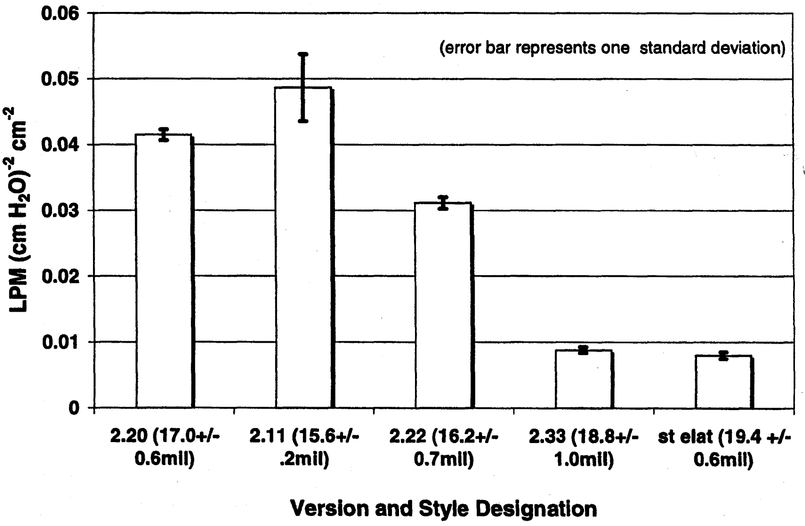

Figure 6: Resistance to flow, derived as discussed in the text, for the various backings.

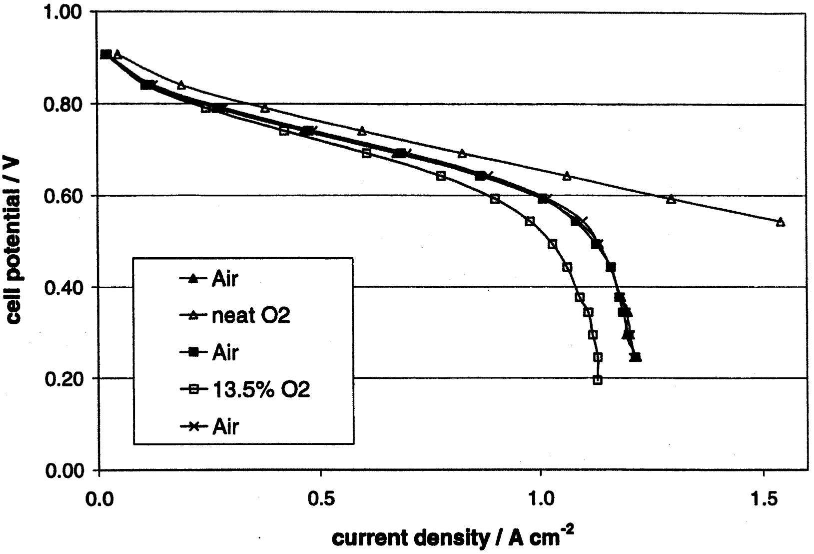

Figure 7: Fuel cell performance as a function of oxygen dilution for gas diffusion backing 2.11. Test conditions: 50 cm^2 cell, Pt loading 0.15-0.2 mg cm^{-2} for anode and cathode; T$_{cell}$= 80°C, anode and cathode back pressure = 30 psig; 1.5 stoich anode and cathode flow rate.

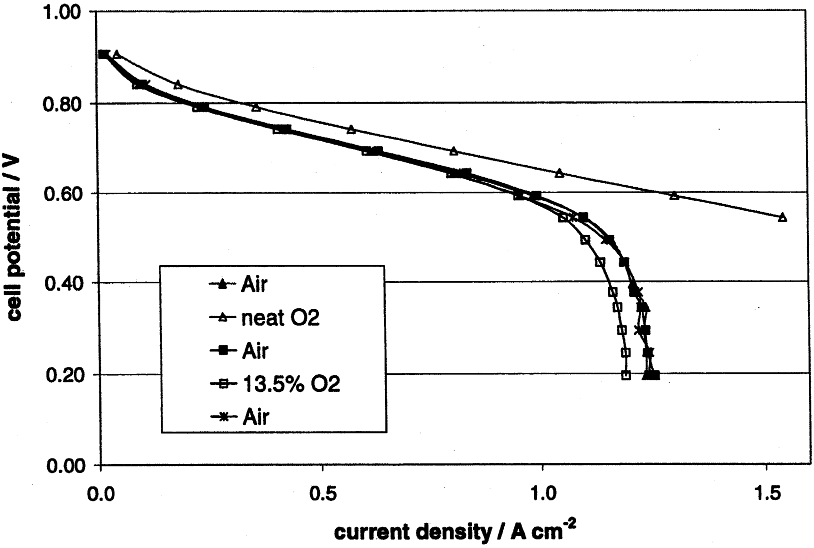

Figure 8: Fuel cell performance as a function of oxygen dilution for gas diffusion backing 2.20. Test conditions as in Figure 7.

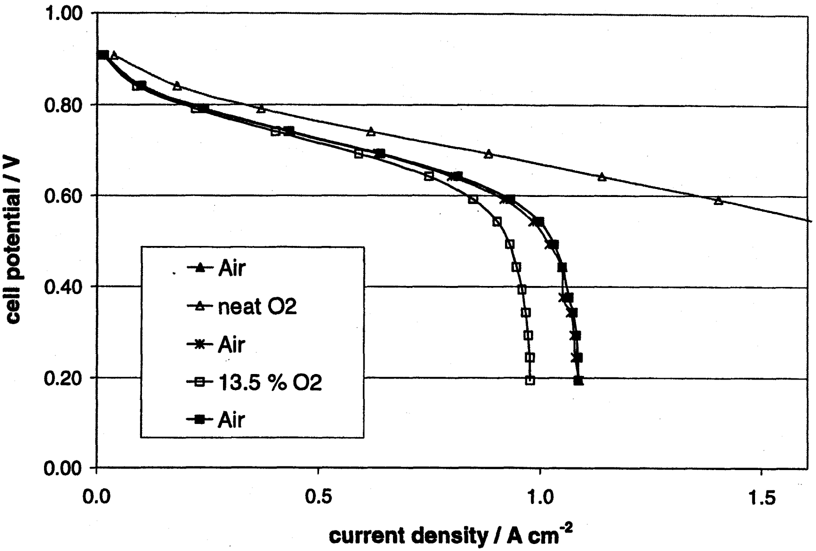

Figure 9: Fuel cell performance as a function of oxygen dilution for standard double-sided ELAT gas diffusion backing. Test conditions as in Figure 7.

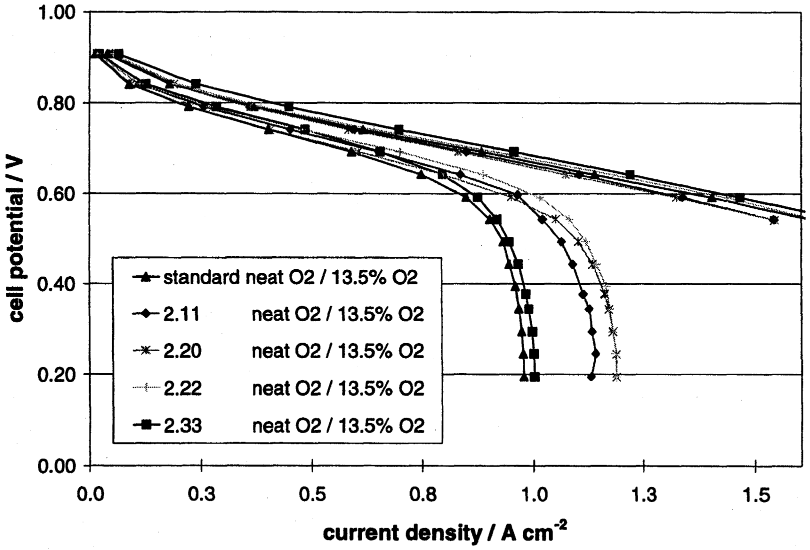

Figure 10: Comparison of fuel cell performance for a series of gas diffusion backings. Test conditions as in Figure 7.

Proton_Conducting_Membrane_Fuel_Cells_II, PV 1998-27, 10-22 (1998)
DOI: 10.1149/199827.0010PV © The Electrochemical Society

AGGREGATION OF IONOMER AND CARBON BLACKS DURING MEA PREPARATION: MODEL TO CHARACTERIZE PARTICLE SIZE AND CATALYST ACCESSIBILITY

Lois Anne Zook, Marc D. DeJohn, and Johna Leddy *
Department of Chemistry
University of Iowa
Iowa City, IA 52242

Aggregates form when ionomers such as Nafion are mixed with small particles. The formation of these aggregates is driven by particle surface area and cohesive energy between ionomer fluorocarbon side chains. A model is suggested for relating the size of aggregates to basic properties of the ionomer and particles. The model is applied to inks of Nafion and the platinized carbon black, Vulcan XC-72. Design notions for varying the properties of MEA inks are presented.

INTRODUCTION

Membrane electrode assemblies (MEAs) for proton exchange membrane (PEM) fuel cells are variously formed by coating inks of polymer and catalyzed carbon black against the outer surfaces of the membrane separator. Typically, the assembly is then heat treated. Using a mixture of polymer and carbon black to form the catalyst layer or interface was first reported by Raistrick (1) in 1986. Polytetrafluorethylene was a commonly used, but it has been largely replaced by ionomers such as Nafion® and Flemion®.

The ionomer in the catalyst layer can serve any of several purposes. Ionomer can increase ionic conduction in the interface; serve as a binding agent for the components in the interface; and help control wetting.

Here, it is suggested that the ionomer also controls the size of the catalyst aggregates in the interface. Experimental results are presented for composites of Nafion and nanostructured materials that illustrate effects of molecular packing and aggregate formation. A model that correlates the size of ionomer/carbon black aggregates with the molecular dimensions of the ionomer and the radius of the carbon black particles is presented. From the model, suggestions are made for controlling the size of carbon black aggregates in the catalyst layer based on ionomer structure and particle size.

EXPERIMENTAL SECTION

Composites were formed by sorption of Nafion onto and into model, nanostructured materials (2–6). Neutron track etched polycarbonate membranes (CoStar, Nuclepore) are 6 μm thick, and traversed by co-linear cylindrical pores. Each membrane contains a single diameter pore, and had pore densities of the order of 10^8 pores/cm^2. Pore diameters of 15, 30, 50, and 100 nm were used (2,3) in Nafion/neutron track etched membrane composites. In Nafion/microsphere composites, polystyrene microbeads (Polyscience) with diameters of 0.11, 0.22, 0.37, and 1.1 μm were used (4,6).

Composite Formation

Nafion/neutron track etched composites were formed by soaking the membranes in Nafion suspension (5% wt/vol Nafion in alcohol/water - Solution Technologies) for 30 minutes. Upon removing the membranes from the soaking solution, the exterior surface was briefly blotted to remove excess suspension adhering to the outer surface of the membrane. The composites were dried overnight in a vacuum desiccator.

Nafion/microsphere composites were formed by cocasting appropriate volumes of Nafion suspension (Aldrich) and microsphere suspension (2.5% wt/vol in water). Casting solvents were allowed to evaporate and the composites were placed in a vacuum desiccator for one hour. Composites contained 50% microbeads by volume, and were approximately 10 μm thick. The density of the microspheres was reported by the manufacturer as 1.05 g/cm^3. The density of the cold cast Nafion was taken as 1.40 g/cm^3, as recently determined (7).

Titration Experiments

The majority of the titration experiments were performed on Nafion/neutron track etched membrane composites. The protocol for these experiments was as follows (3). (1) Weigh the membrane. (2) Soak the membrane in the Nafion suspension, remove excess suspension form the surface of the membrane, and allow the solvents to evaporate. This forms the composite. (3) Soak the dried composite in hydrochloric acid solution to convert the sulfonates to the protonated form. (4) Dry and weigh the composite. (5) Place the composite in 1 M NaCl to flush the protons from the composites, and titrate the protons with NaOH to a phenolphthalein endpoint.

SEM Images

Scanning electron microscopy (SEM) images were taken of the Nafion/microsphere composites by casting the composites on silicon wafers. Micrographs were taken with Hitachi S-2700 and Hitachi S-4000 SEMs. Magnifications of 10× the microbead diameter in each composite were used.

RESULTS

Titration Experiments for Nafion/Neutron Track Etched Composites

The titration experiments yield two different assessments of the amount of Nafion in the Nafion/neutron track etched composites. The difference in the weight of membrane and the composite (membrane + Nafion) yields the actual weight of Nafion in the composite. The titration of the composites yields the millimoles of sulfonate groups in the composites that are actually available for ion exchange. The equivalent weight of the Nafion in the suspension was determined by titration to be 1046 grams of Nafion per mole of SO_3^-.

The surface area of the membranes was known from the pore diameters and the porosity of the membranes. It was found that as the surface area of the membrane increased, the moles of sulfonates found by titration decreased relative to the moles of sulfonates found by weigh. That is, as surface area increased, the moles of sulfonates available for exchange decreased. This is illustrated in Figure 1.

From Figure 1, the fraction of sulfonates available for ion exchange decreases linearly with the surface area over which the Nafion is sorbed. This leads to several observations and conclusions (2).

1. It is the sulfonate groups that interact with the surface that become unavailable for ion exchange.
2. This is consistent with the intercept at zero surface area yielding a value consistent with the 1046 EQWT found for the bulk Nafion material.
3. The slope of the plot yields a cross sectional area per sulfonate unavailable for ion exchange. This cross sectional area has a radius of $0.25_{\pm 12\%}$ nm
4. This radius is consistent with roughly monolayer coverage of sulfonates over the surface of the polycarbonate.

The cylinders of the composite are packed effectively with Nafion. The interior surface of the pore is coated with a monolayer of Nafion where the sulfonates adsorb to the surface and the fluorocarbon tails point radially into the interior of the pore. The remainder of the pore is filled with bulk Nafion, no different in properties than a simple Nafion film.

SEM of Nafion/Microsphere Composites

SEMs of the microsphere composites are shown in Figure 2. It is immediately apparent that the composites formed with microbeads with diameter $\geq 0.22\ \mu m$ form self similar and well distributed clusters. In the composites formed with the smallest microbeads with diameters of 0.11 μm, the beads are not well distributed, and cluster into larger aggregates. The larger aggregates have diameters of 1 to 2 μm.

DISCUSSION

Packing Consideration

The results for the Nafion/neutron track etched materials illustrate that if the support structure is large enough, the ionomer can pack effectively into the structure and form a cohesive monolayer. The result also illustrate that the Nafion preferentially adsorbs to the surface as a monolayer and then fills the remainder of the pore with a structure typical of cast Nafion films.

Titration experiments for the smallest pore diameter of 15 nm were not successful because the uncertainties in determining the weight of sorbed Nafion were too large. However, flux results reported elsewhere (2) indicate that the side chains of the Nafion do not pack effectively into a pore of 15 nm because the tails are too crowded to pack well in the interior of the pore.

Molecular Structure of Nafion 1100

$$-(CF_2CF_2)_8 - CF(CF_2)OCF_2CFOCF_2CF_2SO_3H$$

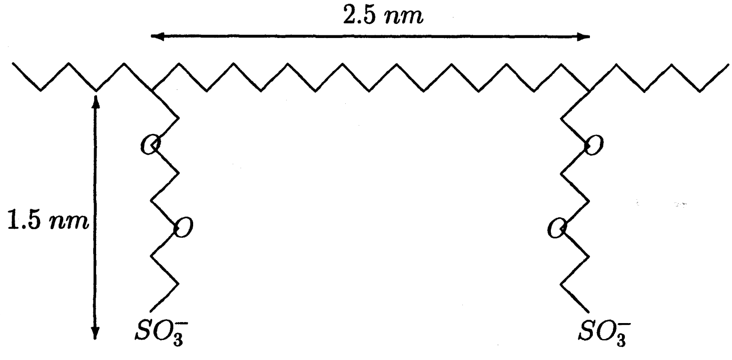

Packing considerations in nanostructured materials have been considered by Halperin, Tirrell, and Lodge (8). They showed that as the characteristic length of nanostructures decreases, the lengths become comparable to the dimensions of the molecules in the system, and this impacts molecular packing. The specific case here can be appreciated by considering the molecular lengths of Nafion. The molecular structure and lengths of the side chains (1.5 nm) and backbone between side chains (2.5 nm) are shown.Based on density calculations for various linear fluorocarbons, the diameter of the tube formed by the side chains is 0.41 nm.

When two sulfonates adsorb next to each other, the monolayer is formed of a thickness of $1.5\ nm + \frac{2.5\ nm}{2} = 2.75\ nm$ because the backbone will bend at its midpoint to allow monolayer formation. This is illustrated.

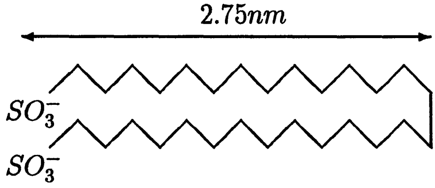

In the 15 nm diameter pore, formation of the monolayer is not possible because cylinder of length 2.75 nm and a diameter of 0.41 nm cannot pack radially and in contact along their lengths inside a circular structure of only 15 nm diameter.

Packing is again a factor in the microsphere composites. For the larger beads, the Nafion can pack effectively along the surface of the beads and sufficiently well into the volumes where two beads touch that each bead is individually wrapped in Nafion. Nafion monolayers can bridge small gaps. As the bead diameter decreases, the fraction of the surface covered by the Nafion decreases because the Nafion cannot pack sufficiently well into the volume where two beads touch, and a different structure is generated. This is illustrated below.

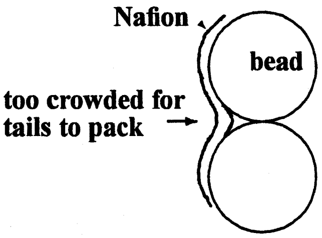

The structure of the microsphere composites is driven by packing and the cohesive energy between fluorocarbon chains. The energy needed to solubilize one CH_2 group in water is 2 to 4 KJ/mol (9); it is expected that the energy to solubilize the CF_2 groups of Nafion will be significantly higher. Thus, the most favored structure for the Nafion will minimize interactions between the CF_2 groups and water while maximizing the interactions between CF_2 groups. Such a structure is best provided by forming a Nafion monolayer at the surface of the inert polymer supports of polystyrene microbeads and polycarbonate membranes. In the microsphere composites for the smallest diameter beads, the cohesive energy between fluorocarbon chains is sufficiently high as to gather the smallest microbeads into a larger aggregate. The aggregate provides a better structure over which the Nafion monolayer can form.

To appreciate the impact of poor packing of the monolayer where two beads touch, consider the diagram of two spheres in contact.

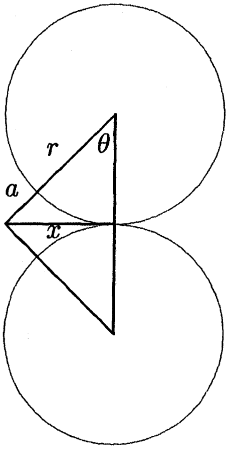

Let r be the radius of the microsphere, and a be the thickness of the adsorbed monolayer. For Nafion, $a = 2.75\ nm$. The left most point in the diagram corresponds to the place where the tails of two adsorbed ionomer monomers collide, one tail on the top bead and one tail on the bottom bead. This collision sets the limit of how well the ionomer packs into the volume where the two spheres touch. This is reflected in the angle θ, where θ measures the cap of each sphere where no coating with ionomer is possible. θ is related to a and r as

$$\theta = \arccos \frac{r}{r+a} \tag{1}$$

It is clear that as a increases, θ increases, and less of the surface is coated by ionomer.

For a 0.11 μm diameter bead coated with Nafion, θ is 17.8°. This is for the point where two beads touch. and represents a significant fraction of the bead surface not covered by ionomer. In a close packed structure, each bead has several nearest neighbors, and the fraction of uncoated surface will be significant. Because the cohesive energy between fluorocarbon chains is sufficiently high it can overcome the drag resistance of the smallest particles, and sequester them into an aggregate with particles on the interior and ionomer monolayer draped around it. It is not dissimilar to marbles inside a balloon, where the air has been vacuumed out of the balloon.

Model

These observations can be generalized with a model to predict the size of an aggregate based on the thickness of the monolayer formed by the ionomer and the size of the beads or particles used in the composite. The model is directly applicable to the inks used to cast MEA catalyst layers, where the particles are the platinized carbon black particles. The model assumes that formation of a monolayer by the ionomer is the driving force for aggregate formation, and that the particles inside the aggregate are close packed.

Define the following variables.

Volume of the aggregate - V_{agg}
Volume of a single spherical particle -v_{part}
Radius of the aggregate - R
Radius of the particle - r
Number of particles in the aggregate - n_{part}
Specific surface area of particles - ssa (cm^2/g)
Avogadro number - N_0
Equivalent weight of the ionomer - $EQWT$
Surface area covered by one chain of the monolayer - σ (cm^2/chain)
Weight of particles per cm^2 - wt_{part}
Weight of ionomer per cm^2 - wt_{ion}

Assume the particles inside the aggregate are close packed. Then, the number of particles in an aggregate is

$$n_{part} = \frac{0.76V_{agg}}{v_{part}} \tag{2}$$

$$= 0.76\left(\frac{R_{agg}}{r_{part}}\right)^3 \tag{3}$$

Note that particles inside an aggregate are less effective catalysts because they are shielded from the environment where the reactants and products are mobile.

Let

$$\alpha = \frac{EQWT \times ssa}{N_0 \times \sigma} \tag{4}$$

Then,

$$\frac{R_{agg}}{r_{part}} = \frac{\alpha}{0.76} \times \frac{wt_{part}}{wt_{ion}} \tag{5}$$

The size of the aggregate is thus determined by the properties and amount of material in the ink. The amount is embedded in the ration wt_{part}/wt_{ion}. The characteristics of the materials used in the ink is embedded in α, where the properties of the ionomer are its equivalent weight and the cross sectional area of the side chains. For the particles (i.e., carbon black), the specific surface area of the particles is important.

Discussion of Nafion and Vulcan XC-62

The aggregates formed when casting an ink of Nafion as ionomer and Vulcan XC-72 as the platinized carbon black particles are characterized by the above model as follows.

Table 1: Materials Properties for Nafion and Vulcan XC-72

	Vulcan XC-72
r_{part}	1.5×10^{-6} cm
ssa	2×10^{6} cm^2/g
	Nafion 1100
$EQWT$	1100 g/mol
σ	1.7×10^{-17} cm^2/chain
α	2.16

From these parameters, the relationship between R_{agg}/r_{part} and wt_{part}/wt_{ion} is shown in Figure 3. The number of particles in an aggregate, n_{part}, is also shown. Note, that as more particles are in an aggregate, the larger the fraction of catalyst buried inside the aggregate, and the lass accessible the catalyst will be.

For typical inks used in MEA fabrication, wt_{part}/wt_{ion} falls in the range between 1 and 10, with values tending to be between 1 and 5. The smaller the ratio of wt_{part}/wt_{ion}, the larger the fraction of catalyst particles on the exterior of the aggregate.

Design Notions for MEA Inks of Ionomer and Carbon Blacks

Several design notions can be extracted from this simple model for changing the characteristics of the catalyst layers produced by forming inks of ionomers and carbon blacks.

- Decreasing aggregate size leaves a larger fraction of the catalyst particles on the exterior of the aggregate, where the particles will be more accessible, and therefore more catalytically active. The size of the aggregates (R_{agg}) can be decreased by each of the following.

  - decrease wt_{part}/wt_{ion}
  - decrease r_{part}
  - decrease $\alpha = \frac{EQWT \times ssa}{N_0 \times \sigma}$
- Forming inks where aggregates do not form would lead to the best dispersion of catalyst as no catalyst particles would be buried inside the aggregates. Small catalyst particles are less likely to form aggregates if the ionomer has the following properties.
  - shorter side chains
  - shorter distances between side chains
  - smaller cross section of the side chains (e.g., hydrocarbon ionomers)

CONCLUSIONS

Aggregates form when ionomers such as Nafion are mixed with small particles. The formation of these aggregates is driven by surface area of the particles and the cohesive energy between the fluorocarbon side chains of the ionomer. A model is developed relating the size of aggregates to basic properties of the ionomer and particles. The model is applied to inks of Nafion and the platinized carbon black, Vulcan XC-72. The properties of MEA inks can be altered by varying wt_{part}/wt_{ion}, and the properties of the ionomer and carbon black.

ACKNOWLEDGMENTS

The financial assistance of the National Science Foundation (CHE-93-20611) is gratefully acknowledged. We also thank Paul D. Moberg for taking the SEM images. Nicholas E. Vanderborgh of Los Alamos National Laboratories is acknowledged for enlightening discussion of MEA catalyst layers.

REFERENCES

[1] Raistrick, I. D. . in *Proceedings of teh Symposium on Diaphragms, Separators, and Ion Excahnge Membranes*; Zee, J. W. V.; White, R. E.; Kinoshita, K.; Burney, H. S., Eds.; The Electrochemical Society, Inc.: 1986.

[2] Fang, Y.; Leddy, J. *J. Phys. Chem.* **1995,** *99*, 6064-6073.

[3] Leddy, J.; Vanderborgh, N. E. *J. Electroanal. Chem.* **1987,** *235*, 299-315.

[4] Zook, L. A.; Leddy, J. Diffusion in Fractal Microstructures. in *Microstructured and Microfabricated Systems II*, Vol. 95-27; Denton, D.; Hesketh, P. J.; Hughes, H., Eds.; The Electrochemical Society, Inc.: 1995.

[5] Zook, L. A.; Amarasinghe, S.; Fang, Y.; Leddy, J. *Nano- and Micro-Structured Materials: The Role of the Interfaces in Tailoring Transport;* Vol. II of *Fundamentals of Materials Research Series* Plenum: New York, 1995 pages 355–364.

[6] Zook, L. A.; Leddy, J. *J. Phys. Chem.* **1998,** *102*,.

[7] Zook, L. A.; Leddy, J. *Anal. Chem.* **1996,** *68*, 3793-3796.

[8] Halperin, A.; Tirrell, M.; Lodge, T. P. *Tethered Chains in Polymer Microstructures;* Vol. 100 of *Advances in Polymer Science* Springer-Verlag: New York, 1992 pages 31–71.

[9] Isrealalchvili, J. N. *Intermolecular and Surface Forces;* Academic Press: New York, 2nd ed.; 1992 page 353.

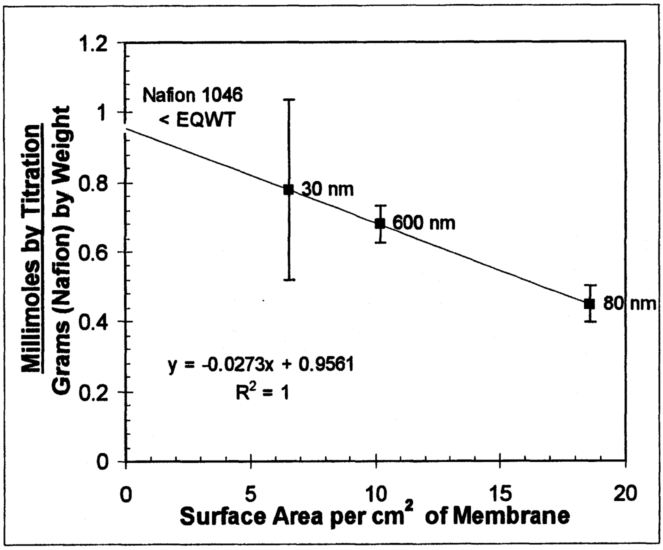

Figure 1: For Nafion/neutron track etched composites, the fraction of sulfonate groups available for ion exchange decreased with the surface area of the membrane.

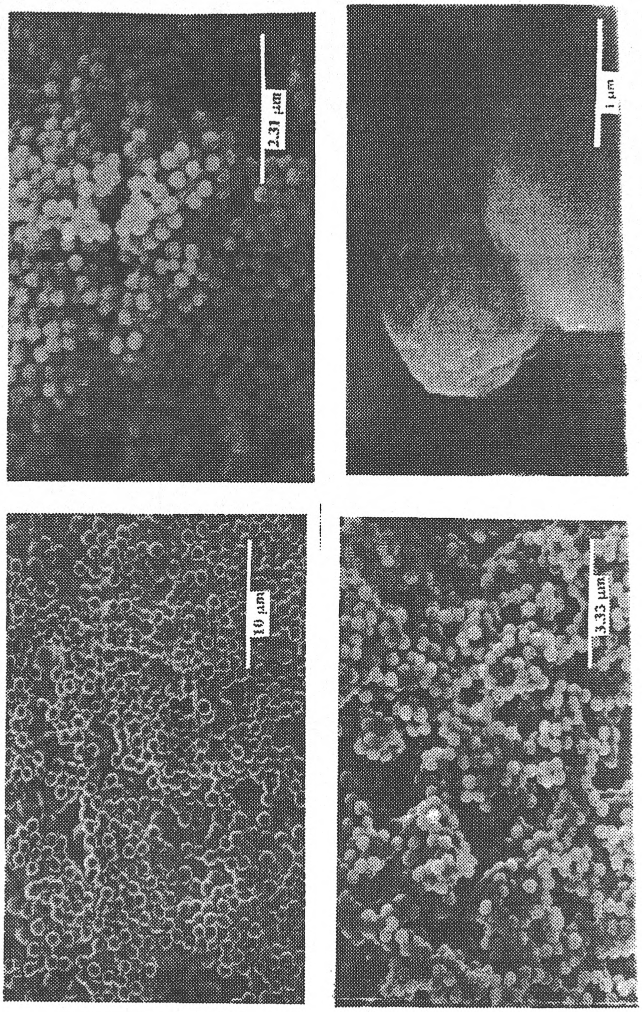

Figure 2: SEM Images of Nafion/microsphere composites. In each Image, the micron bar is 10 × the microbead diameter.

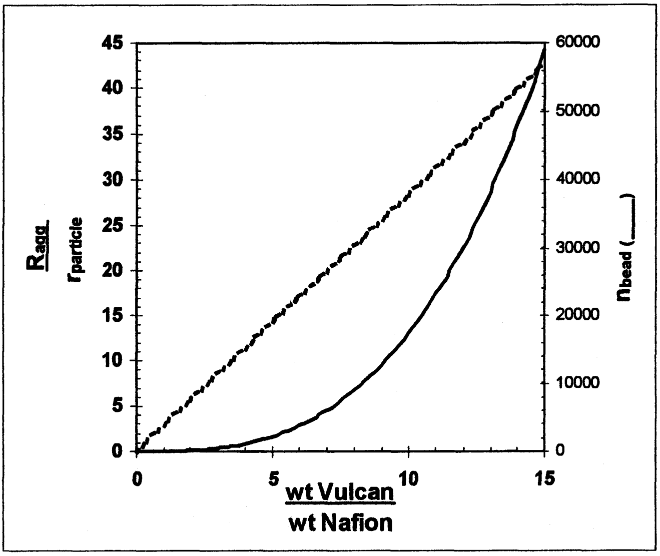

Figure 3: Variation in aggregate size relative to particle size and number of particles per aggregate (n_{bead}) as wt_{Vulcan}/wt_{Nafion} varies in MEA inks. As n_{bead} increases, a larger fraction of particles is embedded inside the aggregates where the catalyst is less accessible.

Proton_Conducting_Membrane_Fuel_Cells_II, PV 1998-27, 23-29 (1998)
DOI: 10.1149/199827.0023PV © The Electrochemical Society

PERFORMANCE IMPROVEMENT OF THE PEMFC BY USING PORE FORMING ADDITIVES IN THE ACTIVE LAYER OF THE OXYGEN (AIR) DIFFUSION ELECTRODE

Sergei Gamburzev, Christopher Boyer, and A. John Appleby

*Center for Electrochemical Systems and Hydrogen Research,
Texas Engineering Experiment Station, Texas A&M University,
College Station, TX 77843 - 3402*

The influence of pore forming additives introduced into the active layer of oxygen (air) gas diffusion electrodes for PEMFCs was studied. Two types of electrodes, with low (LL) and high (HL) platinum loading respectively, were investigated. In both cases, optimal amounts of pore-forming additives were used after experimentation on the increase in the volume porosity of the active layer. The increased volume porosity resulted in a significant reduction in the mass transport resistance in the active layer of the oxygen (air) cathode and therefore in a substantial improvement in electrode performance. Possible positive and negative aspects of changing the volume porosity of the active layer by means of additional pore formation are discussed.

INTRODUCTION

During the past few years, research on proton exchange membrane fuel cells (PEMFCs) has often appeared to have reached a saturation point in regard to performance improvement. Data and scientific efforts and achievements in the performance area were recently summarized by the Ballard team (1). It was concluded that further improvement in PEMFC performance might be achieved by systematic research in: (i) new oxygen reduction electrocatalysts; (ii) new types of polymer electrolyte; and (iii) profound changes in oxygen (air) diffusion electrode structure to minimize all transport limitations. The first direction needs systematic profound research and experimental work in the area of catalyst "construction," while the second mainly involves polymer chemistry. The most promising direction for improvement of PEMFC performance is based on minimization of all transport resistances occurring in the electrochemical reaction by making appropriate changes in the overall electrode structure. One way to minimize the transport resistances in gas diffusion electrodes is to increase their pore volume by using different pore-forming additives (2). It was shown that the pore volume of gas diffusion electrodes could be increased in both the gas distribution layer and the active layer. This paper gives performance results for a hydrogen-oxygen (air) PEMFC which incorporates pore-forming additives during the fabrication of the active layer of the oxygen electrode.

EXPERIMENTAL

Two types of PEMFC with *in-house* fabricated gas diffusion electrodes (3) were studied, namely high platinum loading (HL) with a total of 1.25 mg platinum per cm^2 of membrane-electrode assembly (MEA) and low platinum loading (LL) with 0.25 mg platinum cm^2. Every set of cathodes used proprietary pore-forming (PF) additives in the active layer in amounts varying from 20 to 60 wt %. The pore former was added to the catalyst-Nafion mixture (ink), followed by ultrasonic agitation. After painting the active layers onto the substrate, the electrodes were treated to extract the pore-former. MEAs were fabricated by hot pressing of the cathodes thus prepared and low-platinum-loading (0.05 mg/cm^2) anodes on to Nafion 112 membranes as the polymer electrolyte. The working area of the MEAs was 50 cm^2. The performance of the MEAs was evaluated at 50°C with humidified hydrogen, oxygen and air at atmospheric pressure.

RESULTS AND DISCUSSION

Figure 1 shows the hydrogen-air cell potential versus current density for the set of MEAs with LL-oxygen electrodes as a function of different amounts of the pore-forming additive (PF). The results show that the performance improves when the amount of PF is increased up to a level of 33 wt %. Further increase in the quantity of PF results in a reduction in performance. Figure 2 shows the hydrogen-oxygen cell performance for the above set of MEAs. The influence of amount of pore forming additive on mass transport processes in the active layer of oxygen electrode may be evaluated from both sets of data.

Figure 3 shows the current density generated by hydrogen-air cells at two different cell potentials with LL-oxygen electrodes as a function of amount of PF. It appears that the optimal amount of PF is 33 wt % at 0.6V, and 25 wt % at 0.3 V. This difference may be attributed to the specific distribution of hydrophilic/hydrophobic properties of the pore volume formed in the active layer after extraction of the PF. At high cathode polarization (e.g., at 0.3V cell voltage) the rate of water production in the electrochemical reaction is probably higher that its rate of evaporation. This results in an accumulation of liquid water in part of the hydrophilic pores in the electrode active layer. Thus, this part becomes inaccessible for fast gas-phase diffusion of oxygen from air, which leads to increase in gas diffusion resistance and loss of performance.

Figure 4 shows the influence of the amount of PF on ohmic resistance in the MEAs studied. The ohmic resistance of the MEAs was calculated from the slopes of the linear part of the potential vs. current density plots of PEMFCs operating on hydrogen and oxygen. Because the same membrane (Nafion 112) and MEA structure was used in each case, the only variable parameter was the amount of PF used in the preparation of the active layer of the cathodes, which would be the main influence on the ohmic resistance. The results show the same optimal value (33 wt %) of PF at 0.6 V as in Figure 3.

The set of MEAs with HL oxygen cathodes showed similar behavior to that of the LL electrodes (Figures 5-8). The optimal amounts of PF appeared to be 40 wt %. The higher value for HL compared with LL cathodes results from the different characteristics of the carbon-supported platinum catalysts used in each case. The 30 wt % Pt/C catalyst used to fabricate LL oxygen cathodes gave a higher initial active layer porosity because of its smaller particle size compared with the larger particles of 60 wt % Pt/C catalyst used in HL oxygen oxygen cathodes. If we accept that the optimal porosity (from point of view of transport resistance) of the active layer is practically constant, then more pore forming additive (40 wt. %) is required compared with LL electrodes (33 wt. %).

CONCLUSIONS

1. Introduction of PF into the fabrication procedure for the active layer of LL and HL oxygen gas diffusion cathodes, followed by extraction of the additive, results in an increase in the volume porosity of the active layers and in a consequent significant decrease in mass transport resistance.
2. It was found that volume porosity had an optimal value which was different for both types of electrodes investigated. The electrode performance improvement of the optimal porosity value is correlated in a simple manner with the improved mass transport properties of the electrode active layer.
3. A further increase of porosity beyond the optimal value negatively influences electrode performance because of the appearance of discontinuity of the solid phase in the active layer, and an increase in the active layer thickness. These respectively result in increased ohmic resistance and unfavorable gas diffusion. An unfavorable change in the hydrophobic/hydrophilic pore volume ratio also occurs.
4. At optimal PF loadings, the current density at 0.7 V increased from 200 mA/cm^2 to 320 mA/cm^2 on hydrogen-air with LL cathode and from 370 mA/cm^2 to 480 mA/cm^2 with HL cathodes.

REFERENCES

1. T. R. Ralph, G. A. Hards, J. E. Keating, S. A. Campbell, D. P. Wilkinson, M. Davis, J. St-Pierre, and M. C. Johnson, *J. Electrochem. Soc.* **114**, 3845 (1997).

2. A. Fisher, J. Jindra and H. Wendt, *J. Appl. Electrochem.* **28** , 277 (1998).

3. S. Gamburzev, O.A. Velev, S. Srinivasan and A. J. Appleby, Extended Abstracts, 1996 Fall Meeting, San Antonio, PV 96-2, The Electrochemical Society, Inc., Pennington, NJ, Abstr. No 130.

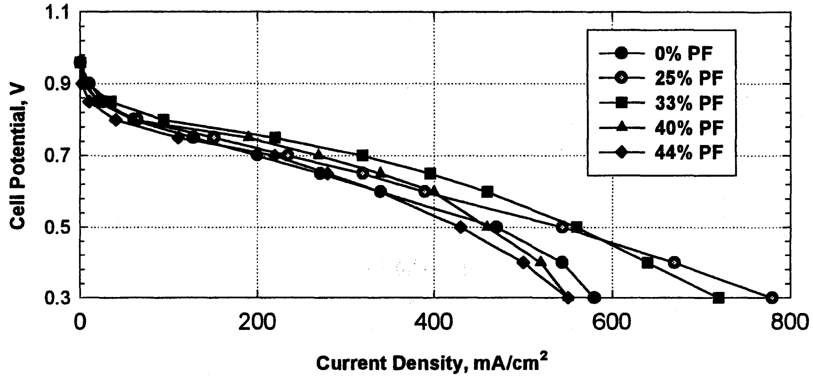

Figure 1. Cell potential vs. current density plots of H_2-air PEMFCs with LL cathodes as a function of amount of pore forming additive in the active layer of air electrode. T = 50°C, P = 1 atma.

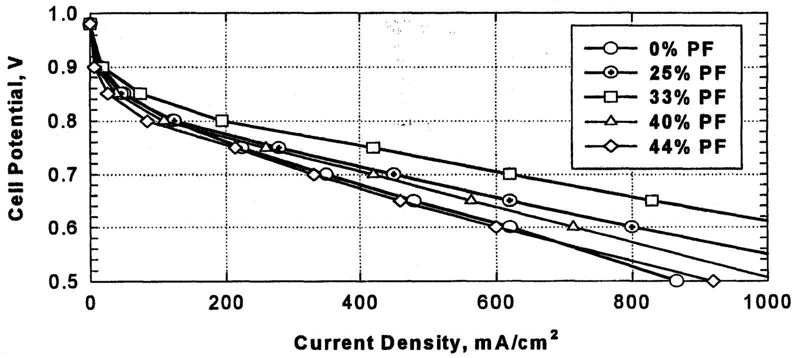

Figure 2. Cell potential vs. current density plots of H_2-O_2 PEMFCs with LL cathodes as a function of amount of pore forming additive in the active layer of air electrode.

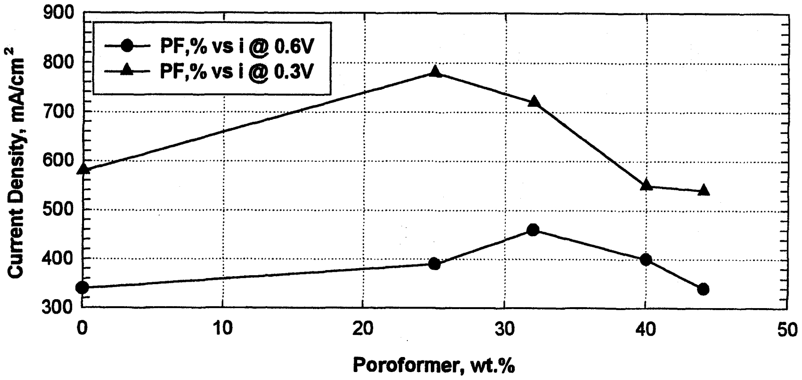

Figure 3. Current density (at E_{cell} = constant) of H_2-air PEMFCs with LL cathodes as a function of amount of pore forming additive in the active layer.

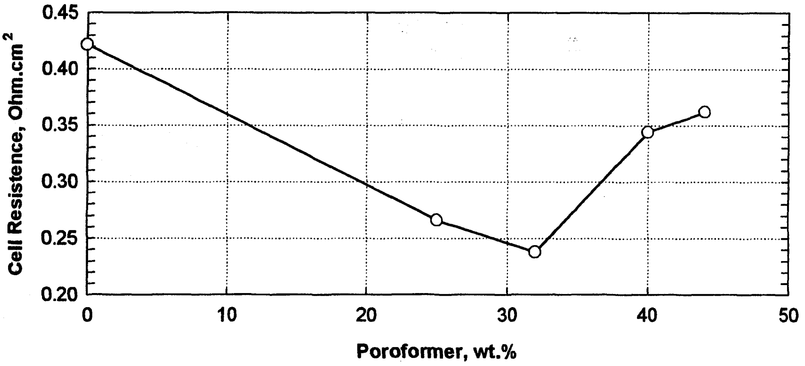

Figure 4. Linear IR resistance of H_2-O_2 PEMFCs with LL cathodes as a function of amount of pore forming additive in the active layer.

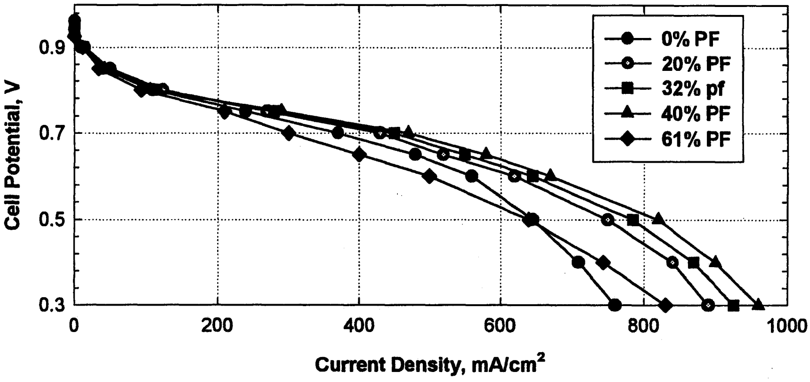

Figure 5. Cell potential vs. current density plots of H_2-air PEMFCs with HL cathodes as a function of amount of pore forming additive in the active layer.

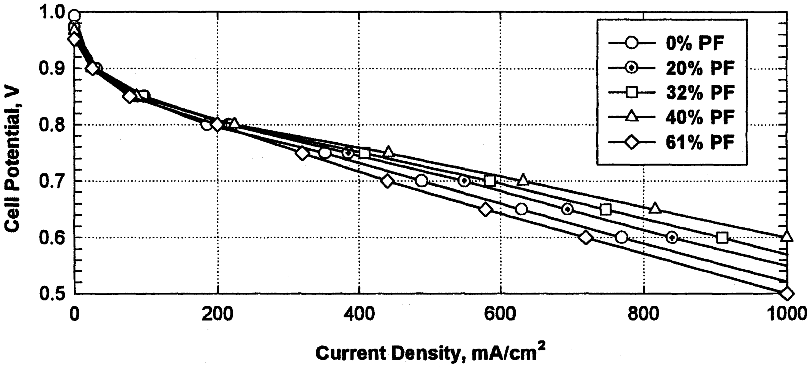

Figure 6. Cell potential vs. current density plots of H_2-O_2 PEMFCs with HL cathodes as a function of amount of pore forming additive in the active layer.

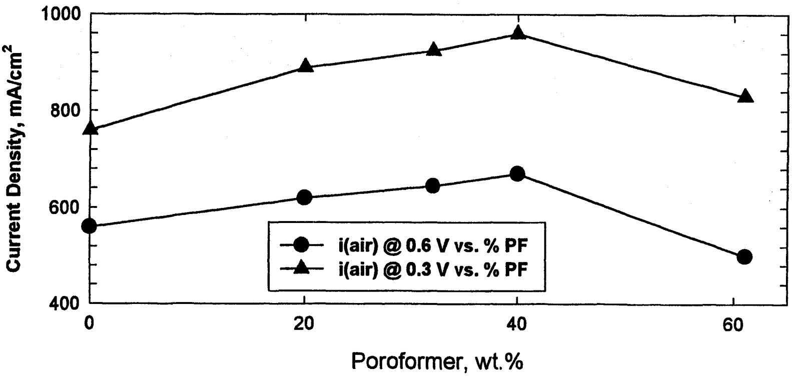

Figure 7. Current density (at E_{cell} = constant) of H_2-air PEMFCs with HL cathodes as a function of amount of pore forming additive in the active layer.

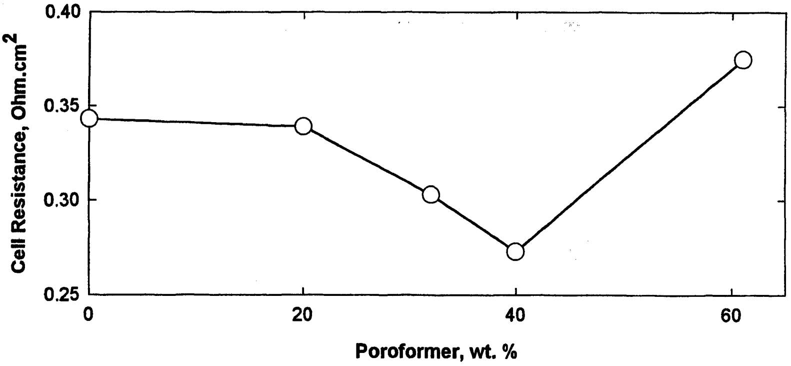

Figure 8. Resistance of H_2-O_2 PEMFCs with HL cathodes as a function of amount of pore forming additive in the active layer.

Proton_Conducting_Membrane_Fuel_Cells_II, PV 1998-27, 30-39 (1998)
DOI: 10.1149/199827.0030PV © The Electrochemical Society

A NEW METHOD TO PREPARE NON-NOBLE METAL BASED CATALYSTS FOR THE REDUCTION OF OXYGEN IN POLYMER ELECTROLYTE FUEL CELLS

G. Faubert, R. Côté, and J.P. Dodelet
INRS-Énergie & Matériaux, 1650 Blvd. Lionel Boulet, C.P. 1020, Varennes, Québec, Canada, J3X 1S2

ABSTRACT

Catalysts for O_2 reduction in PEFCs were prepared from the pyrolysis of Fe acetate adsorbed on perylenetetracarboxylic dianhydride in Ar : H_2 : NH_3 ambient. The amount of adsorbed Fe acetate ranged from 0 to 2.56 wt% Fe nominal. Catalysts are obtained when the pyrolysis temperature is at least 800°C, but 900°C gives the best results. RDE analysis demonstrates that the maximum activity is reached at about 0.2 wt% Fe.

INTRODUCTION

Recently, research on developing electrocatalysts to replace platinum at the cathode of PEFCs has centered on the pyrolysis of (Co, Fe)-N_4 macrocycles (tetraazaannulenes, porphyrins and phthalocyanines) adsorbed on high specific area carbon (1-14). Their use in PEFC single electrode membrane assemblies revealed that the highest activities are obtained for products pyrolyzed at about 600°C, but that pyrolysis temperatures exceeding 800°C are necessary to obtain products exhibiting stable currents in a PEFC (15,16). The reason for this behavior is probably related to changes in the nature of the catalytic site at about 800°C (11,15). There is general agreement that the low temperature active site is of the N_4-Metal type (3), while the nature of the high temperature active site is still controversial.

However, it has been shown that electrocatalysts can also be obtained from precursors other than metal-N_4 macrocycles (17-19). Specifically, catalysts are obtained when the following four ingredients are present in the pyrolysis chamber (20-24):

- A transition metal like Fe, Co or Cr.
- A source of nitrogen which may be: (i) a N-containing solid co-adsorbed with the metal precursor; (ii) N groups on a modified carbon support or (iii) a N-containing gas introduced in the reactor.

- A source of carbon (either carbon resulting from the pyrolysis of the molecular precursors or the conducting carbon used to support the catalytic site).
- A high temperature heat treatment (800°C and above). No catalytic properties are observed for instance for $Fe(OH)_2$ adsorbed on carbon black heat-treated at 600°C in acetonitrile vapour ambient (24).

Up to now, high specific area activated carbons or carbon blacks were always used to support the active site of non-noble metal catalysts for O_2 reduction. One might wonder what kind of catalyst is obtained when the carbonaceous support and the active sites are generated during the same pyrolysis step? To answer this question, various amounts of Fe^{II} acetate adsorbed on perylene tetracarboxylic dianhydride (PTCDA; see Fig.1) were heat-treated at various temperatures in NH_3 ambient. By adsorbing Fe acetate on PTCDA, the precursor of the carbon support, it is hoped to have a better control on the Fe background content of the carbonaceous support and also to have a more homogeneous distribution of active sites.

EXPERIMENTAL

Preparation of pyrolysis precursors

PTCDA was washed overnight with a 1:2 solution of $d.H_2O$ and HCl under magnetic stirring to remove the metallic impurities present in the commercial product. The suspension was filtered, rinsed with $d.H_2O$, and air dried at 75°C. The above steps were repeated twice.

$Fe(CH_3COO)_2$ was added to suspensions of purified PTCDA in $d.H_2O$ in sufficient quantities to yield Fe concentrations of 0, 50, 100, 200, 400, 800, 1600, 3200, 6400, 12 800, and 25 600 ppm (dry weight basis). The mixture of $Fe(CH_3COO)_2$, PTCDA, and $d.H_2O$ was stirred for one hour and then placed in an oven at 75°C to evaporate the $d.H_2O$. The resulting cake composed of $Fe(CH_3COO)_2$ and PTCDA was ground into a fine powder.

Pyrolysis of PTCDA powders

An appropriate amount of the powder was placed in a quartz boat and inserted inside a quartz reactor tube. The tube was purged of air by flowing argon through it for 30 minutes. Next, a 1:2:1 gas mixture of $Ar : NH_3 : H_2$ was introduced into the reactor and the reactor was placed inside a split oven. Hydrogen was added to ensure reducing conditions inside the reactor. The temperature of the oven was increased to 400°C for one hour to ensure complete drying and reaction of the powder with the introduced gas. Next, the powder was pyrolyzed by increasing the temperature to 600, 800, 900, or 1000°C and maintained at that temperature for one hour. The usual pyrolysis temperature utilized was 900°C unless otherwise indicated. At the end of this hour, the reactor was removed from the oven and allowed to cool to room temperature under argon only. The product was then removed from the reactor and ground to a fine powder.

Three samples were also prepared using ambients other than the Ar : NH_3 : H_2 mixture. The other ambients used were the following:

1) A (1:1) Ar : H_2 mixture.
2) A (1:1) mixture of H_2 and Ar/CH_3CN vapor. To generate acetonitrile vapor the argon flow was diverted to a bubbler containing acetonitrile at room temperature before being admitted into the reaction chamber.
3) Ar : CH_3CN vapor. As above, except without hydrogen.

Electrode preparation

The catalysts were evaluated in half and full cells. Measurements in half cells were obtained by the rotating disk electrode technique (RDE). Briefly, 16 mg of finely ground catalyst, 0.400 ml of d.H_2O, and 0.400 ml of a 5 wt% Nafion in alcohol-water solution were ultrasonically blended for 10 minutes. Then 10 µl of this suspension were pipetted onto the vitreous carbon disk of the electrode. The suspension was dried in air at 75°C. RDE measurements were performed at room temperature in a three electrode, one compartment cell containing H_2SO_4 (pH = 0.5) as the electrolyte. The electrolyte was saturated with O_2 prior to the start of an experiment.

Measurements in full cells were obtained with gas diffusion electrodes (GDE) in a fuel cell test station. The catalyst suspension consisted of 17.1 mg of catalyst, 0.240 ml of d.H_2O, and 0.240 ml of 5 wt% Nafion solution blended ultrasonically for one hour. The anode consisted of a 1 cm^2 ELAT electrode catalyzed with 0.37 mg/cm^2 (20 wt%) Pt from Etek. The cathode consisted of a 1 cm^2 uncatalyzed ELAT electrode from Etek. On the active side of the cathode was deposited 4 layers of the catalyst suspension. Each layer was applied by pipetting 60 µl of the catalyst suspension onto the cathode. A hot plate was used to accelerate the drying of the catalyst suspension between each application. The anode received one paint brush applied coating of 5 wt% Nafion solution. Both electrodes were then placed in a vacuum oven at 75°C for one hour. A single cell assembly was prepared by pressing a Nafion 117 membrane between the anode and the cathode under 222 bars of pressure at 140°C for 40 seconds.

RESULTS AND DISCUSSION

Actual Fe content of the catalysts

Table I shows the actual Fe contents of the materials prepared in this study. The first rows of Table I concern the pyrolysis of PTCDA + 1350 ppm Fe (1600 ppm Fe nominal) in $Ar : H_2 : NH_3$ at different pyrolysis temperatures. Rows 5 to 7 of Table I show the effect of utilizing ambients other than NH_3 rich gas on the Fe contents of the products. Pyrolysis at high temperature in $Ar : H_2$ alone is sufficient to remove some organic material yielding a product with a higher Fe content than the precursor. This may be explained by the sublimation of some PTCDA during the heat treatment and also by the loss of the carboxylic moiety of the molecule during polymerization into carbon fibers occurring at temperatures above 520°C (25). Adding CH_3CN to Ar or to $Ar : H_2$ attenuates the loss of organic material. This is a consequence of the decomposition of CH_3CN at high temperature and the subsequent deposition of its decomposition products onto the PTCDA during pyrolysis. A similar behavior was observed in a previous study for the pyrolysis of CH_3CN over iron particles supported on carbon black (24).

Adding NH_3 increases the loss of organic material during pyrolysis. It is known that ammonia acts as an etching agent in the treatment of activated carbon. Ammonia treatment not only incorporates nitrogen into carbon but also profoundly modifies the microstructure of the activated carbon treated. This effect is moderate at 600°C and increases with increasing heat treatment temperature (26). The adsorption of Fe salt on PTCDA helps to retain organic matter, as indicated by the larger increase in Fe content after pyrolysis for lower Fe content materials (compare, for instance, 50 or 100 with 25600 ppm). In the remainder of the text, samples will be identified according to their actual Fe contents.

Electrochemical results

Figure 2 presents the cyclic voltammograms for 47±12 and 1030 ppm Fe. The disk electrode is not rotated during the first scan giving only one peak for O_2 reduction in O_2 saturated H_2SO_4. The second scan is recorded at 1500 rpm. It shows an improvement of the reduction current due to an increase of the O_2 available at the electrode in rotation. It is possible to estimate the relative catalytic effect of materials by the voltage at which the maximum reduction current occurs at 0 rpm. Values closest to the theoretical reversible potential of 0.985 V vs SCE for the reduction of O_2 at room temperature indicate superior catalytic activity. The peak value is at 125 mV for 47 ppm Fe and 405 mV for 1030 ppm Fe. Voltages for maximum reduction current are reported in Table II for all samples presented in Table I. Catalytic activities < 0 mV vs SCE are characteristic of very poor catalysts.

These catalysts' voltammograms show little difference between scans at 0 rpm and at 1500 rpm.

From Table II one may conclude that catalysts for O_2 reduction are obtained for pyrolysis at 800°C and above in Ar : H_2 : NH_3 ambient. Very poor catalytic activity is observed when NH_3 is absent from the gas mixture. This is expected since it has already been demonstrated that a source of nitrogen is necessary during the pyrolysis step to obtain catalytic activity (21). Table II indicates that catalytic activity saturates at around 2000 ppm Fe, which corresponds to 0.2 wt% Fe. Below that content, the catalytic activity decreases rapidly with decreasing Fe content. Similar results (a saturation of the catalytic activity at about 0.2 wt% Fe) were obtained when Fe acetate was adsorbed on nitrogen modified carbon black (23). This saturation effect of the Fe content on activity is interpreted as being a change in the role played by Fe: below saturation, Fe is available in its oxidized state for the generation of the active site, while for Fe contents beyond 0.2 wt%, the iron is chemically reduced and aggregates.

Figure 3 presents the GDE polarization curve of the most active catalyst prepared in this study in comparison to the polarization curve of a commercially produced catalyst containing 2 wt% Pt under the same test conditions. The figure reveals that the PTCDA derived product is more active in the kinetically controlled part of the polarization curve (> 0.8 V), whereas the platinum based catalyst performs better at higher current densities. Both catalysts demonstrated stable behavior in a fuel cell cathode environment at 50°C and at 0.5 V vs RHE over a 24 hour test period. In these stability experiments, current densities of 0.24 A/cm^2 and 0.30 A/cm^2 were measured for the 0.2 wt% Fe-based catalyst and for the 2 wt% Pt catalyst, respectively. Although the Fe content is only 0.2 wt%, the current density obtained with that catalyst is among the highest measured for Fe-based catalysts prepared in our laboratory.

CONCLUSIONS

1. It is possible to obtain catalysts for the reduction of oxygen in PEFCs by pyrolyzing at at least 800°C iron acetate adsorbed on PTCDA in Ar : H_2 : NH_3 ambient. The preferred pyrolysis temperature is, however, 900°C.
2. RDE experiments demonstrate that the catalytic activity increases rapidly with the Fe content and that a maximum in catalytic activity is obtained at about 0.2 wt% Fe. Beyond that value the catalytic activity remains constant even if the Fe content is increased by one order of magnitude.
3. GDE testing of the catalyst containing 0.2 wt% Fe gives a polarization curve similar to the one obtained in the same experimental conditions with 2 wt% Pt. Stable currents of the order of 0.25 A/cm^2 have been obtained at 50°C and 0.5 V vs RHE.

Table I.
Determination[a] of the actual Fe contents of Fe acetate adsorbed on PTCDA before and after pyrolysis. Accuracy ± 5% unless otherwise noted.

Powder & Conditions	Parameters	Actual Fe content before pyrolysis (ppm)	Actual Fe content after pyrolysis (ppm)
PTCDA + 1600 ppm Fe^{II} acetate + $Ar : H_2 : NH_3$	600°C	1350	3480
	800°C	1350	4320
	900°C	1350	4660
	1000°C	1350	4600
PTCDA + 1600 ppm Fe^{II} acetate + 1000°C	$Ar : H_2$	1350	3840
	$Ar : CH_3CN$	1350	2610
	$Ar : H_2 : CH_3CN$	1350	3510
PTCDA + Fe^{II} acetate + $Ar : H_2 : NH_3$ + 900°C	0 ppm Fe	< 35	47 ± 12
	50 ppm Fe	38 ± 12	300
	100 ppm Fe	107 ± 12	790
	200 ppm Fe	210	1030
	400 ppm Fe	370	2030
	800 ppm Fe	740	2530
	1600 ppm Fe	1350	4660
	3200 ppm Fe	2950	8100
	6400 ppm Fe	5500	14 660
	12 800 ppm Fe	11 060	25 160
	25 600 ppm Fe	20 390	55 640

a : determined by neutron activation analysis at the University of Montreal.

Table II.
RDE analysis of catalysts obtained by the pyrolysis of Fe acetate adsorbed on PTCDA.

Powder & Conditions	Parameters	O_2 reduction maximum (mV vs SCE)
PTCDA + 1600 ppm Fe^{II} acetate + Ar : H_2 : NH_3	600°C	< 0
	800°C	400
	900°C	400
	1000°C	350
PTCDA + 1600 ppm Fe^{II} acetate + 1000°C	Ar : H_2	< 0
	Ar : CH_3CN	< 0
	Ar : H_2 : CH_3CN	< 0
PTCDA + Fe^{II} acetate + Ar : H_2 : NH_3 + 900°C	47 ± 12 ppm Fe	125
	300 ppm Fe	275
	790 ppm Fe	360
	1030 ppm Fe	405
	2030 ppm Fe	450
	2530 ppm Fe	375
	4660 ppm Fe	400
	8100 ppm Fe	375
	14 660 ppm Fe	375
	25 160 ppm Fe	375
	55 640 ppm Fe	400

REFERENCES

1. K. Wiesener, *Electrochim. Acta* **31**, 1073 (1986).
2. D. Scherson, A. A. Tanaka, S. L. Gupta, D. Tryk, C. Fierro, R. Holze, E. B. Yeager, and R. P. Latimer, *Electrochim. Acta* **31**,1247 (1986).
3. J. A. R. van Veen, H. A. Colijn, and J. F. van Baar, *Electrochim. Acta* **33**, 801 (1988).
4. M. R. Tarasevich and K. A. Radyushkina, *Materials Chemistry and Physics* **22**, 477 (1989).
5. K. Wiesener, D. Ohms, V. Neumann and R. Franke, *Materials Chemistry and Physics* **22**, 457 (1989).
6. T. Sawaguchi, T. Itabashi, T. Matsue and I. Uchida, *J. Electroanal. Chem.* **279**, 219 (1990).
7. A. Tanaka, S. L. Gupta, D. Tryk, C. Fierro, E. B. Yeager and D. A. Scherson, in *Structural Effects in Electrocatalysis and Oxygen Electrochemistry* (Edited by D. Scherson, D. Tryk, M. Daroux and X. Xing), The Electrochemical Society Proceedings, Vol. **92-11**, 555 (1992).
8. A. Widelöv, *Electrochimica Acta* **38**, 2493 (1993).
9. M. R. Tarasevich, G. V. Zhutaeva and K. A. Radyushkina, *Russ. J. Electrochem.* (Trans. of Electrokhimiya) **31**, 1064 (1995).
10. A. Biloul, P. Gouérec, M. Savy, G. Scarbeck, S. Besse and J. Riga, *J. Appl. Electrochem.* **26**, 1139 (1996).
11. P. Gouérec, A. Biloul, O. Contamin, G. Scharbeck, M. Savy, J. Riga, L. T. Weng and P. Bertrand, *J. Electroanal. Chem.* **422**, 61 (1997).
12. P. Gouérec, M. Savy and J. Riga, *Electrochim. Acta* **43**, 743 (1998).
13. T. Okada, M. Gokita, M. Yuasa and I Sekine, *J. Electrochem. Soc.* **145**, 815 (1998).
14. E. Claude, T. Addou, J. M. Latour and P. Aldebert, *J. Appl. Electrochem.* **28**, 57 (1998).
15. G. Faubert, G. Lalande, R. Côté, D. Guay, J. P. Dodelet, L. T. Weng, P. Bertrand and G. Dénès, *Electrochim. Acta* **41**, 1689 (1996).
16. G. Lalande, G. Faubert, R. Côté, D. Guay, J. P. Dodelet, L. T. Weng and P. Bertrand, *J. Power Sources* **61**, 227 (1996).
17. S. Gupta, D. Tryk, I. Bae, W. Aldred and E. Yeager, *J. Appl. Electrochem.* **19**, 19 (1989).
18. D. Ohms, S. Herzog, R. Franke, V. Neumann, K. Wiesener, S. Gamburcev, A. Kaisheva and I. Iliev, *J. Power Sources* **38**, 327 (1992).
19. M. C. Martin Alves and G. Tourillon, *J. Phys. Chem.* **100**, 7566 (1996).
20. R. Côté, G. Lalande, D. Guay, J. P. Dodelet and G. Dénès, *J. Electrochem. Soc.* in press.

21. G. Lalande, R. Côté, D. Guay, J. P. Dodelet, L. T. Weng and P. Bertrand *Electrochim. Acta* **42**, 1379 (1997).
22. R. Côté, G. Lalande, G. Faubert, D. Guay, J. P. Dodelet and G. Dénès, *J. New Materials for Electrochemical Systems* **1**, 7 (1998).
23. H. Wang, R. Côté, G. Faubert, D. Guay and J. P. Dodelet, *J. Phys. Chem.*, submitted.
24. G. Faubert, R. Côté, D. Guay, J. P. Dodelet, G. Dénès, C. Poleunis and P. Bertrand, *Electrochim. Acta* **43**, 1969 (1998).
25. M. Murakami, S. Iijima and S. Yoshimura, *J. Appl. Phys.* **60**, 3856 (1986).
26. F. Atamny, J. Blöcker, A. Dübotzky, H. Kurt, O. Timpe, G. Loose, W. Mahdi and R. Schlögl, *Molecular Physics* **76**, 851 (1992).

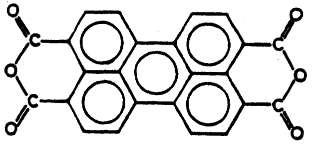

Figure 1. Structure of 3,4,9,10-perylenetetracarboxylic dianhydride (PTCDA).

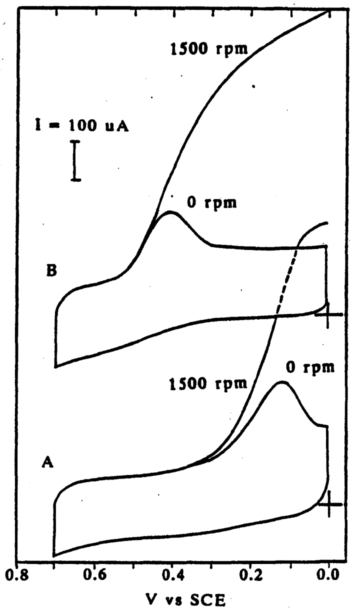

Figure 2. RDE voltammograms (10 mV/s) recorded between 0 and 0.7 V vs SCE for two catalysts at 0 and 1500 rpm. Catalyst A: pyrolyzed PTCDA + 47±12 ppm Fe; catalyst B: pyrolyzed PTCDA + 1030 ppm Fe.

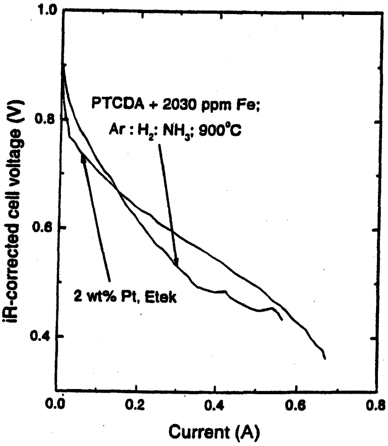

Figure 3. Polarization curves obtained at 50°C in a H_2/O_2 fuel cell using a single cell assembly. $PO_2 = 4.14$ bars @ 402 cm^3/min, $PH_2 = 2.07$ bars @ 127 cm^3/min. Humidifier temperature for both gases = 75°C. Resistances were measured by AC impedance.

Proton_Conducting_Membrane_Fuel_Cells_II, PV 1998-27, 40-51 (1998)
DOI: 10.1149/199827.0040PV © The Electrochemical Society

ANALYTICAL MODEL FOR PEM FUEL CELLS INCLUDING WATER TRANSPORT AND IMPLICATIONS FOR IMPROVING THE MEA STRUCTURE

C. C. Boyer*, S. Gamburzev, R.G. Anthony*, and A. J. Appleby

Center for Electrochemical Systems and Hydrogen Research,
TEES, Texas A&M University, College Station, TX. 77843-3402
**Department of Chemical Engineering*
Texas A&M University, College Station, TX. 77843-3122

ABSTRACT

This paper presents a method for calculating the relative effectiveness of each mass transfer processes in the PEM fuel cell electrode. Such a method is useful for improving the existing design of an MEA and for determining the feasibility of a new electrode material or design. The method was applied to MEAs fabricated in our laboratory and found ionic conductivity in the membrane and electrode dominating the transport losses in the cell. Since conductivity is a function of the water content in the electrolyte, MEA structures fabricated in our laboratory with substrate layers designed to increase the water content in the electrolyte showed significant improvement. These new MEA structures not only improved performance while operating humidified, but also while operating with a dry gas feed.

1. INTRODUCTION

Research on polymer electrolyte fuel cell electrodes is moving from the proof-of-concept stage into commercialization. Research efforts have begun to engineer and optimize the polymer electrolyte membrane (PEM) fuel cell electrode and system. This paper presents a method for calculating the relative effectiveness of each mass transfer processes in the electrode. Such a method is useful for determining the feasibility of a new material and for identifying what needs to be improving in existing designs.

The power plant for light weight transportation applications requires a low-cost, low-maintenance fuel cell system. This requires the membrane and electrode assembly (MEA) to contain only small amounts of platinum and the fuel cell to operate with a relatively simple gas humidification system. MEAs designed to meet these goals were analyzed using the relative effective current method and ionic conductivity dominated the transport losses in the cell. The ionic conductivity can be increased by increasing the water content of the electrolyte. Previous attempts to achieve this goal include water injection techniques (1) and insertion of catalyst into the membrane (2). As a much simpler solution, MEAs with new substrate structures were designed to increase the water content in the electrolyte and they showed significant improvement while operating on humidified and dry gas at atmospheric pressure and 50°C.

2. RELATIVE EFFECTIVE CURRENT OF EACH MASS TRANSFER PROCESS

The components of the fuel cell are multiphase structures such that increasing the transport facility in one phase usually decreases the transport ability of the other phases. For maximum power, it is desirable to design an electrode such that all the transport and kinetic processes in the cell are balanced, i.e. no single process is much more rate limiting than the others. The effective resistance of each process is a non-linear function of current and potential; therefore, one must define an operating point at which the balancing will take place. In this analysis, the fraction of the intrinsic kinetic current that is limited by a mass transfer process defines the operating point used as a basis. This fraction is called the effectiveness factor, Z, and is defined as the true current resulting from limitations by mass transfer, i_m, divided by the intrinsic kinetic current, i_k. It is a function of the dimensionless rate modulus, ϕ, which is defined as the intrinsic kinetic rate divided by the inherent mass transfer rate, α. The square root of the rate modulus as defined here is commonly known as the Theile modulus in heterogeneous catalysis.

$$i_m = i_k Z(\phi) \quad \text{where} \quad \phi = \frac{i_k}{\alpha} = \frac{\text{intrinsic kinetic rate}}{\text{inherent mass transfer rate}} \qquad [1]$$

The electrode needs to be designed such that at a desired operating current, all the mass transfer processes are contributing with equal effectiveness. Conversely, it needs to be designed such that at a tolerable effectiveness factor, each mass transfer process has about the same relative rate. The effectiveness factor used in the evaluation will depend on the loss of kinetic utilization that can be afforded as determined by the designer.

2.1 Intrinsic Kinetic Rate

The amount and activity of the catalyst determines the intrinsic kinetic current. In acid polymer electrolyte fuel cells, the cathode reaction is rate limiting and almost completely determines the kinetic rate. Therefore, the derivations shown here are for the cathode; a similar analysis can be performed on the anode. The Tafel equation with a constant transfer coefficient is sufficient to model the kinetic rate as a function of potential within the operating range of the fuel cell (0.8 to 0.5 volts). The intrinsic kinetic current flux of the electrode, i_k, is a function of the potential, V, the oxygen partial pressure, $x_{O2} P$, the activity of the catalyst surface, k, the active platinum surface area per unit volume, a_V, and the depth of the active region, L.

$$i_k = x_{O_2} P a_V k L \exp\left[\frac{-V}{b}\right] \qquad [2]$$

2.2 Effectiveness Factors for the Mass Transfer Processes

The effectiveness factor of a mass transport process comes from the analytical solution of the volume averaged material balance which considers only kinetics and that mass transport process. The effectiveness factor functions for each mass transfer process have been derived and are summarized in Table I and plotted in Figure 1.

Table I. Summary of effectiveness factors for transport processes

Transport mechanism	Mass transport inherent rate	Effectiveness factor, Z
1) gas diffusion in active region (gas diffusion in agglomerates)	$\alpha_{O_2,act} = \dfrac{4FcD_{O_2}^{act}}{L}$	$Z_{O_2,act} = \dfrac{\tanh\left[\sqrt{\phi}\right]}{\sqrt{\phi}}$
2) proton (electron) migration in active region	$\alpha_{H^+act} = \dfrac{L}{\kappa_{H^+}^{act} b}$	$Z_{O_2,act} = \dfrac{\sin[\varpi]}{\sqrt{\phi/2}}$, $\varpi = \sqrt{\dfrac{\phi}{2}} \cos[\varpi]$
3) gas diffusion through substrate	$\alpha_{O_2,sub} = \dfrac{4FcD_{O_2}^{sub}}{L}$	$Z_{O_2,sub} = \dfrac{1}{1+\phi}$
4) proton migration in membrane (electron in current collector)	$\alpha_{H^+,mem} = \dfrac{R^{mem}}{b}$	$Z_{H^+} = \exp\left[-Z_{H^+}\phi\right]$
5) gas convection in the flow field	$\alpha_{O_2,flow} = \dfrac{x_0 4FQ}{A}$	$Z_{chan} = \dfrac{1-\exp(-\phi)}{\phi}$

The rate modulus, ϕ, will have a certain value at a chosen mass transport effectiveness, Z_r. Since $\phi = i_k/\alpha$, the relative effective current, i_r, can be defined in terms of the transport parameter, α, and the chosen mass transport effectiveness Z_r.

$$i_r = \alpha \frac{\phi(Z_r)}{Z_r} \qquad [3]$$

For example, the relative effective currents at $Z_r = ½$, called here the half-effective currents, are shown in Table II.

2.3 Analysis of MEA Design

The mass transport rates in a typical PEM fuel cell electrode were compared using the relative effective current analysis. Table II also displays estimated values of the half effective currents in a typical PEM fuel cell MEA with low-cost components including a total platinum loading of 0.25 mg/cm^2 and Nafion 112 membrane and operating with air at atmospheric pressure and 50°C. Values for the parameters were estimated from experimental data collected in our laboratory and a number of parameter estimation techniques available in the literature (3-5).

TableII. Half effective currents for mass transfer processes

Transport mechanism	Half effective current	Approximation of $i_{1/2}$ for PEMFCs with low catalyst cathodes
reactant gas in active region	$i_{1/2} = 1.84 \frac{x4FcD_{O_2}^{eff}}{L}$	$1.2 \frac{\mathrm{A}}{\mathrm{cm}^2}$
reactant gas in agglomerates	$i_{1/2} = 1.84 a_b L \frac{4Fc_{O_2} D_{O_2}^{eff}}{\delta}$	$14.4 \frac{\mathrm{A}}{\mathrm{cm}^2}$
reactant gas through substrate	$i_{1/2} = 0.5 \frac{x4FcD}{L}$	$1.9 \frac{\mathrm{A}}{\mathrm{cm}^2}$
proton in active region	$i_{1/2} = 2.5 \frac{b\kappa_{H^+}^{eff}}{L}$	$0.84 \frac{\mathrm{A}}{\mathrm{cm}^2}$
proton in membrane	$i_{1/2} = 0.693 \frac{b\kappa}{L} = 0.693 \frac{b}{R}$	$0.28 \frac{\mathrm{A}}{\mathrm{cm}^2}$

According to this study, proton transport in the membrane and proton transport in the active region had lower half-effective currents than the other processes. Therefore, the MEA performance could be improved by increasing the proton conductivity even at the expense of electron conductivity or some oxygen diffusion in the substrate. The effective proton current could be increased in the membrane by reducing the membrane thickness, in the active region by increasing the polymer volume fraction, or in both layers by increasing the water content in the polymer electrolyte. Reducing the membrane thickness is limited by mechanical stability and gas crossover. An increase of the polymer volume fraction in the active layer will significantly decrease the oxygen diffusivity. Thus, our efforts focused on increasing the water content in the electrolyte by changing the substrate design. The polymer will contain a certain number of water molecules per sulfonic group when equilibrated with fully humidified gas (about 14 in Nafion® membranes with equivalent weight of 1100) (6). The water content almost doubles when equilibrated with liquid water which results in twice the conductivity.

3. WATER TRANSPORT IN THE CELL

The PEM fuel cell requires a careful balance of water content. High ionic conductivity demands the presence of liquid water on the interface of the polymer electrolyte. However, excess water in the porous electrode will block the gas pores and lower the oxygen diffusion from the gas flow fields to the electrode catalyst layer. The ideal electrode will be designed to maintain a high concentration of water in the electrolyte while keeping the gas diffusion layer clear of water.

Traditionally, a hydrophobic agent, Teflon®, has been impregnated into the substrate layer to keep liquid water out. However, the water transport mechanism is not understood and remains one of the challenges to reliable fuel cell stack systems. PEM conductivity is kept high in laboratory evaluations by super-saturating the reactant gas. The parasitic energy required to super-saturate the gas is undesirable and super-saturation creates a problem with two-phase flow in the gas distributors of larger electrode areas and stacks. The efficiency of the fuel cell system can be improved if the reactant gas does not need to be super-saturated. By understanding the water transport mechanisms through the substrate, one should be able to improve the substrate structure so that oxygen diffusion and electrolyte hydration can be balanced at a maximum.

Water flux occurs in the vapor, polymer, and liquid phases. A concentration gradient and interaction with the reactant gas flux drives water transport in the gas phase. A concentration gradient and a drag exerted by the moving protons drives water transport in the polymer phase. Water in the liquid phase may be driven out of the cell by capillary pressure or by a dynamic process of evaporation and condensation that occurs while the interface is at equilibrium, or by a convective turbulence that reaches into the depths of the layer from the gas stream in the channels. From experiment, it has been determined that water is primarily transported in the vapor phase. The effective water vapor diffusivity of the substrate layer most likely includes thermal and capillary pressure effects, because it was found to be higher than an expected gas phase diffusivity estimated from the bulk phase water diffusivity multiplied by the porosity and divided by the tortuosity.

A qualitative model for water transport can be put together based on volume averaged material balances and empiricism. Figure 2 shows a physical picture of the water transport model. The most simplistic method to describe the water concentration in the multiphase porous media uses a single, dimensionless, volume averaged variable called the relative saturation, S. At $S = 0$, the cell is completely dry. At $S = 1$, the pores are flooded which means there is enough water present to block the major gas pathways. In the membrane, the relative water saturation is a function of the water content and relative liquid pressure. In the membrane, the relative saturation is not restricted to a maximum of unity because a liquid pressure gradient across the membrane can increase its value.

For each layer except the cathode, the transport equation for water is:

$$N_w = -D_w \nabla S + \xi\, i/2F \qquad [4]$$

and at each boundary between layers “a” and “b”, $S_a = S_b$. D_w is the effective water diffusivity and ξ is the interaction drag between water and a moving species in the layer. Since water is produced in the cathode, the material balance for this layer will include the divergence term:

$$D_w \nabla^2 S + \frac{j}{2F} = 0 \qquad [5]$$

where j is the local reaction current per volume. The drag term is neglected in the active layer for simplicity and because oxygen drags water toward the membrane in the gas phase and protons drag water away from the membrane in the electrolyte phase; any discrepancy will most likely be internally balanced by inter-phase transport. The overall water balance in the cell from anode to cathode is:

$$N_{\mathrm{cathode}} - N_{\mathrm{anode}} = i/2F. \qquad [6]$$

In this study, the model was used to determine how changes in the diffusivity of water in the substrate would affect the water content in the membrane and electrode. As discussed earlier in the paper, the relative limiting current analysis determined that the cell performance could be improved by increasing the water content in the membrane and electrode. Once the desired diffusivity change was identified, mechanistic models of the water transport helped identify new substrate designs that might accomplish the goal. The results of one of these new substrate designs is presented in the following section.

4. MEAS WITH IMPROVED WATER SATURATION IN THE ELECTROLYTE

The substrate layer was altered to increase the liquid hold up in the electrode and membrane. The MEAs were fabricated as presented previously in the literature (7,8) with Nafion® 112 membranes and a total platinum loading of 0.25 mg/cm^2 for the low platinum content MEAs and 1.30 mg/cm^2 for the high platinum content MEAs. The old type of substrate consisted of a 15 wt% Teflon and Shawnagan Black mixture painted onto a carbon cloth. The new type of substrate used a composite of different polymer/carbon mixtures painted onto a carbon cloth.

The performance of cells with the new substrate design were compared with the standard MEA design at a cell temperature of 50°C, under atmospheric pressure, and using a humidified gas feed. The decrease in the slope of the linear region of the oxygen curve shows that the ionic resistance decreased in the cells with the new substrate in 5 cm^2 tests as seen in Figure 3. The air curve indicates a slight decrease in the oxygen diffusivity, but overall performance is still improved with the new substrate layer. A second test with 50 cm^2 electrodes operating at an oxygen stoichiometry of 2.5 reconfirmed these results as shown in Figure 4.

Performance of MEAs with high platinum loading (1.25 mg/cm^2) did not improve in the 5 cm^2 tests as shown in Figure 5, but did show significant improvement in the 50 cm^2 tests as shown in Figure 6. Both 5 cm^2 and 50 cm^2 tests with high platinum content MEAs show a slight increase in the kinetic rate from the cells with the new substrate layer. This may reflect an increase in the ionic conductivity in the substrate side of the active region which increases the utilization of the catalyst. This effect was predicted by the water transport model. The 5cm^2 test with air does show the onset of oxygen diffusion limitations due to the new substrate layer.

MEAs with thin active layers are more susceptible to the lower water saturation level in the electrolyte because the narrow transition between the "dry" (water vapor) gas diffusion layer and the "wet" (liquid water) electrolyte layer provides a steep water concentration gradient for a fast water flux. As a result, MEAs with thin active layers (low platinum loading) typically exhibit a higher ionic resistance than MEAs with thick active layers. The thicker active region will have a smaller water concentration gradient between the electrolyte membrane and the substrate for slower mass transfer which means a larger build up of the water concentration in the electrolyte. MEAs with thicker active layers can even operate reasonably well when fed dry gas (8).

A 50 cm^2 MEA with the redesigned substrate layer was tested while fed completely dry gas at 50°C and atmospheric pressure. Typical MEA's fabricated in our laboratory show significant performance loss while operating on dry air. There is almost no performance difference when the low loaded and high loaded MEAs with the new substrate layer were operated with dry air as shown in Figure 7 and Figure 8.

5. CONCLUSIONS

A relative effective current analysis can indicate how to better balance the transport losses in the PEM fuel cell for better overall performance. Such an analysis would be useful for optimizing any multiphase electrochemical system. The analysis presented here showed that ionic conductivity in the membrane and active layer were the most rate limited processes in the current MEA design.

PEM cells are very sensitive to water content and understanding the water flux and saturation properties is essential to designing better MEAs and operating procedures. The substrate is a key part to balancing the water content in the MEA. The experiments presented here show that a new substrate layer which increases the water holdup in the electrode and membrane can increase cell performance while operating with humidified air and operate with almost no loss of performance when fed dry air.

NOTATION

a_V	area of catalyst per volume of reaction region (cm^2/cm^3)
A	electrode area (cm^2)
b	effective Tafel slope (mV)
c	molar concentration (mol/cm^3)
D	effective diffusivity (cm^2/s) or for water model (mol/cm^2-s)
F	Faraday's constant (C/equiv)
i	electrode current flux or current density (A/cm^2)
j	current flux produced in a volume of the reaction region (A/cm^3)
k	electrokinetic rate constant (A/cm^2-s-atm)
L	depth of a layer (cm)
N	molar flux (mol/cm^2-s)
P	pressure (atm)
Q	molar gas flow (mol/s)
R	resistance (Ω-cm2)
S	water saturation
V	electric potential (V)
Z	effectiveness factor
α	mass transfer intrinsic rate (A/cm^2)
δ	agglomerate effective thickness (cm)
ϕ	rate modulus
κ	effective conductivity (S/cm)
ξ	interaction drag coefficient

REFERENCES

1. T.V. Ngugen, and R. White, *J. Electrochemical Soc.*, **140**, 2178, (1993).
2. M. Watanabe, H. Uchida, and M. Emori, *J. Phys. Chem.*, **102**, 3129, (1998).
3. A. Parthasarathy, B. Dave, S. Srinivasan, A. J. Appleby, and C.R. Martin, *J. Electrochemical Soc,*, **139**, 1635, (1992).
4. N. Sugumaran and A.K. Shukla, *J. Power Sources*, **39**, 249, (1992).
5. T.E. Springer, M.S. Wilson, and S. Gottesfeld, *J. Electrochemical Soc.*, **140**, 3513, (1993).
6. J.T. Hinatsu, M. Mizuhata, and H. Takenaka, *J. Electrochemical Soc.*, **141**, 1493, (1994).
7. M.S. Wilson, J.A. Valerio, S. Gottesfeld, *Electrochim. Acta*, **40**, 355, (1995).
8. S. Gamburzev, O.A. Velev, S. Srinivasan, and A.J. Appleby, *The Electrochemical Society Meeting Abstracts*, Vol.96-2, The Electrochemical Society, Inc., Pennington, N.J., 1996, Abs. No. 100.

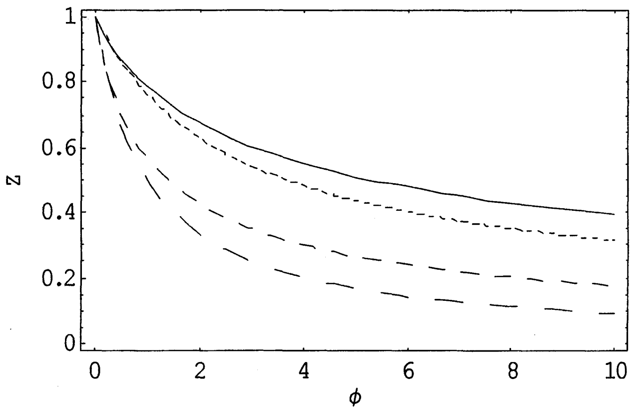

Figure 1. Effectiveness factors as a function of the rate modulus for transport processes in the MEA. Solid line - proton transport in active region; Short dash - oxygen transport in active region; Medium dash - proton transport in membrane; Long dash - oxygen transport in substrate.

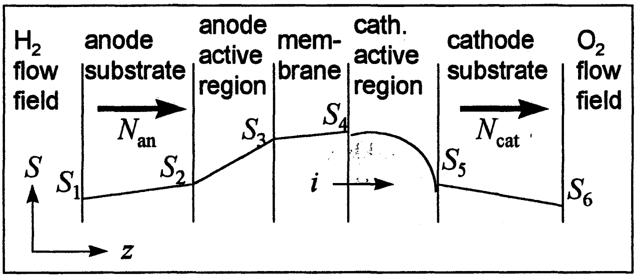

Figure 2. Physical Picture of the water transport model. Layers are not scaled to thickness.

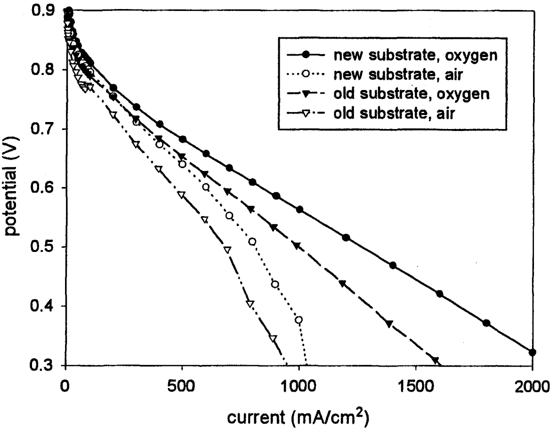

Figure 3. 5 cm^2 tests of low platinum content MEAs comparing the new substrate layer with the existing substrate layer. Gas flow was humidified and high stoichiometry.

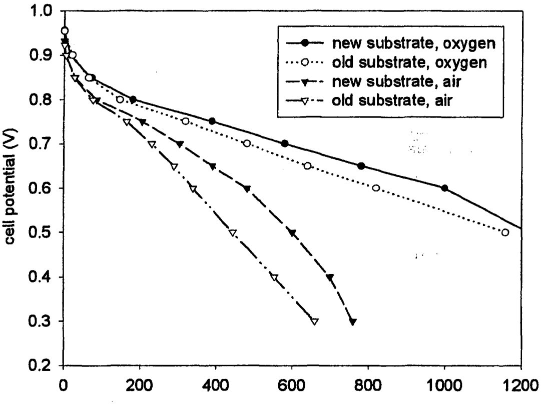

Figure 4. 50 cm^2 tests of low platinum content MEAs comparing the new substrate layer with the existing substrate layer. Gas flow was humidified and $1.1H_2/2.5O_2$ stoichiometry.

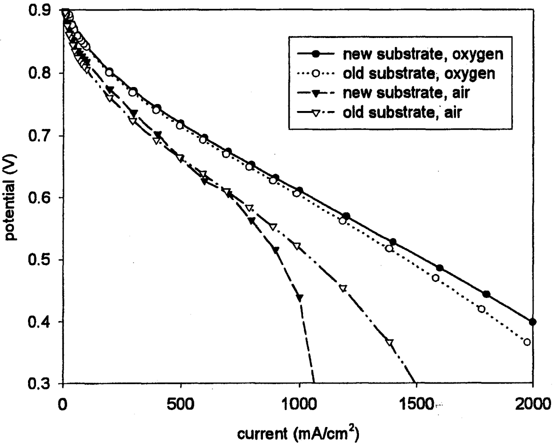

Figure 5. 5 cm^2 tests of high platinum content MEAs comparing the new substrate layer with the existing substrate layer. Gas flow was humidified and high stoichiometry.

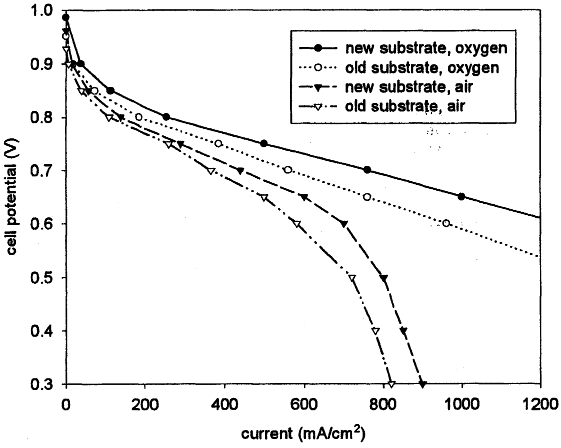

Figure 6. 50 cm^2 tests of high platinum content MEAs comparing the new substrate layer with the existing substrate layer. Gas flow was humidified and $1.1H_2/2.5O_2$ stoichiometry.

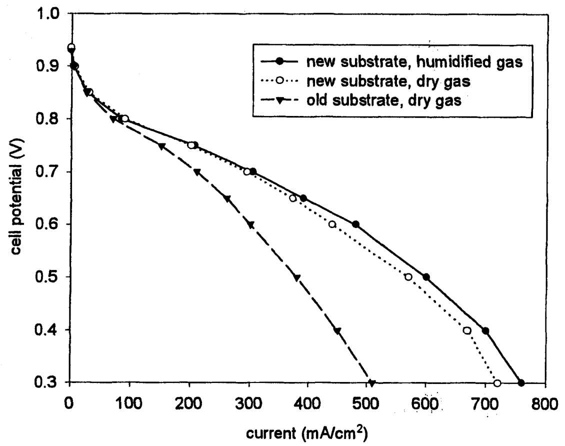

Figure 7. 50 cm² tests with low loaded electrodes showing air curves for old substrate and new substrate operating on dry gas compared to new substrate operating on humidified gas. Gas flow stoichiometry was 1.1H₂/2.5O₂.

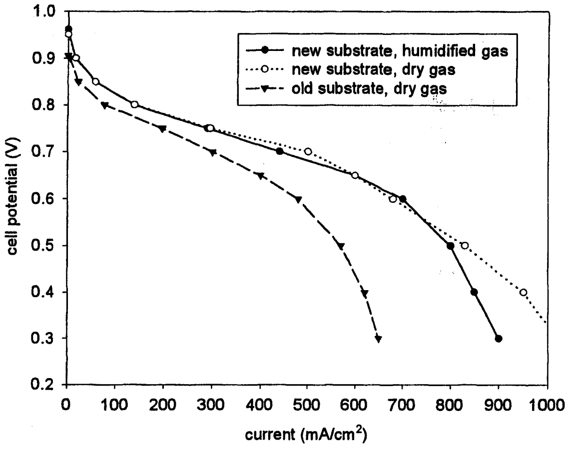

Figure 8. 50 cm² tests with high loaded electrodes showing air curves for old substrate and new substrate operating on dry gas compared to new substrate operating on humidified gas. Gas flow stoichiometry was 1.1H₂/2.5O₂.

Proton_Conducting_Membrane_Fuel_Cells_II, PV 1998-27, 52-65 (1998)
DOI: 10.1149/199827.0052PV © The Electrochemical Society

RECENT PROGRESS IN THE DEVELOPMENT OF THE RADIATION-GRAFTED PSI MEMBRANE

H.P. Brack, F. N. Büchi, J. Huslage, and G. G. Scherer
Paul Scherrer Institut
General Energy Research, Electrochemistry
CH-5232 Villigen, Switzerland

ABSTRACT

Radiation grafting can be used to combine the proton-conducting properties of a partially *para*-sulfonated polystyrene graft component with the thermal and chemical stability of fluoropolymer base films together in membranes suitable for application in Polymer Electrolyte Fuel Cells (PEFC) and other electrochemical devices. Earlier the performance and lifetime of our radiation-grafted membranes were greatly improved after the introduction of our double crosslinking membrane preparation concept and our optimization of the content of the comonomers, divinylbenzene and triallylcyanurate, which are able to introduce crosslinking to the membrane. We now report on further progress with these membranes with respect to (i) the improvement of the PEFC polarizability by using new thinner radiation-grafted membranes, (ii) the improvement of the mechanical properties by changing our irradiation procedure and base polymer type, (iii) testing at higher temperatures (80-85 °C), (iv) long term testing in excess of 5000 hours at 60 °C, and (v) further insight into the degradation of these membranes in the PEFC application as a result of our post-mortem spectroscopic analysis of membranes.

INTRODUCTION

Radiation-Grafting Method

Radiation-grafting can be used to combine the desirable properties of two disimilar polymers in a graft copolymer structure. For example, the chemical and thermal stabilty of commodity fluoropolymers can be combined with the ion-exchange or proton-conducting properties of partially para-sulfonated polystyrene to yield materials useful for electrochemical devices, e.g., fuel and electrolysis cells, batteries, and sensors. Our membrane preparation method is shown schematically in Figure 1.

The radiation-grafting method offers several advantages for the preparation of ion-exchange or proton-conducting membranes for electrochemical applications. For example, the materials and methods are widely available and can be low cost. Such commodity base fluoropolymer films as poly(ethylene-*alt*-tetrafluoroethylene), or ETFE, currently cost less than \$5.00/m^2 for 50 μm thick film (1) and technical grade styrene currently costs less than \$ 1.-/kg in bulk quantities (2). A liter of styrene is about as much monomer as is found in 10 m^2 of a typical radiation grafted film. Industrial-scale electron beam irradiation of bulk film quantities can be purchased for less than \$1.00/m^2 (3), and can be carried out for less than \$0.10/m^2 based on actual operating costs for those purchasing an electron beam irradiation system (4). These prices are provided only to give a crude indication of the commercial viability of the radiation-grafting method, and we are still in the process of estimating the additional costs of special material handling in our preparation method such as material cooling or packing under inert atmosphere and the sulfonation step for a production-scale preparation. It is clear, however, that partially-sulfonated polystyrene-based ion exchange materials find widespread application (5), and, similar to our radiation-grafting method, they are often prepared (5) using chlorosulfonic acid to sulfonate the polystyrene-based precursor after it has been processed into its final bead or film form.

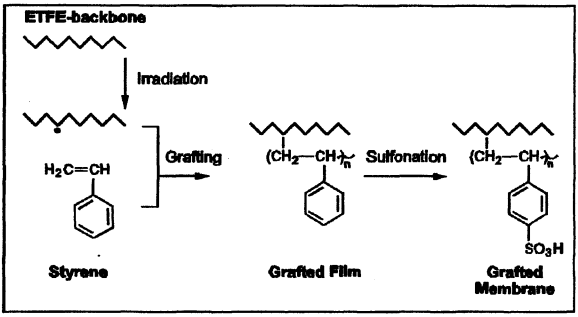

Figure 1 : Schematic illustration of the radiation-grafting method of membrane preparation.

Other advantages of the radiation-grafting method include: (a) Radiation-grafted membranes are readily crosslinked to control swelling, solubility, gas crossover, and degradation by adding an appropriate radically polymerizable crosslinker like divinylbenzene to the grafting mixture. (b) The base polymer is already in the form of a flat thin dense film. Therefore, no extrusion or solution casting of the solid electrolyte is required. This is an advantage because ion-containing polymers often have high melting points and melt viscosities due to the presence of strong hydrogen bonding and/or Coulombic interactions (6). In addition sulfonic acid groups are not stable at temperatures above about 180 °C (7) so that polymers containing sulfonic acid groups can not be readily melt processed without undergoing degradation. (c) Electron beam irradiation is a clean method and does not require an initiator or catalyst, and (d) the initiation reaction can be readily controlled by choice of the irradiation dose, dose rate, and atmosphere. In addition, electron beam irradiation finds widespread industrial application in polymerization, crosslinking, and sterilization.

Radiation-Grafted PEFC Membranes

Our early radiation-grafted PSI membranes were based on sulfonated polystyrene as the graft component and poly(tetrafluoroethylene-*co*-hexafluoropropylene), or FEP, as the base polymer (8). At that time performance and lifetime of these membranes (in terms of a stable *in-situ* membrane resistance) in Polymer Electrolyte Fuel Cells (PEFCs) were limited to 125 mW/cm^2 and less than 500 hours. Membrane lifetime in the PEFC was improved by adding divinyl benzene to our grafting mixture in order to crosslink our radiation-grafted membranes (9). As a result of the crosslinking through DVB, lifetimes were increased up to about 1,000 h or more and the open circuit voltage of cells operated with thinner (70-80 μm thick) radiation-grafted membranes increased from 793 up to 971 mV. Unfortunately, the crosslinking also increased the membrane specific resistance from 10.3 up to 36 Ωcm, and thus the ohmic losses in the PEFC. As Wang and Capuana correctly state in their recent publication (10), the polarization performance of PEFCs containing these radiation-grafted membranes crosslinked using DVB alone was poorer than that of similarly tested PEFCs containing Nafion 117. Wang and Capuano fail to mention however that in that same year we reported that the performance and lifetime of our radiation-grafted membranes were greatly increased after the introduction of our double crosslinking membrane preparation concept and optimization of the content of the crosslinking comonomers (11-13). We reported at that time (11) that a maximum power density of 385 mW/cm^2 was achieved with our optimized membranes and that this value exceeded by 60% that obtained with PEFCs containing Nafion 117 membranes under the same operating conditions (30 cm^2 cell active area, Nafion-impregnated E-Tek electrodes with a platinum loading of 0.8 $mgcm^{-2}$, 60 °C, H_2 and O_2 at atmospheric pressure).

In the following year (14) we reported that our radiation-grafted membranes were able to operate five or six times longer (about 700 h) than two commercially available radiation-grafted membranes from Pall RAI Manufacturing Co., R-1010 and R-4010, without significant degradation in terms of an increase in the *in-situ* membrane area resistance. Those tests were carried out as described. Recently Wang and Capuano successfully demonstrated (10) long-term testing of these same Pall RAI R-1010 and R-4010 membranes over about 1,000 h. It should be noted however that both cell temperature of 50 °C and active areas of 5 cm^2 are significantly lower and smaller than those used in our experiments.

In addition, Wang and Capuano used post-mortem infrared spectroscopy to investigate the degradation processes occurring over the lifetime of in the PEFC application (10). They measured the transmission spectra of membranes that had been tested for various times in PEFCs or soaked for various times in H_2O_2 solution. Unfortunately the region of 925 to 1100 cm^{-1} in their spectra of the untested H^+-form of the membranes was completely obscured by a broad strong absorbance feature and no distinct bands were observable. In general, after testing in a PEFC, bands at 1009 and 1039 cm^{-1} that they assigned to the C-H aromatic in-plane vibration and the S=O symmetric stretching vibration became observable. The absorbance of these two bands was lower in the membranes that were tested longer in a PEFC or exposed longer to H_2O_2 solution.

More than 30 years ago Hodgdon and co-workers (15) investigated the degradation of sulfonated polystyrene membranes in fuel cells. Based on ex-situ degradation studies, they proposed that degradation was primarily caused by (i) weak peroxide linkages introduced into the backbone during polymerization and (ii) by attack of $HO_2\cdot$ radicals generated at the fuel cell anode on the α-H of the sulfonated polystyrene. Büchi and co-workers (9) carried out HPLC analysis of the product water from PEFCs containing radiation-grafted, sulfonated polystyrene-based membranes. The 4-hydroxy- and 4-carboxybenzensulfonic acids and other non-identified benzenesulfonic acids that they found in the product water were consistent with the latter mechanism proposed by Hodgdon and co-workers (attack of *in-situ* generated radicals at the α-hydrogen positions). Büchi and co-workers (9) observed differences between the spectra of the *dried* K^+*-exchanged form* of untested and PEFC-tested FEP-based radiation-grafted membranes that were similar to those reported more recently by Wang and Capuano (9). In the work of Büchi and co-workers (9) the absorbance of the bands at 1009 and 1039 cm^{-1} due to the sulfonated polystyrene-based graft component decreased after membrane testing in a PEFC but that the intensity of the C-F absorption band at 982 cm^{-1} due to the CF_3 group of the FEP base polymer remained unchanged.

Unfortunately, the results of Wang and Capuano (10) are not so easily interpreted because Zundel has shown in his extensive fundamental infrared spectroscopic investigations of sulfonated polystyrene-based membranes that both of these bands at 1009 and 1039 cm^{-1} are highly dependent on the hydration level of the acid form of the membrane (16). Zundel's spectral measurements of membranes at various hydration levels show that the band at 1009 cm^{-1} decreases considerably in intensity upon drying due to strong coupling between the aromatic and sulfonic acid vibrational modes. Likewise Zundel showed that the band at 1039 cm^{-1} also decreases systematically with drying. Unfortunately, Wang and Capuano make no mention (10) of drying the membrane samples prior to spectroscopic analysis. Therefore some of the spectral changes that they reported over this narrow frequency range may be due to not only degradation losses of the sulfonated aromatic groups but also simply to drying out of the membrane in the application or prior to spectroscopic analysis. In addition, they did not report any analysis of spectral features due to the base polymer component of the Pall RAI membranes. In general, post-mortem analysis by transmission mode (through the membrane thickness) infrared measurements of the acid form of radiation-grafted and other PEFC membranes is extremely difficult due to the very strong absorbances of many of the vibrational modes of the sulfonic acid, aromatic, and fluorinated groups and the strong hydration level dependence in the case of the first and sometimes second type of vibrational modes. These problems in the post-mortem spectroscopic analysis of radiation-grafted and other PEFC membranes are addressed in the present work and the post-mortem analysis of membranes based on the partially fluorinated base polymer ETFE are reported.

In addition, we report here on further progress in the development of our PSI radiation-grafted membranes with respect to (i) the improvement of the mechanical properties by changing our irradiation procedure and base polymer type, (ii) the improvement of the PEFC polarizability by using new thinner radiation-grafted membranes, (iii) long term testing in excess in excess of 750 hours at a temperature of 80 °C, and (iv) long term testing in excess of 5000 hours at 60 °C.

EXPERIMENTAL

Membrane preparation and characterization

Nowoflon ET-6235 (ETFE) films from Nowofol GmbH of Siegsdorf, Germany (25, 50, and 100 µm thick) and Teflon FEP films from DuPont of Circleville, OH, USA (25, 50, and 75 µm thick) were used as base polymer films. Our membrane preparation method has been reported earlier (17-18) and is shown schematically in Figure 1. Some important preparation parameters include: (i) polymer film pre-irradiation by electron irradiation under N_2 atmosphere (e^-/N_2) at a dose rate of 15.1 kGy/s or gamma irradiation in air (g/air) at a dose rate of 5.9 kGy/h; (ii) subsequent grafting with a solution of 3.5 M styrene (Fluka purum grade), 0.33 M divinylbenzene (Fluka technical grade, 70-85 % active), and 0.19 M triallylcyanurate (Fluka purum grade) in benzene for 4.5 h at 60 °C; (iii) sulfonation of the graft component using a solution of chlorosulfonic acid, and (iv) generation of the water-swollen acid form of the membrane by treating the sulfonated films in (a) NaOH(aq), (b) HCl (aq), and then approximately 90 °C de-ionized water. The membranes prepared in this manner from the above ETFE and FEP base polymer films are designated here as ETFE-25, ETFE-50, ETFE-100, FEP-25, FEP-50, and FEP-75 depending on the base polymer film type and its thickness.

Stress-strain measurements of the radiation-grafted films and sulfonated and water-swollen membranes were carried out according to DIN 53'455 using a jaw speed of 10 mm/min. Infrared analysis of the films and the dried acid form and the dried K^+-form of the membranes was carried out at a resolution of 1 cm^{-1} in the Attenuated Total Reflectance (ATR) mode using a 45° ZnSe crystal and in the transmission mode on a Perkin Elmer System 2000. FT-Raman spectra of the films and membranes were measured with a Bruker IFS 55/S Equinox Raman FRA 106/S spectrometer at a resolution of 2 cm^{-1} using a laser intensity of 420 mW, 256 scans, and a Ge-detector. An aluminum mirror was placed in the light path behind the membrane sample in order to obtain spectral information through the film and membrane thicknesses.

Fuel Cell Testing

Membranes were tested in fuel cells using our previously reported methods (8). Membranes were tested in stainless steel cells with active areas of 30 cm^2 and graphite cells with active areas of 100 cm^2. Test parameters include: (a) nominal cell temperatures of 60 °C (some single cell experiments with active areas of 30 cm^2 were carried out at a nominal cell temperature of 80 °C), (b) humidified H_2 and O_2 gases at 1 atm, and (c) Nafion-impregnated E-TEK electrodes having a Pt loading of 0.8 mg/cm^2. The stability of the membranes over their lifetime in the PEFCs was evaluated by monitoring the *in-situ* membrane area resistances measured by a current pulse method (19). The performance of the membranes over their lifetime in the application was evaluated based on the polarization characteristics of the PEFCs.

RESULTS AND DISCUSSION

Membrane Mechanical Properties

Previously we used γ-irradiation in air for the pre-irradiation of our perfluorinated FEP base polymer films. Membranes produced using this procedure were brittle and suffered from poor mechanical properties and breakage in cells having active areas much larger than 30 cm^2. The irradiation procedure was optimized and changed to e-beam irradiation in inert gas atmosphere and partially fluorinated poly(ethylene-*alt*-tetrafluoroethylene), or ETFE, base polymer films were used instead of perfluorinated FEP films. Membranes produced using this modified irradiation process and partially fluorinated base fluoropolymer films show improved mechanical properties, both *ex-situ* and in cells having active areas of 100 cm^2. The *ex-situ* characterized mechanical properties typical of these membranes are shown in Figure 2. This improvement in mechanical properties has been ascribed (18) to the lesser extent of chain scission occurring when (i) the pre-irradiation step is carried out more rapidly using the higher dose rate electron beam source, (ii) the pre-irradiation is carried out under inert atmosphere, and (iii) partially fluorinated films are used instead of perfluorinated ones.

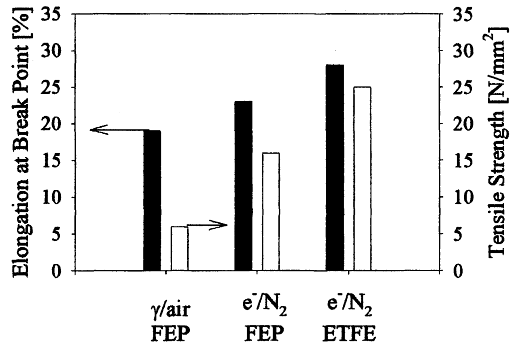

Figure 2 : Mechanical properties of swollen 125 μm FEP-based and 70 μm ETFE-based membranes.

Membrane Ion-Exchange Capacities and Swelling Properties

The ion-exchange capacities (IEC) of the PSI radiation-grafted membranes and Nafion membranes are compared in Table I. The IEC values of the PSI radiation-grafted membranes are considerably higher than those of the Nafion membranes on both a mass (mEq/g) basis, as shown in Table I, and volume (mEq/cm^3) basis. For example, the IECs of the water-swollen PSI membranes are over 200 mEq/cm^3, while the Nafions are less than 50 mEq/cm^3. An important factor is that our membranes are crosslinked so that they can have higher acid group contents than Nafion without excessive swelling. In addition each side chain in Nafion has only one sulfonic acid group. Presumably the grafted chains in our membranes are many monomer units in length and each styrene unit is sulfonated. The higher IEC of our radiation-grafted membranes on a mass basis is also partly a result of the fact that only the main chains (base polymer) in our membrane are partially or fully fluorinated (ETFE or FEP, respectively), whereas in Nafion both the main chain and side chain are fluorinated. The crosslinking in our radiation-grafted membranes restricts their volumetric expansion during swelling and thus favors a higher IEC value on a volumetric basis.

Table I *Ex-Situ* Characterized Membrane Properties

Membrane	Thickness /μm	IEC /mEqg^{-1}	Water swelling /mass %	Water/acid concentration ratio /(H_2O/RSO_3H)
FEP-25	41	2.0	22	6.4
FEP-50	85	1.9	27	7.9
FEP-75	125	1.8	33	10
ETFE-25	39	2.4	27	6.2
ETFE-50	84	2.3	29	7.0
ETFE-100	152	2.4	44	10
Nafion N-112	60	0.91	37	22
Nafion N-115	150	0.91	37	22
Nafion N-117	200	0.91	37	22

As a result of their crosslinking, many of the PSI radiation-grafted membranes swell to a lesser extent in water on a mass basis than Nafion (Table I). It is difficult to readily compare the swelling properties of these different membranes due to their different structures and extents of fluorination. For this reason, the water content in terms of the number of water molecules per acid group in the water swollen membranes (referred to as here as water/acid concentration ratio) is also given in Table I. These values are also lower for our crosslinked radiation-grafted membranes than for the uncrosslinked Nafion membranes. The mass-based water swelling of the ETFE-based membranes are higher than those of their FEP-based counterparts. This difference in swelling is largely a result of the higher extent of fluorination and thus repeat unit weight in the case of the FEP-based membranes because the water/acid concentration ratios are nearly identical for membranes of the same thickness but based on the two different base polymers. For each radiation-grafted membrane type, FEP- or ETFE based, the swelling decreases on a mass basis or in terms of the water/acid concentration ratio as the membranes become thinner. This lower extent of swelling in the thinner membranes has been ascribed (18) to gradients in the concentration of the grafted monomers through the membrane thickness. Thus the thinner membranes have a higher relative content of the larger crosslinking monomer DVB than the thicker membranes do, and thus the thinner membranes are more effectively crosslinked and swell to a lesser extent.

Testing in PEFCs

Thinner Membranes. The *in-situ* characterized properties of our membranes and the comparably thick Nafion membranes are summarized in Table II. The thinner radiation-grafted membranes have lower area resistances than their thicker counterparts (Table II) and thus there is an increase in the PEFC performance with the thinner membranes, as shown by the maximum power densities in Table II and by the polarization curves in Figure 3. Unfortunately, we are not able yet to take complete advantage of the decrease in membrane thickness because the specific resistance of our membranes increases as they become thinner. As mentioned earlier, we have ascribed this effect to inhomogeneities in the grafted monomer distribution through the membrane thickness (18), and we are examining ways of overcoming this challenge. The type of base polymer film, perfluorinated FEP or partially fluorinated ETFE, does not appear to influence the polarization performance of the PEFC, as shown in Figure 4. In spite of the increase in specific resistance as our membranes become thinner, both the polarization curves in Figure 4 and the summarized maximum power densities in Table II indicate that, under the same operating conditions, the polarization characteristics of PEFCs containing our radiation-grafted membranes are comparable or better than those of PEFCs containing Nafion membranes of similar thickness.

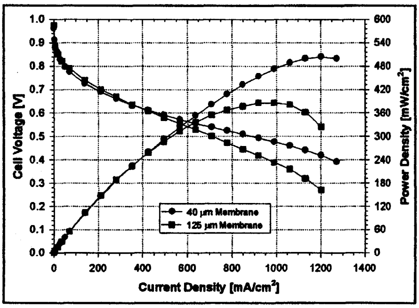

Figure 3 : Performance of 40 and 125 µm thick radiation-grafted FEP-25 and FEP-75 membranes in a H_2/O_2 fuel cell at 60 °C and 1.0 bar (absolute) gas pressure.

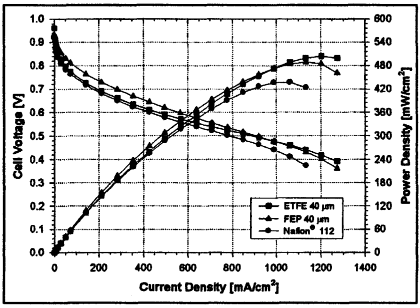

Figure 4 : Performance of 40 µm thick radiation-grafted ETFE-25 and FEP-25 membranes in a H_2/O_2 fuel cell at 60 °C and 1.0 bar (absolute) gas pressure.

Table II *In-Situ* Characterized Membrane Properties: 60 °C, 1 atm. H_2 and O_2

Membrane	Area Resistance /(mΩcm^2)	Specific Resistance /(Ωcm)	Maximum power densities /mWcm^{-2}
FEP-25	65	16	550
FEP-75	120	9.6	450
ETFE-25	66	17	490
ETFE-50	96	11	470
ETFE-100	135	9	390
Nafion N-112	70	11	440
Nafion N-115	150	10	380
Nafion N-117	190	9.5	270

Long-Term PEFC Testing. We have recently obtained reproducible membrane cell lifetimes (in terms of *in-situ* membrane resistance) of greater than 5000 hours at 65°C with our radiation-grafted PSI membranes as shown in Figure 5. In this test the PEFC was restricted to operating at voltages greater than about 650 mV and thus in the cell operating region characterized by useful electrical efficiencies and low heat generation. Over this period of time the membrane resistance increased only by about 0.5 %/100hr, qualitatively indicating that the loss of proton-conducting groups has not been too extensive. More recently, we have begun tests under similar operating conditions at higher temperatures. An example of a long-term test currently in progress at 80 °C is shown in Figure 6. The membrane resistance and the cell current and voltage do not exhibit any large-scale changes indicating that the membrane remains fairly stable during the first 1200 hours of this experiment.

Post-Mortem Membrane Analysis

Transmission mode FTIR measurements were carried out on membranes after their testing in fuel cells was finished. The absorbance of the acid-form of the membranes was too high to yield useful spectra even when the membranes were first dried under vacuum at 80 °C and rapidly transferred to the spectrometer (not shown). Better spectra were obtained by exchanging the membranes into their K^+-exchanged form, but the absorbance of many of the bands of interest were still greater than 2 (less than 1% of the light transmitted) even for the thinnest 40 μm membranes. Useful infrared spectra (all absorbances less than 2) were obtained by measuring in the Attenuated Total Reflectance (ATR) mode. In contrast, FT-Raman measurements were readily measured through the film thickness by placing an aluminum mirror in the light path behind the sample.

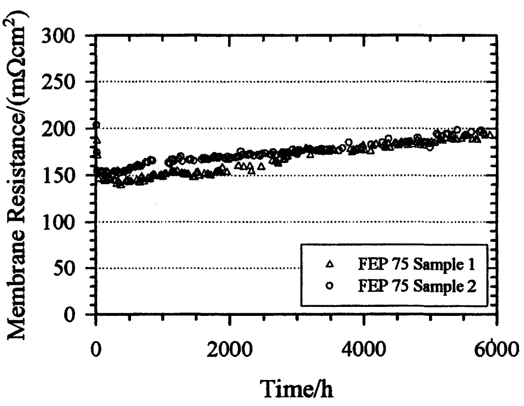

Figure 5 : In-situ membrane resistances of FEP-75 membranes during long-term testing in a H_2/O_2 fuel cell at 60 °C and 1.0 bar (absolute) gas pressure.

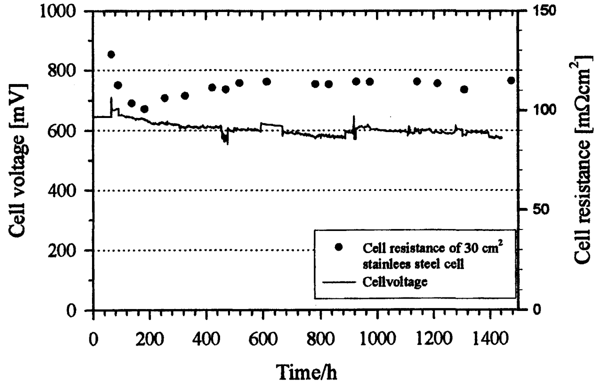

Figure 6 : In-situ membrane resistance of FEP-75 membrane and cell voltage during long-term testing in a H_2/O_2 fuel cell at 80 °C and 1.0 bar (absolute) gas pressure. Current density 0-916 h 0.35 A/cm^2, < 916 h 0.28 A/cm^2.

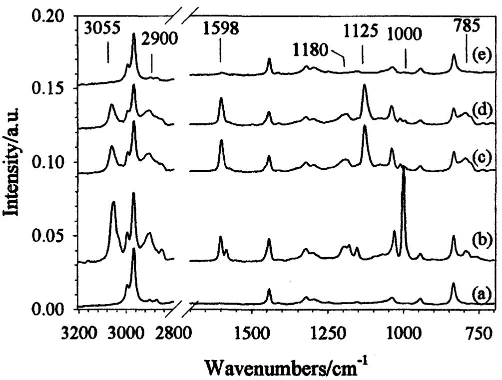

Figure 7. FT-Raman Spectra: (a) 100 μm ETFE film, (b) uncrosslinked grafted film, (c) untested membrane, and tested active areas of membrane regions with (d) normal or (e) white appearance.

Raman spectra of an ETFE base polymer film and an uncrosslinked grafted film and untested and PEFC-tested K+-form membranes prepared from this base polymer are shown in Figure 7. Aromatic bands at about 3050 (C-H stretch), 1600 (quadrant ring stretching), 1130 and 1000 (C-H bending coupled with ring motions) and 785 cm-1 (C-H wag), and aliphatic bands at 2900 cm-1 (C-H and CH2 stretch) are found in the spectra of the grafted film (Figure 7b) but not in that of the base polymer (Figure 7a). After sulfonation in the spectrum of the untested membrane a strong absorption band develops at 1125 cm-1 due to the stretching vibration of the RSO3- anion. This uncrosslinked membrane was next tested in a PEFC. The cell performance was stable for several hundred hours, and then the membrane resistance increased and the cell performance diminished (in terms of polarization properties and power) with further testing. After about 500 hours of testing, the membrane was removed from the PEFC and analyzed. The membrane was observed to have some white regions in the active area. The spectrum of one of these white regions is shown in Figure 7e and appears to be identical with that of the unmodified ETFE base polymer (Figure 7a). The spectra of one of the active area regions having a normal transparent light brown color is shown in Figure 7d and it is essentially identical to that of the untested membrane (Figure 7c). The partially fluorinated base polymer ETFE did not appear to undergo degradation even in the most heavily degraded white region. These Raman spectral results were found to correlate well with infrared spectral changes observed in ATR mode FTIR spectroscopic investigations and ion-exchange capacity measurements on regions of the untested and tested membrane. These results indicate that while some regions of the active area analyzed suffered a complete loss of the sulfonated polystyrene graft component, at least in this particular PEFC test, other regions suffered little degradation. Wang and Capuano reported (10) that they found differences in the extent of degradation of different regions of their membranes in their post-mortem analyses also. We are continuing to investigate this in-situ membrane degradation.

As we reported earlier based on *in-situ* membrane resistance and cell polarization measurements during long-term PEFC testing, the *in-situ* stability of our membranes prepared using the double crosslinking concept (DVB and TAC) is much better than that of uncrosslinked radiation-grafted membranes (11-13). For example, spectroscopic analysis and ion-exchange capacity measurements were carried out also on a crosslinked ETFE-50 membrane after about 500 hours of testing in a PEFC under the same operating conditions (Figure 8). In contrast to the characterization results on the uncrosslinked membrane, no evidence of significant degradation or inhomogeneities in the doubly crosslinked membrane was found by FTIR-ATR or FT-Raman spectroscopic analysis or ion-exchange capacity measurements. It is important to note that in some of our present cell and stack designs, mechanical breakage of the membrane during cell operation can be a problem with either thinner Nafion membranes or the thinner PSI *crosslinked* radiation-grafted membranes. In these cases, mechanical failure, probably due to swelling stresses near the active area (swollen membrane)/gasket (non-swollen) border in the PEFC (14,18) often seem to be solely responsible for the membrane failure. We are currently examining ways to alleviate this problem by still further improving the mechanical properties of our crosslinked membranes and our our cell and stack designs.

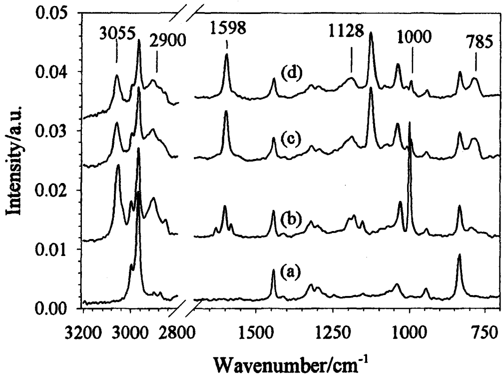

Figure 8. FT-Raman spectra: (a) 50 mm ETFE film, (b) grafted film, (c) untested membrane, and (d) tested active area of membrane.

CONCLUSIONS

The polarization performance of PEFCs containing our radiation-grafted membranes has been improved by the development of thinner membranes based on thinner base polymer films. Membrane mechanical properties have been improved through the use of partially fluorinated ETFE films as base polymers. Long-term testing of our membranes has been carried out for periods of more that 5,000 hours at 60 °C and more than 1400 hours at 80 °C. Post-mortem membrane analysis by means of FT-Raman spectroscopy indicate that membrane degradation is limited to the sulfonated polystyrene-based graft component, even when the partially fluorinated base polymer ETFE is used. Future research efforts will be devoted to improving the mechanical properties and chemical stability of our membranes even further.

ACKNOWLEDGMENTS

Financial support for this work by the Swiss Federal Office of Energy (BFE); electron beam irradiation by Mr. C. Günthard of Studer AG, CH-4658 Däniken; gamma irradiation by Mr. M. Steinemann of the Paul Scherrer Institute (PSI) Hot Laboratory; Melt Flow Index (MFI) measurements on irradiated fluoropolymers by Professor H.G. Bührer and Mr. M. Wyler and Mr. M. Benz of Technikum Winterthur Ingenieurschule (TWI), CH-8401 Winterthur; characterization of membrane mechanical properties by Dr. Ch. Löwe and Mr. Ch. Walder of the Swiss Federal Laboratories for Materials Testing and Research (EMPA), CH-8600 Dübendorf, membrane preparation by Ms. F. Geiger of PSI, are all gratefully acknowledged.

REFERENCES

1. Personal communication, R. Hodann, Nowofol Kunstoffprodukte GmbH, Siegsdorf, Germany, July 1998.
2. Personal communication, E. Chamot, Chamot Labs., July 1998.
3. Personal communication, C. Günthard, Studer AG, Däniken, Switzerland, August 1998.
4. Personal communication, J. Chrusciel, Energy Sciences Inc., Wilmington MA, USA, July 1998.
5. F.D. Dardel and T.V. Arden in Ullmann's Encyclopedia of Industrial Chemistry, Fifth ed., B. Elvers, S. Hawkins, M. Ravenscroft, and G. Schulz Eds., Vol. A 14, p. 393.
6. R.A. Register and R.K. Prud'homme in Ionomers: Synthesis, structure, properties, and applications, M.R. Tant, K.A. Mauritz, and G.L. Wilkes, Eds., Chapman and Hall, London, 1997, Chapter 5.
7. G.E. Boyd, B.A. Soldano, O.D. Bonner Ind. Eng. Chem., 58, 456 (1954).
8. F.N. Büchi, B.Gupta, M. Rouilly, P.C. Hauser, A. Chapiró, and G.G. Scherer, Proceedings of the 27th IECEC Conference, 3, 3.419 (1992)
9. F.N. Büchi, B.Gupta, O. Haas, and G. G. Scherer, Electrochim. Acta, 40(3), 345 (1995).
10. H. Wang and G.A. Capuano, J. Electrochem. Soc., 145(3), 780 (1998).

11. F. N. Büchi, B.Gupta, O. Haas, and G. G. Scherer, J. Electrochem. Soc., *142*, 3044, (1995).
12. M. Rota, H.P. Brack, F.N. Büchi, B.Gupta, O. Haas, and G. G. Scherer, Extended Abstracts, 187th Meeting of the Electrochemical Society, Reno, NE, 1995, Vol. 95-1, p. 719.
13. F.N. Büchi, B. Gupta, G.G. Scherer European Patent Application 94 924 184.8-2111
14. G.G. Scherer, H.P. Brack, F.N. Büchi, B. Gupta, O. Haas, M. Rota; Hydrogen Energy Progress XI, Proceedings of the 11th World Hydrogen Energy Conference, Stuttgart, Germany, June 1996; Vol. 2, p 1727.
15. R. Hodgdon, J.R. Boyack, and A.B. LaConti, in Advance Development and Laboratory Technical Report, No. 65DE5, General Electric Co., West Lynn, MA, USA, 1966.
16. G. Zundel, Hydration and Intermolecular Interaction, Infrared Investigations with Polyelectrolyte Membranes. Academic Press, New York, 1969.
17. B. Gupta, F.N. Büchi, G. G. Scherer, J. Polym. Sci.: Part A: Polym. Chem. 32, 1931 (1994).
18. H.P. Brack and G.G. Scherer Macromol. Symp. 126, 25 (1997).
19. F.N. Büchi, A. Marek, G. G. Scherer, J. Electrochem. Soc. 142(6), 1895 (1995).

Proton_Conducting_Membrane_Fuel_Cells_II, PV 1998-27, 66-70 (1998)
DOI: 10.1149/199827.0066PV © The Electrochemical Society

A NOVEL PROTON CONDUCTIVE MEMBRANE (PCM)

E. Peled, T. Duvdevani and A. Melman
Faculty of Exact Sciences, School of Chemistry, Tel Aviv University,
Tel Aviv, Israel 69978

Abstract

A family of novel proton-conducting membranes (PCMs) has been prepared from low-cost, thermally stable materials and has been preliminarily characterized. These PCMs consist of electronic non-conductive nano-size ceramic powder, polymer binder and an acid. They have the appearance of plastic, good mechanical properties, nano-size pores (typically smaller then 1.5-3 nm) filled with the acid, and room-temperature conductivity of up to 0.21 Scm^{-1} (twice that of Nafion). Their thickness ranges from 30 to 1000 μm. These PCMs are considered to be excellent and low-cost candidates for many electrochemical applications including: fuel cells, electrolyzers, supercapacitors, sensors and batteries.

Introduction

Proton-conducting membranes (PCM), are to be found in many electrochemical applications including: fuel cells, electrolyzers, supercapacitors, sensors and batteries. Nafion, is the most commonly used membrane, in fuel cells operating at near-room temperature (up to 100°C). Nafion, which is a solid polymer electrolyte (SPE), has two major disadvantages-it is very expensive and it dries during fuel-cell operation as a result of water dragging by the proton (1,2).

In recent years, there has been an intensive effort to develop a low cost SPE to replace Nafion and significant progress has been made (3,4). Room-temperature proton-conducting materials are reviewed in reference 5; none of them has a room-temperature conductivity higher then 0.18Scm^{-1}.

The goal of this work was to develop and characterize, a low-cost, highly conductive PCM. It basically consists of nano-sized ceramic powder, having good acid adsorption capacity, a polymer binder and an acid absorbed, by the nano-size ceramic powder, in nano-size pores.

Experimental

The PCMs were formed by a solvent casting technique with the use of K control coater (R K Print, Coat Instruments). A viscous paste was formed by mixing nano-size ceramic powder with Kynar PVDF 2801-00 (ELF Autochem) and a solvent mixture-typically cyclopentanone and propylene carbonate (PC). This paste was poured into the coater which formed a wet film. Upon drying, a flexible film was obtained. The film was washed several times with double-distilled water to remove the residual organic solvents. Following this wash, the film was doped with the acid by immersions in the desired acid, for three hours. This doping was done either at room temperature or at 90-100°C. Using this procedure we prepared PCMs with the following nano-size powders: amorphous fumed 150 nm particle size silicon dioxide, 99.8% (Alfa Aesar, Johnson Matthey), micropolish 50 nm alumina (Buehler), 21 nm particle size Degussa titanium dioxide P25, 99.5% and TiO_2/SiO_2 mixed powder. The thickness of the PCM ranged from 30 to 200 µm. Thicker films (1000 µm) were formed by casting the paste on a Teflon tray. The volume fraction of the ceramic powder was between 0.5 and 15%. The ionic conductivity of the PCM was measured at room temperature (25±3°C) with the use of a 1 cm^2 spring-loaded SS discs cell and a Solatron model SF 1260 AC analyzer (four-electrode measurement). The conductivity test cell is described in ref. 6. The pore-size distribution of dry (with no acid) PCMs was carried out with the use of a Quantachrome NOVA 2200 Surface Area Analyzer.

Results and discussion

In this paper we present preliminary results regarding a narrow range of PCM composition. PCMs which consist of 5-10 volume percent ceramic powder have good mechanical and acid absorption properties. They have the appearance of plastics and can be bent 180°, with no damage to the film. Qualitatively mechanical strength follows the order: $Al_2O_3 \approx TiO_2 > SiO_2/TiO_2 > SiO_2$. The Barrett, Joyner & Halenuda (BJH) method for measuring pore-size distribution, (Fig.1) for a dry PCM which consist of 10% (volume) SiO_2 and 15% (volume) PVDF shows that the dominant pore volume is due to pores smaller than 2 nm. In other PCM samples (depending on composition) a small peak in the PSD curve was found at about 1.5-2.5 nm. For comparison, Nafion has a wide spectrum of pore-sizes ranging from 1 to 100nm with an average value of about 2nm (7). We believe that the pores of the PCM are small enough to prevent H_2 or O_2 gas bubbles to cross the PCM, when it is used in a fuel cell. For conductivity measurement, PCM which consist 10% (volume) ceramic powder and 15% (volume) PVDF were doped by several acids at room temperature, 90°C and 100°C. The results (taken at room-temperature) are summarized in Table.1. Several aqueous solutions of the superacid (SA) CF_3SO_3H were doped at room temperature, in the PCM. This acid is considered (8,9,10) a promising candidate for fuel-cell applications. Changing the SA/water volume ratio from 1:1 to 1:3 has little effect on the PCM conductivity which has a maximum at the 1:2 ratio. Doping the acid at 90°C (for 3 hours) caused a 20% conductivity rise (up to 0.18 Scm^{-1}). The conductivity of the same PCM which was doped (at 100°C) by H_2SO_4:H_2O 1:3 (volume ratio) is 0.21 Scm^{-1}. For comparison the maximum conductivity of Nafion is 0.10 Scm^{-1} (Table 1). The conductivities of H_2SO_4:H_2O 1:3 and SA:H_2O 1:2 solutions were measured, at 25°C, (with a platinized-platinum electrode cell). The values obtained were 0.734 Scm^{-1} and 0.624 Scm^{-1} respectively. The Labyrinth factor (λ) of the PCM can be calculated by comparing the conductivity of the PCM with that of the appropriate acid solution (λ= solution conductivity/ PCM conductivity). Values of λ are 3.5 for both the SA-doped PCM and the H_2SO_4-doped PCM.

A double-layer capacitor was assembled with the use of porous carbon electrodes and 1:3 H_2SO_4:H_2O electrolyte. Two porous carbon electrodes were hot pressed on both sides of the PCM. This capacitor has an equivalent series resistance (ESR) of approximately $0.055\Omega cm^2$ (for a single cell) and capacitance of 0.12 F/cm^2 which is equal to 26 F/gr. A three similar double-layer capacitor was assembled and cycled at 0.1 to 3V (Fig 2). This capacitor ESR was 0.168 Ωcm^2 and it's capacitance was 0.044 F/cm^2. Similarly a supercapacitor with two metal oxide electrodes, like RuO_2, WOx, MnO_2 can be made.

Other solid ionic conductors can be made by doping this membrane by a base like aqueous KOH or other solutions instead of with acids.

Summary

A family of 40-400 μm-thick novel PCMs was developed with the use of low-cost, thermally stable materials. They exhibited room-temperature conductivity higher than any other PCM and double that of Nafion. They are believed to be excellent candidates for many applications including: fuel cells, electrolyzers, supercapacitors, sensors and batteries.

Acknowledgment

We like to thanks Degussa for supplying titania samples and ELF Autochem for supplying Kynar (PVDF) samples.

This research was supported in part by Israel Science Foundation founded by Israel Academy of Science & Humanities.

Reference

1. L.M.J. Blomen; M.N. Mugerwa; Fuel cell systems; Plenum press; 271 (1993).
2. T.Zawodinski, T.E. Springer, F. Uribe and S. Gottesfeld, Solid State Ionics, **60**, 199 (1993).
3. A.E. Steckand C. Stone, New materials for fuel cell and modern Battery System II, O. Savadogo and P.R, Roberge Editors; page 792, Ecole Polytechnique Montreal (1997).
4. F.N. Cornet, G. Geble, R. Mercier, M. Pineri and B. Sillion; ibid, Page 818.
5. S. Chandra, Handbook of Solid State Batteries and Capacitors, p.579, N.Z.A. Munshi Ed. World Scientific (1995).
6. G. Golodnitsky; G. Ardel; E. Strauss; E. Peled; Y. Lareah; Y. Rosenberg; J.Electrochem. Soc. **144**, 3484 (1997).
7. J. Divisek, M.Eikerling, V.Mazin, H.Schmitz, U.Stimming and Yu. M. Volfkovich, J. Electrochem. Soc, in press.
8. A.A. Adams; R.T. Foley; H.J. Barger; J.Electrochem. Soc. **124**, 1228 (1977).
9. A.J. Appleby; B.S. Baker; J.Electrochem. Soc. **125**, 404 (1978).
10. P. Zelenay; B.R. Scharifker and J. O'm. Bockris; J.Electrochem. Soc.

133, 2262 (1986).

Table 1: PCM room temperature conductivity

PCM composition . * [Volume %]	acid [Volume ratio]	Dipping temp. [°C]	Cond. [Scm^{-1}]
8% SiO_2 (12% PVDF)	pure H_2SO_4	25±2	0.04
8% SiO_2 (12% PVDF)	1:3 H_2SO_4:H_2O	25±2	0.18
10%Al_2O_3	1:3 H_2SO_4:H_2O	100	0.07
10%TiO_2	1:3 H_2SO_4:H_2O	100	0.19
10%SiO_2	1:3 H_2SO_4:H_2O	100	0.21
10% SiO_2	1:1 H_3PO_4:H_2O	25±2	0.06
10% SiO_2	1:2 CF_3SO_3H:H_2O	25±2	0.14
10% SiO_2	1:3 CF_3SO_3H:H_2O	25±2	0.12
10% SiO_2	1:1.5 CF_3SO_3H:H_2O	25±2	0.13
10% SiO_2	1:1 CF_3SO_3H:H_2O	25±2	0.11
10% SiO_2	1:2 CF_3SO_3H:H_2O	90	0.18
Nafion**			0.10

* 15% (V/V) PVDF if not otherwise stated

** Ref 2 at 30°C.

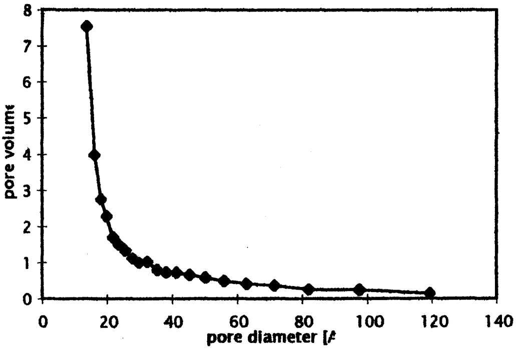

Fig. 1: Pore size distribution (BJH method) for dry PCM.

Proton_Conducting_Membrane_Fuel_Cells_II, PV 1998-27, 71-80 (1998)
DOI: 10.1149/199827.0071PV © The Electrochemical Society

IN-PLANE RESOLVED *IN-SITU* MEASUREMENTS OF THE MEMBRANE RESISTANCE IN PEFCs

F. N. Büchi and G. G. Scherer
Paul Scherrer Institut
General Energy Research, Electrochemistry
CH-5232 Villigen, Switzerland

ABSTRACT

The *in-situ* resistance of Nafion® membranes with different thickness was measured in H_2/O_2 fuel cells as function of current density and gas humidity. The resistance distribution across the thickness of membranes was determined by using membranes composed from several thin sheets with interlaying thin gold wires as potential probes. The same method was used to measure the resistance at different *in-plane* locations (i.e. at gas inlets and outlets). It was found that with increasing current density the resistance at the anode side of the membrane is increasing. When oxygen was fed dry, then complex *in-plane* patterns of membrane hydration distribution were observed.

INTRODUCTION

Polymer Electrolyte Fuel Cells (PEFCs) are a promising candidate as power plant for many future applications [1]. In this type of fuel cell, a thin organic proton exchange membrane plays the dual role as electrolyte and gas separator. Per-fluorinated polymer membranes from DuPont de Nemours (Fayetteville, USA) sold under the trademark of Nafion® are the most common membrane materials used in PEFCs. Only after swelling with water the membrane becomes a reasonable proton conductor (≈ 10 Ωcm at 20 °C) because the membrane bulk separates in at least two phases, a hydrophobic phase containing the backbone and hydrophilic phase containing the sulfonic acid groups and water [2]. In the fuel cell application the protons move through the hydrophilic membrane phase from anode to cathode.

A low electrolyte (membrane) resistance is one of the key parameters for attaining high power densities in PEFC. The specific resistance of the membrane-electrolyte is determined by the concentration of the charge carrier (proton) and its mobility. The most important parameter for the mobility of the protons in the membrane is its water content [3], often expressed as λ = number of H_2O/SO_3H. In the range λ=1 to λ=20 the specific conductivity varies by more than an order of magnitude. The proton mobility is also influenced by the temperature, but in the operating range of PEFCs of 20 to 80 °C, the variation of the water content has a much stronger influence on the membrane resistance than the variation of the temperature.

A high water content of the membrane in the fuel cell is therefore of importance for attaining high power densities. Hence, the water management of the fuel cell, aiming at retaining the highest possible water content in the membrane is one of the most critical operating aspects. To understand the phenomena of membrane water content during fuel cell operation research was carried out investigating the *ex-situ* membrane properties like water-sorption [3-5], water-diffusion [6] and *ex-situ* conductivity [3, 7-9] under well controlled conditions. Model calculations [10-13] have given insight into the complex water management of PEFCs where for the determination of the membrane water content additional parameters, such as current density, dew-point of gases on cathode and anode side, mass-transport in the electrodes, and gas-crossover have to be accounted for. It was established, that the water distribution in the membrane is determined on the one hand by the osmotic drag of water from the anode to the cathode and on the other hand by the back transport of water to the anode.

In earlier work we have investigated the resistance of Nafion® 117 *in-situ* as function of different operating conditions and found, that the resistance increases considerably with current density [14]. However, no efforts have been made to localize the increase of the resistance and the corresponding water loss within the membrane. I.e., the nature of the evolving water profile with current density was not investigated. In order to elucidate the membrane hydration profile Watanabe et al. [15] have performed experiments with very thin layers of recast Nafion (ca. 15 µm) and interlaying Pt-wires as potential probes. In contrast to our previous measurements they have found a decreasing membrane resistance with current density [15]. Using very thick membranes Bellows et al. [16] have recently used neutron scattering and detected a decrease of the water content at the anode with increasing current density.

In this study we present data for the resistance- and water-content distribution across the thickness and *in-plane* of membranes in PEFCs with respect to current density and gas humidity.

EXPERIMENTAL

The Nafion® membranes (N112, N115, N117, N105) were pretreated by heating for 1 hour in half concentrated nitric acid, subsequent washing with pure water (18 MΩ, from Seralpur C90 System) and then boiling for 1 hour in water. The membranes were stored in pure water in the dark. The membrane thickness was measured in the swollen state using a digital thickness gauge (Heidenhain). The following thicknesses were obtained for the swollen membranes, which have, after the described pretreating procedure, a water content of λ=21-22 H_2O/SO_3H : N112 : 58 - 62 μm; N115 : 145 - 150 μm; N117 : 200 - 205 μm; N105 (λ=27-28) : 160 - 165 μm. For fuel cell experiments ELAT-electrodes from E-Tek (Natick, USA) with a Pt-loading of 0.6 mg/cm^2 (20% Pt on C) have been used. To extend the three phase boundary the electrodes were impregnated (0.6 - 0.7 mg/cm^2 dry mass) with solubilized Nafion (1100 EW, Solution Technology, USA).

Stainless steel fuel cells with 1-dimensional geometry [14] (the gases are fed from the back of the current collector) and cells with a grafite channel-type flow field (channel length 370 mm), both with an active area of 28 cm^2 were used. In cells with multiple Nafion® membranes, a 25 μm gold wire was placed as potential sensor in between the individual membrane sheets. For some experiments more than one gold wire was placed between two membrane sheets at different locations.

The resistance of the membranes was measured *in-situ* by the auxiliary current pulse technique [14, 17]. With this technique very fast 5A-pulses are injected into the cell and the voltage change at the end of the pulse is measured in a 1 μs time window. This procedure allows for accurate membrane resistance measurements over the entire current density range. In multiple membrane cells, a fast 4-channel digital oscilloscope (LeCroy 9304) was used to measure simultaneously the voltage change at the end of the current pulse of the entire cell and in-between the gold wire potential probes and the anode. The resistance of the individual membranes was then calculated from the differences of the respective voltage changes. The average water content of an individual membrane sheet was calculated from the resistance by comparison to the *ex-situ* determined resistance, using impedance spectroscopy, of membranes with known water content [9].

RESULTS AND DISCUSSION

1-Dimensional Cell

In the 1-dimensional cell (variation in the direction of the membrane thickness, 1-D) [14], the gases are homogeneously fed from the back of the current-collector to the entire active area. Unlike in cells where the gases flow along the backside of the electrodes humidity, gas composition, temperature, current-density, and membrane resistance are therefore homogeneous over the entire active area.

The membrane resistances as function of current-density @ at 60 °C for 1100 EW Nafion® membranes of different thickness are shown in Figure 1. Except for the cell with a single N112 membrane an increase of the membrane resistance with current density is observed. This increase is a strong function of the membrane thickness. The thicker the membrane in the fuel cell, the stronger is the increase of the resistance with current density. In the current density range from 0 to 0.5 A/cm^2, the increase of the resistance for the cell with a N115 membrane (≈ 150 μm) is 8 mΩcm2 (ca. 5 %) for the cell with 4x N112 membranes (≈ 240 μm) it is 55 mΩcm2 (25%) and for the cell with 2x N117 membranes (≈ 400 μm) it is approx. 130 mΩcm2 (35 %).

The results displayed in Figure 1 reveal only the resistance of the entire membrane. It is now interesting to investigate how the increase of the resistance is developing across the thickness of the membrane. This can be measured in cells with multiple N112 membranes, as the resistance of every individual membrane can be measured separately. Figure 2 displays the resistance of the individual N112 membranes in a cell with 4 membranes at 60 °C as a function of current density. For 3 of the membranes the open circuit resistance is fairly close in the range of 60 - 70 mΩcm^2. For one of the membranes (the third one, counted from the anode side) the open circuit resistance is only about 40 mΩcm^2. We observe such differences for the membrane in the center in most multi-membrane cells. Probably this difference has a geometric explanation : with a diameter of 25 μm the potential sensing wire has a non neglectable size as compared to the thickness of the individual membranes, with a swollen thickness of 58 - 62 μm each.

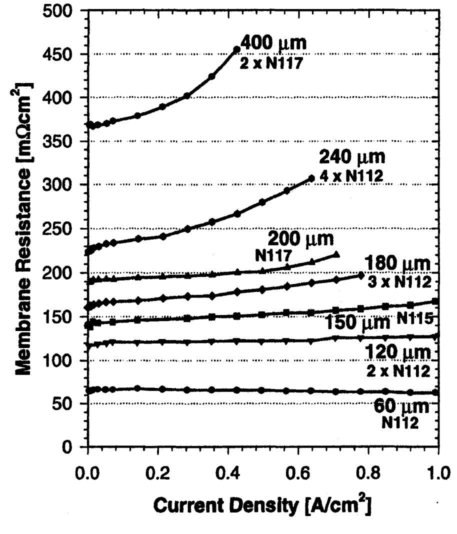

Figure 1 : In-situ resistance of Nafion® membranes (in 1-D cell) with different thickness as function of current density at 60 °C. The thicknesses and nature of the membranes are as indicated.

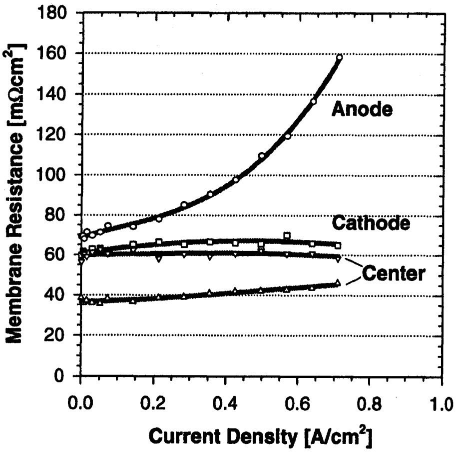

Figure 2 : Resistance of the individual N112 sheets, in a H_2/O_2 fuel cell (1-D) with 4 sheets, as function of current density at a cell temperature of 60 °C.

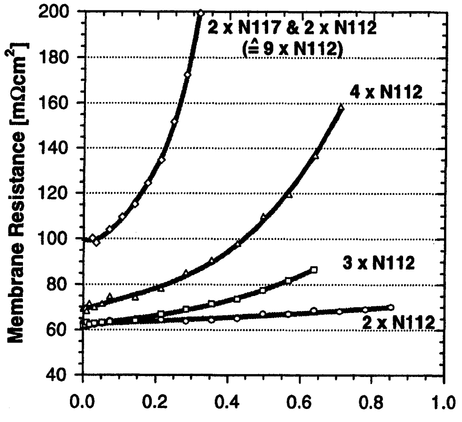

Figure 3 : Resistance of Anode side Nafion® 112 membrane sheet, in cells (1-D) with 2, 3, and 4 N112 membranes, and 2 N117 & 2 N112 membranes as function of current density. Cell temperature 60 °C.

A further indication that the difference is of geometric nature, is that the difference remains unchanged even after the cell has been operated for a considerable time (3 hours) at zero current and humidified gases are fed on both sides. Due to this geometric uncertainties the resistance data do not provide accurate absolute resistance values of the individual membranes. However, changes in the resistance can be measured accurately and are significant.

The only significant resistance change, as function of current density, is observed for the anode side membrane. In fact, the entire increase of the resistance, observed for the fuel cell with 4 N112 membranes takes place within the anode side membrane. The resistance of the anode side membrane is increasing by more than a factor of 2 for the current density increase from 0 to 0.7 A/cm^2. The resistance of the other three membranes is not changing significantly.

The observation that the resistance is confined to anode side is valid for all multi-membrane cells measured (2, 3, 4 x N112). However, as expected from the thickness-dependence of the resistance increase in Figure 1 and as shown in Figure 3 (resistance of anode side membranes in cells with 2, 3, and 4 N112 membranes, and 2 N117 & 2 N112 membranes), the extent of the increase is a function of total membrane thickness. The thicker the total membrane in the fuel cell, the stronger is the increase in resistance observed at the anode side.

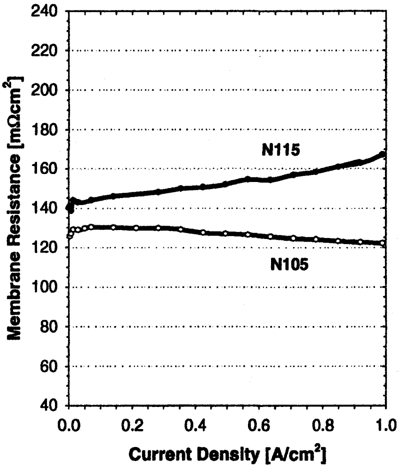

Figure 4 : Resistance of N115 and N105 membranes in H_2/O_2 fuel cell (1-D) as function of current density at 60 °C.

Figure 4 shows the membrane resistance as function of current density for the N115 and N105 membranes. The two membranes have approximately the same thickness (148μm and 155 μm, respectively) but due to the lower equivalent weight, N105 has a considerably higher water content after swelling in water of λ(N105) = 25 - 26 vs. λ(N115) = 21 - 22. Due to the higher water content N105 has a lower protonic resistance at zero current, r_{N105}= 130 mΩcm^2 and r_{N115}= 145 mΩcm^2 at 60 °C. From these resistances membrane water contents of λ(N105) = 21 - 22 and λ(N115) = 13 - 15 respectively may be calculated by comparison to *ex-situ* measurements [9]. No increase of the membrane resistance is observed for N105 up to 1.0 A/cm^2. The small decrease in resistance with current density is attributed to an increase in cell temperature at the higher current densities.

The above observations of the dependence of the membrane resistance as function of current density on the membrane thickness and on the equivalent weight may be explained by the following hypothesis : The transport of water back to the anode is the limiting mechanism of water transport in the membrane. Therefore in thicker membranes the anode needs to dry more (having a higher resistance) to provoke a sufficient water gradient for the transport of water back to the anode in the steady state.

For the transport of water back to the anode two mechanisms are possible : (i) solution-diffusion [10-13] and (ii) convection [19]. The steep gradients in water concentration at the anode side of the membrane and the dependence on the equivalent weight (which is in fact a dependence on the water content of the membrane) require a model in which the water transport is strongly dependent on the local membrane hydration. This is true for the model based on convection of water in the nano-pores of Nafion® and D'Arcy's law [19]. The solution-diffusion models do not predict the observed phenomena correctly. If the experimental results would have to be explained by diffusion, then the water diffuison coefficient D_{H2O}, needed to be strongly dependent on λ as reported i.e. in [17]. But this dependence is not implemented in the diffusion models.

Quasi 2-Dimensional Cell

In cells with a gas flow field, in which the gases flow along a channel along the surface of the electrode backing, volume flow, temperature and humidity of the gases vary along the flow path. Therefore differences in membrane hydration also occur with respect to the *in-plane* location of the MEA. With respect to the width of the channel the parameters in the MEA is assumed to be homogenous, therefore the cell is quasi 2-D.

The membrane resistance of a cell with two Nafion® 117 membranes was measured at the gas-inlets and gas-outlets as shown in the upper part of Figure 5. In case both gases are humidified to a dew-point which is at least as high as the cell temperature, the MEA is in a well humidified condition. As shown in the lower part of Figure 5, the hydration of the anode and cathode side membranes are similar at both ends of the channel when no current is drawn form the cell. A constant membrane hydration of approximately 12 -14 H_2O/SO_3H is calculated from the resistance measurements. When a current of 0.5 A/cm^2 is drawn from the cell, then the anode side membrane is drying and an average water content of 8-9 H_2O/SO_3H is observed. At the cathode side of the membrane no changes in hydration are detected. No significant differences of the membrane hydration between the gas-inlets and gas-outlets are observed, indicating, that the membrane hydration is uniform over the entire active area under these well humidified conditions.

When oxygen is fed dry at a volumetric flow rate (stoich.(O_2)=10) which is representative for operation with air, then a more complex membrane hydration behavior may be observed, as shown in Figure 6. At the ending of the channel, where oxygen is entering dry, the membrane at the cathode side is dry ($\lambda \approx 6$). The anode side membrane in this location however is well humidified ($\lambda \approx 20$). Probably because of the strong water gradient across the membrane, water is diffusing readily into the anode side membrane from the hydrogen gas phase. At the other end of the channel humidified hydrogen is entering and the oxygen has become humid due to the product water. Therefore at this end of the channel the difference in membrane water content is less.

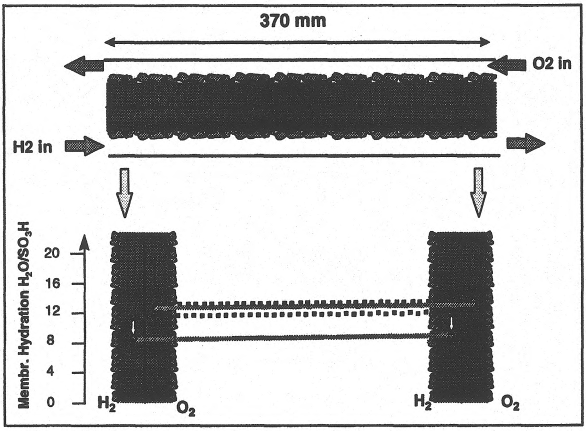

Figure 5 : Top : Schematic drawing of measurement of membrane hydration at two different in-plane locations. Bottom : Profile of hydration of the anode and cathode side membranes along the channel (dotted line at 0 A/cm^2; solid line at 0.5 A/cm^2) at T_{cell} = 60 °C, hydrogen and oxygen humidified at 80 °C. Stoich.(O_2) =10, stoich.(H_2) =6.

Again when current is drawn from the cell the major change is observed in the anode side membrane, which becomes dryer as observed in the 1-D cell and in Figure 5.

This experiment shows clearly, that when the cell is operated with dry oxygen and as a consequence the membrane is not in a well humidified condition, then gradients of membrane hydration across the active area evolve.

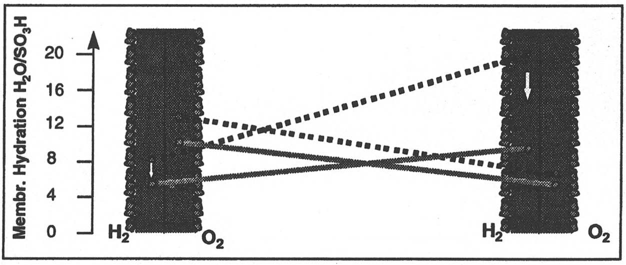

Figure 6 : Profile of hydration of the anode and cathode side membranes along the channel length (dotted line at 0 A/cm^2; solid line at 0.5 A/cm^2) at T_{cell} = 60 °C, hydrogen humidified at 80 °C and oxygen dry. Stoich.(O_2) =10, stoich.(H_2) =6.

CONCLUSIONS

The resistance of Nafion® membranes in PEM fuel cells was investigated. Experiments with multiple membranes have shown that the resistance increase (and corresponding water loss) is confined to the anode side of the membrane when current is drawn from a well humidified cell. If the cell is well humidified, then the hydration of the membrane across the active area is uniform. However, in case the reactant gases are not fully humidified, then a complex water distribution in the membrane over the active area of the fuel cell is observed. The quantitative understanding of this observation will need more work of locally resolved resistance measurements within the active area of the cell.

ACKNOWLEDGMENT

Financial support from the Swiss Federal Office of Education and Science (BBW) for this work, carried out under the program "2nd Generation SPFC" of the EU-research program "Joule III" is gratefully acknowledged.

REFERENCES

[1] A. J. Appleby, F. R. Foulkes, Fuel Cell Handbook, Van Nostrand Reinhold, New York (1989)

[2] T. D. Gierke, G. E. Munn, and F. C. Wilson, J. Polym. Sci. Polym. Phys. Ed., 19, 1687 (1981)

[3] T. A. Zawodzinski, Jr., C. Derouin, S. Radzinski. R. J. Sherman, V. T. Smith, T. E. Springer, and S. Gottesfeld, J. Electrochem. Soc., 140, 1041 (1993) -1047

[4] K.K. Pushpa, D. Nandan, R. M. Iyer, J. Chem. Soc., Faraday Trans 1, 84, 2047 (1988) -2056

[5] J. T. Hinatsu, M. Mizuhata, H. Takenada, J. Electrochem. Soc., 141, 1493 (1994) - 1497

[6] T. A. Zawodzinski Jr.,M. Neeman, L. O. Sillerud, S. Gottesfeld, J. Phys. Chem., 95, 6040 (1991) -6044

[7] J. Halim, F.N. Büchi, O. Haas, M. Stamm, G.G. Scherer, Electrochim. Acta, 38, 1303 (1994)

[8] K. Uosaki, K. Okazaki, H. Kita, J. Electroanal. Chem., 287, 163 (1990) -169

[9] J. Huslage, F.N. Büchi, G.G. Scherer, Extended Abstracts, 9th International Conferece on Solid State Protonic Conductors, Bled, 1998, p. 209

[10] T. V. Nguyen, R. E. White, J. Electrochem. Soc., 140, 2178 (1993)

[11] T. F. Fuller, J. Newman, J. Electrochem. Soc., 140, 1218 (1993)

[12] D. M. Bernardi, M. Verbrugge, J. Electrochem. Soc., 139, 2477 (1992)

[13] T. E. Springer, T. A. Zawodzinski, S. Gottesfeld, J. Electrochem. Soc., 138, 2234 (1991)

[14] F. N. Büchi, G. G. Scherer, J. Electroanal. Chem., 1996, 404, 37

[15] M. Watanabe, H. Igarashi, H. Uchida, and F. Hirasawa, J. Electroanal. Chem., 399, 239 (1995)

[16] R.J. Bellows, M.Y. Lin, M. Arif, and D. Jacobson, Extended Abstract No. 962, 191st Meeting of the Electrochemical Soc., Paris 1997

[17] F. N. Büchi, A. Marek, and G. G. Scherer, J. Electrochem. Soc., 1995, 142, 1895

[18] T. A. Zawodzinski Jr., T. E. Springer, J. Davey, R. Jestel, C. Lopez, J. Valerio, and S. Gottesfeld, J. Electrochem. Soc., 140, 1981 (1993)

[19] M. Eickerling, Yu. I. Kharkats, A.A. Kornyshev, and Yu. I. Volfkovich, J. Electrochem. Soc., 145, 2684 (1998)

Proton_Conducting_Membrane_Fuel_Cells_II, PV 1998-27, 81-90 (1998)
DOI: 10.1149/199827.0081PV © The Electrochemical Society

HIGH TEMPERATURE POLYMER ELECTROLYTE FUEL CELLS

R. F. Savinell, J.S. Wainright and M. Litt
Ernest B. Yeager Center for Electrochemical Sciences
Case Western Reserve University
Cleveland, Ohio 44106

ABSTRACT

Recently, we reported the use of phosphoric acid-doped polybenzimidazole (PBI) membrane as a solid polymer electrolyte for fuel cell applications. The advantages of PBI include: (i), good protonic conductivity at elevated temperatures; (ii), near zero electro-osmotic drag, which means that the proton transport through the PBI membrane does not involve water transport, (iii), low gas permeability, and (iv) low methanol crossover. The purpose of this paper is to present details of polymer processing and methods used to cast acid doped PBI films. Also, we will report and compare the electrical and mechanical properties of these films. A second PBI-like polymer synthesized in our laboratory is introduced with some preliminary characterization that indicates promise for fuel cell applications.

INTRODUCTION

In recent years there has been intense research interest in the development of proton electrolyte membrane (PEM) fuel cells for transportation and portable power applications. Typically, the polymer electrolyte used is a hydrated perfluorosulfonic acid polymer. This type of polymer requires water for proton conductivity; therefore operating temperature is limited to below the boiling point of water. The maximum conductivity of Nafion occurs at about 80 °C at atmospheric pressure. Fuel cell operation at high current densities is complicated by the water drag accompanying proton transport. A water transport imbalance results, leading to dehydration near the anode and cathode flooding with liquid water.

A high temperature polymer electrolyte, which conducts protons with low water content, should ameliorate the water balance problem. There is also increasing interest in the development of a direct methanol/oxygen polymer electrolyte fuel cell [1-4]. The use of methanol as a fuel has several advantages as compared to hydrogen. Methanol is a liquid fuel available at low cost that can be easily handled, stored, and transported. Fuel cell operation at temperatures above 80°C will improve electrode kinetics, improve tolerance to catalyst poisons, and may reduce fuel crossover. A polymer capable of proton conduction at 200 °C opens up the possibility of directly coupling endothermic methanol reforming with the exothermic fuel cell. This could lead to efficient energy integration and reduce size and complexity of the overall fuel cell system. For example, consider a 10% excess over stoichiometric feed of a 50:50 by mole mixture of liquid methanol and water fed to a reformer/fuel cell combination operating at 200 °C. Assuming a fuel cell electrical efficiency of 40%, energy balance calculations show that 10% of the energy in methanol will be utilized in the reformer, 22% will be used to preheat and vaporize the feed streams, and 28% will need to be rejected as waste heat.

A high temperature PEM fuel cell will assist in simplifying fuel cell systems designed to operate on higher molecular weight fuels as well. Tolerance to relatively high CO levels (on the order of mole percents) will reduce the need for extensive prox CO clean-up and other polishing reactor schemes. An example is shown in Figure 1 for a PBI (see below) fuel cell with platinum catalysts operated at 150 °C with 1 % CO in H_2 as the fuel. The excess overpotential of the hydrogen anode is only about 5 mV as compared to operation on pure H_2. Low platinum loading anodes, comparable to those of Nafion PEM fuel cells with high platinum utilization, give excellent performance in the presence of CO at the higher temperatures.

Recently, we reported the use of phosphoric acid-doped polybenzimidazole (PBI) membrane as a solid polymer electrolyte for fuel cell applications [5]. The advantages of PBI include: (i), good protonic conductivity at elevated temperatures; (ii), near zero electro-osmotic drag, which means that the proton transport through the PBI membrane does not involve water transport, (iii), low gas permeability, and (iv) low methanol crossover. In addition, it was shown that acid doped PBI membrane exhibits excellent oxidative and thermal stability [6], and good mechanical flexibility at elevated temperature (200°C) [7]. These properties of PBI membranes offer excellent prospects for the application of acid-doped PBI membranes as a superior polymer electrolyte in fuel cells. The demonstration of PBI in an H_2/O_2 fuel cell [8] and a methanol/O_2 fuel cell [9] have been reported.

The purpose of this paper is to present details of polymer processing and methods used to cast acid doped PBI films. Also, we will report and compare the electrical and mechanical properties of these films. A second PBI-like polymer synthesized in our laboratory is introduced with some preliminary characterization that indicates promise for fuel cell applications.

EXPERIMENTAL RESULTS AND DISCUSSION

PBI Powder and Acid Doping

Polybenzimidazole (PBI) is commercially manufactured by Hoechst-Celanese with primary use in fabrics for fire protection clothing. The polymer is high temperature resistant and is chemically stable. It has a glass transition temperature of about 450 °C because of its all aromatic structure. The benzimidazole group has a pKa of about 5.5, which facilitates its absorption of acid, which can act as a plasticizer. The structure of PBI is shown below in Figure 2.

PBI polymer can be synthesized with a broad range of molecular weights, as shown in Table 1. One measurement often used to characterize the molecular weight of a polymer in the inherent viscosity (I.V.). The I.V. is found by measuring the viscosity of a 0.5 wt% solution of the polymer dissolved in a solvent (concentrated sulfuric acid for PBI). The equation for calculating the I.V. is given below:

$$\text{I.V.} = \frac{\ln\,(\text{viscosity of the solution/viscosity of the solvent})}{(\text{solution concentration in g/dL})}$$

Table 1 shows the I.V. and molecular weight distribution for low, medium, and high molecular weight polymer. The low molecular weight material was purchased from Aldrich Co. The material normally available from Hoechst-Celanese is the medium molecular weight with an I.V. of about 0.7, but some high molecular weight material with an I.V. of about 0.91 has been made available to us. As will be shown later, high molecular weight material is necessary for good mechanical properties following film formation. As it turns out, the I.V. = 0.3 material could not be made into free-standing films. Our understanding is that the high I.V. material is currently a byproduct in PBI manufacturing, but could be the primary product via process adjustments.

Table 1: Characteristics of Commercially Available PBI

Molecular Weight and Inherent Viscosity				
Polymer	I.V. dL/g	M_n	M_w	MWD (M_w/M_n)
Low	0.3	6700	11200	1.7
Medium	0.68	18000	27200	1.5
High	0.97	26300	50300	1.9
all i.V. values for 0.5 wt% solution in sulfuric acid				

In order to increase the average molecular weight of polymer for high quality films, the lower MW components can be extracted by fractionation in dimethyl acetamide (DMAc). Typical extraction results for the yield of undissolved polymer are shown in Table 2. For example, when material initially having an I.V. = 0.91 is extracted at 94 °C, a yield of 69% of the original material is obtained. The I.V. of the extracted material has been increased to 1.14. The yield decreases as the average molecular weight of the material after extraction increases. The yield of these high I.V. fractions would be significantly less for a starting material of 0.71 I.V.

Table 2: PBI Extraction Results using DMAc
Initial I.V. = 0.91

Trial	Fractionation Temperature °C	Yield (%) of undissolved polymer	I.V. (dL/g) of undissolved polymer
A	94	69	1.14
B	110	53	1.19
C	130	41	1.28
D	160	23	1.42

Due to the basic nature of the benzimidazole group, PBI readily absorbs acid. Oxo-acids are required to achieve proton conductivities commensurate with fuel cell operation. Sulfuric acid was originally investigated, but poor film mechanical properties led us to consider phosphoric acid. However, further investigation with different I.V. materials and casting methods may warrant another look at this system. P^{31} NMR indicates that the first two phosphoric acids per repeat unit protonate the two benzimidazole groups, as shown in Figure 3. However, additional phosphoric acid is needed for high levels of conductivity. The additional phosphoric acid is more weakly tied into the PBI structure, but relatively immobile. Still the polymer-acid system is single-phase.

Film Forming Methods and Film Properties

In Figure 4 a schematic of two methods that were investigated for forming films of PBI with phosphoric acid is shown. In the first method, the polymer is dissolved in DMAc and 1-2 wt% LiCl is added to maintain solution stability. A film is cast onto a glass plate, the solvent is evaporated, and then the film is washed in boiling water to remove the residual LiCl. Doping of the film is accomplished by immersion in phosphoric acid solutions. The molarity of the acid determines the final acid loading in the membrane. For example, immersion in 5M acid solution gives a doping level of about 3 moles of acid per PBI repeat unit (this is called 300 mol% doping level). This technique yields a maximum doping level of 520 mol% phosphoric acid by immersion in 11M acid solution.

In the second method, PBI and acid are directly cast together from a co-solvent, trifluoroacetic acid (TFA). The solvent is evaporated and the film is ready for use. Even though the compositions are similar, the properties of the film formed by this process are substantially different than those formed by the DMAc method.

The mechanical properties of DMAc cast films are compared to TFA cast films in Table 3. Films formed by the DMAc casting method are normally stronger and tougher. The TFA films require a polymer of higher I.V. in order to generate films of reasonable strength. The TFA films have much more crystallinity as compared to the DMAc films, and the surface texture is different. The TFA films are more rubbery and softer.

Table 3: Comparison of Mechanical Properties of DMAc and TFA Films

	DMAc Cast, IV = 1.0		TFA Cast, IV = 0.91	
	Modulus 10^9 Pa	Toughness 10^6 Pa	Modulus 10^9 Pa	Toughness 10^6 Pa
Dry	1.94	105.0	1.27	50
doped 100 mol% H_3PO_4	3.53	48.5	1.88	35

In the case of TFA films, the toughness of the acid free polymer increases to about 150 MPa for 1.42 I.V. material as compared to 50 for 0.91 I.V. material. The addition of 50 mol% phosphoric acid drops the toughness to about 100. As acid concentration increases, the toughness increases because of ionic bonding to a maximum value of about 140 MPa. However, once the acid concentration exceeds 200 mol% the excess acid acts as a plasticizer and the toughness decreases (e.g. it drops to about 70 MPa with 500 mol% acid).

Although the mechanical properties of the TFA cast films are not as good as the DMAc cast films, the method of casting is simpler and as shown in Figure 5, the proton conductivity is greater. The proton conductivity of TFA films under dry conditions and temperatures exceeding 180 °C is greater than that of Nafion (for Nafion's optimum operating conditions of 100% RH, 80 °C).

Several techniques have been used to measure the methanol permeability across PBI films [9,10,11]. These techniques include closed receiving volume membrane diffusion cells, limiting current methods, and mass spectroscopy methods. All techniques gave similar results. The crossover equivalent current (50 mol% of methanol in vapor feed at 1 atm pressure) for DMAc cast film is about 5-10 mA/cm^2, which is a factor of 10-20 times less than that reported for Nafion 117. For TFA cast films, the crossover is larger by a factor of 3, but still considerably less than Nafion 117. Of course, the low crossover is reasonable considering that the methanol activity is low in the gas phase at high temperatures and that PBI is a homogeneous system.

Poly (2,5-benzimidazole) (AB-PBI)

AB-PBI is the second PBI-type polymer investigated at CWRU. The polymer is relatively simple to synthesize by a condensation reaction. Figure 6 shows the synthesis route and the chemical structure of the AB-PBI repeat unit. The presence of polyphosphoric acid scavenges the water produced and helps to form high molecular weight material, as shown below in Table 5. Although the DABA starting material is available commercially, purification is critical for high molecular weight polymer. The highest I.V. we have obtained is 7.1 and the preferred reaction conditions were 200 °C for 2 hours with DABA/P_2O_5/H_3PO_4 of 1/7/3.22. (an I.V. of 4.1 corresponds to a M.W. of 71,000.) Reports in the literature indicate that much higher molecular weights are achievable (I.V. up to 12-25). Thermogravimetric (TGA) measurements indicate stability at temperatures below 600 C in an inert atmosphere.

Table 5: Effect of excess phosphoric acid on AB-PBI molecular weight synthesis at 160 °C

Excess P_2O_5, %	I.V. of a 0.5 wt% solution
50	0.84
150	1.28
300	3.31

Doping of acid into AB-PBI is accomplished by submersion into phosphoric acid solution. The mechanical properties of the resulting films are given in Table 6. By drying the film at 140 °C before submersion, a higher doping level can be achieved. Annealing the doped film at temperatures of 150 °C improves film strength to levels about that of PBI/TFA films. We expect better film properties with higher molecular weight material. A remarkable property of this material is the amount of strain before break. Some films have been stretched by a factor of 10 before breaking. Thus the toughness of the AB-PBI films is ca. 100X greater than that of PBI films we have cast.

Table 6 : Mechanical properties of acid doped AB-PBI

Soln. H_3PO_4 molar	H_3PO_4/Repeat	Annealing Temp.C	Modulus Gpa	Strain at Break,%
0	0	25	1.47	256
3	1.29	25	1.77	161
6	1.79	25	.25	437
6*	3.29	25	.069	872
"	"	100	.33	767
"	"	150	1.75	548

* Film dried at 140 C before acid doping

I.V. = 4.27, Measurements at 25 C

The conductivity of AB-PBI was measured in one atmosphere water pressure in the temperature range of 150-200 C. The results are given in Table 7 and it should be noted that temperature effects were not significant. The conductivity of AB-PBI is greater than that of the PBI/DMAc films and nearly equivalent to that of PBI films cast from TFA. To compare acid loadings, a value of 1.3 Acid/Repeat in AB-PBI is equivalent to 2.6 Acid/Repeat in PBI.

Table 7: Conductivity of AB-PBI at 150-200 °C, one atmosphere water pressure

H_3PO_4/Repeat	Conductivity, S/cm
1.3	.022
2.5	.05
3.29	.086

AB-PBI is an attractive polymer for fuel cell applications considering its high conductivity, its good mechanical properties for film formation, and its ease and control of synthesis. We have only begun to develop the PBI-type polymers for fuel cell applications. Further work is needed to understand the conduction mechanism and to optimize the properties for film formation and electrode attachment. These polymers may also find other applications. Some examples include sensors and electrochemical reactors for destruction of toxic volatile organic compounds, among others.

ACKNOWLEDGEMENTS

This work was supported under a University Research Initiate Grant from the Defense Advanced Research Projects Agency, ONR Grant #N00014-92-J-1848.

REFERENCES

1. X. Ren, M. S. Wilson, and S. Gottesfeld, *J. Electrochem. Soc.*, **143**, L12, (1996)
2. D. Maricle and B. L. Murach, *Ext. Abstract* No 478, 187th Electrochemical Society Meeting, Reno, NV, May 21-26, 1995.
3. J. A. Kosek, C. Cropley, G. Wilson and A. B. LaConti, *Ext. Abstract* No 479, 187th Electrochemical Society Meeting, Reno, NV, May 21-26, 1995.
4. S. Surampudi, S. R. Narayanan, E. Vamos, H. Frank, G. Halpert, A. Laconti, J. Kosek, G. K. Surya Prakash, and G. A. Olah, *J. Power Sources,* **47**, 377, (1994).
5. J. S. Wainright, J. T. Wang, D. Weng, R. F. Savinell, and M. Litt, *J. Electrochem. Soc.*, **142**, L121 (1995).
6. S. R. Samms, S. Wasmus, and R. F. Savinell, *J. Electrochem. Soc.*, **143**, 1225, (1996).
7. H. Moaddel, Ph.D. Thesis, Case Western Reserve University, Cleveland OH, 1996.
8. J-T. Wang, R. F. Savinell, J. S. Wainright, M. Litt, and H. Yu, *Electrochim. Acta,* **41** , 193, (1996).
9. J. T. Wang, J. Wainright, R. F. Savinell and M. Litt, *J. Appl. Electrochem.*, **26**, 751, (1996).
10. J-T. Wang, S. Wasmus, and R. F. Savinell, *J. Electrochem. Soc.*, **143**, 1233, (1996).
11. D. Weng, Ph.D. Thesis, Case Western Reserve University, Cleveland OH, 1996.

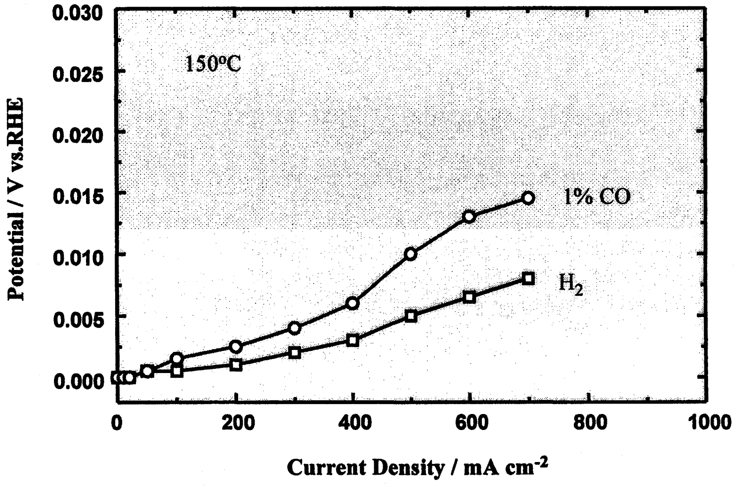

Figure 1: Effect of 1% CO on hydrogen anode performance at 150 C.

Electrode: 1mg/cm^2 Pt black. H_2 and H_2 w/ 1%CO , 1 atm, humidified at 65C.
Electrolyte: PBI/TFA membrane, 600 m/o H_3PO_4

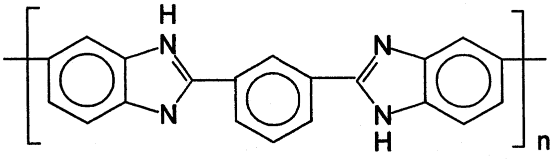

Figure 2: Chemical structure of the PBI repeat unit.

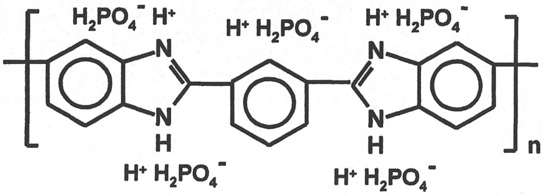

poly[2,2'-(m-phenylene)-5,5'-bibenzimidazole

Figure 3: Five phosphoric acids per PBI repeat unit.

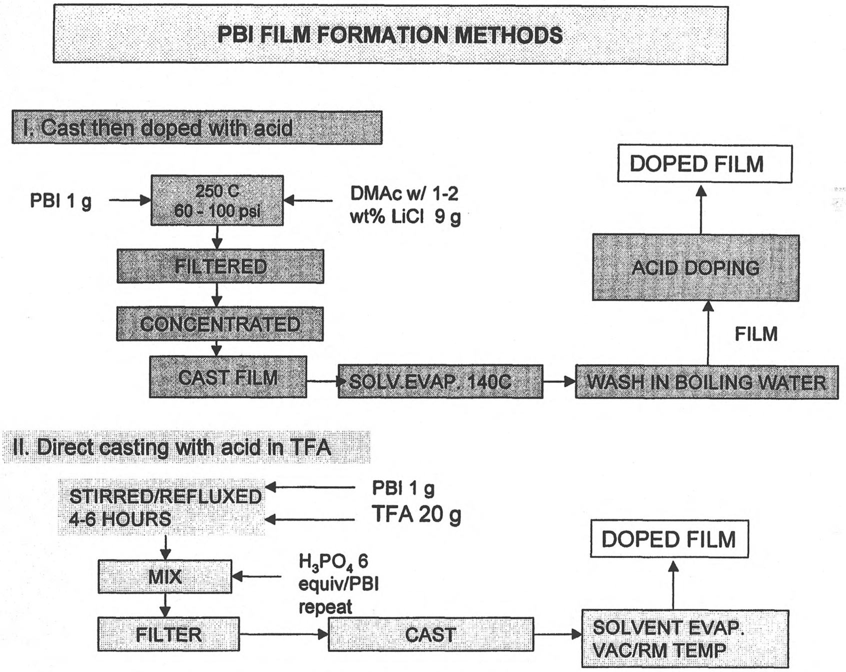

Figure 4: Schematics of two methods to cast PBI films.

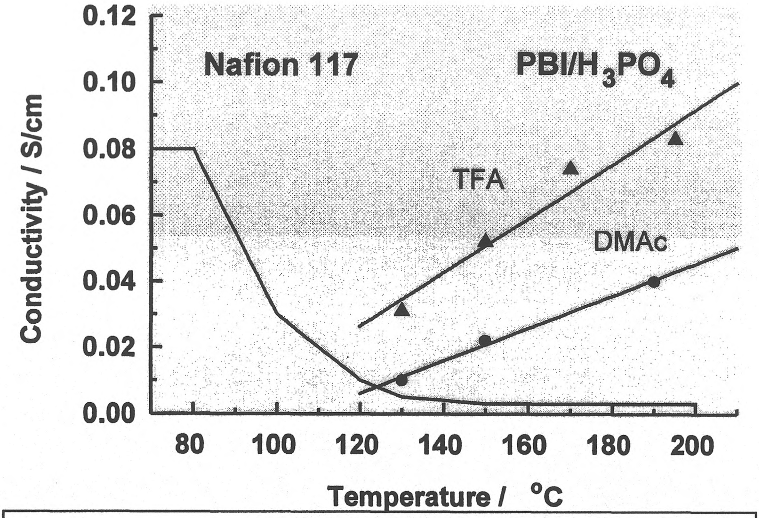

Figure 5: Measured conductivity of PBI doped with 600 m% phosphoric acid for two casting methods as compared to Nafion 117 at 1 atm pressure and .5 atm water partial pressure.

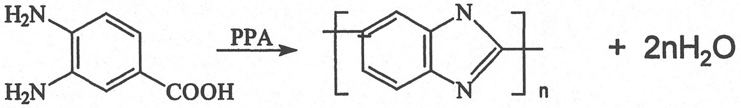

3,4 diaminobenzoic Acid (DABA)
Purified

$$2\,H_2O + P_2O_5 \longrightarrow H_4P_2O_7$$

Figure 6: Synthesis route for ABPBI.

Proton_Conducting_Membrane_Fuel_Cells_II, PV 1998-27, 91-98 (1998)
DOI: 10.1149/199827.0091PV © The Electrochemical Society

SYNTHESISOF CERAMICS/POLYMERNANOCOMPOSITESPROTONIC CONDUCTINGMEMBRANEFOR FUELCELLS APPLICATION

I. HONMA, *S. HIRAKAWA and **J.M. Bae

Energy Division, Electrotechnical Laboratory, AIST, Tsukuba, Ibaraki, 305, Japan,
*Tokyo University of Agriculture and Technology, Koganei, Tokyo, Japan,
**New Energy and Industrial Technology Development Organization (NEDO), Japan

ABSTRACT

High temperature protonic conducting polymer membrane provides new technological applications in the electrochemical devices including electrochromic displays, chemical sensors, fuel cells and others. Organic/inorganic nanocomposites membrane consists of SiO_2 /PEO (Polyethylene Oxides) hybrid are remarkable family of isotropic, amorphous polymer materials, which has been synthesized through sol-gel processes. The hybrid membrane doped with acidic surfactant molecules shows good protonic conductivities at high temperatures above 100C. The membrane was found to be thermally stable at high temperatures because of the inorganic SiO_2 framework in the composites matrix.

INTRODUCTION

Organic/inorganic composite materials are remarkable family of isotropic, amorphous nanocomposites materials, which has been investigated extensively for structural materials. The materials properties of thermal, electrical conductivities, mechanical strength, flexibility, optical density and corrosion toughness can be widely controlled by adjusting compositions, nanophase size, chemical bond between organics and inorganics. The protonic conductor has been studied for a large number of inorganic and polymer materials. A technological applications of those materials are quite promising in electrolytes and electrochemical cells, however, their use in devices are limited by numerous materials requirements.

In this paper, economic organic/inorganic nanocomposites membrane consists of SiO_2 / PEO (Polyethylene Oxides) composite has been synthesized through sol-gel processes. The composite membrane can be derived by hydrolysis and condensation reaction of polymer precursors consists of polyethylene oxides endcapped with triethoxysilane. The membrane doped with acidic surfactant molecules shows good protonic conductivities at high temperatures up to 160 ^{0}C and was found to be a flexible as well as thermally stable conducting polymer electrolyte for high temperature electrochemical devices. The structural stability and conductive properties at the elevated temperatures with various organic/inorganic as well as doping ratio have been investigated. The application to efficient fuel cells will be discussed in comparison to the Nafion membrane which has been widely used as protonic conducting solid polymer electrolytes for H_2 / 0_2 fuel cells.

EXPERIMENT

Synthesis of endcapped precursors for hybrids

Organic/inorganic hybrids membrane have been successfully produced by sol-gel process. Organic polymer of polyethylene oxide (PEO) and inorganic oxides of silica (silsesquioxane; Si_2O_3) have been used as structural element for producing hybrid membrane. The polyethylene oxides polymer (polyethylene glycol) with different molecular weight (200, 300, 400, 600, 2000) (Wako Pure Chemical), mixed with alkoxysilanes precursor of 3-isocyanatopropyltriethoxy silane) have been reacted in N_2 atmosphere at 70 ^oC with stirring. The endcapping reaction to form urethane coupling between two molecules was completed after 5 days aging. The organic/inorganic hybrid precursor was formed as a liquid form, which are easily processed to make large area membrane. The reaction scheme to make endcapped PEO precursors was shown in figure 1. The chain length of PEO; $(CH_2CH_2O)_n$ has been systematically changed as n=13 to 45, i.e., molecular weight, between two endcapping triethoxysilane ($-Si-(OR)_3$), which also controls organics/inorganics ratio. According to the previous studies, the structure of the hybrid membrane was composed of interpenetrated network of nano-sized mixture of silica and PEO phase, in which each silica domain has a distance of approximately 3 nm by chemically bound PEO chain. The structural characterization of the flexible organic/inorganic hybrid materials are studied elsewhere.

Hybrid film producing process

Although the hybrid precursor can form flexible, free-standing composite materials by itself, organo-alkoxysilane of MPH (monophenyltriethoxysilane, or monophenyltrimethoxysilane) were added to control chemical stability and structural flexibility of the membrane. The MPH, with acid catalysts, was hydrolyzed and condensed with the simultaneously hydrolyzing endcapped precursor to modify organic/inorganic hybrid precursors. The MPH was found to increase both chemical as well as thermal stability of the hybrid membrane, especially at elevated temperatures. The compositions of the MPH was changed from 0 % to 80 % by weight ratio with respect to endcapped PEO; the doping ratio η was given by

[η: doping % of MPH] = [MPH (weight)] / [MPH (weight) + PEO (weight)]

The η of 20% was found to be most flexibleand chemically stable composition for the hybrid membrane. The TG-DTA thermal analysis have shown that the decomposition of the membrane (PEO phase) starts from 300C, which indicates the thermal stability enhances enormously compared to bulky PEO polymer. This is probably due to the structural confinement of the PEO chain between the nano-sized silicate domain, which shift chemical as well as thermal stability of the polymer at the vicinity of the inorganic heterointerfaces. Segmental motion, geometrical relaxation and oxygen diffusion are blocked by steric hindrances of the neighboring silica domain. The hybrid membrane can be used for high temperature applications.

Proton conducting membrane

The protonic conductivity of the hybrid membrane was provided by incorporating acidic surfactant molecules such as MDP; monododecylphosphate in the polymer phase, that is PEO domain. The chemical structure of MDP was shown in figure 2. The MDP becomes proton donating molecules in the humidity conditions, where proton dissociates from alkyl-phosphate acid functions to form hydrated protons such as H_3O^+ and $H_5O_2^+$. The anionic alkyl-Phosphate of monododecylphosphate has large molecular size and weight by C_{12} chains, so that it can not diffuse in the polymer phase of the hybrid membrane. The protonic carrier transference number seems to be almost unity in the present case. The protonic carrier concentration is proportional to the MDP doping concentration and conductivity was measured as a function of doping rate.

Film casting

At first, monododecylphosphate THF solution was prepared as follows; MDP, monododecylphosphate (0.2 g) was dissolved in THF (0.2 g), the solution concentration of 1g MDP/g of THF, and mixed with isopropanol (2.0 g). Then, MPH, monophenyltrimethoxysilane was added with stirring. After completely mixed, alkoxysilane-endcapped PEO precursor was added to the above solution. The compositions of MPH/PEO was systematically changed from 0:10 to 8:2, (η = 0 % to 80%) while the total amount of MPH + PEO was kept constant at 2.0 g. When the molecular weight of PEO exceeds 2000, the mixed solution was heated and stirred at 60 C to melt solid PEO polymer. Finally, acidic catalyst of HCl solution (0.01 mol/mol of H_2O) was added, where 1 mol of total alkoxy groups in the precursors meet with 0.01 mol of HCl in 1 mol H_2O solution, and rapidly stirred for 30 seconds. The hydrolysis and condensation reaction of alkoxy silane starts immediately and solution becomes viscous with exothermic heat release. The solution was then casted into a polystyrene substrate and annealed at 60 C for 12 hours to form free-standing, transparent, and flexible membrane. The whole synthetic process was summarized in figure 3. The casted film are further annealed at 100 ^{O}C in N_2 atmosphere to fully polymerized silica network for better mechanical properties. The MDP doping concentration was systematically changed from 10% to 40% by weight ratio with respect to hybrid membrane, where the doping rate ξ was determined by

[ξ: doping % of MDP(weight)] = [MDP(weight)] / [MPH(weight) + PEO(weight)]

The continuous, flat, flexible hybrid membrane was synthesized for all of the MDP concentrations with their thickness of around 400 - 600 μm. At higher concentrations, a part of MDP molecules, which can not be incorporated, are segregated from the casted films, and covering on the membrane surface. Figure 4 shows the TG-DTA thermal analysis with heating rate of 20 ^{O}C/min. The MDP molecules in the membrane decomposes at 300 ^{O}C, followed by complete decomposition of PEO and ,thus, hybrid membrane at 350 ^{O}C. Additionally,there is unknown exothermic peak at 170 ^{O}C. The data suggests that the thermal stability of polymer PEO phase in the composites is highly enhanced by the nano-level confinement in the inorganic SiO_2 framework.

Electrode fabrications onto the hybrid membrane

The membranes were rinsed in a deionized water to remove unnecessary monododecylphosphate on the membrane surface for about six hours and dried in an ambient air. Symmetric electrodes were deposited on both sides of the membrane using a commercially available silver paste (VL-10, Tamura Seisakusho, Japan). The silver paste was tape-casted on the membrane surface and dried at 40 ^{O}C in an oven to form good electrical contact with proton conducting membrane.

Protonic conductivity measurements

Electrical conductivity of hybrid electrolyte membrane was measured by impedance spectroscopic method using a computer-aided frequency response analyzer (Solartron 1260) at frequency range 1Hz~2MHz at various temperatures and humidities. Humidity was controlled by gas bubbling at temperature controlled humidifier units and pressure was applied using needle valves and the total pressure was measured by digital manometers. Nitrogen and hydrogen of research grade were mixed to change partial hydrogen pressures of the cell. The relative humidity was controlled by changing humidifier temperature against cell temperature. The conductivities of membranes were measured in the typical frequency region (~10^4Hz) of relaxations for usual proton-conducting polymer electrolytes.

Results and discussions

Chemical species which comprised the membranes such as polyethylene oxide, silicates, and monododecyl phosphate are known as good insulators against electronic(and/or hole) conduction and their combination is understood to have a very low possibility for further electron/hole conduction. The electrical conduction of organic/inorganic hybrid membranes, therefore, is understandably due to the protonic conduction. The hybrid membrane can be regarded as a novel protonic conducting composite materials.

The protonic conductivities at higher temperatures are measured for different MPH, i.e., silica contents, and MDP concentrations. Figure 5 shows protonic conductivities of three different samples for (a) MPH 10 % / PEO 90 % with 40% doping of MDP, (b) MPH 10 % / PEO 90 % with 30% doping of MDP and (c) MPH 20% / PEO 80% with 20% doping of MDP. As a general tendency for three samples, the conductivity decreases with elevating cell temperature, but surprisingly, sample (c) has good protonic conductivity of the order of 10^{-4} S/cm at temperature range up to 160 ^{o}C. The humidifier temperature is always 10 ^{o}C lower than that of the measuring cell to keep sufficient H_2O partial pressure at constant whole pressure of 3 atm. According to the comparison of the conductivities among (a), (b) and the same membrane doped with 10% and 20% MDP, the increase of the protonic conductivity with MDP doping rate indicates the mobile protonic carriers are originated from MDP, the dissociation of proton from MDP molecules, and protonic carrier density increases with MDP concentrations. The result indicates that the hybrid membrane can be a good protonic conductor at higher temperatures, where other ionic conducting polymer membrane tend to become unstable at these higher temperatures. As a silica content increases, the thermal stability enhances.

Because of the hybrid membrane are consisted of inorganic silica as a part of structural elements, the materials can be a high temperature tolerant protonic conducting polymer membranes. The hybrid materials are designed to have nano-sized composites structure among organic PEO, inorganic silica and functionally doped with acidic surfactant molecules like MDP for the protonic conductivity. The novel properties of the hybrid membrane originated from a controlled mixture of polymer - silica - molecules at nano levels, where the flexibility of polymer, high temperature toughness of silica and protonic carriers of MDP are organically mixed in the composite to functionalize materials properties. The other type of polymer, inorganics and functional molecules can be conjugated to form novel ionic conducting hybrid membrane for electrochemical devices applications.

CONCLUSION

High temperature protonic conducting polymer membrane has been synthesized through the sol-gel processing of organic/inorganic nanocomposites consists of SiO_2 /PEO (Polyethylene Oxides) hybrid materials. The hybrid membrane doped with acidic surfactant molecules such as monododecylphosphates shows good protonic conductivities at high temperatures above 100 ^oC. The membrane was found to be thermally stable at high temperatures because of the temperature tolerant inorganic SiO_2 framework in the composites matrix. The protonic conductivities of 10^{-4} S/cm at 160 ^oC has been achieved at humidity condition. The organic/inorganic hybrid membrane can be identified as a remarkable family of proton conducting solid polymer electrolytes which, potentially, provides new technological applications in the high temperature electrochemical devices including electrochromic displays, chemical sensors, fuel cells and others.

REFERENCES

1. K.D.Kreuer, Solid State Ionics, 97, 1 (1997)
2. N.Ogata, Koubunnsi, 44, 72 (1995)
3. T.Scherban and A.S.Nowick, Solid State Ionics, 35, 189 (1989)
4. H.Iwahara, Solid State Ionics, 77, 289 (1995)
5. B.Gupta, F.N.Buchi and G.G.Scherer, Solid State Ionics, 61, 213 (1993)
6. K.D.Kreuer, A.Fuchs, M.Ise, M.Spaeth and J.Maier, ElectrochimicaActa, 43, 1281 (1998)
7. J.J.Fontanella, M.C.Wintersgill, J.S.Wainright, R.F.Savinell and M.Litt, ElectrochimicaActa, 43, 1289 (1998)
8. M.Nouel and P.S.Fedkin, ElectrochimicaActa, 43, 2381 (1998)
9. A.Kuver and K. P.-Kamloth, ElectrochimicaActa, 43, 2527 (1998)
10. J.J.Sumner, S.E.Creager, J.J.Ma and D.D.DesMarteau, J. Electrochem. Soc. 145, 107 (1998)
11. V.G.Ponomareva and G.V.Lavrova, Solid State Ionics, 106, 137 (1998)
12. T.Kobayashi, M.Rikukawa, K.Sanui and N.Ogata, Solid State Ionics, 106, 219 (1998)
13. E.Quartarone, P.Mustarelli and A.Magistris, Solid State Ionics, 110, 1 (1998)
14. G.G.Scherer, Solid State Ionics, 94, 249 (1997)
15. P.Staiti, S.Hocevar and N.Giordano, Int.J.Hydrogen Energy, 22, 809 (1997)
16. N.Giordano, P.Staiti, S.Hocevar and A.S.Arico, ElectrochimicaActa, 41, 397 (1996)
17. L.Depre, J.Kappel and M.Popall, ElectrochimicaActa, 43, 1301 (1998)
18. M.Popall and H.Durand, ElectrochimicaActa, 37, 1593 (1992)
19. F.Croce, G.B.Appetecchi, L.Persi and B.Scrosati, Nature, 394, 456 (1998)
20. G.R.Goward, F.Leroux and L.F.Nazar, ElectrochimicaActa, 43, 1307 (1998)
21. J-Y.Sanchez, A.Denoyelle and C.Poinsignon, Polymers for Adv. Technologies, 4, 99 (1993)

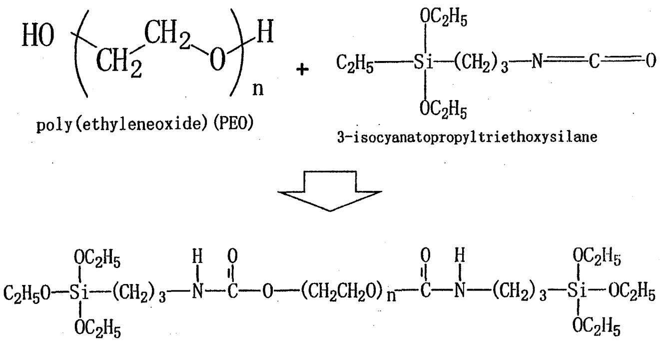

Figure 1 The endcapped precursor for hybrids was formed by reaction between polyethylene oxide (glycol) and 3-isocyanatopropyltriethoxy silane

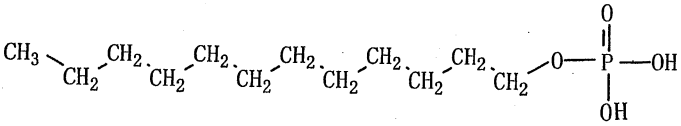

Figure 2 The chemical structure of acidic surfactant molecule, MDP; monododecylphosphate

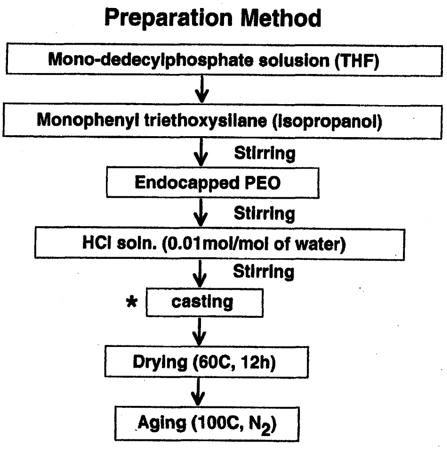

Figure 3 The synthetic procedure of organic/inorganichybrid membrane

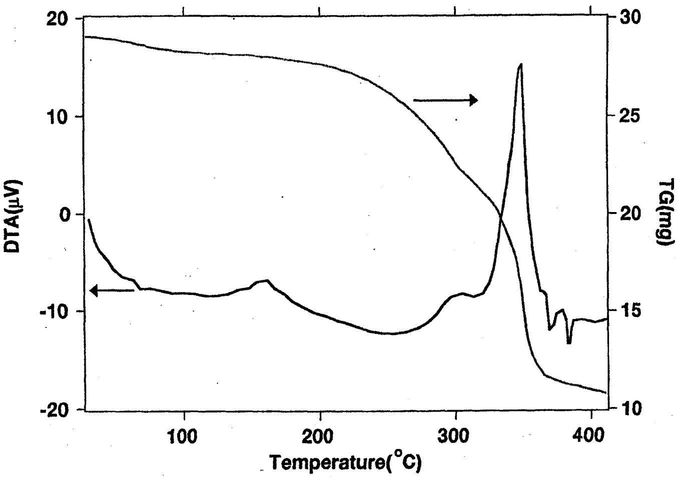

Figure 4 The TG-DTA thermal analysis of the proton conducting hybrid membrane with heating rate of 20 °C/min.

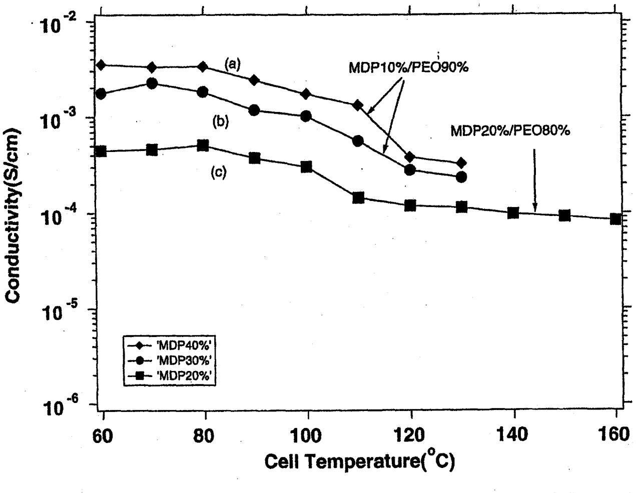

Figure 5 Protonic conductivities of three samples with different organic/inorganic ratio and MDP doping concentrations for (a) MPH 10%/PEO 90% with 40% doping of MDP, (b) MPH 10%/PEO 90% with 30% MDP and (c) MPH 20%/PEO 80% with 20% MDP, respectively.

Proton_Conducting_Membrane_Fuel_Cells_II, PV 1998-27, 99-105 (1998)
DOI: 10.1149/199827.0099PV © The Electrochemical Society

THEORETICAL STRUCTURES OF TRIFLIC ACID-WATER CLUSTERS AND THE MOLECULAR MECHANISM OF PROTON DISSOCIATION

Stephen J. Paddison,[1] Lawrence R. Pratt,[2] and Thomas A. Zawodzinski Jr.[1]

Materials Science and Technology Division[1] and Theoretical Division[2]
Los Alamos National Laboratory,
Los Alamos NM 87545,

Structural and energetic information required for recently proposed quasi-chemical theories of solution chemistry have been obtained for clusters of water with triflic acid, $CF_3SO_3H(H_2O)_n$ for n=1–6. Quantum mechanical calculations on the clusters indicate that the acid proton does not dissociate with n=1 or 2 hydrating water molecules, but does dissociate for n≥3 water molecule partners. The computed minimum energy structures indicate that both "Eigen" $\left(H_9O_4^+\right)$ (n=3,4,6) and "Zundel" $\left(H_5O_2^+\right)$ (n=5) structures are likely to play a role in the molecular mechanism of acid dissociation in Nafion®.

INTRODUCTION

Nafion® has been extensively studied for various applications (1-5). Of considerable current interest is the performance of this and related membrane materials in polymer electrolyte fuel cells. Transport of protons and water in these materials is a key factor in this application. We recently suggested (6,7) that the factors dominating transport in such systems are closely related to the local interactions of sulfonic acid moieties and solvating water molecules, especially the water molecules in the first solvation sphere around the sulfonic acid. Molecular level understanding of the structural and dynamic properties of this portion of Nafion®, which would permit optimized use of the membrane or the design of improved membranes, is currently unavailable.

The number of water molecules per head group has been long recognized as a significant operational parameter. The triflic (trifluoromethanesulfonic) acid molecule is a natural model for the side-chain hydrophilic 'head groups' in Nafion® (6-8). The molecular mechanism of proton dissociation from the sulfonic acid moiety is one essential part of a molecular understanding of the membrane. Focusing attention on the sub-process of proton dissociation, several theoretical ingredients will be required including structural, energetic, and kinetic information encompassing the participation of hydrating water molecules. Here we give results of large-scale electronic structure calculations on the triflic acid molecule with one through six water molecules that illuminate the requirements for the acid proton to dissociate from this highly acidic molecule.

Recently proposed quasi-chemical theories (9-11) provide a motivation for seeking this particular theoretical information. These theories establish a format in which to exploit chemical electronic structure computations to study solution chemistry. The idea is to use electronic structure computational tools to determine the equilibrium coefficients K_n for the formation of precisely defined complexes as

$$CF_3SO_3H + nH_2O \xleftrightarrow{K_n} CF_3SO_3H(H_2O)_n \qquad [1]$$

The K_n are familiar forms

$$K_n = \frac{\rho_{CF_3SO_3H(H_2O)_n}}{\rho_{CF_3SO_3H}\left(\rho_{H_2O}\right)^n} \qquad [2]$$

The ρ_α are number densities for α-molecules. The quasi-chemical approximations require these coefficients in the circumstances of an ideal gas, so that

$$K_n = K_n(T) = \frac{\left(q_{CF_3SO_3H(H_2O)_n}/V\right)}{\left(q_{CF_3SO_3H}/V\right)\left(q_{H_2O}/V\right)^n} \qquad [3]$$

where the q_α are molecule (or cluster) partition functions (12). Standard electronic structure packages such as the Gaussian package (13) can produce these coefficients within the harmonic approximation because they can compute molecular vibrational frequencies for the structures obtained. Moreover, the interactions involved in formation of these complexes are genuinely chemical. Electronic structure methods are appropriate and classical force-field models are currently not available. The adequacy of the harmonic approximation for these purposes has yet to be directly tested and the development of these approaches is in an early stage.

The fundamental thermodynamic parameter addressed by the quasi-chemical approximations is the chemical potential of the solute, here triflic acid. The interaction part of that chemical potential, the part due to interactions of the solute with hydrating water molecules, is then given by

$$\Delta\mu_{CF_3SO_3H} = -RT\ln\left[p_0\sum_{n=0}\tilde{K}_n\left(\rho_{H_2O}\right)^n\right] \qquad [4]$$

The $\tilde{K}_n$ indicates that extra-cluster contributions, due to the environment more distant than the near neighbor water molecules, must be eventually considered (11,14). The notational convention is $K_0 = 1$. p_0 is a probability describing the free energy required to prepare for the cluster, a cavity in the medium. This contribution is associated with packing effects and is expected from an external theory addressing these features [15-20]. Again, we emphasize that the practical adequacy of the current understanding of these additional features has not been directly tested in the present context and subsequent developments will have to focus on these requirements.

We also emphasize that this approach is constructive in style. Only a small number of terms in the series in Eq. [3] are expected to be significant; and the various contributions are well defined and physically natural. Therefore, we can take the attitude that several clear contributions need to be studied and effective descriptions of each contribution need to be secured. See also the relative work (21). Here we address an initial step of determining structures and energies of the complexes $CF_3SO_3H(H_2O)_n$, indicated in Eq. [1].

COMPUTATIONAL METHODS

The electronic structure calculations were carried-out with the GAUSSIAN 94 system of programs [13] using B3LYP density functional theory and the 6-31G** basis set. No *a priori* structural constraints were imposed so all structures presented below were fully optimized. However, particularly for the larger clusters, many local minima exist undoubtedly, some perhaps with similar energies. Each structure presented below is merely the lowest energy structure found in the present work. Corrections for basis set superposition effects were not considered.

RESULTS

Minimum energy structures found for the clusters $CF_3SO_3H(H_2O)_n$ with n=1,2,3 and n=4,5,6 are shown in Figures 1 and 2, respectively. The foremost point is that the acid proton remains associated with the sulfonic acid moiety for n=1 and 2. Three water molecules are required before a definitely dissociated acid proton is recognized in the lowest energy structure. For the simpler case of HCl (22), and for polystyrenesulfonic acid (23) also, the first water of hydration is not sufficient to stabilize an ion pair configuration. The experimental results for polystyrenesulfonic acid (23) indicate that the second water of hydration is sufficient to dissociate the acid proton.

The polystyrenesulfonic acid results also point to the importance of the $H_5O_2^+$ structure, the "Zundel" cation, for this proton dissociation mechanism. The present results suggest that the sufficiency of the second water molecule need not be universal. However, we emphasize that the results of Fig. 1 do not include any affects of a condensed phase environment.

In our results (Fig. 1), when the proton does separate from the acid with the third water molecule, the structure formed is highly suggestive of the "Eigen" cation, $H_9O_4^+$ (24). This could be due to the presence of the three sulfonate oxygen atoms in this particular special case.

The larger clusters (Fig. 2) show both "Eigen" (n=4 and 6) and "Zundel" (n=5) structural patterns associated with the additional proton. Thus, we anticipate that both of these structures should be involved in the fuller molecular description of acid dissociation in these materials.

Plotted in Fig. 3 are the incremental changes of the binding energies for the addition of a water molecule for the structures found. These binding energy increments do not vary monotonically with the size of the cluster; but the largest oscillations have a magnitude typical of hydrogen bonding energies, about 5 kcal/mol.

CONCLUSIONS

Structural and energetic information required for recently proposed quasi-chemical theories of solution chemistry have been obtained for clusters of water with triflic acid, $CF_3SO_3H(H_2O)_n$ for n=1–6. The cluster results indicate that the acid proton does not dissociate with either one or two hydrating water molecules, but does dissociate for n≥3 water molecule partners. The minimum energy structures found, indicate that both "Eigen" $(H_9O_4^+)$ (n=3,4,6) and "Zundel" $(H_5O_2^+)$ (n=5) structures are likely to play a role in the molecular mechanism of the acid dissociation in Nafion®.

ACKNOWLEDGEMENTS

The LDRD program at Los Alamos National Laboratory and the Department of Energy under contract W-7405-ENG-36 supported this work.

REFERENCES

1. G. A. Olah and J. Kaspi, J. Org. Chem. **42**, 4187 (1977).
2. H. S. White, J. Leddy, and A. J. Bard, J. Am. Chem. Soc., **104**, 4811 (1982).
3. G. Fortier, R. Beliveau, E. Leblond, and D. Belanger, Analyt. Lett., **23**, 1607 (1990).
4. R. Lemons, J. Power Sources, **29**, 251 (1990).
5. S. Gottesfeld and T. A. Zawodzinski, in Advances in Electrochemical Science and Engineering, R. C. Alkire, H. Gerischer, D. M. Kolb, and C.W. Tobias, Eds., Vol. 5, pp. 195-301 (1997).
6. S. J. Paddison and T. A. Zawodzinski, Jr., Solid State Ionics, in press.
7. S. J. Paddison, L. R. Pratt, and T. Zawodzinski, Jr., preprint (1998).
8. S. J. Paddison, L. R. Pratt, T. Zawodzinski, and D. W. Reagor, Fluid Phase Equilbrium, **150**, 235 (1998).
9. L. R. Pratt and R. A. LaViolette, Mol. Phys., **94**, 909 (1998).
10. R. L. Martin, P. J. Hay, and L. R. Pratt, J. Phys. Chem. A, **102**, 3565 (1998).
11. G. Hummer, L. R. Pratt, and A. E. García, J. Phys. Chem. A, in press.
12. D. A. McQuarrie, Statistical Mechanics, Harper & Row, New York, 1976. Chapter 9, and particularly Eq. 9-8.
13. M. J. Frisch, G. W. Trucks, H. B. Schlegel, P. M. W. Gill, B. G. Johnson, M. A. Robb, J. R. Cheeseman, T. A. Keith, G. A. Petersson, J. A. Montgomery, K. Raghavachari, M. A. Al-Laham, V. G. Zakrzewski, J. V. Ortiz, J. B. Foresman, J. Cioslowski, B. B. Stefanov, A. Nanayakkara, M. Challacombe, C.Y. Peng, P. Y. Ayala, W. Chen, M. W. Wong, J. L. Andres, E. S. Replogle, R. Gomperts, R. L. Martin, D. J. Fox, J. S. Binkley, D. J. Defrees, J. Baker, J. J. P. Stewart, M. Head-Gordon, C. Gonzalez, J. A. Pople, Gaussian 94 (Revision E.2), Gaussian, Inc., Pittsburgh, PA, (1995).
14. L. R. Pratt, G. J. Tawa, G. Hummer, A. E. García, and S. A. Corcelli, Int. J. Quant. Chem., **64**, 121 (1997).
15. G. Hummer, L. R. Pratt, and A. E. García, Proc. Natl. Acad. Sci. USA, **93**, 8951 (1996).
16. B. J. Berne, Proc. Natl. Acad. Sci. USA, **93**, 8800 (1996).
17. S. Garde, G. Hummer, A. E. García, M. E. Paulaitis, and L. R. Pratt, Phys. Rev. Letts. **77**, 4966 (1996).
18. G. Hummer, S. Garde, A. E. García, M. E. Paulaitis, and L. R. Pratt, Proc. Natl. Acad. Sci. USA, **95**, 1552 (1998).
19. L. R. Pratt, Hydrophobic Effects in The Encyclopedia of Computational Chemistry, P. v. R. Schleyer, N. L. Allinger, T. Clark, J. Gasteiger, P. A. Kollman, H. F. Schaefer III, P. R. Schriener, Editors, John Wiley & Sons, Chichester, (1998).
20. L. R. Pratt, S. Garde, and G. Hummer "Theories of Hydrophobic Effects and the Description of Free Volume in Complex Liquids," in New Approaches to Old and New Problems in Liquid State Theory: Inhomogeneous and Phase Separation in Simple, Complex and Quantum Fluids, proceedings fo the NATO Advanced Study Institute, in press, (1998). LA-UR-98-2712, http://xxx.lanl.gov/abs/physics/9806036.
21. J. R. Henderson, Phys. Rev. E, **55**, 5731 (1997).
22. K. Ando and J. T. Hynes, in Structure and Reactivity in Aqueous Solution, American Chemical Society Series, 568, p. 143, American Chemical Society, Washington D.C. (1994).
23. G. Zundel, Hydration and Intermolecular Interaction, p. 151, Academic Press, New York (1969).
24. M. Eigen, L. DeMaeyer, in The Structure of Electrolyte Solutions, p. 64, John Wiley & Sons, New York (1959).

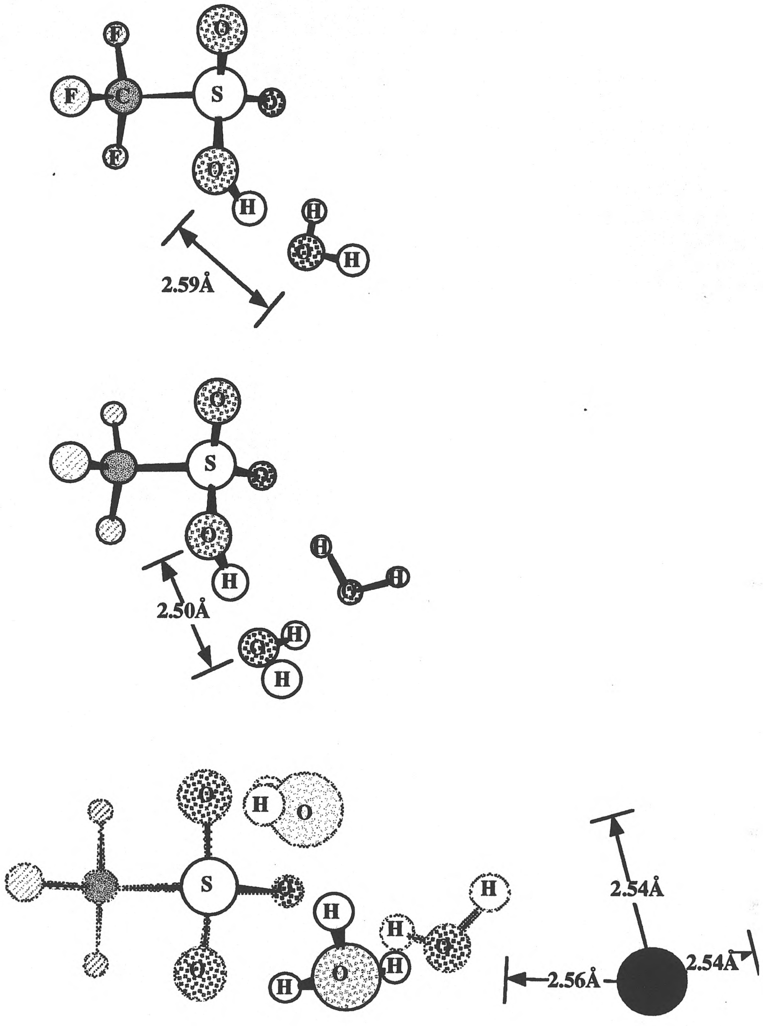

Figure 1: Minimum energy structures found for $CF_3SO_3H(H_2O)_n$ clusters for n=1 (top), n=2 (middle), and n=3 (bottom). Note that the acid proton doesn't dissociate from the sulfonic acid for n=1 and 2 but does dissociate for n=3. In the latter case, the ball and labeled arrows on the right show the distances of near neighbor oxygen atoms to the oxygen atom that bears the additional proton.

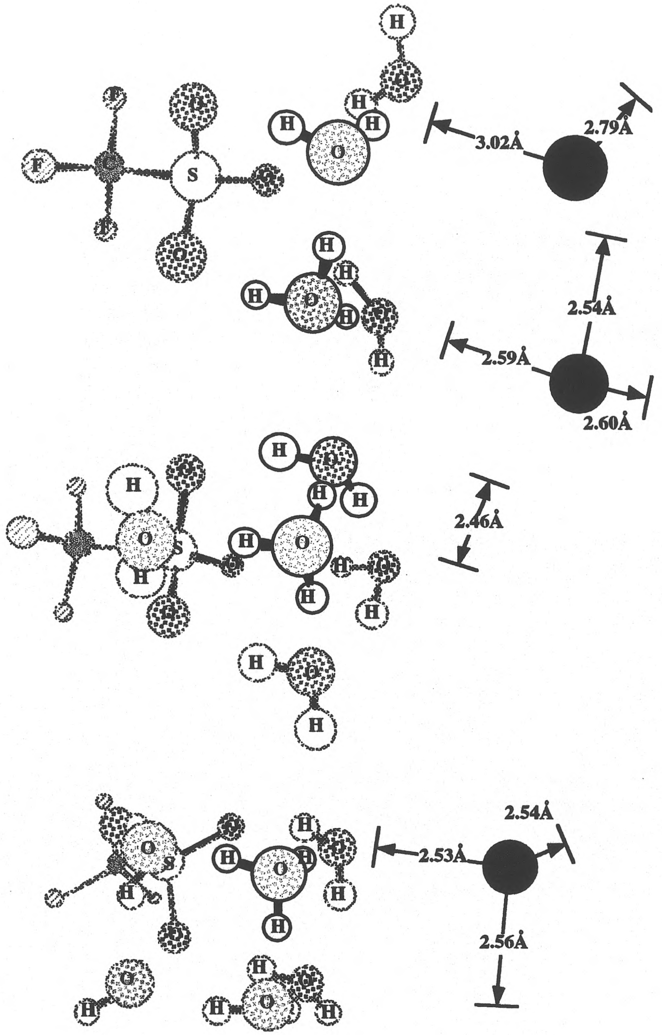

Figure 2: Minimum energy structures found for $CF_3SO_3H(H_2O)_n$ clusters for n=4 (top), n=5 (middle), and n=6 (bottom). The ball and labeled arrows on the right show the distances between interesting oxygen atom neighbors. The n=4 and 6 structures are "Eigen"-like and the n=5 structure is "Zundel"-like.

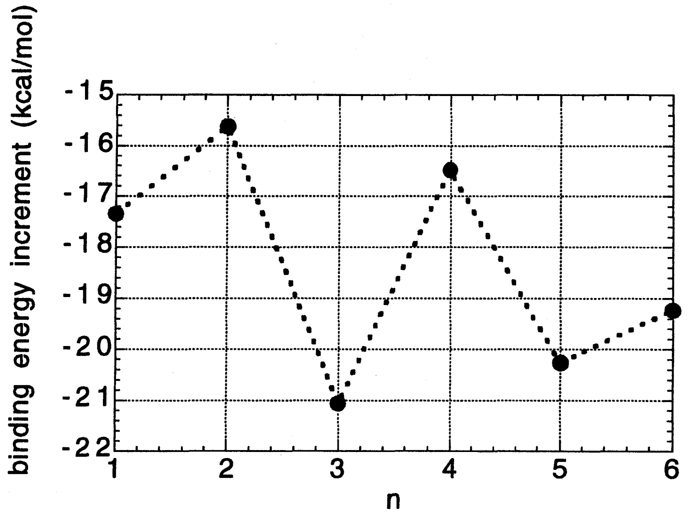

Figure 3: Incremental binding energies for the nth water molecule to form the structures of $CF_3SO_3H(H_2O)_n$. The overall magnitudes are in agreement with previous results of Refs. (1-3) and the largest oscillation has a magnitude similar in size to hydrogen bonding energies, about 5 kcal/mol.

Proton_Conducting_Membrane_Fuel_Cells_II, PV 1998-27, 106-120 (1998)
DOI: 10.1149/199827.0106PV © The Electrochemical Society

ION AND WATER TRANSPORT IN A NAFION® MEMBRANE PORE: A STATISTICAL MECHANICAL MODEL WITH MOLECULAR STRUCTURE

Stephen J. Paddison,[1] Reginald Paul,[2] and Thomas A. Zawodzinski Jr.[1]

[1]Electronic and Electrochemical Materials and Devices Group
Los Alamos National Laboratory,
Los Alamos, NM 87545

[2]Department of Chemistry
The University of Calgary
Calgary, Alberta, Canada T2N 1N4

With the well established importance of the coupling of water and protons through electroosmotic drag in operating PEFCs we present here a derivation of a mathematical model that focuses on the computation of the mobility of an hydronium ion through an arbitrary cylindrical pore of a PEM with a non-uniform charge distribution on the walls of the pore. The total Hamiltonian is derived for the hydronium ion as it moves through the hydrated pore and is effected by the net potential due to interaction with the solvent molecules and the pendant side chains. The corresponding probability density is derived through solution of the Liouville equation. This probability density is then used to compute the friction tensor for the hydronium ion. We find two types of contributions: (a) due to the solvent-ion interactions for which we adopt the conventional continuum model; (b) due to the interaction between the pendant charges and the hydronium ion. The latter is a new result and displays the role of the non-uniform nature of the charge distribution on the pore wall.

INTRODUCTION

Nafion®*, a perfluorosulfonic acid ionomer, continues to see application in fuel-cell systems because it exhibits good chemical stability, remarkable mechanical strength, good thermal stability, and high proton conductivity when sufficiently hydrated. Despite its use in polymer electrolyte fuel cells (PEFCs) and a hosts of other electrochemical devices, the mechanisms of ion and solvent transport in the membrane are incompletely understood. From the extensive experimental investigations (1-4) into proton and water transport within Nafion®, the following conclusions have been drawn: (a) the water self diffusion coefficient increases with increasing water content in the membrane; (b) the proton mobility (conductivity) increases with increasing hydration of the membrane; and (c) the electroosmotic drag coefficient (the number of water molecules associated with each proton) remains a constant value of 1 for membranes equilibrated with water vapor and jumps to values of between 2 and 3 for membranes immersed in liquid water. These observations strongly point to the importance of interactions of water and protons with the interfacial region of the membrane (specifically the pendant side chains terminating with sulfonic acid groups).

Based on characterization of structural and transport properties of these membranes, a number of models of the structure and molecular-level transport in hydrated polymer electrolyte membranes (PEMs) have been proposed (5-11). Their success in predicting transport properties has been varied. However, an important aspect lacking in all these modeling efforts is the specific inclusion of molecular detail or description of the PEM. If one is to really understand the factors that affect transport of water and ions in PEMs to a level at which one can rationally propose new membranes with specific characteristics for particular processes or applications, then models of transport that contain microstructural and local molecular information must be developed and tested.

To this end, we have spend considerable effort to obtain molecular scale information on the structure of Nafion® through *ab initio* electronic structure calculations and dielectric continuum modeling (12-14). These calculations have characterized the hydrophilic sites and their interaction with water along with specific conformations of the pendant side chain. In addition, molecular dynamics simulations were performed (13,14) to obtain statistically significant structural parameters of the pendant side chains.

We present here our initial efforts in developing an ion and water transport model which incorporates molecular scale information for the displacement of an hydronium ion in an arbitrary pore of Nafion®.

BASIC PORE MODEL

As a model we consider a pore to be a cylinder of length L and cross sectional radius R, filled with N water molecules each possessing a dipole moment μ. The walls of the pore will be assumed to consist of a periodic array of fixed anionic groups that exert a periodic potential within the contained volume. In our model we use both hydrodynamics and nonequilibrium statistical mechanics to describe the transport of hydronium ions through the pore. The geometry of our model is presented in the Figure 1. Here, α is an arbitrary hydronium ion that is being transported under the influence of an electric field $\vec{E}$ and subject to the action of intermolecular potentials due to the solvent water, of which only two representative molecules, i and j, are shown, and a periodic potential due to the pendant groups on the wall of the pore.

The hydronium ion conductivity through the pore is derived in two steps: (1) the effective friction coefficient of the hydronium ion under the influence of the solvent and pendant groups is computed while the effect of the field, $\vec{E}$, is ignored; and (2) the electrical conductivity as a consequence of the field $\vec{E}$, with the friction coefficient from the previous step, is calculated assuming a linear ohmic response.

DERIVATION OF MODEL

Governing Equations

The total Hamiltonian H_T for step (1) may be written as:

$$H_T(\vec{p}_\alpha,\vec{r}_\alpha,\vec{p},\vec{r}) = \frac{p_\alpha^2}{2m_\alpha} + \sum_{i=1}^{N}\frac{p_i^2}{2m} + V(\vec{r}_\alpha,\vec{r})\ \vec{p}_\alpha \qquad [1]$$

The quantities appearing in this equation have the following definitions: (a) $\vec{p}_\alpha$ is the momentum of the hydronium ion and m_α its mass; (b) unless explicitly stated to the contrary, any variable without a subscript refers to a collection of N vectors corresponding to the solvent molecules. Accordingly, the momentum and coordinate vectors for the water molecules are given by:

$$\vec{p} = \{\vec{p}_1, \vec{p}_2, \ldots \vec{p}_N\} \qquad \vec{r} = \{\vec{r}_1, \vec{r}_2, \ldots \vec{r}_N\} \tag{2}$$

The mass of a water molecule is indicated by m and is treated as a structure-less particle (i.e. the atoms are not distinguished); (c) $V(\vec{r}_\alpha, \vec{r})$ is the total potential energy of the system and is composed of the following contributions:

$$V(\vec{r}_\alpha, \vec{r}) = \sum_{i=1}^{N} V_{\alpha s}(|\vec{r}_\alpha - \vec{r}_i|) + \Psi(\vec{r}_\alpha) + \sum_{i<j}^{N} V_{ss}(|\vec{r}_i - \vec{r}_j|) + \sum_{i=1}^{N} V_{ps}(\vec{r}_i) \tag{3}$$

Now the various potential energy terms in Eq. [3] have the following functional forms:
(i) $V_{\alpha s}$ is the interaction potential between the hydronium ion and a water molecule. This is assumed to be a typical ion-dipole interaction :

$$V_{\alpha s}(|\vec{r}_\alpha - \vec{r}_i|) = \frac{\mu e \cos\gamma}{4\pi\varepsilon|\vec{r}_\alpha - \vec{r}_i|^2} \tag{4}$$

where γ is the angle made by the vector pointing from α to the center of dipolar axis of water with the dipolar axis itself. Since in most of the work that has so far been done in this field the solvent is assumed to be a continuum we will reduce the level of sophistication in our work by considering a thermal average over γ and thereby ignoring the rotational contribution to the friction coefficient:

$$V_{\alpha s}(|\vec{r}_\alpha - \vec{r}_i|) \approx \frac{2\pi}{K}\int_0^\pi d\gamma \sin\gamma \frac{\mu e \cos\gamma}{4\pi\varepsilon|\vec{r}_\alpha - \vec{r}_i|^2} e^{\frac{-\mu e \cos\gamma}{4\pi\varepsilon kT|\vec{r}_\alpha - \vec{r}_i|^2}}$$

Here, K is a normalization constant for the thermal distribution function. Expanding the exponential and retaining only linear terms we get:

$$V_{\alpha s}(|\vec{r}_\alpha - \vec{r}_i|) \approx -\frac{\mu^2 e^2}{48\pi^2\varepsilon^2 kT}\frac{1}{|\vec{r}_\alpha - \vec{r}_i|^4} \tag{5}$$

ε is the permittivity of the medium, k is the Boltzmann constant, T is the temperature and e the charge of the hydronium ion.
(ii) $\Psi(\vec{r}_\alpha)$ is the periodic potential energy experienced by the hydronium ion due to the pendant groups on the pore wall. If we assume that these groups are located with a spacing of L/n where n is an integer then this potential energy term may be written:

$$\Psi(\vec{r}_\alpha) = \Psi(r_\alpha, \theta_\alpha, z_\alpha) = -V_0 e\left[1 - \sin\left(\frac{2\pi n z_\alpha}{L}\right)\right] \tag{6}$$

where V_0 is the amplitude of the potential and L is the length of the pore.

(iii) $V_{ss}(|\vec{r}_i - \vec{r}_j|)$ is the solvent-solvent interaction potential which is assumed to be a dipole-dipole interaction (thermally averaged over all rotational angles):

$$V_{ss}(|\vec{r}_i - \vec{r}_j|) = \frac{2\mu^4}{3(4\pi\varepsilon)^2 kT} \frac{1}{|\vec{r}_i - \vec{r}_j|^6} \qquad [7]$$

(iv) $V_{ps}(\vec{r}_i)$ is the potential energy of a water molecule (taken as dipole) due to the periodic field, $\vec{E}_p$, produced by the pendant charges. Now from Eq. [6] the pendant field at the location of a solvent molecule i is given by:

$$\vec{E}_p = -\vec{\nabla}_i \Psi(\vec{r}_i) = -\vec{k}\frac{2\pi V_0 en}{L}\cos\left(\frac{2\pi n z_i}{L}\right)$$

where $\vec{k}$ is a unit vector along the z-axis. The potential energy of the dipolar water molecule is:

$$V_{ps}(\vec{r}_i) = -\vec{\mu}\cdot\vec{E}_p = \frac{2\pi\mu V_0 en}{L}\cos\left(\frac{2\pi n z_i}{L}\right)\cos\delta$$

where δ is the angle that the dipole makes with the field $\vec{E}_p$. If we assume, as a first approximation, that the water dipoles are aligned with the field, then we may set $\cos\delta = 1$ which leads to the final form:

$$V_{ps}(\vec{r}_i) \approx \frac{2\pi\mu V_0 en}{L}\cos\left(\frac{2\pi n z_i}{L}\right) \qquad [8]$$

With the description of the system presented above, we are essentially dealing with an $N+1$ body problem composed of the solvent molecules and a single hydronium ion. At this point we will assume that the hydronium ion concentration is low enough so that interactions between them can be ignored and it is sufficient to examine the dynamics of a single ion. The motion of the ensemble of hydronium ions leads to a current and this will be examined in the next step of the calculation. Furthermore, the pendant groups have been treated as fixed objects on the wall of the pore and thus possess no dynamics of their own and serve only to provide a field in which the hydronium ions are transported. It is our objective to compute the contribution made by this field to the ionic friction.

The time dependent distribution function $f_{N+1}(\vec{p}_\alpha, \vec{r}_\alpha, \vec{p}, \vec{r}, t)$ must satisfy the Liouville equation (15):

$$i\frac{\partial f_{N+1}}{\partial t} = L_T f_{N+1} \qquad [9]$$

where L_T is the Liouville operator for the system which is given by:

$$L_T = i\sum_{k=1}^{N}\left(\frac{\partial H_T}{\partial \vec{r}_k}\cdot\frac{\partial}{\partial \vec{p}_k} - \frac{\partial H_T}{\partial \vec{p}_k}\cdot\frac{\partial}{\partial \vec{r}_k}\right) + i\left(\frac{\partial H_T}{\partial \vec{r}_\alpha}\cdot\frac{\partial}{\partial \vec{p}_\alpha} - \frac{\partial H_T}{\partial \vec{p}_\alpha}\cdot\frac{\partial}{\partial \vec{r}_\alpha}\right) \qquad [10]$$

Substitution of H_T from Eqs. [1] and [3] yields:

$$L_T = -i\frac{\vec{p}_\alpha}{m_\alpha}\cdot\frac{\partial}{\partial \vec{r}_\alpha} - i\sum_{k=1}^{N}\frac{\vec{p}_k}{m}\cdot\frac{\partial}{\partial \vec{r}_k} + i\sum_{k=1}^{N}\frac{\partial V_{\alpha s}(|\vec{r}_\alpha - \vec{r}_k|)}{\partial \vec{r}_k}\cdot\frac{\partial}{\partial \vec{p}_k} + i\sum_{k<j}\frac{\partial V_{ss}(|\vec{r}_k - \vec{r}_j|)}{\partial \vec{r}_k}\cdot\left(\frac{\partial}{\partial \vec{p}_k} - \frac{\partial}{\partial \vec{p}_j}\right) +$$

$$i\sum_{k=1}^{N}\frac{\partial V_{ps}(\vec{r}_k)}{\partial \vec{r}_k}\cdot\frac{\partial}{\partial \vec{p}_k} + i\sum_{k=1}^{N}\frac{\partial V_{\alpha s}(|\vec{r}_\alpha - \vec{r}_k|)}{\partial \vec{r}_\alpha}\cdot\frac{\partial}{\partial \vec{p}_\alpha} + i\frac{\partial \Psi(\vec{r}_\alpha)}{\partial \vec{r}_\alpha}\cdot\frac{\partial}{\partial \vec{p}_\alpha} \qquad [11]$$

The total force experienced by the hydronium ion within the pore can be calculated from the Liouville operator:

$$\vec{F}_\alpha(\vec{r}_\alpha) = iL_T\vec{p}_\alpha = -\sum_{k=1}^{N}\frac{\partial V_{\alpha s}(|\vec{r}_\alpha - \vec{r}_k|)}{\partial \vec{r}_\alpha} - \frac{\partial \Psi(\vec{r}_\alpha)}{\partial \vec{r}_\alpha} = \vec{F}_{\alpha s}(\vec{r}_\alpha,\vec{r}) + \vec{F}_{\alpha p}(\vec{r}_\alpha) \qquad [12]$$

The average force experienced by the hydronium ion is given by:

$$\langle \vec{F}_\alpha \rangle(\vec{p}_\alpha,\vec{r}_\alpha,t) = \int d\vec{r}\,d\vec{p}\,\vec{F}_\alpha(\vec{r}_\alpha,\vec{r})f_{N+1}(\vec{p}_\alpha,\vec{r}_\alpha,\vec{p},\vec{r},t) \qquad [13]$$

where the $N+1$ body distribution function $f_{N+1}(\vec{p}_\alpha,\vec{r}_\alpha,\vec{p},\vec{r},t)$ is obtained by solving the full Liouville Eq. [9]. Such an exact calculation is impossible and therefore a more approximate route must be adopted.

In order to simplify the problem we proceed in a manner similar to that adopted in the calculation of the Stokes' friction coefficient in hydrodynamics (16). In this type of calculation the hydronium ion is assumed to move with a fixed velocity $\vec{v}_\alpha$ and the space fixed coordinate system shown in Fig. 1 is replaced by a moving frame of velocity $\vec{v}_\alpha$. These two conditions enable us to eliminate the kinetic energy term of the hydronium ion in the Hamiltonian (Eq. [1]) since this ion may be treated as a fixed object. The solvent molecules in this new coordinate frame, however, now possess an average velocity $-\vec{v}_\alpha$ and thus the ith solvent molecule must have a velocity $\vec{v}_i + \vec{v}_\alpha$ leading to a new Hamiltonian:

$$H_0(\vec{r}_\alpha,\vec{v},\vec{r}) = \sum_{i=1}^{N}\frac{m(\vec{v}_i + \vec{v}_\alpha)^2}{2} + V(\vec{r}_\alpha,\vec{r}) \qquad [14]$$

where, as pointed out earlier, $\vec{v}_\alpha$ is a constant and is now a parameter which will no longer appear as an argument in the various functions to be considered.

The Liouville operator L_0 corresponding to this Hamiltonian is obtained from Eq. [11] after eliminating all those operators that depend upon the momentum, $\vec{p}_\alpha$, of the hydronium ion:

$$L_0 = -i\sum_{k=1}^{N}\frac{\vec{p}_k}{m}\cdot\frac{\partial}{\partial\vec{r}_k} - i\sum_{k=1}^{N}\frac{\partial V_{\alpha s}(|\vec{r}_\alpha - \vec{r}_k|)}{\partial\vec{r}_\alpha}\cdot\frac{\partial}{\partial\vec{p}_k} + i\sum_{k<j}^{N}\frac{\partial V_{ss}(|\vec{r}_k - \vec{r}_j|)}{\partial\vec{r}_k}\cdot\left(\frac{\partial}{\partial\vec{p}_k} - \frac{\partial}{\partial\vec{p}_j}\right) +$$
$$i\sum_{k=1}^{N}\frac{\partial V_{ps}(\vec{r}_k)}{\partial\vec{r}_k}\cdot\frac{\partial}{\partial\vec{p}_k} \qquad [15]$$

At large distances from the hydronium ion the solvent molecules are assumed to be in an equilibrium state ρ_{eq}; the mathematical form for which may be written down immediately from the form of the Hamiltonian in Eq. [14]:

$$\rho_{eq}(\vec{r}_\alpha,\vec{v},\vec{r}) = \frac{1}{Q}Exp\left[-\beta\left(\sum_{i=1}^{N}\frac{m(\vec{v}_i+\vec{v}_\alpha)^2}{2} + V(\vec{r}_\alpha,\vec{r})\right)\right] \qquad [16]$$

here, Q is the partition function for this canonical distribution function, and $\beta = 1/kT$. Assuming that the velocity of the hydronium ion is very small Eq. [16] may expanded as a Taylor series in $\vec{v}_\alpha$ retaining only the zero order and linear terms of this expansion:

$$\rho_{eq}(\vec{r}_\alpha,\vec{v},\vec{r}) \approx \left(1-\beta\sum_{j=1}^{N}\vec{p}_j\cdot\vec{v}_\alpha\right)\frac{1}{Q}Exp\left[-\beta\left(\sum_{i=1}^{N}\frac{p_i^2}{2m} + V(\vec{r}_\alpha,\vec{r})\right)\right] \qquad [17]$$
$$\equiv \left(1-\beta\sum_{j=1}^{N}\vec{p}_j\cdot\vec{v}_\alpha\right)\rho^f(\vec{r}_\alpha,\vec{v},\vec{r})$$

where the definition of ρ^f, an N-body distribution function, is clear from Eq. [17]. The partition function can be obtained by integrating over all the momentum and space variables:

$$Q = \left(\frac{2\pi m}{\beta}\right)^{3N/2} Z; \qquad Z \equiv \int d\vec{r}e^{-\beta V(\vec{r}_\alpha,\vec{r})} \qquad [18]$$

where Z is the so called configuration integral. ρ^f may now be written in the more explicit form:

$$\rho^f(\vec{p},\vec{r}) = \left(\frac{\beta}{2\pi m}\right)^{3N/2} Exp\left[-\beta\sum_{j=1}^{N}\frac{p_j^2}{2m}\right]P_N(\vec{r}) \qquad [19]$$
$$P_N(\vec{r}) \equiv \frac{1}{Z}Exp[-\beta V(\vec{r}_\alpha,\vec{r})] \qquad [20]$$

As the hydronium ion progresses through the solvent it perturbs its equilibrium state into a time dependent state $\rho(\vec{r}_\alpha,\vec{p},\vec{r},t)$ which must satisfy a Liouville equation similar to Eq. [9] but with the reduced Liouville operator L_0:

$$i\frac{\partial \rho(\vec{r}_\alpha,\vec{p},\vec{r},t)}{\partial t} = L_0\rho(\vec{r}_\alpha,\vec{p},\vec{r},t) \qquad [21]$$

In order to obtain $\rho(\vec{r}_\alpha,\vec{p},\vec{r},t)$ Eq. [21] must be solved given the initial condition of Eq. [17]. Such a solution can be obtained using standard methods to yield:

$$\rho(\vec{r}_\alpha,\vec{p},\vec{r},t) = e^{-iL_0 t}\rho_{eq}(\vec{r}_\alpha,\vec{p},\vec{r}) = e^{-iL_0 t}\left(1-\beta\sum_{j=1}^{N}\vec{p}_j\cdot\vec{v}_\alpha\right)\rho^f(\vec{r}_\alpha,\vec{p},\vec{r}) \qquad [22]$$

Using a standard mathematical identity this equation can be rewritten in the following manner:

$$\rho(\vec{r}_\alpha,\vec{p},\vec{r},t) = \rho^f - \beta\left(\sum_{j=1}^{N}\vec{p}_j\right)\rho^f\cdot\vec{v}_\alpha - \frac{\beta}{i}\int_0^t dt' e^{-iL_0 t'}L_0\left(\sum_{j=1}^{N}\vec{p}_j\right)\rho^f\cdot\vec{v}_\alpha \qquad [23]$$

If the transients caused by the perturbations from the moving hydronium ion vanish rapidly then a nonequilibrium stationary state, $\rho(\vec{r}_\alpha,\vec{p},\vec{r})$, is achieved by the solvent, which is mathematically given by allowing $t \rightarrow \infty$ in Eq. [23]. We replace the full $N+1$ body distribution function in Eq. [13] with this more approximate version:

$$\left\langle\vec{F}_\alpha\right\rangle(\vec{r}_\alpha) = \int d\vec{r}d\vec{p}\vec{F}_\alpha(\vec{r}_\alpha,\vec{r})\rho(\vec{r}_\alpha,\vec{p},\vec{r}) \qquad [24]$$

The following identity is well known from nonequilibrium statistical mechanics (5):

$$iL_0\sum_{j=1}^{N}\vec{p}_j = \sum_{k=1}^{N}\frac{\partial V_{\alpha s}(|\vec{r}_\alpha - \vec{r}_k|)}{\partial \vec{r}_\alpha} - \sum_{k=1}^{N}\frac{\partial V_{ps}(\vec{r}_k)}{\partial \vec{r}_k} \equiv \vec{F}_{\alpha s}(\vec{r}_\alpha,\vec{r}) + \vec{F}_{ps}(\vec{r}) \qquad [25]$$

Substituting Eq. [25] in Eq. [23] and the result in Eq. [24] along with the definition of the force on the hydronium ion given in Eq. [12] one may calculate the average force $\left\langle\vec{F}_\alpha\right\rangle$. The friction coefficient is the quantity that relates this force with the hydronium ion velocity, $\vec{v}_\alpha$, in a linear manner and it can be easily seen that such a relationship is given by the second and third terms of Eq. [23]. The second term is, however, odd in the momentum components while Eq. [17] shows that ρ^f is even in these variables hence a zero contribution to the friction coefficient is made by this second term. The third term of Eq. [23] yields a finite friction tensor of second rank and is composed of four terms:

$$\begin{aligned}\underline{\underline{\zeta}} &= \beta\int_0^\infty dt\left\langle\vec{F}_{\alpha s}e^{-iL_0 t}\vec{F}_{\alpha s}\right\rangle_0 + \beta\int_0^\infty dt\left\langle\vec{F}_{\alpha s}e^{-iL_0 t}\vec{F}_{ps}\right\rangle_0 + \beta\int_0^\infty dt\left\langle\vec{F}_{\alpha p}e^{-iL_0 t}\vec{F}_{ps}\right\rangle_0 + \beta\int_0^\infty dt\left\langle\vec{F}_{\alpha p}e^{-iL_0 t}\vec{F}_{\alpha s}\right\rangle_0 \\ &\equiv T_1 + T_2 + T_3 + T_4 \qquad [26]\end{aligned}$$

where the symbol $\langle \, \rangle_0$ implies an average over the distribution function ρ^f. The scalar friction coefficient can be extracted from the second rank tensor by taking one third of its trace, i.e.:

$$\zeta = \frac{1}{3}\sum_{i=1}^{3} \zeta_{ii} \qquad [27]$$

The four terms T_1, T_2, T_3, and T_4 in Eq. [26] can be given the following pictorial representations:

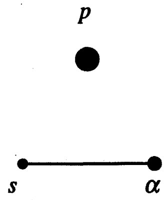

T_1

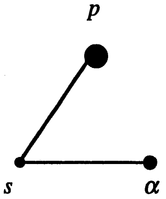

T_2

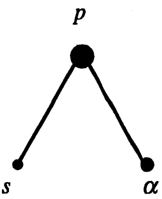

T_3

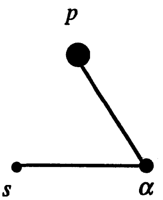

T_4

where p =pendant, s =solvent, and α =the hydronium ion. The term T_1 corresponds to an average force experienced by the hydronium ion due to the solvent molecules, and T_2 is the average force on the hydronium ion due to the pendant groups via the solvent medium. Similar physical meanings can be given to the other representations. In T_4 both the solvent and the pendant groups interact directly with the hydronium ion. In this model we will assume that the last term is the most significant and absorb the first three terms in the friction coefficient $\zeta^{(0)}$ that is computed in traditional ion transport models. An example of this is to be seen in the work of Pintauro and Yang (18) in which the ionic mobility u_i is related to the friction coefficient according to:

$$u_i = \frac{1}{\zeta^{(0)}} \qquad [28]$$

The correction term to the friction coefficient that we seek to calculate in this work is:

$$\zeta^{(c)} = \frac{1}{3}\mathrm{Tr}[T_4] \qquad [29]$$

Prior to turning to the explicit calculation of the effects of the fixed anionic charges groups on the wall of the pore we point out that the derived results thus far still depend on the position of the hydronium ion with respect to the moving coordinate frame (i.e. $\vec{r}_\alpha$). This is a constant since the moving coordinate frame has the same velocity as the hydronium ion.

Correction to Friction Coefficient

Since the pendant groups are treated in our model as fixed charged groups they produce an electrical field in the pore which is not affected by ensemble averaging in Eq. [26]. Therefore, with use of Eqs [6], [12], and [26], we may write for the correction term defined in Eq. [29]:

$$\zeta^{(c)}=-\frac{2\pi V_0 en\beta}{3L}\int_0^\infty dtC(t);\quad C(t)\equiv\left\langle e^{-iL_0t}F_{\alpha sz}\right\rangle_0 \qquad [30]$$

where $\vec{F}_{\alpha sz}$ is the z-component of the force $\vec{F}_{\alpha s}$. Eq. [30] is developed in the following steps:

1) The time displacement operator e^{-iL_0t} may be expanded as a power series according to:

$$C(t)=\sum_{p=0}^{\infty}(-1)^p\frac{c_{2p}}{(2p)!}t^{2p} \qquad [31]$$

where c_{2p} are the even moments of the distribution function ρ^f. The moments of this correlation function are defined according to:

$$c_p=(-i)^p\left\langle(-iL_0)^pF_{\alpha sz}\right\rangle_0 \qquad [32]$$

and it can be shown that only the even moments do not vanish.

2) The Laplace transform of Eq. [31] is:

$$\tilde{C}(s)=\sum_{p=0}^{\infty}(-1)^p\frac{c_{2p}}{s^{2p+1}} \qquad [33]$$

where s is the Laplace transform variable.

3) Eq. [33] may be expressed in the form of a continued fraction (19):

$$\tilde{C}(s)=\cfrac{a_0}{s+\cfrac{a_1}{s+\cfrac{a_2}{s+\cfrac{a_3}{s+\ddots}}}} \qquad [34]$$

The coefficients of this continued fraction are related to the moments c_p in the following manner:

$$a_0=c_0,\quad a_1=\frac{-c_2}{c_0},\quad a_2=\frac{c_4+a_1c_2}{a_0a_1},\quad a_3=\frac{-c_6-(a_1+a_2)c_4}{a_0a_1a_2},\quad \textbf{etc.} \qquad [35]$$

4) Taking the simplest approximant from Eq. [34]:

$$\tilde{C}(s) = \frac{a_0}{s + a_1} \qquad [36]$$

5) Laplace inversion of Eq. [36] gives:

$$C(t) = -a_0 e^{-a_1 t} \qquad [37]$$

6) Finally, substitution of Eq. [37] into Eq. [30] and employing the definitions in Eq. [35] gives for the friction coefficient the following expression:

$$\zeta^{(c)} = \frac{2\pi V_0 en\beta}{3L} \frac{c_0^{\ 2}}{c_2} \qquad [38]$$

Calculation of Moments

In order to calculation the correction to the friction coefficient we need to compute the two moments c_0 and c_2 appearing in Eq. [38]. The relevant definitions may be extracted from Eq. [32], i.e.:

$$c_0 = -\langle F_{\alpha sz} \rangle_0 \qquad [39]$$

$$c_2 = \langle L_0^{\ 2} F_{\alpha sz} \rangle_0 \qquad [40]$$

where $\vec{F}_{\alpha sz}$ is given by the negative gradient (along the z-axis) of $V_{\alpha s}$ (Eq. [5]). With explicit evaluation this becomes:

$$F_{\alpha sz} = b_1 \sum_{k=1}^{N} \frac{z_\alpha - z_k}{r_{\alpha k}^{\ 6}} \qquad [41]$$

where:

$$b_1 = \frac{-\mu^2 e^2}{12\pi^2 \varepsilon^2 kT}; \quad r_{\alpha k} = \left[(x_\alpha - x_k)^2 + (y_\alpha - y_k)^2 + (z_\alpha - z_k)^2 \right]^{1/2}$$

The second moment, c_2, requires application of $L_0^{\ 2}$ (Eq. [15]) to $F_{\alpha sz}$ and the result may be written as the sum of four terms:

$$L_0^{\ 2} F_{\alpha sz} = Y_1 + Y_2 + U + Y_3 \qquad [42]$$

where:

$$Y_1 = \frac{-\mu^2 e^2}{6\pi^2 \varepsilon^2 m^2 kT} \sum_{k=1}^{N} Y_{1k} \qquad [43]$$

$$Y_2 = \frac{-\mu^4 e^4}{144\pi^4 \varepsilon^4 m(kT)^2}\sum_{k=1}^{N} Y_{2k} \qquad [44]$$

$$U = \frac{\mu^6 e^2}{48\pi^4 \varepsilon^4 m(kT)^2}\sum_{k=1}^{N}\sum_{j\neq k}^{N} U_{kj} \qquad [45]$$

$$Y_3 = \frac{-\mu^3 e^3 n^2 V_0}{3mkTL^2 \varepsilon^2}\sum_{k=1}^{N} Y_{3k} \qquad [46]$$

The summands appearing in Eqs. [43]–[46] are quite complicated involving powers of the position and momenta coordinates of both the solvent molecules and the hydronium molecule; and thus the reader is spared the explicit details. It is clear from the coefficients in these Eqs. that both Y_2 and U are of an insignificant magnitude relative to $F_{\alpha sz}$; and therefore these terms will be neglected. In any case, our calculations (c_0 and c_2) require evaluation of the ensemble average of the quantities in Eqs. [41] and [42]. In computing the averages of these functions we recognize the fact that all these terms are sums of one body functions. The ensemble averaging in Eqs. [39] and [40] involves the N-body distribution function ρ^f defined in Eq. [19] and since all solvent molecules are treated as identical, the following simplifications result:

$$\langle F_{\alpha sz}\rangle_0 = \frac{-\mu^2 e^2 N}{12\pi^2 \varepsilon^2 kT}\int d\vec{r}\,\frac{(z_\alpha - z)}{|\vec{r}_\alpha - \vec{r}|^6}P_1(\vec{r}) \qquad [47]$$

$$\langle Y_1\rangle_0 = \frac{3\mu^2 e^2 NkT}{\pi^2 \varepsilon^2}\int d\vec{r}\,\frac{(z_\alpha - z)}{|\vec{r}_\alpha - \vec{r}|^8}P_1(\vec{r}) \qquad [48]$$

$$\langle Y_3\rangle_0 = \frac{-\mu^3 e^2 n^2 V_0 N}{3m\varepsilon^2 kTL^2}\int d\vec{r}\left[\frac{1}{|\vec{r}_\alpha - \vec{r}|^6} - \frac{6(z_\alpha - z)^2}{|\vec{r}_\alpha - \vec{r}|^8}\right]\sin\!\left(\frac{2n\pi z}{L}\right)P_1(\vec{r}) \qquad [49]$$

P_n is an n-body reduced distribution function given by:

$$P_n(\vec{r}_1,\vec{r}_2,\ldots\vec{r}_n) = \int d\vec{r}_{n+1}\ldots d\vec{r}_N P_N(\vec{r}_1,\vec{r}_2,\ldots\vec{r}_N) \qquad [50]$$

At this stage of the development, the integrals over the momenta and coordinates of the N solvent molecules have been reduced to integrals over the coordinates of an arbitrary solvent molecule.

In order to make further progress with these equations we must calculate an explicit form for the distribution function $P_1(\vec{r})$. In principle this can be done by using Eq. [50] along with the definition of $P_N(\vec{r}_1,\vec{r}_2,\ldots\vec{r}_N)$ given in Eq. [20]. It is, however, easier to obtain this function as a functional derivative of the configuration integral (20). Written explicitly, Eq. [18] is of the form:

$$Z=\int\int\ldots\int d\vec{r}_1 d\vec{r}_2\ldots d\vec{r}_N\prod_{i=1}^{N}Exp\left[-\beta\left\{\frac{a_1}{\left|\vec{r}_\alpha-\vec{r}_i\right|^4}+a_3\cos\left(\frac{2n\pi z_i}{L}\right)\right\}\right]\prod_{i<j}^{N}Exp\left[-\beta\frac{a_2}{\left|\vec{r}_i-\vec{r}_j\right|^6}\right]$$

where:

$$a_1=\frac{-\mu^2e^2}{48\pi^2\varepsilon^2kT};\qquad a_2=\frac{-2\mu^4}{3(4\pi\varepsilon)^2kT};\qquad a_3=\frac{2\pi\mu V_0en}{L}\tag{51}$$

With the following definitions:

$$z(\vec{r}_i)\equiv Exp\left[-\beta\left\{\frac{a_1}{\left|\vec{r}_\alpha-\vec{r}_i\right|^4}+a_3\cos\left(\frac{2n\pi z_i}{L}\right)\right\}\right];\quad f(\vec{r}_i,\vec{r}_j)\equiv Exp\left[-\beta\frac{a_2}{\left|\vec{r}_i-\vec{r}_j\right|^6}\right]-1\tag{52}$$

the configuration integral may be written:

$$Z[z]=\int\int\ldots\int d\vec{r}_1d\vec{r}_2\ldots d\vec{r}_N\prod_{i=1}^{N}z(\vec{r}_i)\prod_{i<j}^{N}\left[1+f(\vec{r}_i,\vec{r}_j)\right]\tag{53}$$

where $f(\vec{r}_i,\vec{r}_j)$ in Eqs. [52] and [53] is the Mayer Cluster function. The symbol $Z[z]$ is used to indicate the functional dependence of the configuration integral on the function z. We now approximate $Z[z]$ by the simplest cluster integral:

$$\begin{aligned}Z[z]&\approx\int\int\ldots\int d\vec{r}_1d\vec{r}_2\ldots d\vec{r}_N\prod_{i=1}^{N}z(\vec{r}_i)+\int\int\ldots\int d\vec{r}_1d\vec{r}_2\ldots d\vec{r}_N\prod_{i=1}^{N}z(\vec{r}_i)\sum_{i<j}^{N}f(\vec{r}_i,\vec{r}_j)\\&=\left[\int d\vec{r}z(\vec{r})\right]^N+\frac{N(N-1)}{2}\left[\int d\vec{r}z(\vec{r})\right]^{N-2}\int\int d\vec{r}d\vec{r}'f(\vec{r},\vec{r}')z(\vec{r})z(\vec{r}')\\&\equiv g_1(z)^N+\frac{N(N-1)}{2}g_1(z)^{N-2}g_2(z)\end{aligned}\tag{54}$$

where the definitions of $g_1(z)$ and $g_2(z)$ are clear from development of Eq. [54]. Therefore the one body distribution function is given by:

$$P_1(\vec{r})=\frac{1}{Z}z(\vec{r})\frac{\delta Z}{\delta z(\vec{r})}\tag{55}$$

Carrying out the functional differentiation gives for the one body function:

$$P_1(\vec{r})=\frac{Ng_1(z)^{N-3}}{Z}\left[g_1(z)^2+\frac{(N-1)(N-2)}{2}g_2(z)+(N-1)g_1(z)\chi(\vec{r})\right]z(\vec{r})\tag{56}$$

where use has been made of the following relations:

$$\frac{\delta g_1(z)}{\delta z(\vec{r})}=1; \quad \frac{\delta g_2(z)}{\delta z(\vec{r})}=2\chi(\vec{r}); \quad \chi(\vec{r})=\int d\vec{r}' f(\vec{r},\vec{r}'); \quad \frac{\delta \chi(z)}{\delta z(\vec{r}')}=f(\vec{r},\vec{r}')$$

Before proceeding further it is prudent to consider the magnitude of the various terms in Eq. [56]. The magnitude of these three terms can be traced back to the numerical values of the three coefficients in Eq. [51]. The evaluation of the coefficients indicates that while a_1 and a_3 are comparable in magnitude, a_2 is approximately 20 orders of magnitude smaller. This leads to the conclusion that the Mayer Cluster function is essentially zero, and thus the one body function of Eq. [56] will simplify to:

$$P_1(\vec{r})=\frac{N}{g_1(z)}z(\vec{r}) \qquad [57]$$

Substituting Eq. [57] into Eqs. [47]–[49], we obtain for the moments c_0 and c_2:

$$c_0=\frac{\mu^2 e^2 N^2}{12\pi^2 \varepsilon^2 kT g_1}\int d\vec{r}\frac{(z_\alpha - z)}{|\vec{r}_\alpha - \vec{r}|^6}z(\vec{r}) \qquad [58]$$

$$\begin{aligned} c_2 &= \frac{3\mu^2 e^2 N^2 kT}{\pi^2 \varepsilon^2 g_1}\int d\vec{r}\frac{(z_\alpha - z)}{|\vec{r}_\alpha - \vec{r}|^6}z(\vec{r}) \\ &\quad -\frac{\mu^3 e^2 n^2 V_0 N^2}{3m\varepsilon^2 kTL^2 g_1}\int d\vec{r}\left[1-\frac{6(z_\alpha - z)^2}{|\vec{r}_\alpha - \vec{r}|^2}\right]\frac{z(\vec{r})}{|\vec{r}_\alpha - \vec{r}|^6}\sin\left(\frac{2n\pi z}{L}\right) \end{aligned} \qquad [59]$$

The integrals in Eqs. [58] and [59] may be evaluated numerically most easily in cylindrical coordinates (the geometry of the pore making this the obvious choice) and the result leading to the correction to the friction coefficient according to Eq. [38].

Conductivity of Pore

Under the influence of the electric field $\vec{E}$ (due to the potential difference between the anode and cathode) the hydronium moves through the pore and may be assumed to obey Newton second law according to:

$$m_\alpha \frac{d\vec{v}_\alpha}{dt}=-\zeta\vec{v}_\alpha + e\vec{E}$$

where friction has been included explicitly. When a stationary state has been achieved $\vec{v}_\alpha$ becomes the drift velocity. Assuming that the electric field acts along the pore axis (z-axis) the drift speed becomes:

$$v_\alpha = \frac{eE}{\zeta}$$

The current density in the pore may be expressed in terms of the concentration of the hydronium ions, c, according to:

$$J = \Im c v_{\alpha} = \frac{e\Im c}{\zeta} E = \kappa E \qquad [60]$$

where $\Im$ is the Faraday constant and κ the conductivity. The molar conductivity, Λ, may then be expressed in terms of our derived correction to the friction coefficient according to:

$$\Lambda = \frac{e\Im}{\zeta^{(0)} + \zeta^{(c)}} \qquad [61]$$

If the contribution of the pendant groups is ignored ($V_0 = 0$) then the conductivity is simply as derived by Pintauro and Yang (6).

CONCLUDING REMARKS

We have derived a mathematical model that describes the transport of a molecule of water (vehicle-type mechanism) via the displacement of an hydronium ion through a cylindrical pore in a PEM with incorporated molecular structural potentials due to pendant side chains along the inside of the walls. This is essentially the first attempt at combining features of continuum mechanics with statistical mechanics into a unified theory. Numerical work is currently being undertaken to calculate the conductivity of a Nafion® pore as a function water content.

ACKNOWLEDGMENTS

We gratefully acknowledge the support of the LANL LDRD program for the funding of this work.

REFERENCES

* DuPont registered trademark polymer.

1. T. A. Zawodzinski, M. Neeman, L. D. Sillerud, and S. Gottesfeld, J. Phys. Chem., **95**, 6040 (1991).
2. T. A. Zawodzinski, T. E. Springer, F. A. Uribe and S. Gottesfeld, Solid State Ionics, **60**, 199 (1993).
3. T. A. Zawodzinski, C. Derouin, S. Radzinski, R. J. Sherman, V. T. Smith, T. E. Springer, and S. Gottesfeld, J. Electrochem. Soc., **140**, 1041 (1993).
4. T. A. Zawodzinski, J. Davey, J. Valerio and S. Gottesfeld, Electrochimica ACTA, **40**, 297 (1995).
5. T. D. Gierke, G. E. Munn, and F. C. Wilson, J. Polym. Sci. Polym. Phys., **19**, 1687 (1981).
6. W. Y. Hsu and T. D. Gierke, Macromol., **15**, 101 (1982).
7. W. Y. Hsu and T. D. Gierke, J. Membrane Sci., **13**, 307 (1983).

8. S. W. Capeci, P. N. Pintauro, and D. N. Bennion, J. Electrochem. Soc., **136**, 2876 (1989).
9. M. W. Verbrugge and R. F. Hill, J. Electrochem. Soc., **137**, 886 (1990).
10. M. Eikerling, A. A. Kornyshev, and U. Stimming, J. Phys. Chem., **101**, 10807 (1997).
11. X.-D. Din and E. E. Michaelides, AIChE J., **44**, 35 (1998).
12. S. J. Paddison, L. R. Pratt, T. A. Zawodzinski and D. W. Reagor, Fluid Phase Equilibria, in press.
13. S. J. Paddison and T. A. Zawodzinski Jr., Solid State Ionics, in press.
14. S. J. Paddison, L. R. Pratt, T. A. Zawodzinski Jr., J. Phys. Chem., submitted.
15. P. M. V. Resibois, Electrolyte Theory: An Elementary Introduction to a Microscopic Approach, Chap. 4, Harper and Row, New York (1968).
16. R. M. Fuoss and F. Accasina, Electrolytic Conductance, p. 53, Interscience Publishers, New York (1959).
17. D. A. McQuarrie, Statistical Mechanics, p. 508, Harper and Row, New York (1973).
18. P. N. Pintauro and Y. Yang, in Fundamentals of Electrochemical Process Design: A Tutorial, J. B. Talbot and J. M. Fenton, Editors, PV 95-11, p. 266, The Electrochemical Society Proceedings Series, Pennington, NJ (1995).
19. R. Paul, J. Mol. Structure, **85**, 215 (1981).
20. J. P. Hansen and I. R. McDonald, Theory of Simple Liquids, 2nd Ed., Chap. 4, Academic Press, London (1986).

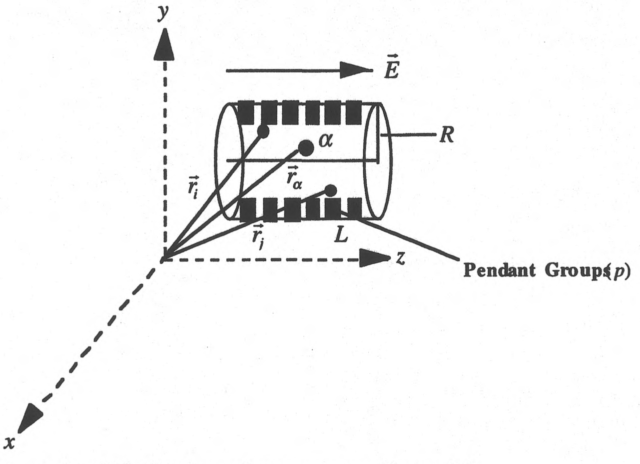

Figure 1 Schematic of idealized membrane pore used in model.

Proton_Conducting_Membrane_Fuel_Cells_II, PV 1998-27, 121-126 (1998)
DOI: 10.1149/199827.0121PV © The Electrochemical Society

PROPOSED MECHANISM OF CO MITIGATION IN PEMFCS BY USING DILUTE H_2O_2 IN THE ANODE HUMIDIFIER

R.J. Bellows, E. Marucchi-Soos and R.P. Reynolds
Exxon Research and Engineering, Rt. 22 East, Annandale, NJ 08801, USA

ABSTRACT

CO poisoning in proton exchange membrane fuel cells (PEMFCs) can be mitigated by using dilute H_2O_2 in the anode humidifier. However, mitigation appears to be provided by an "unintended" O_2 bleed produced by decomposition of H_2O_2 in the humidifier, rather than by H_2O_2 vapors transported from the humidifier to the anode. CO mitigation was effective when significant levels of O_2 were present in the anode feed. The effectiveness of CO mitigation disappeared when non-catalytic materials were used to suppress H_2O_2 decomposition in the humidifier. (**Safety Note**: H_2O_2 decomposition in the anode humidifier may produce flammable compositions in the anode feed.)

INTRODUCTION

There is an extensive literature describing how CO poisoning reduces the performance of proton exchange membrane fuel cells (PEMFCs). Recent proceedings provide excellent bibliographies concerning CO tolerance relative to the use of reformate fuels (1,2). Typical performance for a PEMFC operating on impure H_2 feed decreases with increasing levels of CO as shown in Figure 1 (3). The electro-oxidation of H_2 requires two adjacent Pt sites. CO poisoning is caused by chemisorption of CO onto the anode catalyst, forming a nearly complete CO monolayer which blocks sites for electro-oxidation of H_2 (4). H_2 oxidation becomes severely polarized as this monolayer approaches complete coverage. This polarization can be reduced by removing a small fraction (typically 5-10%) of the CO from the Pt surface (5,6).

Bleeding small amounts of O_2 into H_2-rich feeds is reported to mitigate CO poisoning at impurity levels up to 100 ppm CO (7,8). This O_2 reacts chemically with the CO, but its selectivity is low. Typically, O_2 is fed at roughly 100-200 times the stoichiometric requirement for CO oxidation. The excess O_2 consumes H_2 fuel via a non-electrochemical reaction. The O_2 bleed provides large voltaic improvements which greatly exceed the coulombic losses caused by H_2 consumption.

A novel method for mitigating CO poisoning in PEMFCs was recently described wherein dilute 5% H_2O_2 was used in an anode humidifier to successfully mitigate 100 ppm CO in a H_2 rich feed (9). A schematic of Schmidt's anode humidifier system is shown in Figure 2. A mechanism was proposed which involved vapor transport of the H_2O_2 from the anode humidifier to the anode where it reacted on a Pt-Ru electro-catalyst via the following reactions:

$$H_2O_2 + M \rightarrow H_2O + M(O)_{ad} \qquad [1]$$

$$M\text{-}CO + M(O)_{ad} \rightarrow 2M + CO_2 \qquad [2]$$

In analyzing this performance, we estimated that the humidified anode feed would contain on the order of 100 ppm H_2O_2. This suggested that CO oxidation via reactions [1] and [2] might be more selective than those using the O_2 bleed. The higher selectivity using H_2O_2 additions could provide a technical and economical advantage over using the O_2 bleed. For fuel cell powered electric vehicle applications, we estimated that a small bottle (<100 cc) of 30 wt% H_2O_2 would be sufficient to mitigate 100 ppm CO for over 1000 miles of driving range.

Our work essentially reproduced the experimental findings of Schmidt et al. (9), showing successful mitigation of CO poisoning on Pt anodes. In our work, we mitigated approximately 100 ppm CO in the H_2 feed by using <1% H_2O_2 in the anode humidifier. However more significantly, our data shows that successful mitigation depends on the slow decomposition of H_2O_2 in the humidifier and that suppressing this decomposition suppresses the mitigation effect.

EXPERIMENTAL

The membrane electrode assembly (MEA) was prepared by General Motor's Global Alternative Propulsion Center using a 40 wt% Pt/Vulcan XC-72 at a loading of 0.4 mg Pt/cm^2 on both sides of a Nafion 112. The MEA was mounted in a Globetech test fixture having 5 cm^2 active area.

Performance tests were run using a commercial Globetech GT-120 test station which controls gas flow rates, pressures and humidifier temperatures. The cell was run at 80°C and ambient pressure at both electrodes. Humidifiers were approximately 60-70% filled with liquid. Our initial anode humidifier used Globetech's standard 1000 mL heated stainless steel humidifier bottle. In subsequent testing, this was replaced by a heated polypropylene (PP) humidifier chamber. The PP humidifier was made from a Nalgene 250 mL narrow mouth square bottle. The lines connecting the humidifier to the fuel cell were changed from stainless steel to polyethylene (PE). The temperature of the PP humidifier was controlled by partially immersing it in a water bath heated on a hot plate. The cathode humidifier was always run at 82°C. The anode humidifier was controlled between 25° and 45°C in various experiments. House H_2 was used for the anode feed after passing through a butyl lithium getter (Supelco, OMI 2 Indicator Tube). Cylinders of impure H_2 were research grade, prepared by MG Products. House air was used for the cathode feed.

Performance curves for the fuel cell were run using a power supply and an HP 6050A System DC Electronic Load. Test protocol held the anode and cathode flow rates constant during performance measurements. The cell was held at constant potential for 60 seconds prior to recording each current. Transients were allowed to stabilize for at least 30 minutes, after switching from pure to impure H_2 or changing the H_2O_2 concentration in the anode humidifier. H_2O_2 (J.T. Baker, 30 wt%, Reagent Grade) was diluted with deionized H_2O between 0.5 and 15 wt%.

Gas analysis was performed on a Wasson modified HP 5890 GC. Anode feed samples were collected in a double-valved stainless steel sample bomb. Anode gases were allowed to flow through the humidifier for at least 90 minutes prior to sampling. GC analysis for N_2 confirmed that the sampling procedure had not been contaminated with traces of air.

RESULTS AND DISCUSSION

Our initial performance curves for pure and impure H_2, with and without H_2O_2, are plotted in Figure 3. Without H_2O_2, the performance on impure H_2 containing 96 ppm CO was severely degraded. However, with 0.75 vol% H_2O_2 in the stainless steel humidifier, performance was restored, approaching that for pure H_2. This performance mitigation is comparable to that reported in previously by Schmidt et al. using Pt-Ru anodes (9).

We observed small gas bubbles in the sight glass of the stainless steel anode humidifier. This suggested that H_2O_2 might be decomposing via [3] to form O_2 in the humidifier, with the reaction being catalyzed by the metallic walls in the humidifier. (Schmidt et al. also suggest the possibility of H_2O_2 decomposing in their humidifier and stainless steel anode feed lines.) We analyzed the anode feed (100 mL/min., humidifier temperature = 45°C) using a GC, and found approximately 2% O_2 in H_2. This O_2 level is in the range reported to be effective for CO mitigation using the O_2 bleed (7,8).

$$2\ H_2O_2\ \text{->}\ 2\,H_2O + O_2 \qquad [3]$$

At this point, a PP humidifier and PE feed lines were substituted at the anode in order to suppress H_2O_2 decomposition, as shown schematically in Figure 4. Qualitatively, almost no bubbles were observed on the walls of the PP vessel, showing that this material did not catalyze H_2O_2 decomposition at temperatures up to 50°C.

The H_2O_2 treatment became ineffective at mitigating CO poisoning (96 ppm) when using the PP humidifier, even when the humidifier contained as much as 15 wt% H_2O_2 at 45°C. GC analysis of the feed gases from the PP humidifier showed that the O_2 was now below measurable levels (less than 10 ppm).

This change in O_2 content of the anode feed gases is best explained by a slow decomposition of H_2O_2 in the reservoir. Metallic surfaces are known to catalyze H_2O_2 decomposition, while polyolefinic materials are not likely to catalyze this reaction. The effective CO mitigation when using the stainless steel humidifier and the loss of mitigation when using the polypropylene humidifier is best explained by the well known O_2 bleed effect rather than by the vapor transfer of H_2O_2 from the humidifier to the anode. Our interpretation is that an unintended O_2 bleed provided the primary mechanism for CO mitigation when using the stainless steel humidifier. Furthermore, if the CO mitigation mechanism involved a vapor transfer of H_2O_2 from the humidifier to the electrode, there is no reason to expect that changing the material of the humidifier would affect the CO mitigation.

In further support of our interpretation, the literature describes H_2O_2 reduction on Pt, Ru and Pt-Ru electrodes as proceeding via a two electron reduction, with H_2O being the final product (10). This suggests that reaction [1], the formation of stable $M(O)_{ad}$, is unlikely.

Finally, our proposed O_2 bleed mechanism will not be economically attractive in PEMFCs. Compared to air, H_2O_2 is an expensive source of O_2. The low selectivity for O_2 bleed (~1%) would require costly amounts of H_2O_2 to achieve CO mitigation.

Safety Note: Decomposition of H_2O_2 in heated metallic humidifiers can proceed at unknown rates. This decomposition has the potential to produce flammable mixtures of H_2 and O_2 in the anode feed, which should be avoided. The lower flammable limit for pure O_2 in H_2 is 6.1 vol% (11).

REFERENCES

1. D.P. Wilkinson and D. Thompett, in Proceedings of the 2nd International Symposium on New Materials for Fuel Cell and Modern Battery Systems, Montreal, Canada, 266, (1997).
2. S.J. Cooper, A.G. Gunner, G. Hoogers and D. Thompsett, ibid, p. 286.
3. R.J. Bellows, E. Marucchi-Soos and D.T. Buckley, *Electrode Materials and Processes for Energy Conversion and Storage IV*, **PV 97-13**, 1-14, Electrochemical Society Proceedings, Pennington, NJ (1997).
4. P. Stonehart and P.N. Ross, Cat. Rev.-Sci. Eng., **12**, 1-35 (1975).
5. H.A. Gasteiger, N.M. Markovic and P.N. Ross, *J. Phys. Chem.*, **99**, 16757, (1995).
6. T. Springer, T. Zawodzinski and S. Gottesfeld, *Electrode Materials and Processes for Energy Conversion and Storage IV*, **PV 97-13**, 15-24, Electrochemical Society Proceedings, Pennington, NJ (1997).
7. S. Gottesfeld and J. Pafford, *J. Electrochem. Soc.*, **135**, 2651-2652 (1988).
8. D.P. Wilkinson, H.H. Voss, J. Dudley, G.J. Lamont, and V. Basura, U.S. Patent 5,432,021, (1995) and U.S. Patent 5,482,680, (1996).
9. V.M. Schmidt, H.-F. Oetjen, and J. Divisek, *J. Electrochem. Soc.*, 144, L237-238, (1997).
10. K. Kinoshita, "Electrochemical Oxygen Technology", John Wiley & Sons, Inc., New York, 1992, Chapter 2, pp.19-112.
11. Handbook of Physics and Chemistry, 45th Edition, R.C. Weast, Ed., p. D-55, Chemical Rubber Company, (1964).

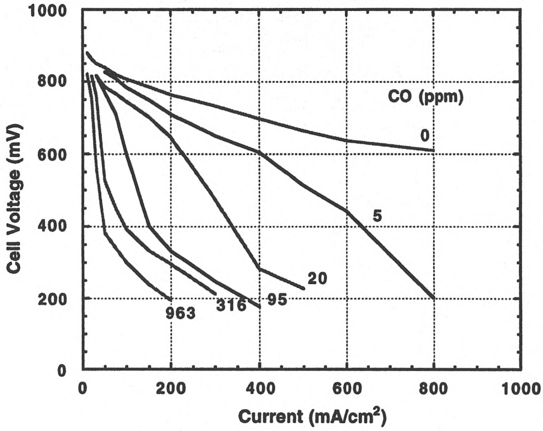

Figure 1: PEMFC Performance on H_2/Air on Pt Anodes, 80°C, 0.3 mg Pt/cm^2

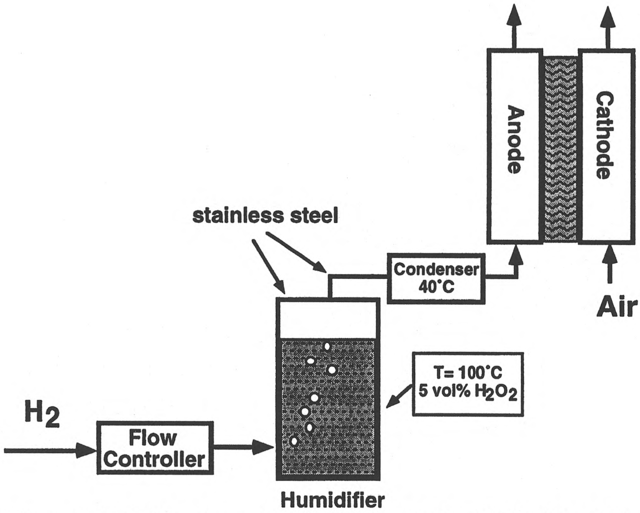

Figure 2: CO Mitigation using H_2O_2 in Anode Humidifier (Schmidt)

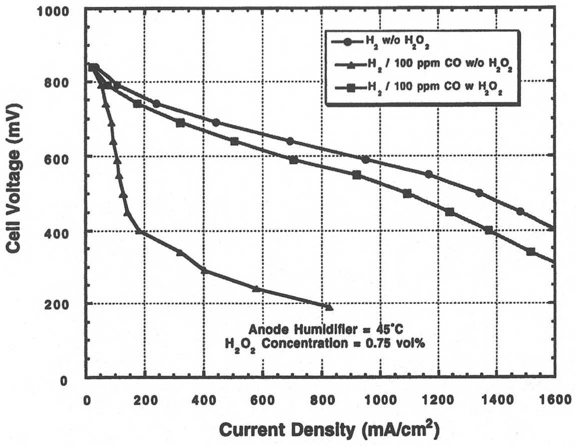

Figure 3: Steady state performance of PEMFC on pure and impure H_2, T_{cell} = 80°C; catalyst loading = 0.4 mg Pt/cm^2

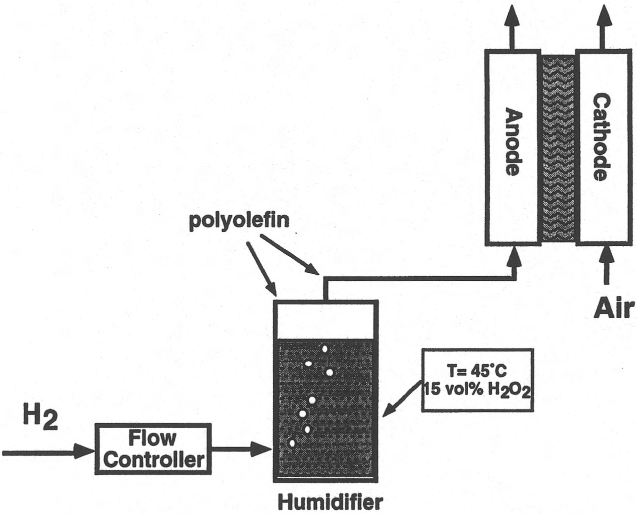

Figure 4: CO Mitigation using H_2O_2 in Polyolefin Humidifier

Proton_Conducting_Membrane_Fuel_Cells_II, PV 1998-27, 127-135 (1998)
DOI: 10.1149/199827.0127PV © The Electrochemical Society

PERFORMANCE OF PEM FUEL CELLS OPERATING ON SYNTHETIC REFORMATE: EXPERIMENTAL AND MODELING STUDIES

T. Zawodzinski, T. Springer, J. Bauman, T. Rockward, F. Uribe and S. Gottesfeld

Electronic and Electrochemical Materials and Devices Group
Los Alamos National Laboratory
Los Alamos, NM 87545

ABSTRACT

Experimental results and modeling simulating PEM Fuel Cell operation on reformed gasoline are reported. These studies cover observed and calculated effects of hydrogen dilution at the level expected from gasoline reforming and the extent of catalyst poisoning by CO under such anode operation conditions. At flow rates corresponding to less than 80% hydrogen utilization, modest losses in cell power density are observed experimentally from hydrogen dilution alone. Modeling suggests that the performance loss caused by hydrogen dilution stems primarily from combined effects of limited protonic conductivity and gas permeability within the thin film anode catalyst layer. Effects due to limited transport through the gas diffusion backing are expected to be relatively minor. Under the experimental conditions employed, little evidence was found for deleterious effects caused by internal generation of CO from CO_2. Finally, we demonstrate complete tolerance to 100 ppm CO in a 40% H_2 inlet stream at stoichiometric flow of 1.3, using air injection into the anode.

INTRODUCTION

Polymer electrolyte fuel cells (PEFCs) show promise as power sources for electric vehicles. Near-term strategies to bring such vehicles to market apparently require fuels other than hydrogen. Anode feedstreams derived from reformed gasoline or, perhaps, methanol, are thus the consequence of the practical need to have a suitable fuel delivery infrastructure for fuel cell powered transportation. Reforming gasoline leads to an anode feed that contains, in addition to hydrogen, substantial content of nitrogen + carbon dioxide, as well as impurity levels of CO, estimated at 10-100 ppm. Combined N_2 and CO_2 content of at least 60% by volume of the anode feedstream is expected.

Dilution of the hydrogen stream by these gases has several possible consequences, as does the presence of low levels of CO. The effect of carbon monoxide on PEFC cell anode performance has been recently studied leading to significant level of understanding. Typically, the performance of PEFCs employing Pt or Pt alloy anode catalysts is substantially degraded at 80°C when CO is present at levels of as little as a few ppm. However, several strategies exist for ameliorating the effects of CO on the fuel cell anode. Some of our own previous work has shown that PEFC anode tolerance to CO in neat hydrogen can be improved through the use of alloy catalysts (1). We have described modeling and experimental studies of CO tolerance of Pt and Pt alloy catalysts [1,2].

On the other hand, little has been reported regarding the possible pitfalls of operation on diluted hydrogen streams, particularly when high fuel utilization is demanded. In that case, sections of the anode near the outlet would be fed with extremely dilute hydrogen when a simple flow field is employed. For example, for 90% utilization of a stream containing 40% H_2 (with the balance consisting of inert gases), the outlet will have a hydrogen concentration of roughly 6%. This can yield a significant performance drop if the anode catalyst layer and anode backing layer are not optimized.

The combined effects of dilution and CO impurity must be dealt with in a cell operating on reformate. We recently described some preliminary experimental studies and modeling of the effects of dilution of the anode feedstream on anode polarization [3]. More extensive experimental studies are reported here.

EXPERIMENTAL

All experiments were performed on 50 cm^2 single cells operating at 80°C and 30 psig on both anode and cathode sides. The membrane and electrode assemblies (MEAs) were prepared, as described in more detail elsewhere [5], by painting the catalyst on the surface of a Teflon blank and then hot-pressing both anode and cathode to a Nafion membrane. For experiments involving air injection into the anode , LANL reconfigured anodes were used to increase effectiveness at low catalyst loadings. All results shown were obtained with MEAs prepared with a Nafion^{TM} 1135 membrane (EW= 1100, thickness = 88 μm).

A variety of modifications in hardware and testing methods were introduced to allow operation with reformate. The higher anode gas flow rates that have to be used, requires some modification of the anode flow field to avoid excessive pressure drop across the cell. We also need to allow for effective mixing of gases and for well-controlled stoichiometric flows into the cell. Finally, when anode flow rate was increased as required for work with diluted hydrogen streams, it was difficult to adequately humidify the anode feedstream using our simple sparging systems.

Using mass flow controllers, we produced 40% H_2 anode feedstreams by mixing neat H_2 either (a) with neat N_2 or (b) with a mixture of 42%CO_2 + 58%N_2 or (c) with a mixture of 42%CO_2 + 58%N_2 + 100 ppm CO. Humidification of these gas streams was carried out by passing the gas through a humidifier bottle which was fitted with a length of 1/8 inch O.D. Nafion tubing (Perma-Pure, Inc, Tom's River, NJ) connected to the inlet. This tubing is fed into the bottle inside a 1/4 inch 316 stainless steel spring coiled inside the bottle thus protecting the Nafion tubing from direct contact with the bottle wall and avoiding kinking of the tubing inside the bottle. Use of the Nafion tubing allowed for effective humidification of the anode gas stream.

Gas flows were controlled by our data acquisition computer, operating via a LabView program in conjunction with a series of programmable mass flow controllers (MKS Instr.Model RS 485). Before each experiment, flow controllers were calibrated using a digital flowmeter. The calibration factor necessary for the flow-tracking algorithm was determined by dividing set flow by measured flow.

Injection of air into the anode feed was performed by introducing a separate feed line at the anode inlet. Air was thus injected into the humidified gas stream. This allowed us to achieve improved mixing of the air with the reformate stream. A time of 30 minutes was allowed upon switching gas mixtures, to properly reach steady state in the cell before beginning data collection (while holding the cell at constant voltage of, typically, 0.5V). The experiments shown use a uniform stoichiometric ratio set at each point on the polarization curve. This is done via the following algorithm: the cell voltage is first changed to a new value. After the cell settles to a steady current, typically 30 seconds (except for low stoichiometric flows when longer times are used to allow for complete equilibration), the current is measured and the cell is switched to constant current mode. The gas flow rate is then switched to correspond to the stoichiometric flow times the current.

RESULTS AND DISCUSSION

1. Experimental Studies

Typical experimental studies of a given cell consisted of a series of tests using various anode feedstreams. First, neat hydrogen performance was determined at the desired stoichiometric flow. We then measured polarization curves for 40% H_2/60% N_2, 40% H_2/35% N_2/25% CO_2 ('reformate without CO'), and 40% H_2/35% N_2/25% CO_2 with 100 ppm CO ('reformate'). Tests using reformate as the anode feed were typically carried out with several levels of air injection to probe conditions required to obtain complete CO tolerance. The effect of dilution of hydrogen on the performance of a cell operating at a stoichiometric flow ('stoich') of 1.5 (utilization of 67%) is shown in Figure 1. Little performance loss was experimentally observed for hydrogen feedstreams diluted with nitrogen or with nitrogen plus carbon dioxide. A specific parameter which could be relevant in determining the extent of the effect of CO generation from CO_2 at the anode, is the time left for full equilibration. As in all of our other measurements, the polarization curves shown in Figure 1 were collected 30 minutes after introduction of the CO_2 containing anode feed stream. Therefore, excluding the possibility of a much slower process, comparison of the results of dilution with N_2 and with N_2+CO_2 indicates that little of the reverse water-gas shift reaction occurs within our anode. We have argued before [6] that the extent of reverse shift within the anode could be determined by details of anode catalyst layer preparation, particularly by the degree of direct exposure of catalyst sites to the gas stream.

In Figure 2, we show the performance of a cell operating on simulated reformate at hydrogen flow rate of 1.3 stoich. This figure highlights the strong performance loss associated with CO poisoning at 100 ppm CO and our ability to completely recover that loss with 4% air injection. The final voltage loss observed with air bleed *vs.* an anode operating on neat hydrogen is seen to be < 50 mV at 1 A/cm^2. When comparing with reported results which have focussed on 100 ppm CO in an otherwise pure hydrogen feedstream, the performance restoration shown in figure 2 is more demanding because of operation on reformate, *i.e.*, on diluted hydrogen with 100 ppm CO. At given ppm CO, the P_{CO}/P_{H2} ratio in the reformate (40% H_2) is 2.5 times larger than in the CO/ H_2 mixture. Since the competition of CO for a catalyst surface site is determined by this ratio of partial pressures, the deleterious effect of 100 ppm CO in the reformate is expected to be similar to that of 250 ppm CO in a CO/ H_2 mixture. This suggests the need for increasing the amount of air injected into the anode feedstream vs. the case of 100 ppm CO in hydrogen. Use of a reconfigured anode composition/structure allowed us to achieve complete tolerance at 100 ppm CO in reformate with only 4% air bleed. While this provides good base for operation with less than fully polished anode feed stream (possibly eliminating the need for the last stage of a multi-stage PROX) the overall amount of air injected leads to a rather high fuel efficiency penalty of 4%, somewhat higher than desired.

Our attempts to operate with simulated reformate at stoichiometric flows lower than 1.3 (fuel utilization larger than 77%) have not yielded conclusive results as yet, most probably because of residual leaks and imperfect flow control at the relatively low flow rates involved. We have tested, however, the implication of hydrogen dilution to the level expected near the anode outlet when operating with 40% H_2 inlet and 90% fuel utilization. Under such conditions, the outlet hydrogen concentration is calculated near 6% and we used H_2/N_2 gas mixtures with 6% H_2 as inlet stream of high stoichiometric flow to probe anode performance. While the anode exhibits lowered performance under these conditions, the performance loss seen is by no means dramatic. We thus concluded that operation on reformate (40% H_2) at 90% fuel utilization (1.1 stoich), should be possible with a performance penalty only marginally higher than that seen at 1.3 stoich (figure 2).

2. Modeling of Dilution Effects

We have previously reported a model for accounting the effect of CO poisoning in CO/H_2 mixtures [2]. To complete modeling of anode performance on reformate feed streams, effects of hydrogen dilution need to be addressed. Anodes operating on a diluted feedstream were modeled by adapting our previously described air cathode model [4] that addresses the similar case of a diluted gaseous reactant inlet stream (air). Here we focus briefly on results of the modeling and some indications of important contributors to loss in fuel cell voltage arising from various anode parameters. The base case model parameters employed have been:

Physical parameters: Catalyst layer thickness: 5 μm; backing layer thickness: 300 μm; inlet hydrogen mole fraction: 0.35; total pressure: 3 atm

Anode Catalyst and Catalyst Layer Properties: Effective ionic conductivity: 0.01 S/cm; effective hydrogen diffusion coefficient: 2.8×10^{-5} cm^2 sec^{-1}; Tafel slope for the HOR : 60 mV; exchange current density at 1 atm H_2 per cm^2 of geometric area: 0.5 A cm^{-2}

Backing layer properties: H_2 diffusion coefficient in the gas phase : 0.541cm^2 sec^{-1}; porosity: 0.4; tortuosity: 7.7

A limitation of the present anode modeling results is that they rely on a slight modification of the mixed-mean condition assumed in [4] to describe the effects of hydrogen concentration variation along the flow channel. Thus, the results are most appropriate for higher stoichiometric flows of hydrogen and need further refinement to consider the variation of hydrogen concentration along the flow channel under high utilization. Diagnostics and an analysis of sensitivity to various parameters were developed by varying model parameters , revealing that the two key anode parameters which determine loss from inlet hydrogen dilution are the ionic conductivity and gas permeation rate within the catalyst layer, and, to more limited degree, the porosity and tortuosity of the backing. We explore the relative importance of these anode components by calculating polarization losses for a series of reasonable parameter values [4], demonstrating the potential negative impact of each.

In Figure 3, we show the effects of dilution of the hydrogen stream on performance for the base case parameters. Decreasing the mole fraction of hydrogen is clearly calculated to have a substantial effect under base case parameter assumption. In comparing notes with the experimental result shown in figure 1, the actual effect of dilution to mole fraction of 0.4 was similar but somewhat smaller than calculated here, about 50 mV around 1A cm^{-2}. This suggests that the actual anode is associated with better protonic conductivity and/or higher hydrogen permeability than assumed in the base case. In Figure 4, we illustrate the effect of catalyst layer protonic conductivity on anode polarization losses with a 35% hydrogen inlet stream. This parameter is predicted to have a marked effect on performance: decreasing, for example, the conductivity by an order of magnitude (while holding all other parameters at base case values) increases the anode polarization loss, relative to the base case, by 90 mV at a current density of 0.6 A cm^{-2}. Explanation for the critical effect of catalyst layer conductivity on electrode performance with diluted gaseous reactant is provided in [4]. In Figure 5, we show the effect on anode polarization of decreasing the hydrogen permeation rate through the catalyst layer holding all other parameters at base case values. As with the effect of conductivity, this has a marked effect on the polarization loss. In Figure 6 , we illustrate the effect of increasing backing layer thickness on anode polarization. Increasing the thickness by factor 5 has only marginal effect on polarization of the anode, ca. 10 mV difference at a current density of 0.6 A cm^{-2}. Varying the backing layer porosity has a similarly small effect, as shown in Figure 7.

To summarize, in addition to the inescapable 'Nernstian' (thermodynamic) voltage loss of 12 mV associated with diluting hydrogen from 100% down to 40%, key contributors to higher dilution losses observed include limited catalyst layer protonic conductivity and/or hydrogen permeation rate through the catalyst layer. The gas diffusion backing apparently plays only a minor role as a source of loss on dilution.

The observed performance loss incurred from dilution was generally in agreement with model predictions, particularly in showing overall small effects compared with the effects of ppm level CO in the reformate feed stream. Complete reformate anode modeling should include the combined effects of hydrogen dilution and CO deactivation effects, under high fuel utilization conditions. Results from such a comprehensive model will be reported later elsewhere.

REFERENCES

1. T. Zawodzinski, C. Karuppaiah, F. Uribe and S. Gottesfeld in *Proc. Symp. on Electrode Materials and Processes for Energy Conversion and Storage IV*, PV 97-13, The Electrochemical Society, p. 139, 1997.

2. T. E. Springer, T. Zawodzinski and S. Gottesfeld in *Proc. Symp. on Electrode Materials and Processes for Energy Conversion and Storage IV*, PV 97-13, The Electrochemical Society, p. 15, 1997.

3. T. Zawodzinski, T. E. Springer, J. Bauman, S. Savett, F. Uribe and S. Gottesfeld, Extended Abstracts of the San Diego ECS Mtg., Abstract # 881.

4. T. E. Springer, M. S. Wilson and S. Gottesfeld, *J. Electrochem. Soc.*, 140, 3513 (1993).

5. M. S. Wilson, Judith A. Valerio and S. Gottesfeld, Electrochim. Acta, **40**, 355 (1995).

6. M.S. Wilson , T.E. Springer, T.A. Zawodzinski and S. Gottesfeld, Proc. 28th Intersociety Energy Conversion Engineering Conf. (IECEC) 1993, Vol 1 pp 1203-1208; see also S.Gottesfeld and T.A. Zawodzinski, in "Advances in Electrochemical Science and Engineering" , Vol. 5, Ed. R.C. Alkire, H. Gerischer, D.M. Kolb and C.W. Tobias, Wiley/VCH, 1997.

ACKNOWLEDGMENT

We gratefully acknowledge the support of the US DOE Office of Advanced Automotive Technology for this work.

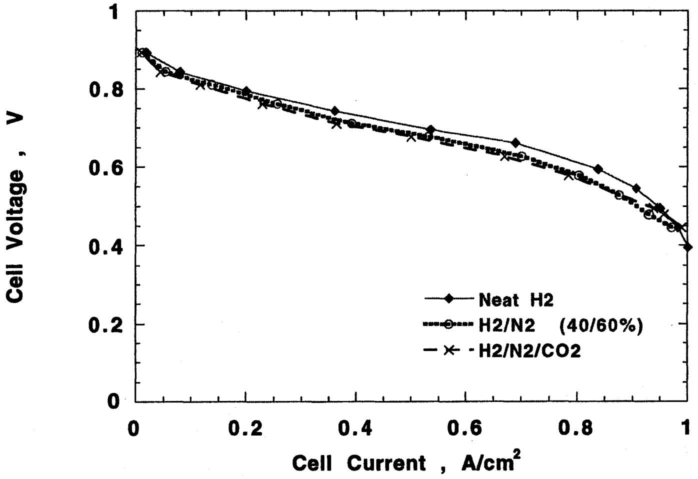

Figure 1: The measured effect of dilution of a hydrogen feed stream on PEFC performance. Fuel cell operating conditions: 50 cm^2; 0.4 mg/cm^2 Pt anode, 0.2 mg/cm^2 Pt cathode; T_{cell} = 80°C,; $T_{hum,,anode}$ = 105°C, $T_{hum,,cathode}$ = 80°C; P_{anode}= $P_{cathode}$=30 psig; Hydrogen flow rate = 1.5 stoich with flow tracking; Air flow rate = 2.5 stoich at 1 A/cm^2

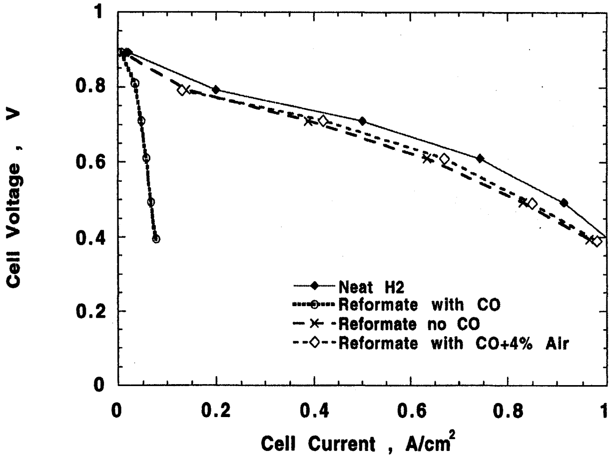

Figure 2: Polymer electrolyte fuel cell performance on anode feed streams at 1.3. stoich., of diluted (40%) hydrogen, reformate (40% H_2 with 100 ppm CO) and reformate + air bleed at 4% . LANL reconfigured anodes employed, optimized for minimizing both catalyst loading and air bleed level.

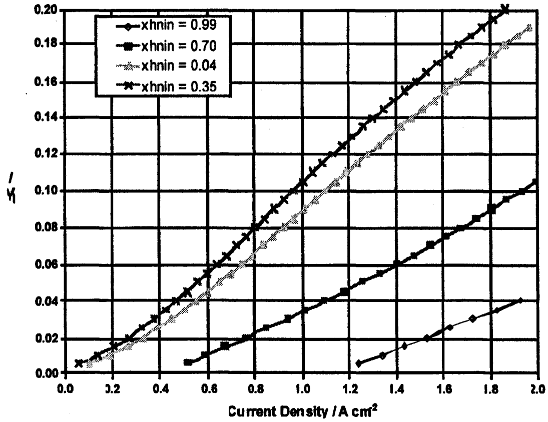

Figure 3: Calculated effect of inlet hydrogen mole fraction (xhnin) on anode polarization. Other parameters as in base case.

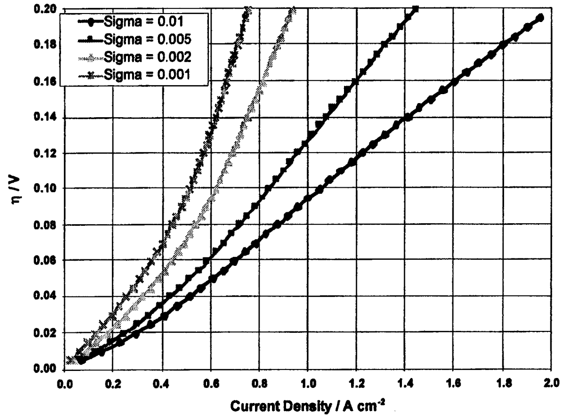

Figure 4: Calculated effect of catalyst layer ionic conductivity (sigma) on anode polarization. Other parameters as in base case.

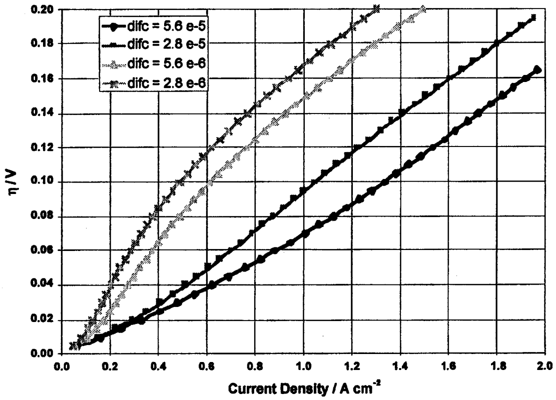

Figure 5: Calculated effect of the diffusion coefficient of hydrogen (difc) in the catalyst layer on anode polarization. Other parameters as in base case.

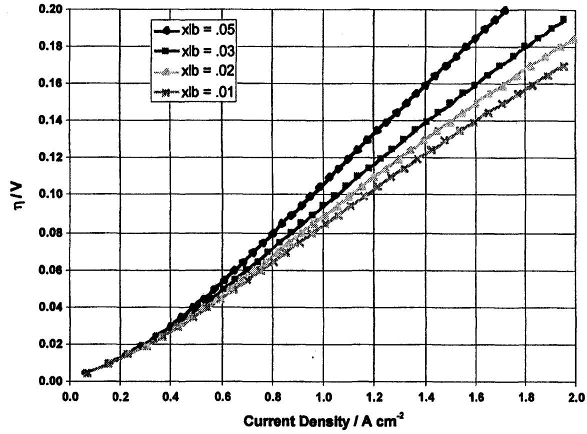

Figure 6: Calculated effect of anode backing layer thickness (xlb) on anode polarization. Other parameters as in base case.

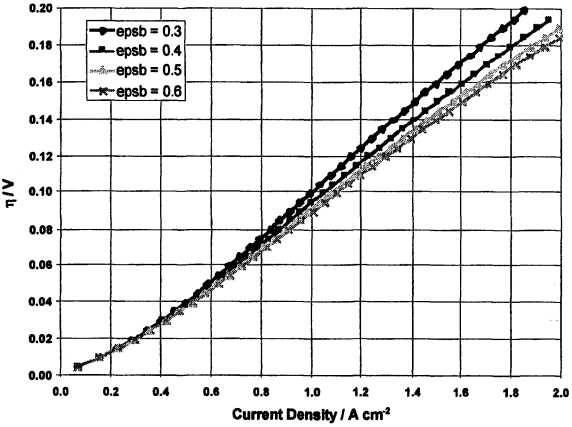

Figure 7: Calculated effect of backing layer porosity (epsb) on anode polarization. Other parameters as in base case.

Proton_Conducting_Membrane_Fuel_Cells_II, PV 1998-27, 136-149 (1998)
DOI: 10.1149/199827.0136PV © The Electrochemical Society

AN INVESTIGATION OF TRANSIENT CARBON MONOXIDE POISONING EFFECTS IN POLYMER ELECTROLYTE FUEL CELLS

Jayson W. Bauman, Thomas A. Zawodzinski, Jr., and Shimshon Gottesfeld

Electronic and Electrochemical
Materials and Devices Group

Los Alamos National Laboratory
Los Alamos, NM 87545

Abstract

We describe studies of performance decay and recovery in polymer electrolyte fuel cells in response to step changes in the level of CO in the anode feed stream. Following a step from 0 to 100 ppm CO in the hydrogen anode feed, completion of current decay at constant cell voltage of 0.6V in a 50 cm^2 cell operating at 80°C with anode loading of 0.2 mg Pt cm^{-2} took 300 seconds. The observed current decay is controlled by the rate of surface dosing, determined primarily, if not exclusively, by inlet flow of CO, and the non-linear dependence of anodic HOR rate on $(1-\theta_{CO})$. Performance recovery in response to a pure hydrogen purge at 80°C was found to be sluggish, with full recovery taking as long as 1000 seconds. The rate of recovery upon exposure to a hydrogen purge is a function of temperature and is apparently controlled by the rate of thermal desorption of CO. Cell performance decay was found much faster (1-10 sec) for a step from 10 ppm to 200 ppm inlet CO. The recovery time was very slow (> 1500 sec) on return from 200 ppm to 10 ppm inlet. Air bleed into the anode significantly slows down decay times and shorten recovery times in operation with transient levels of CO.

Introduction

If reformed hydrocarbons are to be used as the fuel source for polymer electrolyte fuel cells (PEFCs), the catalyst-poisoning effects of carbon monoxide must be significantly reduced. To date, experimental and theoretical work has focused on steady-state poisoning effects of carbon monoxide on anode catalysts in neat hydrogen with some added P_{CO} or in the presence of simulated reformates. However, in a transportation power system hydrocarbon reformers do not always operate at steady state. A nominal output of 100 ppm CO or less could jump to a much higher mole fraction of CO in the event of a rapid change in power demand or under start-up conditions. CO tolerance approaches optimized for steady-state operation may be inadequate for these step changes in the amount of CO released from the reformer.

Here we describe the measured response to step changes in the CO level in the anode stream fed to a PEFC single cell. Determination of the characteristic rate of cell performance decay and recovery during such changes in input CO level should lead to optimized CO tolerance approach(es) and help in power system design.

Experimental

The MEAs tested were made by the ink decal technique [1], and had an active area of 50 cm^2. All anodes had a catalyst loading of approximately 0.2 mg cm^{-2}. Single channel serpentine flowfields for both the anode and cathode were used. The cathode gas diffusion layer (GDL) was uncatalyzed single-sided ELAT (E-Tek, Inc.), and the anode GDL was uncatalyzed double-sided ELAT. The designations single- and double-sided refer to backing structures with microporous layers on one or both faces of the carbon cloth, respectively. These backings are discussed in more detail in this volume [2]. Unless otherwise indicated, the cell temperature was held constant at 80°C.

To isolate the effects of CO transients, the apparatus shown in Figure 1 was used. A feed stream consisting of either neat hydrogen or simulated reformate (40% H_2, 25% CO_2, 35% N_2, 100 ppm CO) was fed to the fuel cell anode. The CO level in the feedstream was increased by injection of CO at the anode inlet without running the CO through the dead space of the anode humidifier sparger bottle or other volume of anode plumbing feed. Using this apparatus, there is nearly zero dead volume (< 1 cm^3) between the CO source and the anode inlet. Therefore the time lag between opening the valve and the actual introduction of the carbon monoxide into the anode is negligible. This allows an accurate determination of the time of CO introduction into the anode.

Three types of transient measurements were taken. In each method, the fuel cell was held at 0.6 V until the current stabilized. The hydrogen flowrate was held at a constant 1.5 times the stoichiometric flow of hydrogen (hereafter referred to as 1.5 stoich) at the steady state current before CO injection. In the first type of experiment, the cell was running at steady state on neat H_2. The current obtained at 0.6 V with neat H_2 was recorded for 60 seconds under steady-state conditions before the introduction of CO. At $t = 60$ s, the cell was exposed to either 50, 100 or 200 ppm CO. The cell current was monitored as a function of time. At an arbitrary time of 450 seconds, after the cell current had stabilized at a lower value due to the catalyst poisoning effect of the injected CO, the CO injection at the inlet was turned off and the anode feed returned to neat H_2. In the second type of experiment, the cell was operating at steady state on 10 ppm CO, without the benefit of air bleed. At $t = 60$ s, the CO level was jumped to 200 ppm CO and at 450 seconds the cell was returned to neat H_2. In the third type of experiment, the cell was operating on simulated reformate gas, with CO tolerance facilitated by 6% air bleed. At $t = 60$ s, the CO concentration was spiked to 500 ppm for 30 seconds.

These experiments were conducted at different temperatures and flowrates. The data acquisition software, developed in-house using LabVIEW (National Instruments), measured the current and voltage each second through the course of the experiment.

Results and Discussion

To estimate the current decay time following a step in concentration of CO in the anode inlet stream, one needs to know (1) the variation with time of catalyst surface coverage by CO as determined by the inlet flow of CO, (2) any significant transport barriers within the anode, and (3) any deviation from unity sticking coefficient for CO on the Pt sites at the relevant cell temperature. In addition, knowledge of the functional dependence of hydrogen electro-oxidation rate on CO coverage is required. At each point in time during the transient observed, the change in cell current is controlled by the change in anode current, given in general terms by:

$$J_{HOR}(\theta_{CO},\eta)=J_{HOR}(\eta)_{\theta_{CO}=0}f(\theta_{CO}) \qquad [1]$$

where

θ_{CO} is the time dependent CO coverage,

η is the anode overpotential (also time dependent in all experiments where overall cell voltage is kept constant), and

$f(\theta_{CO})$ reflects the effect of given coverage of CO, at given anode overpotential, on attenuation of J_{HOR}.

Clearly, the variation with time of the function $J_{HOR}(\theta_{CO},\eta)$ following a step of CO inlet concentration is quite complex. Nevertheless, insight into the factors that control the rate of cell performance decay under cell operation conditions can be obtained by examining expected rates of decay under some simple assumptions.

We start such an examination by estimating the time required for completion of catalyst coverage by CO, following a step in inlet CO mole fraction from zero to some X_{co}, and assuming fast mass transport within the anode and unity sticking probability of CO to Pt sites at any CO coverage lower than 1. Under these conditions, on stepping the inlet CO level from 0 to X_{co}, the rate of increase in CO surface coverage is fully controlled by inlet flow rate of CO. In other words, every CO molecule that enters the anode is immediately adsorbed on the time scale of the experiment. Under this assumption, the time required for completion of monolayer coverage by CO will be given by the ratio between total surface area of the Pt anode catalyst and the inlet flow rate of CO, according to:

$$\tau = N_{\theta=1}\frac{3m}{r\rho}\cdot\frac{1}{f_{in,anode}X_{CO}} \qquad [2]$$

where

$N_{\theta=1}$ is the maximum number of adsorbed CO molecules per cm^2 of catalyst area, assuming one molecule adsorbed per Pt site,

m is the mass of catalyst per geometric surface area,

r is an average radius of catalyst particles (assumed spherical)

ρ is the mass density of the catalyst

$f_{in,\ anode}$ is the anode inlet flux per geometric surface area, and

X_{co} is the constant mole fraction of CO in the inlet stream.

$f_{in,anode}$ is determined under conditions relevant to fuel cell operation by the requirements of stoichiometric flow of the hydrogen fuel. At the hydrogen inlet flow rate employed in our experiments, *i.e.* 1.5 stoichiometric flow @ 1 A cm^{-2}, for a CO concentration step from zero to 100 ppm and anode catalyst loading of 0.2 mg Pt cm^{-2}, and assuming a radius of Pt particles (mass density of 20 g cm^{-3}) of 1.5 nm, and $N_{\theta=1} = 2.3 \times 10^{-9}$ mol cm^{-2}, equation [2] yields $\tau = 604$ seconds for the time required for completion of surface coverage by CO under full dosing control by CO inlet flow rate.

Figure 2 shows the transient decay and recovery data for a cell with this type of Pt anode (0.2 mg cm^{-2}) running at 80°C at a constant voltage of 0.6V on 1.5 stoich. of H_2 at 1A cm^{-2}. At t = 60 seconds on the time axis shown in the figure, the anode feed was stepped from neat H_2 to 100 ppm CO. The anode feed was next returned to CO free H_2 at t = 450 seconds. The first curve in figure 2 shows the initial performance decay on stepping from 0 to 100 ppm inlet CO and the subsequent recovery on switching back to anode inlet with no CO. (Prior to this first experiment, the anode had not been exposed to CO.) The initial decay time measured experimentally is close to 300 seconds.

The actual performance decay time suggests several conclusions. The first is that, indeed, the time frame for completion of performance loss on stepping inlet CO level from 0 to 100 ppm is on the order of several minutes. This very long time frame may suggest a general slow response of a PEFC to steps in inlet CO concentration. However, this response time may be significantly shortened under other CO concentration step conditions, as shown and discussed below. The second observation is that the response time is certainly not slower than calculated by assuming full control by inlet CO flow, meaning that, on the slow time scale for introduction of CO determined by the stoichiometric flow of hydrogen and the relatively low concentration (100 ppm) of CO, any mass transport or sticking barriers are negligible.

There are several possible reasons why the anode current decay is somewhat faster than the calculated rate of catalyst site blocking as given in Eq. [2]. First, the decay of J_{HOR} has been reported to scale with $(1-\theta_{CO})^2$ [3]. In fact, Igarashi *et al.* [4] recently argued that, as CO coverage exceeds about 70%, the fall of the HOR rate at a Pt electrode surface is even steeper than expected from the $(1-\theta_{CO})^2$ dependence. In addition to the effects of $f(\theta_{CO})$ (see Eq. [1]), if the anode catalyst utilization is incomplete, less than the expected number of Pt surface sites will be available even under CO-free conditions. The latter could happen for reasons of insufficient ionic or gas access to all potential catalyst sites [5]. For incomplete utilization, then, less than complete coverage of sites by CO will be required to substantially decrease the observed hydrogen oxidation rate. Between these two effects of the non-linear sensitivity of J_{HOR} to CO coverage and incomplete catalyst utilization caused by imperfect gas access, it can be understood why J_{HOR} decay time observed is somewhat shorter than the time calculated for surface dosing by CO as controlled by inlet flow rate.

The second curve in figure 2 shows a repeat of the decay-recovery cycle, started 20 minutes after the previous run had been completed with prolonged pure hydrogen purge; the third run shown was obtained under similar initial conditions and is identical to the second. The second and third exposures of the cell to 100 ppm CO both show a much faster performance decay time, on the order of 100 s. After the third cycle had been completed, the anode was purged with H_2 + 10% air for 20 minutes. After such an oxidative purge of the catalyst surface, the cell response (run 4) to CO step is similar to that observed for first exposure to 100 ppm CO. As seen in figure 2, the cell always recovers to its initial performance upon removal of the CO from the hydrogen feed stream at relatively fast initial rate, however the remainder of performance recovery under pure hydrogen purge is very sluggish. At 80°C, full recovery is seen to require several minutes under such hydrogen purge conditions.

To understand the shorter decay times on re-exposure to 100 ppm CO, we highlight cyclic voltammetry studies of PEFC Pt anodes reported on more extensively elsewhere in this volume [6]. Although purging with neat hydrogen allows, eventually, full recovery of the fuel cell from effects of CO exposure (see Figure 2), cyclic voltammetry shows that only a small fraction (10-15%) of the CO covering the surface is removed by purging with hydrogen at 80°C. (Previous modeling [7] indicates that such a small fraction of catalyst sites is sufficient to allow adequate active area for high rates of hydrogen electrooxidation.) Since not all of the CO is removed at 80°C by the hydrogen purge, it takes a shorter time at a given inlet flow of CO to cover a smaller number of CO-free Pt sites and complete the decay of anode current. This irreversible nature of the adsorption of a fraction of CO on Pt at 80°C thus explains the difference between the response of a cell not previously exposed to CO (run 1) and subsequent runs (2 and 3). Air bleeding eliminates all of the CO from the anode catalyst surface, thus replicating in run 4 the cell response recorded in run 1.

The discussion presented above suggests that there are multiple types of CO adsorption sites present on the Pt catalyst with different characteristic CO binding strength. The more strongly bound CO is not removed by H_2 purge at 80°C, in contrast to some more loosely bound CO. It is well-known that differences exist in CO bonding to the different Pt crystal planes [*e.g.* 8, 9]. The high surface area catalyst used in our fuel cell anodes is polycrystalline with very small particles and a surface structure that is likely to have defects. Such defects, coupled with the range of different crystalline structures at the catalyst surface, could account for the apparent different Pt-CO bond energies encountered . Chang *et al.* reported that the bonding mode of adsorbed CO molecules on Pt is dependent on the CO coverage, and that the ratio of bridged to linear CO decreases with increasing CO coverage [10]. Igarashi *et al.* reported it is most reasonable to assume that most of the adsorbed CO will be linearly bonded at full surface coverage [4]. Some rearrangement of adsorbed CO may thus take place as limited CO desorption occurs, possibly stabilizing remaining CO surface molecules by bridge bonding to Pt sites.

To further probe the dynamics of slow CO desorption by hydrogen purge, the length of neat H_2 purge following complete performance decay was varied and the effect on subsequent decay time was measured. The results are shown in Figure 3. The first and second runs are the same as in figure 2. Two additional runs are included, which show the transient decay curves after purging with H_2 for 14 hours and for 5 days, respectively. The decay times are only marginally longer after such long purge and never reach the decay time measured after oxidative cleansing of the anode.

Figure 4 shows the effect of the anode flow rate on current response to a CO transients. Both initial and subsequent anode performance decays occur more quickly when the inlet flow rate is doubled, as expected from decay controlled by rate of CO supply with the inlet fuel stream. The decay time is, in fact, roughly halved, as expected from full control of the decay on this time scale by inlet flow of CO. In contrast, the recovery curves are virtually identical for the various flow rates, showing that CO desorption is unaffected by flowrate. The concentration of CO in the hydrogen purge is expected to be negligible and the recovery rate is apparently fully controlled by the rate of thermal desorption of CO from the Pt sites, with the distribution of CO bonding energies affecting the significant distribution of desorption times observed in the recovery branch.

Figure 5 shows the effects of CO concentration on the transient cell performance phenomena. As inlet CO concentration increases, cell current at the steady state level of poisoning decreases. At 50 ppm, 100 ppm, and 200 ppm CO, the steady state cell currents were 10 A, 6 A, and 4 A, respectively. This is obviously the result of higher equilibrium coverage of CO as CO partial pressure is increased in the anode feed stream. The time it takes the cell to reach low steady state current (corresponding to full effect of CO at given CO partial pressure), is inversely proportional to the CO concentration in the anode feed, in accord with CO surface dosing controlled by CO inlet flow rate.

Figure 6 shows the effects of cell temperature on anode current decay and recovery resulting from introduction and removal of CO. As expected, performance on neat H_2 increases with increasing cell temperature in a well-humidified cell. The time required for complete performance decay does not vary significantly with temperature over this narrow range. However, minimum cell current decreases with decreasing cell temperature, indicating that the equilibrium coverage of CO is temperature-dependent. There is little difference between the 80°C and 90°C recovery curves, as 95% of the original current is returned by 600 seconds after removing the CO source. However, the 60°C CO recovery takes much longer to achieve initial performance. At a time of 2000 seconds after CO was removed from the hydrogen stream, only 80% of the original performance had returned. This clearly points to thermal CO desorption as the rate limiting step for cell recovery and highlights the substantially higher sensitivity of the PEFC to CO at lower temperatures with obvious impacts on system start up dynamics.

The cell current response to CO level changes from either 0 to 200 ppm or 10 to 200 ppm CO are shown in Figure 7. The decay time for the jump from 10 to 200 ppm CO is much shorter than for the jump from neat H_2 to 200 ppm—half the current is lost within several seconds and current decay is practically complete after 30 seconds. This result is readily understood. With 10 ppm CO in the anode feed stream, significant CO coverage on the (Pt-Ru) anode has already been achieved. Therefore, when the CO level is further increased, it takes a much shorter time to dose a small number of CO free surface sites and deactivate the anode. A similar difference is observed in the recovery, shown in Figure 8. When the CO source is completely removed, the recovery takes nearly 10 minutes. However, when the CO is stepped from 200 ppm back to 10 ppm, recovery takes more than twice as long. The results shown in figures 7 and 8 highlight a time scale for performance decay which may be more technically significant in anodes which do not employ air bleed. An anode which exhibits sufficient tolerance to 10 ppm CO (with no air bleed) is seen to be associated with a relatively quick loss in performance when the input CO level rises temporarily to hundreds of ppm CO and, not less importantly, with very sluggish recovery on return to the 10 ppm CO level.

Figure 9 deals with another situation of potential technical significance, looking at a cell (with a Pt-Ru anode) where complete CO tolerance had been maintained at the 100 ppm level with continuous bleed of 6% air [11-13] and the CO level was then stepped from 100 to 500 ppm for 30 seconds. After the inlet CO level was returned to 100 ppm, 6% air bleed is seen to be insufficient to restore the original performance. It took 10% air bleed to restore cell performance. The much higher concentration of CO in the anode stream probably results in an extremely small number of sites for oxygen adsorption, thus limiting the effectiveness of air bleeding by substantially inhibiting the oxidative (chemical) removal of CO. The latter process requires dissociative adsorption of oxygen on the catalyst surface and thus may be especially sensitive to availability of the small number of CO-free sites on the surface.

(*Note that the surface coverage of CO from CO/H_2 mixtures involves competition between CO and H_2 for Pt catalyst sites, with this competition being essentially controlled by the ratio P_{CO}/P_{H2}. At given ppm CO, P_{CO}/P_{H2} is higher by factor 2.5 in simulated reformate with 40% hydrogen vs. the case of CO in neat H_2. Therefore, the residual number of CO-free sites at nominal 500 ppm CO, for example, could be significantly smaller in the case of 500 ppm CO in reformate (40% hydrogen) than in the case of 500 ppm CO in neat hydrogen).

Conclusions

The rate of PEFC performance decay in response to a rise of CO level in the anode inlet stream (without resorting to air bleed) is sensitive to a variety of factors. Under full control by inlet flow of CO, the time for complete dosing of active anode catalyst sites is of the order of several hundred seconds at typical inlet flow rates, with CO levels of the order of 100 ppm, even when anode catalyst loading is as low as 0.2 mg Pt cm^{-2}. The measured time for complete performance decay on stepping inlet CO level from 0 to 100 ppm, is about 50% of the calculated total catalyst surface dosing time, because of the non-linear dependence of J_{HOR} on θ_{CO} and, possibly, because of incomplete catalyst utilization in operation on CO-free H_2. It does not seem that, on this slow dosing time scale which is determined by the inlet fuel flow and by typical P_{CO}, the rate of dosing is significantly limited by anything other than CO inlet flux.

Of technical significance is the observation that first exposure to 100 ppm CO shortens the decay time observed on second exposure to 100 ppm CO when anode recovery between the two exposures is by pure hydrogen purge alone. This shows that, in operation with a continuously changing CO level, the drop in cell performance decay on exposure to higher CO levels will be much faster than expected from calculated total surface dosing, as long as the anode is relieved of CO only by pure hydrogen purge at 80°C. The performance decay will be even faster—on the order of a few seconds for a 50% performance fall and 30 seconds for complete performance decay—when the level of CO is stepped up not from zero, but rather from steady state 10 ppm. The latter is probably a more realistic scenario and point out the time frame relevant to evaluation of power system dynamics and to upstream CO sensing.

Of particular concern for a PEFC system designed on shuttling between steady state hydrogen streams with very low CO levels and transient hydrogen streams with hundreds of ppm CO, is the very slow recovery time of the cell at 80°C on CO-free hydrogen purge. Thermal desorption of CO into a CO free gas stream is a sluggish process at 80°C, resulting in complete anode recovery by CO-free hydrogen purge lasting 10 minutes. Even longer recovery times are recorded when the purge is with low, but non-zero CO levels.

It is important to note that the above conclusions refer to an anode exposed to variable CO levels with performance recovery limited to purge with CO-free hydrogen at 80°C. Under any given CO level transient scenario, significantly faster recovery times and significantly slower decay times on re-introduction of CO are expected when air bleed is applied. The reason is that the Pt surface could be completely freed of CO, at high rate, by air bleed when low levels of injected air are used. Air bleed level into the cell could, in fact, be adjusted based on cell current as input, matching the duration of higher level air injection with the duration of high CO inlet level transients.

Acknowledgment

We gratefully acknowledge the US DOE Office of Advanced Automotive Technology for support of this work.

References

1. M.S. Wilson, J.A. Valerio and S. Gottesfeld, Electrochim. Acta, **40**, 355 (1995)
2. B. Mueller, T. Zawodzinski, J. Bauman, F. Uribe, S. Gottesfeld, , E. DeCastro, and M. DeMarinis. *This Proceedings Volume.*

3. REF 2: T. E. Springer, M. S. Wilson, and S. Gottesfeld, *J. Electrochem. Soc.* **140,** 3513 (1993).
4. H. Igarashi, et al. J. Electroanalytical Chem. **391** (1995) 119.
5. W. Vogel, J. Lundquist, P. Ross and P. Stonehart, Electrochim. Acta, **20**, 79 (1975)
6. T. Zawodzinski, C. Karuppaiah, Y. Wu, S. Savett, F. Uribe, and S. Gottesfeld. *This Proceedings Volume.*
7. T. Springer, et al., Proceedings of the Symposium on Electrode Materials and Processes for Energy Conversion and Storage IV, **97-13**, 15.
8. L. Palaikis *et al., Surface Science* **199** (1988) 183.
9. K. Kinomoto *et al., Surface Science* **242** (1991) 538.
10. S.C. Chang and M.J. Weaver, *J. Phys Chem.* **93** (1989) 5341.
11. S. Gottesfeld and J. Pafford, *J. Electrochem. Soc.* **135**, 2651-2652 (1988)
12. S. Gottesfeld, U.S. Patent No. 4,910,099 (March 20, 1990)
13. M. S. Wilson, T. E. Springer, T. A. Zawodzinski, and S. Gottesfeld, Proceedings of the 26th Intersociety Energy Conversion Engineering Conference, August 4-9, 1991, Boston, MA, Vol. **3.**, pp. 636 - 641.

Figures

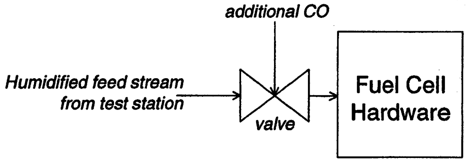

Figure 1. Schematic of Transient Hardware

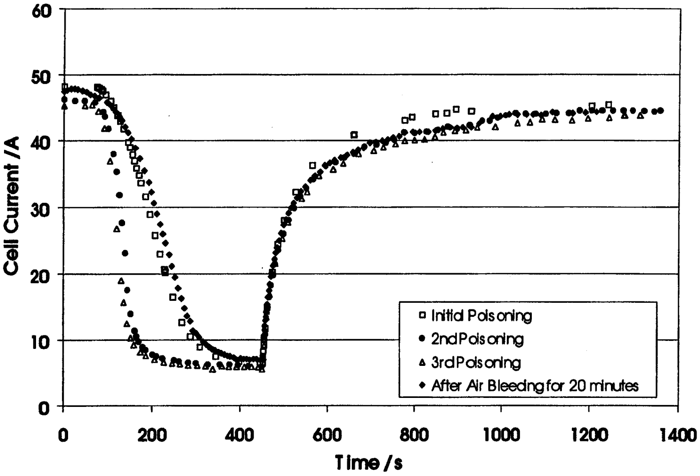

Figure 2. Initial and subsequent poisonings on Pt anode, 80°C

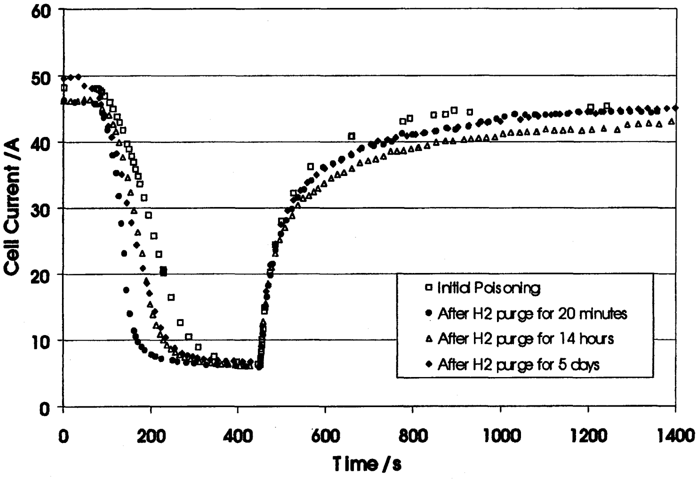

Figure 3. Transient Effects on Pt for 100 ppm CO, 80°C.

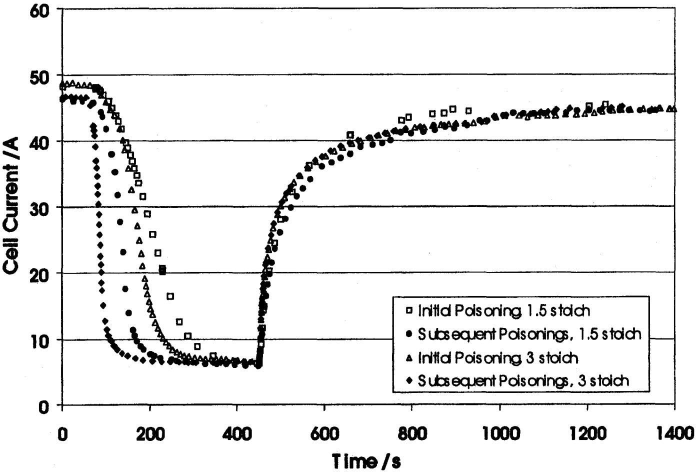

Figure 4. Transient Effects on Pt for 100 ppm CO, 80°C, with varying H_2 flowrates

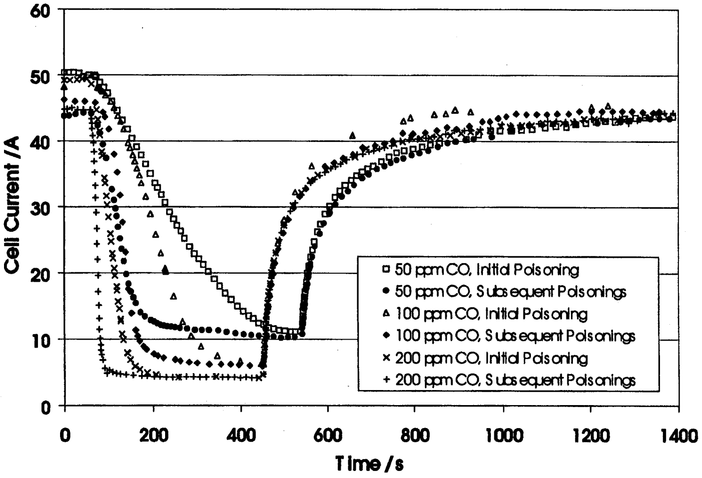

Figure 5. Transient Effects on Pt for 1.5 stoic 80°C, for 50, 100, and 200 ppm CO

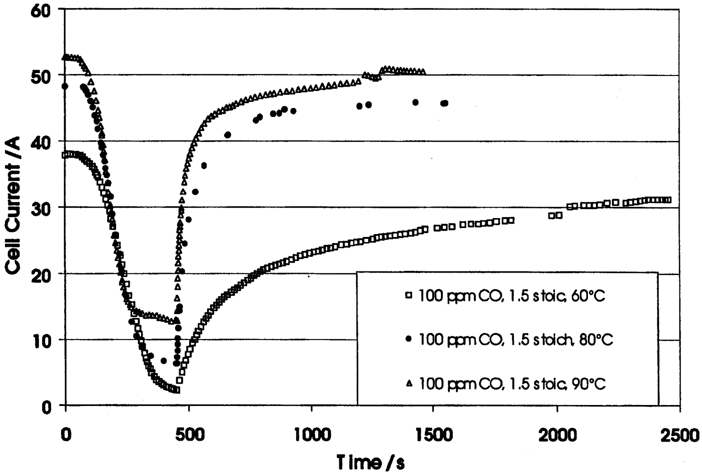

Figure 6. Transient Effects on Pt for 100 ppm CO, 1.5 stoic, for varying cell temperatures

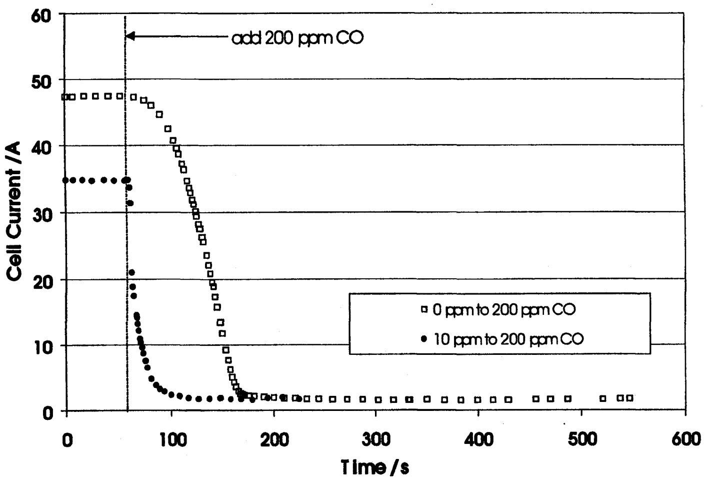

Figure 7. Transient response of a Pt-Ru anode to a jump in CO concentration of 0 to 200 ppm CO and 10 to 200 ppm CO

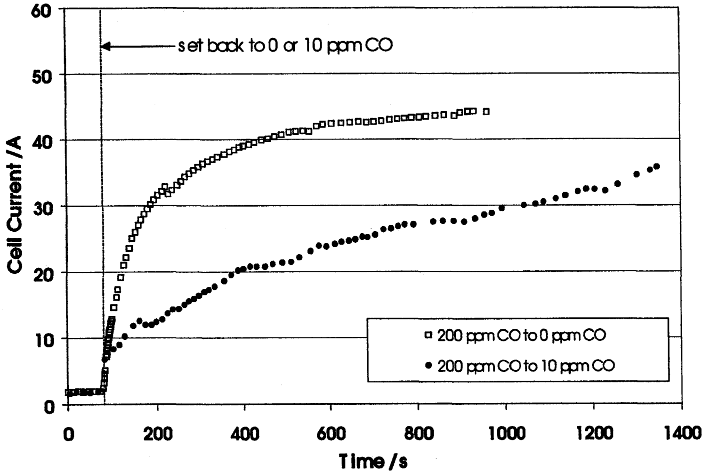

Figure 8. Transient CO recovery curves for 200 to 10 ppm CO and 200 to 0 ppm CO.

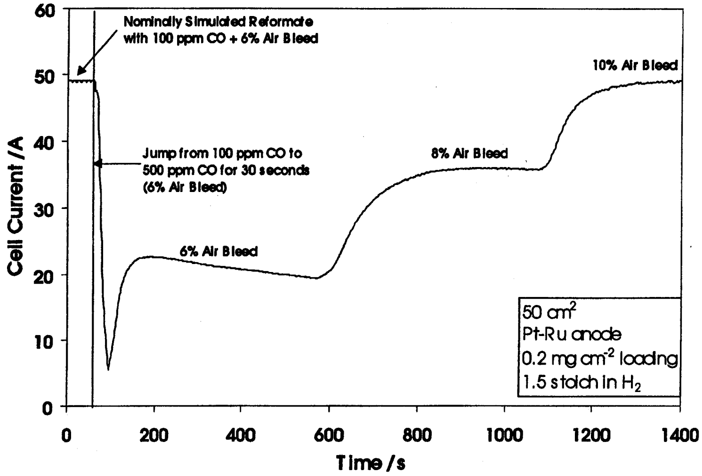

Figure 9. Transient effects of jumping from 100 to 500 ppm CO for 30 seconds.

Proton_Conducting_Membrane_Fuel_Cells_II, PV 1998-27, 150-161 (1998)
DOI: 10.1149/199827.0150PV © The Electrochemical Society

CARBON MONOXIDE TOLERANT ANODES FOR PROTON EXCHANGE MEMBRANE (PEM) FUEL CELLS.
II. ALLOY CATALYST DEVELOPMENT

Gerhard L. Holleck, David M. Pasquariello and Susan L. Clauson
EIC Laboratories, Inc.
111 Downey Street, Norwood, MA 02062

ABSTRACT

PEM fuel cells are highly attractive for distributed power and cogeneration systems. To be competitive, they must operate on fuel mixtures obtained by reforming of widely available natural gas. Such fuels invariably contain CO, a strong poison for Pt. Therefore, CO tolerant anode catalysts are essential for wide spread PEMFC introduction. Ternary PtRuX alloy catalysts where X= Ni, Pd, Co, Rh, Ir, Mn, Cr, W, Nb, Zr, were synthesized and evaluated as fuel cell anodes in the presence of CO. The alloys were prepared as well defined thin films on standard TFE-bonded carbon substrates via a dc magnetron sputtering technique. W containing catalysts with substantially increased tolerance towards the presence of CO were developed.

INTRODUCTION

Recent advances in the performance of proton exchange membrane (PEM) fuel cells make them highly attractive for distributed power, cogeneration and transportation systems. They are efficient and function virtually without noise or pollution. To be economically competitive, PEM fuel cells must operate on H_2 rich fuel mixtures obtained by reforming of widely available natural gas or liquid hydrocarbons. Reformed fuel gas mixtures invariably contain CO. Catalytic shift reactors can reduce the concentration to 10 to 100 ppm, but even at those levels CO is a strong poison for Pt (1-3). Therefore, CO tolerant anode catalysts are essential for wide spread PEMFC introduction. Alloying with Ru facilitates the oxidative removal of adsorbed CO from Pt, and PtRu alloy catalysts represent the state of the art for anodes operating on reformed gas mixtures (4,5).

Our goal is to further improve the CO tolerance of fuel cell anodes with new, multi component, bi-functional transition metal catalysts. We aim to provide, in close proximity to Pt, surface sites which can adsorb –OH at cathodic potentials and facilitate oxygen transfer to the Pt-CO_{ads} species and/or modify the Pt surface environment to reduce the coverage of CO_{ads}. Specifically we explore here the catalytic activity of ternary PtRuX alloys where X represents the transition metals Ni, Pd, Co, Rh, Ir, Mn, Cr, W, Nb and Zr. To permit a truly comparative evaluation of the catalyst activity in a representative fuel cell configuration, we developed a new technique to synthesize multi-component alloy catalysts as well defined thin films on standard TFE-bonded carbon substrates via dc magnetron sputtering (6). The thin catalyst layer (e.g. 100 nm) is located at the electrode-membrane interface, permitting complete catalyst utilization difficult to achieve in conventional TFE bonded electrodes, where some parts are always inaccessible by either the gas or the electrolyte. Further, the catalysts are tested in an electrode structure which is identical for all alloy compositions and which has, due to its availability, become almost a standard in many fuel cell research laboratories.

EXPERIMENTAL

Electrode Catalyst Fabrication

The sputter deposition was performed with a custom designed Microscience IBEX-2000 system. A schematic of the IBEX deposition system is shown in Figure 1. The system permits simultaneous sputtering of up to four different metals with independent control of the deposition rate and hence the amount of each metal in the catalyst coatings. The substrates (2.5 x 5.0 cm glass slides and uncatalyzed carbon electrodes) are mounted on a circular plate that rotates at 105 rpm beneath the sputter guns. At this rotation rate, less that one monolayer of metal from each sputter gun is deposited during a single pass, ensuring that the films have homogeneous compositions. For the work described here, the catalysts are generally deposited at a pressure of 10 mTorr, and an Ar flow rate of 10 sccm, with the substrates mounted on the rotating planet. The substrates were at ambient temperature, and at a distance of 6.5 cm from the targets. The typical sputter time was 30 minutes following an equally long pre-sputtering period to condition and clean the target surfaces. During these periods the substrates were shielded. The metal deposition and thus the alloy composition was controlled by the power (current and voltage) applied to the respective targets.

Our principal substrate was a standard but uncatalyzed TFE-bonded carbon fuel cell electrode purchased from E-TEK. Simultaneously the alloy film was also deposited onto microscope glass slides. These were used for the alloy characterization including measurement of film thickness, crystal structure, and elemental composition.

Film thickness was measured with a Dektak profilimeter using an edge created by partially masking (e.g., painting an ink line on the substrate) the clean glass slide before catalyst deposition. This mask, along with the overlying film, was removed with a cotton swab dampened with isopropanol.

The crystal structure of the catalyst films was determined by X-ray diffraction in a Rigaku spectrometer using the Bragg-Brentano geometry.

The surface morphology of the deposited catalysts was evaluated via scanning electron microscopy (Cambridge Instruments, Stereoscan 120). Film composition was determined semi-quantitatively from energy dispersive X-ray spectroscopy (EDS) in the SEM.

Electrochemical Test Arrangement

Electrode performance was evaluated in the modified fuel cell arrangement illustrated in Figure 2. The fuel cell cathode was replaced by 0.5M H_2SO_4 electrolyte and a Pt wire counter electrode. This permitted the unambiguous measurement of anode potentials against a dynamic H_2 reference electrode (DHE). The DHE consisted of a TFE bonded Pt black electrode (~0.2 cm^2) to which a cathodic current of 0.2 mA was applied that maintained the reference electrode potential about 1 to 2 mV cathodic of the reversible H_2 potential. The test cell was constructed of Teflon with Viton O-ring seals. We pressurized the counter electrode compartment to 0.5 atm above atmospheric pressure to provide a uniform contact force between the back side of the anode and the graphite insert, that resulted in a low resistance electrical contact. The pressure was maintained independent of the H_2 evolution rate at the counter electrode by a pressure regulating vent.

Gas composition and gas flow were controlled via a system of mass flow controllers (Tylan) connected to compressed gas cylinders (H_2 grade 4.7, H_2 + 99 ppm CO, N_2 prepurified from AIRCO). Gas flow rates were generally 0.5 to 2.0 cc/s, and the gas stream was humidified before use by passage through distilled H_2O held at the same temperature as the test cell. Potential and/or current was controlled by a potentiostat/galvanostat (EG&G PAR Mod. 363 and Universal Programmer Mod. 175). The ohmic resistance component of the measured potential was monitored continuously by a current interrupter (ESC Model 800 IR measurement system). Current, voltage, and resistance data were acquired with a computer-based data acquisition system. The experimental setup is schematically illustrated in Figure 3.

Electrode Test Procedures

For the electrochemical evaluation, the catalyzed electrodes were bonded to a proton exchange membrane Nafion 117 (DuPont). The membrane was hydrated by boiling in distilled water for 1h, followed by immersion in 5% H_2O_2 at 70°C to 80°C for 1 h and then in 1M H_2SO_4 at ~80°C for 0.5 h. Repeated treatments with boiling distilled water were performed until the pH of the rinse water indicated that all excess H_2SO_4 had been removed.

Catalyzed electrode discs (2.2 cm diameter) were die cut from the coated substrates. These specimens were impregnated with about 0.3 mg/cm^2 Nafion using an alcoholic solution of Nafion 117 (Aldrich) applied with a spray atomizer to the catalyzed side of the electrode. The catalyzed side was placed face-down onto a 4.5cm diameter wet Nafion membrane and the two components were bonded by hot pressing at 130°C and 80 atm for 90 seconds. The active electrode diameter in our test cell was 1.6 cm, and yielded an active electrode of 2 cm^2.

The anode performance characterization was generally carried out at 60°C with H_2 and H_2-CO gas mixtures containing 10 and 100 ppm CO. Selected tests were also performed with H_2 containing other CO concentrations. A standard test regime consisted of the following sequence: (1) slow anode polarization at 1 mV/s in pure H_2; (2) a sequence of cyclic voltage sweeps at 1 mV/s between 0 and 180 mV in H_2 + 10 ppm CO; (3) extended (~1h) polarization of the electrode at ~100 mV and monitoring of the current to establish steady state conditions with H_2 + 10 ppm CO gas (4) slow (1 mV/s) cyclic voltage sweeps to ~600 mV or 1000 mA with H_2 + 10 ppm CO; (5) switch over and electrode equilibration in H_2 + 100 ppm CO; (6) slow (1mV/s) cyclic voltage sweeps to 180 mV and then to ~600 mV or 1000 mA with H_2 + 100 ppm CO; (7) change over to N_2 and then H_2 followed by polarization at 1 mV/s to 1000 mA. This test regime was developed to achieve reproducible, near steady state conditions, and to detect any time or test induced changes in electrode activity.

RESULTS AND DISCUSSION

Catalyst and Electrode Structure

The surface morphology of the catalysed electrode structures is illustrated in the scanning electron micrographs of Figure 4.). At low magnification, the uncatalyzed electrode shows a tile-like pattern, and evidence of processing. Higher magnification reveals the agglomerates observed typically with Teflon-bonded carbon. SEM examination of all carbon substrates with deposited metals or alloys show surface structures identical to those for the $Pt_{0.55}Ru_{0.47}$ and $Pt_{0.55}Ru_{0.30}W_{0.15}$ catalyzed electrodes. They are characterized by nearly spherical particles with diameters of 200 to 200 nm nucleated around the surface aggolomerates. The morphology of the catalyst layer was clearly controlled by the substrate. Thus, a macroscopically two-dimensional but microscopically three-dimensional rough alloy catalyst interface was obtained. From Pt deposits of the same structure we determined, via H adsorption and stripping, surface roughness factors of 10 to 13. The catalyst surface area was found to be fairly insensitive to changes in deposit thickness, and agreed well with calculations based on dimensions obtained from the SEM photographs. Thus, a 100 nm Pt catalyst layer is equivalent to a 0.2 mg/cm^2 loading and a specific catalyst surface area of 5 m^2/g.

The catalyst films were mostly crystalline, as indicated by X-ray diffraction. Figure 5 shows a comparison of the X-ray diffraction patterns obtained for Pt, Ru, $Pt_{0.52}Ru_{0.48}$, and $Pt_{0.55}Ru_{0.30}W_{0.15}$, clearly demonstrating that we are depositing alloys as opposed to merely mixtures of the individual components. The pattern for Pt shows a strong, sharp, well-defined peak for the 111 plane, whereas those for the 222, 311, 220, and 200 reflections were weak. This is a result of the preferred orientation common to thin films. Pt has a cubic close-packed structure, while Ru is hexagonal close-packed. These structures are more compatible with each other than with the W structure. Consequently, PtRu alloys preserve the Pt lattice structure, with a shift toward higher angles. The main diffraction peak in the pattern for the PtRuW ternary is still shifted toward higher angle, but there is also a more significant reduction in the overall intensity of the diffraction. We have observed that the alloys have more amorphous character when the third constituent has a crystal structure that differs significantly from those of Pt and Ru.

Anode Catalyst Performance

Characteristic potential-current relationships measured with a Pt catalyzed anode in the absence and presence of CO are reproduced in Figure 6. For H_2 the IR corrected electrode polarization was very small. The addition of only 10 ppm CO changed the potential–current behavior very dramatically. The anode polarized quickly beyond 400 mV. Higher current densities could be maintained only around 600 mV, where the surface $-OH_{ads}$ concentration on Pt was sufficient to allow effective oxidative removal of adsorbed CO. Clearly, such electrode polarizations are not acceptable in a practical fuel cell. The improvement achieved with a Pt-Ru alloy catalyst is demonstrated in Figure 7.

Again, in the absence of CO, H_2 oxidation occurred at very low polarization. The onset of substantial electrode polarization in the presence of CO was shifted to higher current densities. Also, the potential at which H_2 – CO mixtures could be oxidized at high rates was significantly reduced occurring now between 300 and 400 mV. This has been attributed to the facilitated oxidation of CO_{ads} on Pt by the proximity of $-OH_{ads}$ at Ru sites.

We synthesized and characterized ternary PtRuX alloys where X=Ni, Pd, Co, Rh, Ir, Mn, Cr, W, Nb, Zr. All alloy catalysts showed low polarization with pure H_2. In the presence of CO, the potential-current relationships were fundamentally similar for all alloys and resembled those shown for PtRu in Figure 7. Differences were observed in the current density at which significant electrode polarization occurred and in the plateau voltage at which CO_{ads} was effectively oxidized. These parameters are summarized for the alloys in Table 1. In general we found that the partial replacement of Ru by another transition metal lowered the alloy activity both in the low potential and the plateau regions. At low levels of Ru substitution the effect was small for most elements but it was quite significant for Pd, Ni and Nb. A striking exception was W where the partial substitution of Ru resulted in a significantly increased tolerance to the presence of CO at 10 and 100 ppm levels. A graphic representation of the results and a comparison with the binary alloys is shown in Figure 8.

In the presence of CO the binary PtRu and PtW alloy catalysts were far superior to pure Pt. Of the two, PtRu was better in the low potential region while PtW proved superior in the plateau region except at very high current densities. The performance of the ternary PtRuW alloy, however, exceeded both binaries in the low potential and the potential plateau regions. To probe whether our results are indeed representative for steady state conditions, we held the potential of the ternary catalyst at 100 mV and at 200 mV. The currents remained, except for minor fluctuations, flat at 85 mA and 250 mA respectively over the entire 90 min test period.

A similar series of potential-current curves for Ir containing Pt alloys is reproduced in Figure 9. Again, the ternary alloy catalyst was more active for H_2 oxidation in the presence of CO than any of the binary catalysts. Ru was, however, more effective than Ir in improving the CO tolerance as can be seen from the activity decrease when Ru was substituted by Ir in the PtRu alloy.

in improving the CO tolerance as can be seen from the activity decrease when Ru was substituted by Ir in the PtRu alloy.

To translate our results into the realm of practical fuel cells, we need to consider the relatively low surface area of our catalysts. A practical PEM fuel cell electrode may contain a loading of e.g. 1 mg/cm^2 of a catalyst with a specific surface area of 30 m^2/g. This would translate into a real catalyst surface of 300cm^2/cm^2 of electrode. If 70% of the catalyst were accessible, such an electrode should, neglecting IR and transport limitations, be able to support about 20 times the current measured with our thin layer electrodes. Thus, with the goal of lower catalyst loadings in mind, our results up to ~100 mA/cm^2 would be most relevant for practical full size fuel cells.

CONCLUSIONS

Using a new technique we synthesized multi-component Pt–transition metal alloy catalysts as thin layers on standard fuel cell electrode substrates. This permitted a true comparative evaluation of catalyst activity for the oxidation of H_2 in the presence of CO. The partial substitution of Ru in PtRu by Ni, Pd, Co, Rh, Ir, Mn, Cr, Nb and Zr resulted in a moderate decrease in activity for H_2 oxidation in the presence of 10 or 100 ppm CO. The effect increased with increasing level of metal substitution. In contrast, PtRuW alloy anodes showed a substantially improved tolerance towards the presence of CO.

ACKNOWLEDGEMENTS

This work is supported by the U.S. Department of Energy under Grant DE-FG02-96ER82157.

REFERENCES

1. V. M. Schmidt, R. Ianniello, H. F. Oetjen, H. Reger, U. Stimming and F. Trila, in ECS Proc. Vol. PV95-23, p.1, The Electrochemical Society, Pennington, NJ (1995).
2. S. F. Simpson, C. E. Salinas, A. J. Cisar and O. J. Murphy, in ECS Proc. Vol. PV95-23, P.182, The Electrochemical Society, Pennington, NJ (1995).
3. J. Sobkowski and A. Czerwinski, J. Phys. Chem., 89, 365 (1985).
4. M. Iwase, S. Kawatsu, in ECS Proc. Vol. PV95-23, p. 12 (1995). The Electrochemical Society, Pennington, NJ.
5. H. A. Gasteiger, N. M. Markovic, P. N. Ross Jr., and E. J. Cairns, J. Phys. Chem. 98, 617 (1994).
6. G.L. Holleck, D.M. Pasquariello and S.L. Clauson, Proc. 33rd Intersoc. Energy Conversion Engineering Conf.,Colorado Springs, August 1998. Paper 38.

Table I. Summary of Catalyst Performance

Alloy	H_2+10 ppm CO			H_2 + 100 ppm CO		
	I (mA/cm^2)	E (V)		I (mA/cm^2)	E (V)	
	at 100 mV	at 100 mA/cm^2	at 300 mA/cm^2	at 100 mV	at 100 mA/cm^2	at 300 mA/cm^2
$Pt_{0.53}Ru_{0.47}$	57	0.256	0.311	19	0.309	0.364
$Pt_{0.55}Ir_{0.45}$	29	0.314	0.489	11	0.446	--
$Pt_{0.82}W_{0.18}$	31	0.172	0.493	6.8	0.469	0.670
$Pt_{0.52}Ru_{0.15}Cr_{0.33}$	32	0.238	---	14	0.316	---
$Pt_{0.52}Ru_{0.33}Cr_{0.15}$	60	0.186	0.282	25	0.265	0.374
$Pt_{0.52}Ru_{0.14}Mn_{0.34}$	33	---	---	10	0.292	0.386
$Pt_{0.54}Ru_{0.36}Mn_{0.10}$	59	---	---	19	0.305	0.354
$Pt_{0.44}Ru_{0.14}Zr_{0.42}$	26	---	---	5	0.362	0.421
$Pt_{0.52}Ru_{0.35}Zr_{0.14}$	52	---	---	13	0.333	0.350
$Pt_{0.40}Ru_{0.10}Ni_{0.50}$	25	0.294	0.342	4	0.414	0.471
$Pt_{0.47}Ru_{0.13}Ni_{0.40}$	38	---	---	10	0.324	---
$Pt_{0.52}Ru_{0.32}Ni_{0.16}$	49	0.253	0.316	9.2	0.347	0.391
$Pt_{0.49}Ru_{0.14}Rh_{0.37}$	45	---	---	10	0.356	---
$Pt_{0.49}Ru_{0.33}Rh_{0.18}$	50	---	---	18	0.340	0.371
$Pt_{0.46}Ru_{0.13}Co_{0.41}$	21	0.310	0.364	6.2	0.404	0.449
$Pt_{0.50}Ru_{0.33}Co_{0.17}$	35	---	---	17	0.316	0.364
$Pt_{0.54}Ru_{0.32}Ir_{0.17}$	57	0.233	0.304	24	0.308	0.372
$Pt_{0.6}Ru_{0.2}Ir_{0.2}$	36	0.266	0.326	9	0.339	0.406
$Pt_{0.54}Ru_{0.14}Pd_{0.32}$	35	---	---	13	0.433	0.462
$Pt_{0.51}Ru_{0.34}Pd_{0.15}$	35	---	---	13	0.364	0.415
$Pt_{0.57}Ru_{0.37}Nb_{0.07}$	39	0.354	0.454	12	0.411	0.551
$Pt_{0.53}Ru_{0.32}W_{0.15}$	85	0.142	0.248	34	0.251	0.385
$Pt_{0.53}Ir_{0.18}W_{0.29}$	57	0.132	0.255	33	0.206	---
$Pt_{0.51}Ir_{0.43}W_{0.06}$	93	0.157	0.309	28	0.279	0.430
$Pt_{0.52}Ir_{0.47}W_{0.01}$	85	0.161	0.299	28	0.365	0.613

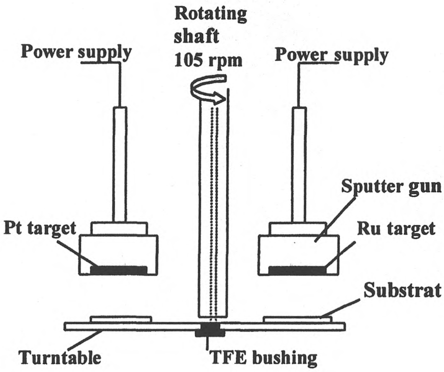

Figure 1. Schematic diagram of *in-vacuo* apparatus used for sputter deposition of alloy catalysts. For clarity only two sputter targets, Pt and Ru, are shown. Shields, masks, and substrate heaters are also omitted from the drawing.

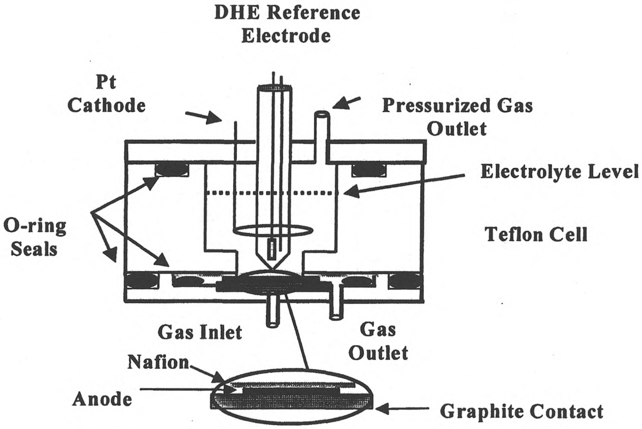

Figure 2. PEM fuel cell anode test cell.

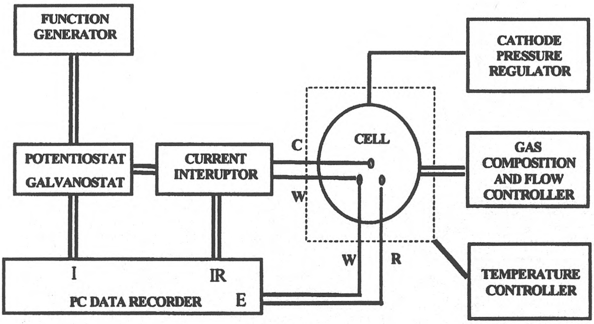

Figure 3. Test arrangement for fuel cell anode performance evaluation.

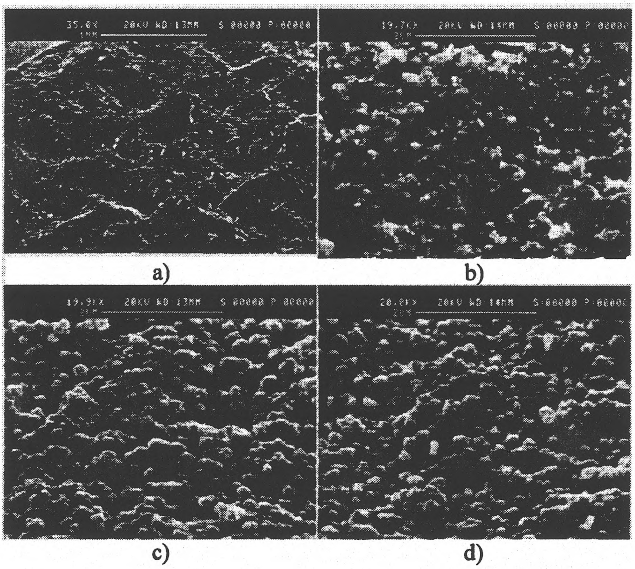
a) b) c) d)

Figure 4. Scanning electron micrographs of (a,b) uncoated TFE-bonded carbon electrode, and electrodes catalyzed with (c) $Pt_{0.53}Ru_{0.47}$, and (d), $Pt_{0.55}Ru_{0.30}W_{0.15}$.

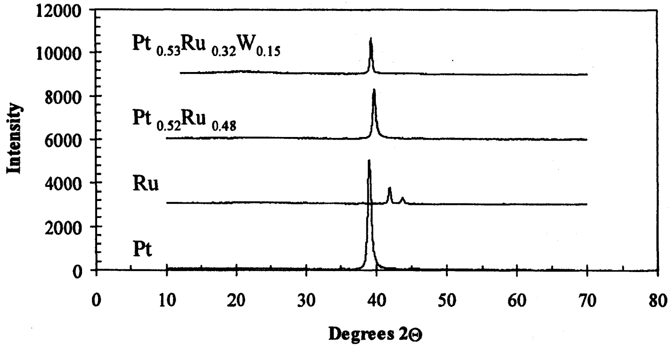

Figure 5. X-ray diffraction patterns of sputter deposited catalysts. The patterns are offset and intensities are in arbitrary units.

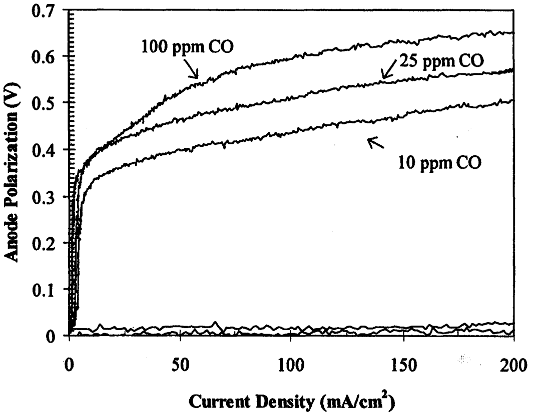

Figure 6. Polarization of a Pt catalyzed fuel cell electrode in H_2 (lower unlabeled trace) and H_2-CO mixtures. 60°C, sweep rate 1 mV/s.

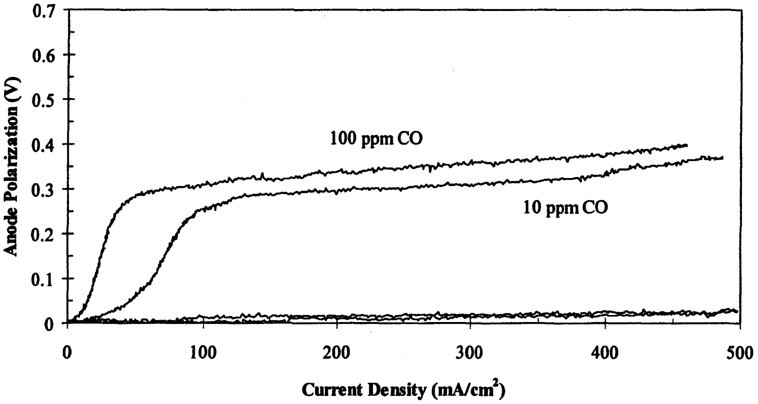

Figure 7. Polarization of a $Pt_{0.53}Ru_{0.47}$ catalyzed fuel cell electrode in H_2 (lower unlabeled trace) and H_2-CO mixtures. 60°C, sweep rate 1 mV/s.

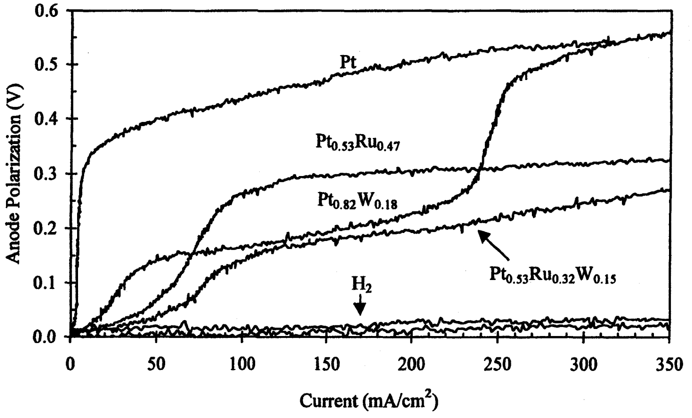

Figure 8. Comparison of anode polarization measured for electrodes catalyzed with Pt, PtRu, or PtW, and a PtRuW ternary in a mixture of H_2 with 10 ppm CO. Typical performance in pure H_2 is included for comparison.

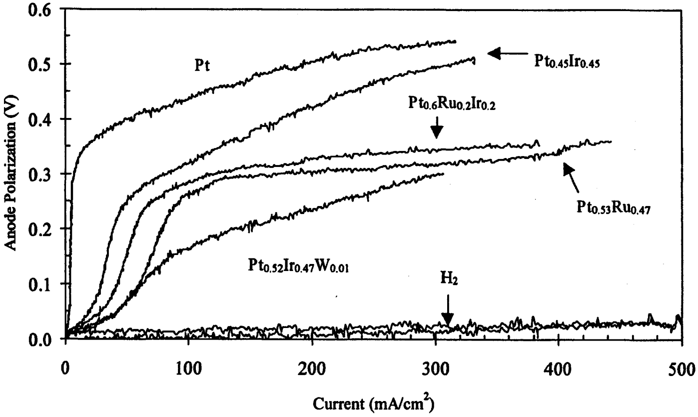

Figure 9. Comparison of anode polarization for Pt, PtIr, PtRuIr, PtRu, and PtIrW alloys in pure H_2 and in a mixture of H_2 with 10 ppm CO.

Proton_Conducting_Membrane_Fuel_Cells_II, PV 1998-27, 162-175 (1998)
DOI: 10.1149/199827.0162PV © The Electrochemical Society

ELECTROCATALYSIS OF CO TOLERANCE IN H_2/CO MIXTURES BY CARBON SUPPORTED PtMo IN A PROTON EXCHANGE MEMBRANE FUEL CELL

E. A. Ticianelli, S. Mukerjee, S. J. Lee, and J. McBreen
Department of Applied Science, Brookhaven National Laboratory
Upton, NY 11973

J. R. Giallombardo, and E. S. De Castro
E-TEK, Inc., 6 Mercer Road
Natick, MA 01760

ABSTRACT

We report 2 to 3 fold enhancement in activity for CO oxidation in PEM fuel cell by highly dispersed carbon supported PtMo alloy nano-crystals (PtMo/C) as compared to the current state of the art PtRu/C at 85°C with 100 ppm CO in H_2. The half-cell polarization characteristics show a lower susceptibility to changes as a function of temperature (below 100°C), CO concentration (5-100 ppm) and alloy composition (1:1 to 1:5, Mo:Pt) in contrast to Pt/C and PtRu/C. Cyclic voltammograms show both Pt and Mo features and a redox couple involving Mo (at ~0.5 V). CO stripping voltammograms show two peaks, the first at low overpotentials (~0.05 V) followed by a second initiated at ~ 0.5 V, the second peak is akin to oxidation of CO on Pt/C. Preliminary analysis of the Mo K edge XANES confirmed the presence of Mo as an oxide at potentials as low as 0.0 V and the redox couple at ~ 0.5 V.

INTRODUCTION

CO tolerance in reformer based low and medium temperature H_2/O_2 PEM fuel cells is crucial for the viability of this technology for applications in transportation and, portable power generation applications. The choice of an appropriate anode electrocatalyst with low susceptibility to CO poisoning and a high kinetic rate for hydrogen oxidation is therefore paramount. The most commonly used anode electrocatalyst, Pt/C, is very susceptible to poisoning by CO, leading to high overpotentials. Alternate binary electrocatalysts containing a more oxidizable element with ability to nucleate oxygenated species at lower potentials and hence initiate CO oxidation on the surface with lower overpotentials have been the focus of several decades of research. Prior literature is replete with investigations on alloys such as PtSn (1-2), PtRh (3), PtRu (4-6) and Pt with oxygen adsorbing ad-atoms such as Ge, Sb and Sn (7-8) *etc.* In recent years PtRu alloys have received renewed attention as promising candidates for CO oxidation in PEM fuel cells (9-11). A recent report by Oetjen *et al.,* (12) have exhibited a four fold performance enhancement with highly dispersed PtRu as compared to Pt at 80°C with CO concentrations up to 250 ppm. Despite these improvements the overpotential with CO concentrations of 100 ppm at moderate temperatures such as 85°C is substantial, resulting in a loss of 270 mV at 1 A/cm^2 (12).

Recent reports by Grgur *et al.,* (13-14) have reported interesting results on electro-oxidation of H_2/CO mixtures with addition of Mo to Pt using well characterized PtMo bulk alloys. Electrochemical characterization, using rotating disk electrodes (RDE), showed that like PtRu bulk alloys, Mo alloyed with Pt is able to initiate H_2 oxidation at or near complete CO coverage with 50 times higher current density as compared to Pt. They pointed out the possibility of different roles played by Mo and Ru in these alloys due to inherent differences in the elements. The exact mechanism remains uncertain. Unlike Ru, in the Mo alloy, the bulk of the CO is stripped above 0.6 V, with evidence of a smaller oxidation at lower potentials in the range of 0.05 to 0.5 V (13,14).

Presented here are results of our investigation on highly dispersed PtMo/C in PEM fuel cells demonstrating enhanced CO tolerance. Studies were conducted at several temperatures, CO/H_2 contents, and Pt/Mo compositions and the results were compared with those of standard Pt/C and PtRu/C materials. Single and half cell polarization measurements and cyclic voltammetry in the presence and absence of CO were employed in the experimental investigation. In addition, efforts to understand the role of Mo in these alloys using ***in situ*** X-ray absorption spectroscopy are included.

EXPERIMENTAL

The PtMo/C electrocatalysts were obtained from ETEK Inc. (Natick, MA). The nominal compositions of the PtMo/C catalyst were 1/1, 3/1, and 4/1, Pt/Mo atom/atom based on the ratio of the starting materials and the loading on carbon was 30 w/o. For control experiments, Pt/C and PtRu/C from ETEK were used. The PtRu/C was an alloy with an atomic composition of 50% Pt, 50% Ru, the loading on carbon for both Pt/C and PtRu/C being 20 w/o. Anode electrodes were prepared by a brushing/rolling technique developed in house. They comprised of a carbon cloth substrate (ETEK, Carbon Cloth), with diffusion layer of Teflonized carbon (35 w/o PTFE) with average thickness of 35 μm, which was pre-sintered at 320 °C under Ar. The reaction layer comprised of catalyst + Nafion (0.4 mg/cm^2 Pt or Pt alloy loading). The gas diffusion side of the electrode had a thinner diffusion layer of C/PTFE (30 w/o) of ~15 μm thickness. Steady state polarization measurements on CO tolerance were carried out in a fuel cell test station using a cell fixture for a 5cm^2 membrane-electrode assembly, which allowed for both single and half-cell polarization measurements. The test station was built in-house and had provisions for controlling temperature, pressure, humidification and flow (mass flow) of reactant gases. The bipolar plates made of carbon with resin impregnation (Poco graphite) had standard ribbed flow channels and the anode chamber had a built in hydrogen reference electrode (RHE) with separate flow channels allowing for simultaneous half cell measurements. Details of the fuel cell test station and the single cell test fixture are given elsewhere (15). Membrane electrode assemblies were made for anodes Pt/C, PtRu/C and PtMo/C while keeping the cathode electrode the same (Pt/C, ETEK electrode, 0.4 mg/cm^2 Pt loading). The membrane was Nafion® (115) which was cleaned by a procedure described in detail elsewhere (15). The Nafion loading (solubilized Nafion® [Aldrich Chemicals]) in the reaction layer of the electrodes was ~ 1.9 mg/cm^2 and the assembly was made by hot pressing at 1000 Kg$_f$/cm^2, 140 °C for 3 minutes. Simultaneous measurements of single and half-cell performance were made at several temperatures, with corresponding anode/cathode humidification temperatures 15°/5°C above that of the cell. Pressures in the anode and cathode chambers were regulated at each temperature to maintain the H_2 and O_2 partial pressures 1 atm. For H_2/CO mixtures, premixed gas cylinders were used (Matheson, NJ).

Cyclic voltammetries in the PEM cell were carried out using the same single cell set-up at 25 °C. To investigate catalyst behavior with respect to the CO oxidation process, H_2 containing 100 ppm of CO was passed through the electrode for at least 1 h maintaining a constant electrode potential (0.05 V vs. RHE). At the same time pure hydrogen was passed through the counter electrode which also served as a RHE reference. After passing the CO mixed gas, the anode compartment were purged with N_2 for about 30 min to remove residual H_2 gas and non-adsorbed CO.

XAS measurements were conducted at beam line X11A at the National Synchrotron Light Source (NSLS) both at the Pt L (L_3 and L_2) and Mo K edges. Details of the beam line optics, monochromator and detuning *etc.* are given elsewhere (16). Electrodes for XAS measurements were prepared according to the methodology described elsewhere (16), the catalyst loading on the electrode was 45 mg/cm^2. All electrodes were soaked in 1 M $HClO_4$ for 48 hr. and wetted by a vacuum procedure prior to XAS experiments. The electrolyte of choice, 1 M $HClO_4$, exhibits negligible anion adsorption in contrast to other aqueous acids such as H_2SO_4 and hence is closest to proton conductors such a Nafion®. Two types of *in situ* spectro-electrochemical cells were used (17-18). A compression cell was used for measurements in 1 M $HClO_4$ as a function of potential (17). Experiments with and without adsorbed CO were conducted in a cell, which allowed CO feed to the electrode and *in situ* measurements under conditions of CO adsorption and desorption (18). For these experiments a pure CO stream was passed through the working electrode for one hour, with the electrode polarized at 0.0 V vs. RHE. Polarizing the electrode to more positive potentials subsequently stripped this CO. Details of the spectro-electrochemical cells, data acquisition and XANES and EXAFS analysis are given elsewhere (16-18).

RESULTS AND DISCUSSION

Single and half cell measurements

Figure 1 compares the single cell performance of Pt/C, PtRu/C and 3/1-PtMo/C (0.4 mg/cm^2) as anode electrodes (cathode: Pt/C, 0.4 mg/cm^2) in H_2/CO [100 ppm]//O_2 at 85°C with the respective anode/cathode pressures of 16/11 psig and humidification temperatures of 100/90°C. Inset in Fig. 1 shows the corresponding polarization behavior of the anodes. Figure 2 presents the effect of temperature on the single cell performance and in the anode polarization for the fuel cell equipped with 3/1-PtMo/C anode at a CO concentration of 20 ppm. The effect of the CO partial pressure on the single cell performance and the corresponding polarization of the hydrogen electrode is presented in Figure 3, for the same electrode at a constant temperature (85°C). Finally, Figure 4 presents the effect of Pt/Mo composition ratio on the single cell and hydrogen electrode polarization in the presence of 100 ppm of CO at 85°C.

As evident from the polarization behavior relative to the data for Pt/C anode without CO presented in Fig. 1, PtMo/C exhibits higher CO tolerance than PtRu/C. Comparison of the half-cell polarization and the overall single cell performance behavior of these electrocatalysts in H_2/O_2 (without CO) shows negligible differences (not shown), indicating that the hydrogen polarization characteristics without CO is essentially the same for all the electrode materials considered here. This observation is consistent with that presented for bulk electrodes prepared with the same materials (13,14). However the polarization characteristics in the presence of CO (Fig. 1, inset) result in marked differences. Comparison of current densities at 50 and 100 mV using the polarization plot for hydrogen oxidation in the presence of 100 ppm CO indicates two to three fold enhancement of anode electrode performance in going from PtRu/C (current state of the art) to PtMo/C.

Figure 2 shows that the CO poisoning effect (20 ppm CO) on the PtMo/C anode is negligible for temperatures above 100°C, this result is similar to those reported earlier (19,20) on Pt/C and PtRu/C. On the other hand, while Pt/C or PtRu/C show marked performance degradation at low temperatures (19,20), the fuel performance degradation due to CO poisoning is small for PtMo/C, even for temperatures as low as 40°C. Also, contrarily to Pt/C, PtSn/C or PtRu/C (19,20), the single and half cell performance data in Fig. 3 shows that PtMo exhibits a much smaller effect as a function of CO partial pressure, the results with 20, 50, and 100 ppm CO being approximately coincident. Another important observation is that the CO tolerance factor of the PtMo/C alloy nano-crystals are essentially independent of composition in the range 1:1 to 1:5 Mo:Pt, as evident from the results of Figure 4.

Fig. 1 (inset) shows that in the presence of CO, the hydrogen electrode polarization for Pt/C exhibits a clear tendency for a liming current, this is less evident for PtRu/C and absent for PtMo/C. This behavior for PtMo/C was also observed at all temperatures, CO partial pressures, and Pt/Mo compositions (Fig. 2-4). According to previous reports (19,21), the appearance of a limiting current is due to the occurrence of a free site attack CO poisoning mechanism given by

$H_2 + 2\,S \rightarrow 2\,S\text{—}H$	(Tafel reaction)	[I]
$S\text{--}H \rightarrow S + H^+ + e$	(Volmer reaction)	[II]
$CO(g) + n\,S \Leftrightarrow S_n\text{--}CO$	(Free site attack)	[III]
$S\text{--}H_2O + S\text{--}CO \rightarrow S + CO_2 + 2H^+ + 2e$	(CO oxidation)	[IV]

where S represents an active site in the catalyst surface and n = 1 for linear bonded CO and n = 2 for bridge bonded adsorbed CO, which are the predominant CO adsorbed species found on the catalyst surface. In this mechanism, reactions (I) and (II) correspond to the Tafel/Volmer reactions usually considered for the HOR in acid media (22,23). Reaction (III) represents the CO adsorption process, and reaction (IV) is responsible for CO oxidation leading to CO_2. S-H_2O represents the catalyst-hydrated oxide, which is formed in different regions of potential depending on the nature of the electrode material (1,6,24-30).

The analysis of the polarization response of the hydrogen electrode can be more appropriately made using the corresponding Tafel response. Figure 5 presents these plots for the polarization of the hydrogen electrode in presence of 20 ppm of CO at 55°C. In absence of CO, both reactions (I) and (II) are very fast, the overall reaction kinetics is described by a very large exchange current density and a Tafel slope (b) close to b = 30 mV dec^{-1} (22,23). On the other hand, in the presence of CO there is a large fraction of the surface covered with CO, hence reaction (I) may become the rate-determining step. However, at low overpotential or low current densities the surface coverage of H may be enough to allow reaction (II) to occur at full speed which explains the value of Tafel slopes of 20-30 mV dec^{-1} obtained experimentally for overpotentials less than 50 mV (Fig. 5) for all catalysts. At higher overpotentials, while the rate of reaction (IV) is negligible, the current generation is controlled by the rate of H adsorption, and a limiting current may be observed in the polarization diagram. Under this condition the hydrogen current originates only from the oxidation of the S-H being formed on the holes of a compact CO surface monolayer (1,13,31).

As pointed out above, for Pt/C limiting currents were clearly seen either at 85°C, CO 100 ppm (Fig. 1, inset) or at 55 °C, 20 ppm CO (Fig. 5). The appearance of limiting current is less evident for PtRu/C and not observed for PtMo. According to the above mechanism the absence of limiting currents can be explained either by a weakening of the CO adsorption process (reaction (III)) and/or to a 'cleaning' of the surface by the CO oxidation step (reaction (IV)). Smaller CO adsorption will allow for a larger coverage of S-H which can dislocate the limiting current to very high values, while the onset of reaction (IV) will lead to an opening of free catalyst sites (S) also leading to an increase of the H coverage. In this case the consequence is the increase of the current for hydrogen oxidation, and a prevention of establishment of limiting currents.

To check these two possibilities, the experimental results in Fig. 5 were analyzed by means of kinetic equations derived previously for the above mechanism (19,21). Briefly, in this treatment the expression for the current for hydrogen oxidation was derived from the expression for the steady state coverages of hydrogen and carbon monoxide, that is, taking n = 2,

$$k_1 P_{H_2}(1-\theta_C-\theta_H)^2 - k_{-1}\theta_H^2 - 2k_2^\eta\theta_H = 0 \qquad [1]$$

$$k_3 P_{co}(1-\theta_H-\theta_C)^2 - k_{-3}\theta_C^2 - k_4^\eta = 0 \qquad [2]$$

Where *k's* are the rate constants of the forward and backward reactions (I) to (IV) expressed in A/cm^2. The current density for the hydrogen oxidation reaction (j_{H2}) was taken as

$$j_{H_2} = 2k_2^\eta\theta_H = 2k_2\theta_H\eta \qquad [3]$$

Where the dependence with the electrode overpotential (η) is expressed assuming a linear polarization approximation. The current for CO oxidation (j_{co}) was calculated using the equation derived in the thin film model of gas diffusion electrodes (19), that is,

$$j_{co} = \frac{k_4\sinh(\eta/b)}{1+\Gamma k_4\sinh(\eta/b)}; \qquad \Gamma = \frac{1}{j_{co}^l} = \frac{\delta}{FDHP_{co}} \qquad [4]$$

and the final expression for the degree of CO coverage was taken as

$$\theta_C^d = \theta_C - j_{co}\Gamma \qquad [5]$$

Where j_{co}^l is the limiting current for CO oxidation, η is the electrode overpotential, b is the Tafel slope for the CO oxidation reaction, δ is the thickness of the thin film of electrolyte covering the catalyst particles, H is the Henry constant for CO polymer/gas solubility to pressure equilibrium and D is the diffusion coefficient of CO in the electrolyte. θ_C is the CO coverage calculated assuming $k_4 = 0$, and θ_C^d is the final value. This is replaced into equation (1) to obtain the corresponding value of the hydrogen coverage, which was then used to calculate the current vs. overpotential relationship for the HOR in the presence of CO oxidation.

The results of the theoretical analysis in terms of the hydrogen oxidation currents are those presented as solid lines in Fig. 5, and in terms of the CO oxidation currents as inset in the same Figure. For derivation of the above curves the following set of values was used for the parametrization of the theoretical equations: $\delta \cong 1 \times 10^{-5}$ cm (15), H = 4.8 x 10^{-6} mol cm^{-3} atm^{-1} and D = 5.0 x 10^{-6} cm^2 s^{-1} (32), $K_1 = k_1/k_{-1}$ = 400 atm^{-1}, k_2 = 18 A V^{-1} cm^{-2}, $K_3 = k_3/k_{-3}$ = 2 x 10^9 atm^{-1}, and b = 0.09 V/e-fold (19). The values of k_4 depended on the catalyst and resulted 2 x 10^{-11} A V^{-1} cm^{-2} for Pt/C, 8 x 10^{-9} cm^{-2} A V^{-1} for PtRu/C and 8 x 10^{-8} A V^{-1} cm^{-2} for PtMo/C.

The most important observations derived from the above analysis can be summarized as follows: (i) Consistent with the experimental results in absence of CO, kinetics of the hydrogen oxidation was independent of the catalysts. The same values of the equilibrium constant K_1 and the kinetic constant k_2 were appropriate in representing the responses of the three materials. (ii) The extent of CO adsorption is similar in all catalysts since the same value for the equilibrium constant of reaction (III) was adequate to fit all the experimental responses. (iii) The extension of the CO oxidation process is quite different for the different catalysts, as observed by the distinct values for the rate constant of reaction (IV). As derived from the kinetic analysis, inset in Fig. 5 shows that the onset of CO oxidation starts at ca. 0 V for PtMo/C, 0.2 V for PtRu/C and 0.5 V for Pt/C. A clear conclusion from these observations is that the main factor for the increased CO tolerance of PtMo relative to the other catalysts is not related with a lower affinity to CO, but rather with the ability of promoting the CO oxidation process at very low electrode potentials. This conclusion is the same as that proposed previously based on the investigations using bulk catalyst alloys (4-6,13).

Cyclic voltammetry

Cyclic voltammograms for PtMo/C in 1M $HClO_4$ in the *in situ* spectro-electrochemical cell at ambient temperature (25°C) in the flooded electrode mode are presented in Figure 6. The results obtained under similar conditions, after a CO purge for 1 hr (electrode polarized at 0.0 V), on Pt/C and PtMo/C are presented in Figure 7. Finally, the cyclic voltammograms at 55 °C of the PtMo electrode in the PEM cell environment in absence and in the presence of adsorbed CO are presented in Figure 8, which also includes the anodic scan for the Pt/C and PtRu/C catalysts in the presence of CO.

Results for PtMo/C in absence of CO (Figs 6 and 8) show evidences of both Pt and Mo features, although the Pt-H_{upd} region is not as defined as on the Pt/C or PtRu/C electrodes (4-6). However, the Pt-H feature is evident from the peak for hydrogen desorption for the electrode polarized at 0.0 V (N_2 purge) for 1 hr (Figure 6). As in the case of bulk alloy (13), voltammograms of PtMo/C in absence of CO show a redox behavior at potentials of 0.43/0.50 V vs. RHE involving Mo (Figs. 6 and 8). Comparison with the Pourbaix diagram (33) for Mo indicates that this redox behavior is most likely due to $Mo^{4+} \leftrightarrow Mo^{6+}$ oxidation states. Repeated cycling between 0.05 V and 1.2 V for 50 cycles showed no changes indicating minimal dissolution of Mo from these electrocatalysts.

Experiments in the liquid acid electrolyte in the presence of adsorbed and dissolved CO (Fig. 7), and in the PEM environment with only adsorbed CO seem to indicate that both Pt and Mo are active for the CO oxidation. CO oxidation is first initiated at lower potentials by oxygenated species on the Mo surface at ca. 0.05 V, followed by Pt above 0.55 V. Comparison of the corresponding voltammogram for Pt/C confirms the CO oxidation at 0.55 V to be due to Pt. The presence of two distinct peaks is significant, in that it is in complete contrast to the corresponding voltammetric response from electrocatalysts such as PtRu/C and PtSn/C. This indicates a unique role for Mo in these electrocatalysts in contrast to a simple bifunctional mechanism where the oxides on the more oxidizable element provide the necessary oxygenated species for CO oxidation on Pt.

A qualitative comparison of the voltammograms in the presence of adsorbed CO in Fig. 8 shows that at 55 °C the onset of the CO oxidation process occurs at very low electrode potentials for PtMo/C (probably at around 0 to 0.05 V), followed by PtRu/C at ca. 0.3 V and by Pt/C at around 0.6 V. This is in agreement with the onset of the CO oxidation reaction, as derived from the kinetic analysis, which occurs at around 0 V for PtMo/C, ~ 0.2 V for PtRu/C, and ~ 0.5 V for Pt/C (Fig. 5, inset). Naturally, the higher magnitude of currents observed in the voltammetric experiments is expected for this potentiodynamic technique ($v = 20$ mV s^{-1}), as compared with the polarization response which corresponds to a steady state condition. Also the difference on the onset potentials are undoubtedly related with the different temperature of both experiments.

In situ XAS results at Pt L and Mo K edge

The ratio of Pt to Mo atoms in the electrocatalyst was determined from the edge jumps at the Pt L_3 and Mo K edges using methodology described elsewhere (16), this indicated 72.5 a/o Pt for PtMo/C 3/1 and 87 a/o for the 4/1 alloy. Figure 9 shows the representative Pt-Pt phase corrected k^3 weighted Fourier transform at the Pt L_3 edge in 1 M $HClO_4$ for Pt/C and PtMo/C (3/1) at 0.54 V. Slight differences in the radial coordinate distances as well as the nature of interactions in the short-range atomic order around Pt is evident, indicating alloy formation. Alloy formation was also confirmed using powder x-ray diffraction analysis (not shown). Inset in Figure 9, shows corresponding Pt XANES spectra for Pt/C and PtMo/C (3/1) at 0.54 V in 1 M $HClO_4$. Increased magnitude of the normalized absorption (referred to as the 'white line') indicates increase in the *d-band* vacancy of Pt as a result of alloying with Mo. Such an increase in *d-band* vacancy as a result of alloy formation is expected as shown previously on binary alloys of Pt with Ru (16) and the first row transition elements (17).

Figure 10 presents the XANES at the Mo K edge for PtMo/C at 0.0 and 0.54 V in 1 M $HClO_4$ and for a Mo foil reference standard. As evident from the spectra, Mo in PtMo/C is oxidized with the edge positions shifted positive to the Mo reference foil.

Preliminary analysis of the spectrum with known standards (not shown) have indicated an oxidation state of (+ IV) at potentials as low as 0.0 V. This suggests its presence in the electrocatalyst as some sort of a hydrated oxide close to $MoO(OH)_2$. Comparison of the spectra at 0.0 and 0.54 V shows a change in oxidation state (Fig. 10), which corresponds to the redox couple observed in the cyclic voltammograms (Figs. 6 and 8). These changes in the oxidation state were reversible. This preliminary analysis indicates that, most probably, $MoO(OH)_2$ is present in the surface of the alloy catalyst and is active for the CO oxidation especially at low electrode potentials.

CONCLUSIONS

Results of this investigation point to significant improvements in CO tolerance with PtMo/C, which shows a two to three fold enhancement in performance compared to the current state of the art PtRu/C at 85°C with 100 ppm CO in H_2. Cyclic voltammograms show evidence of both Pt and Mo features and of a redox couple involving Mo. Voltammograms for CO stripping shows two distinct peaks. The first peak for CO oxidation occurs at very low potentials (~ 0.05 V) and corresponds to CO oxidation initiated by Mo alloyed to Pt. This is followed by CO stripping at 0.55 V, a potential akin to CO oxidation on Pt/C. Voltammograms also show PtMo/C is very stable and there is no evidence of any Mo dissolution in the potential window of –50 mV to 1.2 V. Kinetic analysis of the hydrogen electrode polarization data in presence of CO shows that the CO tolerance can not be related with a lower affinity to CO, but rather with the ability of promoting the CO oxidation process at very low electrode potentials.

The half cell and single cell polarization curves show that unlike PtRu/C, PtSn/C and Pt/C there is no significant change in the polarization characteristics as a function of temperature (below 100°C) and CO concentrations (in the range 5 to 100 ppm). Further, the effect of changes in the alloy composition (in the range 1:1 to 1:5 for Mo:Pt) had little effect on the steady state hydrogen polarization characteristics.

The short-range atomic order and *d-band* vacancies around Pt atoms in PtMo/C clearly show alloy formation as evidenced from XAS at the Pt L_3 edge. The Mo K edge XANES spectra at 0.0 V shows that Mo is present as a hydrated oxide species with an approximate oxidation state of (+IV), such as $MoO(OH)_2$.

In situ XAS studies are in progress to understand the mechanism for CO tolerance exhibited by PtMo/C. This involves detailed EXAFS and XANES analysis at both Pt L and Mo K edges in 1 M $HClO_4$ with and without CO. In addition, comparison with corresponding data on highly dispersed intermetallic alloys of PtMo/C, with different Pt/Mo ratio are in progress to examine the effect on CO tolerance relative to alloy composition.

ACKNOWLEDGEMENTS

The authors gratefully acknowledge the support of the U.S. Department of Energy, Division of Material Science, under contract number DE-FG05-89ER45384 for its role in the development and operation of beam line X11A at the NSLS. The NSLS is supported by the Department of Energy, Division of Material Science under contract number DE-AC02-98CH10886. E. A. T. is on leave of absence from Instituto de Química de São Carlos/USP, Brazil, with a scholarship from Fundação de Amparo a Pesquisa do Estado de São Paulo (FAPESP). S. J. L. was supported from a 1996 post doc. Program of the Ministry of Education, South Korea.

REFERENCES

1. H. A. Gasteiger, N. M. Markovic, and P. N. Ross Jr., *J. Phys. Chem.*, **99**, 8945 (1995).
2. M. R. Andrew, B. D. McNicol, R. T. Short, and J. S. Drury, *J. Appl. Electrochem.* **7**, 153 (1977).
3. P. N. Ross Jr., K. Kinoshita, A. J. Scarpellino and P. Stonehart, *J. Electroanal. Chem.*, **59**, 177 (1975).
4. L. W. Niedrach, D. W. McKee, J. Paynter, and I. F. Danzig, *Electrochem. Technol.* **4**, 318 (1967).
5. P. N. Ross Jr., K. Kinoshita, A. J. Scarpellino and P. Stonehart, *J. Electroanal. Chem.*, **63**, 97 (1975).
6. H. A. Gasteiger, N. M. Markovic, and P. N. Ross Jr., *J. Phys. Chem.*, **99**, 16757 (1995).
7. M. Watanabe, M. Shibita, and S. Motoo, *J. Electroanal Chem.*, **187**, 161 (1985).
8. M. Shibata, and N. Furuya, *J. Electronal. Chem.*, **269**, 217 (1989).
9. H. A. Gasteiger, N. M. Markovic, P. N. Ross Jr., and E. J. Cairns, *J. Phys. Chem.*, **98**, 617 (1994).
10. R. Ianiello, V. M. Schmidt, U. Stimming, J. Stumper, and A. Wallau, *Electrochim. Acta.*, **39**, 1863 (1994).
11. T. Iwasita, R. Dalbeck, E. Pastor, and X. Xia, *Electrochim. Acta.*, **39**, 1817 (1994).
12. H. -F. Oetjen, V. M. Schmidt, U. Stimming and F. Trila, *J. Electrochem. Soc.*, **143**, 3838 (1996).
13. B. N. Grgur, G. Zhuang, N. M. Markovic, and P. N. Ross Jr., *J. Phys. Chem.*, (In Press)
14. B. N. Grgur, N. M. Markovic, and P. N. Ross, *J. Phys. Chem.*, (Submitted).
15. S. J. Lee, S. Mukerjee, J. McBreen, Y. W. Rho, and T. H. Lee, *Electrochim. Acta.*, (In Press).
16. J. McBreen, and S. Mukerjee, *J. Electrochem. Soc.*, **142**, 3399 (1995).

17. S. Mukerjee, S. Srinivasan, M. P. Soriaga, and J. McBreen, *J. Electrochem. Soc.*, **142**, 1409 (1995).
18. J. McBreen, *J. Electroanal. Chem.*, **357**, 373 (1993).
19. E. A. Ticianelli, S. Mukerjee, S. J. Lee, and J. McBreen, *J. Electrochem. Soc.*, submitted.
20. S. J. Lee, S. Mukerjee, E. A. Ticianelli, and J. McBreen, *Electrochim. Acta.*, submitted.
21. T. A. Zawodzinski Jr., C. Karuppaiah, F. Uribe and S. Gottesfeld, *Electrode Materials and Processes for Energy Conversion and Storage IV*, S. Mukerjee and J. McBreen (Eds.), Vol. **97-13**, pp. 15-24. The Electrochemical Society Inc. (1997).
22. W. Vogel, J. Lundquist, P. N. Ross Jr., and P. Stonehart, *Electrochim. Acta.*, **20**, 79 (1975).
23. R. M. Q. Mello and E. A. Ticianelli, *Electrochim. Acta*, **42**, 1031 (1997).
24. H. A. Gasteiger, N. M. Markovic, and P. N. Ross Jr., *J. Phys. Chem.*, **99**, 8290 (1995).
25. K. Wang, H. A. Gasteiger, N. M. Markovic and P. N. Ross Jr., *Electrochim. Acta*, **41**, 2587 (1996).
26. W. T. Napporn, J.-M. Leger, C. Lamy, *J. Electroanal. Chem.*, **408**, 141 (1996).
27. K. L. Ley, R. Liu, C. Pu, Q. Fan, N. Leyarovska, C. Segree, and E. S. Smotkin, *J. Electrochem. Soc.*, **144**, 1543 (1997).
28. K. Y. Chen, P. K. Shen, and A. C. C. Tseung, *J. Electrochem. Soc.*, **142**, L185 (1995).
29. K. Y. Chen and A. C. C. Tseung, *J. Electrochem. Soc.*, **143**, 2703 (1996).
30. K. A. Friedrich, K.-P. Geyzers, U. Linke, U. Stimming, J. Stumper, *J. Electroanal. Chem.*, **402**, 123 (1996).
31. A. Couto, M. C. Pérez, A. Rincón, and C. Gutiérrez, *J. Phys. Chem.*, **100**, 19538 (1996).
32. R. H. Perry, D. W. Green, and J. O. Maloney, pp. 3-101, *'Chemical Engineers Handbook'*, Mc.Graw Book Company, New York, (1984).
33. M. Pourbaix, pp. 272-279, *Atlas of Electrochemical Equilibria in Aqueous Solutions*, National Association of Corrosion Engineers, Houston, TX (1994).

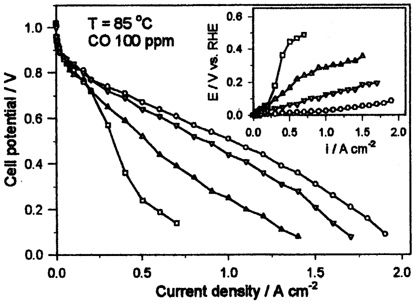

Fig. 1 - Cell potential-current density plots for a 5 cm^2 cell with H_2/CO[100ppm]//O_2, Nafion® 115 membrane, respective anode/cathode pressures of 16/11 psig, and humidification temperature of 100°/90°C. Cathode: Pt/C (0.4 mg/cm^2). The anodes were: {□}Pt/C, {Δ}PtRu/C, {∇}3/1-PtMo/C in presence of CO; {O}Pt/C in absence of CO. Inset: Polarization of the anode electrodes.

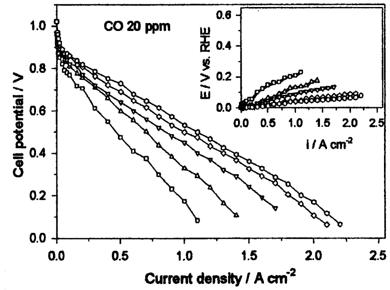

Fig. 2 - Cell potential - current density plots at several temperatures for a 5 cm^2 cell with H_2/CO[20ppm]//O_2, Nafion® 115. Cathode: Pt/C (0.4 mg/cm^2). Anode: 3/1-PtMo/C: {□}55, {Δ}70, {∇}85, {◊}100, and {O}115 °C. Inset: Polarization of the anode electrodes.

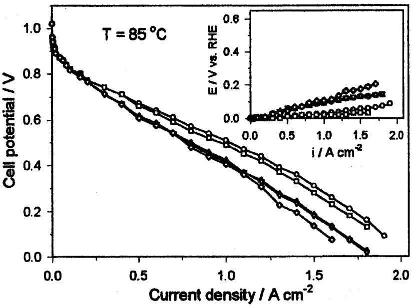

Fig. 3 - Cell potential - current density plots at several CO concentration for a 5 cm^2 cell with H_2/CO//O_2, Nafion® 115 membrane. Cathode: Pt/C (0.4 mg/cm^2). Anode: 3/1-PtMo/C: {O}0, {□}5, {Δ} 20, {∇}50 {◊}100 ppm. Inset: Polarization of the anode electrodes.

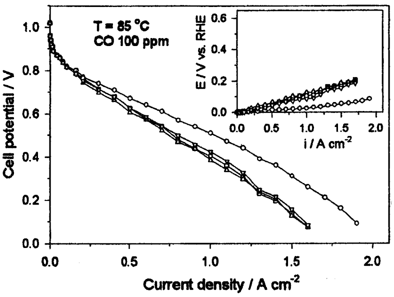

Fig. 4 - Cell potential - current density plots for a 5 cm^2 cell with H_2/CO[100ppm]//O_2, Nafion® 115 membrane. Cathode: Pt/C (0.4 mg/cm^2). Anodes: {□}3/1-PtMo/C, {Δ}4/1-PtMo/C, {∇}5/1-PtMo/C in presence of CO; {O}Pt/C in absence of CO. Inset: Polarization of the anode electrodes.

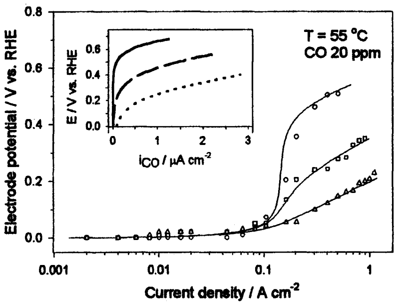

Fig. 5 - Tafel plots for the polarization of the hydrogen electrode for a 5 cm^2 cell with H_2/CO[20ppm]//O_2, Nafion® 115. Cathode: Pt/C (0.4 mg/cm^2). Experimental results: {O} Pt/C, {□}PtRu/C, {Δ}3:1 PtMo/C. Solid lines: theoretical lines obtained from kinetic analysis. Inset: CO oxidation currents obtained from the kinetic analysis: {—} Pt/C, {---} PtRu/C, {···} 3/1-PtMo/C.

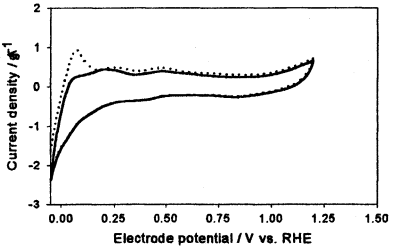

Fig. 6 - Cyclic voltammograms in 1 M $HClO_4$ at 25°C, at 5 mV/s in flooded electrodes for 3/1-PtMo/C, N_2 purge with (····) and without (—) polarization at 0.0 V for 1 h.

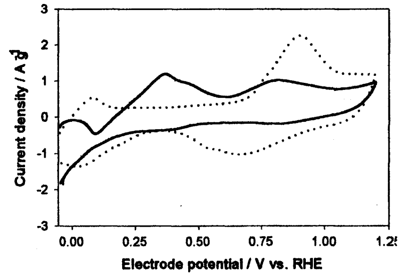

Fig. 7 - Cyclic voltammograms in 1 M $HClO_4$ at 25°C, at 5 mV/s in flooded electrodes for Pt/C (····) and 3/1-PtMo/C (—) after purging with CO for 1 hour at 0.09 and 0.0 V, respectively.

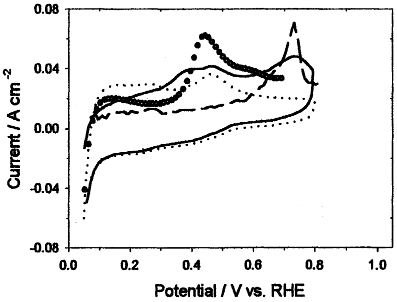

Fig. 8 - Cyclic voltammograms in the PEM cell at 55°C, at 20 mV/s in Nafion® covered electrodes for 3:1-PtMo/C without CO (····). In addition, data for 3/1-PtMo/C (—), PtRu/C (o) and Pt/C (---) after purging with CO [100ppm]/H_2 for 1 hour at 0.05V followed by N_2 purge (30 min) to remove excess of CO/H_2 is shown.

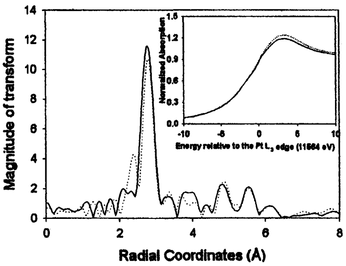

Fig. 9 - Representative plots of XAS in 1 M $HClO_4$ showing the Pt-Pt phase corrected Fourier transform at the Pt L_3 edge for Pt/C (—) and 3:1-PtMo/C (····) at 0.54 V, Δk = 3.1 - 15.5, k^3 weighted.
Inset: corresponding XANES spectra for Pt/C (—) and PtMo/C (····) at 0.54 V.

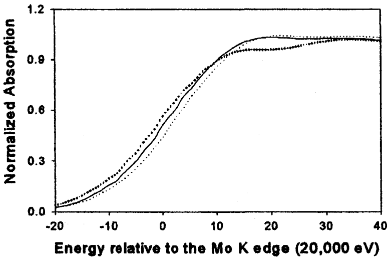

Fig. 10 - XANES spectra at the Mo K edge for PtMo/C at 0.0 (—) and 0.54 V (····); data for a Mo foil reference standard shown for comparison (+).

Proton_Conducting_Membrane_Fuel_Cells_II, PV 1998-27, 176-186 (1998)
DOI: 10.1149/199827.0176PV © The Electrochemical Society

ON THE MECHANISM OF CO-TOLERANCE OF PT-MO ALLOY ELECTROCATALYSTS

B. N. Grgur, N. M. Markovic and P. N. Ross, Jr.
Materials Sciences Division
Lawrence Berkeley National Laboratory
Berkeley, CA 94720

ABSTRACT

A mechanism of action of Mo atoms in the Pt-Mo alloy surface for the electrooxidation of CO and H_2/CO mixtures is proposed. The Mo atoms nucleate reactive OH groups which oxidize CO adsorbed at neighboring Pt sites at much lower overpotentials than on the pure Pt surface. In the case of H_2/CO mixtures, the rate of oxidation of CO even at very low overpotential is sufficiently high such that the steady-state coverage by CO of Pt sites is significantly less than the saturation coverage, creating a steady-state level of vacant Pt sites for the oxidation of H_2 to take place at a high rate. A mathematical model is derived which produces simulated i-E curves that are in reasonable agreement with experiment.

INTRODUCTION

Recent work from our laboratory (1, 2) has demonstrated that Pt-rich Pt-Mo alloy surfaces have shown the highest steady-state currents for the oxidation of H_2 in the presence of CO at the operating conditions of a polymer electrolyte fuel cell, i.e. so-called CO-tolerance of the anode electrocatalyst. In the present communication, we report further more detailed studies on the mechanism of action of Mo atoms in the alloy surface. We show that in the potential range of stability of Pt-Mo alloys, Mo surface atoms have multiple oxygenated ligands, the stoichiometry of which various with potential. The oxidation states of Mo surface atoms as well as the nature of Mo surface oxides is proposed to be determining factor in the electrocatalysis of H_2, CO and H_2/CO mixture on these alloys. A mathematical model is derived based on the proposed surface chemistry. The mathematical correctly simulates the potential dependence of the rate of CO electrooxidation on the alloy surface, and provides a reasonable mechanistic explanation for the enhancement in the rate of hydrogen electrooxidation of H_2 in the presence of CO.

EXPERIMENTAL

The electrooxidation kinetics of H_2, CO and H_2/CO mixtures were studied on UHV-prepared, well-characterized solid Pt-Mo alloy surfaces in 0.5 M H_2SO_4 at 60° C as described previously (1,2). Surface compositions were determined by low energy ion scattering spectroscopy (LEIS) and were varied systematically by a combination of ion bombardment, thermal annealing and plasma deposition in UHV; the surface compositions reported here were 15, 23 and 33 at. % Mo. The chemical state of Mo in the surface as a function of potential was determined by *ex-situ* x-ray photoelectron spectroscopy (XPS). Following preparation and characterization in UHV, the solid alloy samples were transferred into the disk position of an insertable rotating ring-disk electrode arbor (Pine Instruments) as described in detail previously (3).

RESULTS

Oxidation States of Mo in the Alloy Surface in Electrolyte

The composition dependence of the base cyclic voltammetry of the Pt-Mo surfaces is shown in Fig. 1 in comparison to that of a pure Mo surface prepared in UHV and treated in the same way. In what follows, we try to resolve the transitions of Mo valence states in PtMo surface by comparing the electrochemical behavior of Mo metal with that of PtMo electrode in 0.5 M H_2SO_4. We take advantage of the reasonably complete knowledge of the surface chemistry of the pure Mo surface in acid electrolyte, and make use of the additional in-parallel characterization of both pure Mo and PtMo alloy surfaces by ex-situ XPS. We do not claim to make a definitive determination of the surface chemistry of Mo in PtMo alloy surfaces, but rather a determination that provides a reasonable explanation for the role of Mo in enhancing the kinetics of CO electrooxidation in the low overpotential region of interest for PEM fuel cells. The voltammetry in Figure 2 revealed that at least three anodic peaks are observed in the cyclic voltammetry of the Mo metal in 0.5 M H_2SO_4, *e.g.* on the positive sweep direction at 0.1 V, 0.22 V and 0.4V. These voltammetric features serve as an evidence for multiple higher valence-states of Mo surface atoms. At more positive potentials, e.g. just before the onset of Mo dissolution at 0.4 V, it seems likely that the surface is predominantly in the +VI state, as the dissolved state of Mo is identified as H_2MoO_4 (4). The fact that the dissolution of Mo at 0.4 V is mirrored with the broad peak at 0.4 - 0.45 V in the voltammetry for 23 and 33 % Mo alloys suggests that at this potential Mo atoms in the surface are also predominantly in the +VI valence state. In contrast to the pure Mo electrode, in the alloy Mo atoms are stabilized on the surface by Pt-Mo intermetallic bonding, a result we had seen previously (and even more dramatically) with Pt-Sn alloys (5). By further analogy, if the anodic peak in the voltammetry of Mo metal electrode at *ca.* 0.25 V corresponds to the transition of Mo^{+III} to Mo^{+IV} valence state, than it is also reasonable to suggest that a peak observed at 0.25 V in the voltammetry of Pt-Mo alloys may also be assigned to the oxidation of Mo atoms from Mo^{+III} to Mo^{+IV}. These valence state assignments are consistent with the ex-situ XPS analyses of both pure Mo electrodes (6) and Pt-Mo alloy electrodes (2). Figure 2 shows that voltammetric peak(s) recorded on Mo electrode at potentials negative of *ca.* $E < 0.2$ V indicate an even more reduced state of Mo than + III may exist at these potentials. However, these peaks are not clearly resolved in the voltammetry of the alloys, due to the extensive hydrogen evolution reaction (HER) on Pt sites in the same potential range. As a consequence, a similar processes may also occur on Mo in the Pt-Mo surface, but these processes are masked by the HER which occur in the same potential range. Because of this uncertainty, we shall not use the +II state in our subsequent modeling.

The above analysis indicates that under our experimental conditions, Mo surface atoms in the PtMo alloy have multiple O and/or OH ligands on them *at all potentials* of interest, the stoichiometry of which various with electrode potential. We will assume that at a constant pH of ≈ 1 that any change in the valence state is charge compensated by change in surface protonation that retain the net surface charge. The surface redox processes on the Mo sites are then postulated to be represented by the following reactions: the Mo(+III)/Mo(+IV) at the surface is represented as

$$MoOOH \rightarrow MoO_2 + H^+ + e^- \qquad [1]$$

while the Mo(+IV)/Mo(+VI) equilibrium is represented as

$$MoO_2 + 2H_2O \rightarrow MoO_2(OH)_2 + 2H^+ + 2e^- \qquad [2]$$

The ΔG's (and thus the E_o's) for rxns. 1&2 on the alloy surfaces may not be the same as those for pure Mo, but for the present purposes we shall use the values given in Pourbaix (7) for bulk Mo. In the latter case, MoOOH does not actually exist as a bulk phase, and we assume this state exists as a surface (2D phase) having an E_o approximately equal to that for the Mo^{3+}/MoO_2 equilibrium, 0.311 V. For simplicity, we neglect any non-ideality and use purely Nernstian relations for the surface activities of the various species,

$$n(E - E_o)F / RT = \ln \Gamma_o / \Gamma_R \qquad [3]$$

where Γ_o and Γ_R are the surface concentrations of the oxidized and reduced forms, respectively. For kinetic analysis, it is convenient to use relative coverages of the total surface by a particular species, Θ_j, which are obtained by the normalization

$$\Theta_j = \Gamma_j / \sum_j \Gamma_j \qquad [4]$$

The resulting "isotherms" for the various oxy/hydroxide species are shown in Figure 2. The isotherms from eqns. 1-4 clearly show in a quantitative way what we had deduced from the voltammetry and XPS results described above: that a mixture of both different oxidation states and different oxide phases of Mo surface atoms coexist over the potential range of interest; a significant change in the state of oxidation of Mo and the surface concentration of OH species occurs in the $0.3 < E < 0.5$ V potential region . As we discuss further below, the oxidation state of Mo surface atoms as well as the nature of Mo surface oxides with nominally the same valence state of Mo, are postulated to be *the* determining factors in the electrocatalysis of CO and H_2/CO mixture on PtMo alloys. More specifically, we postulate that only the OH species of the oxyhydroxide states (for example, $MoO(OH)_2$) are reactive with CO_{ads}, but because of its size oxyhydroxide states may reduce the availability of adjacent Pt surface atoms for the dissociative adsorption of molecular hydrogen. De-protonated oxide states (for example, MoO_3) are proposed to have a lessor screening effect on the adjacent Pt surface atoms, but are inactive for reaction with CO_{ads}. Translated to the development of PtMo catalyst, the surface concentration of Mo atoms should be such as to be capable both to provide (continuously) reactive oxyhydroxide species, but not to screen adjacent Pt sites on which the HOR (when not covered by CO_{ads}) takes place.

The role of the surface concentration of Mo atoms on the availability of Pt surface sites can be assessed from its effects on the electrooxidation of pure H_2 (no CO) on Pt-Mo alloys, as shown in Figure 3. The alloy surfaces containing 15 and 23 at. % Mo have polarization curves indicative of pure diffusion control, i.e. equivalent to a pure Pt RDE. Increasing the Mo surface concentration from 23 up to 33 at. % produced a dramatic reduction in the activity of Pt-Mo alloy surfaces for the oxidation pure H_2, even exhibiting a *reaction limiting current* (no dependence on the rotation rate) below 0.4 V. Interestingly, above 0.4 V, the 33% Mo surface becomes re-activated for the oxidation pure H_2, apparently due to a change in the oxidation state of Mo atoms in the surface as we have discussed above. Note that the deactivating effect of too much Mo in the surface is not a simple blocking relation, i.e. the effect is much bigger than the change in $1 - x_{Mo}$. For that reason, we will not attempt to model the blocking effect in this work, and only model the two surfaces where the blocking effect appears to be negligible, the 15 and 23 at. % Mo surfaces.

The Electrooxidation of Adsorbed CO and Dissolved CO in Solution

We had suggested in previous studies (1,2) of the oxidation of H_2 in the presence of CO that the superior kinetic properties of the Pt-Mo alloy surface relative to Pt or any other Pt alloy surface (such as Pt-Ru) was due to the oxidation of *both* adsorbed CO and CO dissolved in solution in the low overpotential region. We illustrate independent physical evidence for this process with kinetic studies on the 15 % Mo surface summarized in Figure 3. The quasi-steady-state electrooxidation (1 mV/s) polarization curves for CO in argon show a *positive* reaction order in CO partial pressure, and clearly indicates that a *continuous* oxidation of CO occurs at a finite rate even at potentials < 0.2 V. The anodic stripping of CO_{ads} is also shown in this figure. There are three states of CO_{ads} on the Pt-Mo surface, only two of which are observed in anodic stripping (at 0.2 - 0.5 V and 0.6 - 0.8 V), which we call the "strongly" adsorbed states (2), while the "weakly" adsorbed state is oxidized when CO is purged from solution. Below 0.2 V, oxidation of CO (gas) occurs via this weakly adsorbed state, which as we show below constitutes about 10 % of the saturation coverage of CO_{ads}. This weakly adsorbed state of CO is created by strong repulsive interaction between CO_{ads} molecules on the Pt sites, which has been clearly demonstrated with Pt(hkl) low index single crystal surfaces (8), but in our kinetic modeling we find that it is characteristic of all Pt and most Pt alloy surfaces. What is unique about Pt-Mo is not the occurrence of the weakly adsorbed state, or the amount of it, but that it is oxidized at potentials < 0.2 V, and this appears to be due to unique reactivity of the OH_{ads} on the Mo sites in this potential region.

We derive here a quantitative mathematical model for the CO electrooxidation process in terms of the concepts enunciated above. The elementary steps are assumed to be

$$CO \Leftrightarrow CO_{ads} \quad [5]$$

$$CO_{ads} + Mo(OH)_n \Rightarrow CO_2 + Mo(OH)_{n-1} + H^+ + 1\ e^- \quad [6]$$

$$Mo(OH)_{n-1} + H_2O \Leftrightarrow Mo(OH)_n + H^+ + 1\ e^- \quad [7]$$

where the second step is assumed to be rate determining. We are interested primarily in simulating the shape of the polarization curve, rather than the absolute value of the current, we will assume Tafel kinetics of the form

$$i = nFk\Theta_{OH}\Theta_{CO}\exp(FE\ /\ RT) \quad [8]$$

where Θ_{OH} as a function of potential is given by eqns. 3&4. Following from the discussion above of the concepts of "weakly adsorbed" and "strongly adsorbed" states of CO, the chemical rate constant, k, is a function of Θ_{CO}, and Θ_{CO} is a function of potential. We will use semi-empirical relations for both $k(\Theta_{CO})$ and $\Theta_{CO}(E)$ that captures what we know (or have postulated) about the chemistry of adsorbed CO. It is known from careful studies in UHV (9) that the heat of adsorption of CO on Pt decreases linearly with coverage as the coverage approaches saturation. This decrease in the heat of adsorption is caused by strong repulsive interaction between adsorbed CO molecules and in effect creates the "weakly bonded" state. We will assume that a similar repulsive interaction exists near saturation coverage for CO on Pt in solution. This linear decrease in the heat of adsorption can then be related to a linear decrease in the activation energy for CO electrooxidation through the Bronsted relation,

$$\Delta\Delta G^{\diamond} = \beta\Delta\Delta H_{ads}$$

where β is the symmetry factor. The higher reactivity of the weakly adsorbed state is then clearly seen as a consequence of a lowered free-energy of activation for its oxidation, $\Delta G_o^{\diamond}$, which will then be represented mathematically by a Temkin-type relation

$$\Delta G^{\diamond} = \Delta G_o^{\diamond} - r\Theta_{CO} \quad [9]$$

where r is the interaction parameter (r>0 is repulsive). For the purposes of obtaining an expression for free-energy of activation as a function of potential, we shall assume that Θ_{CO} varies linearly with potential in the region of interest, e.g. 0 - 0.4 V, and we will neglect the contribution of this potential-dependence of Θ_{CO} in the pre-exponential term, , but we will include a P_{CO} dependence as indicated by the experimental data. After re-arranging, the final form for simulation of the i-E curve is

$$i = nFk_o P_{CO}{}^m \Theta_{OH} \exp[(-\Delta G_o^\circ - \gamma E) / RT] \exp(FE / RT) \qquad [10]$$

where ΔG_o° and γ are semi-empirical parameters, the reaction order (m) in CO is experimentally approximately 0.5 and k_o is essentially a scale factor. ΔG_o° can be obtained independently from the experimental temperature dependence of the current, $(\partial \log i / \partial T)_E$, while γ is best obtained by fitting the simulated i-E curve to experiment. The simulated i-E curve for CO electrooxidation on PtMo alloy for $\Delta G_o^\circ = 80$ kJmol^{-1} and $\gamma = 34$ kJmol^{-1}V^{-1} is shown in Figure 5, along with the observed i-E curve on the 23 at. % Mo alloy surface. The simulated curve reproduces both the shape of the observed curve, and captures the physical concepts described, i.e. it is not just "curve-fitting". In the low overpotential region, < 0.2 V, the oxidation proceeds through the "weakly adsorbed" state of CO, which produces the lowest activation energy; OH groups are provided exclusively by the MoOOH state on the Mo surface atoms. With increasing potential, the weakly adsorbed state is depleted, increasing the activation energy, and causing the current to increase much less than the Tafel factor, (F/RT). Above about 0.3 V, there is a significant change in the OH population on the surface, as seen in Figure 2, where the decrease in OH from the deprotonation of the MoOOH state is more than compensated for by the production of OH from the $MoO_2(OH)_2$ state. Again, the slope of the i-E curve in this region matches the experimental slope extremely well, but the potential where the transition occurs is not well represented by the E_o's used in eqn. 3, i.e. the values for pure Mo. It is not unreasonable to use adjusted values for the effect of Pt-Mo intermetallic bonding on the O and OH formation chemistry. Note that such adjustments would be physically in the right direction, i.e. increasing the values of E_o corresponds to bonding with Pt stabilizing the more *reduced* states of Mo. If we make the E_o's about 0.1 V more positive, the agreement with experiment is essentially perfect (!).

Oxidation of Hydrogen in the Presence of CO

A basic hypothesis of this work is that the model for the electrooxidation of CO contains all the ingredients necessary to understand the oxidation of H_2 in the presence of CO. The physical concept is that the electrooxidation of CO creates vacancies on Pt surface atoms on which H_2 oxidation occurs. We assume that for very high coverages of CO, where we are concerned with only the weakly adsorbed state of CO, the oxidation takes place via the Heyrovski-Volmer single-site mechanism (9). This is a different mechanism than we found in our previous study of H_2 oxidation on pure Pt covered only by the irreversibly or strongly adsorbed state of CO (2), which was the Tafel-Volmer dual-site mechanism. Mathematically, we represent the single-site mechanism by the simple site-blocking model,

$$i = i_{H_2}(1 - \Theta_{CO}) \qquad [11]$$

where i_{H_2} is the current in the absence of CO, and for our purposes here we will treat it as a scale factor for the current, i.e. the potential dependence of i_{H_2} is neglected since it reaches the diffusion limiting current above ca. 0.02 V. Thus, the i-E curve is given entirely by the potential dependence of the steady-state coverage by adsorbed CO. Thus, the more accurately this potential dependence is represented, the closer the simulation will be to experiment. To derive the most accurate representation of the steady-state coverage of CO, we return to the elementary steps represented by eqns. 5 & 6, and note that these are steps in series, and that a more accurate analysis would not assume the second is rate determining but that at steady-state the two steps proceed at equal rates, i.e. the rate of adsorption = rate of oxidation. Using (i/nF) from eqn. 10 for the rate of oxidation, and using a simple form for the rate of adsorption of CO we have,

$$k_{ads}P_{CO}(1-\Theta_{CO}) = k_o P_{CO}{}^{0.5}\Theta_{OH}\exp[(-\Delta G_o^{\Diamond} - \gamma E)/RT]\exp(FE/RT)$$

where k_{ads} is the rate constant for CO adsorption, and P_{CO} is the CO partial pressure. Then rearranging,

$$(1-\Theta_{CO}) = KP_{CO}{}^{-0.5}\Theta_{OH}\exp[(-\Delta G_o^{\Diamond} - \gamma E)/RT]\exp(FE/RT) \qquad [12]$$

Multiplying eqn 12 by the scale factor i_{H_2} is then the simulated i-E curve, which is shown in Figure 6 together with the observed curve on the 23 % Mo alloy surface with 0.1 % CO in H_2. The potential dependence is extremely well represented by the simulated curve in the potential region 0.05 - 0.3 V, but the model overestimates the kinetic effect of oxidation of oxidizing the "strongly bonded" CO from the surface at $E > 0.3$ V. There are two other pieces of experimental data, presented in our previous paper (2), that are also well represented by the model: the reaction order in CO, which is ca. - 0.5 both experimentally and in the model as well ($m \approx 0.5$); and an apparent activation energy that increases linearly with potential in the region $0.05 < E < 0.4$ by a nearly identical amount as in our simulation, 25 kJ/mol.

SUMMARY

A mechanism of action of Mo atoms in the Pt-Mo alloy surface for the electrooxidation of CO and H_2/CO mixtures is proposed. The Mo atoms nucleate reactive OH groups which oxidize CO adsorbed at neighboring Pt sites at much lower overpotentials than on the pure Pt surface. In the case of H_2/CO mixtures, the rate of oxidation of CO even at very low overpotential is sufficiently high such that the steady-state coverage by a specific state of adsorbed CO on the Pt sites, a state we term "weakly adsorbed, is significantly reduced, creating a steady-state level of vacant Pt sites for the oxidation of H_2 to take place at a reasonably high rate. A mathematical model is derived which captures the proposed surface chemistry of both the OH groups on the Mo sites and the weakly adsorbed state of CO on the Pt sites. The mathematical model produces simulated i-E curves that are in reasonable agreement with experiment.

ACKNOWLEDGMENT

This work was supported by the Office of Advanced Automotive Technologies (OAAT) of the U.S. Department of Energy under contract DE-AC03-76SF00098.

REFERENCES

1. B. Grgur, G. Zhuang,; N. Markovic, and P. Ross, J. Phys. Chem. B, 101, 3910(1997)
2. B. Grgur, G. Zhuang,; N. Markovic, and P. Ross, J. Phys. Chem. B, 102, 2494(1998).
3. Pine Instrument Co., 101 Industrial Dr., Grove City, PA 16127.
4. A. A. Pozdeeva, E. I. Antonovskaya and A. M. Sukhotin, Corros. Sci., 6, 149(1966).
5. H. Gasteiger, N. Markovic, P. Ross, J. Phys. Chem., 99, 8945(1997).
6. Y. C. Lu and C. R. Clayton, Corros. Sci., 29, 927(1989).
7. E. Deltombe, N. De Zoubov, and M. Pourbaix, in Atlas of Electrochemical Equilibria in Aqueous Solutions, M. Pourbaix, Editor, pp. 272-279, Pergammon Press, New York, 1966.
8. G. Ertl, M. Neuman, and K. Streit, Surf. Sci., 64, 393(1977).
9. N. Markovic, B. Grgur, and P. Ross, J. Phys. Chem. B, 101, 5405(1997).

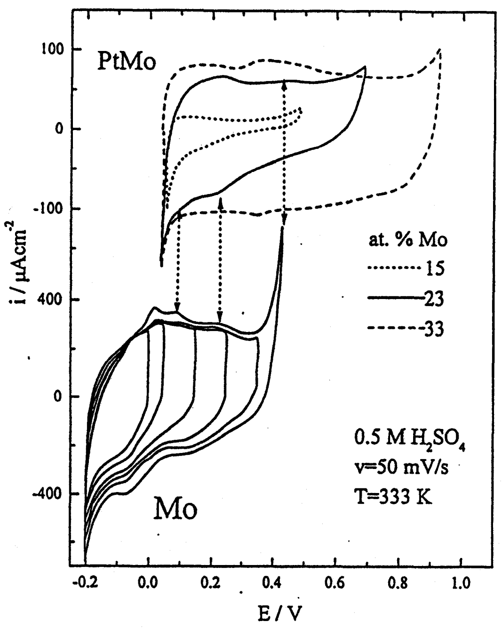

Figure 1. Cyclic voltammetry of Pt-Mo alloy surfaces having surface concentrations of 15, 23 and 33 at. % Mo compared to that of a pure Mo surface pre-treated in an identical fashion (see text). 20 mVs^{-1}, 0.05 M H_2SO_4, 333°K.

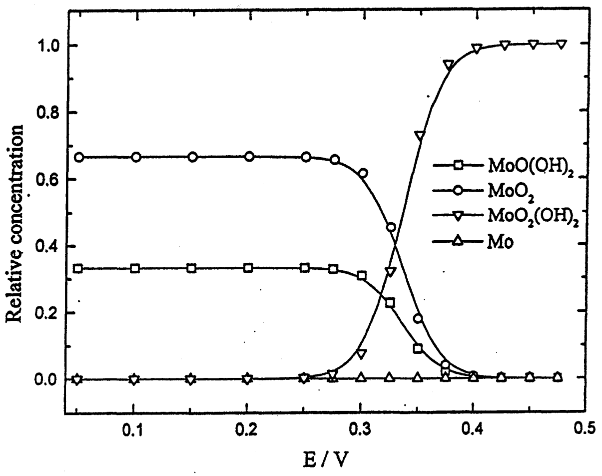

Figure 2. Plots of relative surface concentrations of various Mo oxide species as a function of potential according to eqns. 3&4.

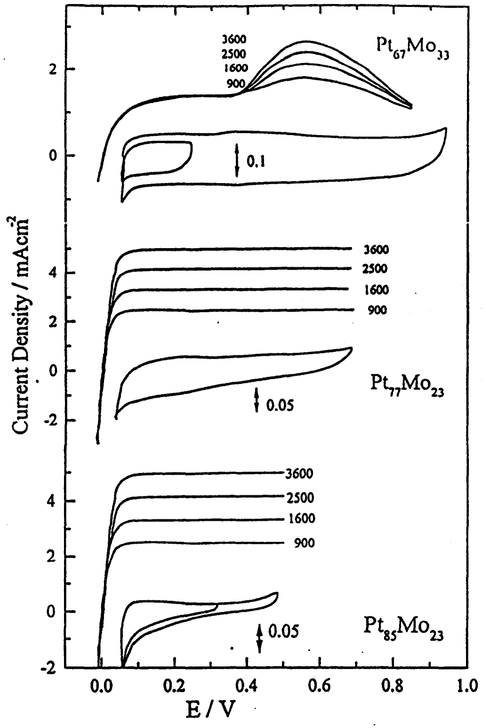

Figure 3. Cyclic voltammetry of the three Pt-Mo alloy surfaces of Fig. 1 as RDE electrodes in H_2-saturated. Base voltammetry in Ar-purged solution shown for comparison. 20 mVs^{-1}, 0.05 M H_2SO_4, 333°K.

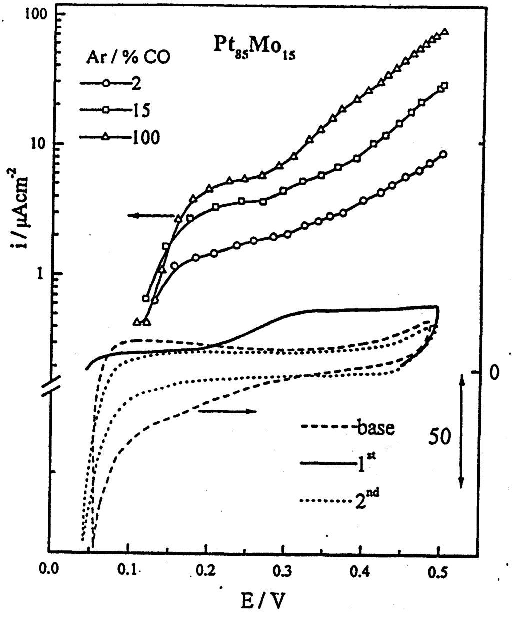

Figure 4. Quasi-steady-state i-E curves for CO oxidation on the 15 at. % Mo alloy electrode at different CO partial pressures. 2500 rpm, 1 mVs^{-1}; CO stripping voltammetry for CO adsorbed at 0.1 V, following Ar-purging. 20 mVs^{-1}, 0.05 M H_2SO_4, 333°K.

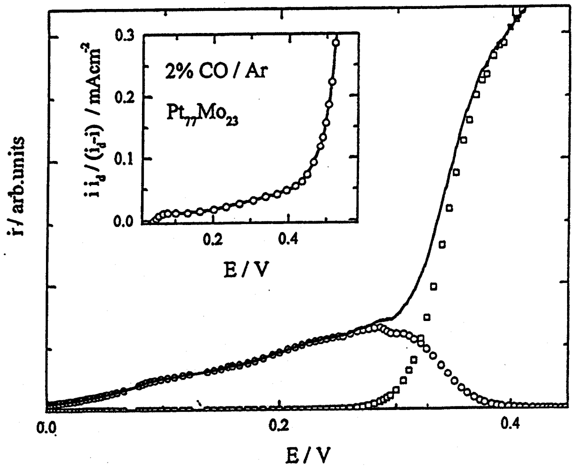

Figure 5. Simulated i-E curve for CO oxidation on a Pt-Mo alloy surface accoding to eqns. 3, 4 & 10. Open symbols denote contribution of OH in the +III and +VI oxide states, respectively. (insert) Experimental curve for 23 at. % Mo alloy electrode shown for comparison.

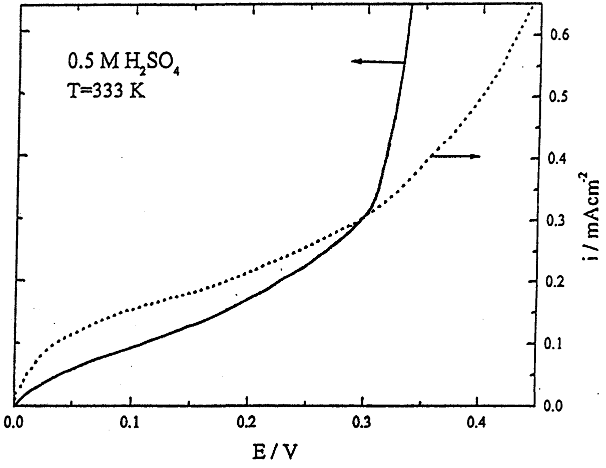

Figure 6. (solid) Simulated i-E curve for the oxidation of H_2 containing 0.1 % CO according to eqns. 3, 4 &12. (dashed) Experimental curve for the 23 at. % Mo alloy electrode shown for comparison.

Proton_Conducting_Membrane_Fuel_Cells_II, PV 1998-27, 187-199 (1998)
DOI: 10.1149/199827.0187PV © The Electrochemical Society

CHANGE OF ELECTROCHEMICAL IMPEDANCE SPECTRA (EIS) WITH TIME DURING CO-POISONING OF THE Pt-ANODE IN A MEMBRANE FUEL CELL

B. Müller, N. Wagner, W. Schnurnberger

Institute of Technical Thermodynamics
German Aerospace Center (DLR)
Pfaffenwaldring 38-40
D-70569 Stuttgart
Germany

ABSTRACT

The most common method used to characterize the electrochemical performance of a fuel cell is the recording of current/voltage U(i) curves. However, separation of electrochemical and ohmic contributions to the U(i) characteristics requires additional experimental techniques. The application of electrochemical impedance spectroscopy (EIS) is an approach to determine, which have proved to be indispensable for the development of fuel cell electrodes and membrane electrode assemblies (MEA`s).

The impedance spectra measured during CO poisoning of the anode in galvanostatic mode at 217 $mAcm^{-2}$ show a strong time dependency. From the evaluation of the spectra with an equivalent circuit we suggest that the hydrogen dissociation reaction is the reaction rate determining step. At lower cell voltages the CO oxidation reaction occurs and the Faraday impedance of the anode shows an inductive response at frequencies lower than 3 Hz.

INTRODUCTION

Polymer Electrolyte Fuel Cells (PEFC) have been receiving more and more attention due to their high energy conversion efficiency and emission free-operation for powering electric vehicles [1]. The highest performance is achieved with neat hydrogen (H_2) which is the preferred fuel for low-temperature fuel cells. However, neat H_2 has several limitations. The storage systems for liquid or compressed H_2 are heavy and bulky. Furthermore, H_2 refueling is costly and takes time. An additional obstacle is the lack of an infrastructure to distribute H_2 to the consumer [2].

A solution is to generate hydrogen on board of the electric vehicle by reforming either hydrocarbons (e.g. natural gas) or alcohols (e.g. methanol). The reformate feed gas may contain up to 2.5% carbon monoxide (CO) by volume, which can be reduced to about 50 ppm CO using a selective oxidizer [3].

Although Pt has proven to be the most effective catalyst for hydrogen oxidation in polymer membrane fuel cells, even small traces of carbon monoxide can cause significant decrease in fuel cell performance. It was reported that only 5 ppm CO in the hydrogen stream leads to a drop of the maximum power density to less than half the value obtained for neat hydrogen [4]. The decrease of the cell performance is caused by the adsorption of carbon monoxide on the platinum electrocatalyst. The CO blocks or at least limits the number of the active catalyst sites and inhibits the hydrogen oxidation reaction (HOR) [5]. To develop CO tolerant anodes, it is important to understand the mechanisms that occur during the poisoning of the platinum catalyst.

Therefore, electrochemical impedance spectroscopy (EIS) during galvanostatic operation is applied to analyze the time dependency of the anode potential decay during poisoning. In our experiments the PEFC was anodically operated “dead end“ with a mixture of hydrogen and 100 ppm CO.

EXPERIMENTAL

The measurements were carried out in a 23 cm^2 single cells with stainless steel sinter plates having a porosity of 50 % as the gas distribution structure. The membrane electrode assembly (MEA) consisted of two electrodes with 20%wt Pt/C (purchased from E-TEK) hot pressed (1.6 MPa, 10 min, increasing temperature up to 160°C) onto a Nafion 117 membrane.

The cells were run at 80 °C. We used neat hydrogen or H_2 with 100 ppm CO on the anode side and oxygen on the cathode side (H_2 5.0 and O_2 2.0, Messer Griesheim), both at 2.0 bar absolute. The hydrogen or the hydrogen/carbon monoxide mixture flow as “dead end“ whereas the cathode received oxygen at eight times the stoichiometric requirement for the applied current (5A) to ensure steady state conditions at the cathode side. The clearance volume of the cell was 31 cm^3; thus during the first minute of operation with H_2/CO at 5 A (35 cm^3/min hydrogen consumption) the neat hydrogen was substituted by the gas mixture.

The electrochemical impedance measurements were carried out with a Zahner IM6 (Kronach, Germany) impedance device in galvanostatic mode. The data was both collected and analyzed with “Thales“ software from Zahner Meßtechnik. All impedance spectra reported herein were measured between the FC cathode and anode. In the galvanostatic mode with a constant current (5A or 217 mA/cm^2) the impedance of the cathode and the membrane resistance can be assumed to be constant and the changes in the impedance spectra during poisoning with CO can be attributed to the anode. The current and the potential were each collected with two interwired circuit cables. At each potential, a small AC perturbation (200 mA amplitude) was applied between the anode and the cathode of the fuel cell. The impedance spectra were obtained by varying the frequency of the current perturbation signal from 0.05 Hz to 20 kHz in order to take several measurements during the poisoning period. One of the prerequisites of impedance measurements is a quasi-steady state of the system studied. Thus, recording of impedance spectra of a system which changes its electrochemical state leads to the possibility that at each frequency a significantly different potential is present. Provided that the time of acquisition is available for each frequency sample, data can be transformed by interpolation to generate impedance spectra which belong to well defined times. Then, each of these interpolated spectra represents a certain quasi-steady state of the system. As a result of the evaluation the dependency on time of the impedance controlling parameters is obtained [6].

The interpolated impedance spectra can be described by a model (equivalent circuit) of elementary impedance elements. The numeral values of the parameters will be calculated by a fitting procedure of the model to the measured data. The measured data will be represented in the following diagrams as symbols and the modeled curves as lines. The equivalent circuit contains various elementary impedance elements representing the involved reaction and mass transfer steps. These elements are generally represented as ohmic, capacitive or inductive components with particular dependencies of their complex impedance upon the frequency of the AC signal. The particular linking of these impedance elements is based upon the relationship between the processes represented by these elements. Subsequently occurring steps are represented by a series connection of the elements while steps occurring simultaneously are represented by a connection in parallel.

Impedance spectra can be presented as Bode plots, where the logarithm of the impedance magnitude and phase-shift are plotted vs. the logarithm of the frequency. However, to identify and separate different diffusion processes, it is useful to represent the measured impedance spectra as Nyquist diagrams (imaginary part vs. real part of the impedance). In the Nyquist diagram one can observe the finite diffusion as an additional loop at the lowest part of the frequency range, the infinite diffusion is a straight line with a slope of 1 (real part = imaginary part). Due to the logarithmic scale of the impedance, the difference of the two kinds of diffusion can not seen so clearly in the Bode diagram. In general, the Bode plot provides a clearer description of the electrochemical system's frequency-dependent behavior than does the Nyquist plot, in which frequency values are implicit. Steady-state current-voltage curves (Fig.1) shows deviation from linear behavior for $i > 500$ mAcm^{-2}, indicating additional diffusion overvoltage.

Changing the anode feed gas from neat H_2 to H_2/100ppm CO at a current density of 217 mAcm^{-2} one can observe (Fig.2a) the time dependency of the cell voltage during poisoning of the anode with CO. Three different sections can be recognized: a nonlinear decrease of the cell voltage immediately after adding 100 ppm CO to the hydrogen feed gas (point 1, t=0). The transition behavior between 500 mV and 300 mV (point 5 to 8) leads to slow voltage decay at low cell voltage (points 9 to 12).

An overview of the impedance spectra measured at different times indicated by points 1 to 12 is given in Fig.2b. The first impedance spectrum was recorded starting with neat hydrogen (point 1, t=0). Afterwards, the anode feed gas was switched to the mixture of H_2/100 ppm CO and measurements were taken every 10 minutes.

The Nyquist representations of the interpolated impedance spectra at different times during CO poisoning of the anode indicate a significant change of the spectrum with time.

MODEL DISCUSSION

A theoretical expression for the expected shape of the impedance spectra can be derived only if a particular kinetic mechanism is chosen.

We assume two fundamental steps that control the CO poisoning effect of PEFC-anodes:

I) CO adsorbed on the catalyst surface blocks the adsorption of H_2, thus decreasing the available active sides. Consequently the "effective" HOR current density increases (in galvanostatic mode) and an additional overvoltage according to the U(i) characteristic occurs.

II) The adsorption of CO at the surface of the Pt catalyst will change the electronic structure of the catalyst. From this one has to expect the electrochemical reactivity (electron transfer symmetry factors) of the HOR to be changed.

The oxidation of hydrogen was shown [7] to proceed according to the Tafel-Volmer sequence:

$$H_2 + 2M \Leftrightarrow 2MH \quad \text{(Tafel)} \tag{1}$$

$$MH \Leftrightarrow M + H^+ + e^- \quad \text{(Volmer)} \tag{2}$$

with the dissociation reaction reaction rate controlling.

Another mechanism proposed for the HOR is the Volmer-Heyrowsky sequence [8]:

$$H_2 + M \Leftrightarrow MH + H^+ + e^- \quad \text{(Heyrowsky)} \tag{3}$$

$$MH \Leftrightarrow M + H^+ + e^- \quad \text{(Volmer)} \tag{4}$$

Equation 1-4 shows that the reaction rate is sensitive to the surface coverage (MH) and surface poisoning with CO by blocking the active platinum (M) sites.

The impedance of a fuel cell can be separated [9] into the membrane resistance (the impedance above 10 kHz) and the impedance contribution of the anode and cathode. The impedance of the cathode and anode can be represented each by an equivalent circuit consisting of a parallel connection between the Faraday impedance and the double (or dielectric) layer capacitance. In the simplest case, only one charge transfer reaction is present and the Faraday impedance can be represented by the charge transfer resistance. In most cases the Faraday impedance is more complicated and had to be derived from kinetical equations or from experience.

For the Heyrowsky-Volmer sequence Vetter [8] derived the Faraday impedance as a series combination of the Faraday resistance R_f and Faraday capacitance C_f by combining the charge transfer reaction (Volmer) and the electrochemical reaction (Heyrowsky). Vetter remarks that this "capacitance" response of the electrode (adsorbed surface) should turn over in an inductive response, observed experimentally by Gerischer and Mehl [10], if the degree of surface coverage (Θ_H) changes. Thus in the mathematical expression for the Faraday capacitance the term $(\alpha_V-\alpha_H)(1-2\Theta_H)$ reaches values <0. α_V and α_H represent the two electron transfer symmetry factors.

Up to now there is no experimental evidence to separate the "geometrical blocking" term $(1-2\Theta_H)$ from "electronic structure" of the catalyst surface represented by the electron transfer symmetry factors α_{ij}.
Therefore $(\alpha_V-\alpha_H)(1-2\Theta_H) < 0$ can be reached by either:

$$(\alpha_V-\alpha_H) < 0 \text{ and } (1-2\Theta_H) > 0 \quad \text{or} \quad (\alpha_V-\alpha_H) > 0 \text{ and } (1-2\Theta_H) < 0 . \qquad (5)$$

Keddam has shown [11] that the inductive behavior (low frequency inductive arc in the Nyquist representation) is observed when the values for α_V and α_H are different.
An inductive behavior in the low frequency range of the impedance spectra seems to appear in systems in which a reaction consisting of two successive electron transfer steps proceeding by an adsorbed intermediate species [12]:

$$\text{reactant(s)} \pm e^- \Leftrightarrow \text{adsorbate} \qquad \text{step 1} \qquad (6)$$
$$\text{(reactant)} + \text{adsorbate} \pm e^- \Leftrightarrow \text{product(s)} \qquad \text{step 2} \qquad (7)$$

This mechanism was proposed to evaluate EIS for cathodic production of hydrogen by the metallic electrodeposition reaction and anodic oxidation reaction of metals (e.g. iron) close to their corrosion potentials.
This kind of reaction mechanism can be expressed as an equivalent circuit to fit experimental EIS data [13]. If the impedance at the low frequency range of the impedance spectra is smaller than the impedance at intermediate frequencies then the capacitance C_{ad} from the equivalent circuit should be replaced by an inductance. This behavior of the anode can be explained with the surface relaxation [14] according to the model of the Faraday impedance at non-equilibrium potential with a potential dependent transfer reaction rate.
The evaluation of the interpolated impedance spectra (Fig.3-5) was performed with the equivalent circuit represented in Fig.6. Since the impedance of the cathode (R_c and $C_{dl,c}$) and membrane resistance R_M are constant in the galvanostatic mode, we analyze in detail the time (potential) dependency of the impedance elements of the anode.
The impedance elements from the equivalent circuit (Fig.6b) are defined as following:

C_A = capacity of the anode
C_C = capacity of the cathode
L_k = low frequency inductance
R_M = membrane resistance
R_k = resistance of relaxation
R_η = heterogeneous reaction resistance or charge transfer resistance
Z_N = Nernst impedance
Z_k = impedance of relaxation
τ = time constant of relaxation = L_k/R_k

According to [14], the Faraday impedance of the electrode (anode, Z_F) is given by equ. 8:

$$Z_F = (R_\eta + Z_N)/(1 + R_\eta/Z_k) \qquad (8)$$

$$Z_k = (1+j\,2\pi f\,\tau)/(i_F\,\mathrm{dln}k/\mathrm{d}E) \qquad (9)$$

$$\text{for } f \rightarrow 0\text{: } Z_k \rightarrow R_k = 1/(i_F\,\mathrm{dln}k/\mathrm{d}E) \qquad (10)$$

CONCLUSION

Impedance spectra measured in the galvanostatic mode during poisoning of the anode with CO show a strong time and a strong potential dependency respectively. A significant change of the shape of the spectra with time is observed. Three different sections can be recognized. In the first section (Fig.3), the nonlinear decrease region of the cell voltage from t = 0 (740 mV) to t = 4200 s (443 mV), the most sensitive impedance elements are R_k (increases from 1.3 mΩ to 7 mΩ), τ increases from 165 ms to 346 ms, the reaction resistance R_η increases from 18 mΩ to 48 mΩ, the Nernst impedance $Z_{n,1}$ from 5 $m\Omega s^{-1/2}$ to 172 $m\Omega s^{-1/2}$, and the capacitance C_A decreases from 106 mF to 39 mF. The high value of C_A is explained by the fact that C_A is the sum of the adsorption capacity and double layer capacity. The two capacities can be separated if we modify the equivalent circuit (two capacities in parallel). The double layer capacity (29 mF) is not sensitive to the potential. So we can attribute the decrease of the capacity to the adsorption capacity (from 77 mF to 10 mF) due to the decrease of hydrogen adsorption because the surface is blocked with CO.

In the transition region (Fig.4) from t = 4200 s (443 mV) to t = 5400 s (308 mV) only R_k shows a different behavior (decreases from 7.2 mΩ to 1.6 mΩ). At the cell voltage of 344 mV we have an overvoltage due to CO poisoning of the anode of 396 mV (740 mV-344 mV). From previous impedance measurements at different current densities we calculate for the anode at 217 $mAcm^{-2}$ an overvoltage of 75 mV. Adding to the overvoltage at this current density (the overvoltage due to CO poisoning) we obtain the potential of the anode (471 mV). At this potential the CO oxidation reaction will contribute with H_2O dissociation as a precursor step and at the Pt surface both reactions - hydrogen and CO oxidation - take place. A parallel current pathway (high resistance) due to CO oxidation is opened, with small influence on the Faraday impedance due to the high resistance of this parallel reaction. Therefore, the equivalent circuit from Fig.6b could be extended by a parallel resistance. However, this parallel resistance can hardly be separated under the experimental conditions chosen.

In the third section (Fig.5) from t = 6000 s (292 mV) to 12000 s (244 mV) we observe a linear decrease (6.5 µV/s) of the cell voltage. For this further decrease of the cell voltage mainly R_k and $Z_{N,1}$ (finite diffusion) are responsible. The fuel cell was operated at "dead end" and we have an increasing concentration of inert CO_2 in the anode gas supply.

The equivalent circuit proposed here can be extended by the porous electrode model and has to be verified by further impedance measurements under different operation conditions like different CO concentration, pressure, temperature and stoichiometry.

REFERENCES

1. S. J. C. Cleghorn, T. E. Springer, M. S. Wilson, C. Zawodzinski, T. A. Zawodzinski and S. Gottesfeld, International Journal of Hydrogen Energy, 22, 1137 (1997).
2. C. Borroni-Bird, J. Power Sources, 61, 33 (1996).
3. D. P. Wilkinson and D. Thompsett, in Proceedings of the Second National Symposium on New Materials for Fuel Cell and Modern Battery Systems, O. Savadogo and P. R. Roberge, Editors, p. 268, Montreal (Quebec) Canada (1997).
4. M. S. Wilson, C. Derouin, J. Valerio, T. A. Zawodzinski and S. Gottesfeld, Electrocatalysis, Issues in Polymer Electrolyte Fuel Cells. Proc., 28th IECEC, 1.1203-1.1208 (1993).
5. P. Stonehart and P. N. Ross, The Commonality of Surface Processes in Electrocatalysis and Gas Phase Heterogeneous Catalysis, Catal. Rev.-Sci. Eng., 12, 1 (1975).
6 N. Wagner, Thesis, University Erlangen, (1989).
7. W. Vogel, J. Lundquist, P. Ross and P. Stonehart, Electrochimica Acta, 20, 79 (1975).
8. K.J. Vetter, in "Elektrochemische Kinetik", Springer-Verlag, Berlin, Göttingen, Heidelberg, 1961, p.484.
9. N. Wagner, W. Schnurnberger, B. Müller and M. Lang, Electrochim. Acta, (1998) (in press).
10. M. Keddam, Thèse, Universitè de Paris, (1968).
11. H. Gerischer and W. Mehl, Z. Elektrochem., 59, 1049 (1955).
12. J.-P. Diard, B. Le Gorrec and C. Montella, J. Electroanal. Chem., 326, 13 (1992.
13. H. Göhr, Ber. Bunsenges. Phys. Chem., 85, 274 (1981).
14. H. Göhr and C.-A. Schiller, Z. Phys. Chemie Neue Folge, 148, 105 (1986).

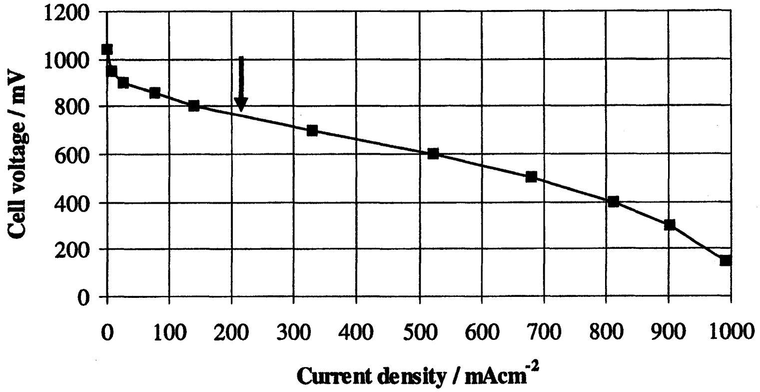

Fig.1: Steady-state current-voltage curve with pure hydrogen and oxygen, both at 2 bar absolute, cell temperature 80°C, E-TEK-electrodes. The arrow indicate the starting point of the galvanostatic impedance measurements

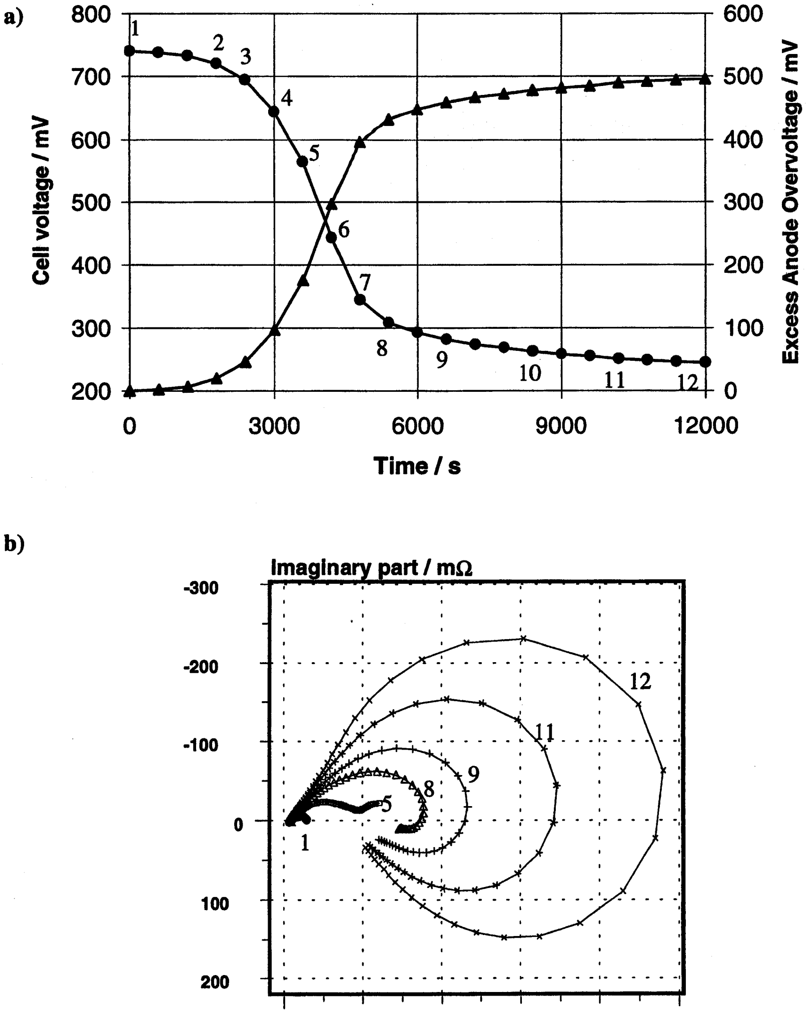

Fig.2: Time dependency during poisoning of the anode with CO, with hydrogen + 100 ppm CO at 2 bar absolute, cell temperature 80°C, E-TEK-electrodes:
a) cell voltage (●) and excess anode overvoltage (◆)
b) interpolated impedance spectra (Nyquist representation)

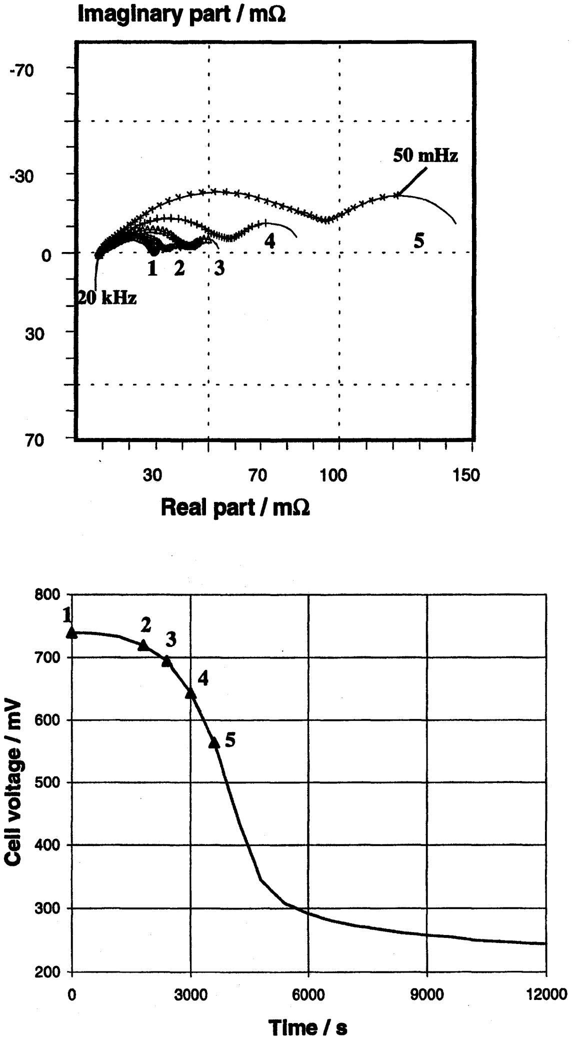

Fig.3: Time dependency of the impedance spectra (Nyquist representation) and cell voltage (Δ) during poisoning of the anode with CO, with hydrogen + 100 ppm CO at 2 bar absolute, cell temperature 80°C, E-TEK-electrodes.

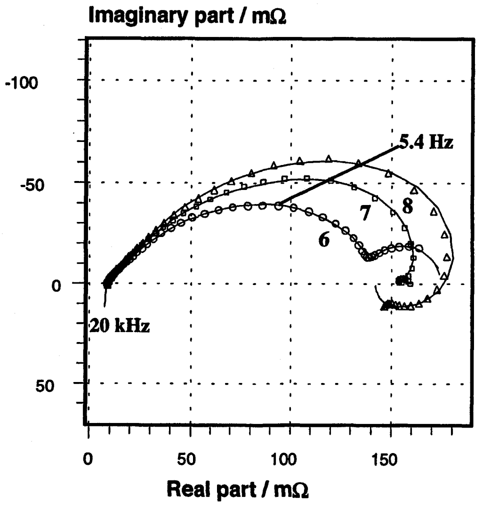

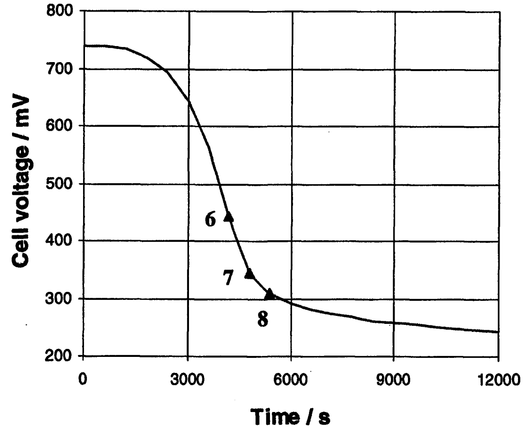

Fig.4: Time dependency of the impedance spectra (Nyquist representation) and cell voltage (Δ)during poisoning of the anode with CO, with hydrogen + 100 ppm CO at 2 bar absolute, cell temperature 80°C, E-TEK-electrodes.

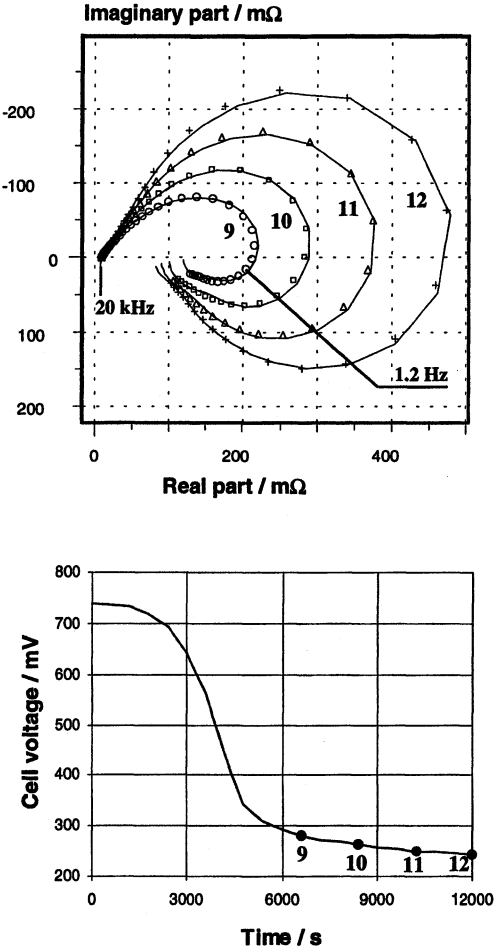

Fig.5: Time dependency of the impedance spectra (Nyquist representation) and cell voltage (●)during poisoning of the anode with CO, with hydrogen + 100 ppm CO at 2 bar absolute, cell temperature 80°C, E-TEK-electrodes.

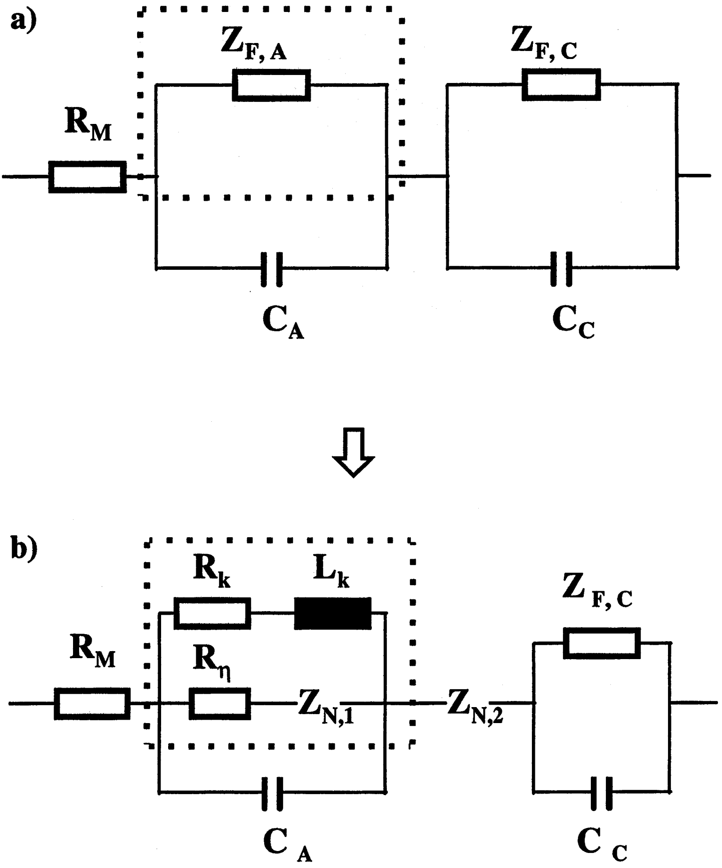

Fig.6: Equivalent circuits of the fuel cell:
a) general equivalent circuit
b) equivalent circuit for evaluation of interpolated impedance spectra measured during poisoning the anode with CO

Proton_Conducting_Membrane_Fuel_Cells_II, PV 1998-27, 200-208 (1998)
DOI: 10.1149/199827.0200PV © The Electrochemical Society

ENHANCED CO TOLERANCE IN POLYMER ELECTROLYTE FUEL CELLS WITH PtMo ANODES

T. Zawodzinski, J. Bauman, T. Rockward, P. Haridoss, F. Uribe and S. Gottesfeld

Electronic Materials and Devices Group
Los Alamos National Laboratory
Los Alamos, NM 87545

ABSTRACT

We demonstrate that fuel cells using supported PtMo anode electrocatalysts can exhibit excellent tolerance to 20 ppm CO in H_2. Only some of the supported PtMo samples tested appeared highly tolerant to CO. A key factor correlating with good anode performance in the presence of CO is the particle size of the supported PtMo catalyst.

INTRODUCTION

Anodes for polymer electrolyte fuel cells that are tolerant to carbon monoxide at levels of 10 to 100 ppm are important for the development of fuel cells as vehicular power sources. CO levels in this range are likely to be present in anode feed streams derived from processing of fuels such as gasoline. Work toward this goal has focused on several different strategies, including injection of air into the anode flow stream, operation of the cell at elevated temperatures and development of improved anode electrocatalysts, typically Pt alloys. The latter strategy, if successful, leads to the most straightforward mode of improving cell performance.

Ross and co-workers (1,2) have carried out extensive work to identify appropriate alloy catalysts based on fundamental electrochemical studies of hydrogen oxidation in the presence of CO on well-characterized surfaces of bulk electrodes. A series of alloy catalysts have been spotlighted in this work, including PtRu of various alloy compositions, Pt_3Sn and, most recently, PtMo with various component ratios. These catalysts all exhibit lower onset potentials for CO electrooxidation than Pt. Furthermore, a common and important feature for their behavior as CO tolerant electrocatalysts for fuel cell applications is a small but finite oxidation current observed near 0 V vs. hydrogen. This current, observed to be on the order of mA on disk electrodes studied by this Berkeley group, is magnified substantially by the high surface area of the typical supported catalyst used in the fuel cell. By definition, complete CO tolerance requires a substantial hydrogen oxidation current in the presence of CO at minimal anode polarization.

We report here on comparative studies, performed in PEFCs , of the CO tolerance of dispersed, carbon-supported Pt, PtRu and PtMo alloy electrocatalysts. These studies include work using hydrogen and simulated reformate feedstreams with various levels of CO. We find that some compositions of supported PtMo catalysts are completely tolerant to 20 ppm CO in hydrogen at 80C, a significant improvement over previously observed levels of tolerance for PtRu under similar conditions.

EXPERIMENTAL

Carbon-supported Pt, PtRu and PtMo alloy electrocatalysts were all obtained from E-TEK. Membrane/electrode assemblies were prepared as described elsewhere (3). Fuel cell tests were carried out using standard test stands and methods described in more detail elsewhere in this volume (4). Gas mixtures were prepared using calibrated automated mass flow controllers (MKS) to mix feedstock gases or gas mixtures in appropriate quantities. Simulated reformate was prepared by mixing hydrogen gas with an appropriate $N_2/CO_2/CO$ mixture. Gases were humidified by passage through a humidifier bottle upstream of the cell.

A series of different C/PtMo samples were tested. No unusual measures were taken in preparing inks from various supported PtMo samples. The C/PtMo samples were studied for extent of alloying and crystallite sizes using X-ray diffraction techniques on the Pt (111) peak. These studies were carried out on a Siemens D5000 diffractometer equipped with a Huber incident beam germanium curved crystal monochrometer with Cu K-α radiation.

RESULTS AND DISCUSSION

Figure 1 shows a series of polarization curves obtained for PtMo exposed to various levels of CO in H_2. We previously showed extensive results for PtRu catalysts (3) and one curve obtained under similar conditions is also shown in Figure 1. At 80°C, PtRu alloys are capable of delivering slightly improved tolerance to 20 ppm CO compared to Pt, at somewhat higher loadings than typically used in our anodes. Figure 1 shows that PtMo exhibits complete tolerance to 20 ppm CO in H_2.

In Figure 2, we show a series of plots obtained for various anode catalysts, of the excess anode potential measured on adding 20 ppm CO to H_2 shown as function of current density. PtMo sample number 1, revealed to be poorly alloyed, showed relatively poor tolerance (high excess overpotential) to 20 ppm CO. In contrast, improved samples of carbon-supported PtMo have shown excellent tolerance to 20 ppm CO, as can be seen in Figure 2 for sample PtMo #4.

In Figure 3, we show a series of polarization curves obtained for fuel cells operating on H_2 + 20 ppm CO, with anodes using all six PtMo samples studied in this work. Clearly, there are significant differences from sample to sample, reflecting improvements in catalyst preparation methods. PtMo sample number 4 shows complete tolerance to 20 ppm CO. Unfortunately, however, cells using this catalyst do not maintain such perfect CO tolerance at higher CO volume fractions, as indicated by Figure 4.

In an effort to obtain some information about the state of the different supported PtMo catalysts tested , we performed XRD studies. A typical XRD scan is shown in Figure 5. Unfortunately, little information could be obtained concerning the extent of alloying of the sample from these data, for the following reason. Typically, when one element dopes substitutionally into the structure of another element, if the atomic radii of the two elements differ by a significant amount, there is a distinct expansion of the host lattice associated with doping. Such an expansion of the host lattice will lead to a shift of the host lattice X-ray diffraction peaks. Such shift in peak positions can then be used to calculate the extent of doping into the host material. However, in the case of platinum and molybdenum, their atomic radii differ only by about 1.75% (5,6). Such difference in atomic radii is too small to cause an identifiable shift in the peak positions of platinum when doped with molybdenum. The X-ray scans do not reveal the presence of second phases, as evidenced by the absence of any peaks other than those of the carbon and platinum. This indicates that, within detection limits, platinum may indeed be doped with molybdenum, however, as explained above, it is difficult to identify the extent of doping attained in each of the samples.

The full width at half maximum of the (111) peak could be used to characterize the average crystallite size using the Debye-Scherrer relation. The Debye-Scherrer relation is quantitatively represented as:

$$L = \frac{0.9\lambda}{B\cos\theta_b}$$

, where L is the average crystallite size in the platinum particles, λ is the wavelength of X-rays used (this experiment used Cu Kα radiation, λ = 1.540562 Å), B is the full width at half maximum of the (111) peak, measured in degrees 2θ (not θ) and corrected for instrument broadening (0.2 degrees for the 0.6 mm exit slit used in the x-ray diffractometer). The value of B after the correction for instrument broadening is then converted to radians from degrees and used in the Debye-Scherrer relation. θ_b is the Bragg angle for the (111) peak. The values obtained for crystallite sizes from the (111) peak have been confirmed with similar calculations on the other peaks as well.

In Figure 6, we show a plot of anode polarization loss caused by adding 20 ppm CO to H_2 , versus PtMo catalyst particle size. Clearly, the quality of the PtMo catalyst correlates strongly with particle size, samples of larger particle sizes exhibiting better CO tolerance. The reason underlying the correlation is not fully clear, however it is possible that the method used to prepare the dispersed catalyst samples resulted in larger particle sizes when the components were well alloyed.

Finally, we have carried out several experiments investigating the performance of C/PtMo anode catalysts on reformate streams. The results are consistent with results described for other catalysts in reference 4. In particular, no 'reverse shift' effect was observed with this catalyst in the presence of CO_2. Because of the higher CO/H_2 ratio in the diluted stream at nominal 100 ppm CO, the tolerance to 20 ppm CO in H_2 is essentially equivalent to tolerance to ca. 10 ppm in reformate.

Complete tolerance to even 10 ppm in reformate could provide some important advantages. Gasoline processing and fuel stream clean-up technologies are presently being further refined and CO levels of 10 ppm or less have been reported for steady-state operation. This opens up the possibility of using the intrinsic tolerance of PtMo for steady state operation, combined with air bleeding added to deal with any transient CO excursions. Thus, during 'cruising', any loss of fuel utilization associated with air injection may be avoided. Obviously, such an approach requires an effective CO sensor upstream the stack.

We have recently performed systematic studies of the response of PEFCs to CO level variations (7). Figure 7 shows the consequence of step increase in CO level in a reformate stream from 20 to 100 ppm, comparing Pt and PtMo anodes and using continuous 2% air bleeding into the anode in each case. Clearly, the PtMo anode maintains a substantially higher (ca. fivefold) performance than the Pt cell when temporarily exposed to 100 ppm CO.

CONCLUSIONS

We have shown that PtMo is a promising catalyst for achieving high tolerance to low levels (10 - 20 ppm) of CO in H_2 or in reformates of liquid hydrocarbons, without the need of air bleed. However, at CO levels above 20 ppm, the benefit of this catalyst is lessened. The best CO tolerance has been achieved with PtMo samples of larger particle sizes, possibly correlating with more complete alloying. This suggests that further improvements could possibly be made in processing these catalysts to further enhance their performance.

ACKNOWLEDGMENTS

We gratefully acknowledge the support of the US DOE Office of Advanced Automotive Technology for this work. We also acknowledge E-TEK Inc of Natick, MA for providing the carbon-supported PtMo samples. We particularly appreciate discussions with Emory DeCastro, Jim Giallombardo and Bob Allen. Finally we thank Phil Ross and Nenad Markovic of LBNL for stimulating discussions related to fuel cell anode electrocatalysis.

REFERENCES

1. H. A. Gasteiger, N. M. Markovic and P. N. Ross, *J. Phys Chem.*, **99,** 16757 (1995).

2. H. A. Gasteiger, N. M. Markovic and P. N. Ross, *J. Phys Chem.,* **99**, 8290 (1995).

3. M. S. Wilson and S. Gottesfeld, J. Applied Electrochem, **22**, 1 (1992).

4. T. Zawodzinski, T. Springer, J. Bauman, T. Rockward, F. Uribe and S. Gottesfeld, *This Proceedings Volume.*

5. Swanson, Tatge, Natl. Bur. Stand. (U.S.), Circ. 539, 1 31 (1953)

6. Swanson, Tatge., Natl. Bur. Stand. (U.S.), Circ. 539, 1 20 (1953

7. J. Bauman, T. Zawodzinski and S. Gottesfeld, *This Proceedings Volume.*

FIGURES

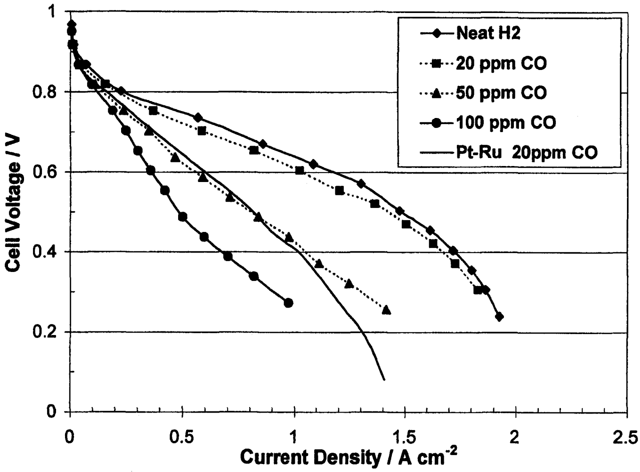

Figure 1: Fuel cell performance with PtMo anode catalyst exposed to various levels of CO in H_2. A polarization curve obtained for PtRu exposed to 20 ppm CO is included for comparative purposes. Test conditions: Pt loadings 0.3 mg/cm^2 for anode and cathode of all cells; T_{cell}= 80°C, anode and cathode back pressure = 30 psig; 2 stoich anode flow rate.

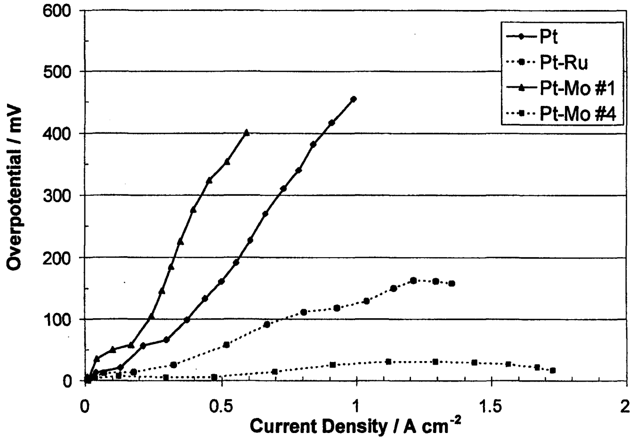

Figure 2: Excess anode polarization at 20 ppm CO in H_2. Curves demonstrate improvement in preparation of PtMo/C catalysts, optimizing composition and degree of alloying. Test conditions as in Figure 1.

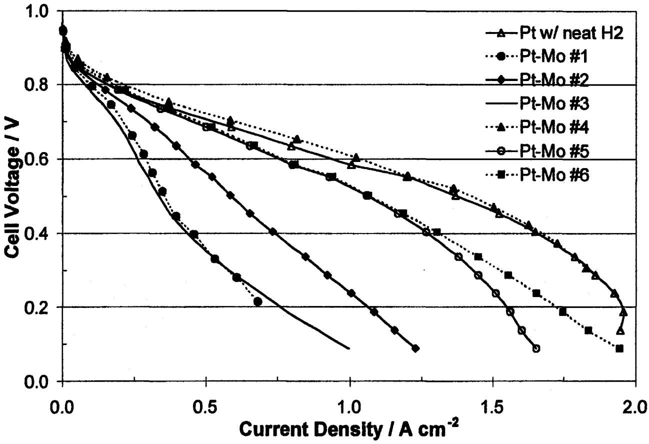

Figure 3: Polarization curves for a series of PtMo samples exposed to 20 ppm Co in hydrogen. Other test conditions as in Figure 1.

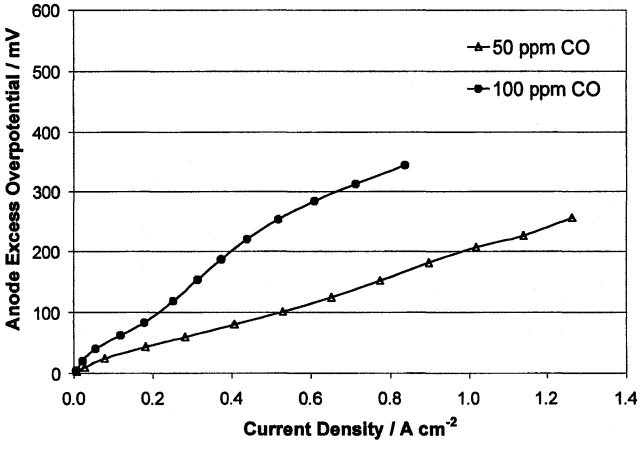

Figure 4: Anode loss for a cell with a PtMo #4 anode catalyst at two different CO levels. Test conditions as in Figure 1.

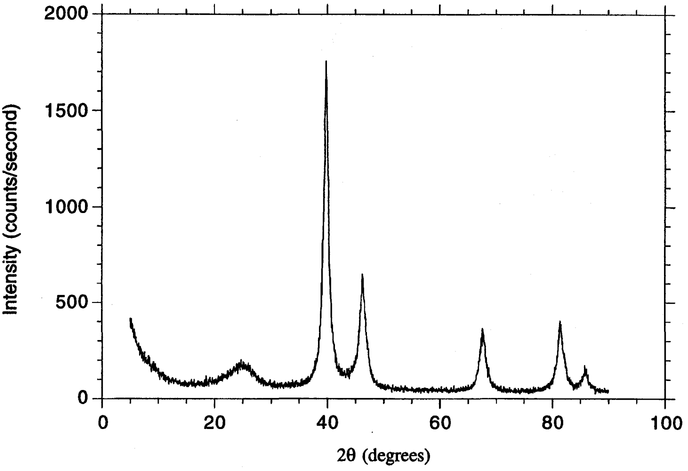

Figure 5: XRD scan obtained for a sample of PtMo sample number 4.

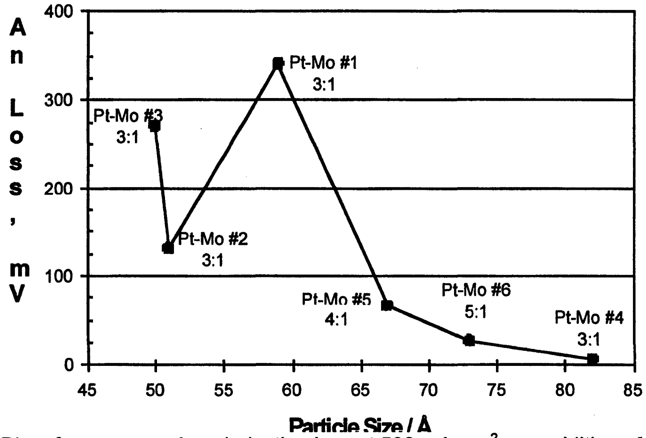

Figure 6: Plot of excess anode polarization loss at 500 mA cm^{-2}, on addition of 20 ppm CO to H_2, vs. particle size for a series of PtMo samples. Fuel cell data from Figure 2.

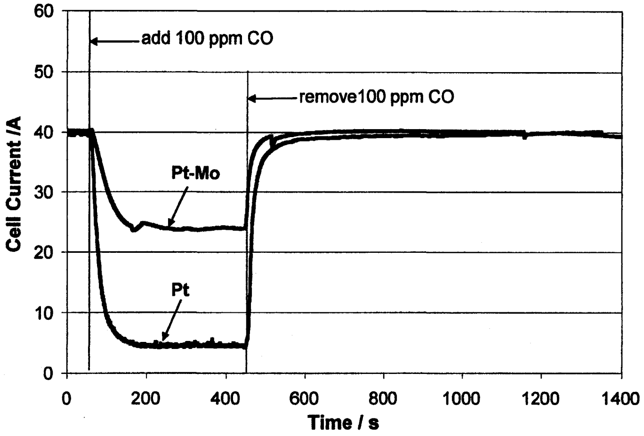

Figure 7: Transient response of cells with PtMo and Pt anodes. For t < 60 sec, cells are exposed to simulated reformate containing 20 ppm CO with a 2% airbleed. At t = 60 sec, CO level is increased to 100 ppm. At t = 450 sec, CO level is returned to 20 ppm. Test conditions: Pt loadings 0.3 mg/cm^2 for anode and cathode of all cells; T_{cell}= 80°C, anode and cathode back pressure = 30 psig; 2 stoich anode flow rate.

Proton_Conducting_Membrane_Fuel_Cells_II, PV 1998-27, 209-217 (1998)
DOI: 10.1149/199827.0209PV © The Electrochemical Society

PERFORMING CO TOLERANT ANODE CATALYST FOR POLYMER ELECTROLYTE FUEL CELLS

M. C. Denis, G. Lalande, D. Guay, and J. P. Dodelet
INRS-Énergie et Matériaux, C. P. 1020, Varennes, Québec, Canada, J3X 1S2
and
R. Schulz
IREQ, Hydro-Québec, C. P. 1000, Varennes, Québec, Canada, J3X 1S1

ABSTRACT

High energy ball-milling of Pt, Ru, and Al in a 1:1:8 atomic ratio has been used to produce CO tolerant unsupported Pt-Ru based catalysts for the oxidation of hydrogen in polymer electrolyte fuel cells. After leaching Al, this catalyst [$Pt_{0.5}$ -$Ru_{0.5}$ (Al_4)] displays a specific area of 38 m^2/g. It shows hydrogen oxidation performance and CO tolerance equivalent to those of $Pt_{0.5}$ -$Ru_{0.5}$ Black from Johnson Matthey, the commercial catalyst which was found to be the most CO tolerant one in this study. $Pt_{0.5}$ -$Ru_{0.5}$ (Al_4) is a composite catalyst. It consists of two components: (i) small crystallites (~ 4 nm) of a Pt-Al solid solution (1-3 Al wt%) of low Ru content, and (ii) larger Ru crystallites. The providers of oxygenated species necessary for the electrochemical oxidation of CO on Pt are either oxidized Al or Ru. The latter may be either on the surface of the Pt-Al (+Ru) alloy crystallites or at the surface of the larger Ru crystallites. $Pt_{0.5}$ -$Ru_{0.5}$ (Al_4) provides a stable current under H_2 + 100 ppm CO.

INTRODUCTION

Polymer electrolyte fuel cells (PEFCs) operate typically at 80-100°C on H_2 mostly obtained by steam reforming methanol or other light hydrocarbon fuels. Contrary to phosphoric acid fuel cells operating at higher temperatures, PEFCs are not able to tolerate a CO level of about 1% by volume obtained, for instance, at the output of a methanol reformer. This level has to be lowered further to a few ppm by using a shift process and a subsequent catalytic oxidizer.

CO concentration in the hundred ppm range have already a strong effect on the performances of PEFCs (1,2). Poisoning occurs because CO binds strongly to Pt sites resulting in a high Pt surface coverage of CO at the operating temperature of PEFCs. Since the chemisorption of CO is exothermic, a possible solution to this problem is to increase the temperature, but the operating temperature is limited to a maximum of about 120°C by the need for effective humidification of the membrane (3). A second solution consists of injecting a small amount of O_2 (up to about 2%) to oxidize CO chemically (1). However, the explosion threshold for H_2/O_2 mixtures is 5% O_2 in H_2. This limits to about 100 ppm the maximum level of CO that can be treated effectively by oxygen bleeding in PEFCs (3).

A third solution to the poisoning problem is to use Pt alloy catalysts that are more tolerant towards CO poisoning than pure Pt. Among all binary alloys that have been considered for CO tolerance, Pt-Ru alloys are certainly those that have been the most studied. The use of Pt-Ru as oxidation catalyst for H_2 containing CO at the anode leads to a lowering of the CO oxidation potential (onset of CO oxidation at ~ 0.4 V vs RHE in 0.5 M H_2SO_4 (4)) compared with the oxidation potential of CO on pure Pt (onset of CO oxidation at ~ 0.7 V vs RHE in 0.5 M H_2SO_4 (4)). The activity of Pt-Ru alloys towards CO oxidation is related to their bifunctional properties (4-7) : a nucleation at low potentials of oxygen containing species (OH_{ads}) on Ru atoms and the bimolecular reaction of OH_{ads} with CO adsorbed on Pt. The optimum Pt-Ru surface composition for CO oxidation is $Pt_{0.5}$-$Ru_{0.5}$. It results from two opposite effects: an increase in the coverage of the electrode with OH_{ads} increasing with the fraction of Ru and a decrease in the possibility of reaction between OH_{ads} with CO_{ads} as the number of Ru-Ru pair sites increases.

The aim of this paper is to see if it is also possible to obtain performing unsupported Pt-Ru catalysts by using High Energy Ball-Milling (BM), a technique which is industrially amenable. It is known that by using the BM technique, it is possible to form a large number of nanocrystalline alloys by direct reaction in the solid state between elemental components which are subject to intense mechanical deformations (8). BM is obtained by the rapid movement of a hermetically sealed crucible containing the metal powders to be alloyed and several balls with which they enter in collision. The macroscopic temperature of the container and its contents barely increases a few tens of degrees during the process and it seems that the microscopic or local temperature does not increase more than 300°C (9). Alloys are then produced by the diffusion of the elements in the solid state which is favored by the appearance of defects in the crystalline structure after mechanical deformation. This paper will demonstrate that it is possible to obtain CO tolerant Pt-Ru catalysts with performances at least equivalent to those of the commercially available catalysts containing Pt and Ru.

EXPERIMENTAL

Catalyst preparation and characterization

The various metal powders used in catalyst preparation were: Pt, < 74 μm (-200 mesh) in size, 99.8% (Alfa AESAR); Ru, < 44 μm (-325 mesh), 99.95% (Omega); Al, 44-

420 μm (-40 +325 mesh) (Johnson Matthey Electronics). The catalysts were prepared using a Spex 8000 mixer/mill. Metal powders and WC balls were loaded in a 70 ml WC crucible. Six grams of powder were used, and the ball-to-powder weight ratio was always 4/1. All powder handling was performed in an Ar-filled glove box. Milling times of 40h were routinely used.

The ball-milled materials were characterized by (i) X-ray diffraction (XRD) using a Siemens D-500 diffractometer equipped with a Cu $K\alpha$ radiation source; (ii) surface area measurements by N_2 adsorption (multipoint BET) using a Quantachrome Autosorb Automated Gas Sorption System; (iii) neutron activation analysis to obtain bulk concentrations of metals milled; and (iv) XPS using a VG Escalab 220i-XL equipped with an Al $K\alpha$ monochromatic source.

<u>Electrochemical measurements</u>

The electrocatalytic performances of the catalysts were evaluated for pure H_2 (UHP, Praxair) and H_2 + 100 ppm CO (UHP, BOC Canada) in a GT60 GlobeTech fuel cell test station. The ink was prepared by sonicating for 20 min 40 mg of metal powder, 150 μl of a Nafion 5 w/o solution (Aldrich), 400 μl of methanol (J. T. Baker, CMOS Electronic Grade), and 60 μl of glycerine (Fisher Scientific, ACS). A volume of 305 μl of the ink was pipetted onto a 5 cm^2 uncatalyzed ELAT backing layer from E-TEK which was then dried in a vacuum oven for 1h at 75°C. The resulting catalyst loading was 4 mg/cm^2 with a catalyst/Nafion weight ratio of 85/15. A Pt catalyzed ELAT backing layer (E-TEK, 0.37 mg Pt/cm^2) painted with a 5 w/o Nafion solution was used as the cathode. After drying in a vacuum oven at 75°C, the Nafion deposited on the cathode amounted to 0.6 mg/cm^2.

Nafion 117 was used as the polymer electrolyte in the membrane electrode assembly. The membrane electrode assembly was obtained by hot-pressing a clean Nafion 117 membrane between the anode and the cathode at 140°C for 40 sec under 2500 psi. Current stabilization at 0.5V was reached before recording the polarization curves. These were obtained under the following conditions: cell temperature = 80°C; temperature of water humidifying the anode and cathode gases = 110°C; H_2 (or H_2 + 100 ppm CO) pressure = 30 psig; O_2 (UHP, Praxair) pressure = 60 psig. H_2 and O_2 flow rates = 0.2 slm. For experiments involving CO, H_2 + 100 ppm CO was fed into the cell during 30 min in open circuit potential conditions before measuring the polarization curve.

Three commercial catalysts were used as references for the fuel cell tests. They were: Platinum Black (Fuel Cell Grade, Alfa AESAR, Johnson Matthey) [Pt Black]; Platinum Ruthenium Black (Pt 66%, Ru 34% (w/w), Alfa AESAR, Johnson Mattey) [$Pt_{0.5}$-$Ru_{0.5}$ Black]; and $PtRuO_x$ (Pt/Ru = 1/1 at, E-TEK) [$PtRuO_x$].

RESULTS and DISCUSSION

When Pt and Ru powders in a 1:1 atomic ratio are milled together, a $Pt_{0.5}$ -$Ru_{0.5}$ nanocrystalline alloy is obtained after 20h. This alloy shows poor catalytic performances even for pure H_2 oxidation because its specific area is very low (3.8 m^2/g). This is the result of the agglomeration of alloy nanocrystallites as it is often the case when ball-milling is used. A successful way to improve the specific area of the ball-milled catalyst is to mill Pt, Ru, and Al together and to leach the resulting material in 1M NaOH. The atomic ratio of Pt, Ru, and Al is 1:1:8, respectively. The catalyst obtained according to this procedure is labelled $Pt_{0.5}$ -$Ru_{0.5}$ (Al_4). Its specific area is 38 m^2/g which is still smaller than 44.3, 145, and 63.2 m^2/g for Pt Black, $PtRuO_x$, and $Pt_{0.5}$ -$Ru_{0.5}$ Black, respectively. This does not affect the performance of the catalyst as shown in Figs. 1 and 2. These figures display the polarization curves of $Pt_{0.5}$ -$Ru_{0.5}$ (Al_4) (dark circles) in pure H_2 and in H_2 + 110 ppm CO, respectively. Figure 2 indicates that $Pt_{0.5}$ -$Ru_{0.5}$ (Al_4) and $Pt_{0.5}$ -$Ru_{0.5}$ Black have comparable CO tolerance.

Neutron activation analysis reveals, however, the presence of 1-3 wt% of unleacheable Al in $Pt_{0.5}$ -$Ru_{0.5}$ (Al_4). To determine the effect of Al vs Ru in $Pt_{0.5}$ -$Ru_{0.5}$ (Al_4), a catalyst consisting of Pt (Al_4) was fabricated by ball-milling Pt and Al together in a 1 to 4 Pt/Al atomic ratio. The polarization curves of Pt (Al_4) (dark triangles) in pure H_2 and in H_2 +110 ppm CO at the anode are also presented in Figs. 1 and 2, respectively. Figure 2 indicates that even if Ru is absent from the composition of Pt (Al_4), the catalyst shows however a better CO tolerance than that displayed by Pt Black (open squares). However, this CO tolerance slowly decreases under potentiostatic control at 0.5V, while $Pt_{0.5}$ -$Ru_{0.5}$ (Al_4) tested in the same conditions stabilizes at an even higher current density than $Pt_{0.5}$ -$Ru_{0.5}$ Black.

$Pt_{0.5}$ -$Ru_{0.5}$ (Al_4) and Pt (Al_4) were characterized. Their XRD diffractograms are given in Fig. 3, curves A and B, respectively. Except for the sharp Ru diffraction peaks in $Pt_{0.5}$ -$Ru_{0.5}$ (Al_4), both diffractograms are similar. They both show broad Pt peaks shifted towards larger diffraction angles, indicating some dissolution of Al in the Pt lattice. The existence of a Pt-Al solid solution is expected for low Al content on the basis of the phase diagram for the binary Pt-Al alloys (10). A low content of Ru in the Pt-Al alloy is expected since it is possible to obtain Pt-Ru alloys by ball-milling when these two metals are milled together. However, in the present case, the dilution effect of Al lowers the probability of interaction of Pt and Ru powders during the milling procedure. An average nanocrystallite size of 3.8 nm has been evaluated from the width at half height of the main diffraction peak (Pt(111)) of Pt (Al_4) in Fig. 3B. Since the same peak shows a similar broadness for $Pt_{0.5}$ -$Ru_{0.5}$ (Al_4), a similar nanocrystallite size is also expected for that catalyst.

The surface species of $Pt_{0.5}$ -$Ru_{0.5}$ (Al_4) have been evaluated by XPS. Figure 4 presents the XPS spectra at the Pt 4f core level of Pt Black (curve A) and $Pt_{0.5}$ -$Ru_{0.5}$ (Al_4)

(curve B). The XPS spectrum at the Pt 4f core level of $Pt_{0.5}$ (Al_4) has already been presented (11). It is the same as that of Pt Black. The vertical lines at 71.0 eV, 72.4 eV and 73.8 eV are the binding energies reported for the $4f_{7/2}$ peak of Pt (12), $Pt(OH)_2$ (12) and PtO (13), respectively. From Fig. 4, one may deduce that both Pt Black (curve A) and $Pt_{0.5}$ -$Ru_{0.5}$ (Al_4) (curve B) show similar XPS spectra characteristic of metallic Pt.

Figure 4 also presents the XPS spectrum at the Ru 3d core level of $Pt_{0.5}$ -$Ru_{0.5}$ (Al_4) (curve C). The vertical lines at 280.0 eV and 280.7 eV are the binding energies reported for the $3d_{5/2}$ peaks of Ru and RuO_2, respectively (14). From Fig. 4, one may deduce that $Pt_{0.5}$ -$Ru_{0.5}$ (Al_4) contain both metallic and oxidized Ru.

In order to obtain the oxidation state for Al on the surface, it was necessary to measure the Al 2s XPS spectrum. Al 2p which is the principal peak of Al was not accessible since its binding energy coincides with that of Pt (72.65 eV for metallic Al (15)). Furthermore, its sensitivity factor is only 0.537 vs 15.46 for Pt. It was therefore not possible to determine the presence of Al at the surface of the catalyst from the Al 2p peak. The Al 2s core level of $Pt_{0.5}$ -$Ru_{0.5}$ (Al_4) is given in Fig. 4D. The vertical lines in Fig. 4D indicate the binding energy of metallic Al (117.8 eV), Al_2O_3 (119.6 eV) and oxidized metallic Al (120.5 eV). Metallic Al and oxidized Al are therefore present at the probed surface of $Pt_{0.5}$ -$Ru_{0.5}$ (Al_4).

CONCLUSION

The characterization of $Pt_{0.5}$ -$Ru_{0.5}$ (Al_4) indicates that this catalyst is a composite of small Pt-Al alloy nanocrystallites with a low content of Ru in contact with larger Ru nanocrystals. In the Pt-Al (+Ru) alloy nanocrystallites, Pt is exclusively metallic while Al is partially oxidized. On the other hand, larger Ru nanocrystals are also partially oxidized. This catalyst is as CO tolerant as $Pt_{0.5}$ -$Ru_{0.5}$ Black. Its composite structure ressembles that of Pt/WO_3 and $Pt\text{-}Ru/WO_3$, two CO tolerant catalysts which have also been tested as catalysts for the direct oxidation of methanol (16,17). In $Pt_{0.5}$ -$Ru_{0.5}$ (Al_4), the providers of oxygenated species necessary for the electrochemical oxidation of CO on Pt are either oxidized Al at the surface of the Pt-Al (+Ru) alloy or oxidized Ru. The latter may be either at the surface of the Pt-Al (+Ru) alloy or at the surface of the larger Ru nanocrystals adjacent to the Pt-Al nanocrystallites. A similar conclusion can be drawn for Pt (Al_4) except that there is no Ru in this case. Pt (Al_4) is not stable. It is possible that some of the Al is slowly leached in the acidic medium of the membrane electrode assembly. The stability of $Pt_{0.5}$ -$Ru_{0.5}$ (Al_4) indicates a fundamental difference with Pt (Al_4) probably related to the presence of Ru in the catalyst. The fabrication of $Pt_{0.5}$-$Ru_{0.5}$ (Al_4) powders as CO tolerant catalysts for H_2 oxidation in polymer electrolyte fuel cells using the ball-milling technique is industrially amenable.

ACKNOWLEDGEMENTS

This work was supported by Hydro-Québec and a Collaborative R&D Grant from NSERC

REFERENCES

1. Sh. Gottesfeld and J. Pafford, *J. Electrochem. Soc.* **135**, 2651 (1988).
2. D. Wilkinson and D. Thompsett, "Proceedings of the Second International Symposium on New Materials for Fuel Cell and modern battery systems", Edt. by O. Savadogo and P. R. Roberge, Ecole Polytechnique Montreal, 1997, p.266.
3. Sh. Gottesfeld and T. A. Zawodzinski, *Adv. Electrochem.Sci.Eng.* **5**, 195 (1997).
4. H. A. Gasteiger, N. Markovic, P. N. Ross, Jr. and E. J. Cairns, *J. Phys. Chem.* **98**, 617 (1994).
5. M. Watanabe and S. Motoo, *J. Electroanal. Chem.* **60**, 267 (1975).
6. H. A. Gasteiger, N. M. Markovic and P. N. Ross, Jr., *J. Phys. Chem.* **98**, 8290 (1994).
7. H. A. Gasteiger, N. M. Markovic and P. N. Ross, Jr., *J. Phys. Chem.* **99**, 8945 (1995).
8. C. C. Koch "Materials Science and Technology, Vol 15, Processing of Metals and Alloys", edt. By R. W. Cahn, VCH, Verlagsgesellschaft, Weinheim, (1991), Chapter 5, p. 193.
9. R. M. Davis, B. McDermott, C. C. Koch, *Metallurgical Transactions* **19A**, 2867 (1988).
10. T. B. Massalski ed. "Binary Alloy Phase Diagram 2nd ed., ASM Int. Materials Park, OH., U.S.A., 1990.
11. M. C. Denis, G. Lalande, D. Guay, J. P. Dodelet and R. Schulz, "Proceedings of the Symposium on Electrode Materials and Processes for Energy Conversion and Storage IV", edt. by J. McBreen, S. Mukerjee, S. Srinivasan, The Electrochemical Society, Pennington, NJ, U.S.A. **97-13**, 119 (1997).
12. J. S. Hammond and N. Winograd, *J. Electroanal. Chem.* **78**, 55 (1977).
13. J. B. Goodenough, A. Hamnett, B. J. Kennedy, R. Manoharan and S. A. Weeks, *J. Electroanal. Chem.* **240**, 133 (1988).
14. K. S. Kim and N. Winograd, *J. Catal.* **35**, 66 (1974).
15. C. D. Wagner, W. W. Riggs, L. E. Davis, J. F. Moulder, G. E. Muilenberg, "Handbook of X-Ray Photoelectron Spectroscopy" Perkin-Elmer Corporation, 1978.
16. P. K. Shen and A. C. C. Tseung, *J. Electrochem. Soc.* **141**, 3082 (1994).
17. P. K. Shen, K. Y. Chen, A. C. C. Tseung, *J. Electrochem. Soc.* **142**, L85 (1995).

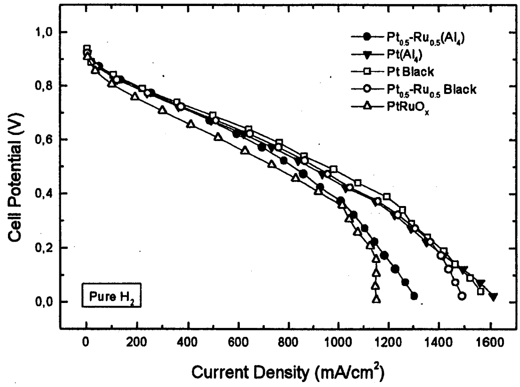

Fig. 1 H_2 / O_2 polarization curves at 80°C for a single membrane electrode assembly using Pt (Al_4) and $Pt_{0.5}$ -$Ru_{0.5}$ (Al_4) at the anode. The polarization curves with Pt Black, $Pt_{0.5}$ -$Ru_{0.5}$ Black, and $PtRuO_x$ at the anode are given for comparison.

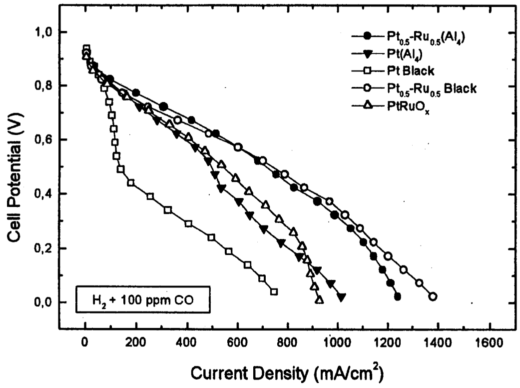

Fig. 2 H_2 + 100 ppm CO / O_2 polarization curves at 80°C for a single membrane electrode assembly using Pt (Al_4) and $Pt_{0.5}$ -$Ru_{0.5}$ (Al_4) at the anode. The polarization curves with Pt Black, $Pt_{0.5}$ -$Ru_{0.5}$ Black, and $PtRuO_x$ at the anode are given for comparison.

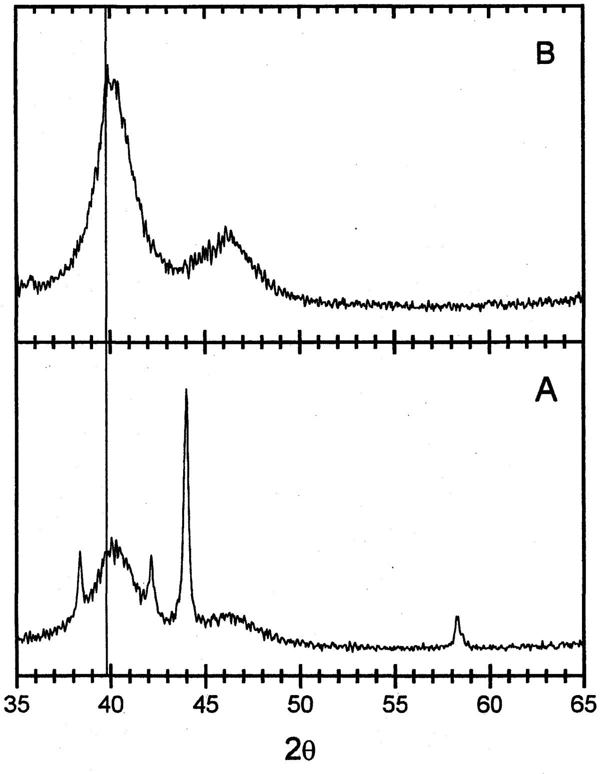

Fig. 3 X-ray diffractograms of: (A) $Pt_{0.5}$ -$Ru_{0.5}$ (Al_4); (B) Pt (Al_4). The vertical line indicates the diffraction position of unalloyed Pt(111).

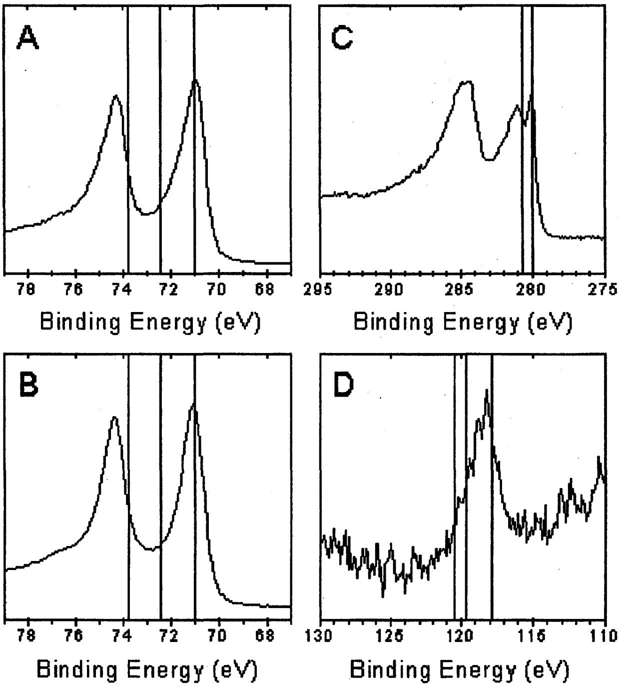

Fig. 4 XPS spectra: at the Pt 4f core levels of (A) Pt Black and (B) $Pt_{0.5}$ -$Ru_{0.5}$ (Al_4). The vertical lines at 71.0, 72.4 and 73.8 eV are the binding energies reported for the $4f_{7/2}$ peaks of Pt, $Pt(OH)_2$ and PtO, respectively; (C) XPS spectrum at the Ru 3d core levels of $Pt_{0.5}$ -$Ru_{0.5}$ (Al_4). The vertical lines at 280.0 and 280.7 eV are the binding energies reported for the $3d_{5/2}$ peak of Ru and RuO_2, respectively; (D) XPS spectrum at the Al 2s core level of $Pt_{0.5}$ -$Ru_{0.5}$ (Al_4). The vertical lines at 117.8, 119.6 and 120.5 eV are the binding energies for the Al 2s of Al, Al_2O_3 and oxidized metallic Al, respectively.

Proton_Conducting_Membrane_Fuel_Cells_II, PV 1998-27, 218-228 (1998)
DOI: 10.1149/199827.0218PV © The Electrochemical Society

COMPARISON OF CO TOLERANCE ON Pt and Pt-Ru ANODES IN PEMFCS

R.J. Bellows, E. Marucchi-Soos
Exxon Research and Engineering, Annandale, NJ 08801

Trace CO impurities can polarize the electro-oxidation of H_2 in the proton exchange membrane fuel cell (PEMFC). CO polarization can severely decrease the PEMFC's power and efficiency. CO polarization data from several groups are compared for PEMFCs using Pt and Pt-Ru anodes with impure H_2. Anodic polarization, in the presence of ppm levels of CO, shows surprisingly high slopes on semi-logarithmic plots. These polarization slopes exceed typical Tafel slopes and are consistent with a non-Faradaic rate limiting step. The onset of severe anode polarization, $I_{crit.}$, correlates with noble metal loading, CO concentration level, and temperature. The dependence of I_{crit} on CO level supports the use Temkin adsorption isotherms for modeling CO tolerance behavior.

INTRODUCTION

The objective of this work was to develop a correlation for CO polarization losses in the proton exchange membrane fuel cell (PEMFC), in order establish a benchmark for anticipated improvements in CO tolerance. The PEMFC has emerged as a promising candidate for distributed power applications and for powering electric vehicles. Many groups are now considering supplying H_2 for PEMFCs by reforming natural gas, alcohols or various hydrocarbons fuels (1-4). This "reformate H_2" avoids many of the limitations anticipated with storing and distributing pure H_2 fuel. Unfortunately, reformate H_2 contains CO impurities, which cause large polarization losses, thereby reducing the PEMFC's efficiency and power output.

Several groups have reported PEMFC performance using impure H_2 on Pt and Pt-Ru catalyzed anodes (5-12). Typical performance curves for on Pt anodes using impure H_2 are shown in Figure 1. The highest performance is always obtained when using pure H_2. The performance using impure H_2 decreases with both increasing CO and with increasing current density. Interestingly, at low current densities, the voltage can remain close to pure H_2, even at the higher CO levels.

Several research groups are trying to develop "CO tolerant" anodes. "CO tolerance" is usually defined as the ability to electro-oxidize H_2 in the presence of CO at an acceptable polarization loss. CO tolerance is usually quantified at some current density in terms of the maximum CO concentration (typically ppm) which can be tolerated, as defined by some nominal polarization loss at the anode (typically 20-100 mV). Losses are referenced to performance on pure H_2. Pt-Ru anodes are reported to show increased CO tolerance over Pt anodes in PEMFCs (8). Pt3Sn and $Pt_{75}Mo_{25}$ are reported to oxidize CO at low potentials (13,14). Pt-Ru/WO_3 is reported to tolerate higher CO levels than Pt in gas diffusion electrodes (15).

There is a need for a benchmark for comparing CO tolerance data from various sources. This would be especially useful since typically the workers have conducted experiments using differing PEMFC designs, materials, noble metal loadings, CO impurity levels and test protocols. In earlier work, the onset of CO polarization on Pt anodes was correlated with noble metal loading, CO concentration level and temperature (11). In this presentation, we extend our correlation to Pt-Ru anodes and we discuss our correlations relative to the modeling of CO tolerance behavior.

THEORY

Anode Surface Chemistry

Fuel cell performance curves are interpreted using polarization theory (16). At any current density, the terminal voltage is a combination of the theoretical voltage (1.23V) minus various polarization losses attributed to O_2 activation at the cathode, O_2 concentration polarization in air cathodes, internal resistance in the cell and H_2 activation losses at the anode. This paper considers an additional H_2 activation loss which is caused by the presence of CO in the H_2. This loss can be interpreted as an additional polarization term, CO polarization (η_{CO}), which is defined as the difference between cell performance on pure H_2 and that with some level of CO.

The electro-oxidation of H_2 on Pt is a two step reaction which proceeds first by the dissociation of H_2, followed by the discharge of adsorbed monatomic H (17). Dissociation is the rate limiting step and requires two adjacent bare Pt sites. CO is a well known poison for the electro-oxidation of H_2 on Pt. CO binds strongly to Pt sites, thereby blocking the H_2 dissociation reaction, even at trace levels (18). Adsorbed CO can be removed from Pt via electro-oxidization but this is a sluggish reaction which generally occurs only at much higher potentials than H_2 electro-oxidation. H_2 electro-oxidation activity on Pt surfaces in the presence of CO ($i_{H2/CO}$) is reported by Ross and Stonehart to be a function of anode activity on pure H_2 (i°_{H2} (V, T)) multiplied by a poisoning parameter ($[1-\Theta_{CO}]^2$), where V = potential, T = temperature, Θ_{CO} = fraction of Pt surface covered by CO, and $[1-\Theta_{CO}]$ = fraction of Pt surface not covered by CO (17,18).

$$i_{H2/CO} = i^\circ_{H2}(V, T) \bullet [1-\Theta_{CO}]^2 \qquad [1]$$

Their interpretation is that the limiting reaction mechanism requires two adjacent sites and that the probability of finding two adjacent sites is reduced by the square of the surface fraction not poisoned by CO. Equilibrium considerations suggest that CO coverage on Pt should be decreased by using lower CO partial pressures and/or higher temperatures.

The activity on gas diffusion electrodes is given by [2], where S = Pt surface area factor in cm^2 Pt per cm^2 superficial electrode area, i_o = exchange current density and b = the Tafel slope for H_2 on Pt. Based on these considerations, an implicit relationship for CO polarization in the H_2 electro-oxidation is given by:

$$I_{crit} = S \bullet i_o \bullet \exp(2.3\,\eta_{CO}/b) \bullet [1-\Theta_{CO}]^2 \qquad [2]$$

CO Tolerance Correlation for Pt Anodes

PEMFC performance curves, taken in this laboratory, are shown as a function of CO concentration in Figure 1. At low current densities, performance on impure H_2 is nearly identical to that for pure H_2. At some intermediate current density, the voltage begins to drop below that for pure H_2 and at slightly higher currents, the voltage drops quite rapidly. At still higher currents, the slope of the performance curve changes, showing a positive second derivative. After this inflection, the voltage remains relatively constant.

The polarization caused by trace CO, η_{CO}, is defined as the difference in cell voltage at constant current, between performance on pure and impure H_2. η_{CO} is plotted vs. current density on a semi-logarithmic scale in Figure 2. For each CO level, η_{CO} shows three distinct behaviors: 1) $\eta_{CO} = 0$, at lower current densities, 2) $\eta_{CO} = 50\text{-}350$ mV, where η_{CO} increases very rapidly with increasing current density and 3) $\eta_{CO} \approx$ constant, at higher current densities. Region 2 of Figure 2 is particularly interesting because the slope for each curve is quite large, i.e., about 800-900 mV/decade.

In region "1" , the "open CO monolayer region", there is enough bare Pt (i.e., not covered by CO) to support H_2 electro-oxidation at low current densities with no polarization losses, because i_o for H_2 on Pt is quite high (11).

In region "2", the "non-Faradaic region", the current density for H_2 oxidation on bare Pt exceeds i_o and η_{CO} grows rapidly. The slope of the polarization between 50 and 350 mV is much higher than expected electro-chemical Tafel slopes, which are typically 30-120 mV/decade. We believe that these large slopes have not been appreciated previously.

The high slope suggests that a non-Faradaic chemical step is rate limiting, possibly the dissociation of H_2 into monatomic H. This is consistent with the two step mechanism proposed previously (17). This high slope is of critical importance in understanding CO tolerance. If the rate limiting step in H_2 oxidation was Faradaic, the Tafel slope would be much lower and CO poisoning in PEMFCs might be minor problem.

In region "3", the "CO overpotential region", at higher current densities the high η_{CO} starts to promote simultaneous oxidation of adsorbed CO. CO oxidation on Pt has been reported to start between 150-300 mV/RHE at 60°C (19). CO oxidation rates increase with increasing η_{CO} until CO oxidation starts to exceed the rate of adsorption for incoming CO in the feed. At the potentials in region "3", our interpretation is that CO oxidation begins to decrease Θ_{CO}, opening additional bare Pt sites so that further increases in current density require almost no increase in η_{CO}.

The onset of CO polarization provides a useful basis for correlating various CO poisoning studies. The onset of CO polarization in Figure 2 was defined by extrapolating the steep slope in region "2" back to the intercept where $\eta_{CO} = 0$ mV for each level of CO. We interpret this intercept as a "critical" $I_{H2/CO}$ ($I_{crit.}$), above which the available bare Pt can no longer support reversible H_2 electro-oxidation. CO polarization plots (similar to Figure 2) were prepared from CO tolerance studies reported in the literature (5,6,8,9,10,12). The I_{crit} values estimated from these various studies are plotted in Figure 3 (normalized to a Pt loading of 0.4 mg Pt/cm^2). The comparison shows a surprisingly consistent correlation for the onset of the non-Faradaic region, despite differing fabrication procedures, differing experimental conditions and differing CO poisoning protocols.

The normalization to a constant loading improved the correlation, suggesting that the I_{crit} is proportional to Pt loading (more probably Pt surface area). The outliers in the trend line in Figure 3 (Wilson (ref. 6) and Iwase (ref. 8)) may be caused by differences in Pt surface area, Pt utilization or O_2 crossover. (Pt surface areas and other experimental details were generally not reported in the original references.) I_{crit} decreases with increasing CO level in Figure 3 because higher CO levels decrease the available bare Pt sites. Figure 3 shows a power law correlation where I_{crit} is proportional to $[CO]^{-0.6}$, ([CO] = CO concentration). The data at 120°C suggest that I_{crit} has an apparent activation energy = 100 kJ/mol. (Note: The apparent activation energy was incorrectly stated as 25 Kcal/mol in ref. 11.)

Modeling of CO Polarization at LANL

Los Alamos National Labs (LANL) has published a useful phenomenological model which describes their CO polarization results in PEMFCs (20). Their model assumes a "Tafel" relationships for the electro-oxidation of H_2 and CO on Pt, a Langmuir adsorption isotherm for CO on Pt and the poisoning parameter as described above. The LANL interpretation of the CO polarization is generally consistent with our discussion of the three regions in Figure 2. The LANL model predicts that the onset of severe CO polarization decreases as a function of increasing CO. The LANL model can be used to predict how changing significant parameters (increasing CO oxidation rate or decreasing CO adsorption strength) would improve CO tolerance.

EXPERIMENTAL DETAILS

The CO tolerance tests were conducted on a GT-120 test station with a 5 cm^2 fuel cell test fixture manufactured by Globetech, Bryan, TX. The membrane electrode assembly (MEA) was fabricated on Nafion™ 112 by General Motors, using a spray technique. Catalysts were 40 wt% Pt and 20 wt% Pt-Ru on Vulcan XC72, as supplied by E-tek (Natick, MA). Both anode and cathode had a loading of 0.3 mg Pt/cm^2. For Pt-Ru, the anode loading was 0.225 mg Pt/cm^2. The pure H_2 feed was passed through a butyl-Li getter to remove trace impurities. Air was provided by Exxon house gas systems. Cylinders containing pre-mixed CO and H_2 were supplied by MG Gases. The trace CO levels are based on the manufacturer's analysis, as delivered. Anode and cathode pressure were 10 and 15 psig respectively and anode and cathode flow rates were 0.11 and 0.43 liters/min., under all operating conditions.

The experimental protocol used to evaluate the "CO Tolerance" was as follows (21):

1. Anode feed was held at a constant flow rate during the scan, so that H_2 stoichiometry is well above 1.0, especially at low current densities.
2. Each data point in performance scan was recorded after 1 minute at constant voltage.
3. Anode was exposed to impure H_2 for at least 1 hour prior to scan (longer for 5 ppm CO).

RESULTS AND DISCUSSION

CO tolerance studies for Pt-Ru anodes were conducted and analyzed in the same manner as those for Pt (11). Representative PEMFC performance curves using Pt-Ru anodes, taken in this laboratory, are shown as a function of CO concentration level in Figure 4. The behavior is qualitatively similar to that observed on Pt anodes.

η_{CO} for Pt-Ru anodes is plotted vs. current density on a semi-logarithmic scale (similar to Figure 2) in Figure 5. As with Pt anodes, η_{CO} shows three distinct behaviors at each CO level: 1) $\eta_{CO} = 0$, at lower current densities, 2) η_{CO} = 50-300 mV, where η_{CO} increases very rapidly with current density and 3) $\eta_{CO} \approx$ constant, at higher current densities. The slope in Region "2" is again quite large, i.e., about 500-800 mV/decade but somewhat less than the 800-900 mV/decade observed for Pt anodes.

Similar PEMFC performance curves using Pt-Ru anodes with impure H_2, have reported by other groups (8,9,10). CO polarization curves estimated from published performance, showed regions similar to the three regions seen in Figure 5. Table I summarizes the slopes found in the non-Faradaic region.

The onset of CO polarization, I_{crit}, for these various studies is plotted in Figure 6, normalized to a Pt loading of 0.4 mg/cm^2. The normalization to a constant loading improved the correlation, again suggesting that I_{crit} is proportional to noble metal loading (or probably surface area). The dashed lines in Figure 6 summarize our earlier correlation lines for Pt anodes (Figure 3) and are included for comparison purposes. Generally, Figure 6 suggests that $I_{crit.}$ averages about 3-4 fold higher on Pt-Ru than on Pt anodes. The comparison however, shows wider variability than we found with Pt anodes in Figure 3 and therefore we did not attempt to characterize Pt-Ru using a single correlation line. The spread in the Pt-Ru data suggest differences among the Pt-Ru catalysts (or perhaps among MEA fabrication procedures, experimental conditions or CO poisoning protocols). The extent of alloy formation in Pt-Ru catalysts is reportedly variable (22).

In all cases, I_{crit} decreases with increasing CO level. Our Pt-Ru data for $I_{crit.}$ vs. CO level show that a power law correlation exponent of -0.6. This is similar to the overall power law dependence on Pt anodes, as shown in Figure 3. However, separate power law correlations for the data of either Schmidt or Acres both show power law exponents of -0.25. The reason for this variability in CO dependence is not understood.

Proposed Improvement in LANL Model for CO Tolerance

Values for $I_{crit.}$ were estimated from the LANL model (using Figure 1 in ref. 5) and are plotted vs. CO level in Figure 7 (20). Values of $I_{crit.}$ were also estimated from LANL's experimental data (using Figure 1 from reference 5) and these are also plotted for comparison in Figure 7. The dashed lines again represent our correlation for Pt anodes as shown in Figure 3. A power law fit of I_{crit} vs. CO level, as predicted by the LANL model, shows an exponent of -1.7. It can be shown mathematically that this predicted power law dependence is related to the assumed Langmuir adsorption constant. The inconsistency between the LANL model and our correlation of experimental data as shown in Figure 3 suggests that the LANL model can be further improved by using an isotherm where the adsorption strength varies with CO coverage, such as a Temkin or Freundlich isotherm. Of course, the use of more complicated isotherms has the disadvantage of introducing additional fitting parameters.

CONCLUSIONS

The CO polarization behavior for Pt-Ru catalyzed anodes in PEMFCs at 80°C was analyzed. Data from several sources consistently showed 3 regions of behavior:

1. An "open CO monolayer region" which shows no polarization losses. At low current densities, there is sufficient bare Pt to effectively catalyze H_2 oxidation.

2. A "non-Faradaic region", where η_{CO} is between 50 and 300 mV, shows surprisingly high "Tafel" slopes. High slopes suggest that the rate limiting step in H_2 electro-oxidation is non-Faradaic, probably the H_2 dissociation step.

3. A "CO overpotential region" which shows a relatively constant η_{CO} at about 250-400 mV, depending on CO level, which correlates with the onset of significant CO oxidation on Pt-Ru.

The onset of severe polarization, $I_{crit.}$, correlates with Pt loading and CO impurity level, similar to the correlation previously observed on Pt anodes. In general, $I_{crit.}$ is about 3-4 times higher for Pt-Ru than for Pt anodes. The variability of the I_{crit} correlation for Pt-Ru is greater than that for Pt. Also the power law dependence for Pt-Ru anodes shows a greater range of CO dependence than Pt. A possible interpretation for this variability is that there was greater variability among Pt-Ru than Pt catalysts.

The CO dependence of $I_{crit.}$ suggests that accurate modeling of CO tolerance should use a coverage dependent isotherm such as the Temkin isotherm.

FUTURE EFFORTS

A series of CO tolerance experiments are planned using Pt anodes where both Pt loading and Pt surface area will be systematically varied.

REFERENCES

1. D.P. Wilkinson and D. Thompett, *Proceedings of the 2nd International Symposium on New Materials for Fuel Cell and Modern Battery Systems*, Montreal, Canada, 266, (1997).
2. C. Borroni-Bird, J. Power Sources, **61**, 33-48 (1996)
3. J. Bentley, B.M. Barnett and S. Hynek, 1992 Fuel Cell Seminar - Ext. Abs., 456, 1992.
4. R.D. Sutton and N.E. Vanderborgh, 1992 Fuel Cell Seminar - Ext. Abs., 201, 1992.
5. S. Gottesfeld and J. Pafford, J. Electrochem. Soc., **135**, 2651-2652 (1988).
6. M.S. Wilson, C. Derouin, J. Valerio, and S. Gottesfeld, Proc. 28th IECEC, 1.1203-1.1208, 1993.
7. T.R. Ralph, G.A. Hards, D. Thompsett and J.M. Gascoyne, 1994 Fuel Cell Seminar - Ext. Abs., 199, 1994.
8. M. Iwase and S. Kawatsu, Proton Conducting Membrane Fuel Cells I, Gottesfeld, S.; Halpert, G.; Landgrebe, A.; Editors, 12-23, The Electrochem. Soc.: Pennington, NJ, 1995.
9. V.M. Schmidt, R. Ianniello, H.-F. Oetjen, H. Reger, U. Stimming, and F. Trila, Proton Conducting Membrane Fuel Cells I, Gottesfeld, S.; Halpert, G.; Landgrebe, A.; Editors, 1-11, The Electrochem. Soc.: Pennington, NJ, 1995.
10. T. Zawodzinski, presentation at DOE Fuel Cells for Transportation Exploratory R&D Program, Washington, DC, Sept. 25, 1996.
11. R.J. Bellows, E. Marucchi-Soos and D.T. Buckley, *Electrode Materials and Processes for Energy Conversion and Storage IV*, **PV 97-13**, 1-14, Electrochemical Society Proceedings, Pennington, NJ (1997).

12. G.K. Acres, J.C. Frost, G.A. Hards, R.J. Potter, T.R. Ralph, D. Thompsett, G.T. Burnstein, G.J. Hutchings, Catalysis Today, 38, 393-400, (1997).
13. H.A. Gasteiger, N.M. Markovic and P.N. Ross, Catalysis Letters, **36**, 1-8 (1996).
14. B.N. Grgur, N.M. Markovic, and P.N. Ross, Jr., J. Phys. Chem. B, **102**, 2494-2501, (1998).
15. P.K. Shen, K.Y. Chen, and A.C.C. Tseung, J. Electrochem. Soc., **142**, L85-L86, 1995.
16. A.J. Appleby and F.R. Foulkes, Fuel Cell Handbook, 19-28, Van Nostrand Reinhold, New York, 1989.
17. P. Stonehart, and P.N. Ross, Cat. Rev.-Sci. Eng., **12**, 1-35 (1975).
18. P.N. Ross and p. Stonehart, J. Cat., 35, 391-400 (1974).
19. R.J. Bellows, E. Marucchi-Soos and D.T. Buckley, IE&C Res., **35**, 1235 (1996).
20. T.E. Springer, T.A. Zawodzinski, and S. Gottesfeld, *Electrode Materials and Processes for Energy Conversion and Storage IV*, **PV 97-13**, 15-24, Electrochemical Society Proceedings, Pennington, NJ (1997).
21. T. Zawodzinski, personal communication, Jan. 10, 1997.15. D. Thompsett, S.J. Cooper, Electrochem. Soc., Fall Ext. Abs., No. 607, 948, 1994.
22. P.J. Hagans, K.E. Swider, D.R. Rolison, *Electrode Materials and Processes for Energy Conversion and Storage IV*, , **PV 97-13**, 86-105, Electrochemical Society Proceedings, Pennington, NJ (1997).

Table I: Summary of "Tafel Slopes in the Non-Faradaic Regime"

First Author	Slope (mV/decade)
Bellows	500
Schmidt	510
Iwase	720
Acres	775

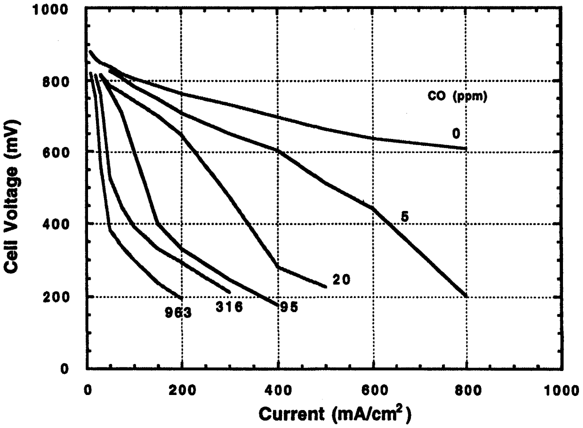

Figure 1: PEMFC Performance with H_2/Air on Pt Anodes with Increasing CO, 80°C, 0.3 mg Pt/cm^2

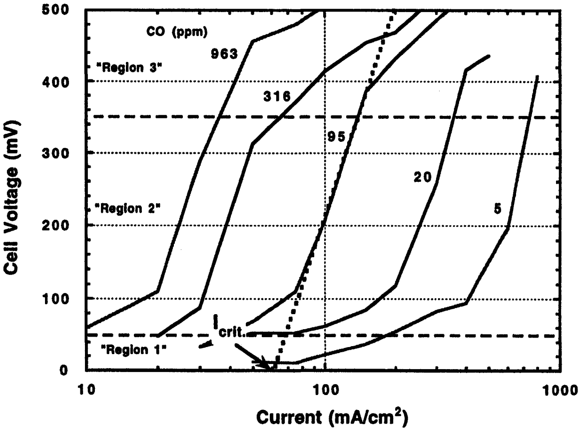

Figure 2: CO Polarization with H_2/Air on Pt Anodes with Increasing CO, 80°C, 0.3 mg Pt/cm^2

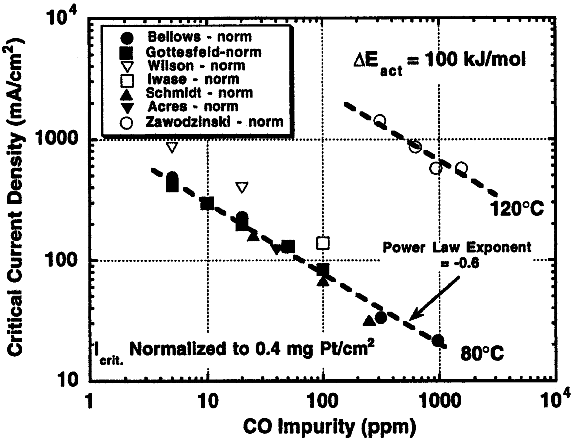

Figure 3: $I_{crit.}$ on Pt for H_2/Air PEMFCs Increases with Decreasing CO Level and Increasing Temperature

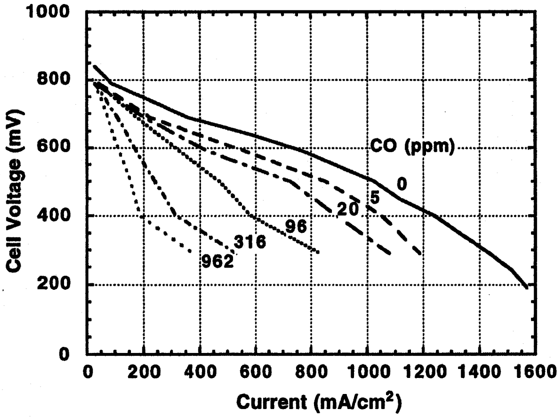

Figure 4: PEMFC Performance with H_2/Air on Pt-Ru Anodes with Increasing CO, 80°C, 0.225 mg Pt/cm^2.

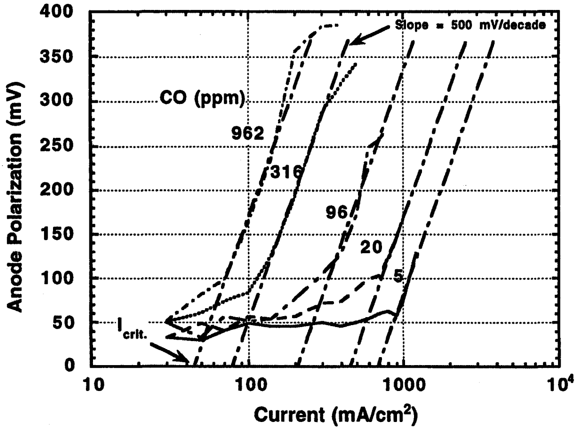

Figure 5: CO Polarization with H_2/Air on Pt-Ru Anodes with Increasing CO, 80°C, 0.225 mg Pt/cm^2.

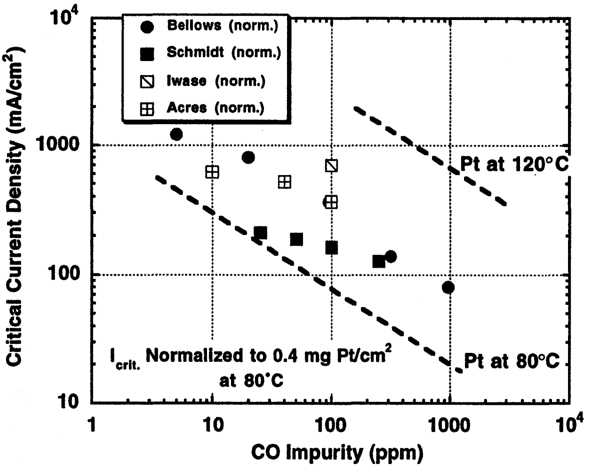

Figure 6: Comparison of $I_{crit.}$ on Pt-Ru and Pt Anodes vs CO Level

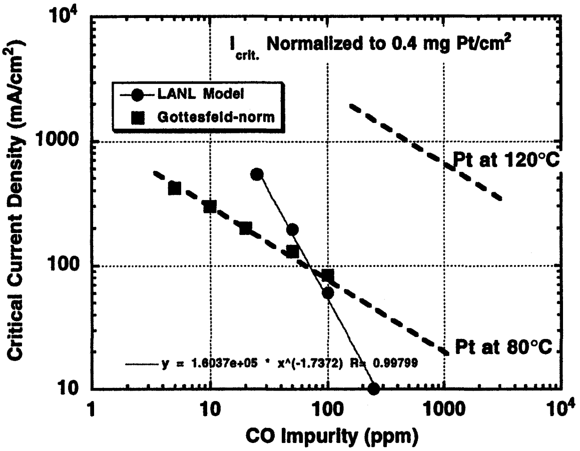

Figure 7: Comparison of $I_{crit.}$ on Pt Anodes and LANL Model vs. CO Level.

Proton_Conducting_Membrane_Fuel_Cells_II, PV 1998-27, 229-237 (1998)
DOI: 10.1149/199827.0229PV © The Electrochemical Society

EFFECT OF AMMONIA AS POSSIBLE FUEL IMPURITY ON PEM FUEL CELL PERFORMANCE

Francisco A. Uribe, Thomas Zawodzinski Jr., and Shimshon Gottesfeld

Electronic and Electrochemical Materials and Devices
MST-11, MS-D429
Los Alamos National Laboratory
Los Alamos, NM 87545

ABSTRACT

Effects of NH_3 on PEM fuel cell performance are reported. Traces of NH_3 in the anode feedstream cause a decrease in cell current. The extent of the effect depends on NH_3 concentration and time of exposure of the anode to NH_3. We discuss possible mechanisms by which NH_3 affects cell performance.

INTRODUCTION

Polymer electrolyte membrane fuel cells (PEFC) designed for stationary power generation or for transportation applications, will likely operate on reformed fuels. The primary source of H_2 can be methane, methanol or gasoline. Documented reforming processes are used to obtain H_2 from methane [1] or other hydrocarbon fuels. One is the autothermal (ATR) fuel reforming, for which the inlet mixture is CH_4, H_2O, O_2 and N_2 (the last two gases from air) and the outlet major components are H_2, H_2O, N_2, CO_2 and CO. An alternative method, partial oxidation (POX) reforming, requires the same inlet composition except water and produces the same major outlet components as ATR. Both processes produce CO as the most important impurity but also may produce traces of NH_3, estimated in the range of 30 to 90 ppm [1], by the reaction of N_2 and H_2 at high temperatures. With on-board processing of gasoline at relatively early phase of development, outlet NH_3 levels are not well documented and may be a sensitive function of the exact nature of the fuel processor. The report in [1] seems, however, to provide sufficient reason for evaluation of the severity of effects of trace NH_3 on cell performance.

To date, most of the efforts in dealing with impurities in reformates have been centered around the CO catalyst poisoning problem whereas little attention has been given to the effects of trace NH_3 in the fuel feedstream. Szymanski et al. [2] found, for phosphoric acid fuel cells, that NH_3 present as impurity in either fuel or oxidant streams reacts with the electrolyte to form $(NH_4)H_2PO_4$. They concluded that this conversion of protons to ammonium ions lowers the O_2 reduction rate at the cathode, leading to cell performance losses. Recently we examined the effect of traces of ammonia in PEM fuel cell anode feed streams [3] and reported that traces of the order of tens of ppm NH_3 lead to considerable performance losses. Depending on the length of time that the cell is exposed to ammonia, the losses may become irreversible [3]. Here we report our latest results, including description of our attempts to elucidate the nature of the deleterious effect of NH_3 in a PEM fuel cell and to improve NH_3 tolerance.

EXPERIMENTAL

Figure 1 shows the schematics for testing NH_3 tolerance in Nafion™ membrane based H_2-Air fuel cells. We prepared membrane and electrode assemblies (MEA) following a reported procedure from our laboratory [4]. The electrode catalyst layers were prepared from carbon-supported 20 % Pt (E-TEK). The catalyst loadings were in the range 0.15 to 0.20 mg Pt/cm^2. Both the anode and the cathode catalyst layers were pressed onto a Nafion™105 membrane using decals. A carbon cloth backing, not shown in the figure, was used as a gas diffuser. We injected NH_3 as an aqueous solution or in the gas phase (diluted in H_2 or Ar) into a humidified H_2 stream entering the cell. The same port was used for injecting aqueous H_2SO_4. For injecting the liquid solutions, we used a peristaltic pump. Fuel cells were operated at 80°C, and the anode and cathode humidifier temperatures were 105 °C and 90 °C respectively. We operated the cells with H_2 and air flows of 160 and 550 standard cm^3 against 30 and 60 psig back pressure respectively. The cell size (electrode geometric active area) was 5 cm^2. For cyclic voltammetry (CV) we flowed N_2 on the side of the MEA acting as the working electrode and H_2 on the other side which we used as counter/reference electrode. We carried out CV scans with a PAR Model 173 Potentiostat coupled with a PAR Model 175 Programmer.

RESULTS AND DISCUSSION

Transient effects of NH_3. Ammonia was added at the point of fuel injection into the cell. The extent of the effect measured depended on the concentration of NH_3 in the fuel inlet stream and the duration of NH_3 addition (though the ammonia was added as injected aqueous solution in this experiment, little difference was observed when ammonia was injected as a gas). Fig. 2 shows the cell current density, measured at a cell voltage of 0.5 V, as a function of time following the injection of NH_3 at final concentrations in the fuel stream of 13 and 130 ppm. After I hour of continuous NH_3 injection, the currents were still decreasing. At this point, we recorded polarization curves for each NH_3 concentration. These are shown in Fig. 3 along with the polarization curve obtained with neat H_2. The results clearly show the negative effect that the presence of NH_3 has on fuel cell performance even at such low levels as 13 ppm.

By analogy to observations on CO-poisoned cells, we thought that changing the anode feed back to pure H_2 would purge NH_3 out allowing complete recovery of the original performance. We thus made a first attempt of recovering cell performances by turning the NH_3 off and running on a pure H_2 feed. The results, presented in Fig. 2, show that after turning off NH_3, the current increased very slowly. In fact, it took about 12 hours for complete recovery to initial cell current (1.2 A/cm^2). This behavior is thus quite different from that of CO, which can be purged from the anode with pure H_2 resulting in complete performance restoration within a few minutes. This difference suggests either a completely different poisoning mechanism than CO or a much higher energy of adsorption on Pt anode sites.

Long term exposure to NH_3. When the fuel cell anode was exposed to NH_3 for several hours, the cell performance dropped to impractical low levels. Fig. 4 shows the polarization curve after 15 hours of continued supply of H_2 containing 30 ppm of NH_3. At that time NH_3 injection was turned off and the cell was operated on pure H_2 for several days. After 17 hours the cell performance showed some recovery, but beyond this time no further improvement was achieved, as shown by the polarization curve recorded 88 hours after NH_3 had been turned off. This result shows that long term exposure to NH_3 could degrade the cell performance irreversibly. For comparison, Fig. 4 also shows the initial performance on H_2 with no NH_3, and the polarization curve after I hour of exposure to NH_3.

Possible mechanism by which NH_3 affects cell performance. Several routes could be suspected as mechanisms by which NH_3 affects PEM fuel cell performance. NH_3 may react with the protons of the protonic membrane, forming NH_4^+ and decreasing membrane conductivity. The same effect on ionic conductivity could take place within the catalyst layer, particularly the anode catalyst layer, which contains recast ionomer in protonic form. Anode catalyst poisoning due to NH_3 adsorption onto Pt could inhibit hydrogen oxidation. Finally, NH_3 may cross over to the cathode, inhibiting the O_2 reduction reaction (ORR)[2]. We have examined these alternatives by the following experiments.

To address the possible effect on membrane conductivity, we measured the high frequency resistance (HFR) of the cell. Fig. 5 shows HFR measurements obtained simultaneously with the polarization curves of Fig. 4. After 1 hour of exposure to NH_3 the cell performance clearly dropped compared to the original performance on neat H_2 (this is best seen in figure 2). However, as shown in Fig.5, the corresponding HFR's are practically the same. In the short term, as loss of performance is already clearly observed, the presence of NH_3 in the anode feedstream appears not to affect the conductivity of the membrane (the conductivity of Nafion membranes in ammonium form is lower by roughly a factor of 4 relative to that in the protonic form).

However, Fig. 5 shows that when NH_3 is kept flowing for longer periods of time, the HFR is affected. After 15 hours of continued H_2/NH_3 flow the HFR more than doubled at higher cell current densities and was significantly higher at low currents. Stopping the flow of NH_3 into the cell and allowing it to run on pure H_2 for several days did not improve the membrane conductivity. Recall (see Fig. 4) that, under these conditions, the cell had irreversibly lost performance.

We used cyclic voltammetry (CV) to investigate the possibility of NH_3 adsorption on the Pt anode catalyst. Once a cell was brought to some performance level in operation on H_2/air or H_2+NH_3/air, operation was interrupted, the H_2 feed into the anode was replaced by N_2 and the air at the cathode was replaced by H_2 (safety note: nitrogen purge should be applied between O_2 and H_2 operation of the same cell electrode). In this two electrode configuration, the MEA was studied by cyclic voltammetry where the cell anode was now the "working electrode" and the original cell cathode became the counter/reference electrode. Cyclic voltammograms were first recorded after operation of the cell with neat H_2 and then after operation with H_2 + 30 ppm NH_3 for 90 minutes. The results are shown in Fig. 6. The two CV's are practically the same. The H adsorption potential domain (0.1 to 0.4 V) is not affected by the presence of NH_3 in the cell, suggesting that NH_3 does not adsorb significantly on the Pt surface sites. Remember that under similar conditions, i.e., after 90 minutes of exposure to NH_3 at this level, the fuel cell current density at 0.5 V dropped from 1.3 to 0.8 A/cm^2.

The possibility of NH_3 crossover to the cathode catalyst was also investigated with CV in a similar fashion as described above. In this experiment, the gases flowing to the electrodes were exchanged such that pure hydrogen was fed to the original anode and nitrogen was fed to the original cathode, the latter becoming the working electrode for CV experiments. After operating the cell with H_2 contaminated with NH_3, the CV recorded for the cathode catalyst was similar to those in Fig. 6, showing no sign of catalyst poisoning by NH_3 adsorption.

The remaining alternative explanation for the observed performance loss is that the ionic conductivity of the catalyst layer is the first to be adversely affected by neutralization of protons with ammonia, leading to an ammonium-form Nafion ionomer in the catalyst layer. Such loss of protonic conductivity in the anode catalyst layer nay be detrimental to cell performance as the protonic flux required to maintain a current of the order of 1 A/cm^2 throughout he anode cannot be sustained after protons in the anode have been significantly replaced by NH_4^+ ions. If the anode is first to be affected, as expected because NH_3 is a component of the anode feed stream, the high frequency resistance may still show no rise as cell performance starts to drop. One may ask why then is the effect seen on the CV of the anode catalyst so small after prolonged exposure to NH_3 (Fig. 6). One could expect some effect on the process: $Pt + H^+ + e^- = Pt\text{-}H_{ads}$ as proton population diminishes by neutralization with NH_3, However, such effect on the CV may be relatively much smaller than that observed on cell current at given level of proton replacement because CV current densities are 3 orders of magnitude lower than cell current densities. It is interesting to point out that the CV results are very different from those obtained in the presence of CO impurity at similar anodes. For instance, 100 ppm of CO introduced in the anode fuel stream brings about strong performance loss after 2 minutes [5]. Concurrently, the H adsorption peaks in the CV completely disappear [6].

We attempted to accelerate the recovery of performance of the cell described in Fig.2 (lower curve) by injecting a 10 mM solution of H_2SO_4 into the anode. Equivalents of acid injected were more than 10 times the original amount of base (NH_3) introduced into the cell. The recovery rate was, however, unaffected. We also briefly attempted to chemically oxidize NH_3 with O_2 at the anode catalyst layer, by bleeding 6% of air along with a fuel stream containing 30 ppm NH_3. However, the presence of air in the fuel feed stream under these conditions had no beneficial effect.

CONCLUSIONS

The presence of trace NH_3 in the anode fuel feedstream clearly degrades the PEM cell performance. The extent of performance deterioration depends on NH_3 impurity level and the time of cell exposure to it. With short times of exposure (1 to 3 hours) the original performance can be fully recovered (the mechanism of recovery probably involves proton generation by anodic hydrogen oxidation current). Longer times of exposure (e.g. 15 hours) decrease the cell performance to impractical levels and the cell does not recover even after several days of operation on pure H_2

Cyclic voltammetry shows that Pt catalyst surfaces both in anode and cathode are not directly poisoned by NH_3. The conductivity of the membrane is affected after longer times of exposure, whereas cell performance starts dropping as soon NH_3 is brought to the cell. It thus seems that replacement of H^+ by NH_4^+ ions within the anode catalyst layer is a primary reason for cell current drop, with drop in membrane conductivity adding to the problem at longer times.

ACKNOWLEDGMENT

We gratefully acknowledge the US DOE Office of Advanced Automotive Technology for support of this work.

REFERENCES

1. “Multi-Fuel Reformers for Fuel Cells Used in Transportation”. Phase I, Final Report, May 1994 by Arthur D. Little, Inc. for US DOE-OTT.

2. S. T. Szymanski, G. A. Gruver, M. Katz, and H. R. Kunz, *J. Electrochem. Soc.*,**127**,1440 (1980).
3. F. A. Uribe, T. Zawodzinski Jr., and S. Gottesfeld, Electrochemical Society Meeting, San Antonio, October 1996. Vol.96-2, Abstract No. 783.
4. M. Wilson, J. Valerio and S. Gottesfeld, *Electrochim. Acta.*, **40**, 355(1995).
5. J. Bauman, T. Zawodzinski Jr., and S. Gottesfeld, this Proceedings Volume.
6. T. Zawodzinski, C. Karuppaiah, Y. Wu, S. Savett, F. Uribe, and S. Gottesfeld, this Proceedings Volume.

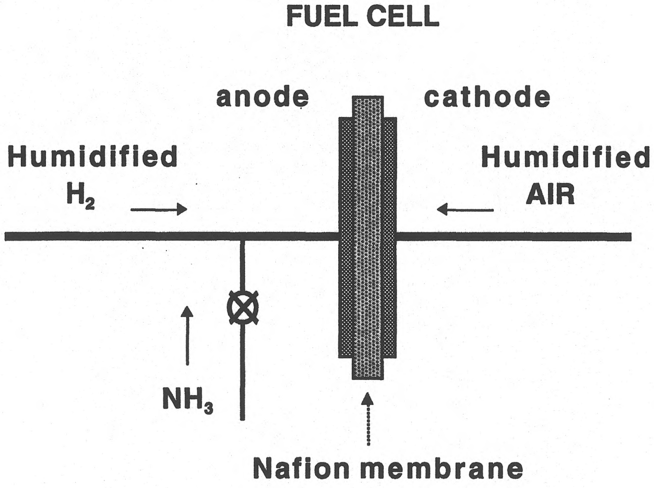

Figure 1: Scheme for testing NH_3 tolerance in H2-Air PEM fuel cells

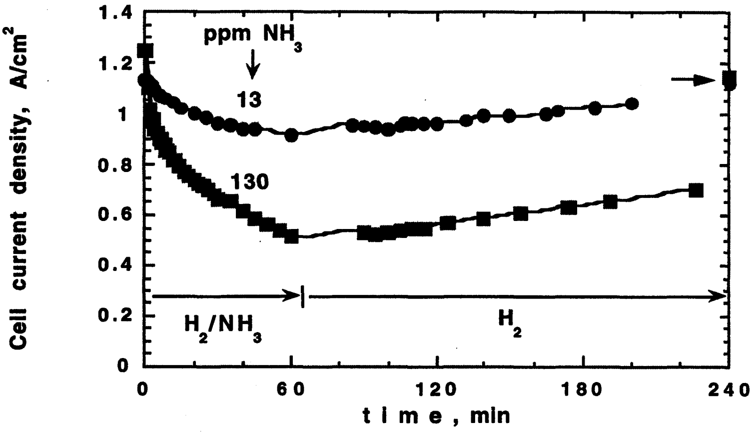

Figure 2: Effect of two concentrations of NH_3 on cell current at 0.5 V cell voltage. The impurity was injected as an aqueous solution into the anode feedstream. Catalyst loadings: 0.17 mg Pt/cm^2 in both anode and cathode. Cell temperature was 80 °C. Initial currents (t=0) were obtained on neat H_2. The uppermost point on the right indicates the current density after 12 hours of operation on neat H_2, following thel hour exposure to NH_3.

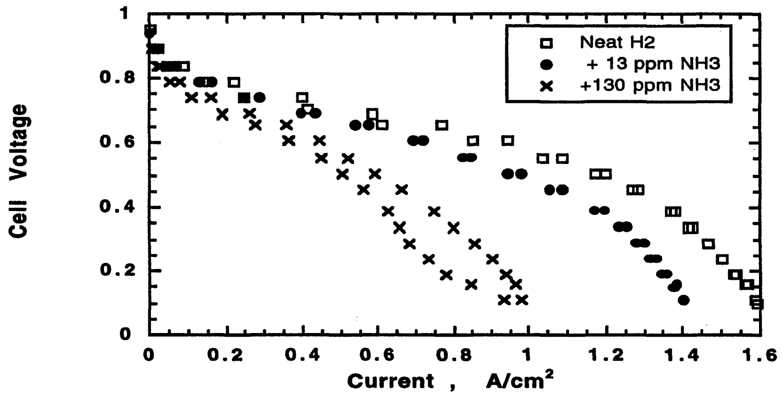

Figure 3: Effect of NH_3 on H_2-Air fuel cell performance at 80 °C. Same cell as in Fig. 2, one hour after NH_3 injection had started.

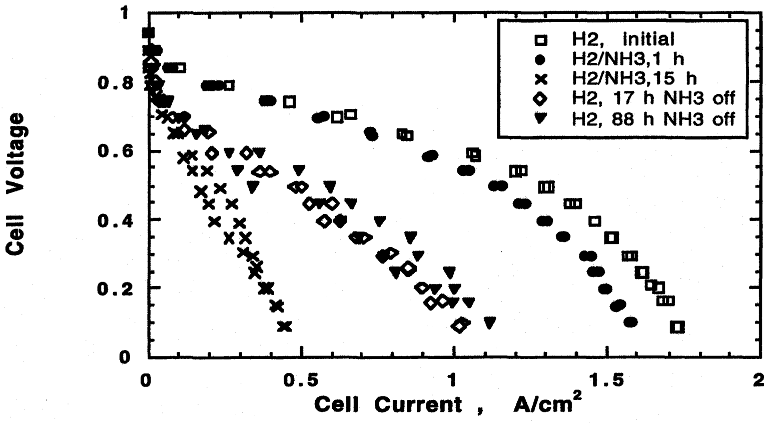

Figure 4: Effects of long term NH_3 exposure on H_2-air fuel cell performance at 80 °C. 30 ppm $NH_3(g)$ were injected into the anode feedstream.

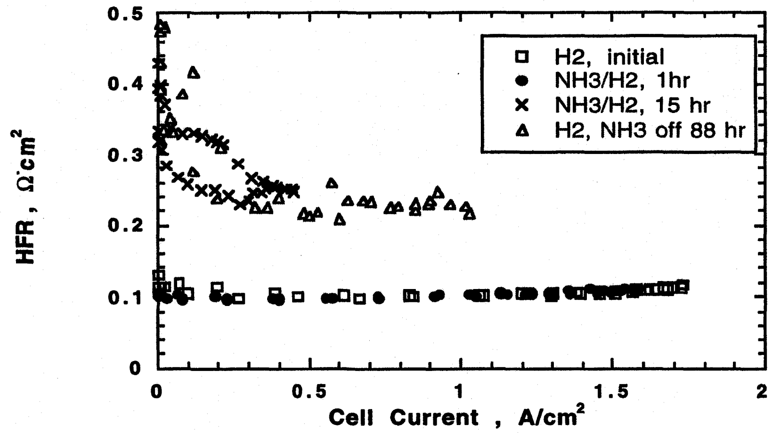

Figure 5: Effects of long term NH_3 exposure on H_2-air fuel cell high frequency resistance at 80 °C. 30 ppm $NH_3(g)$ were injected into the anode feedstream. These curves were simultaneously recorded with polarization curves in Fig. 4.

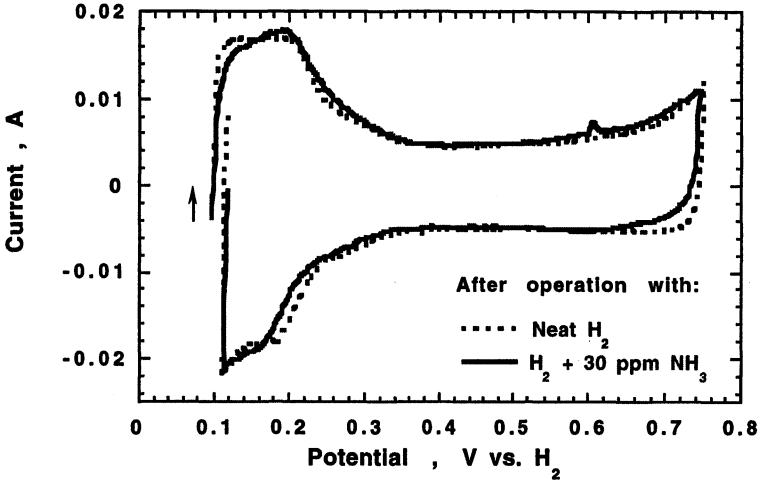

Figure 6: Cyclic voltammetry at the electrode used as the anode in a 5 cm^2 fuel cell after operation with neat H_2 and with H_2 + 30 ppm NH_3 injected at the anode feedstream for 1.5 hour. CV's were obtained with N_2 flowing at this electrode and H_2 at the other side of the MEA. Cell temperature: 80 °C.

Proton_Conducting_Membrane_Fuel_Cells_II, PV 1998-27, 238-248 (1998)
DOI: 10.1149/199827.0238PV © The Electrochemical Society

ELECTRODE PERFORMANCE AND DESIGN FOR STRIP-CELL DIRECT METHANOL FUEL CELLS

S. Calabrese Barton,[†] T. Patterson,[‡] E. Wang,[‡] T. F. Fuller,[‡] and A. C. West[†]
[†]Columbia University, New York, NY 10027
[‡]International Fuel Cells, South Windsor, CT 06074

ABSTRACT

A feasibility analysis of a mixed-reactant, strip-cell direct methanol fuel cell concept is presented. In this type of cell, selective electrodes are mounted in an alternating fashion on the same side of a membrane electrolyte, which minimizes the need for ancillary equipment, and maximizes power density. At low current density, the fuel efficiency of the direct-methanol strip cell is shown to be higher than that of a bipolar cell with typical cathodes. The effect of geometric parameters on the performance of strip cells is discussed, and design recommendations are given for a simple geometry.

INTRODUCTION

High power density, small-scale direct methanol fuel cell stacks require minimization of weight and volume due to ancillary system components. One way to accomplish this is to use a "strip cell" arrangement, in which strips of anode and cathode material are alternated over strips of membrane electrolyte on the same side of a non-conducting support film. A diagram of this scheme is shown in Fig. 1. Selective electrodes that are active only to one reactant are employed to prevent parasitic chemical reactions. This approach reduces weight and volume by eliminating seals, separator plates, and load-bearing structures.

Previous reports have considered the merits of conventional strip cells, in which the cells are arranged in-plane, but the reactants are separated on opposite sides of the cell (1,2). Such designs provide high stack voltage in a small volume, but require complicated sealing to prevent leaks between reactant streams. Selective electrode fuel cells with mixed reactant feed have been considered for solid oxide (3) and proton-exchange membrane fuel cells (4,5). In none of these studies were the electrodes in a strip-cell arrangement.

Two selective cathode catalysts of current interest are iron tetramethoxyphenyl porphyrin (FeTMPP), and a transition metal cluster catalyst (Ru-Se-Mo). Both catalysts have been shown to be methanol tolerant (6,7). The main motivation for development of these selective cathode catalysts has been to reduce the effect of methanol crossover. As will be demonstrated, an important advantage of the selective electrode approach for direct methanol fuel cells is that methanol crossover is eliminated as an issue.

The strip cell geometry places a premium on electrolyte and electrode conductivity, because current flows perpendicular to the thickness of these components. Proper electrolyte-membrane thickness, electrode widths, and electrode spacing must be chosen to minimize ohmic losses and maximize electrode utilization. This paper will conclude with a discussion of these issues.

FUEL EFFICIENCY

As previously stated, an important advantage of selective electrodes for direct methanol fuel cells is the elimination of the issue of methanol crossover. This can be demonstrated in Fig. 2. Here the polarization performance and the fuel efficiency of a selective-electrode cell with FeTMPP cathode catalyst and mixed feeds are compared with a more "traditional" DMFC with platinum catalysts and pure feeds. For these cells a constant rate of methanol crossover, N_{XO} = 0.35 μmol/cm^2/s, was assumed, equivalent to a crossover current of 200 mA/cm^2 (8). The fuel efficiency is defined by

$$\eta = \frac{IV}{\Delta H\left(N_a + N_{XO}\right)} \qquad [1]$$

where ΔH is the heat of combustion of the fuel, which for pure methanol at 20°C and 1 atmosphere is 0.78 MJ/mol.

Both cells use a Nafion 117 membrane, which is highly permeable to methanol. The temperature of the cell is 80°C and at ambient pressure. Air is supplied to the cathode and 1 molar methanol to the anode. Although the performance of the "traditional" cell is better, its fuel efficiency is lowest at low current densities. The cell with mixed reactants and selective electrodes has an efficiency that is proportional to the cell potential. This highlights the key advantage of the selective electrodes. High fuel efficiency can be achieved if the selective-electrode cell is limited to low current density.

CELL GEOMETRIC DESIGN

The strip-cell configuration introduces an additional issue of possibly high ohmic losses. As shown in Fig. 3a, current passes in the plane of a strip cell, normal to the thickness and along the width of the electrodes and the membrane electrolyte. An appropriate strip-cell geometry must be chosen to minimize ohmic losses compared to those associated with electrode kinetics. In the following, the appropriate cell geometry will be discussed for a simple configuration.

Cell Conditions

The strip-cell assembly of Fig. 3a was simplified to a two-dimensional model, as shown in Fig. 3b. The important parameters in this geometry are the electrode widths, w_c and w_a, the electrode spacing, s, and the thickness, t, of the membrane electrolyte. It is assumed here that the length, L, of the electrodes is much greater than their width or thickness. The width of each electrode is defined by the amount of overlap between the electrode and membrane. Base-case values for these parameters are specified in Table I. For simplicity, a constant cell current density of 20 mA/cm^2 was assumed, although other design constraints may alternatively be chosen.

Table I. Base Case Cell Parameters

Parameter	Value
Conductivity, κ (mS/cm)	100
Anode width, w_a (cm)	2×10^{-2}
Relative cathode width, w_c/w_a	1
Relative electrode spacing, s/w_a	0.1
Relative membrane thickness, t/w_a	2
Cell current density, I (mA/cm^2)	20

Each electrode is considered planar and infinitely conductive. Although electrode porosity is necessary for gas access, it was not considered here. High electrode conductivity may be practically achieved by addition of a conductive filler such as graphite. Tafel kinetics were assumed. Tafel parameters, which are representative of the anode and two cathode materials discussed above, are given in Table II. The assumption of Tafel kinetics is limited to current densities less than 100 mA/cm^2, such that mass-transfer effects may be neglected. Ohmic cell resistance was calculated using the Schwarz-Christoffel method (9,10), and the overall cell polarization was calculated using a boundary element method.

Table II. Kinetic Parameters for Selective Electrodes

Parameter	Anode	FeTMPP Cathode	Ru-Se-Mo Cathode
Open Circuit Half-cell Potential, (V)	0.0	1.23	1.23
Exchange Current Density, (mA/cm^2)	6.88×10^{-4}	4.95×10^{-6}	4.75×10^{-4}
Tafel slope, (V)	2.25×10^{-2}	3.74×10^{-2}	6.58×10^{-2}

Ohmic Cell Resistance

The ohmic resistance, *i.e.* the cell resistance for infinitely fast electrode kinetics, provides a preliminary understanding of the effects of geometry on true cell resistance. Such information indicates the ranges of geometric parameters for which ohmic losses may be minimized in the actual cell. Fig. 4 shows the variation of the dimensionless ohmic resistance of the cell, $L\kappa R$, with electrode spacing, s, plotted with membrane thickness, t, as a parameter. In this plot, spacing and thickness are normalized by electrode width, w. As expected, the ohmic resistance decreases uniformly with decreasing electrode spacing. In contrast, as thickness decreases, the ohmic resistance is seen to increase. For $t/w > 2$ at small spacing, the resistance becomes essentially independent of thickness. For $s/w \leq 0.1$, this independence may be extended to $t/w = 1$. One may thus conclude that a practical design target is to set the electrode width to less than half the membrane thickness.

Overall Cell Polarization

Effect of electrode width. The kinetics of the chosen selective cathode materials, as given in Table II, are slow compared to supported noble metals. Such slow kinetics control the polarization behavior of the cell in cases where ohmic losses are low, such as when the membrane thickness is large and the electrode spacing is small.

For example, Fig. 5 is a plot of cell power density as a function of electrode width, $w = w_a = w_c$, for two cathode materials. The values of all fixed parameters are given in Table 1. The power density is defined as

$$P = \frac{IV}{L\left(w_a + w_c + s\right)} \qquad [2]$$

where the quantity (w_a+w_c+s) is an estimate of total cell width. For both cathode materials, cell power density increases as electrode width decreases and ohmic losses are reduced. The sensitivity of the power density to electrode width decreases with decreasing electrode width, however, as the cell polarization falls under the control of electrode kinetics. For both cell types, the power density begins to plateau as the electrode width decreases below 0.1 cm, and is insensitive to electrode width for $w < 0.01$ cm. For these electrode materials, therefore, an electrode size on the order of 0.1 cm may be appropriate.

Effect of membrane thickness. Fig. 6 shows the variation of cell power density with membrane thickness, with all fixed-parameter values given in Table 1. Power density appears to be only weakly dependent on membrane thickness over the range shown. As indicated by the primary cell resistance, the cell power density is independent of membrane thickness for $t/w > 1$. A relative membrane thickness of $t/w = 1.0$ is sufficient to minimize ohmic losses under these conditions.

Effect of electrode spacing. In Fig. 7, the cell power density for a fixed cell current density is plotted as a function of electrode spacing for two cathode materials. Cell power density is shown to be only weakly dependent on electrode spacing for small spacing, such that $s/w < 0.1$. Under such conditions, cell polarization falls under mainly kinetic control. Under purely kinetic control, the electrode current density is uniform, and the electrode width, w, becomes an important length scale for current flow. As electrode spacing decreases to much less than this width, the potential drop across this width becomes small compared to the total ohmic potential drop. One may conclude from these results that a normalized electrode spacing of $s/w = 0.1$ is the minimum from which practical benefit may be derived in this case.

Effect of relative electrode width. In a strip cell, electrodes of unequal macroscopic area can be employed in the same cell. Whether this added dimension can be exploited for performance gains depends on cell design criteria, *e.g.*, whether cell potential or cell current is held fixed.

For example, Fig. 8 is a plot of cell power density as a function of cathode-anode width ratio, w_c/w_a, for two cathode materials. The values of all fixed parameters are given in Table 1, with the exception that cell potential, not current density, is held fixed at 0.4 V. For fixed potential, a weak maximum appears for electrode width ratio $w_c/w_a > 1$. For the Ru-Mo-Se catalyst, a 13% increase in power density can be achieved by setting the cathode width to be about three times that of the anode. This maximum occurs at a width ratio such that decreased cathode losses, due to lower cathode current density, are matched by anode losses that increase with increasing anode current density. In this case, the value of w_c/w_a at maximum power density is greater than unity because the cathode kinetics are slower than are those of the anode. It should be noted that such performance gains may also be obtained by increasing the cathode catalyst loading.

No such maximum occurs for fixed cell current. Under electrode kinetic control, cell potential displays a weak, logarithmic dependence on cathode width; under resistance control, cell potential decreases with increasing cathode width. The linear increase in cell width therefore causes the fixed-current power density, as defined by Eq. 2, to decrease monotonically with increasing cathode width.

A strip cell with the FeTMPP cathode, in the base-case configuration, gives an ohmic potential loss of only 4 mV at 20 mA/cm^2 current density. Such losses are small compared to the combined kinetic overpotential of about 800 mV. In terms of performance, therefore, the strip cell may be a practical configuration for the implementation of selective electrodes in a mixed-reactant, direct methanol fuel cell. The manufacturability of such strip cells with small electrode thickness and spacing is a separate, important issue that will not be discussed here.

Overall system power density. The power densities presented herein should not be mistaken for overall system values; they only reflect the power density of the electrochemical cell itself. An estimate of overall system power density, the minimization of which is a primary motivation for pursuit of mixed-reactant designs, requires detailed knowledge of a complete system, and will not be attempted here. Clearly, the power densities presented in Figures 5 to 8 are quite low compared to conventional DMFC systems with noble metal catalysts. This is particularly true for the Ru-Se-Mo cathode, which gives only 1.2 mW/cm^2 at 20 mA/cm^2, compared to ~11 mW/cm^2 at the same current density for the platinum-cathode cell of Fig. 2. For the present strip-cell system to be practical, such deficiencies must be redressed by elimination of ancillary structures.

CONCLUSIONS

This paper has discussed aspects of a direct methanol fuel cell in a strip-cell configuration, with selective electrodes and a mixed-reactant feed. The fuel efficiency of the strip cell configuration was demonstrated to be higher than that of a bipolar cell with noble-metal electrodes at low current density.

A design analysis of a simple strip-cell DMFC with selective electrodes was discussed. For the electrode materials considered, the following geometry is appropriate:

1. An anode width of about 0.1 cm.
2. A membrane thickness 1 to 2 times the average electrode width.
3. An electrode spacing one tenth the average electrode width.

Additionally, the cathode width ratio may be chosen to be different from that of the anode to take advantage of mismatched electrode kinetics. For an electrode width of 0.02 cm, using FeTMPP cathode material, these dimensions lead to an ohmic overpotential of just 4 mV at 20 mA/cm^2 cell current density. This demonstrates the viability of the strip cell configuration for the mixed-reactant feed DMFC. A complete strip-cell system is required to demonstrate that overall power-density improvements are achievable using such a configuration.

ACKNOWLEDGMENTS

This work was supported by the Defense Sciences Office of DARPA under contract N00014-94-C-0290 through the Office of Naval Research.

REFERENCES

1. R. Nolte, A. Kolbe, and K. Ledjeff-Hey, in *Proceedings of the 37th Power Sources Conference*, p. 77, U. S. Army Research Laboratory, Fort Monmouth, NJ (1996).
2. D. Modroukas, P. Rohonyi, and O. Adlhart, in *Proceedings of the 37th Power Sources Conference*, p. 85, U. S. Army Research Laboratory, Fort Monmouth, NJ (1996).
3. K. Asano and H. Iwahara, *J. Electrochem. Soc..*, **144**, 3125 (1997).
4. G. A. Louis, J. M. Lee, D. L. Maricle, and J. C. Trocciola, U. S. Pat. 4248941 (1981).
5. C. K. Dyer, *Nature*, **343**, 547 (1990).
6. S. L. Gupta, S. K. Zecevic, W. Aldred, G. Du, and R. F. Savinell, Abstract 792, The Electrochemical Society Extended Abstracts, Vol. 96-2, San Antonio, TX, October, 1996.
7. C. Fischer, N. Alonso-Vante, S. Fiechter, and H. Tributsch, *J. Appl. Electrochem.*, 25, 1004 (1995).
8. F. J. Luczak, B. L. Murach, P. A. Plasse, and D. L. Maricle, Abstract 787, The Electrochemical Society Extended Abstracts, Vol. 96-2, San Antonio, TX, October, 1996.
9. V. I. Ivanov and M. K. Trubetskov, *Handbook of Conformal Mapping with Computer-Aided Visualization,* p. 275, CRC Press, Boca Raton, (1995), 275-277.
10. H. F. Moulton, *Proc. London Math. Soc.* (ser. 2), **3**, 104 (1905).
11. B. A. Fuchs and B. V. Shabat, *Functions of a Complex Variable and Some of Their Applications* (vol. 1), p. 394, Pergamon, NY, (1964).

LIST OF SYMBOLS

I ....Cell current (mA)
L ....Electrode length (cm).
N_a....................Rate of methanol consumption at the anode (mol/s).
N_{XO} ....Methanol crossover rate (mol/s).
P ....Cell power density, defined by Eq. 2 (W/cm^2).
R ....Cell resistance (Ω).
s ....Electrode spacing (cm).
t.......................Membrane thickness (cm).
V.....................Cell potential (V).
w ....Anode and cathode width (cm).
w_a....................Anode width (cm).
w_c....................Cathode width (cm).

<u>Greek</u>

ΔH..................Heat of combustion of methanol (J/mol).
κ ....Electrolyte conductivity (mS/cm).

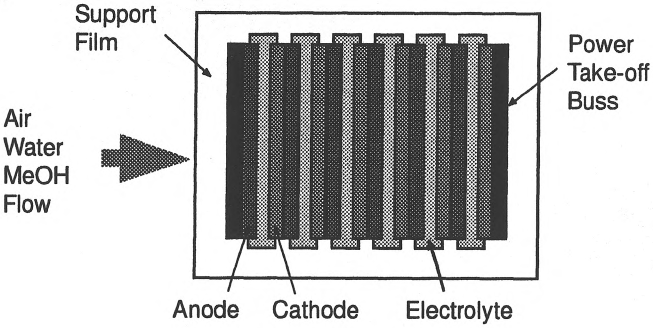

Figure 1. Strip Cell Concept.

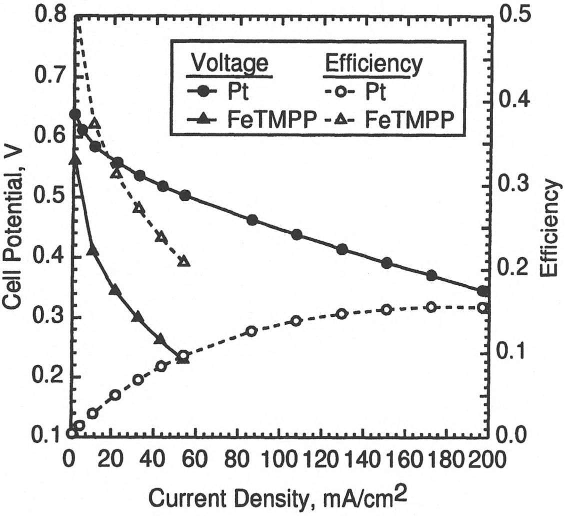

Figure 2. Performance and fuel efficiency of a traditional DMFC compared to one with selective electrodes. The efficiency of the selective-electrode cell is highest at low current density, whereas that of traditional cell increases with current density.

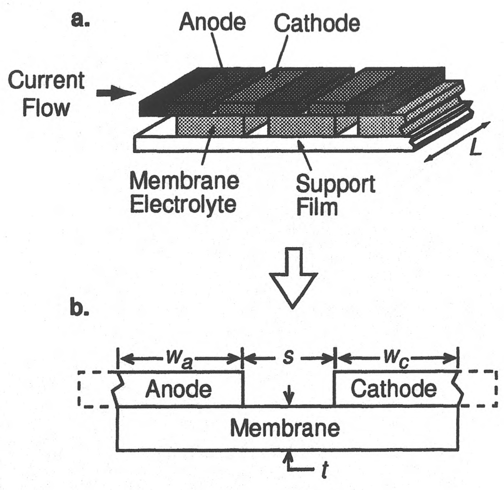

Figure 3. Simplified Strip Cell Model.

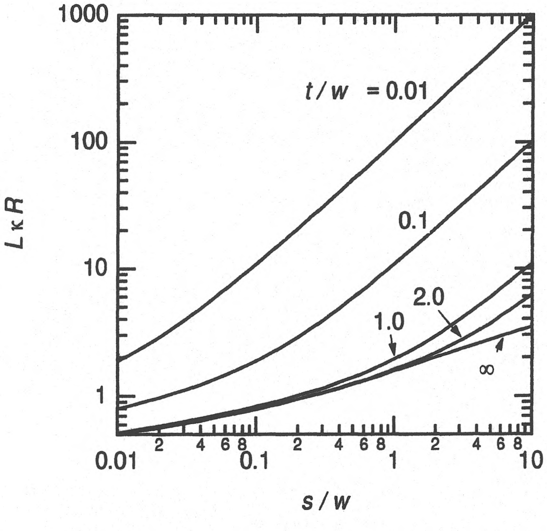

Figure 4. Dimensionless resistance of strip cell, as calculated by Schwarz-Christoffel transformation. Resistance increases with increasing electrode spacing and with decreasing membrane thickness, and is independent of membrane thickness at high thickness and low spacing.

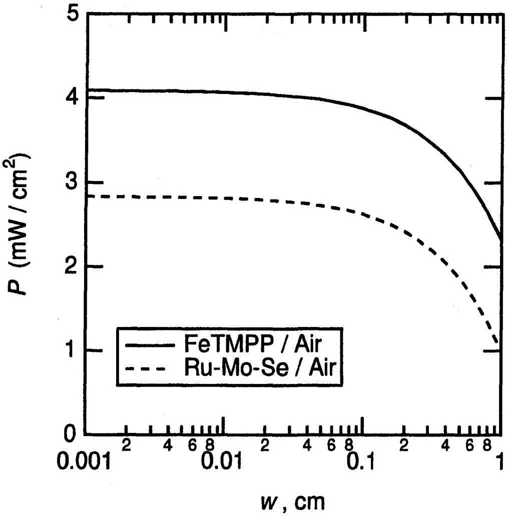

Figure 5. Effect of electrode width on cell performance. Both cells are sensitive to electrode width for $w > 0.1$ cm.

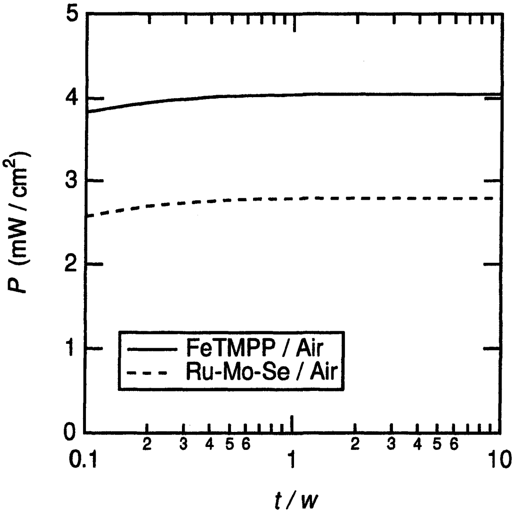

Figure 6. Effect of membrane thickness on cell performance. The performance of both cells is weakly dependent on membrane thickness, and is independent of thickness for $t/w > 1$.

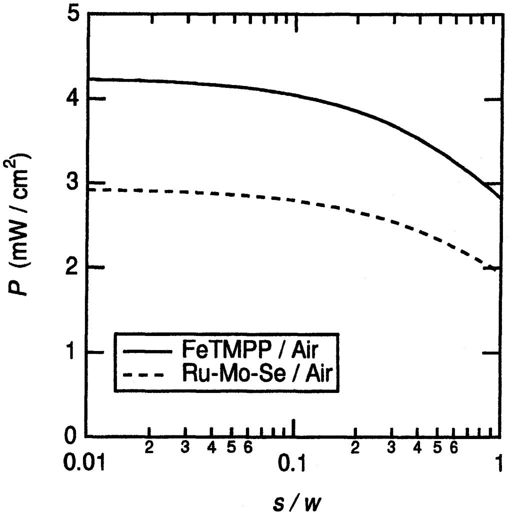

Figure 7. Effect of electrode spacing on cell performance. Thickness dependence becomes weak for $s/w < 0.1$.

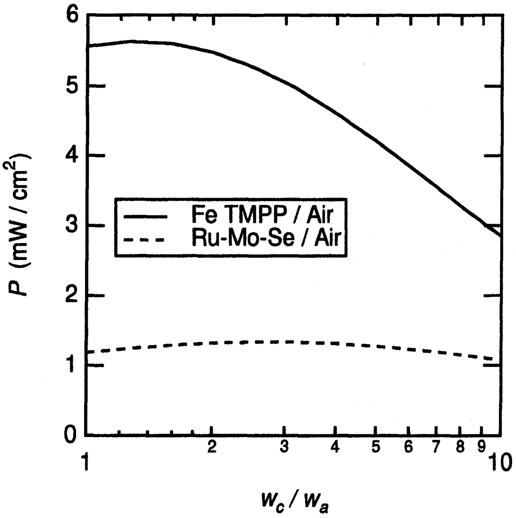

Figure 8. Effect of cathode width on cell power density, at 0.4 V cell potential. The cell with Ru-Se-Mo cathode displays a strong maximum at $w_c/w_a = 3$. The maximum in the FeTMPP cell is weak.

Proton_Conducting_Membrane_Fuel_Cells_II, PV 1998-27, 249-258 (1998)
DOI: 10.1149/199827.0249PV © The Electrochemical Society

PLATINUM-BASED ANODE CATALYST DISPERSED IN POLYANILINE FOR THE DIRECT METHANOL FUEL CELL

J. M. Rheaume, J-M. Léger, M.-J. Croissant, S. Srinivasan and C. Lamy

« Electrocatalyse », UMR n°6503-CNRS-Université de Poitiers
40 Avenue du Recteur Pineau
F-86022 Poitiers Cedex France

ABSTRACT

Polymer electrolyte fuel cell anodes containing noble metals, including either Pt, Pt-Ru, or Pt and Sn particles were dispersed in a thin film of polyaniline (PAni) on carbon cloth and tested as anodic material in a direct methanol fuel cell and polarization curves were recorded. Even if the performance of these anodes remained in general inferior to that of conventional electrodes, the curves obtained with Pt-Sn/PAni were encouraging, at least at low current densities.

INTRODUCTION

Fuel cells (FCs) which produce electricity directly from the electrochemical oxidation of hydrogen or fossil fuels boast higher efficiencies and significantly lower emissions than heat engines, which have conventionally been used for power generation. For these reasons, fuel cells would be nearly ideal for automobile propulsion, especially if they could operate from a liquid fossil fuel such as methanol which could be distributed in much the same manner as gasoline, whose infrastructure is already in place. One highly promising way to use methanol is to directly oxidize it in a Direct Methanol Fuel Cell (DMFC). Doing so would avoid the otherwise necessary costly and cumbersome ancillary reforming equipment to be reform into hydrogen gas. Both direct oxidation and reforming of methanol are plagued by the tenacious problem of electrode poisoning due to strongly adsorbed CO on the active sites of the electrodes containing platinum which is the only acceptable catalyst in acid medium (1-3). Thus the development of new, CO tolerant electrodes is the focus of much research.

Several approaches to the CO poisoning problem have been attempted. One attempt consisted of dispersing Pt in various conducting supports. Numerous other groups have published papers on methanol oxidation by Pt combined with other metals. For example, Laborde et al. belong to one of several groups reporting that Ru promotes the formation of adsorbed oxygenated species at lower potentials than Pt when oxidizing methanol and CO, facilitating more complete oxidation of the methanol (4). It is now clear that the catalysts best suited to methanol oxidation are multimetallic metals which do not necessarily have to be alloys (5). For CO oxidation, Pt-Ru and Pt-Sn bimetallic electrodes were often considered, and the modification by tin appears as the most promising one (3,6).

Obviously, not only the nature of the metallic catalyst is crucial, but also the membrane electrode assembly (MEA) preparation is vitally important to cell performance to ensure good contact between the catalyst layer and the ionomeric membrane. The mass transport and charge transfer characteristics can be highly improved by directly applying a thin film of intermixed ionomer and catalyst directly to the membrane (7). This is generally obtained by brushing or spraying a thin layer a Nafion® solution followed by hot-pressing (at 140°C) to recast the ionomer layer.

Conductive organic polymers are an alternative possibility for a convenient support for the catalyst particles because of their high surface area which is sometimes higher than that of a carbon-based substrate's resulting from high film porosity and rough morphology. (4, 8-10). Poly(methyl)thiophene, polypyrrole or polyaniline are generally the polymers considered. Remarkable stability in the form of film integrity and electrocatalytic activity for polyaniline based electrodes with electrodeposited Pt microparticles was reported after half cell endurance tests lasting 30 hours (11).

In this paper, we present and discuss the polarization curves obtained with anodes composed of electrodeposited Pt, Pt-Ru, and Pt-Sn particles dispersed in a 0.5 µm thick layer of polyaniline previously electropolymerized on a carbon cloth.

EXPERIMENTAL PROCEDURES

Fuel Cell Preparation

Preparation of Anodes. Anodes were prepared by electropolymerization of a PAni film using cyclic voltammetry as previously described (4,8). A carbon cloth tissue (E-TEK, Natick, MA) was used as the supporting material (instead of a gold sheet) and the deposition was carrying out during voltammetric cycles between 0 and 1.0 V. All potentials are given on the reversible hydrogen electrode (RHE) scale. Following deposition of the polymer layer, several potential cycles between 0 and 0.55 V were performed to stabilize the polymer. The metallic particles were then electrodispersed in the PAni film from the following appropriate salt solutions mixed in 0.5M H_2SO_4 : 10^{-3}M K_2PtCl_6, $7.5 \cdot 10^{-4}$M K_2RuCl_5, and $3 \cdot 10^{-3}$M $SnCl_4$. In all three cases, the final total metal loading was fixed at 1 mg/cm^2. It should be noted that the composition of the deposition solution for bimetallic catalysts were chosen in order to obtain the most active electrode as previously determined (8).

Preparation of Membrane Electrode Assemblies. Nafion® 117 membrane was used in all experiments as the solid electrolyte. Pretreatment of the membrane was performed according to the conventional method. A 2 mg/cm^2 Pt/C Etek electrode was always used as cathode. The electrode area measured 5 cm^2. On the active surface of the anodes, different amounts of Nafion® solution were tested (from 0.9 to 4.6 mg/cm^2 for Pt/PAni/C, Pt-Ru/PAni/C, Pt-Sn/PAni/C and the reference anode, a 2 mg/cm^2 Pt/C Etek electrode).

Since the anodes were composed of a PAni layer, the classical hot-pressing procedure was not used due to the possible degradation of the conducting polymer film at the temperature necessary to recast the Nafion® evaporated layer. In the results section, the effect of hot pressing will be discussed.

Fuel Cell Testing Procedure

Fuels and Oxidant. The tests were conducted in a complete, unpressurized fuel cell (GlobeTech). Oxygen was introduced in the cell by a humidification system (GlobeTech) which allowed to control the temperature and the pressure in addition to the amount of oxidant and its humidity. All the results presented here were however carried out at ambient pressure.

Methanol can be introduced in the cell through two different ways: by bubbling nitrogen through a 2M methanol aqueous solution (typically at a flow rate of 400 cm^3/min) and the direct introduction of methanol (2M) with a peristaltic pump which allows the circulation of methanol though the cell in a closed circuit, at the controlled temperature of 85°C.

Polarization Curves. A potentiostat (Wenking POS 73, Bank Elektronik) with a variable resistance box was used to impose currents on the cell. Once the cell reached a stable potential with reactants flowing at open circuit, i.e. steady state, the measurements were carried out according to the following procedure: starting at open circuit, the overall and anodic potentials were measured at the imposed current. The anodic potential was measured using a reference electrode (mercurous sulfate) plunged in 0.5 M sulfuric acid to make the ionic contact with the membrane, of which a portion was also plunged into the same acidic aqueous solution.

RESULTS

Anode Preparation

The characterization of the metallic particles formed by simultaneous electrodeposition of several metals in a PAni/C matrix is difficult. However, it was recently proved by « in situ » EXAFS-XANES measurements (12) that, in the case of platinum-ruthenium codeposit, it is possible to form a real alloy. This point is very important because it allows the correlation of the results obtained with bulk alloys (13) with the results recorded with small particles. In the case of platinum-tin codeposit, no evidence of the formation of an alloy was found.

After the preparation of these electrodes, two types of MEAs were prepared. The first one according to the commonly used technique, with a solution of Nafion® brushed on both electrodes (Pt-based/PAni/C for the anode and Pt/C Etek for the cathode) before being hot-pressed with a Nafion® 117 membrane. The second type of MEA was obtained without Nafion® solution and hot-pressing on the anode side, the cathode alone being previously hot pressed on the membrane.

Effect of the presence of Nafion® at the electrode interface

The effect of the presence of Nafion® at the interface was studied in the case of different electrodes, Pt, Pt-Ru and Pt-Sn deposited in PAni, and compared to the behavior of a Pt/C-Etek reference electrode (Figures 1-4).

In Figure 1, the positive influence of the presence of a thin layer of Nafion® is clearly confirmed in the case of Pt/C Etek electrode. The presence of this thin layer of recasted Nafion® increases the conductivity of the interface and allows better utilization of the metallic site.

Such a positive effect of a Nafion® solution is not at all observed with a Pt/PAni/C anode (Figure 2). Conversely, a strong inhibition phenomena is observed when a Nafion® solution is added, even after hot pressing. With this electrode, the best conditions seem to be without the addition of Nafion®. The hot pressing procedure has to be avoided, in order to not compromise the stability of the conducting polymer used. The temperature necessary to recast the Nafion® is too high for PAni; it modifies its conducting properties.

In the case of Pt-Ru/PAni/C (Figure 3) and Pt-Sn/PAni/C (Figure 4), the effect of the presence of a thin layer of Nafion® is smaller than with pure platinum particles.

The Pt-Ru/PAni/C anode yielded better results without a layer of evaporated Nafion® on the active surface of the electrode, i.e. the cells depolarized at higher current densities. In the case of Pt-Sn/PAni/C electrode, the effect is completely different, and the best results were obtained with the presence of a thin layer of evaporated Nafion®, without further hot pressing the membrane electrode assembly.

Comparison of Polarization Curves

A comparison of the better of the results obtained with the different anodes, either with or without evaporated Nafion® are reported in the Figure 5. Even if the best anode remains Pt/C-Etek (with recasted Nafion® obtained by hot-pressing), the performance of the Pt-Sn/PAni/C electrode, at least at low current densities (below 50 mA/cm^2) are encouraging. This observation is rather surprising; this electrode appears more active than the Pt-Ru/PAni/C electrode, which contradicts the results obtained with « classical » Pt-Ru/C, which is recognized as the best electrocatalyst for methanol.

Comparison of Anodic Curves

Figure 6 shows the anodic curves for the electrodes discussed in the above section. The anodes with the best performance (i.e. lowest overpotentials) exhibit a low potential at open circuit. The anodic polarization curves of the PAni anodes parallel the findings for the full cells described above. The results noted from the polarization curves are confirmed and the best anode was that composed of Pt-Sn/PAni/C, the worst performers were the Pt/PAni/C and the Pt-Ru/PAni/C. The potential shift in the negative direction observed for the Pt-Sn electrode is around 150 mV, if we compared to an electrode of similar structure (Pt/PAni/C) and the comparison with Pt-Ru/PAni/C electrode confirms that Sn appears surprisingly to give best results than Ru when as a second component added to platinum.

It should be noted that the Pt/C Etek electrode did not perform as well as expected in view of the high performance of the MEAs in the full cells reported in Figure 5. However, at current densities greater than 50 mA/cm^2, this electrode is the best one.

CONCLUSION

In this preliminary study of the performance of electrodes composed of a electrodeposit of Pt-based catalyst in a conducting polymer (polyaniline), several points were observed: the electrode membrane assembly manufacturing is different from the procedure used with conventional membrane electrode assemblies. The hot-pressing procedure needs to be avoided due to the rather poor thermal stability of the conducting polymer. However, the presence of a small amount of Nafion® solution brushed on the electrode before annealing at 80°C seems to be necessary to improve the contact between the electrode and the electrolyte. Under these conditions of preparation, encouraging results were obtained, with Pt and Pt-based electrodes, mainly for low current densities (typically below 50 mA/cm²). However, for higher current densities, the results are quite low due to the poor contact between electrode and electrolyte.

However, the most interesting result obtained is the behavior of the Pt-Sn/PAni/C electrode. It is quite surprising that the modification by tin gives better results than those with modification by Ru, which is widely recognized as the best candidate to improved the properties of platinum for methanol electrooxidation. These results are different from the observation made with particles deposited only on a carbon substrate. If a definitive interpretation is difficult to give at the present state, it could be related to the strong positive effect already found for the CO oxidation on Pt-Sn electrodeposited into a into a PAni layer (6). It seems clear that the metallic particles electrodeposited into a conducting polymer have some interactions with the polymer surface which can modify the adsorption (and then the dissociation) of methanol). The adsorbed CO species formed are probably much easily oxidized by platinum modified by tin leading to a low coverage of poisonous species.

PAni films show promise for being matrices for dispersion of metallic crystallites in fuel cell electrodes. However, the working temperature seems to be limited up to 80°C, but other conducting polymers can be considered for this purpose. In addition, the thickness of the PAni film and the electrocatalyst loading need to be optimized, in addition to the procedure to obtain the membrane electrode assembly.

REFERENCES

1. B. Beden, C. Lamy and J-M. Léger in, Modern Aspects of Electrochemistry, J. O'M Bockris, B.E. Conway and R.E. White, Editors, Vol. 22, p. 97, Plenum Press, New-York (1992).

2 C. Lamy and J-M Léger, in New materials for fuel cell and modern battery systems, O. Savadogo and P.R. Roberge, Editors, p. 477, Editions de l'Ecole Polytechnique, Montreal (Canada) (1997).

3. K. Wang, H. Gasteiger, N. Markovic and P. N. Ross, Electrochim. Acta 41, 2587 (1996).

4. H. Laborde, J-M. Léger and C. Lamy, J. Appl. Electrochem., 24, 1019 (1994).

5. P. Ross, in Direct Methanol-Air Fuel Cells, P. Langrede, Editor, 92-14, p. 61, The Electrochemical Society Proceedings Series, Pennington, NJ (1993).

6. W. Nappom, J-M. Léger and C. Lamy, J. Electroanal. Chem., 408, 141 (1996).

7. M. Wilson, J. Valerio and S. Gottesfeld, Electrochim. Acta, 40, 355 (1995).

8. C. Lamy, J-M. Léger and F. Garnier, in Handbook of Organic Conductive Molecules and Polymers : Vol 3. Conductive Polymers: Spectroscopy and Physical Properties, H.S. Nalwa, Editor, p. 471, John Wiley and sons, (1997).

9. S. Swathirajan and Y. Mikhail, J. Electrochem. Soc., 139, 2105 (1992).

10. C. Hable and M. Wrighton, Langmuir, 9, 3284 (1993).

11. K. Kost, D. Bartak, B. Kazee and T. Kuwana, Anal. Chem., 60, 2379 (1988).

12. J. McBreen, S. Mukerjee, S. Srinivasan, J-M. Léger, W. Nappom, C. Lamy,, The 1997 Joint International Meeting (192nd Electrochemical Society Meeting and 48th International Society of Electrochemistry Meeting), Paris, August 31 - September 5, p 1241.

13. A. Kabbabi, R. Faure, R. Durand, B. Beden, F. Hahn, J-M. Léger and C. Lamy, J. Electroanal. Chem., 444, 41 (1998).

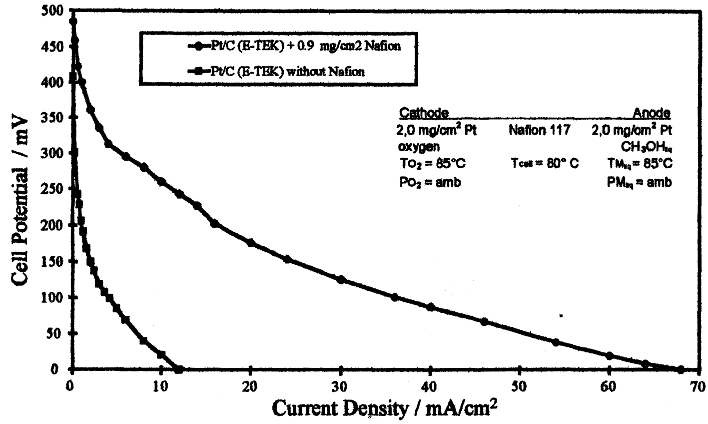

Figure 1 : Potential versus Current Density for a methanol (liquid) /oxygen cell. Effect of the presence of Nafion® at the interface. Case of the Pt/C Etek electrode.

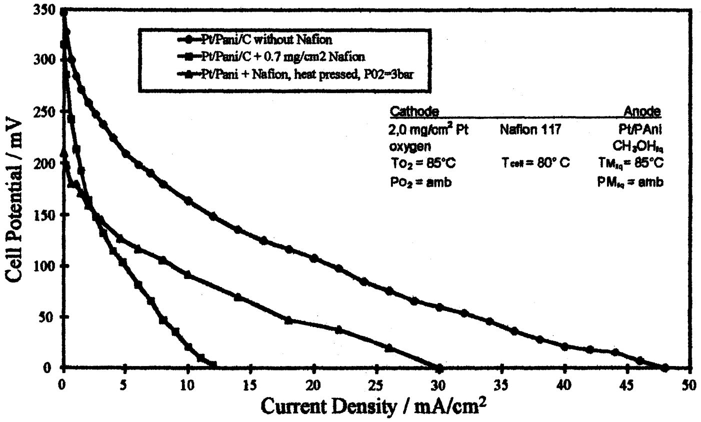

Figure 2 : Potential versus Current Density for a methanol (liquid) /oxygen cell. Effect of the presence of Nafion® at the interface and of the hot-pressing during the manufacturing of the membrane electrode assembly. Case of the Pt/PAni/C electrode.

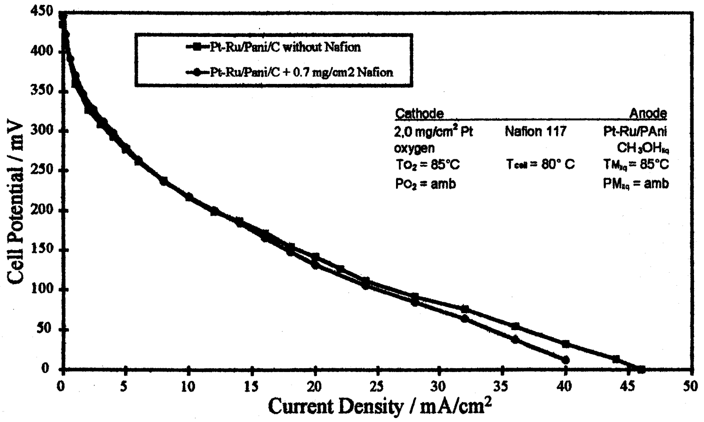

Figure 3 : Potential versus Current Density for a methanol (liquid) /oxygen cell. Effect of the presence of Nafion® at the interface. Case of the Pt-Ru/PAni/C electrode.

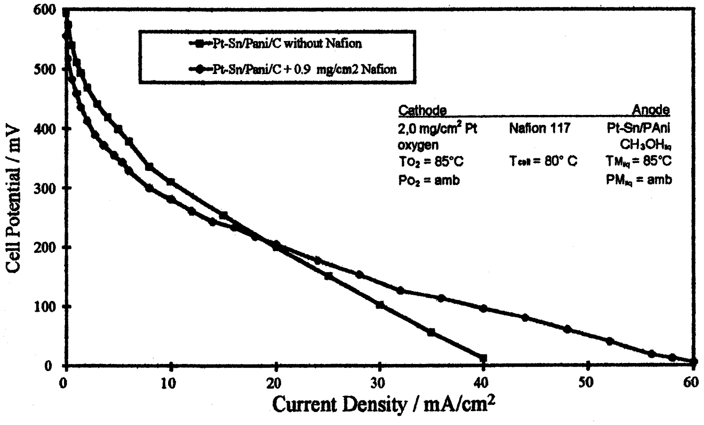

Figure 4 : Potential versus Current Density for a methanol (liquid) /oxygen cell. Effect of the presence of Nafion® at the interface. Case of the Pt-Sn/PAni/C electrode.

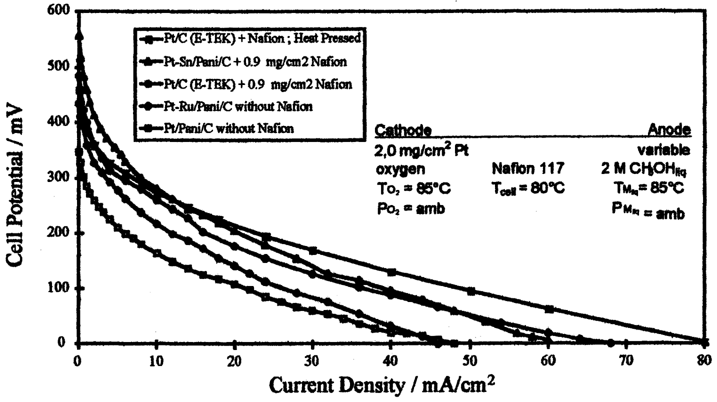

Figure 5 : Potential versus Current Density for a methanol (liquid) /oxygen cell. Effect of the nature of electrode, for various PAni/C supported electrodes in comparison to the behavior of the Pt/C Etek electrode.

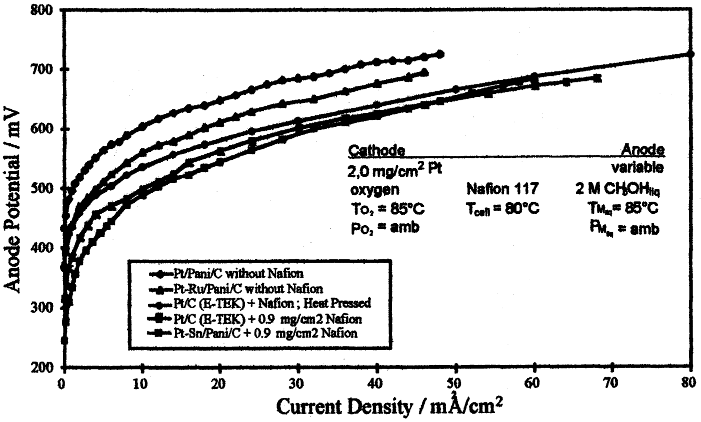

Figure 6 : Anodic curves for a methanol (liquid) /oxygen cell. Effect of the nature of electrode, for various PAni/C supported electrodes in comparison to the behavior of the Pt/C Etek electrode.

Proton_Conducting_Membrane_Fuel_Cells_II, PV 1998-27, 259-266 (1998)
DOI: 10.1149/199827.0259PV © The Electrochemical Society

DIRECT METHANOL FUEL CELL : STUDY OF IMPROVED Pt-Ru ANODE MATERIALS

A. Oliveira Neto, J. Perez, W.T. Napporn, A.L.N. Pinheiro and E.R. Gonzalez
Instituto de Química de Sao Carlos-USP,
C.P. 780, 13560-970 São Carlos (SP), Brazil.
e-mail : ernesto@iqsc.sc.usp.br

ABSTRACT

The electrocatalytic oxidation of methanol on Pt-Ru dispersed on carbon thin porous coating electrodes using an alternative preparation method was investigated. The EDX analysis confirmed that the simultaneous reduction of the precursor salts of Pt and Ru leads to the presence of these materials in the nominal composition initially calculated. The polarization data shows that, for all concentrations of methanol, Tafel plots present two slopes.

INTRODUCTION

Because of the use of a liquid fuel, the direct methanol fuel cell (DMFC) is an attractive alternative power source for transportation applications. Many investigations concerning the fabrication of the anode and the cathode were made in order to decrease the catalysts loading, while obtaining very active materials. For the anode materials, dispersed catalysts, modified in their composition and structure, seem to give promising results. It has been shown that the addition of Ru and/or Sn to platinum has improved the activity towards the oxidation of methanol in acid media. Until now, Pt-Ru alloys seem to be the best anode materials, because the problem of poisoning of the electrode by strong adsorbed species, like carbon monoxide, is less severe than in pure Pt (1,2). As an added benefit when these alloys are used, there is an increase in the long-term stability of the electrocatalysts. On the other hand, there is still margin to develop alternative methods of preparation capable of producing catalysts with better characteristics.

For fuel cell applications, the catalysts are generally dispersed on a high surface area carbon support using a low catalyst loading. The use of those electrocatalyts under operational conditions and their characterization have proved that the method of preparation is a key aspect for their performance, particularly when they are used for the fabrication of gas diffusion electrodes. It has been shown in this laboratory that the electrocatalysts for these electrodes can be conveniently studied using the thin porous coating (TPC) electrode technique (3).

In this work, an alternative route was used to prepare Pt-Ru catalysts, supported on high surface area carbon (4). The characterization of these materials was made by Electron Dispersion X-Ray (EDX). The electrooxidation of methanol was studied on TPC electrodes, made with the catalysts, by cyclic voltammetry and steady state polarization techniques with various methanol concentrations in sulphuric acid.

EXPERIMENTAL

The Pt-Ru electrocatalysts dispersed on carbon (Vulcan XC-72) were prepared by the simultaneous reduction of platinum and ruthenium salts (H_2PtCl_6 and $RuCl_3$ from Merck) using the method described elsewhere (4). TPC electrodes were made by mixing the catalyst powders with a dilute suspension (2% w/w) of PTFE emulsion (Dupont TM 30) and applied into a recess made in the PTFE holder of a conventional rotating electrode. A conventional one-compartment electrochemical glass cell with a Luggin capillary was used in the electrochemical experiments. The counter electrode was a platinum foil and the reference was a reversible hydrogen electrode (RHE).

The electrocatalytic activities of the electrodes were estimated in 0.5 M sulphuric acid (high purity from Merck) solution, prepared with ultrapure water from a Milli-Q Millipore system. All the electrochemical experiments (voltammetry and polarization) were performed under nitrogen atmosphere and at room temperature (25±1°C) using a Princeton Applied Research (PAR) 273A potentiostat coupled with an IBM-PC compatible microcomputer.

RESULTS AND DISCUSSION

After the preparation, the dispersed Pt-Ru materials with various Pt:Ru ratios were characterized by EDX and the results are presented in Table 1. The EDX results show values of platinum and ruthenium contents which are very close to the nominal composition of the materials.

Figure 1 shows the voltammograms, obtained with different thin porous coating Pt-Ru electrodes, recorded at 10 mV s^{-1} in 0.5 M H_2SO_4. When the Ru contents increases from 10 to 40 atom %, the double layer current increases progressively indicating an increasing adsorption of oxygen-like species as OH_{ads}.

The charge corresponding to the hydrogen region is the same for Pt-Ru catalysts containing 10, 20 and 30 atom % of Ru but lower for that with 40 %. The size of the particles and their distribution on the carbon support are certainly responsible of this phenomenon.

According to Ticianelli et al. (5) the presence of Ru leads to the formation on the surface of OH_{ads} species at potentials as low as 0.25 V vs.RHE. The surface composition of the Pt-Ru electrodes appears to be stable for potentials up to 1.0 V vs.RHE. From the mechanism proposed for the electrooxidation of methanol on Pt in acid medium (6), it is evident that adsorbed oxygen, or the surface oxide, is the convenient oxygen species, which can easily be involved in the oxidation process. The formation of oxygenated species on a pure platinum surface seems to control the oxidation of the primary alcohols (7) which, on Pt electrodes, begin to occur at a potential as high as 0.8 V vs. RHE. On Pt-Ru catalysts the oxidation process starts at 0.25 V, a much lower potential. The conclusion is that the methanol molecule can be oxidized at much lower potentials on Pt-Ru catalysts than on pure Pt catalysts.

Figure 2 shows cyclic voltammetric curves for methanol oxidation on carbon supported Pt-Ru (80:20) catalysts, for different concentrations of methanol. It can be observed from these results that the onset of methanol oxidation on this catalyst is almost independent of the concentration of methanol.

Figure 3 shows polarization curves for methanol oxidation obtained with a Pt-Ru (70:30) catalyst, for different concentrations of methanol. In this case it can be seen that for a methanol concentration of 1 M, a potential shift of 50 mV to more positive potentials is observed in comparison with the concentration of 0.1 M, for potentials up to 0.55 V. Above this value the behaviour seems to be independent of the concentration of methanol. An explanation for this behaviour is that at high methanol concentrations the contribution of the hydroxyl species for the oxidation process is low, due to the competition between their formation and the occupation of the surface by adsorbed methanol species. These results on the effect of methanol concentration are very important for methanol fuel cells using a liquid-feed system.

Figure 4 shows the voltammograms of different C/Pt-Ru electrodes, recorded at 10 mV s^{-1} in 0.5 M H_2SO_4, in the presence of 0.1 M CH_3OH. It can be seen that the carbon supported 60:40 Pt-Ru catalyst gives the higher current density. But when for the all catalysts the current density is corrected for the background current due to the supporting electrolyte, the Tafel plots obtained show that the sample which gives the best catalytic effect is that with the 70:30 Pt-Ru composition. This difference between the polarization and the voltammetric is due to the effect of the double layer, which is highest in the case of the 60:40 Pt-Ru sample (cf. Figure 1). These observations agree with reports in the literature (1, 2, 8), which indicate the Pt-Ru containing ~30 atom % of Ru as the best catalyst. According to Gasteiger et al. (8), the electrocatalytic activity of Pt-Ru towards methanol oxidation starts being observed with a coverage of 10 atom % of Ru. However, this initial coverage depends on temperature.

Figure 5 shows Tafel plots for the different catalysts in 0.5 M H_2SO_4 containing 0.1 M CH_3OH. Almost the same behaviour is observed for the catalysts containing 10, 20 and 30 % atom of Ru but, for potentials above 0.35 V, the catalyst with 40% Ru presents a shift of 50 mV toward more positive potentials. The Tafel plots (in the case of 0.1 M CH_3OH) for all the catalysts present two slopes: ~ 60 mV dec^{-1} between 0.25 and 0.32 V and ~250 mV dec^{-1} between 0.32 and 0.6 V. Wieckowski et al. (9) have also observed two Tafel slopes for the electrooxidation of methanol on Pt-Ru electrodes using Pt single crystals. In previous work (8) a bifunctional mechanism was proposed for the oxidation of methanol on Pt-Ru catalysts. Methanol will be preferentially adsorbed on the platinum atoms, while the Ru atoms will generate the oxygen-like species. The tendency that has the Ru atoms to favour the formation of these species at low potentials confirms this hypothesis. For small organic molecules such as CH_3OH, CO and also for O_2, it was shown that the size of the catalyst particles and their distribution can modify their catalytic activity (10). With pure platinum dispersed on carbon, it was also shown that the Pt mass available and the specific activity for methanol oxidation increase with the amount of platinum surface oxide on the carbon support (11).

The surface structure of the Pt-Ru catalysts prepared here may show predominant crystallographic facets (12). This may be important, because recently it has been shown that the surface structure has an important effect on the mechanism of methanol oxidation (9). At the same time, no change is observed in the Tafel slopes when the methanol concentration increases from 0.1 to 1 M, indicating that the poisoning effect on these catalysts is independent of the concentration of methanol.

CONCLUSIONS

The experiments described in this work show that an alternative preparation method of Pt-Ru catalysts allows to obtain active materials. The addition of Ru to Pt in order to improve its catalytic activity has until now been an option to decrease the poisoning phenomenon during methanol oxidation on these materials.

The two Tafel slopes obtained in our case are in agreement with those obtained recently by Wieckowski et al. (9). This can be related to the structure of the electrode and to the preferential orientation of the Pt-Ru catalyst particles which are key points in the real activity of these materials.

REFERENCES

(1) F. Richarz, B. Wohlmann, U. Vogel, H. Hoffschelz, K. Wandelt, Surface Sci., **335**, 361 (1995).

(2) R. Ramkumar, S. Dheenadayalan and R. Pattabiraman, J. Power Sources, **69**, 75(1997).
(3) J. Perez, A.A. Tanaka, E.R. Gonzalez and E. A. Ticianelli, J. Electrochem. Soc., **141**, 431 (1994).
(4) E.R. Gonzalez, E.A. Ticianelli, A.L.N. Pinheiro and J. Perez, Brazilian Patent, deposited.
(5) E.A. Ticianelli, J.G. Beery, M.T. Paffett and S. Gottesfed, J. Electroanal. Chem., **258**, 61 (1989).
(6) B. Beden, C. Lamy and J-M. Léger in "Modern Aspects of Electrochemistry", J.O'M. Bockris, B.E. Conway and R.E. White (Eds), Vol 22, Plenum, New York (1992) p. 97.
(7) N-H. Li, S-G. Sun, S-P. Chen, J. Electroanal. Chem., **430**, 57 (1997).
(8) H. Gasteiger, N. Markovic, P.N. Ross Jr., E. J. Cairns, J. Phys. Chem., **97**, 12020 (1993).
(9) W. Chrzanowski and A. Wieckowski, Langmuir, **14**, 1967 (1998).
(10) S. Mukerjee, J. Appl. Electrochem., **20**, 537 (1990).
(11) F. Gloaguen, J-M. Léger and C. Lamy, J. Appl. Electrochem., **27**, 1052 (1997).
(12) J. Perez, E.R. Gonzalez and E. A. Ticianelli, Electrochim. Acta, **in press**

ACKNOWLEDGMENTS:

The authors thank FAPESP (Proc 97/02471-6 and 95/0692-0), PRONEX / FINEP, CNPq, and CAPES, Brazil for financial support.

Table I . Composition analysis by EDX of the TPC Pt-Ru electrodes.

Nominal composition of the TPC Pt-Ru catalysts	EDX Pt content Atom %	EDX Ru content Atom %
90 : 10	88	12
80 : 20	81	19
70 : 30	71	29
60 : 40	62	38

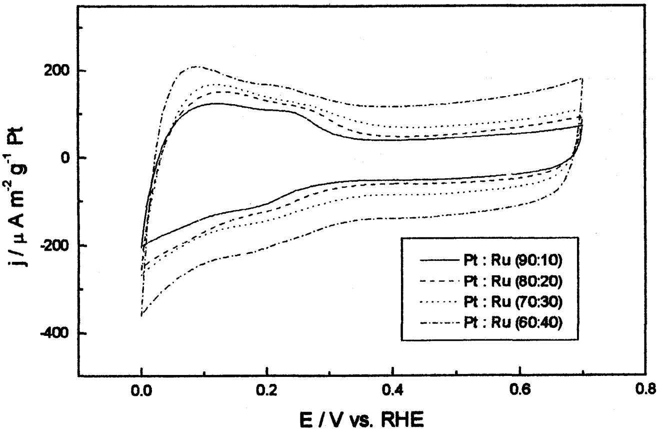

Figure 1. Voltammograms for different Pt-Ru electrodes recorded at 10 mV s^{-1} and 25°C in 0.5 M H_2SO_4.

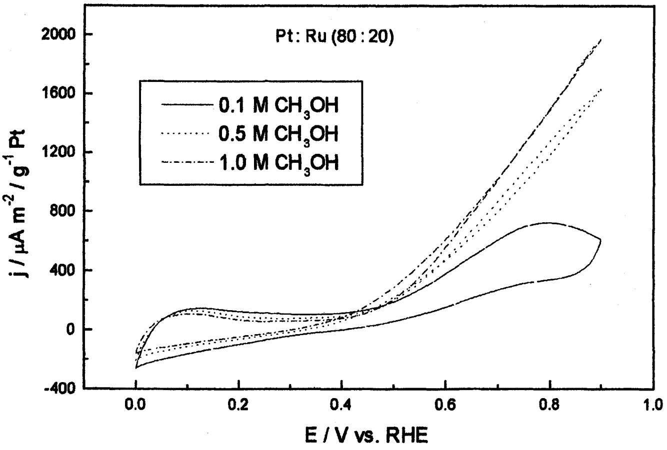

Figure 2. Voltammograms for Pt-Ru (80:20) recorded at 10 mV s^{-1} and at 25°C in 0.5 M H_2SO_4 in the presence of various methanol concentrations.

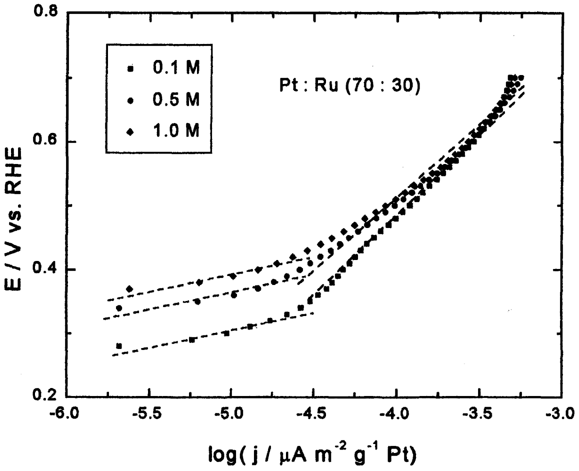

Figure 3 : log(j) vs. E curves for methanol oxidation on Pt-Ru catalysts in 0.5 M H_2SO_4.

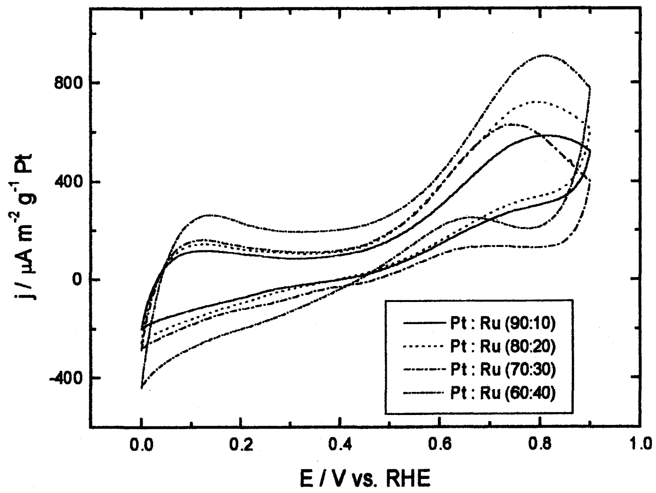

Figure 4. Voltammograms for the different Pt-Ru electrodes recorded at 10 mV s^{-1} and at 25°C in 0.5 M H_2SO_4 in the presence of 0.1 M CH_3OH.

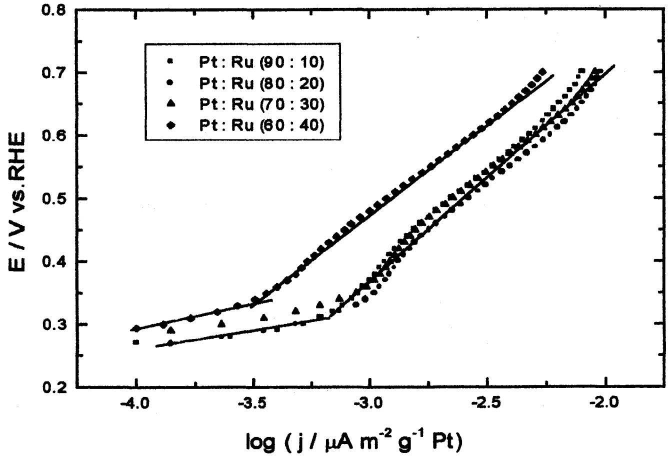

Figure 5. Tafel plots for the different TPC Pt-Ru electrodes in 0.5 M H_2SO_4 containing 0.1 M CH_3OH.

Proton_Conducting_Membrane_Fuel_Cells_II, PV 1998-27, 267-279 (1998)
DOI: 10.1149/199827.0267PV © The Electrochemical Society

DIRECT METHANOL FUEL CELLS: CATALYST IONOMER CONTENT AND ANODE PERFORMANCE

S. C. Thomas, X. Ren and S. Gottesfeld
Los Alamos National Laboratory
Los Alamos, NM 87545

ABSTRACT

In a study of DMFC anode catalyst layers, we have found that addition of recast ionomer does not improve anode performance when some unsupported PtRu catalysts are used. It seems that the protonic conductivity of a Ru oxide component in such catalysts is sufficient to allow effective utilization of catalyst sites. To examine possible interpenetration of catalyst and membrane material, ultramicrotomed thin sections of the MEA were examined by SEM. Images of such sections have not revealed significant catalyst/membrane interpenetration, supporting the interpretation that hydrous RuOx may provide sufficient protonic conductivity in some PtRu catalyst layers prepared with no added ionomer.

INTRODUCTION

Thin film catalyst layers for electrodes structures, a technology developed at Los Alamos National Laboratory (LANL) (1, 2) have been utilized in much of recent work involving both hydrogen and direct methanol polymer electrolyte fuel cells. Results obtained with such catalyst layers illustrate the importance of the thinness of the catalyst films with respect to proton and reactant accessibility to catalyst sites and, in the case of the direct methanol fuel cell (DMFC), CO_2 removal. These thin catalyst layers are cast from dispersions of the catalyst particles in an aqueous, solubilized ionomer solution. Not only does the inclusion of the recast ionomer within the catalyst layer provide structural integrity to the catalyst layer; it has also been shown to be essential for sufficient ionic conductivity within the electrode structure. By varying the relative weight percentages (and hence volume percentages) of ionomer and catalyst in the catalyst layer, the relative ionic and electronic conductivities in the catalyst layer are varied, as is the average density of the layer. It has been recognized for some time that the optimal structure for high catalyst utilization is a catalyst layer that is as thin as possible, with an appropriate mixture of catalyst and ionomer (1, 3). However, past work has focused on carbon supported Pt catalysts utilized in the hydrogen PEFC, not on unsupported PtRu and Pt black catalysts used in the anode and cathode, respectively, of the DMFC. In the work reported in this paper, the wt. % of ionomer in thin film catalyst layers prepared for DMFC anodes was systematically varied to determine the effect, if any, on DMFC performance.

EXPERIMENTAL

Pretreatment of the proton form of the Nafion 117 membrane, preparation of membrane electrode assemblies (MEA) for a DMFC using a decal technique, and the single-cell fuel cell hardware have been previously described (2) as has the cell testing system used (4). Two unsupported PtRu blacks of nominal 1:1 atomic ratio were used, one supplied by E-TEK, Inc., Natick, MA, and the other by Johnson Matthey. Anode inks were made by dispersing appropriate amounts of the PtRu catalyst, deionized water and 5 % Nafion solution (900 equivalent weight (EW), Solution Technology Inc.). The cathode inks contained unsupported Pt black (30 m^2/g, Johnson-Matthey), deionized water and 5 % Nafion solution (1100 EW Solution Technology Inc.). The geometric active area of all the MEAs prepared was 5 cm^2.

In all experiments, 1 mol/L methanol solution was pumped through the DMFC anode flow field at 1 – 2 mL/min. A back pressure, which varied with cell operating temperature, was imposed upon the anode outlet flow at temperatures above 80°C to ensure that the membrane would be in contact with a liquid solution of methanol. When operated in fuel cell mode, the cathode gas feed was air, at 60 psig pressure and a flow rate of 0.5 L/min. The air was sometimes pre-humidified at the same temperature as the operating temperature of the cell; occasionally no humidification of the air was used. When operated in driven cell mode to measure methanol anode polarization, the cathode gas was humidified hydrogen. The back pressures and humidification temperatures of the hydrogen gas varied with the operating temperature of the cell.

To prepare samples of MEAs for microscopy examination, 1 mm wide strips were cut from the middle of a MEA, the performance of which had been previously evaluated in a fuel cell. A silicone embedding mold was slit to open when bent and the MEA strip was positioned in the slit to allow cross-sectioning. LR White epoxy in the "hard" formulation was used as the embedding resin. Sections of selected MEAs were prepared by ultramicrotomy using a Reichert Ultracut S ultramicrotome. All sections were cut using a diamond knife for materials science from SPI Supplies with a clearance angle of 4°. Sections were cut with the interfaces in the MEAs perpendicular to the knife edge. Best results were obtained using a cutting speed of 0.05 mm/s and section thickness of 2.5 µm. The sections were retrieved from the water bath contained in the diamond knife boat onto Formvar-coated copper grids. The sections were examined with a JEOL JSM-6300FXV scanning electron microscope (SEM) using 25 kV accelerating voltage and a working distance of ca. 15 mm.

X-ray diffraction (XRD) data for the anode catalyst powders were obtained using a Siemens diffractometer D5000. The operating conditions were 50 kV accelerating voltage and 40 mA of beam current using Cu K_α radiation with a Ge crystal monochromator.

RESULTS AND DISCUSSION

The anode catalyst used in this series of experiments was an unsupported alloy with a 1:1 PtRu atomic ratio, designated as RV3030, supplied by E-TEK, Inc. of Natick, MA. The loading of the PtRu alloy was kept at 2 ± 0.3 mg/cm^2. The wt. % of recast ionomer (900 EW) in the anode catalyst layers was varied from 0 % to 30 %. It was found that decreasing the amount of solubilized ionomer resulted in inks that were increasingly more difficult to paint on the Teflon blank (from which the catalyst film is transferred in a "decal" process to the membrane). With no recast ionomer in the anode ink, it became necessary to change the ink solvent from deionized water to isopropanol in order to obtain an ink that would wet the Teflon blank. All MEAs that were tested contained, in addition to the various anode catalyst layers, Nafion^{TM} 117 membranes and cathode catalyst layers composed of 90 wt. % Pt black, loaded at 2.5 ± 0.5 mg/cm^2, and 10 wt. % recast ionomer (1100 EW).

The MEAs were first tested in a cell using a 1 mol/L aqueous methanol feed to the anode and humidified hydrogen gas to the cathode side of the cell. The cathode in this driven cell configuration acts as a counter/reference hydrogen electrode. To investigate anode catalyst layer performance in the oxidation of methanol, anode current dependence on potential vs. the H_2 electrode was measured. These anode polarization data provide a direct tool for comparing activities of anode catalyst layers. As shown in Figure 1, the current density achieved at an overpotential of 0.4 V (RHE) during a potential scan of the anode at 2 mV/s increased with decreasing wt. % of recast ionomer in the anode catalyst layer. This trend was observed at all temperatures tested. It was also repeated when the MEAs were operated in DMFC configuration, as shown in Figure 2, pointing to the dominant effect of the anode on overall DMFC performance. As the recast ionomer in the catalyst layer is an ionic conductor, and hence should enable mobility of hydrogen ions in the layer, the results shown in figures 1 and 2 were unexpected.

Several reasons can be hypothesized for this trend of increased current with decreased wt. % of recast ionomer in these PtRu anode catalyst layers. At given precious metal loading, decreasing the wt. % (and hence vol. %) of recast ionomer would decrease anode catalyst layer thickness with possible beneficial effects. For example, if hot pressing of the anode catalyst layer to the Nafion 117 membrane results in some embedding of catalyst into the membrane, a larger fraction of PtRu catalyst sites may establish sufficient protonic contact with the membrane when the catalyst layer is thinner. It can also be argued in the same context that less recast ionomer in the catalyst layer would result in a catalyst layer of greater hardness that would "bite" more deeply into the polymeric membrane. Thus, for the same loading of PtRu, the current achieved could increase if more significant catalyst/membrane interpenetration takes place during hot press. The finding presented in figure 1 could also mean that a possible limitation to catalyst utilization is poor electronic conductivity of the catalyst layer, since the electronic conductivity would decrease with increasing ionomer content in the composite layer.

Figure 3 shows a scanning electron micrograph of a cross section of a MEA. The MEA section is supported on a Cu grid covered with a thin Formvar polymer film. This particular MEA, with no recast ionomer in the anode catalyst layer, had been tested in a DMFC. The cross section displays carbon cloth electrode backings on either side of the anode and cathode catalyst layers. It can be seen that both the anode and cathode catalyst layers are noncontinuous in this section and similar discontinuities were observed in other sections of this MEA, as well as other MEAs. It is unknown as to whether such cracking of the catalyst layers occurred during preparation of the MEA, operation of the fuel cell, embedding of the used MEA into resin, or sectioning of the embedded MEA.

Figures 4, 5 and 6 are micrographs of the anode catalyst layers containing no recast ionomer, 10.5 % recast ionomer, and 30.7 % recast ionomer in the anode catalyst layers, respectively. For the sections sampled, the anode catalyst layer with no recast ionomer had an average thickness of ca. 1 µm. The average thickness of the anode catalyst layer containing 10.5 wt. % recast ionomer was ca. 7 µm while that of the anode containing 30.7 wt. % recast ionomer was ca. 15 µm. All MEAs showed a distinct interface between the anode catalyst layer and the membrane, with no evidence of greater penetration of the membrane by the anode catalyst layer containing no recast ionomer.

It is interesting to compare the observed thicknesses of the anode catalyst layers with the calculated thicknesses based on zero porosity. If it is assumed that the catalyst was 1:1 metallic PtRu black, with an average density of 17.2 g/cm^3, the calculated thickness of the anode catalyst layer containing no recast Nafion is 0.97 µm. If it is assumed that the catalyst was Pt/RuO$_2$, with an average density of 11.6 g/cm^3, the calculated thickness of this same catalyst layer is 1.4 µm. The observed thickness of this anode catalyst layer was ca. 1 µm. For the anode catalyst layer containing 10.5 % recast ionomer, the average density of the anode catalyst layer, assuming a density of 1.8 g/cm^3 for the ionomer, is 7.4 g/cm^3 if the catalyst is assumed to be Pt/RuO$_2$ and 9.2 g/cm^3 if the catalyst is assumed to be PtRu. These values provide calculated thicknesses of the anode catalyst layer of 2.8 µm and 2.2 µm, respectively. Contrast these values with the observed thickness of ca. 7 µm. Obviously, introduction of the recast ionomer into the anode catalyst layer introduces a degree of porosity that increases with increasing amounts of ionomer. This decrease in particle interconnectivity could explain a decrease in electronic conductivity within the anode catalyst with increased ionomeric content. Enhanced porosity in such catalyst layers would explain the relatively high permeabilities of gaseous reactants, as concluded before from modeling and diagnostics of PEFC air cathodes [3].

In the absence of evidence for significant embedding into the membrane of anode catalyst layers prepared with no recast ionomer, we must conclude that protonic conductivity in a PtRu anode catalyst layer with no recast ionomer might possibly arise from another source. If the RV3030 catalyst powder, nominally PtRu black with a 1:1 atomic ratio, contains some form of ruthenium oxide, RuO$_x$, the RuO$_x$ in hydrous form could provide the necessary protonic conductivity (5, 6). Hence both the electronic and protonic conductivity necessary in the anode catalyst layer would be provided by the RV3030 itself and addition of recast ionomer would serve only to increase the thickness of the catalyst layer and thereby decrease access to catalyst sites. An additional beneficial effect of RuOx in the catalyst layer, replacing recast PFSA material, may be lowering the local acidity of the system, which would improve the interfacial kinetics of methanol electro-oxidation.

Figure 7 is the XRD spectrum of the as-received E-TEK catalyst, RV3030, that was used in this series of experiments. Figure 8 is the XRD spectrum of the same catalyst after reduction with H$_2$. The presence of amorphous RuO$_x$ in the as-received catalyst is inferred from the broad peaks (Figure 7) which are substantially lessened upon reduction of the RuO_x to alloyed PtRu (Figure 8). This suggests that the amount of RuO_x in the as-received catalyst is sufficient to provide protonic conductivity.

Figure 9 is the XRD spectrum of an as-received, unsupported PtRu sample provided by Johnson Matthey. The spectrum shows more complete alloying of the Pt and Ru, with far less of the Ru being present as RuO_x. Anode layers for MEAs with identical loading of the JM catalyst were prepared using 0 wt. % and 15 wt. % recast ionomer. The results summarized in Table I indicate that the addition of recast ionomer to this PtRu catalyst, of less RuO_x content, increases anode (and DMFC) performance. With this latter anode catalyst composition, the increased thickness of the anode catalyst layer caused by the inclusion of recast ionomer is apparently more than compensated for by increased ionic conductivity within the anode. Without addition of recast ionomer to the anode catalyst layer, the relatively small amount of RuO_x present in the Johnson Matthey catalyst does not provide sufficient protonic conductivity.

Table I.
Effect of Ionomer Content in Anodes using Johnson-Matthey PtRu Black Catalyst on Current Density Obtained at 80°C in Driven Cell and Fuel Cell Configurations

Ionomer content (wt. %)	i (mA/cm^2) at anode overpotential of 0.35 V (RHE)	i (mA/cm^2) at cell potential of 0.5 V
0	130	150
15	200	170

It is important to stress here that the presence of Ru oxide in PtRu anode catalysts is not necessarily the key for maximizing DMFC anodic activity. Whereas the results presented here indicate that RuOx, probably in its hydrous version, can provide protonic conductivity within the catalyst layer, the overall electrocatalytic process of anodic methanol oxidation involves much more than proton transport. In fact, some other PtRu catalysts of stronger metallic character (lower RuOx content) as received seem to exhibit the highest electrocatalytic activity in polymer electrolyte DMFC anodes. As expected, such catalysts would require the addition of recast ionomer to the formulation to achieve the maximum activity of the anode catalyst layer.

CONCLUSION

When a component of the catalyst itself provides sufficient protonic conductivity, for example, RuO_x in PtRu catalysts, maximum DMFC anode performance can be achieved by reducing, or even eliminating, the recast ionomer in the catalyst layer. The optimal ionomer content in the PtRu anode catalyst layer will thus be a function of the RuO_x content of the catalyst and hence may vary with catalyst supplier and catalyst batch.

ACKNOWLEDGMENTS

This work was supported by the Defense Advanced Research Projects Agency through the Defense Sciences Office and by the U.S. Department of Energy through the Office of Transportation Technology. Acknowledgment is made to Kurt Sickafus for the use of his ultramicrotome and to the Electron Microscopy unit of Los Alamos National Laboratory for the use of the scanning electron microscope. Financial assistance to S.C.T. from the Natural Sciences and Engineering Research Council of Canada is also gratefully acknowledged.

REFERENCES

1. M. S. Wilson, and S. Gottesfeld, *J. Appl. Electrochem.*, **22**, 1 (1992).
2. X. Ren, M. S. Wilson, and S. Gottesfeld, *J. Electrochem. Soc.*, **143**, L12 (1996).
3. S. J. Lee, S. Mukerjee, J. mcBreen, Y. W. Rho, Y. T. Kho and T. H. Lee, *Electrochim. Acta*, **43**, 3693 (1998).
4. T. E. Springer, M. S. Wilson, and S. Gottesfeld, *J. Electrochem. Soc.*, **140**, 3513 (1993).
5. I. Raistrick, U.S. Pat. 4,876,115, (1989).
6. K. E. Swider, C. I. Merzbacher, P. L. Hagans, and D. R. Rolison, *Chemistry of Materials*, **9**, 1248 (1997).

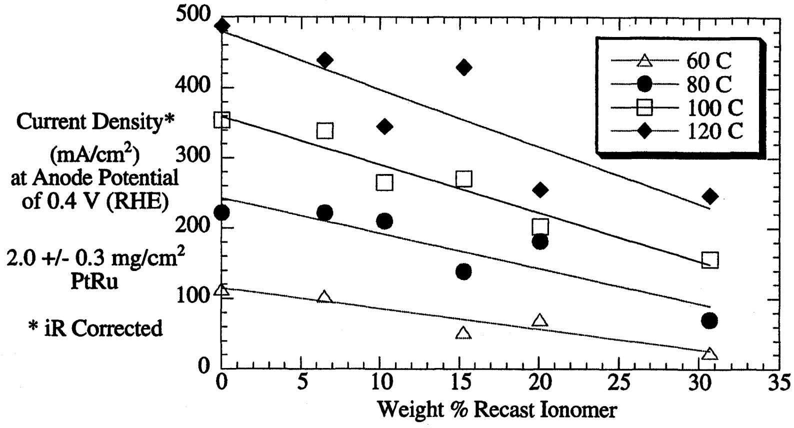

Figure 1 Effect of wt. % recast ionomer in the anode catalyst on iR corrected current density as a function of cell temperature. Anode: 1 mol/L methanol at 2 mL/min. with 0, 0, 20, and 40 psig back pressures at cell temperatures of 60°C, 80°C, 100°C and 120°C, respectively. Cathode: Humidified H_2 at 0.3 L/min. and back pressure of 15 psig.

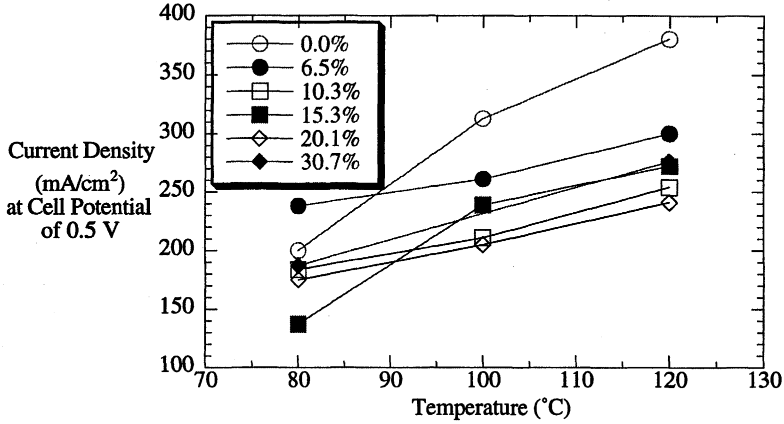

Figure 2 Effect of wt. % recast ionomer in the anode catalyst on non iR corrected DMFC current density at cell voltage of 0.5 V as a function of cell temperature. Anode: 1 mol/L methanol at 2 mL/min. with 0, 20, and 40 psig back pressures at cell temperatures of 80°C, 100°C and 120°C, respectively. Cathode: Air at 0.5 L/min. and 60 psig, humidified at 80°C at 80°C cell temperature and bypassed at cell temperatures of 100°C and 120°C.

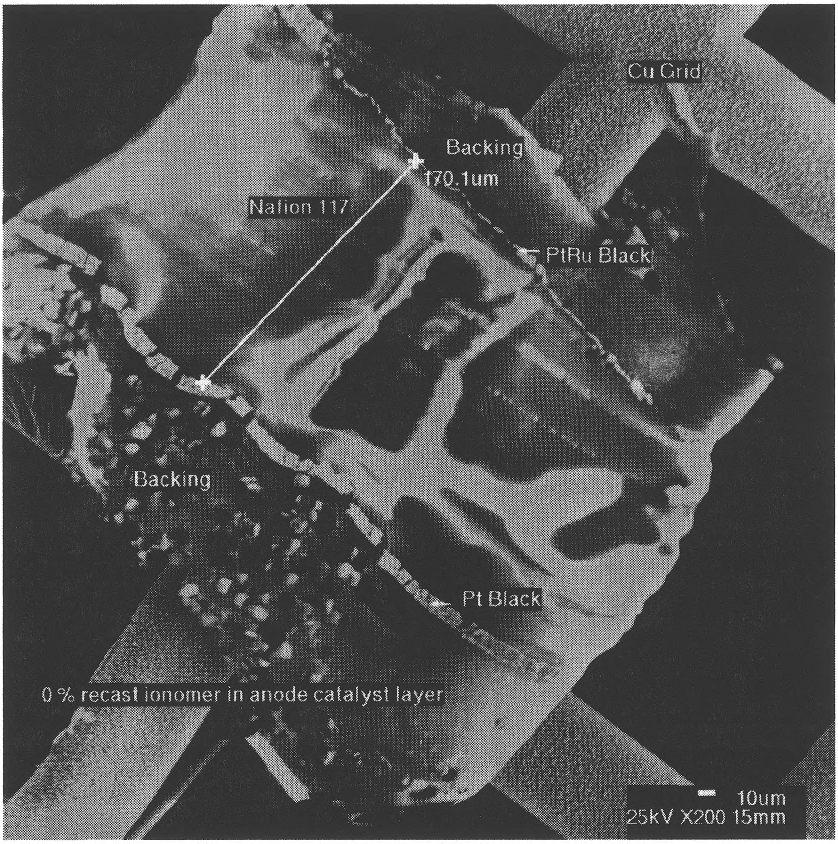

Figure 3 Scanning electron micrograph of a cross section of a membrane electrode assembly that has been previously used in a fuel cell with portions of backing on each side of the catalyst layers

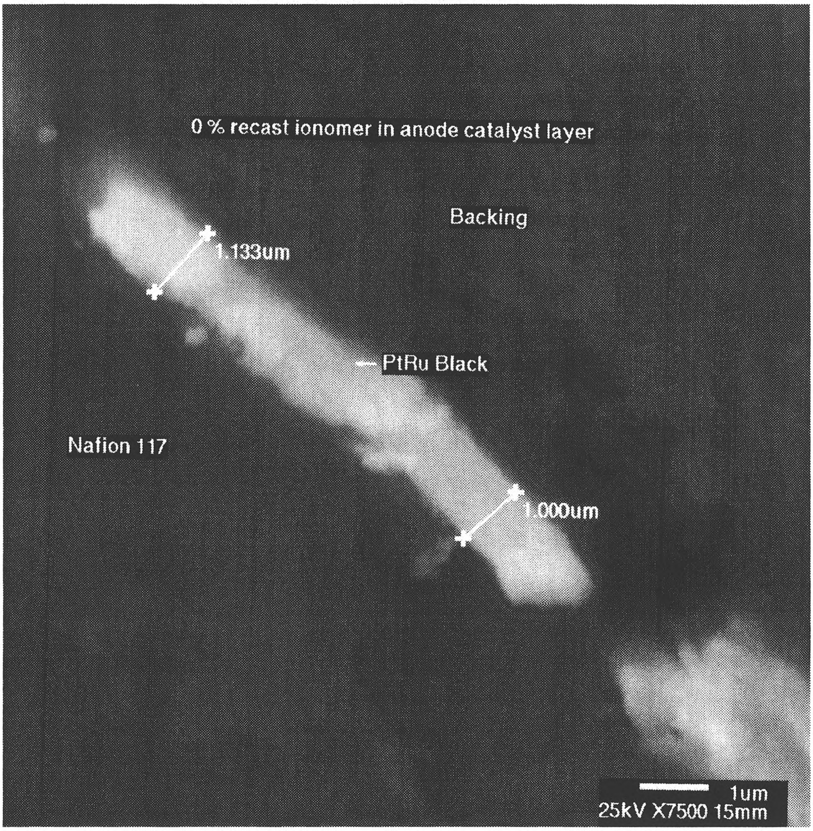

Figure 4 Scanning electron micrograph of PtRu anode catalyst layer containing no recast ionomer in the anode catalyst layer

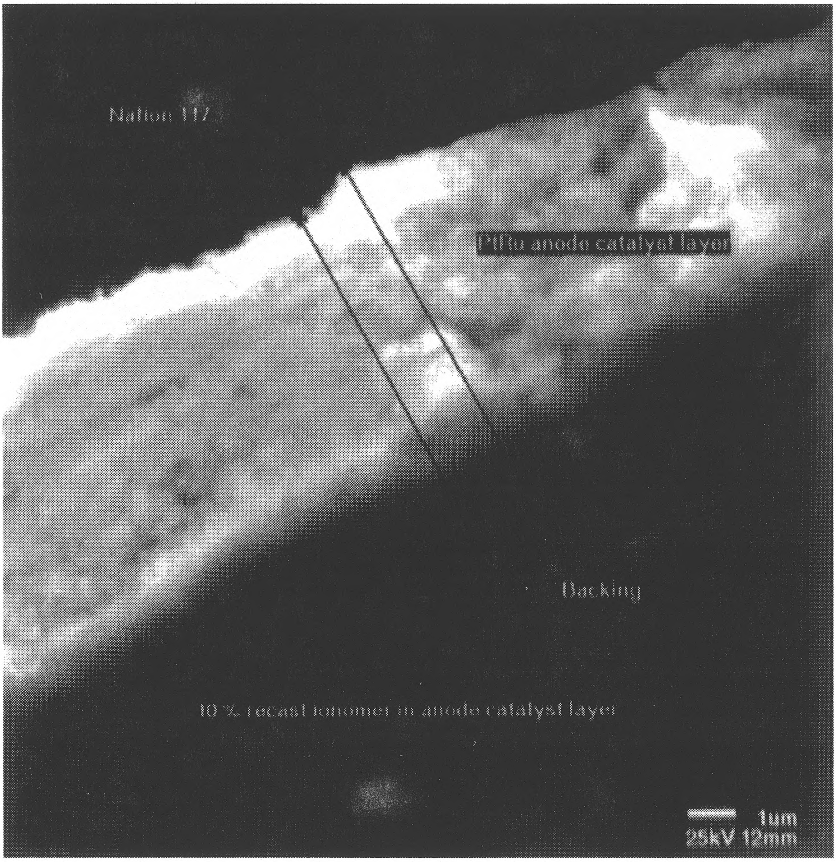

Figure 5 Scanning electron micrograph of PtRu anode catalyst layer containing 10.5 % recast ionomer in the anode catalyst layer

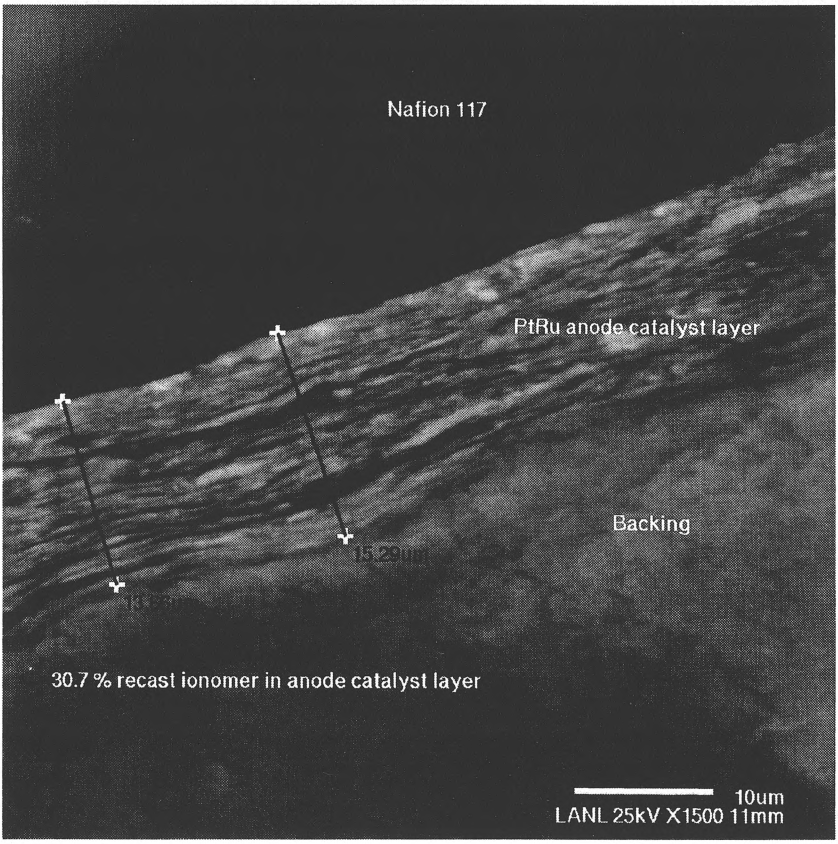

Figure 6 Scanning electron micrograph of PtRu anode catalyst layer containing 30.7 % recast ionomer in the anode catalyst layer

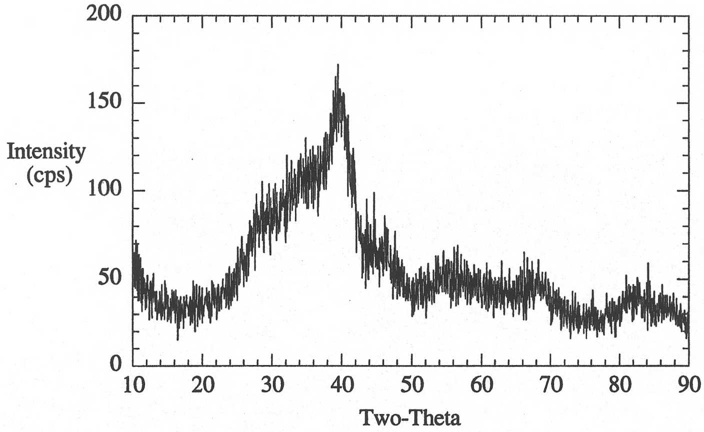

Figure 7 XRD spectrum of as-received E-TEK unsupported PtRu anode catalyst, RV3030

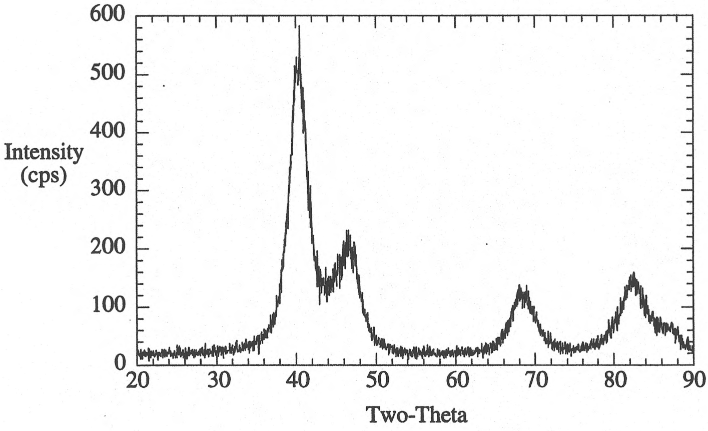

Figure 8 XRD spectrum of E-TEK unsupported PtRu anode catalyst, RV3030, after reduction with H_2.

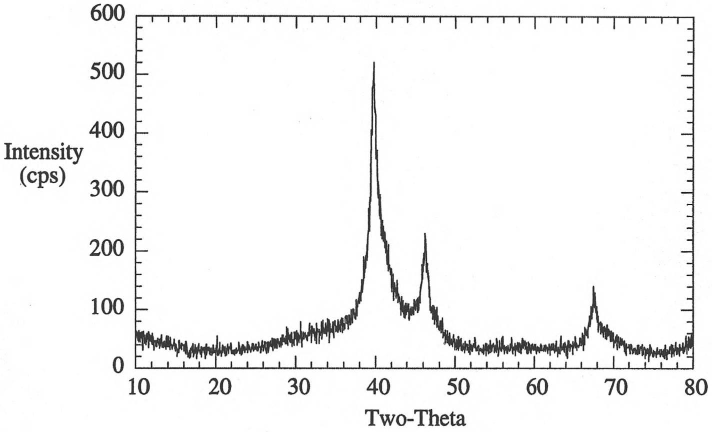

Figure 9 XRD spectrum of as-received Johnson Matthey unsupported PtRu anode catalyst

Proton_Conducting_Membrane_Fuel_Cells_II, PV 1998-27, 280-290 (1998)
DOI: 10.1149/199827.0280PV © The Electrochemical Society

Ceramic Supported Pt and Pt-Ru Catalysts for Methanol Oxidation

David J. Tarnowski, Cong Pu, John White, Michael R. Wixom, and Levi T. Thompson
T/J Technologies, Inc. 3850 Research Park Drive. Ann Arbor, MI 48108.

Introduction

Pt and Pt-Ru are the primary catalysts used for electrodes in direct methanol fuel cells (DMFCs). Noble metals are expensive, and present a significant cost barrier to commercially viable fuel cells. Dispersing these catalysts onto support materials has effectively reduced the noble metal loading required for fuel cell electrodes and reduced fuel cell costs. High surface area carbon has been the most popular fuel cell catalyst support material. While relatively stable, carbon serves only to disperse the noble metal catalysts. No catalytic activity is displayed by the carbon support material, either directly or indirectly, toward methanol oxidation. Additionally, the density of carbon is low, hence a large volume of supported catalyst is required for higher Pt loadings needed for high power density DMFCs. Large volumes of supported catalysts impose detrimental mass transport effects on fuel cell performance through necessarily thick catalyst layers and limit DMFC power densities (1, 2).

Transition metal oxides have shown catalytic activity toward methanol oxidation in concert with noble metal catalysts (3). However, high degrees of electronic resistance within the oxide contribute to larger ohmic potential losses (3). We address the need for improved anode electrocatalysts for use in DMFCs by dispersing Pt and Pt/Ru onto high surface area conducting ceramic supports. Our approach investigates the catalytic activity of noble metal catalysts dispersed onto the surface of high surface area metal carbide and metal nitride support materials (4). These supported catalysts possess high catalytic activities due to dispersed noble metal sites in intimate contact with the electronically conductive ceramic support materials. Further, the support materials studied in this work are 3-5 times more dense than carbon, which reduces mass transport effects that limit the power density of the anode. The use of noble metal catalysts supported on high surface area conductive ceramics should therefore be useful for improving the performance and cost of direct methanol fuel cells.

Experimental

Preparation of high surface area ceramic support materials-

High surface area carbide and nitride support materials were prepared by temperature programmed reactions (TPR) under controlled atmospheres (5). Precursors used were either oxide or metal amide/imide powders. Precursors were heated in a 1 inch diameter quartz tube positioned in a horizontal tube furnace. Reactant gas compositions and flow rates were controlled through a manifold of Tylan precision mass flow controllers. Results will be presented for two carbides and a nitride support material (see Table I). Support material phases and compositions are considered proprietary and will not be identified.

Table I. Metal Carbides and metal nitride used as noble metal support materials.

Support Material†	Reference Code	with Pt dispersion	with Pt-Ru dispersion
T/J Metal Carbide I	MC1	Pt/MC1	Pt-Ru/MC1
T/J Metal Carbide II	MC2	Pt/MC2	Pt-Ru/MC2
T/J Metal Nitride	MN1	Pt/MN1	Pt-Ru/MN1

† Reference codes do not imply material stoichiometry.

Noble metal dispersion onto ceramic support materials-

Small platinum clusters were dispersed onto the surface of the high surface area ceramic supports using methods similar to those described by Watanabe *et al.* (6,7,8). 200 mL of chloroplatinic acid (0.5% by weight in water) was converted to platinum sulfite acid by slowly mixing in ~ 4 g of sodium bisulphite. The solution was diluted to 700 mL and the pH was adjusted to 5.0 by adding 1 M sodium carbonate solution. Binary Pt/Ru catalysts were prepared in a similar manner, except Ru salts ($RuCl_3$) were dissolved in water and then added to the Pt precursor solution to a achieve the desired Pt:Ru ratio. Noble metal solutions were then converted to metastable oxide salts by slowly adding 30 wt % H_2O_2 while stirring. Solution pH was maintained at 5.0 by adding 1 M sodium carbonate solution when necessary. Noble metal particles were reduced onto the support materials by bubbling hydrogen gas through the solution overnight. The supported catalysts were collected and washed thoroughly with deionized water and then dried at 100°C.

Support materials characterization-

Support material phases and compositions were examined by x-ray diffraction using a Rigaku DMAX-B x-ray diffractometer with a Digital VAXstation II/GPX. Powder patterns were compared with existing x-ray diffraction files for identification. Surface areas were determined by single point BET using a Quantasorb Jr. Surface Area Analyzer with 29% N_2/He as adsorption gas and N_2 calibration gas. The weight % of noble metals in each supported catalyst was determined using atomic absorption spectroscopy. Prior to analysis, supported catalysts were dissolved in aqua regia and diluted to a known volume. Analyses were made with a Perkin Elmer 1100 B spectrometer.

Electrochemical measurements were made with the use of an EG&G Versastat Potentiostat/Galvanostat interfaced with a personal computer through an IEEE-488 interface board and run by M270 electrochemical software. Measurements were made in a three electrode glass cell with a Pt foil counter electrode and a reversible hydrogen electrode (RHE) in a separate compartment connected to the analyte through a ground glass frit and Luggin capillary. All experiments were run in 1.0 N H_2SO_4 at room temperature (23 ± 2°C). Solutions were purged of oxygen using argon gas unless otherwise stated. All voltages are reported vs. RHE.

Catalyst inks were prepared by mixing supported catalysts with Nafion (15% by weight, Nafion/catalyst) and diluting to an appropriate volume with isopropanol (9). Aliquots of ink were withdrawn with a micropipette and weighed after being allowed to dry. In this way the mass of solids per unit volume of ink was determined for each catalyst ink.

Electrochemical analyses were performed with carbon current collectors. Graphite rods (0.32 cm^2) were cleaned on abrasive paper, sonicated in 18 MΩ water to remove polishing debris, and air dried. Appropriate volumes of each ink were withdrawn with a micropipette and carefully placed on the end of the graphite rods and then cured at 120°C for 30 minutes. After curing, the barrel of each electrode was wrapped with Teflon tape to prevent any interference from the graphite rod.

Results and Discussion

Surface area analysis-

MC1 and MC2 were produced with BET surface areas of 90 m^2/g and 113 m^2/g, respectively. MN1 displayed surface areas exceeding 100 m^2/g. Surface areas were dependent on the precursors used and TPR profile followed. Pores of less than 10 nm were minimized in order to ensure adequate mass transfer of reactants to catalyst surfaces (10). Higher surface area support materials with pore size distributions optimized for DMFC applications will be produced in the future by further modifying reaction conditions.

X-ray diffraction-

Diffraction patterns for supported catalysts were highly dependent on the support material used. Noble metals dispersed onto MC1 generated no Pt diffraction patterns in conjunction with the diffraction pattern for the support material (see Figure 1). Subsequent electrochemical analysis, coupled with evidence from atomic absorption spectroscopy (vida infra), suggested that the noble metals were finely dispersed on the surface of MC1, either as Pt sites too small to be detected by x-ray diffraction, or as an amorphous species dispersed on the MC1 support (11).

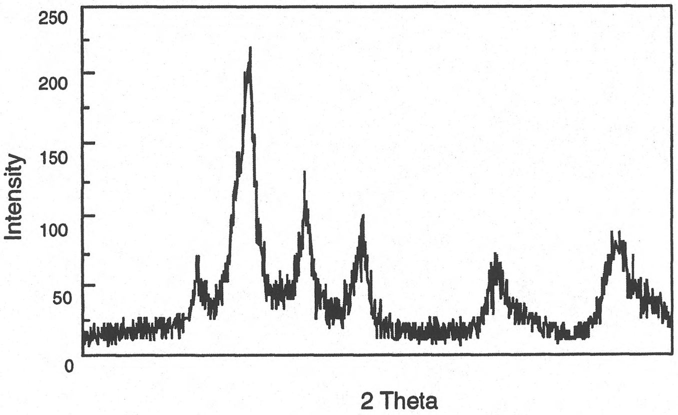

Figure 1. X-ray diffraction pattern for Pt/MC1. Pt particle size estimation impossible, possibly due to amorphous Pt or very small Pt domains.

The diffraction pattern for Pt/MN1 allowed for an estimation of Pt particle sizes of ~9 nm. Pt catalysts supported on MC2 exhibited noble metal particle sizes of ~6 nm. Diffraction patterns for MC2 and MN1 become less pronounced following Pt dispersion (see Figure 2). Changes in diffraction patterns following dispersion indicates structural changes in MC2 and MN1 during the dispersion processes.

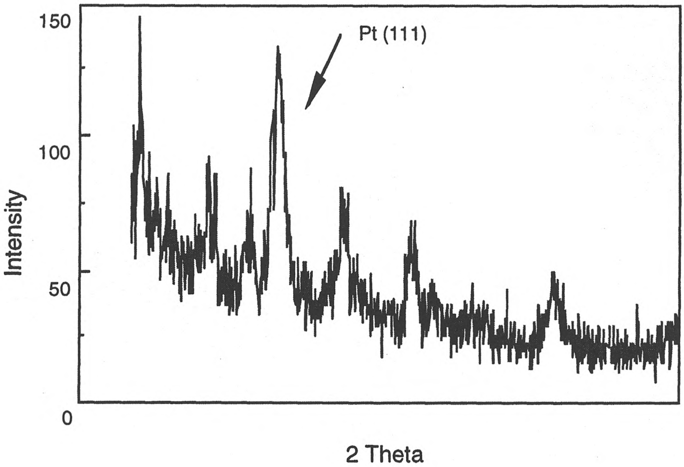

Figure 2. X-ray diffraction pattern for Pt/MC2. Pt particle size estimated to be ~6 nm.

Atomic absorption analysis-

Atomic absorption analysis confirmed that noble metals were successfully dispersed onto the high surface area carbide and nitride support materials. Pt weight percentages exceeding the expected value (Pt/MC2, Pt/MN1) suggest dissolution of support materials during the dispersion process.

Table II. Pt content of T/J supported catalysts.†

Catalyst Type	Pt Content (wt %)	Ru Content (wt %)
Pt/MC1	12	--
Pt-Ru/MC1	9	4.5
Pt/MC2	27	--
Pt/MN1	10	--

† Expected Pt content of 10 wt %.

Electrochemical Characterization-

Cyclic voltammetry performed on supported catalyst inks revealed differences in catalytic activity toward methanol oxidation. Catalyst activity depended highly on the support material used. The Pt/MN1 catalyst demonstrated a high electrochemical surface area with no distinct voltammetric features (Figure 3). Methanol oxidation occurred in a manner typical for Pt catalysts, oxidizing methanol on both positive-going and negative-going sweeps. Current densities for the Pt/MN1 catalyst were less than current densities observed for equivalently produced Pt/C catalysts. Differences in activity may be due to inaccessible Pt sites within the MN1 support following dispersion. Future research will examine the effects of alternative dispersion methods on catalyst performance.

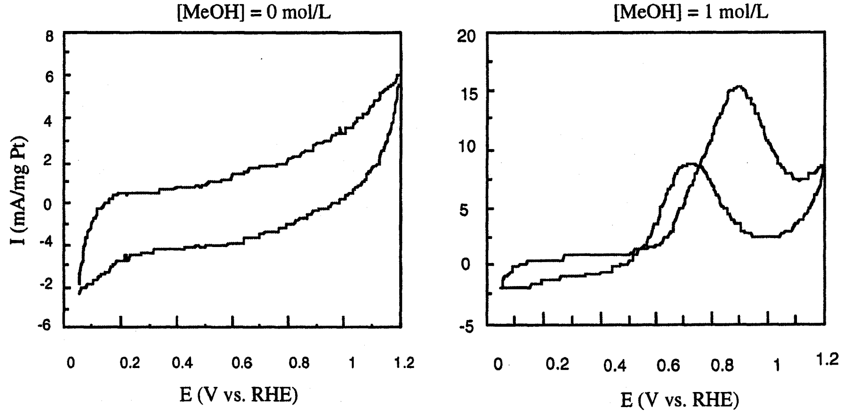

Figure 3. Cyclic voltammograms for the Pt/MN1 catalyst recorded at scan rates of 20 mV/s in 1 N H_2SO_4 with methanol concentrations of 0 mol/L and 1 mol/L. Currents are normalized by Pt content of catalyst (mA/mg Pt).

Platinum catalysts supported on MC2 displayed voltammetry indicating surface interactions between the carbide and noble metal domains (see Figure 4). Reversible waves observed in the potential region between 0.05 and 0.3 V suggested a high degree of hydrogen adsorption/desorption on this supported catalyst. The voltammetry in blank electrolyte differed significantly from the independent voltammetries of MC2 and Pt, indicating the electrochemical activity is due to the two species acting in concert. Methanol oxidation activity for the Pt/MC2 catalyst was comparable to Pt/C catalysts under equivalent conditions.

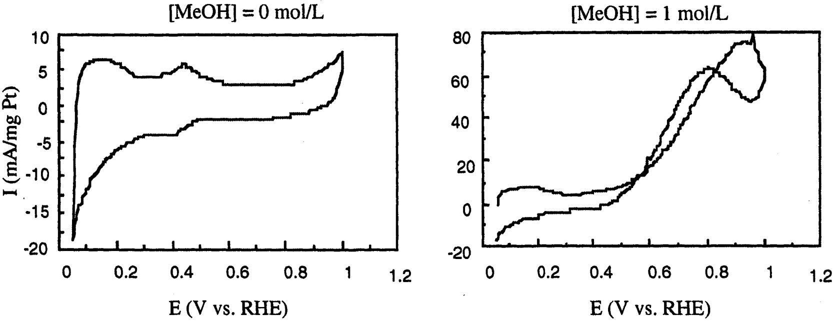

Figure 4. Cyclic voltammograms for the Pt/MC2 catalyst recorded at scan rates of 20 mV/s in 1 N H_2SO_4 with methanol concentrations of 0 mol/L and 1 mol/L. Currents are normalized by Pt content of catalyst (mA/mg Pt).

The most dramatic results were observed for the Pt/MC1 supported catalyst (see Figure 5). Blank voltammetry clearly indicated intimate surface interactions between the MC1 support and Pt particles in the hydrogen adsorption/desorption region. Waves due to Pt oxide formation and reduction were observed. The electrochemical surface area for this catalyst was high, supporting the assertion that Pt domains on this catalyst are small. The methanol oxidation activity for the Pt/MC1 catalyst was significantly higher than for equivalently produced Pt/C supported catalysts.

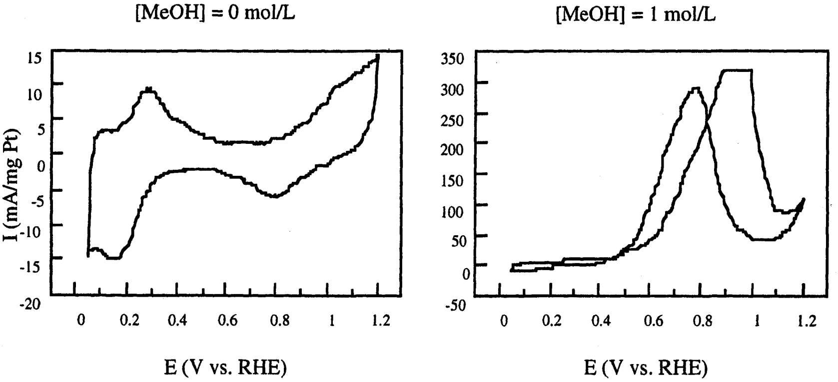

Figure 5. Cyclic voltammograms for the Pt/MC1 catalyst recorded at scan rates of 20 mV/s in 1 N H_2SO_4 with methanol concentrations of 0 mol/L and 1 mol/L. Currents are normalized by Pt content of catalyst (mA/mg Pt).

In addition to high catalytic activity, Pt/MC1 supported catalysts displayed tolerance to poisoning by CO during methanol oxidation. Three consecutive scans following dosing with methanol show a gradual shift in the overpotential for methanol oxidation at the Pt/MC1 catalyst (see Figure 6a). In contrast, Pt/C catalysts develop almost the full overpotential for methanol oxidation after only the first scan (Figure 6b). These results indicate MC1 promotes CO tolerance by Pt.

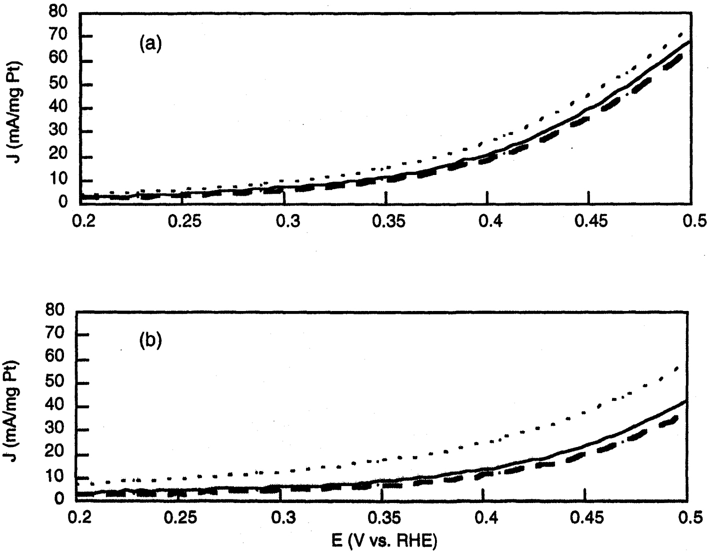

Figure 6. Cyclic voltammograms recorded at 25 mV/s for (a) Pt-MC1 and (b) Pt/C catalysts in oxygen-free solutions of 1 M methanol in 1 N H_2SO_4. First scans (·····) for each catalyst exhibit high activities. Scans 2 (—) and 3 (---) for the Pt/C catalyst (b) exhibit a large increase in overpotential for methanol oxidation, due to CO formation on Pt sites. The Pt-MC1 catalyst (a) displays only small changes in overpotential for scans 2 and 3, indicating catalyst tolerance to CO. Methanol oxidation activities (normalized to mA/mg Pt) for the Pt-MC1 catalyst are twice those observed for the equivalently produced Pt/C catalyst.

Further CO tolerance was imparted to the MC1 supported catalysts through the dispersion of Pt-Ru instead of pure Pt. Similar to Pt-MC1 supported catalysts, x-ray diffraction revealed no peaks due to Pt or Pt-Ru alloys on the surface of Pt-Ru/MC1 catalysts, despite the presence of noble metal sites confirmed by both voltammetry and atomic absorption spectroscopy. Figure 7 shows differences in voltammetry between Pt-MC1 and Pt-Ru/MC1 supported catalysts. Voltammograms recorded for both supported catalysts exhibit waves indicative of hydrogen adsorption/desorption between 0.05 V and 0.3 V vs. RHE. The Pt-Ru/MC1 supported catalyst showed reduction of Pt-oxides formed on the anodic sweep at a potential of ~100 mV cathodic of the Pt/MC1 supported catalyst, due to the lower potentials for oxide formation on Pt-Ru alloys.

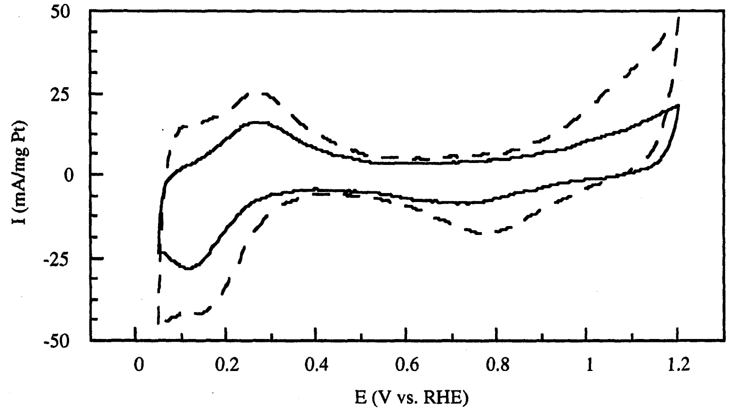

Figure 7. Cyclic voltammograms recorded at 20 mV/s in 1.0 N H_2SO_4. Data for Pt/MC1 (dashed line) and Pt-Ru/MC1 (solid line) catalysts shown. Peak positions for oxide reduction waves at 0.7 V and 0.8 V for the Pt-Ru and Pt supported catalysts, respectively, indicate a higher affinity of the Pt-Ru catalyst toward surface oxides.

A direct comparison of methanol oxidation activities was made between Pt-Ru/MC1 supported catalyst produced at TJ and Pt-Ru/C catalysts purchased from major catalyst suppliers. In these tests, catalyst activity was determined by chronoamperometric methods using the potential waveform shown in Figure 8. The pulsed potential waveform electrochemically cleans working electrodes prior to methanol oxidation, ensuring a clean and reproducible surface for each experiment. Similar potential waveforms are commonly used in studies of organic oxidation reactions (12). Initially the working electrode was pulsed to 1.1 V for 10 s. At this potential carbon monoxide and other passivating species deposited on the working electrode during previous experiments are oxidized to CO_2 and removed from the working electrode surface. The poison-free electrode was then pulsed to a potential of 0.05 V for 10 s. At this potential Pt oxides are reduced to metallic Pt, the species responsible for the adsorption and subsequent oxidation of methanol. Finally, the working electrode was pulsed to the potential of interest (E_2) for 60 s. Currents were recorded before and after the addition of methanol. Current differences obtained at the end of E_2 were used to determine methanol oxidation currents for each type of catalyst.

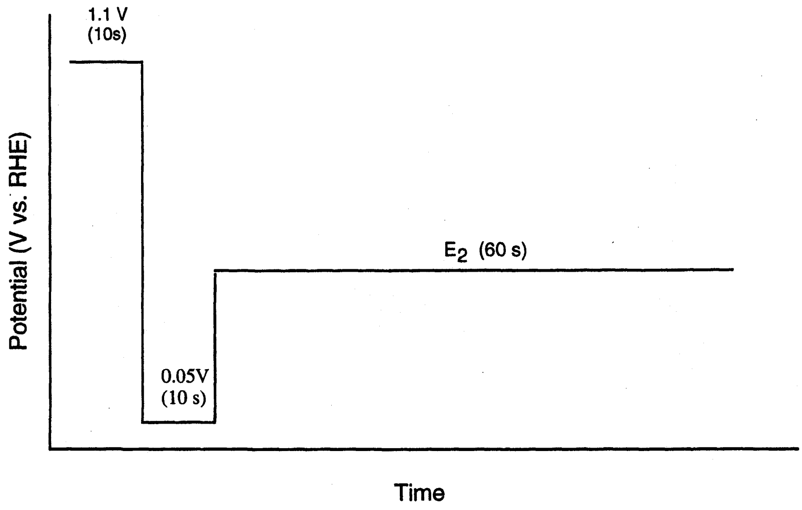

Figure 8. Schematic of the potential sequence used for chronoamperometric experiments.

Figure 9 shows Tafel plots constructed from current densities (normalized to mA/mg Pt) due to methanol oxidation at Pt-Ru/MC1 and two commercially available Pt-Ru/C supported catalysts. At potentials below 0.4 V, the Pt-Ru/MC1 supported catalyst produced at T/J Technologies is significantly more active than either of the Pt-Ru/C supported catalysts. We believe this is due to the greater dispersion of noble metals on the MC1 surface and promotion of Pt activity by the support material. At potentials greater than 0.4 V, the Pt-Ru/MC1 supported catalyst maintains activities equal to or slightly less than those observed for the carbon supported catalysts.

Future research will examine the activity of Pt-Ru/MC1 catalysts as functions of temperature and Pt:Ru ratio. Pt-Ru black and carbon supported Pt-Ru realize an optimum level of methanol oxidation activity for an atomic ratio of 1:1 Pt:Ru at elevated temperatures. The catalytic promotion of Pt activity by the MC1 support, as well as a degree of CO tolerance, may make it possible to increase the Pt-Ru ratio for noble metals dispersed on MC1 supports. A higher Pt:Ru ratio is desirable, since Ru serves only to facilitate the oxidation of CO from Pt surfaces, and does not participate directly in methanol oxidation. Minimizing the amount of Ru will increase Pt site density and overall catalyst activity.

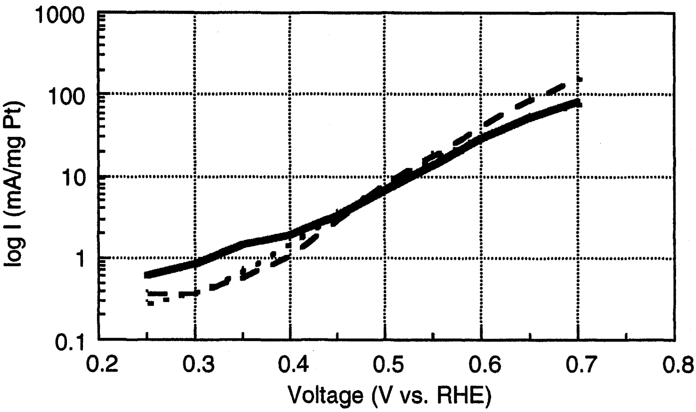

Figure 9. Tafel plots for the oxidation of 1 M MeOH in 1 N H_2SO_4. Catalysts composed of 15% Nafion inks on glassy carbon electrodes. — Non-optimized T/J Pt-Ru-Carbide I (6.7% Pt). ······ Purchased Pt-Ru/C catalyst (20% Pt). ----- Purchased Pt-Ru-C (10 % Pt). Methanol oxidation activity of the T/J catalyst is greater than the activity of either of the carbon supported catalysts for E< 0.45 V, the potential region most desirable for DMFC anode operation.

A further advantage conducting ceramic supports have over carbon supports is a higher density. Higher density support materials enable greater amounts of catalyst (mg catalyst/cm^2) to be used without imposing diffusion limitations on electrode performance due to catalyst layer thickness. Experiments indicate diffusion limitations within the catalysts layer are less with the use of noble metal catalysts supported on MC1 than for carbon supported catalysts. Further experiments will determine the electrode loadings possible without significant loss of performance due to diffusion limitations.

Conclusions

The catalytic promotion of noble metal catalyst activity toward methanol oxidation by high surface area conducting ceramic support materials has been demonstrated. Catalyst activity depends strongly on the composition of the ceramic support material. T/J Technologies has developed a carbide support material (MC1) upon which noble metal dispersion is very high, and support sites promote the activity of Pt. High catalytic activities toward methanol oxidation were displayed by the Pt/MC1 supported catalyst, due to high dispersion of Pt sites. MC1 was also observed to promote CO tolerance in the Pt supported catalyst. Tests with Pt-Ru/MC1 supported catalyst indicate greater CO tolerance than observed for Pt/MC1. The higher density of MC1 allows greater catalyst loadings to be applied without imposing diffusion limitations on DMFC anode performance. Hence, a highly active (mA/mg Pt) supported catalyst can be applied with sufficient noble metal loadings (mg Pt/cm^2) to produce direct methanol fuel cells with higher power densities than are currently possible using carbon supported catalysts.

Acknowledgment

We gratefully acknowledge support by grants from the United States Department of Energy DE-FG02-97ER82494 and the National Science Foundation DMI-9660664 through the Small Business Innovation Research program. We also thank Professor Eugene Smotkin at Illinois Institute of Technology and Professor Robert Savinell at Case Western Reserve University for their technical assitance and consultation during this research.

References

1. C. Pu, E.S. Smotkin, R. Liu, and Q. Fan, in The 192nd Meeting of the Electrochem. Soc. no 77, Paris, 1997.
2. X. Ren, M.S. Wilson, and S. Gottesfeld, *J. Electrochem. Soc.* **143**, L12 (1996).
3. P.K. Shen and C.C. Tseung. *J. Electrochem. Soc.* **141**, 3082 (1994).
4. C. Pu, M.R. Wixom, and L.T. Thompson, U.S. Provisional Patent Application 60/075,541 (1998).
5. L.T. Thompson, M.R. Wixom, and J. M. Parker, U.S. Patent 5,680,292 (1997).
6. M. Watanabe, K. Makita, H Uami, and S. Motoo, *J. Eletroanal. Chem.*, **197**, 195 (1986).
7. M. Watanabe, M. Uchida, and S. Motoo, *J. Electroanal. Chem.*, **229**, 395 (1987).
8. M. Watanabe, S. Sawgusa, and P. Stonehart, *J. Electroanal. Chem.*, **271**, 213 (1989).
9. M.S. Wilson and S. Gottesfeld, *J. Electrochem. Soc.*, **1**, 22, (1992).
10. M. Uchida, Y. Fukuoka, Y. Sugawara, N. Eda, and A. Ohta, *J. Electrochem. Soc.*, **143** 2245 (1996).
11. C. He, H.R. Kunz, and J.M. Fenton, *J. Electrochem. Soc.*, **144** , 970 (1997).
12. D.J. Tarnowski and C. Korzeniewski, *Anal Chim Acta*, **332**, 111 (1996).

Proton_Conducting_Membrane_Fuel_Cells_II, PV 1998-27, 291-299 (1998)
DOI: 10.1149/199827.0291PV © The Electrochemical Society

SCREENING BINARY AND TERNARY CATALYST FORMULATIONS FOR DIRECT-METHANOL-PEM FUEL CELLS

M. Götz, H. Wendt, Institute for Chemical Technology , Technical Universtiy Darmstadt,
Petersenstrasse 20, 64287 Darmstadt, Germany

Abstract

In an exploratory approach binary and ternary nanodisperse alloy catalysts were synthesized containing the elements Pt, Ru and W, Mo or Sn, respectively. The catalysts were prepared applying a colloid method developed by Bönnemann, which was found to be highly suitable for synthesizing this kind of supported catalyst, as determined by TEM, EDX and electrochemical measurements. The catalysts were tested for their activity towards anodic oxidation of H_2/CO-mixtures and methanol in PEM single cells. It turned out that for H_2/CO oxidation, the systems Pt/Ru/W and - at higher overpotentials -Pt/Ru/Sn were the most active systems, for methanol oxidation again Pt/Ru/W was the most active system. By varying the molar composition of the system Pt/Ru/W it was found that both for oxidation of H_2/CO and methanol the most active system tested was a ternary catalyst with a molar ratio Pt/Ru/W of 1/1/1,5.

In another series of experiments the cocatalytic activity of some transition metal phtalocyanine complexes was investigated. It turned out that none of the systems tested had a beneficial effect on oxidation of H_2/CO, for methanol oxidation the systems Pt/Cobaltphtalocyanine and Pt/Nickelphtalocyaninetetrasulfonic acid showed a cocatalytic activtiy. For Pt/Nickelphtalocyaninetetrasulfonic acid, the effect can still be enhanced by pyrolyzing the complex.

Furthermore, a pre-screening method for methanol oxidation is introduced which makes it possible to test a number of electrocatalyst systems at the same time using graphite model electrodes which are covered with a thin layer of catalyst and ionomer.

Introduction

Although today the car manufacturers have apparently focused on the indirect methanol fuel cell system, the long term aim is to avoid the chemical factory in the car and use a direct methanol system for PEM driven cars. However, with established Pt/Ru anode catalysts acceptable power densities of DMFCs can only be achieved with relatively high noble metal loadings of several mg cm^{-2} that are economically unacceptable. Therefore new catalyst systems are essential for the viability of the direct methanol fuel cell concept.

Apart from ruthenium, cocatalytic effects have also been reported for a number of other elements if they are used together with Platinum, such as S, Se, Te, Sb, Ir, Os[1], W[2], Mo[3], Sn[4], Pb[5] and others. Almost all these investigations have been performed in liquid electrolyte and with bulk electrodes, with the cocatalyst either being alloyed with platinum or present as an adsorbate layer on the electrode surface. Therefore it had to be investigated whether the reported effects also occur in the case of highly dispersed, carbon-supported catalysts and if these systems are stable in the corrosive matrix of the ion-exchange polymer at the potentials of the DMFC anode. As W, Sn, and Mo seemed to be the most promising cocatalyst-candidates, we mainly focused on these elements. Furthermore it was our intention to find out whether the catalytic activity of the system Pt/Ru could be further improved by formulating ternary catalyst systems with the respective elements.

The system Pt/W has repeatedly been subject to research. Cocatalytic effects for both methanol oxidation [6] and oxidation of H_2/CO [7], [8], are reported for this system, although the effects are not as strong as in the case of ruthenium. At the actual working potential of the anode it seems likely that tungsten is active as a redox catalyst which is present in an oxidized state written as WO_{3-x}, possibly a tungsten bronze. The cocatalytic activity is supposed to be due to a rapid change in the oxidation state of W, involving the redox couples W(VI)/W(IV) [9] or W(V)/W(VI) [10], respectively. This redox activity renders active sites for the dissociative adsorption of water and for the oxidation of adsorbed hydrogen generated by dehydrogenation of methanol.

In case of tin as cocatalyst the results are less consistent. For anodic oxidation of H_2/CO the positive effect of tin has been confirmed several times [11] and usually is explained by the activity of tin for dissociative adsorption of water. In contrast to ruthenium, tin does not adsorb CO and thus cannot be poisoned by it [12]. Concerning the effect of tin for anodic methanol oxidation, a number of contradictory results have been published, ranging from a huge enhancement to a strong decrease of catalytic activity [13], [14], [15], [16], [17]. In the more recent literature cocatalytic activity of Sn could not be confirmed for methanol electrooxidation.

Little has been published on the effect of molybdenum. Shropshire found an increase in activity of Pt for methanol oxidation in H_2SO_4 when Na_2MoO_4 was present as an adsorbate on the electrode surface [3]. Like tungsten molybdenum is known to form bronzes which seem likely to be responsible for the cocatalytic activity of Mo. Kita et al. confirmed this effect, claiming that the redox couple Mo(IV)/Mo(III) is responsible for the cocatalytic activity [18]. However, in contrast to Shropshire et al. they could not find Mo(VI) as catalytically active species. In rotating disc electrode experiments using an unsupported $Pt_{0,75}Mo_{0,25}$ alloy in H_2SO_4 Grgur et al. found an activity comparable to that of a $Pt_{50}Ru_{50}$ alloy electrode for oxidation of H_2 containing 100 ppm of CO [19].

The phtalocyanines have been intensively investigated because of their activity for cathodic oxygen reduction, but little is known about their catalytic activites for anodic reactions. Only for one structural relative of the phtalocyanines - cobalt-dihydrodibenzotetraazaannulene - an activity for anodic oxidation of formic acid, oxalic acid, hydrazine and also quite low activity for oxidation of formaldehyde and CO in sulfuric acid was reported. In contrast to this, no activity had been found when cobalt-phtalocyanine was used as electrocatalyst for these and other anodic reactions [20], [21]. For oxygen reduction it is known that a catalyst with enhanced activity and stability is obtained when phtalocyanines are pyrolyzed at moderate temperatures of 500 to 800 °C. It is believed that after this heat treatment isolated metal sites coordinated by a thermally modified ligand are formed on the surface of the carbon suppot besides a small amount of metallic particles [22].

All these different approaches had to be verified and further investigated with active carbon as catalyst support under real fuel cell conditions.

Experimental

Preparation of catalysts and MEAs

For the binary and ternary alloy catalysts, a synthesis method developed by Bönnemann and coworkers [23] was used in a slightly modified form. The respective metal chlorides are dissolved, or suspended, respectively, in tetrahydrofuran and then treated with an appropriate amount of a solution of tetraoctylammoniumhydrotriethylborate. This leads to formation of colloidal metal solutions from which the metal particles can easily be adsorbed on active carbon - in this case Vulcan XC-72 - to prepare supported catalysts. To get rid of the tetraoctylammonium ions on the surface the supported catalysts are suspended in ethanol, refluxed for 2 hrs, filtered off and dried at room temperature. Unless otherwise noted, the molar composition of these catalysts is 1/1 or 1/1/1, respectively.

In case of the catalysts containing transition metal complexes a commercially available carbon-supported Pt catalyst (E-TEK, 20% Pt-loading), was suspended in a solution of the respective complex in an appropriate solvent and stirred for 12 hrs. Then the solvent is destilled off. In some cases, the catalyst was heat-treated for 2 hrs at 700 °C in a nitrogen atmosphere. The molar ratio Pt/Co or Pt/Ni, respectively, was 5/1.

MEAs are manufactured by a spraying method developed at our laboratory which is based on the method of Gottesfeld and described elsewhere [24]. Usually catalysts with a metal loading of 20 % were used, the noble metal loading of each electrode was 0,4 mg cm^{-2}. Cathode catalyst was a Pt catalyst (20% on VucanXC-72) supplied by E-TEK.

Catalysts were morphologically characterized by TEM and their chemical composition analyzed by EDX.

Pre-screening method

The setup for the pre-screening experiments consists of a PTFE-beaker containing the electrolyte (1 mol/l methanol in 0,5 mol/l sulfuric acid or phosphoric acid, respectively). In the PTFE lid eight working electrodes, reference and counter electrode, a gas inlet for argon purge and a gas outlet with reflux condenser are inserted. The working electrodes are made of graphite, are 8 mm in diameter and 130 mm in length. A graphite screen (diameter 45 mm, thickness 0,5 mm) is used as counter electrode and a reversible hydrogen electrode as reference. The solution is magnetically stirred and can be thermostated to temperatures up to 100°C. For preparation of the working electrodes, a small amount of the carbon supported catalyst is suspended in a suitable liquid and a defined drop of this suspension is put on the electrode surface. Typically 0,5 mg of a 20 % metal on carbon catalyst are used, leading to a noble metal loading of 0,2 mg/cm^2. The catalyst is fixed on the electrode surface with a drop of dissolved ionomer. For this purpose either Nafion© or other ionomers such as S-PSU and S-PEEK are used.

This setup has the advantage that in each experiment eight different catalyst formulations can be tested in parallel and thus numerous longer term investigations can easily be performed simultaneously, although only in the so-called liquid methanol mode. The whole multielectrode assembly can be operated galvanostatically or potentiostatically.

Screening Measurements in MEAs

To ensure the relevance of the electrode kinetic results, membrane-electrode asemblies (MEAs) with an active electrode area of 25 cm^2 were manufactured with the catalysts, using Nafion© 117 membranes and Nafion© solution for manufacturing the electrodes. The MEAs were fitted into a commercially available graphite cell block (supplied by Electrochem inc.) and operated with hydrogen containing 150 ppm of CO to simulate reformate gas, or with evaporated 1 molar aqueous methanol solution, respectively. Cathode gas was oxygen in both cases. Cell temperature for operation on H_2/CO was 75°C, for DMFC operation 95°C. The current voltage curves of the different cells were compared, giving a direct indication of the electrocatalytic activity of the anode catalyst, as the cathode was always prepared in the same manner using the same catalyst. Current voltage curves were recorded after 14 days of continious cell operation. However, it turned out that this method of testing takes too long to screen a large number of catalysts in a short time. Therefore the pre-screening method described above was developed for evaluating the most promising catalysts, which were then tested in MEAs.

Results

TEM and EDX analysis of the colloid catalysts

Bönnemann et al.reported that in case of the binary systems Pt/Ru and Pt/Rh nanodisperse alloys can be achieved using his synthesis method [23], [25]. Applying this procedure binary and ternary colloids of a quite narrow particle size distribution with a mean particle size of about 2-3 nm as determined by TEM were synthesized, as can be seen in fig.1. EDX analysis showed that the molar composition of the catalyst was locally homogenous over each sample. Therefore in case of the ternary systems the formation of a ternary alloy phase seems likely, but as the spot size of the TEM is 20 nm in diameter no single particles could be examined, so no definite claim can be made concerning the composition of each particle.

Fig. 1: TEM micrograph of a Pt/Ru/W catalyst synthesized by the colloid method

Electrochemical measurements

Bi- and Trimetallic Catalysts

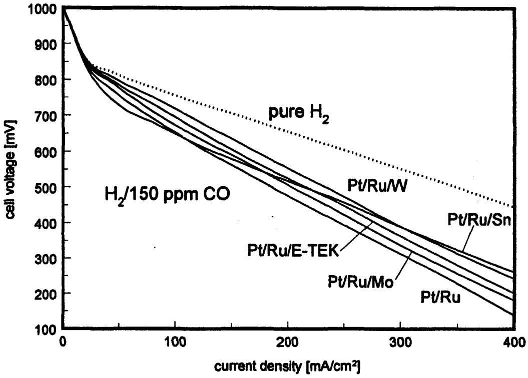

Fig. 2: Current voltage curves of cells with binary and ternary anode catalysts operated on H_2/CO

Fig.2 shows the current-voltage curves of cells manufactured with alloy catalysts in operation with H_2 containing 150 ppm of CO to simulate reformate gas. A Pt/Ru catalyst synthesized by the Bönnemann method and a commercially available Pt/Ru catalyst (E-TEK) were used as reference systems. It can be seen that in operation on H_2/CO the ternary systems Pt/Ru/W, Pt/Ru/Mo and - at current densities higher than 200 mA cm^{-2} - also the system Pt/Ru/Sn are superior to a binary Pt/Ru catalyst synthesized by the same method. The Pt/Ru/W catalyst and - at current densities higher than 220 mA cm^{-2} - the Pt/Ru/Sn catalyst are even superior to the commercially availble Pt/Ru catalyst in this mode of operation.

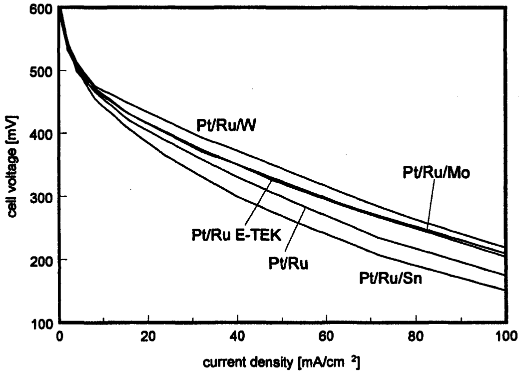

Fig. 3: Current voltage cures of cells with binary and ternary anode catalysts operated on methanol

Current voltage curves for operation on methanol are shown in fig. 3. It can be seen that in this case again the Pt/Ru/W catalyst is the most active system, followed by Pt/Ru/Mo and Pt/Ru (E-TEK) which exhibit about the same activity. The selfmade Pt/Ru and especially the Pt/Ru/Sn catalysts are considerably less active.

As the ternary catalyst Pt/Ru/W (with a molar ratio Pt/Ru/W of 1/1/1) turned out to be the most active of the ternary systems the molar composition was varied to find out whether further improvements could be achieved. Fig 4 shows the results for operation of these cells with H_2/150 ppm CO, fig. 5 for operation on methanol. In both series of experiments it turns out that the most active system tested has a molar ratio Pt/Ru/W of 1/1/1,5. Further increasing the tungsten content - demonstrated by the system Pt/Ru/W 1/1/2 - leads to a considerable decrease in catalyst activity for oxidation of H_2/CO as well as for methanol oxidation.

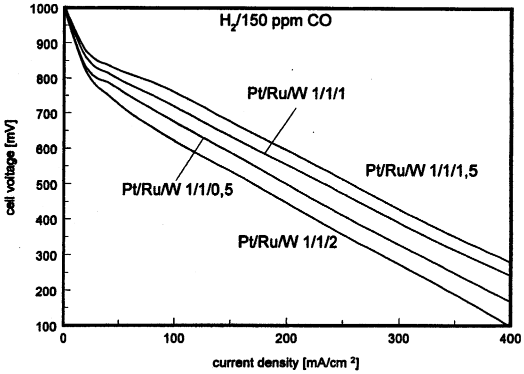

Fig. 4: Current voltage curves of cells with Pt/Ru/W anode catalysts operated on H_2/CO

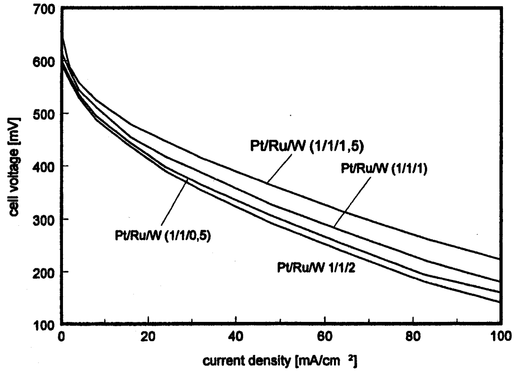

Fig. 5: Current voltage curves of cells with Pt/Ru/W anode catalysts operated on methanol

For the catalysts containing transition metal phtalocyanines the current voltage curves for operation on methanol are shown in fig. 6.

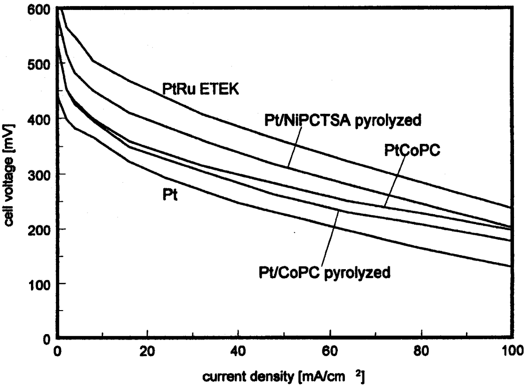

Fig. 6: Current voltage curves of cells with binary Pt/transition metal phtalocyanine catalysts in operation on methanol
(PC = phtalocyanine,
PCTSA = phtalocyanine-tetrasulfonic acid)

Curves for oxidation of H_2/CO are not included as no increase in activity could be achieved for this mode of operation.

From the complexes tested as cocatalysts - which were phtalocyanines of iron, cobalt, manganese, copper, vanadium, cobalt and nickel (in the form of Nickelphtalocyaninetetrasulfonic acid) - only the nickel and cobalt complexes showed a cocatalytic activity. Therefore, we only included these results in fig. 5. It can be seen that both complexes improve the catalytic activity of the Pt catalyst. In case of nickel complex heat treatment at 700°C in N_2 turned out to beneficial for the activity, but has the opposite effect on the cobalt complex.

Discussion

Pt/Ru

It turned out that a binary Pt/Ru catalyst manufactured by the colloid method is somewhat less active than a commercially available E-TEK catalyst of the same composition. Most likely this is due to the slightly higher particle size in case of the colloid catalyst, leading to a decreased active surface and thus decreased catalyst activity. As shown by Bönnemann et al. it is possible to synthesize Pt/Ru colloids of a smaller particle size using this method [25], which should lead to an increased activity.

Pt/Ru/Sn

A possible explanation that for tin there is a cocatalytic activity for CO-oxidation and no activity for methanol oxidation - which also involves poisoning of the platinum surface by strongly adsorbed CO - is given by Wang et al. by postulating that CO adsorbates generated by CO adsorption on Pt are of a different chemical nature than adsorbates generated by dehydrogenation of methanol [26]. Furthermore it can be seen from the current voltage curves in fig. 1 that the beneficial effect of tin becomes significant only at relatively high current densities, i.e. at high overpotentials. Possibly in case of the direct methanol fuel cell the anode potential is in a region in which tin is not active as cocatalyst.

Pt/Ru/Mo

The formulation of a ternary system containing molybdenum leads to an increased activity compared to the binary Pt/Ru catalyst both for oxidation of H_2/CO and methanol. It is believed that this cocatalytic activity is due to a rapid change of the oxidation state of Mo - possibly involving the formation of molybdenum bronzes - providing an oxygen-containing species for oxidation of the CO adsorbate.

Pt/Ru/W

A ternary catalyst containing Pt, Ru and W turned out to be the most active system both for oxidation of methanol and H_2/CO. It also can be seen that the optimum tungsten content must be close to a ratio Pt/W of 1/1,5 if Pt/Ru is 1/1. However, more experiments must be performed to find the optimum composition.

Phtalocyanine Complexes

No definite explanation can be given for the cocatalytic activity of cobaltphtalocyanine, nickelphtalocyaninetetrasulfonic acid and the catalyst obtained from pyrolysis of the latter. However, as both metals can easily be oxidized it appears possible that these systems are active for the dissociative adsorption of water. As a beneficial effect is only shown for methanol oxidation it seems possible that the anode potential of a PEMFC operated on H_2/CO is not in the correct potential range for these effects. However, the adsorption of the relatively large phtalocyanine complexes on the supported platinum catalyst might not be the best method for synthesizing these catalysts, as a part of the platinum is inevitably covered by the complex. Better results can be expected by treating the carbon support with the complexes before adsorbing the noble metal compounds. Possibly the decrease in activity of the Pt/CoPC catalyst upon pyrolyzing the complex is due to evaporation of the complex; therefore, the experiment is to be repeated with cobaltphtalocyaninetetrasulfonic acid, which is expected to withstand evaporation at the temperature of the heat treatment.

Conclusion

This investigation showed that nanodisperse, ternary phases of a suitable particle size for fuel cell purposes can be achieved by using the colloid method developed by Bönnemann. Furthermore it turned out that for oxidation of H_2/CO as well as for methanol oxidation the cocatalytic effects of Ru and a second transition metal are additive to a certain extent and thus more active systems than Pt/Ru can be synthesized by formulating ternary catalysts, best being Pt/Ru/W. For a Pt/Ru molar ratio of 1/1 the optimum Pt/W ratio was found to be close to 1/1,5. However, it is not sure nor likely that in case of ternary systems the optimum Pt/Ru ratio is 1/1, thus more systems with different Pt/Ru ratios have to be investigated. It must also be kept in mind that all effects found are still too weak, bringing about a considerable enhancement in catalyst activity but not a real breakthough in anodic CO- or methanol oxidation. From a number of transition metal phtalocyanine complexes that were investigated only cobaltphtalocyanine and nickelphtalocyaninetetrasulfonic acid exhibited cocatalytic effects, the activity of the latter being considerably enhanced by pyrolysis of the complex.

Acknowledgment
The authors want to thank Dr. Eigenberger and Dr. Kerres from the ICVT at Stuttgart for providing S-PEEK and S-PSU. The authors also thank the Bundesministerium für Wirtschaft and the Dechema e.V for financial support of this work which was part of the AIF project (AIF-Nr. 11032).

References

[1] G. Sandstede ed., *From Electrocatalysis to fuel cells*, University of Washington Press, Seattle, London, 1971.

[2] P.K. Shen, A.C.C. Tseung, *J. Electrochem. Soc.* **141** (1994), 3082-3090.

[3] J.A. Shropshire, *J. Electrochem. Soc.* **112** (1965), 465-469.

[4] M.M.P.Janssen, J. Moolhuysen, *Electrochim. Acta* **21** (1976), 861-868.

[5] B. Beden, F. Kadirgan, C. Lamy, J.M. Leger, *J. Electroanal. Chem.* **127** (1981) 75-85.

[6] P.K. Shen, A.C.C. Tseung, *J. Electrochem. Soc* **141** (1994), 3082-3090.

[7] K.Y. Shen, P.K. Shen, A.C.C. Tseung, *J. Electrochemical Society* **142** (1995), L185-L187.

[8] P.K. Shen, K.Y. Shen, A.C.C. Tseung, *J. Electrochem. Soc.* **142** (1995), L85-L86.

[9] A.K. Shukla, M.K. Ravikumar, A.S. Aricò, G. Candiano, V. Antonucci, N. Giordano, A. Hamnett, *J. Appl. Electrochem.* **25** (1995), 528-532.

[10] K. Machida, M. Enyo, G. Adachi, J. Shiokawa, *J. Electrochem. Soc.* **135** (1988), 1955-1961.

[11] Y. Morimoto, E.B. Yeager, *J. Electroanal. Chem.* **441** (1998), 77-81.

[12] H. A. Gasteiger, N.M. Markovic, P.N. Ross, Jr., *J Phys. Chem.* **99** (1995), 8945-8949.

[13] K.J. Clathro, *J. Electrochem. Soc.* **116** (1969), 1608-1611.

[14] M.M. Janssen, J. Moolhuysen, *J. Catal.* **46** (1977), 289-296.

[15] M. Watanabe, Y. Furuchi, S. Motoo, *J. Electroanal. Chem.* **191**(1985), 367-375.

[16] T. Frelink, W. Visscher, J.A.R. van Veen, *Electrochim. Acta* **39**(1994), 1871-1875.

[17] A.N. Haner, P.N. Ross, *J. Phys. Chem.* **95**(1991), 3740-3746.

[18] J. Wang, H. Nakajiama, H. Kita, *Electrochim. Acta* **35** (1990), 323-328.

[19] B.N. Grgur, G. Zhuang, N.M. Marcovich, P.N. Ross, Jr. , *J. Phys. Chem. B* **101** (1997), 3910-3913.

[20] H. Jahnke, M. Schönborn, G. Zimmermann in *Topics in current chemistry* **61**, Springer Verlag Heidelberg 1976, 133-181.

[21] H. Jahnke, M. Schönborn, G. Zimmermann in *Batelle, Frankfurt, Informationshefte* **11** (1971), 62.

[22] J.A.R. van Veen, H.A. Colijn, *Ber. Bunsenges. Phys. Chem.* **85** (1981), 700-704.

[23] H. Bönnemann, W. Brijoux, R. Brinkmann, E. Dinjus, T. Joußen, B. Korall, *Angew. Chem. Int. Ed. Engl.* **30** (1991), 1312-1315.

[24] A. Fischer, J. Jindra, H. Wendt, *J. Appl. Electrochem.* **28**, (1988), 277-282.

[25] T.J. Schmidt, M. Noeske, H.A. Gasteiger, R.J. Behm, P. Britz, W. Brijoux, H. Bönnemann, *Langmuir* **13** (1997), 2591-2595.

[26] K. Wang, H.A. Gasteiger, N.M. Marcovic, P.N. Ross, *Electrochim. Acta* **41** (1996), 2578-2593.

Proton_Conducting_Membrane_Fuel_Cells_II, PV 1998-27, 300-315 (1998)
DOI: 10.1149/199827.0300PV © The Electrochemical Society

DIRECT METHANOL FUEL CELLS: RECENT PROGRESS IN FUEL EFFICIENCY, CELL PERFORMANCE AND PERFORMANCE STABILITY

Piotr Zelenay[1], S. C. Thomas and Shimshon Gottesfeld
Los Alamos National Laboratory
Los Alamos, New Mexico 87545, USA

ABSTRACT

Research presented in this paper focuses on several factors affecting the performance of direct-methanol fuel cells (DMFCs), under development for either transportation or portable power applications. In particular, we discuss (i) variations in electrocatalytic activity of a variety of Pt-Ru anode catalysts, (ii) long-term stability of the anode, and (iii) crossover of methanol. We report on recent accomplishments in cell performance, fuel utilization (overall conversion efficiency), and lowering Pt loading in DMFCs designed for the potential use in automotive transportation.

INTRODUCTION

Although direct-methanol fuel cells trail hydrogen/air fuel cells in power density, they do not require a bulky and heavy reforming subsystem, thus presenting an attractive alternative to the reformate-fed devices. Overall performance of DMFCs, currently developed for transportation and portable applications, depends on several factors, of which the most important ones are:

(i) electrocatalytic activity of the anode;
(ii) ionic conductivity and resistance to methanol crossover of the proton conducting membrane;
(iii) water management on the cathode side of the cell (function of flow-field and backing designs).

As described previously[1,2], optimization of different components of DMFCs may lead to a considerable increase in power density and fuel efficiency (utilization). In this paper, we report on recent efforts at Los Alamos National Laboratory (LANL) aimed at potential application of DMFCs as (i) a primary power source for fuel cell vehicles (FCVs), and (ii) portable power sources at the 50 W level. Different system constraints,

---

[1] *On leave from the Department of Chemistry, Warsaw University, Warsaw, Poland.*

e.g., stack power, temperature of operation and catalyst loading, require substantially different approaches in the development of both systems. For example, DMFCs for transportation application have been designed by us to operate at a temperature around 100°C, with as low as possible precious metal loading. On the other hand, the temperature of DMFCs intended for portable power applications would be much lower, only about 60°C, while the amount of Pt is not as crucial as in the case of automotive-market oriented systems.

In the present paper, we focus our attention on recent accomplishments in DMFC research in both areas: transportation and portable power systems. In particular, we demonstrate enhanced activity and stability of the anode, reduction of crossover rate and continuing improvement in the stability of the cell performance.

EXPERIMENTAL

Pretreatment of Nafion™ 117 and 1210 membranes in the H^+ form, preparation of membrane electrode assemblies (MEAs) for a DMFC using a decal technique, and the single-cell fuel cell hardware have been previously described[3,4], as has the cell testing system used.[5] Several unsupported Pt-Ru blacks of a nominal 1:1 Pt:Ru atomic ratio were used for anode preparation. They were supplied by different manufacturers, and some fabricated in-house. Anode inks were made by dispersing appropriate amounts of the Pt-Ru catalyst in deionized/distilled water and adding 5% Nafion™ solution (1200 in equivalent weight, Solution Technology Inc.). The cathode inks contained unsupported Pt black (30 $m^2 g^{-1}$, Johnson-Matthey), deionized/distilled water and 5% Nafion™ solution (1100 equivalent weight, Solution Technology Inc.). In some cases, the catalyst layer preparation involved direct application of the catalyst inks to conventionally PTFE-treated wet-proofed carbon cloths. The geometric active area of all the MEAs prepared was 5 cm^2.

Methanol solutions, between 0.25 and 2.0 M in concentration, were pumped through the DMFC anode flow field at precisely controlled rates (0.5-3.0 mL min^{-1}) using a Shimadzu LC-10AS HPLC pump. A back pressure of between 15 and 30 psig was imposed upon the anode outlet flow to ensure that the membrane would be in contact with a liquid solution of methanol whenever the cell operating temperature was in excess of 90°C (potential transportation application). The cathode gas feed in the transportation-oriented work was air at a pressure of 30 psig and relatively high flow. In the work aimed at portable power systems, the air pressure was typically ambient (0.76 atm at the altitude of Los Alamos) and the flow was 0.05 L min^{-1} (stoichiometry of 2 at the point of maximum power, *i.e.* at a cell voltage close to 0.4 V). The air was usually pre-humidified at the same, or similar, temperature as the operating temperature of the cell. In some cases, especially at low cell operating temperatures required by portable power systems, humidification of air was found unnecessary.

The crossover of methanol as a function of cell current density was recorded at the same time as the corresponding cell polarization (V-i_C) plot. The determination was based upon the amount of carbon dioxide present in the cathode exhaust, as measured using a GMM12 Carbon Dioxide IR Sensor (Vaisala Oy, Finland). (The IR detector was pre-calibrated with a gaseous mixture of 4% CO_2 and 96% N_2.) The CO_2 content in the cathode exhaust was then converted into the corresponding amount of methanol that had crossed through the membrane, expressed as current density of MeOH oxidation on the cathode, i_X. The crossover of methanol at open-circuit was also determined electrochemically by measuring oxidation current of MeOH at the cathode.[2]

RESULTS AND DISCUSSION

DMFC anode research

Since the electrocatalytic activity of the Pt-Ru anode catalyst and long-term stability of the anode reflect directly on the fuel cell performance, we invested substantial effort in the optimization of the anode catalyst. Among others, we tested a number of presumably identical unsupported Pt-Ru catalysts of a nominal Pt:Ru atomic ratio of 1:1 (**Table I**). In addition to the catalysts obtained from two different manufacturers (*A* and *B*), we also tested two in-house fabricated anode catalysts, listed in Table I as *LANL-1* and *LANL-2*. Activity of the anode catalysts was determined at 0.35 V *vs.* a hydrogen evolving counter electrode saturated with humidified hydrogen-gas. The catalyst layers were prepared using exactly the same procedure in each case, with the Pt-Ru catalyst loading and the ionomer content in the ink kept as close as possible to 5 mg cm^{-2} and 15%, respectively. Repeatability of preparation was confirmed by measuring several cells prepared with the same catalyst batch. Performance of such cells was repeated to within ±10%.

The anode performance varies a lot from one catalyst batch to another. For example, despite being synthesized by the same manufacturer, catalysts *A-8* and *A-6* exhibit electrocatalytic activity that at 0.35 V differ by as much as an order of magnitude (Table I). Similar differences can be seen for catalysts *B-1* (or *B-2*) and *B-3* from the other manufacturer. At present, it is too early to state unequivocally the reasons for the variations in the performance of such Pt-Ru catalysts. However, our preliminary investigation of this subject points to three possible factors:

(i) Electrocatalytic activity of the anode increases with an increase in the real surface area of the Pt-Ru catalyst, as measured by BET method. Other factors notwithstanding, a surface area of around 80 $m^2 g^{-1}$ generally warrants satisfactory performance of the catalyst.

(ii) As concluded from the XRD measurements, better alloying of the two component metals typically leads to higher electrocatalytic activity of the anode in methanol oxidation.

(iii) The oxidation state of the Ru component in the alloy (XRD measurements) may affect the anode performance. The anode appears to benefit from the presence of Ru in more reduced (metallic), rather than oxidized, state.

Table I

Variations in anode performance at 80°C with various batches of unsupported Pt-Ru catalyst. Methanol feed: c=1 M, f=1.0 mL min^{-1}. Catalyst loading *ca.* 5 mg cm^{-2}. Cell voltage was *iR*-corrected.

Catalyst	Current density at 0.35 V ($A cm^{-2}$)
A-1	0.330
A-2	0.160
A-3	0.360
A-4	0.245
A-5	0.090
A-6	0.030
A-7	0.310
A-8	0.340
A-9	0.310
A-10	0.250
B-1	0.225
B-2	0.235
B-3	0.040
LANL-1	0.280
LANL-2	0.305

Whatever the complete reasons are for the inconsistent performance of Pt-Ru catalysts, clearly no standard of the unsupported Pt-Ru catalyst is currently available for DMFC anodes. Either commercial or in-house fabricated catalyst batches need to be carefully scrutinized before being used in direct-methanol fuel cells.

Fortunately, the best Pt-Ru catalysts available allow preparation of active DMFC anodes that can be operated for prolonged periods of time without noticeable loss in performance. A life test of such an anode at 80°C is shown in **Figure 1**. The test indicates that state-of-the-art anodes are capable of stable operation for weeks. The spikes on the current density *vs.* time plot in Figure 1 are due to either opening of the cell circuit for 30-60 min or stopping the feed of methanol for 15-30 min. Although not absolutely necessary for stability of anode performance, opening of the cell circuit and/or cutting off the flow of methanol both lead to a temporary increase in anode activity. This may be useful in any DMFC applications that will involve intermittent operation of the fuel cell.

An interesting observation has been the dissimilar increases in anode and cell performance with temperature. This is illustrated in **Figure 2**, where changes in the anode current over the temperature range from 60°C to 100°C are compared with the corresponding changes in the V-i_C cell plots in the same temperature range. The figure clearly indicates that DMFC performance increases with temperature less than does the electrocatalytic activity of the anode. For the sake of comparison, we can examine the voltages ratio of anode current at 0.35 V (*vs.* hydrogen evolving electrode) to cell current at 0.5 V at different temperatures. If *iR*-corrected values are consistently used, this ratio assumes the values of 0.6, 0.8 and 1.1 at 60°C, 80°C and 100°C, respectively. The observed gradual increase in the anode-to-cell current ratio with temperature appears too high to be fully accounted for by the concurrent rise in the methanol crossover through the Nafion™ 117 membrane. (Depending on temperature, the potential shift of the cathode due to crossover can be estimated at 10-25 mV for a DMFC operating near 0.5 V.)

Fuel Utilization

Partial use of fuel because of fuel/oxygen recombination at the cathode is often considered a "soft" point of the direct-methanol fuel cell and a major stumbling block on the path to making DMFC power systems practical. As we show in this work, and in companion papers[6,7], this difficulty is significantly overcome when the DMFC is operated under optimized conditions.

One effective way for the reduction of methanol crossover through the membrane is to operate the fuel cell using relatively "lean" anode feed – in terms of MeOH concentration and, to a lesser extent, flow rate of the MeOH solution (**Figures 3** and **4**). This lowers the MeOH concentration gradient across the membrane and thus the crossover rate. Additionally, methanol crossover could greatly depend on the cell current. An increase in cell current leads to a decrease in the concentration of methanol next to the membrane on the anode side, that is, to a drop in the concentration gradient across the membrane and, consequently, to the reduction of crossover. The amount of methanol crossing through the membrane under open-circuit conditions (which represents the upper crossover value, Figure 3) is often reduced by half, or even more, near the maximum power point. As a result, fuel utilization at high current densities may reach values in excess of 90% (Figure 4).

A possible implication of the effect of methanol concentration in the feed stream on fuel utilization and, consequently, on energy conversion efficiency, is to operate a DMFC at varied methanol feed concentration. This concept is discussed in more detail in a companion paper.[6]

DMFC Operation Conditions Applicable to Potential Application in Automotive Power Systems

Operation at higher DMFC cell temperature is key for approaching the power densities of reformate/air fuel cells. Based on DMFC performance already demonstrated, we have projected that the system power density and overall conversion efficiency of both direct and indirect methanol fuel cell systems would be similar.[7,8] Recent demonstrations using optimized anode catalysts focused on a combination of high power density, high fuel utilization, good performance stability and, most recently, limited overall catalyst loading. High power density, very high fuel utilization and stable fuel cell operation have been achieved in single DMFCs operating at 100°C, with 0.5-1.0 M methanol feed streams and 30 psig air at high flow rate. **Figure 5** shows results of a 2000-hour life test of a single cell DMFC, demonstrating a combination of peak power density near 0.2 W cm^{-2} and fuel utilization over 90%, both maintained continuously. One important feature established here is excellent stability of the anode catalyst at 100°C (in addition to the anode stability already demonstrated at 80°C, Figure 1).

Cell voltage and power density *vs.* current density plots obtained with total Pt loading lowered to 2.6 mg cm^{-2} are given in **Figure 6**. They demonstrate that even with relatively low concentration of methanol in the feed stream (0.5 M) it is possible to achieve with this reduced overall loading, at or near 100°C, peak DMFC power density of at least 0.15 W cm^{-2} and overall energy conversion efficiency (voltage efficiency × fuel utilization) of 36%. The keys to these achievements have been the optimization of anode catalyst formulation and preparation, improvements in membrane and cell structure as well as operation conditions that ensure the highest ratio of cell current to crossover current.

Progress in fuel utilization has been achieved by lowering concentration of methanol in the feed stream and, to a lesser degree, by controlling flow rate of the solution.

Our more recent data, obtained with only slightly higher total loading of Pt (3.0 mg cm^{-2}) and 1.0 M MeOH solution, gave higher peak power of 0.28-0.29 W cm^{-2} at 100°C, and an overall energy conversion efficiency only a little lower than that obtained with 0.5 M solution above. Thus, Pt loading required for 1 W of electricity in a direct methanol cell is at present at a 10 mg level. Considering a pitch per cell of 2 mm, as successfully demonstrated in some initial testing of single cells, the volume power density projected for a DMFC stack operating at 100°C is at least 1 kW L^{-1}. It is worth mentioning that the power density is expected to drop by only about 25% in operation on ambient air, instead of 30 psig.

DMFC Research for Potential Application in Portable Power Systems

Liquid fuel storage is an important advantage of methanol vs. hydrogen for portable power source applications. This is because the effective energy density of methanol, assuming a DMFC voltage of 0.5 V (a typical design point) and 90% fuel efficiency, is 2.25 kWh kg^{-1}. In comparison, for hydrogen stored as metal hydride at 2% by weight and, assuming hydrogen/air cell voltage of 0.7 V, the effective energy density of the fuel is 0.4 kWh kg^{-1}. However, in order to benefit fully from the "energy density advantage", DMFCs should achieve sufficient power density under benign cell operation conditions, typically around cell temperatures of 60°C, at 1 atm pressure and at low flows of air (stoichiometry less than 3). Such conditions are required to ensure that the cell could reach and maintain the design temperature in the simplest operation mode using blown dry air.

In response to this challenge, we have been active at LANL in the development of efficient direct-methanol fuel cells capable of sustained operation under conditions specific to portable fuel cell systems. **Figure 7** shows the results obtained with a 5 cm^2 (catalyst rich) cell at ambient pressure and 0.05 L min^{-1} flow of air. At present, such a cell can deliver around 0.230 A cm^{-2} at 0.4 V, which corresponds to a maximum power density of 0.09 W cm^{-2}.

In recent work at LANL, we have demonstrated a 50 cm^2 cell which is to serve as a building block for a 50 W DMFC stack. The performance of this cell at 60°C, anode feed of 1 M MeOH, ambient air (0.76 atm at the elevation of Los Alamos), with very little pressure drop in the cathode flow channels, is only slightly below that obtained with the cell of surface area ten times smaller. The ability to obtain more than 0.150 A cm^{-2} at 0.4 V puts the maximum power density projected for a portable DMFC stack design around 0.2 kW L^{-1}, quite substantial for such benign operation conditions.

SUMMARY

The outcome of the work presented in this paper can be summarized as follows:

(i) Irreproducible preparation of commercial unsupported Pt-Ru catalysts used for fabrication of DMFC anodes can lead to variations in the anode activity as large as one order of magnitude between batches of catalysts supplied. This presents difficulty in establishing good benchmark for evaluation of alternative anode catalysts and forces careful testing prior to stack fabrication.

(ii) Rate of the crossover of methanol through commonly used polymer electrolyte membranes can greatly be reduced – by 50% or more – by adjusting the concentration of methanol in the anode feed stream according to the power requirement from the cell. At higher cell current densities, fuel utilization of 80-90%, or even higher, can be achieved.

(iii) Thanks to further optimization of the anode (including catalyst and catalyst layer) and the cathode structure (backing, flow-field, etc.), substantial improvement in cell performance has been accomplished that has allowed the precious metal loading to be significantly reduced without severe drop in the cell performance. Power density of almost 0.3 W cm^{-2} can be reached in DMFC operating at 100°C, with total Pt loading at or below 3.0 mg cm^{-2}.

(iv) Increase in power density of cells operating at 60°C, at ambient pressure and low stoichiometric flow of air, promises good progress in application of DMFCs for portable power sources.

ACKNOWLEDGMENTS

This work was supported by the Defense Advanced Research Projects Agency (DARPA) through the Defense Sciences Office and by the U.S. Department of Energy through the Office of Advanced Automotive Technology.

REFERENCES

1. S. Gottesfeld, *Polymer Electrolyte Fuel Cells*, in *Advances in Electrochemical Science and Engineering*, C. Tobias, H. Gerischer, R Alkire and D. Kolb (Eds.), vol. 5, John Wiley & Sons, New York, 1997.

2. S. Cleghorn, P. Zelenay, X. Ren and S. Gottesfeld, *Ionomeric Membranes for Direct Methanol Fuel Cells,* Meeting Abstracts, vol. 98-1, Abstract No. 894, The Electrochemical Society, Pennington, New Jersey, 1998.
3. X. Ren, M. S. Wilson and S. Gottesfeld, *J. Electrochem. Soc.*, **143**, L12 (1996).
4. X. Ren, W. Henderson and S. Gottesfeld, *J. Electrochem. Soc.*, **144**, L267 (1997).
5. T.E. Springer, M. S. Wilson and S. Gottesfeld, *J. Electrochem. Soc.*, **140**, 3513 (1993).
6. R.M. Moore, S. Gottesfeld and P. Zelenay, *Optimizing the Overall Conversion Efficiency of a Direct-Methanol Fuel Cell,* in *Proton Conducting Membrane Fuel Cells (Second International Symposium)*, S. Gottesfeld, T.F. Fuller and G. Halpert (Eds.), Proceedings Volume 98-27, Electrochemical Society, Pennington, New Jersey, 1998.
7. R.M. Moore, S. Gottesfeld and P. Zelenay, *Comparison of the Conversion Efficiency of a Direct-Methanol vs. a Hydrogen Fuel Cell,* in *Proton Conducting Membrane Fuel Cells (Second International Symposium)*, S. Gottesfeld, T.F. Fuller and G. Halpert (Eds.), Proceedings Volume 98-27, Electrochemical Society, Pennington, New Jersey, 1998.
8. S. Gottesfeld, S.J.C. Cleghorn, X. Ren, T.E. Springer, M.S. Wilson and T.A. Zawodzinski, *Polymer Electrolyte Direct Methanol Fuel Cells; An Option for Transportation Applications,* Fuel Cell Seminar Abstract Book, p. 521, 1996.

FIGURES

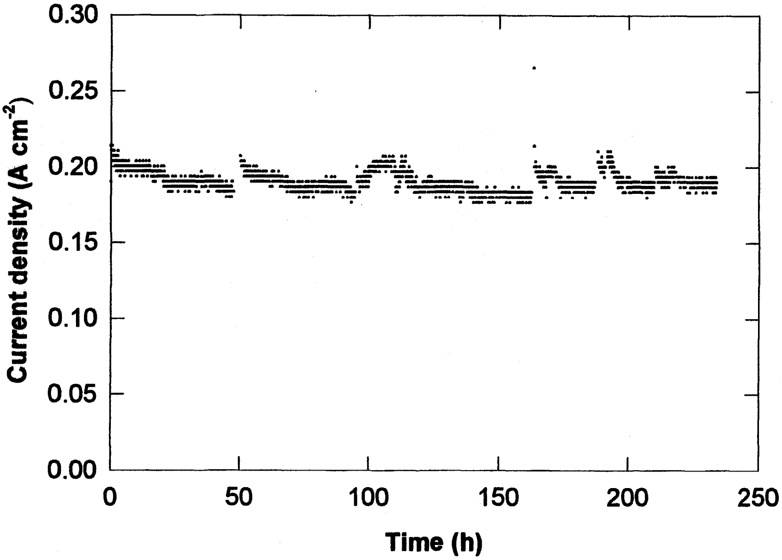

Figure 1. Stability test of a DMFC anode with unsupported Pt-Ru catalyst at 0.35 V (DHE), 80°C. Anode feed: c=1.0 M, f=1.0 mL min^{-1}.

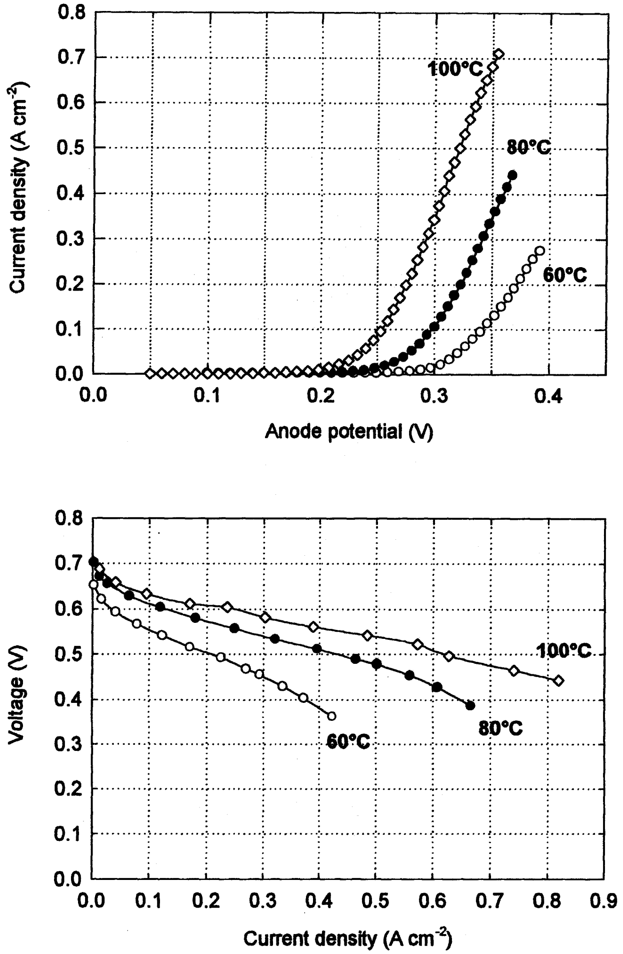

Figure 2. Effect of temperature on DMFC anode activity (top) and DMFC polarization (bottom) at 80°C. Nafion™ 117 membrane. Anode feed: c=1.0 M, f=1.0 mL min^{-1}. Cathode feed: Air at 30 psig, high stoichiometric flow. All voltage values are iR-corrected.

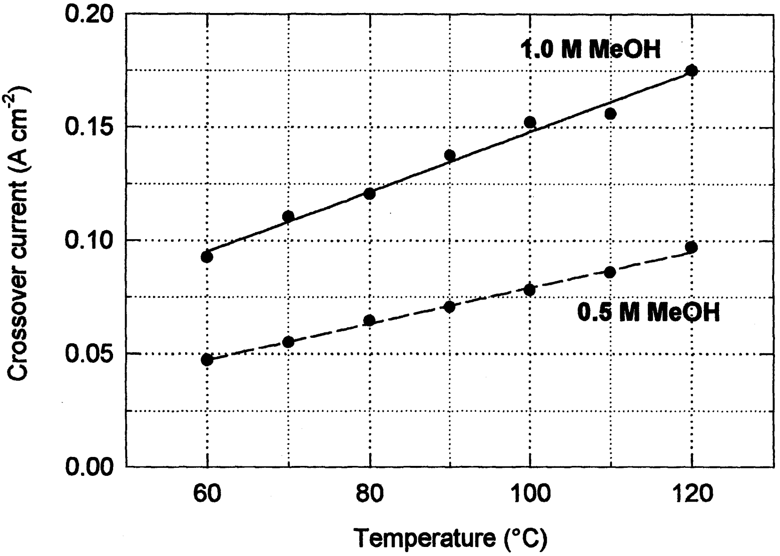

Figure 3. Crossover of methanol through a Nafion™ 117 membrane in a DMFC at open circuit; *f*=2.0 ml min^{-1}. Anode exhaust at temperatures above 90°C back-pressurized to 15-30 psig.

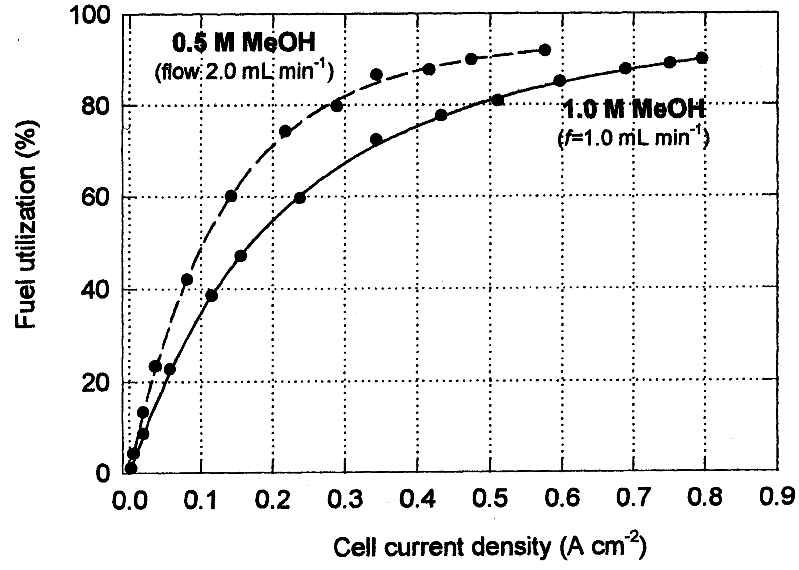

Figure 4. Fuel utilization as a function of cell current density at 100°C. Nafion™ 117 membrane. Anode exhaust back-pressurized to 15 psig. Cathode feed: Air at 30 psig, high stoichiometric flow.

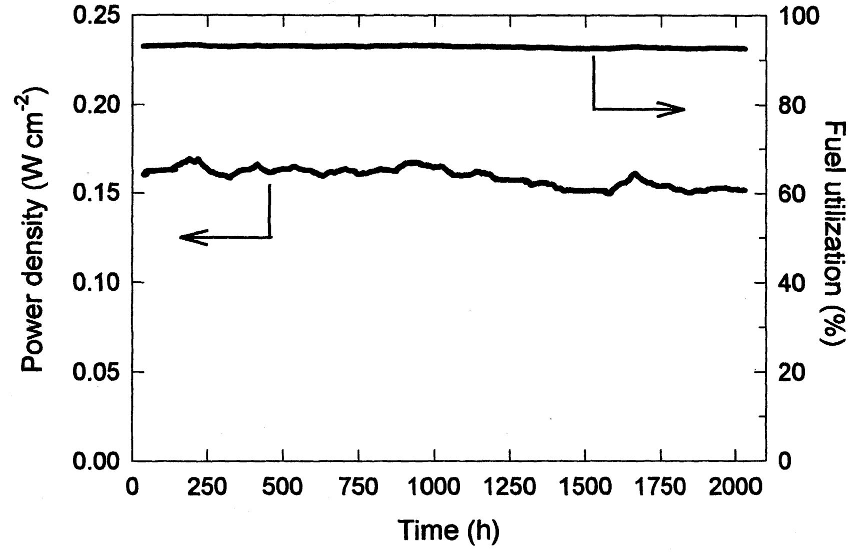

Figure 5. Life test of DMFC power density and fuel utilization at 0.4 V and 100°C. Anode feed: c=1.0 M, f=1.0 mL min^{-1}. Cathode feed: Air at 30 psig, high stoichiometric flow.

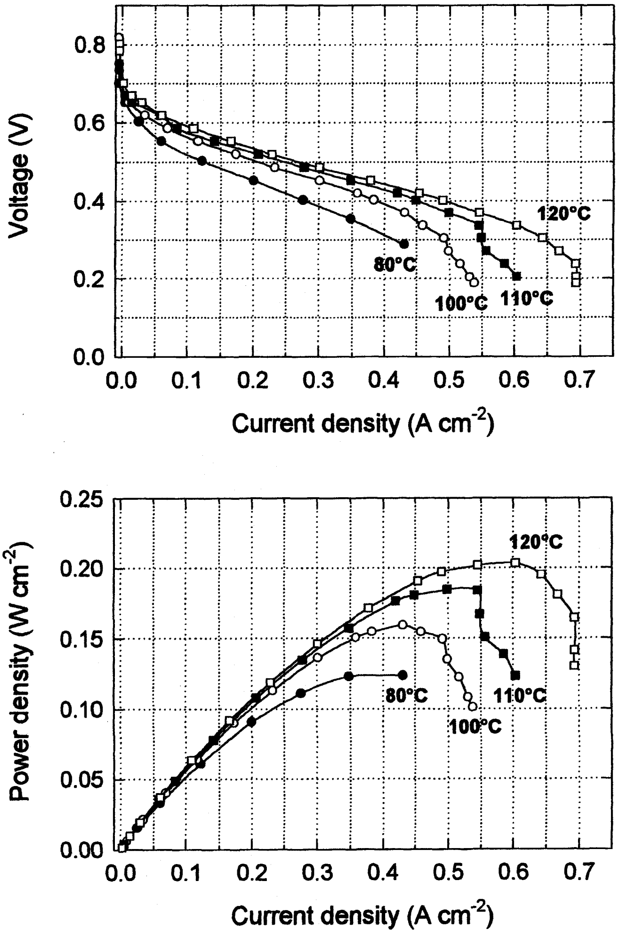

Figure 6. Voltage (top) and power density (bottom) as a function of current density for a DMFC with total precious metal loading limited to 2.6 mg cm^{-2}. Anode feed: c=0.5 M, f=2.0 ml min^{-1}. Cathode feed: Air at 30 psig and high stoichiometric flow.

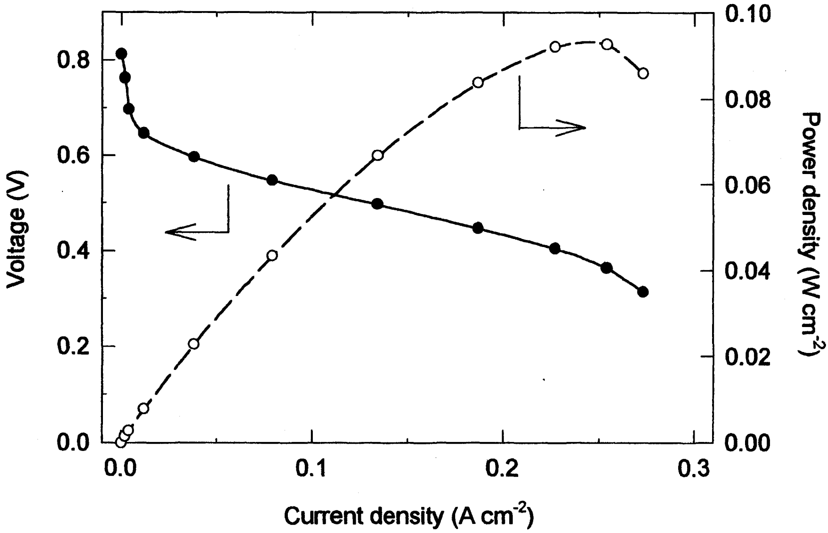

Figure 7. Cell polarization and power density plots for a DMFC operated at 60°C with highly catalyst-loaded anode (8.9 mg of Pt-Ru per cm^2). Anode feed: c=0.5 M, f=1.0 mL min^{-1}. Cathode feed: Air at ambient pressure (0.76 atm) and 0.05 L min^{-1} flow.

Proton_Conducting_Membrane_Fuel_Cells_II, PV 1998-27, 316-326 (1998)
DOI: 10.1149/199827.0316PV © The Electrochemical Society

ELECTROCHEMICAL FACTORS IN DESIGN OF DIRECT METHANOL FUEL CELL SYSTEMS

S. R. Narayanan, T. I. Valdez, N. Rohatgi, J.Christiansen, W.Chun and G. Halpert
Jet Propulsion Laboratory, California Institute of Technology, Pasadena, CA 91109

Abstract

The design of direct methanol fuel cell based portable power source is being pursued at JPL. Performance data obtained on Nafion-based fuel cells have been used to develop a closed loop system model. The model has been exercised to obtain information on the impact of the various possible operating conditions on size, mass and efficiency of portable systems. Flow rate of air, methanol concentration and temperature are found to key controllable variables that significantly impact system size and efficiency. The results of the modeling studies are discussed.

Background

Recent advances in the performance of direct methanol fuel cells [1-8] are sufficiently attractive for the design of complete power systems. Portable power sources based on this technology are currently being considered for various military applications. The development of a 150 W portable power system based on direct methanol fuel cells is currently being pursued at the Jet Propulsion Laboratory (JPL).

After the initial concept development at JPL over 6 years ago[1], the various factors governing the performance of direct methanol fuel cells have been studied by various groups in the United States and abroad. Performance levels shown in Fig. 1 characterize the status of Nafion-based direct methanol fuel cells being developed at JPL .

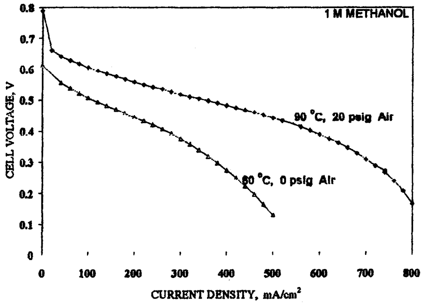

Fig. 1. Performance of a direct methanol fuel cell based on Nafion 117 with Pt-Ru anode and Pt cathode.

These fuel cells use in-house developed Pt-Ru catalysts and membrane-electrode assemblies and operate on a liquid feed of aqueous solutions of methanol. While the research in the area of new membranes and catalysts continues, it is important to understand the impact of the current performance levels on the design of systems

Brief description of direct methanol fuel cell system

A portable power system based on the concept of the direct methanol fuel cell is shown in Fig. 2.

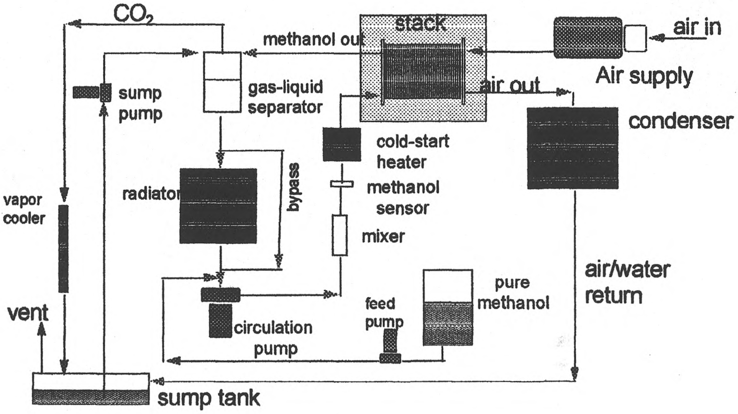

Fig. 2. Schematic of a direct methanol fuel cell system for portable applications

In this arrangement the fuel feed subsystem delivers pure methanol into a circulating loop of dilute methanol. Dilute methanol of a specified concentration constitutes the fuel solution entering the fuel cell stack. During operation, the concentration of methanol solution exiting the stack is reduced, and pure methanol must be added to restore the solution to the specified original concentration. Carbon dioxide is rejected from the solution loop at a gas-liquid separator. Air is introduced in the stack with an appropriate device such as a blower or compressor. The exiting air passes through a condenser that serves to recover water and reject heat. A portion of the recovered water may be returned to the fuel circulation loop. Additional heat rejection is accomplished by means of a heat exchanger in the fuel circulation loop. Some of the intrinsic advantages of this arrangement, relative to the hydrogen systems, are that the liquid feed of methanol allows the attainment of a uniform stack temperature and maintenance of membrane humidity.

Overview of factors affecting system design

In the design of portable systems based on direct methanol fuel cells the most important performance parameters are: system power density (W/kg, W/L), system energy density (Wh/kg, Wh/L), efficiency (methanol to electricity), performance under transient loads, and long-term stability during operation and storage. Table 1 shows that there are several electrochemical factors that affect system performance .

Table 1. System Performance Characteristics and Electrochemical factors

SYSTEM PERFORMANCE CHARACTERISTICS	ELECTROCHEMICAL FACTORS
Power Density, W/Kg, W/L • Stack Mass • Balance of Plant Mass **Efficiency** • Stack Heat generation processes • Energy required by pumps and blowers • Energy required by heat exchangers • Energy required power conditioning equipment **Load handling capability** • Reactant/Product concentration deviations caused by load • Response mechanisms for coping with changes **Environment –System sensitivity** • Response to temperature, humidity and pressure changes **Operating life** • Stable operation for desired periods	**Power Density, mW/cm^2** (operating point on V-I curve) • Catalytic activity (Pt-Ru, ...) • Ionic conductivity (Nafion, ...) • Electrode/ MEA characteristics **Reactant and Product Mass Transfer** • Concentration (Methanol Molarity) • Pressure (Air) • Flow rates (Relative to stoichiometric) • Temperature • Humidity • Flow field design features **Water handling through the stack** • Electro-osmotic transport (membrane type) • Temperature of operation **Heat generation processes** • Irreversibility (Deviation from Thermoneutral potential) • Crossover Rate (parasitic heat generation) **Degenerative processes** • Short term stability (for. e.g. flooding, dry out) • Long term irreversible loss (catalyst poisoning , membrane degradation)

Studies at the single cell and stack level have shown that improvements in performance (operating current density and voltage) can be achieved by changing various parameters such as the temperature, concentration and air flow rates and pressures. For example, the data in Fig. 3 shows that considerably higher performance can be attained by operating at high air flow rates. This observation suggests that such an operating mode with enhanced air flow rates will result in improved system performance. Similarly, higher current densities are attainable at higher concentrations of methanol as shown in Fig. 4. This again suggests that higher concentrations of methanol are to be preferred. However, since the system performance, weight and volume are governed by performance characteristics of various subsystems and their interactions with the stack, it is possible that the improvements achieved in stack performance are only ostensible improvements at the system level and may even have a negative impact on the system characteristics. Therefore improvements at the stack level must be assessed in the system context. The present study focuses on the identification of the key stack performance factors that are important to achieving a lightweight efficient design for portable applications.

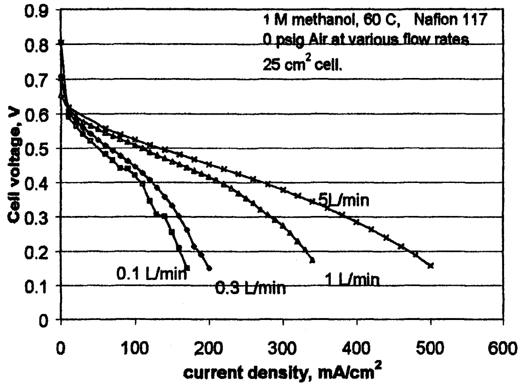

Fig. 3 Effect of air flow rate on the performance of Nafion-based direct methanol fuel cells

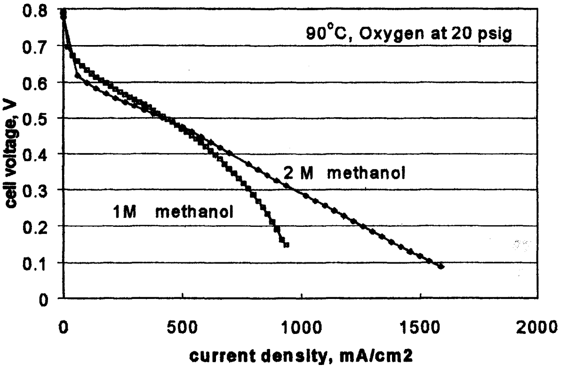

Fig. 4 Effect of methanol concentration on the performance of Nafion-based fuel cells

System Modeling

In order to carry out such an analysis a closed loop steady state system model was developed and exercised. The model sought to relate the inputs and outputs as shown in Fig. 5.

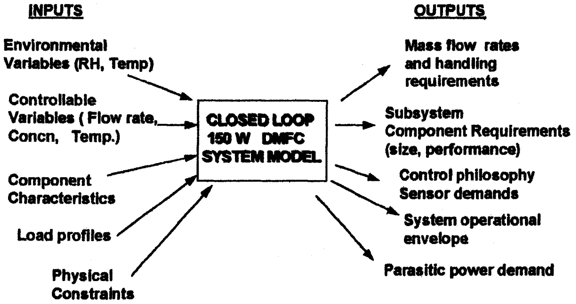

Fig. 5. Inputs and outputs relating to the system model

The model was developed using a set of performance data obtained on a five-cell stack and individual cells fabricated and tested at JPL. Such performance data has been reported earlier [2,5,8]. This data was used to derive multi-variable mathematical correlations to represent the following :

a. Dependence of stack voltage on current density as a function of temperature and air flow rate.
b. Dependence of methanol crossover rate on current density, methanol concentration and temperature.
c. Dependence of water transport rates across the stack on temperature and current density.

In the model the following assumptions have been made. Ambient pressure air flows across the cathodes in the stack. The air exiting the stack is saturated with water vapor. An ambient-air cooled condenser allows recovery of water and rejection of part of the heat generated in the stack. An appropriate portion of the liquid water is returned to the methanol circulation loop and the excess water is rejected. The methanol loop in the process flow diagram consists of a circulating pump, start-up heater for very low temperature start-up (<10°C), and an air-cooled radiator for heat rejection. The carbon dioxide produced in the stack is separated from the liquid stream at a gas-liquid separator. The methanol vapor carried by the exiting carbon dioxide is recovered in an air-cooled condensing unit and returned to the circulation loop.

Upon exercising the model the various sensitivities could be determined. Three controllable variables, namely air flow rate, methanol concentration and stack temperature had the most impact on the system size and efficiency. The results in this regard are discussed in the following.

Air flow rates and Water Recovery
One of the desirable features of a light-weight system would be not to have to supply or carry water to sustain the operation of the power source. Thus during system operation no more water should be required except for a small initial charge that will be contained in the dilute methanol fuel loop shown in Fig. 2. This would entail restricting water loss from the system to just the amount produced by the reactions. Thus liquid water appearing at the cathode by various processes and the water carried as vapor by the air stream must be largely recovered and returned to the anode side.

Water recovery in small portable systems can be achieved by condensers that use forced ambient air cooling. Under these circumstances, the amount of water recovered is dependent on the ambient temperature, the flow rate of air through the stack, and the heat transfer efficiency of the condenser.

The performance of the single cell and hence the stack is a strong function of the air flow rate as shown in Fig. 3. The stoichiometric air flow rate at any current density is calculated based on the amount of oxygen required for sustaining the electrochemical current producing reaction plus the amount of air consumed by the parasitic oxidation of methanol crossing over to the cathode. The stoichiometric flow rate can be calculated at each value of applied load using the measured value of crossover. An example of this calculation is as follows. A cell operating at 100 mA/cm^2, with a crossover rate of 40 mA/cm^2, and an active area of 25 cm^2, the stoichiometric flow rate of air is about 0.066 liters/min. The air flow in an operating cell can be expressed as a multiple of the stoichiometric rate. Thus a cell operating at 0.33 L/min of air in the above example would correspond to about 5 times the stoichiometric rate. Water recovery parameters can be related to a stoichiometric rate rather than an absolute flow rate.

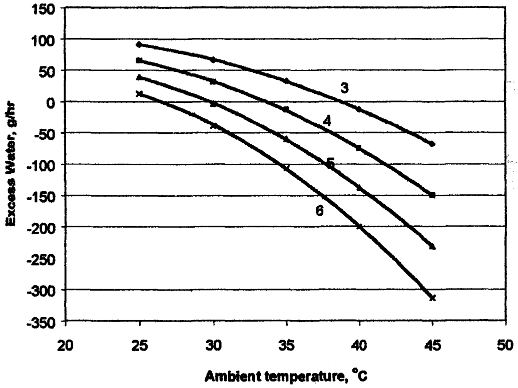

Fig. 6 . Water excess at various stoichiometric rates of air flow (indicated on the lines) at inlet RH=0%, Cathode exit =60°C, 1M methanol, I=100ma/cm^2, power ~180 W, MeOH Flow rate 2L/min.

The model was exercised to understand the recovery of water at various stoichiometric flow rates and ambient temperatures. These results are shown in Fig. 6.

The results in Fig. 6 show that at stoichiometric flow rates of about 6 or greater, it is not possible to recover enough water at an ambient temperature of about 25°C and there will be a water imbalance. At a lower stoichiometric rate of about 3, water balance can be achieved up to about 37°C. Thus if the fuel cell system has to operate in environments as high as 42°C, the stoichiometric flow rate of 3 will result in a water imbalance condition. Thus the stoichiometric flow rate of air that will allow the maintenance of a water balance is a strong function of the ambient temperature. In order to extend the range of operation to higher ambient temperatures and also ensure water balance, we must operate at stoichiometric flow rates below 3. The condenser duty (heat rejection load) under these conditions is shown in Fig. 7.

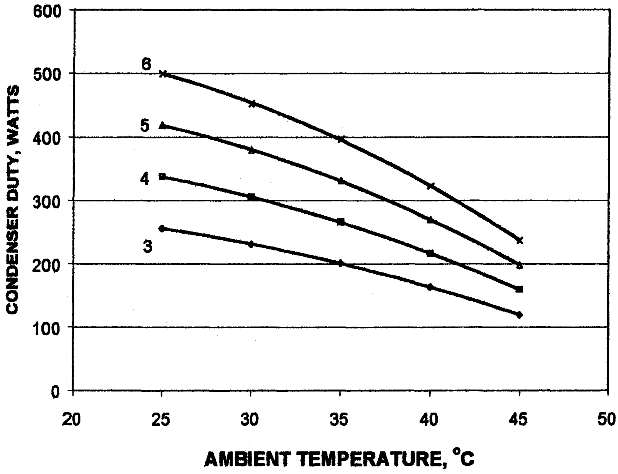

Fig. 7. Condenser duty as a function of stoichiometric flow rate RH=0%, Cathode exit =60°C, 1M methanol, I=100ma/cm^2, power ~180 W, MeOH Flow rate = 2L/min

The condenser duty increases with stoichiometric flow rate because of the larger amount of water that needs to be recovered. At higher ambient temperatures water cannot be recovered to the same extent as at lower temperatures and the condenser duty decreases. Thus the stoichiometric flow rate has a significant impact on condenser requirements. Metal-based condensers are generally heavy components. Off-the-shelf forced air – cooled condensers are rated at about 200 W$_{th}$/kg for such applications. Thus even at a stoichiometric flow rate of 3 the condenser mass is significant. Condensers need air moving equipment such as fans so that they can maximize their heat transfer efficiency. The power demand by such fans is of the order of 1Watt-electric for 25 thermal watts. For cooling air to move in and out of the condenser, sufficient volume allowance must be made in the system design. Also, associated with the passage of the cathode stream down the condenser is a pressure drop that adds to the ancillary power demand from the air pumping equipment.

Thus, the need to maintain a water balance and the process of water recovery entails a significant increase in the mass, volume and ancillary power demand. It would therefore be preferable to consider a condition where a condenser need not be used. In order to achieve a water balance without condensing equipment, the model predicts that the stoichiometric flow rates must be as low as 1.75 times the stoichiometric flow rate when the cell is operating at 50-55°C. Under these conditions, the acceptable stoichiometric flow rate becomes a strong function of the operating temperature of the stack. Partial water recovery may be an alternative with minimal impact on mass of the system so that slightly higher flow rates than 1.75 stoichiometric can be used. Therefore performance improvements in the cell at low stoichiometric flow rates is important to achieving a lightweight system.

By operating the stack at temperatures such as 90°C, it is possible to realize higher power densities (see Fig. 1) thus resulting in lower stack mass. However, it is now apparent from this study that operation of the stack temperatures as high as 90°C will necessarily have to involve intensive water recovery, and is not a desirable operating point for realizing a lightweight portable system.

Methanol concentration and temperature

The results in Fig.4 show that by increasing the concentration of methanol, higher power density can be achieved. It is also known that increasing the concentration results in a proportionally higher rate of crossover [2,3,6]. Yet another fact is that the crossover rate in an operating cell decreases as the operating current density is increased [7]. While at higher temperatures the attainable current density is higher, the crossover rate is also strongly increased [1,2,4]. Thus for a particular polymer electrolyte membrane and electrode configuration such as Nafion 117 where the crossover of methanol is a significant process, methanol concentration and temperature strongly impact the overall efficiency of the operating cell. In general, lower cell efficiencies result in a larger heat management system.

The methanol to electric efficiency of the operating cell can be defined as a product of the voltage efficiency and the efficiency of methanol utilization in the current generation process. Such an efficiency product is given by equation (1).

$$\eta_{stack} = (V_{load}/V_{tn}) \, . \, (I_{load}/(I_{load} + I_{cr,I}) \qquad (1)$$

Where η_{stack} is the efficiency of the operating stack, V_{tn} is the thermoneutral potential, V_{load} is the cell voltage under an operating load, I_{load} is the operating current density and $I_{cr,I}$ is the crossover current density measured at the operating current density.
The crossover rate is dependent on current density and this is dependent on electrode and membrane parameters and for the most part can be modelled by a simple linear diffusion model[2]. Introducing such a description of the dependence of crossover rate the efficiency may be expressed as:

$$\eta_{stack} = \{(V_{load})/V_{tn})\} \,.\, I_{load}/(I_{load} + \{I_{cr,o} - \gamma I_{load}\}) \qquad (2)$$

where $I_{cr,o}$ is the crossover rate under open circuit conditions and γ is a property of the membrane-electrode assembly and is given by $1/\{1+ (D_{el}\ \delta_{mem}/D_{mem}\ \delta_{el})\}$, D_{el} is the apparent diffusion coefficient of methanol in the electrode structure, D_{mem} the apparent diffusion coefficient of methanol in the membrane ,δ_{mem} the thickness of the membrane and δ_{el} the thickness of the electrode structure[2].

Substituting for γ from experimental data into equation (2) and by using appropriate mathematical correlations for the dependence of cell voltage on load, the stack efficiency can be estimated over a wide range of current densities The current density at which the efficiency attains a maximum value can also be calculated. These results are presented in figures 8 and 9.

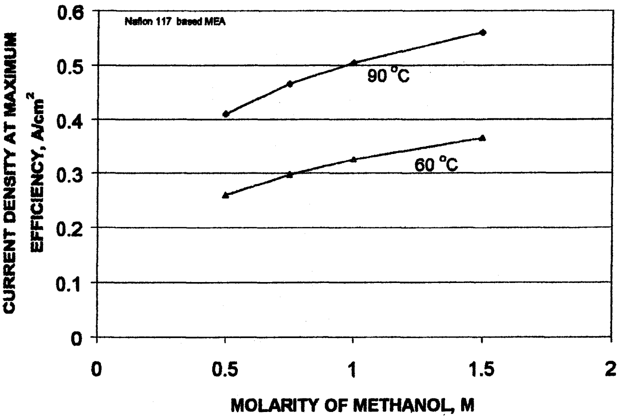

Fig. 8. Effect of methanol molarity on the current density attained at maximum efficiency

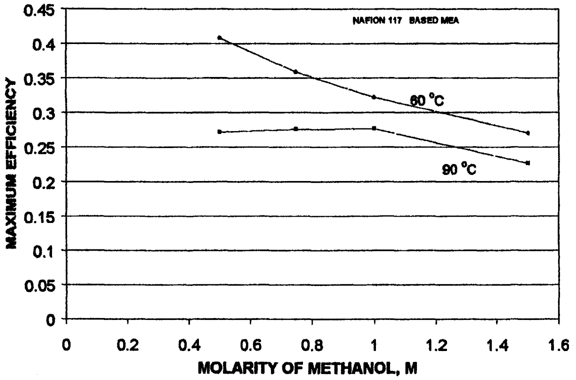

Fig.9. Dependence of maximum stack efficiency on molarity of methanol and temperature

These results show that the efficiency of the fuel cell stacks is a strong function of the temperature and concentration. The results also show that current densities as high as 300- 500 mA/cm^2 , and efficiency in the range of 25-40% , can be over a wide range of operating conditions.

For lightweight portable systems, high efficiency is a prime requirement. Figs. 8 and 9 show that in order to attain high efficiencies of 40% with Nafion 117 membrane, it is necessary to operate at 60°C and with 0.5 M methanol. The current density values for these operating conditions however would significantly depend on the air flow rates as pointed out earlier here. Experimental data at low stoichiometric flow rates[9] show that the optimal current density under these conditions is in the range 100-120 mA/cm^2.

Results in Fig. 9 show that the efficiency curve at 60°C decreases with increasing methanol concentration rather steeply. Thus, operating a fuel cell to maintain the maximum efficiency needs close control of methanol concentration and temperature. Maintenance of concentration of methanol requires an in-line concentration sensor that has a response time sufficient to react to the control requirements in a system. Such a sensor has been developed at JPL and has been found to perform satisfactorily in a system configuration.

Conclusions

The key factors governing the size and mass of state-of-art portable systems based on the direct methanol fuel cell concept are air flow rate, methanol concentration and temperature. By operating at low air flow rates of about 1.75 times stoichiometric, the size of the water recovery system can be minimized or even eliminated. This can be approached by improving the cathode structures to reject water more effectively[9] and by reducing the crossover of methanol through the membrane. The modeling studies suggest that the stack operating temperature of 60°C, appears to be the upper limit for maintaining a thermal and water balance within the size and mass constraints for portable systems. The study also shows that operating systems at a methanol concentration of about 0.5 M allows attainment of high efficiencies with Nafion 117 membranes. Control of concentration is very important in the design of portable systems if high efficiency and thermal balance must be maintained.

Acknowledgements
The work described herein was carried out at the Jet Propulsion Laboratory, California Institute of Technology under contract with the National Aeronautics and Space Agency(NASA) and was supported by the Defense Advanced Projects Agency.

References

1. S.Surampudi, S. R. Narayanan, E. Vamos, H. Frank and G.Halpert, A. Laconti, J. Kosek, G. K. Surya Prakash, and G. A. Olah, J. Power Sources, **47** 377 (1994).
2. S. R. Narayanan, A. Kindler, B. Jeffries-Nakamura, W. Chun, H. Frank, M.Smart , S. Surampudi and G. Halpert, Proceedings of the First International Symposium on Proton Conducting Fuel Cells I, p.261-283, The Electrochemical Society, 1995 (Eds. S. Gottesfeld, G. Halpert and A. Landgrebe)
3. X. Ren, M. S. Wilson and S. Gottesfeld, J. Electrochem. Soc., **143** L12 (1996)
4. X. Ren, T. A. Zawodinski, F. Uribe, H. Dai and S. Gottesfeld, in Proton Conducting Fuel Cells I, S. Gottesfeld, G. Halpert and A. Landgrebe, Editors, Electrochemical Society, Pennington, NJ, (1995) p. 284.
5. S. R. Narayanan, A. Kindler, B. Jeffries-Nakamura, W. Chun, H. Frank, M.Smart, T. I. Valdez , S. Surampudi, J. Kosek and C. Cropley, " Recent Advances in PEM Liquid Feed Direct Methanol Fuel Cells," Proceedings of the Eleventh Annual Battery Conference on Applications an Advances, Long Beach, CA, January 1996.
6. S. R. Narayanan, G. Halpert, W. Chun, B. Jeffries- Nakamura, T. I. Valdez, H. Frank and S.Surampudi, Proceedings of the Power Sources Conference, Cherry Hill, New Jersey, June 1996 .
7. S. R. Narayanan, T. Valdez, N. Rohatgii, J. Christiansen, W.Chun, G. Voecks and G. Halpert, Proceedings of the Power Sources Conference, Cherry Hill NJ, June 1998.
8. T. I. Valdez, S. R. Narayanan, H. Frank and W. Chun, " Direct Methanol Fuel Cell for Portable Applications," p. 239-244, Proceedings of the Twelfth Annual Battery Conference on Applications an Advances, Long Beach, CA, January 1997.
9. T. I. Valdez and S. R. Narayanan, "Recent Studies on Methanol Crossover in Liquid-Feed Direct Methanol Fuel Cells" Proceedings of Symposium on Proton Conducting Fuel Cell 2, this volume.

Proton_Conducting_Membrane_Fuel_Cells_II, PV 1998-27, 327-340 (1998)
DOI: 10.1149/199827.0327PV © The Electrochemical Society

DIRECT METHANOL FUEL CELLS: CATHODE EVALUATION AND OPTIMIZATION

S. C. Thomas, X. Ren, P. Zelenay* and S. Gottesfeld
Los Alamos National Laboratory
Los Alamos, NM 87545

ABSTRACT

Direct methanol fuel cell (DMFC) performance has been improved as a result of Pt cathode optimization based upon the process of robust design. Cathode performance has been evaluated using cathode polarization curves generated from DMFC data. The effects of variation of temperature and nature of cathode backings on DMFC cathode potential were investigated. Our results show that Pt rich DMFC cathodes, operating on ambient air at 60°C, can exhibit high performance of >0.85 V vs. RHE at 100 mA/cm^2.

INTRODUCTION

Demonstrated DMFC performance has improved significantly in recent years. Much attention has been devoted to evaluation of anode catalysts and optimization of anode structure, characterization of existing membranes and searching for alternatives (1, 2). Of equal importance is the contribution of the cathode to performance and performance stability, yet comparatively little effort has been devoted to this component of the DMFC (3 – 5). The work reported here describes some of the recent efforts undertaken in this laboratory to evaluate and optimize cathode performance in a DMFC, employing Pt black as the cathode catalyst. The results show that, in spite of the frequently mentioned lack of "methanol tolerance", Pt cathodes in optimized DMFCs can exhibit high performance which is only marginally lower than their methanol-free performance.

**On leave from the Department of Chemistry, Warsaw University, Warsaw, Poland*

EXPERIMENTAL

The cathode catalysts used in this series of experiments were unsupported Pt blacks. The anode catalyst was an unsupported PtRu alloy. Both catalysts were supplied by Johnson-Matthey. Inks were made by dispersing appropriate amounts of catalyst in deionized water and 5 % Nafion solution (Solution Technology Inc.). Inks were then applied to Nafion 117 membrane (DuPont) either directly or by a decal transfer process. The geometric active area of all membrane electrode assemblies (MEAs) prepared was 5 cm^2. Pretreatment of the proton form of the Nafion 117 membrane, preparation of MEAs for a DMFC using a decal technique, and the single-cell fuel cell hardware have been previously described (1) as has the cell testing system used (6).

For a given series of experiments, the anodes in all MEAs tested were identical, while parameters of the cathodes were varied. Cell, methanol anode and hydrogen anode performances were investigated at temperatures from 60°C to 100°C. When operated at 60°C, 0.5 mol/L methanol solution was used; 1 mol/L methanol solution was used at 80°C and 100°C. The methanol flow rate was held constant at 1 – 2 mL/min. A backpressure of 15 psig was imposed upon the anode outlet flow at 100°C to ensure that the membrane would be in contact with a liquid solution of methanol.

When operated in fuel cell mode, the anode feed was either hydrogen or methanol solution and the cathode feed was air. When operated in driven cell mode to measure methanol anode polarization, the cathode gas was humidified hydrogen. When operated in hydrogen pump mode, humidified hydrogen gas was supplied to both anode and cathode. The backpressures, flow rates and humidification temperatures of the cathode gases, air or hydrogen, varied with the operating temperature of the cell.

Programs written in Labview (National Instruments) and run from a Power Macintosh computer were used to control the experiments as well as generate cathode polarization and cathode loss curves.

RESULTS AND DISCUSSION

Optimization of Cathode Catalyst Layer Composition/Structure Using Robust Design

In this work, the process of robust design (7) was used to systematically investigate the effect of several variables on cathode performance. Robust design is a method, similar in concept to other techniques (8 – 10), of optimizing an experimental approach to effectively achieve a desired outcome. This method uses the mathematical tool of orthogonal arrays in which a large number of factors are investigated with a small number of experiments. In the matrix of experiments, an optimized set is performed in which the levels of various factors are changed from one experiment to another. The data for all experiments in the matrix are analyzed together to determine the effect of each factor.

Three steps, each involving several components of the robust design process are typically followed. Only the main features are summarized in this paper.

(1) Planning the matrix of experiments. For the work reported in this paper, the desired outcome was identified as achieving the highest DMFC current density, J, at 80°C, at a cell voltage of 0.5 V. Statistical treatment of the data was then based on a "larger-the-better" scenario in which a function, designated as η, was defined as $\eta = -10 \log (1/n \sum 1/J_i^2)$ where n is the number of trials of each experiment number i. The objective of maximizing the current density then became equivalent to maximizing η.

Typically 4 to 8 factors are optimized in one matrix of experiments. In this work, ionomer equivalent weight (EW) and ionomer content in the cathode catalyst layer, cathode catalyst loading and hot pressing temperature during the decal transfer process of the catalyst layers to the membrane were the factors investigated. Levels of each of these 4 factors were chosen. Typically three levels sufficiently far apart, the level currently in use and a level on either side of it, are employed. Although construction of an orthogonal array specific to the project under consideration is possible, a standard array of 9 experiments (7), shown in Table I, was adopted to study the effect of the 4 factors, in contrast to the 81 experiments required for a full factorial analysis.

Table I
Orthogonal Array Matrix Experiment

Expt. #	Factor and Level Assigned			
	Factor A	Factor B	Factor C	Factor D
1	1	1	1	1
2	1	2	2	2
3	1	3	3	3
4	2	1	2	3
5	2	2	3	1
6	2	3	1	2
7	3	1	3	2
8	3	2	1	3
9	3	3	2	1

(2) Performing the experiments. After the orthogonal array was chosen, the matrix of experiments could be performed, as shown in Table II. It is important to stress that control of all variables, other than the factors being tested, should be as stringent as possible. For example, the same batch of Pt black catalyst as well as a standard anode formulation were used for all experiments. Importantly, all experiments in a matrix of experiments must be completed. If data are missing, orthogonality is lost and analysis of such experiments is complicated.

Table II
Experimental Log Sheet

Exp. #	Factor and Level Assigned			
	Ionomer EW	Ionomer Content (wt. %)	Cathode Loading (mg/cm^2)	Hot Press Temp (°C)
1	900	4	3.5	80
2	900	10	6.0	125
3	900	16	8.5	140
4	1100	4	6.0	140
5	1100	10	8.5	80
6	1100	16	3.5	125
7	1200	4	8.5	125
8	1200	10	3.5	140
9	1200	16	6.0	80

In this work, only one MEA was prepared for each of the 9 experiments. The average, from three consecutive trials, of the current densities achieved with each MEA at 0.5 V and 80°C, was used for analysis of the data. Table III summarizes these average DMFC current densities and the value of the η function for each of the 9 experiments.

Table III
DMFC Current Densities @ 0.5 V @ 80°C and η Values for the Matrix of Experiments

Expt. #	1	2	3	4	5	6	7	8	9
Current density (mA/cm^2)	210	285	125	190	250	235	255	255	285
Value of η function	46.4	49.1	41.9	45.6	48.0	47.5	48.1	48.1	49.2

(3) Analyzing and verifying the experimental results. The effect of each factor is estimated by a statistical treatment of the data during which average values of the η function are calculated for each level of each factor. For example, the effect of an ionomer content of 4 wt. % is determined from averaging the η values from experiments 1, 4 and 7. The optimum level of each factor is determined as that level of the factor that gives the largest average value of η. This matrix of experiments indicated that the highest DMFC performance at 0.5 V at 80°C should be obtained with a cathode fabricated with an ink made with Nafion of EW = 1200, at 10 % recast ionomer by weight, loaded at 6 mg of Pt/cm^2 of electrode area, and hot pressed to the decal at 125°C.

The analysis method used in the robust design process allows estimation of the η value that would be obtained under optimized conditions. Once the "optimized" η value is determined, the current density resulting from the optimized factors can be calculated. Based on the analysis of the η values determined from the 9 experiments, DMFC cell performance at 0.5 V at 80°C under the optimized conditions was predicted to be 300 mA/cm^2. A verification experiment was conducted with one MEA fabricated using the optimized levels of each factor. The actual average performance achieved, based on three consecutive trials, indeed was 300 mA/cm^2. Robust design is an iterative method; additional matrix experiments could next be designed to further optimize the formulation and conditions.

The following work, in which other factors were studied to determine their effect on cathode performance, used MEAs fabricated at the levels of ionomer EW, ionomer content, Pt loading and hot press temperature determined to be optimum from the preceding robust design process.

Cathode Potential vs. Current Density Curves

To evaluate a DMFC air cathode performance, it would obviously be desirable to know the potential of the cathode under DMFC operation conditions. The use of a reference electrode to obtain the cathode potential in an operating DMFC frequently poses problems of instability. We preferred here to evaluate the DMFC cathode potential from ordinary, two electrode cell polarization measurements. Using a two electrode configuration within the operating cell, current density vs. potential curves for a DMFC air cathode were derived from three iR corrected voltage/current density $V^{*}(J)$ measurements for (i) a methanol/air cell, (ii) a driven cell with the same methanol anode and a hydrogen evolving cathode, and (iii) a driven "hydrogen pump" cell with a hydrogen oxidation anode and a hydrogen evolving cathode.

The iR corrected potential differences measured in these three cells at given J, can be written as:

$$V^{*}_{MeOH/air}(J) = E_{air}^{MeOH}(J) - E_{MeOH}(J) \qquad [1a]$$

$$V^{*}_{MeOH/H2}(J) = E_{MeOH}(J) - E_{HER}(J) \qquad [1b]$$

$$V^{*}_{H2/H2}(J) = E_{HOR}(J) - E_{HER}(J) \qquad [1c]$$

where the asterisk designates "iR corrected" and the potential differences are written to yield positive voltage values in each case. The E's are electrode potentials (vs. some arbitrary fixed reference potential) at current density J for a methanol anode at the relevant DMFC anode conditions, E_{MeOH} (J), a DMFC air cathode at relevant DMFC cathode conditions, E_{air}^{MeOH} (J), and (well humidified) hydrogen oxidation electrode, E_{HOR}(J), and hydrogen evolution electrode, E_{HER} (J), in contact with the ionomeric membrane. The superscript $^{(MeOH)}$ in the symbol for the DMFC air cathode potential, E_{air}^{MeOH} (J), indicates that this cathode suffers the effects of methanol penetration. Each value of E is, obviously, a function of the concentration of reactants, pressure of gases and activity of protons and water, but all of those are maintained identical in the three cell measurements [1a] – [1c]. Summing [1a] and [1b], and subtracting [1c], one obtains:

$$E_{air}^{MeOH}(J) - E_{HOR}(J) = V^*_{MeOH/air}(J) + V^*_{MeOH/H2}(J) - V^*_{H2/H2}(J) \qquad [2]$$

Equation 2 explains the derivation of DMFC cathode potential at given J vs. the potential of a hydrogen oxidation anode operating at the same J. Figure 1a displays the results of the process for such a cathode operating at 60°C.

Unlike an ideal reference electrode, the HOR electrode potential varies somewhat with J. However, one can readily compare measured E_{air}^{MeOH} (J) vs. E_{HOR} (J) to measured air cathode potential vs. E_{HOR} (J) in a hydrogen/air fuel cell – the latter value is simply the iR corrected voltage of the hydrogen/air fuel cell:

$$E_{air}(J) - E_{HOR}(J) = V^*_{H2/air} \qquad [3]$$

The cathode loss specifically caused by methanol penetration to the DMFC air cathode can thus be evaluated directly from the difference between E_{air} (J) and E_{air}^{MeOH} (J), as derived from equations [3] and [2], respectively, demonstrated in Figure 1b.

As Figure 1a reveals, the potential of this, heavily Pt loaded air cathode, operating in a DMFC at 60°C on ambient air, is rather high: 0.85 V vs. the HOR electrode potential at 100 mA/cm^2. That this is very close to the full activity of this air cathode is seen in Figure 1b, which confirms that the presence of methanol has only marginal effect on the air cathode potential at 100 mA/cm^2.

Effect of temperature on cathode potential. Computer generated cathode polarization curves based on three, iR corrected cell polarization curves, as described by equations [1] and [2], were used to assess the effect of methanol crossover on cathode potential at different temperatures. As shown in Figure 2a, the increase in DMFC performance is not nearly as significant when the temperature change is from 80°C to 100°C as it is when the cell temperature is increased from 60°C to 80°C. Polarization of the anode against a hydrogen evolving electrode (cell [1b]) indicates that anode performance increases monotonously with increase in temperature, as shown in Figure 2b. The cathode polarization curves (Figure 2c) show that the cathode potential increases (cathode activity increases) with temperature between 60°C and 80°C but the potential of the cathode at 100°C is, in fact, below that at 80°C. This deviation from the behavior expected based on monotonous oxygen reduction rate enhancement with temperature must be explained by more substantial effects of methanol crossover on cathode performance at the elevated temperature of 100°C (11). Under the simplest circumstances, methanol entering the cathode from the membrane would cause a shift of air cathode potential, given by

$$\Delta E_{air} = b \log [(J_{orr} - J_{crossover}) / J_{orr}] = b \log [1 - (J_{crossover} / J_{orr})] \qquad [4]$$

where b is the Tafel slope for the ORR, J_{orr} is the oxygen reduction current density at the relevant cathode potential E and $J_{crossover}$ is the methanol crossover current density. Equation [4] describes the shift of the DMFC air cathode potential under the conditions described in (12) as "no apparent interaction". As the temperature increases, $J_{orr,}$ an interfacial process with activation energy of ca. 15 kcal/mol (13), should increase proportionately more than $J_{crossover}$ which is determined by methanol diffusivity through the ionomeric membrane, associated with an activation energy of the order of only 5 – 6 kcal/mole (11). Hence, the drop of cathode potential with temperature between 80 and 100°C must be the result of additional effects of methanol penetration on cathode potential, possibly excessive flooding.

Cathode catalyst evaluation using cathode polarization curves. Different batches of Pt black were tested to determine their effectiveness as cathode catalysts. Figure 3a shows the performance of three MEAs in DMFC configuration at 80°C, each of the MEAs using a different batch of Pt black. Figure 3b provides the cathode polarization curves for the same three Pt black cathode preparations. The relative performance of the three Pt black cathodes, as indicated by their polarization curves (Figure 3b), matches well the relative DMFC performance (Figure 3a). This result demonstrates the good repeatability of DMFC anode performance in repeated MEA fabrication and clearly points to possible gains, particularly at higher cell currents, derived from further optimization of cathode catalysts and catalyst layer preparation.

Effect of cathode backing on cathode potential. Evaluation of DMFC cathode polarization has also allowed us to isolate the effect of the nature of the air electrode backing on DMFC performance. The effect of applying the carbon powder-PTFE mixture to different substrates is indicated in Figure 4a. Under comparable conditions of carbon powder-PTFE mixture composition and loading, our DMFC cathode (and cell) performances were consistently better when a carbon cloth substrate was used for preparation of the cathode backing. A cell with cathode backing based on a carbon cloth substrate was operated continuously for a period approaching 400 hours. This cell showed stable performance at different temperatures and there was no visible deterioration of the cathode backing material after such testing.

With a carbon cloth based cathode backing selected, several types of such backing layers with somewhat different structures were evaluated for their effect on DMFC performance. Figure 4b shows the results, in terms of cathode polarization plots, for three such cathode backing layers. The commercial E-TEK backing consisted of carbon-Teflon® mixture applied to both sides of a carbon cloth, the experimental E-TEK backing had the same carbon-Teflon® mixture applied to one side of the cloth only and the "LANL backing" was also a construction based on the application of a carbon-PTFE mixture to carbon cloth. Clearly, the mode and extent of application of the carbon powder-PTFE mixture to the carbon backing affects performance, particularly at higher current densities. These advantages in cathode performance were also reflected in the performance of the corresponding methanol/air cells.

SUMMARY AND CONCLUSIONS

This work indicates that investigation and optimization of variables related to DMFC Pt cathode construction can result in better DMFC cathode performance. It points to robust design techniques as means for minimizing the number of experiments required in such optimization efforts. DMFC cathode polarization curves, generated from polarization data for three, two-electrode polymer electrolyte cells, enable evaluation of air cathode performance in presence of the methanol "leaking" through the membrane. The results show clearly that, when the Pt air cathode in a DMFC is of sufficient loading and cell operation conditions are optimized, cathode loss in the DMFC caused by methanol is marginal (< 20 mV at 100 mA/cm^2). It is thus important to realize that the net performance of a Pt cathode in a DMFC could be really high (>0.85 V vs. RHE at 100 mA/cm^2) in spite of the activity of Pt as a methanol electrooxidation catalyst. This is the result of the intrinsically superior activity of Pt as an ORR catalyst and the possibility to minimize, under some conditions, the penalty of the methanol in the cathode to only mixed potential effects (12).

Higher DMFC air cathode performance loss around temperatures of 100°C, as revealed in this work for DMFC cathodes of high Pt loading, remains a challenging target for further improvements.

ACKNOWLEDGMENTS

This work was supported by the Defense Advanced Research Projects Agency through the Defense Sciences Office and by the U.S. Department of Energy through the Office of Advanced Automotive Technology. Financial assistance to S.C.T. from the Natural Sciences and Engineering Research Council of Canada is also gratefully acknowledged.

REFERENCES

1. X. Ren, M. S. Wilson and S. Gottesfeld, *J. Electrochem. Soc.*, **143,** L12 (1996).
2. J. S. Wainwright, J-T. Wang, D. Weng, R. F. Savinell and M. Litt, *J. Electrochem. Soc.*, **142,** L121 (1995).
3. S. C. Roy, P. A. Christensen, A. Hamnett, K. M. Thomas, and V. Trapp, *J. Electrochem. Soc.*, **143,** 3073 (1996).
4. V. Trapp, P. Christensen, A. Hamnett, *J. Chem. Soc. Faraday Trans.*, **92**, 4311 (1996).
5. S. Gupta, D. Tryk, S. K. Zecevic, W. Aldred, D. Guo and R. F. Savinell, *J. Appl. Electrochem.*, **28**, 673 (1998).
6. T. E. Springer, M. S. Wilson, and S. Gottesfeld, *J. Electrochem. Soc.*, **140**, 3513 (1993).
7. M. S. Phadke, *Quality Engineering Using Robust Design*, Prentice Hall PTR, Englewood Cliffs, NJ (1989).
8. G. E. P. Box and N. R. Draper, *Empirical Model Building and Response Surfaces*, John Wiley & Sons, New York (1987).
9. G. E. P. Box, W. G. Hunter and J. S. Hunter, *Statistics for Experimenters*, John Wiley & Sons, New York, (1978).
10. F. Delime, J. M. Leger and C. Lamy, *J. Appl. Electrochem.*, **28**, 27 (1998).
11. X. Ren, T. A. Zawodzinski, F. Uribe, H. Dai & S. Gottesfeld, in Proton Conducting Membrane Fuel Cells I, S. Gottesfeld, G. Halpert and A. Landgrebe, Editors, PV 95-23, p 284, The Electrochemical Society Proceedings Series, Pennington NJ (1995).
12. D. Chu and S. Gilman, *J. Electrochem. Soc.*, **141**, 1770 (1994).
13. B. R. Scharifker, P. Zelenay, and J. O'M. Bockris, *J. Electrochem. Soc.*, **134**, 2714 (1987).

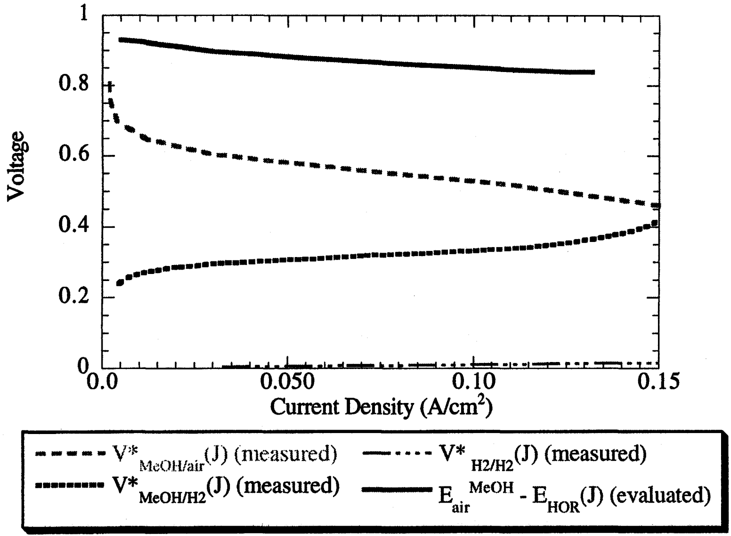

Figure 1a Derivation of DMFC cathode potential (6 mg Pt/cm^2) vs. a hydrogen oxidation anode at 60°C. CH_3OH, 0.5 mol/L and 0 psig. Air at 0 psig and 50 sccm. H_2 at 10 psig, 0.3 L/min and 100°C humidification. Active area of cell is 5 cm^2.

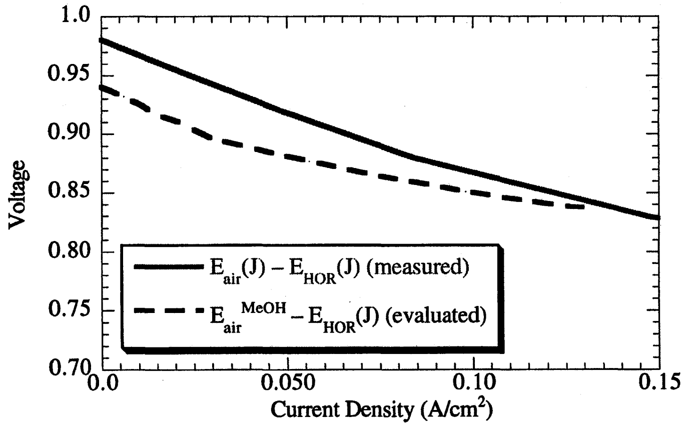

Figure 1b Evaluation of cathode loss caused by methanol penetration to the DMFC air cathode with 6 mg Pt/cm^2 at 60°C. CH_3OH, 0.5 mol/L and 0 psig. Air at 0 psig and 50 sccm. H_2 at 10 psig, 0.3 L/min and 100°C humidification. Active area of cell is 5 cm^2.

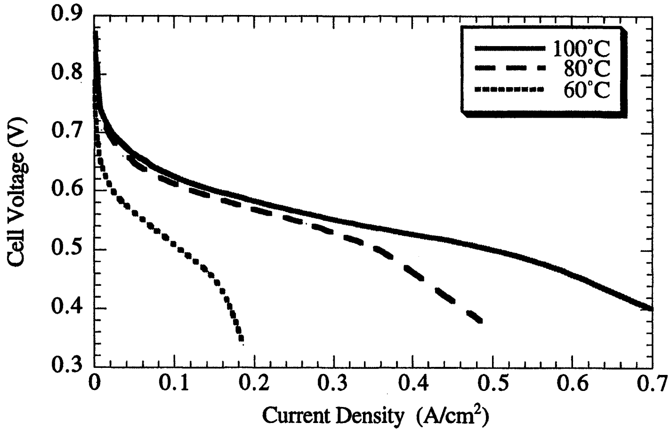

Figure 2a Effect of temperature on DMFC polarization curves. CH_3OH, 0.5 mol/L and 0 psig at 60°C; 1 mol/L and 0 psig at 80°C; 1 mol/L and 15 psig at 100°C. Air at 0 psig with no humidification at 60°C; 30 psig and 110°C humidification at 80°C and 100°C.

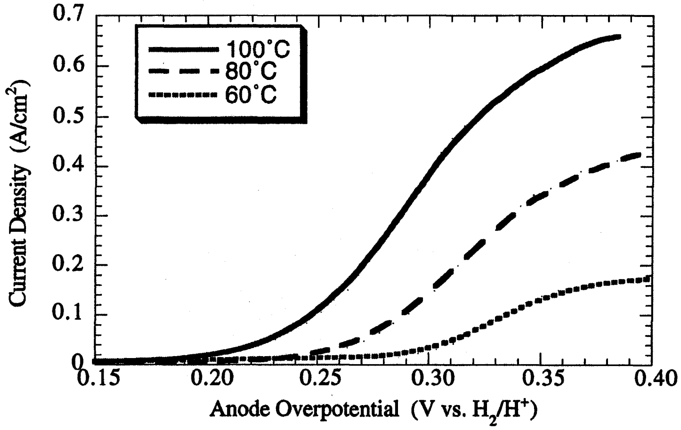

Figure 2b Effect of temperature on polarization curves in a CH_3OH/H_2 (driven) cell. CH_3OH, 0.5 mol/L and 0 psig at 60°C; 1 mol/L and 0 psig at 80°C; 1 mol/L and 15 psig at 100°C. H_2 at 10 psig and 100°C humidification at 60°C; 30 psig and 105°C humidification at 80°C and 100°C.

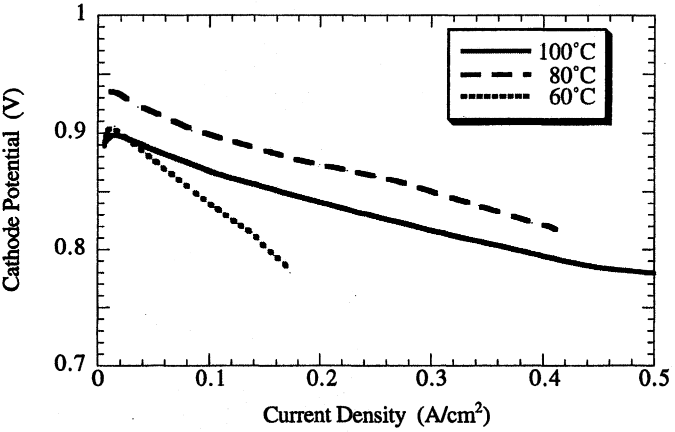

Figure 2c Effect of temperature on DMFC cathode potential (vs. potential of a hydrogen oxidation electrode operating at the same current density). CH_3OH, 0.5 mol/L and 0 psig at 60°C; 1 mol/L and 0 psig at 80°C; 1 mol/L and 15 psig at 100°C. Air at 0 psig and no humidification at 60°C; 30 psig and 110°C humidification at 80°C and 100°C.

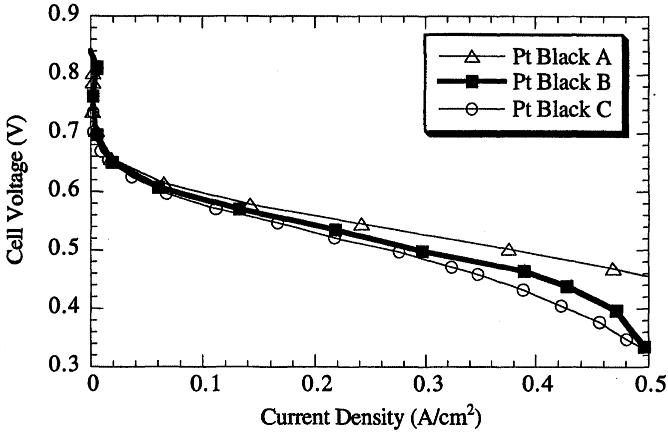

Figure 3a Polarization curves for three CH_3OH/air cells at 80°C with MEAs containing three different Pt black cathode catalysts. Pt black loading in each case: 1.6 ± 0.1 mg/cm^2. 1 mol/L CH_3OH; air at 30 psig and 0.45 L/min

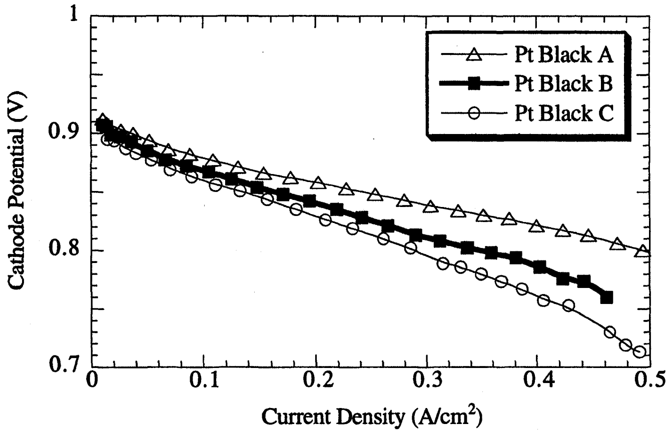

Figure 3b Cathode polarization curves at 80°C of three different Pt black cathode catalysts. Pt black loading 1.6 ± 0.1 mg/cm^2. 1 mol/L CH_3OH; air at 30 psig and 0.45 L/min.

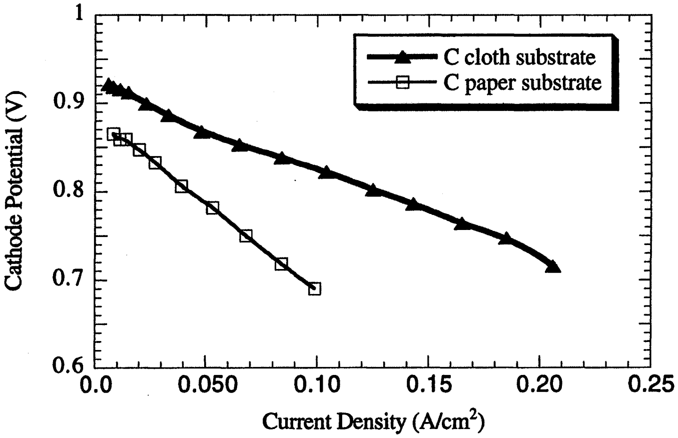

Figure 4a Effect of cathode backing substrate material on cathode polarization (potential vs. HOR) in DMFC at 60°C. 0.5 mol/L CH_3OH; air at 0 psig and 50 sccm.

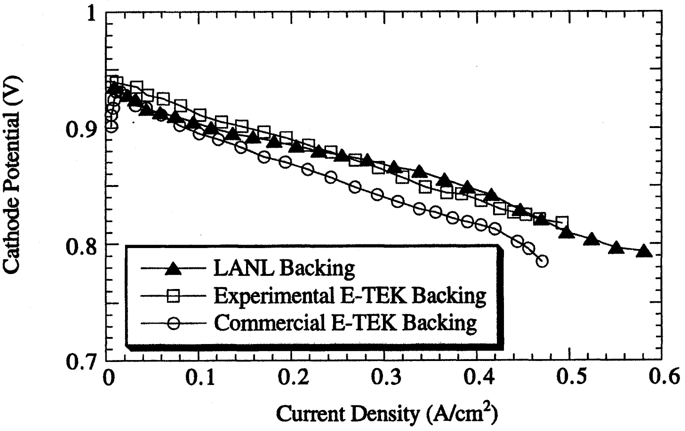

Figure 4b Effect of fine structure of the treated cathode backing layer on DMFC cathode polarization at 80°C, shown for three such layers based on the same carbon cloth substrate

Proton_Conducting_Membrane_Fuel_Cells_II, PV 1998-27, 341-357 (1998)
DOI: 10.1149/199827.0341PV © The Electrochemical Society

DIRECT METHANOL FUEL CELL: TRANSPORT PROPERTIES OF POLYMER ELECTROLYTE MEMBRANE AND CELL PERFORMANCE

X. Ren, T. E. Springer, and S. Gottesfeld

Electronic and Electrochemical Materials and Devices, MS-D429
Los Alamos National Laboratory, Los Alamos, NM 87545

ABSTRACT

Methanol and water absorption in 1100 and 1200 e.w. Nafion® membranes was determined by weighing P_2O_5 dried and methanol solution equilibrated membranes. Both methanol and water absorption in the 1200 e.w. membrane is about 70-74 % of that in the 1100 e.w. membrane. The methanol cross-over rate corresponding to that in a direct methanol fuel cell (DMFC) at open circuit was measured using a voltammetric method in the DMFC configuration and under the same cell operating conditions (temperature, humidification and concentration of feed methanol solution). Accounting for the thickness difference between the membrane samples, the methanol cross-over rate through a 1200 e.w. membrane is 52 % of that through a 1100 e.w. membrane. To resolve the cathode and anode performances in an operating DMFC, a dynamic hydrogen electrode (DHE) was used as a reference electrode. Results show that in DMFC operation the cathode could be flooded due to the high water and methanol cross-over rates, especially through the 1100 e.w. membrane at a cell temperature below 80 °C. An increase in methanol cross-over rate as incurred by increasing the concentration of the feed methanol solution, increasing the cell operating temperature or using a membrane more permeable to methanol decreases the cathode potential of the DMFC at open circuit. As the cell current density is increased, the cathode potential of the DMFC can approach the cathode potential of a H_2/air cell, thanks to the consumption of methanol at the anode and consequent decrease in methanol cross-over rate.

INTRODUCTION

Recently, direct methanol fuel cells (DMFCs) using polymer electrolyte membrane have demonstrated improved performance (1-5). Compared to fuel cell systems using H_2 from methanol reforming, DMFCs have the advantage of simpler system, and with further development may even achieve higher overall energy efficiency(6). Two major obstacles that currently delay application of DMFCs are the low activity of methanol electro-oxidation catalysts and the cross-over of methanol through the polymer electrolyte membrane. It has been realized that methanol cross-over to the cathode not only lowers fuel utilization but also adversely affects the oxygen cathode (7), resulting in a relatively low cell performance. Two methods of measuring methanol cross-over rate in the fuel cell configuration are currently in use; an optical, infrared (IR) method measuring CO_2 emission flux in the cathode effluent (8,9), and a voltammetric method developed in this laboratory (10,11). The IR method can be used to study effects of the DMFC operating conditions, particularly cell current, on methanol cross-over rate. The voltammetric method gives the methanol cross-over current relevant to the cross-over rate in the DMFC at open circuit, and is especially useful for membrane characterization. In this paper, the methanol cross-over currents through 1100 e.w. and 1200 e.w. membranes were measured using the voltammetric method. IR measurements for the DMFC at O.C. conditions were also used to confirm the methanol cross-over rate. The effects of methanol cross-over on DMFC performance were evaluated using a dynamic hydrogen reference electrode (DHE).

EXPERIMENTAL

The thin-film catalyst layers on the Nafion® membranes were formed using the decal method developed in this laboratory previously for H_2/air fuel cell (12). The anode catalyst for methanol oxidation was unsupported $Pt\text{-}RuO_x$ (RV 30-30 from E-Tek, Inc) and the cathode catalyst for oxygen reduction was 60% Pt on carbon support (from E-Tek, Inc). To prepare the catalyst ink mixtures, 5% Nafion® solution (1100 E.W., Solution Technology, Inc) was added to the water-wetted catalysts. Suitable anode ink composition was 85 weight percent (w/o) $Pt\text{-}RuO_x$ and 15 w/o Nafion®, and the cathode ink composition was 88.5 w/o 60% Pt on carbon support and 11.5 w/o Nafion®. To prepare the membrane/electrode assembly (MEA), anode and cathode inks were uniformly painted onto two Teflon blanks (5 cm^2) to give a 2 $mgcm^{-2}$ $Pt\text{-}RuO_x$ on the anode and 1.2 $mgcm^{-2}$ Pt on the cathode. After drying at 145 °C for 10 minutes, the catalyst layers were transferred and bound to a pre-dried Nafion® membrane (60 °C on a vacuum table for 45 min.) by hot pressing at 125 °C and 105 atm for 120 s. After the Teflon blanks were peeled off, the cells employing the catalyst/membrane assembly were assembled as shown in Fig.1. It should be noted that in our more recent DMFC studies, we have reached MeOH/air cell current densities of 0.3 A cm^{-2} at 0.5 V using higher catalyst loading, more active anode catalyst and further optimized MEA preparation (5). While the MEA's prepared here were somewhat less active, they were prepared identically for the two membranes.

RESULTS AND DISCUSSION

Water And Methanol Absorption

Samples of Nafion® 117 and Nafion® 1210 (10 mil, 1200 e.w.) membranes were pretreated as previously described (4), *i.e.*, by boiling for over 1 hour in each step in 3% H_2O_2, deionized (D.I.) water, 0.5 M H_2SO_4, and again in D.I. water. Wet membrane porosity(ε) and water/methanol fluid uptake were determined at 22 °C by weighing P_2O_5 dried and solution equilibrated membranes. Eq. 1 was used to calculate the membrane porosity (13):

$$\varepsilon = \frac{\text{fluid uptake volume}}{\text{total volume}} = \frac{\left(W_{\text{wet}} - W_{\text{dry}}\right) \cdot \rho_{\text{dry}}}{\left(W_{\text{wet}} - W_{\text{dry}}\right) \cdot \rho_{\text{dry}} + W_{\text{dry}} \cdot \rho_{\text{sol}}} \qquad [1]$$

where ρ_{dry} is the dry membrane density (2.0 gcm^{-3} for non-porous PTFE assumed for the dry Nafion® membrane) and ρ_{sol} the solution density. The overall uptake of solution molecules per sulphonic acid group in the membranes was calculated using Eq.2, and the results are listed in Table 1 and 2 for N117 and N 1210 membranes, respectively.

$$\lambda_{total} = \frac{(W_{wet} - W_{dry})}{W_{dry}} \bullet \frac{E.W.memb.}{18x_{H2O} + 34(1 - x_{H2O})} \qquad [2]$$

where x_{H2O} is the molar fraction of water in the solution. Our previous NMR and voltammetric experiments have shown that the water and methanol reside almost completely in the ion-cluster pores and the connecting channels of the membranes (10), confirming that water and methanol are excluded from the hydrophobic PTFE region due to their very low solubility in that region. Furthermore, the NMR studies showed that the composition of the fluid within the membrane is nearly identical with that of the equilibrating solution (10). The uptake of water molecules per sulphonic acid group (λ_{H2O}) and uptake of methanol molecules per sulphonic acid group (λ_{MeOH}) were then calculated from the λ_{total} using Eq. 3;

$$\lambda_{H2O} = \lambda_{total} \bullet x_{H2O} \; ; \; \lambda_{MeOH} = \lambda_{total} \bullet (1 - x_{H2O}) \qquad [3]$$

From the results listed for both membranes in Tables 1 and 2, it shows that for a membrane in contact with a methanol solution the water molecule uptake remains nearly constant while the methanol molecule uptake increases with the concentration of methanol solution. The methanol molecule uptake is in addition to the water molecules uptake by the membrane in contact with pure water, only with the most concentrated (>10 M) methanol solutions, some drop in water uptake is observed. This result indicates that the degree of membrane swelling increases as the concentration of contacting methanol solution is increased. For the methanol concentration region studied, the water uptake by a N1210 membrane is about 73 % of that by a N117 membrane. The methanol uptake by a N1210 membrane is also 70-74 % of that by a N117 membrane.

Methanol Permeation Rate

The limiting currents (J_{lim}) of methanol permeating through our MEA's in fuel cell configuration were measured using the voltammetric method as previously described(10). Figure 1 (bottom) shows the transport processes and electrode reactions involved during the measurement. A methanol solution was fed to the left-side electrode as in a DMFC. Methanol would permeate through the left carbon cloth backing, the thin (~ 3 μm) Pt-RuO_x catalyst layer, and the Nafion® membrane. Permeated methanol flux was determined by measuring the limiting current density (J_{lim}) resulting from the mass transport controlled methanol electro-oxidation at the Nafion® membrane/Pt catalyst interface on the right side of the cell. The right side compartment was kept in inert atmosphere of humidified N_2 or pure water. The cell used for permeation measurement (thereafter referred as "permeation cell") is operated by imposing an external voltage, with hydrogen evolution as the counter process on the left side of the cell in Figure 1. The equivalent methanol cross-over currents in the DMFC ($J_{cross\text{-}over}$) at open circuit are actually higher than the measured J_{lim}. This is because in the "permeation cell" there is a backward methanol transport associated with the electro-osmotic drag of fluid by the reverse protonic current of J_{lim}. The difference between J_{lim} and $J_{cross\text{-}over}$ increases with more concentrated methanol feeds. We have recently developed a mathematical model to derive a correction which shows that Eq. 4 can be used to calculate $J_{cross\text{-}over}$ from J_{lim} (11). The correction factor K_{dl} is a function of the overall electro-osmotic drag coefficient of the proton transport in the membrane and the concentration of feed methanol solution. Table 3 lists the methanol cross-over rate through N117 and N1210 membranes at 80 °C.

$$J_{cross-over} = \frac{J_{\lim}}{k_{dl}} \qquad [4]$$

In Fig.2, J_{lim} and $J_{cross\text{-}over}$ from Table 3 are plotted against the concentration of feed methanol solution. If the cross-over current is limited by methanol diffusion through the membrane, then $J_{cross\text{-}over} = 6FD_mCp/d$ (where D_m is the methanol diffusion coefficient in membrane; C - concentration of feed methanol solution; p - partition coefficient and d - membrane thickness). $J_{corss\text{-}over}$ exhibits the expected linear dependence on methanol concentration. The dependence of measured J_{lim} on C had noticeable curvature explained by the effect of electro-osmotic drag (11).

DMFC Performance

Figs. 3 and 4 show the performance of DMFC's using N117 and N1210 membranes at 80 °C, using liquid methanol solution/air (20psig, humidified at 85 °C) feeds. Higher methanol cross-over rate through the N117 membrane than that through the N1210 membrane results in lower OCV of the cell using N117 membrane. For each membrane, increase in the concentration of methanol feed solution lowers the cell potential at open circuit. Even though the cell resistance with membrane N1210 is higher than that of the cell with N117 (0.36 Ω cm^2 *vs.* 0.16 Ω cm^2), the DMFC using N1210 shows better performance at 80 °C than the DMFC using N117. To resolve the anode and cathode performance, our cells also contained a dynamic hydrogen electrode (DHE) as reference. Our DHE exhibited good stability with no serious potential drifting even at a cell current up to 1000 mAcm^{-2} (a potential drift amounting to ± 50 mV at a cell current up to 500 mAcm^{-2} was reported by Küver *et al* for their DHE (14)).

Validity of DHE as Reference Electrode in an Operating DMFC. Fig. 5 shows the schematic diagram of DHE in DMFC structure. The DHE electrodes are a pair of carbon cloth discs (1.5 mg cm^{-2} Pt on carbon support and 0.5 mg cm^{-2} 1100 e.w. Nafion® loadings) of 3 mm in diameter. The center of DHE electrode was separated from the edge of fuel cell electrodes by 5.5 mm. A galvanostatic circuit provided a current density of 6 mA cm^{-2}, which is 140 times higher than that used by Küver *et al* (14). Our DHE electrode exhibited stable potential, and also eliminated the pre-charge step used by Küver *et al* (14). Following are descriptions of a set of experiments we performed to verify the validity of DHE in an operating fuel cell.

DHE in H_2/H_2 Cell. By feeding both cell anode and cathode with H_2 (20 psig, 0.6 L min^{-1} and 115 °C humidified), the fuel cell electrodes act at zero cell current as reversible hydrogen electrode (RHE). The measured potential of the DHE vs. the RHE was -3 mV for the current density used in the reference electrode loop. By applying an external voltage across the H_2/H_2 cell, the cell acts like a H_2 pump. Fig. 6 shows the electrode polarization curves of H_2 oxidation on Pt-RuO$_x$ and H_2 evolution on Pt obtained by using the DHE. The polarizations are small and of similar magnitude, reflecting the fast and reversible electrode processes of H_2 oxidation and H_2 evolution.

One of the problems of the previously reported DHE in fuel cell structure was the serious potential drift when the cell was under high current (14). This was explained as due to changes in the water (and therefore, the protonic) activity in the vicinity of the reference electrode caused by the electro-osmotic drag of water along the protonic cell current. This problem was solved in our DHE by separating the DHE and the fuel cell electrodes sufficiently apart (4 mm) so that the membrane potential at DHE is fixed at mid potential drop across the membrane. This was verified by measuring the membrane resistances across ref-anode, and across ref-cathode. As shown in Fig. 7, the potential drops across ref-anode and across ref-cathode were identical, at half of the potential drop between anode and cathode, even at a cell current density up to 1200 mA cm^{-2}. The potential drop between the two reference electrodes at zero current in the reference electrode loop (both electrodes act as RHE) was also measured and found to be essentially zero with the H_2 pump cell under current.

DHE in DMFC. Fig. 8 compares three methanol anode polarization curves, two were measured against DHE and one against H_2 evolution counter electrode in a well humidified N_2 atmosphere in the driven two electrode cell configuration. The polarization curves of methanol oxidation in DMFC measured with DHE reference and with the driven two electrode cell (H_2 evolution on the counter cell electrode in a well humidified N_2 atmosphere) are nearly identical. This verified that a stable DHE potential in the operating DMFC. In comparison, the H_2 evolution counter cell electrode serves as a poor reference electrode in the driven two electrode cell. At a too low cell current, the counter electrode had a higher potential than the DHE reference electrode; and at a too high cell current, the counter electrode had a lower potential than the DHE reference. In the former case, trace amount of O_2 in the N_2 stream may affect the counter electrode potential, and in the latter case, the over-potential of H_2 evolution at the counter cell electrode (as shown in Fig. 6) becomes noticeable.

Resolved Anode and Cathode Performance in DMFC. By using DHE as reference electrode, the DMFC performance shown in Figs. 3 and 4 could be further resolved to show anode and cathode polarizations. Figs.9 and 10 show anode polarization with various concentrations of feed methanol solutions. The sharp cell potential drops at a cell current density above 50 mAcm^{-2} seen in Figs.3 and 4 with 0.2 M methanol feed were now clearly due to the anode concentration polarization of methanol transport through the anode carbon cloth backing. With 1 M methanol feed, some concentration polarization still exists at a cell current density above 200 mA cm^{-2}. The anode of the DMFC using a N1210 membrane showed slightly better activity than that of the DMFC using a N117 membrane.

Figs.11 and 12 show the air cathode polarization curves in DMFC's and H_2/Air cells constructed from anode and cell polarization curves. The air cathode of the H_2/air cell using a N117 membrane had better performance than that of the H_2/air cell using a N1210 membrane (at 0.8 V, cell current is 350 mA cm^{-2} for N117, and below 200 mA cm^{-2} for N1210). The air cathode with a N1210 membrane showed significant histeresis in the downward and upward cell voltage scans, exhibiting higher potential in the upward cell voltage scan (after passing high current). This phenomenon indicates a poorly hydrated N1210 membrane. Uribe *et al* reported that in a less well humidified Nafion® membrane, the O_2 reduction electrode process at Pt becomes sluggish (15). In the upward potential scan of the H_2/Air cell, arrival of water by electro-osmotic drag and water formed through

O_2 reduction at a higher current density earlier applied hydrates the membrane near the vicinity of cathode, and thus cathode potential increases. In contrast, the air cathode polarization curves in the DMFC using a N1210 membrane did not show such histeresis. This indicates that the air cathode in the DMFC is well hydrated due to the fact that the anode is in contact with a liquid methanol solution feed.

Fig. 11 shows that the cathode potential of DMFC at open circuit decreases with increase in methanol cross-over rate, caused by increasing the concentration of feed methanol solution. There is also a rapid decrease in the cathode potential at a cell current density > 200 mA cm^{-2}, which we believe is due to cathode flooding. More evidence for cathode flooding is indicated in Fig.13, which shows that there is a quite different changes in the cathode potential at a cell current > 200 mA cm^{-2} below and above 80 °C. With the cell operated at a temperature above 80 °C, cathode water removal becomes more efficient, and the cathode is less likely to be flooded. The methanol cross-over rate in an operating fuel cell measured using an optical IR method, showed that as the cell current is increased the methanol cross-over rate decreases (8,10). This is because more methanol is consumed at the anode catalyst layer before it reaches the membrane. Consequently, the cathode potential in DMFC approaches that in the H_2/air cell as shown in Fig. 12 and 13 for the non-flooded cathodes. The increase in methanol cross-over rate caused at a higher cell temperature is also shown in Fig.13 to decrease the cathode potential of the DMFC at open circuit.

Although the air cathode with a N1210 membrane has poorer performance than that with a N117 membrane in H_2/air cell, the air cathode with a N1210 membrane performed considerably better in DMFC than that with a N117 membrane (Figs. 11 and 12). There is a relatively small potential loss at open circuit, and the polarization curves at higher current density matches more closely to the air cathode polarization curve in the H_2/air cell. The lower methanol cross-over rate as well as the lower water cross-over rate through a N1210 membrane are responsible to the better cathode performance in DMFC.

CONCLUSIONS

The following conclusions summarize the results presented here:

A Nafion® 1200 e.w. membrane exhibits lower water and methanol absorption than an 1100 e.w. membrane. Adjusted for the thickness difference, the methanol cross-over rate through a 1200 e.w. membrane is only half of that through a 1100 e.w. membrane. A product of the methanol cross-over current density (mA cm^{-2}) and membrane resistance (Ω cm^2) can be used to select membranes for DMFC application, since this number eliminates thickness dependence of membrane protonic conductance and methanol flux. The smaller the product the better. The values of this product for 1200 e.w. and 1100 e.w. Nafion® membranes (for 1 M methanol feed) are 38.5 and 44.3 (mA Ω), respectively at 80 °C.

We verified that a DHE can serve as a stable reference electrode in a DMFC. Using a DHE, we found that, with our DMFC configuration, there is a noticeable methanol concentration polarization with 1 M methanol feed in the anode carbon cloth backing when cell current density is >200 mA cm^{-2}. The anode of a DMFC using a N1210 membrane exhibits slightly better polarization curves than those of DMFC using a N117 membrane.

An increase in methanol cross-over rate decreases the air cathode potential at open circuit. Such methanol cross-over increase can be caused by using a feed methanol solution of higher concentration, a more methanol permeable membrane or a higher cell temperature.

Although the air cathode of H_2/air cell using a N1210 membrane is considerably poorer than that of H_2/air cell using a N117 membrane, the air cathode of a DMFC using a N1210 membrane has much better performance than that of DMFC using a N117 membrane, thanks to lower permeability of the MeOH solution at a given temperature. The higher water and methanol permeation through a N117 membrane causes cathode flooding in DMFC operation. Such cathode flooding can be relieved by operating the DMFC at a temperature above 80 °C, or using non-humidified air feed at a cell temperature below 80 °C. We have aslo optimized the cell structure recently to relieve the cathode flooding at a cell temperature below 80 °C to achieve better DMFC performance with a N117 membrane.

ACKNOWLEDGMENT

This work was supported by the U. S. Department of Energy and by the Defense Advanced Research Project Agency (DARPA).

REFERENCES

1. S. Gottesfeld, G. Halpert, and A. Landgrebe, Eds., *Proton Conducting Membrane Fuel Cells 1.* PV 95-23, The Electrochemical Society, Pennington, NJ, (1995).
2. J.A. Kosek, C.C. Cropley, G. Wilson, A.B. LaConti, and S. Narayanan. *Proceedings of the 28th Intersociety Energy Conversion Engineering conference (IECEC),* Vol. 1,p.1209 (1993).
3. S. Surampudi, S. R. Narayanan, E. Vamos, H. Frank, G. Halpert, A. Laconti, J. Kosek, G. K. S. Prakash, and G.A. Olah, *Journal of Power Sources.* **47,** 377 (1994).
4. X. Ren, M. S. Wilson, and S. Gottesfeld, *J. Electrochem. Soc.* **143**, L12 (1996).
5. X. Ren, S.C. Thomas, P. Zelenay, and S. Gottesfeld, "Direct Methanol Fuel Cells: Developments for Portable Power and for Potential Transportation Applications", 1998 Fuel Cell Siminar, Palm Springs, California.
6. X. Ren, M. S. Wilson, and S. Gottesfeld in *Proton Conducting Membrane Fuel Cells 1,* S. Gottesfeld, G. Halpert, and A. Landgrebe, Eds. PV 95-23, The Electrochemical Society, Pennington, NJ, p.252 (1995).
7. D. Chu and S. Gilman, *J. Electrochem. Soc.* **141,** 1770 (1994).
8. S. R. Narayanan, H. Frank, B. Jeffries-Nakamura, M. Smart, W. Chun, and G. Halpert, in *Proton Conducting Membrane Fuel Cells 1,* S. Gottesfeld, G. Halpert, and A. Landgrebe, Eds. PV 95-23, The Electrochemical Society, Pennington, NJ, p.278 (1995).
9. D. L. Maricle, B.L. Murach, and L.L. Van Dine, Abstract 35, The Electrochemical Society Extended Abstracts, Vol 94-1, San Francisco, CA., May 22, (1994).

10. X. Ren, T. A. Zawodzinski, F. Uribe, H. Dai, and S. Gottesfeld, in *Proton Conducting Membrane Fuel Cells 1*, S. Gottesfeld, G. Halpert, and A. Landgrebe, Eds. The Electrochemical Society, Pennington, NJ, p.284 (1995).
11. X. Ren, T.E. Springer, T. Zawodzinski, and S. Gottesfeld, "Methanol Transport through Nafion Membranes: Electroosmotic Drag Effects on Potential Step Measurements", manuscript to be submitted to *J. Electrochem. Soc.*.
12. M. S. Wilson and S. Gottesfeld, J. Appl. Electrochem. 22, 1 (1992).
13. M. W. Verbrugge, J. Electrochem. Soc. 136, 417 (1989).
14. A. Küver, I. Vogel, W. Vielstich, J. Power source, 52,77 (1994).
15. F.A. Uribe,T.E. Springer, and S. Gottesfeld, J. Electrochem. Soc.,139,765 (1992).

Table 1. Nafion®117 membrane porosity and λ (uptake of solution molecules per sulphonic group) at 22 °C.

MeOH conc. mol. dm^{-3}	Membrane Porosity	λtotal	λH_2O [b]	λMeOH
0.0 (D.I.Water)	0.4048 ± 0.0112 a	20.76 ± 0.96	20.76 ± 0.96	0.0
1.0	0.4131	21.07	20.69	0.38
2.0	0.4233	21.52	20.71	0.81
4.0	0.4396	22.13	20.40	1.73
6.5	0.4571	22.47	19.46	3.01
8.0	0.4953	25.31	20.99	4.32
10.0	0.5052	25.11	19.48	5.62

a-- Average and standard deviation from ten samples;

b-- Average value of λH_2O for membrane in contact with all methanol solutions is 20.29 ± 1.21.

Table 2. Nafion® 1200 ew 10 mil membrane porosity and λ at 22 °C.

MeOH conc. mol. dm^{-3}	Membrane Porosity	λtotal	λH_2O [b]	λMeOH
0.0 (D.I.Water)	0.3142 ± 0.003 [a]	15.29 ± 0.22	15.29 ± 0.22	0.0
1.0	0.3236	15.60	15.32	0.28
2.0	0.3303	15.77	15.17	0.59
4.0	0.3376	15.64	14.42	1.22
6.5	0.3671	16.88	14.61	2.26
8.0	0.3788	17.16	14.23	2.93
10.0	0.3950	17.52	13.60	3.93
13.0	0.4249	18.34	12.56	5.78

a-- Average and standard deviation from 7 samples;

b-- Average value of λH_2O for membrane in contact with all methanol solutions is 14.56 ± 0.64.

Table 3. Measured limiting current (J_{lim}) and calculated DMFC open-circuit cross-over current ($J_{cross\text{-}over}$) for N117 and N1210 membranes at 80 °C.

MeOH conc. mol dm^{-3}	k_{dl}	N117 J_{lim} mA cm^{-2}	N117 $J_{cross\text{-}over}$ mA cm^{-2}	N1210 J_{lim} mA cm^{-2}	N1210 $J_{cross\text{-}over}$ mA cm^{-2}
0.10	0.9869	7.8	7.9	-	-
0.20	0.9745	-	-	7.5	7.7
0.25	0.9676	22.8	23.6	10.3	10.6
0.50	0.9373	58.0	61.9	22.2	23.7
1.00	0.8829	116	131	42	47.6
2.00	0.7930	220	277	85	107

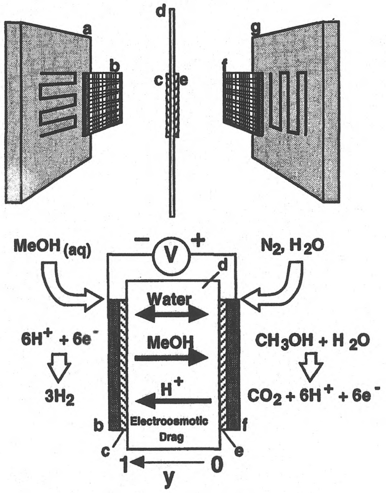

Figure 1. Schematic diagrams showing methanol permeation measurement in DMFC configuration; (a) and (g) graphite blocks with cross-patterned flow field; (b) and (f) carbon cloth backings; (c) Pt-RuO_x thin film catalyst layer; (d) Nafion® membrane; (e) Pt black thin film catalyst layer. For the permeation measurement, the humidified air feed in DMFC is replaced by a humidified nitrogen feed. The electro-oxidation of methanol permeated through membrane/electrode assembly takes place at e.

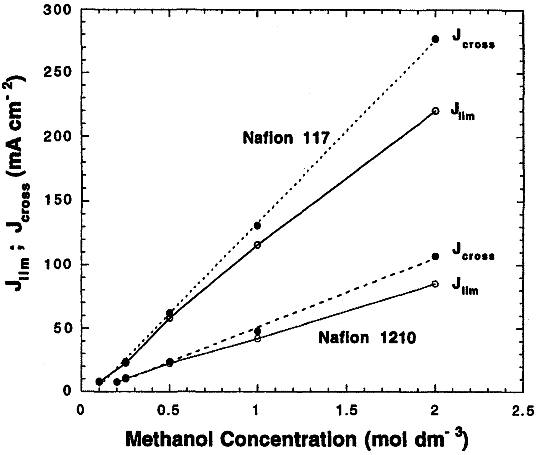

Figure 2. Plots of J_{lim} , measured in the permeation cell, and $J_{cross\text{-}over}$ for the DMFC at open-circuit calculated from J_{lim} using Eq. 4 *vs.* the concentration of feed methanol solution at 80 °C.

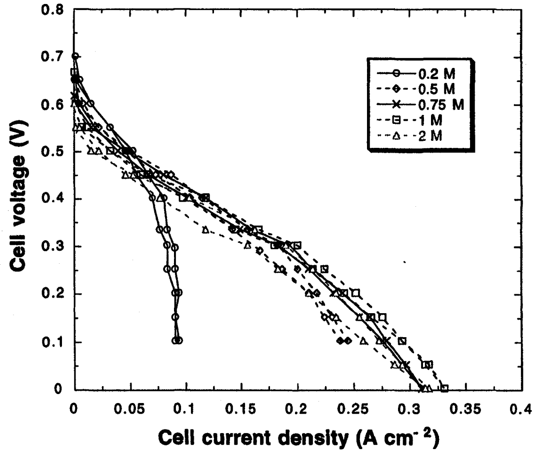

Figure 3. DMFC (MeOH/air) polarization curves using a N117 membrane with different MeOH feed concentration. Air at 20 psig at 0.6 L min^{-1}, 85 °C humidified, cell at 80 °C.

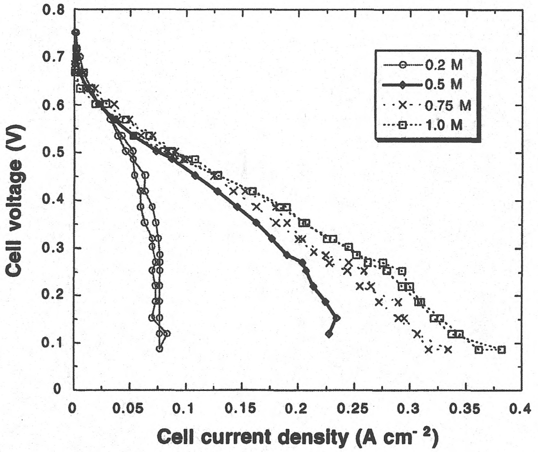

Figure 4. DMFC (MeOH/air) polarization curves using a N1210 membrane with different MeOH feed concentration. Air at 20 psig at 0.6 L min^{-1}, 85 °C humidified, cell at 80 °C.

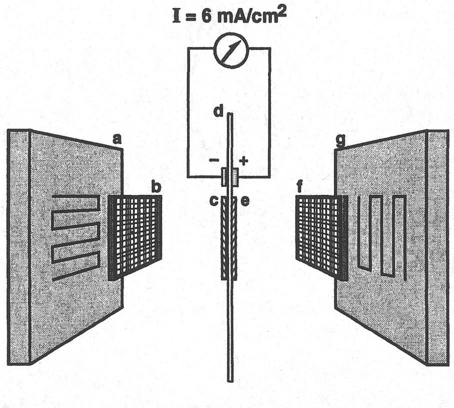

Figure 5. Schematic diagram showing DHE circuit in DMFC structure. (a) and (g) graphite blocks with cross-patterned flow field; (b) and (f) carbon cloth backing; (c) Pt-RuO$_x$ thin film anode catalyst layer; (d) Nafion® membrane; (e) Pt thin film cathode catalyst layer. The flow channels were designed to pass over the pair of electrodes in the DHE circuit.

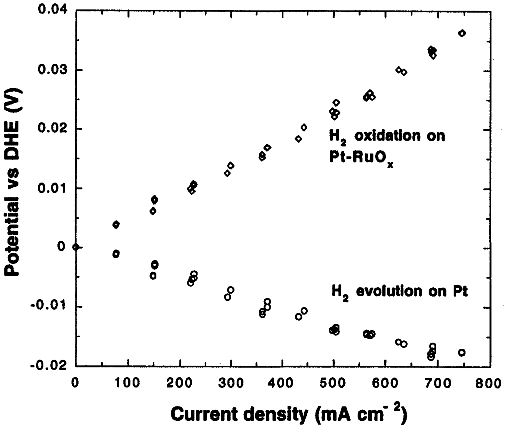

Figure 6. Polarization curves of H_2 oxidation on Pt-RuO_x and H_2 evolution on Pt electrodes at 80 °C (with IR correction) measured with a DHE reference electrode. H_2 feed is at 20 psig, 0.6 L min^{-1} and 115 °C humidified.

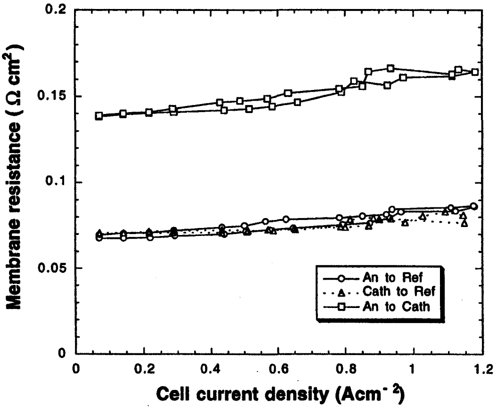

Figure 7. Membrane high frequency (8 k Hz) resistances measured between anode-cathode, anode- DHE ref and cathode- DHE ref at 80 °C, for a hydrogen pump cell with H_2 (20 psig, 0.6 L min^{-1}, 115 °C humidified) feed.

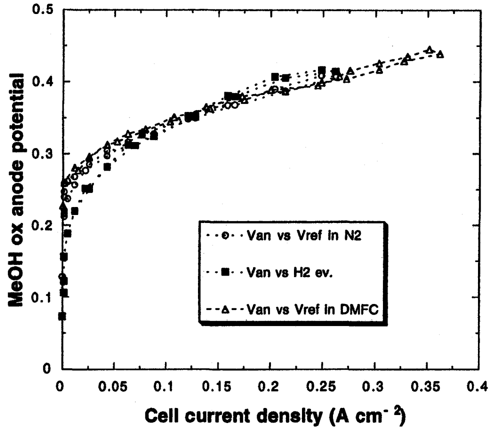

Figure 8. Methanol anode polarization curves at 80 °C measured in DMFC using DHE and in two electrode driven cell using H_2 evolution counter electrode. The DMFC was fed with 1 M methanol/air (20 psig, 0.6 L min^{-1}, 85 °C humidified) and the 2-electrode cell was fed with 1 M methanol/N_2 (20 psig, 0.6 L min^{-1}, 115 °C humidified).

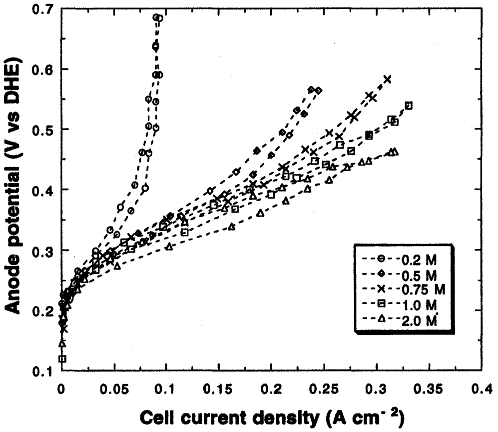

Figure 9. DMFC anode polarization curves using a N117 membrane at 80 °C (iR corrected). See Figure 3 for cell operating conditions.

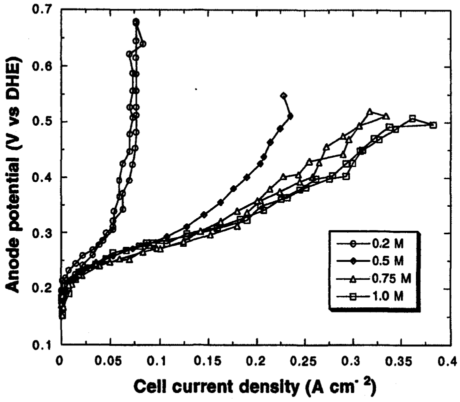

Figure 10. DMFC anode polarization curves using a N1210 membrane at 80 °C (iR corrected). See Figure 4 for cell operating conditions.

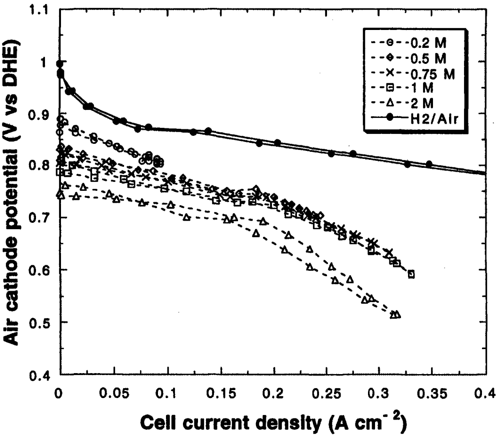

Figure 11. DMFC cathode polarization curves using a N117 membrane at 80 °C (iR corrected). See Figure 3 for cell operating conditions.

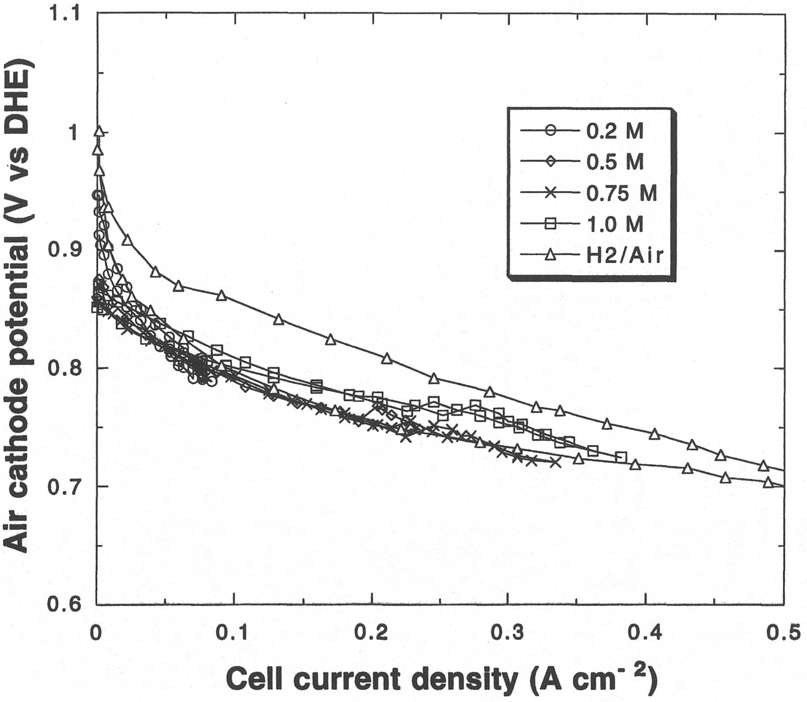

Figure 12. DMFC cathode polarization curves using a N1210 membrane at 80 °C (iR corrected). See Figure 4 for cell operating conditions.

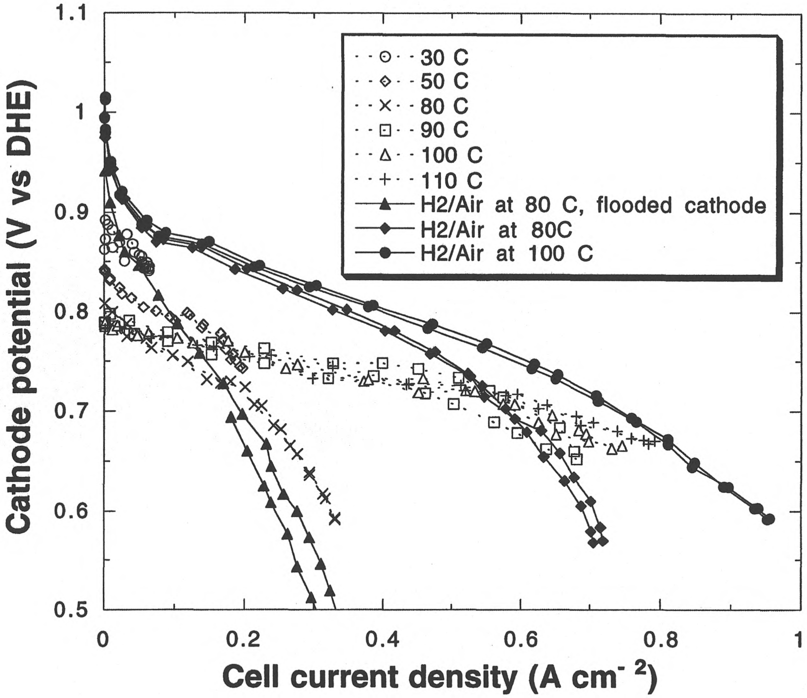

Figure 13. Cathode polarization curves of DMFC and H_2/air cell using a N117 membrane at various cell temperatures (iR corrected). DMFC was fed with 1 M MeOH/air (20 psig, 0.6 L min^{-1}, humidified at 5 °C higher than the cell temperature). H_2/air cell was fed with H_2(20 psig, 0.6 L min^{-1}, humidified at 105° C) and air (20 psig, 0.6 L min^{-1}, humidified at 115 °C for the flooded cathode, and 5 °C higher than the cell temperature for the normal cathode).

Proton_Conducting_Membrane_Fuel_Cells_II, PV 1998-27, 358-364 (1998)
DOI: 10.1149/199827.0358PV © The Electrochemical Society

CS^+- DOPED POLY-PERFLUOROSULFONATE MEMBRANES FOR APPLICATION IN DIRECT METHANOL FUEL CELLS

Vincenzo Tricoli

Dipartimento di Ingegneria Chimica, Chimica Industriale e Scienza dei Materiali
University of Pisa – 56126 – Pisa, ITALY

Abstract

Poly-perfluorosulfonic acid membranes were doped with cesium ions to several degrees. These, along with the H^+- form membrane, were investigated in relation to methanol permeability as well as to hydrogen ion conductivity at room temperature. While retaining considerable conductivity, the cesium doped membranes are highly impermeable to methanol. We found that methanol permeability in the membrane reduced by almost two orders of magnitude, owing to the presence of cesium ions. These findings are discussed on the ground of the alterations produced by cesium in membrane micro-structure. Also presented are some preliminary results relative to the permeability and conductivity in these membranes at temperatures up to 60 °C.

Introduction

Low temperature polymer electrolyte fuel cells (PEFCs) are receiving increasing attention as modular power sources that combine high energy efficiency and nonpolluting emission. Application of these devices in vehicular transportation represents an enormous potential market. Significant advances in the H_2/O_2 PEFC technology have been recorded during the last few years (1). However, the use of hydrogen as a fuel in electric vehicles entails obvious problems. Methanol is a low cost liquid fuel having conspicuous electrochemical activity. Recently, great attention has especially been devoted to liquid-feed methanol PEFCs (2). However, large scale commercialization of the direct methanol fuel cell (DMFC) is at present inhibited by two major technical problems. One is slow methanol oxidation kinetics on the anode catalyst. The second is methanol diffusion from the anode to the cathode side, across the polymer electrolyte membrane. That causes loss of fuel, reduced cathode voltage, and excess thermal load in the cell. Poly-perfluorosulfonic acid (Nafion®) membranes are commonly used as electrolytes in DMFCs, owing to good chemical and thermal resistance and ionic conductivity. However, it has been found that over 40% methanol is wasted in DMFCs across such membranes (3). Remarkable improvement in energy efficiency and in cell voltage would result from drastic reduction of methanol cross-over. Thus, novel ion conductive membranes are sought (4). It was the purpose of the present work to attain a membrane which combines the features of Nafion® films with substantially reduced methanol permeability.

Nafion® is a noncross-linked ion-exchange polymer comprised of a perfluorinated backbone with sulfonate ionic groups attached to pendant side chains. It is now widely accepted that Nafion® has a microphase-separated structure with a hydrophobic perfluorinated region interspersed with ion-rich hydrophilic domains (5). The most direct evidence of such a picture comes from small-angle *X*-ray and neutron scattering investigations (6). Nafion® swells in the presence of water, the latter being uptaken within the ion-rich domains; thus an inverted micellar structure has been suggested with water pools surrounded by a low dielectric polymer matrix and ionized sulfonate groups located at the polymer-water interface (7). The hydration energy of the sulfonate anions as well as of the mobile counter-ions is the driving force to swelling. Accordingly, the micelles may be swollen to different extents, by exchanging H^+ with another counter-ion to various degrees. Also, it has been proposed that the reverse micelles are somehow interconnected; that would account for the good ion-transport properties of Nafion® (8).

However, small hydrophilic molecules may also dissolve into the micelles and diffuse. We consider that methanol diffuses primarily through the water-rich domains of Nafion®; an account of this hypothesis is given further below. The swelling degree of the micelles – whose size is of the order of 20 Å (6) – is anticipated to remarkably affect methanol transport. Rearrangement of the solvent molecules – which is essential to methanol diffusion – is hindered in highly confined domains and is expected to reduce dramatically with increasing confinement. On the other hand, the hydrogen ion mobility is also likely to drop as the size of the water-rich clusters decreases. H^+ migration may occur also by a *chain* mechanism in aqueous solutions (9). If this mechanism contributes to proton migration through the aqueous domains of Nafion® membranes as well, minor rearrangement of water molecules would be required unlike for methanol diffusion. As a consequence, it would appear plausible that proton conductivity be less dramatically depressed by increased confinement (*i.e.* reduced micellar size). If these conjectures are correct, it should be possible to depress the rate of methanol cross-over through Nafion® membranes, with less marked decrease in conductivity, by reducing the size (*i.e.* the water content) of the inverted micelles.

We have exchanged H^+ in Nafion® 117 membranes with Cs^+ to several degrees. Cesium ion has considerably smaller hydration energy compared with proton, thus the former has lower affinity toward water (10). That implies lower water content in the membrane as also experimentally confirmed (11). Accordingly, one expects the size of hydrophilic clusters to be smaller in Cs^+- doped membranes. We investigated methanol permeability and proton conductivity at 21 °C in Cs^+- doped as well as in H^+- form membranes. We show how the permeability and conductivity at room temperature in Nafion® 117 can be manipulated by controlling the amount of cesium counter-ions in the membrane. Some preliminary data obtained at temperatures up to 60 °C are also reported.

Experimental methods

Membranes preparation. As received Nafion® 117 membranes (*Aldrich*) were soaked in 1M CsOH (*Aldrich*) at room temperature for 24 hr. We also investigated films partially exchanged with cesium ions. These were prepared by soaking Cs^+- form membranes in 5×10^{-2} M H_2SO_4 (*Carlo Erba*) for 60 seconds or 180 seconds. They are respectively referred to as M_{60} and M_{180} in the following account. For conductivity tests at higher temperature the membranes were pre-treated for two hours in de-ionized water at 80 °C, before being exchanged (entirely or partially) with cesium ions. De-ionized water (18 MΩ·cm) was employed to prepare all solutions.

Hydrogen ion conductivity measurements. Proton conductivity tests were carried out using a four probes d.c. technique. The details of the experimental set-up are described elsewhere (12).

Methanol permeability measurements. A two-compartments glass cell was utilized for permeability tests. One compartment (V_A=10 ml) was filled with a solution of methanol (8 vol.%) and n-buthanol (0.2 vol.%) in de-ionized water. The other (V_B=13.4 ml) was filled with a n-buthanol (0.2 vol.%) solution in de-ionized water. The membrane (area 4.9 cm^2) was clamped between the two compartments and these were kept under stirring during an experiment. Methanol flux establishes across the membrane owing to the concentration difference between the two compartments. V_A and V_B were chosen sufficiently large so as pseudosteady-state condition occurred during these experiments, after an initial transient. Moreover, the methanol concentration in the receiving compartment was always negligible compared to that on the source side, while the latter remained essentially unchanged during the experiment. Accordingly, the flux of methanol was constant and its concentration in the receiving compartment as a function of time is given by:

$$c_B(t) = \frac{A}{V_B}\frac{P}{L}\, c_A\,(t - t_0) \qquad (1)$$

P is the membrane permeability. t_0, also termed *time lag*, is explicitly related to the diffusivity: $t_0 = L^2/6D$ (13).

c_B is measured at several times during an experiment and the permeability is calculated from the slope of the straight-line. The methanol concentrations were measured by a capillary gas chromatograph (*Fisons, mod. 8000*) fitted with a FID. N-buthanol was used as internal standard.

Results and discussion

a) T=21 °C The methanol permeabilities in the membranes investigated were calculated from the slopes of the experimental straight-lines (eqn. 1). These, along with the hydrogen ion conductivities, are reported in Tab. 1. There is excellent accordance between the conductivity in the H^+- form membrane measured in the absence of absorbed methanol by our experimental set-up, $6.6\times10^{-2}\ \Omega^{-1}cm^{-1}$, and the value $5\times10^{-2} \div 7\times10^{-2}\ \Omega^{-1}cm^{-1}$ commonly reported in the literature.

It can be noted that the presence of cesium ions in the membrane – specifically in the water-rich domains – causes remarkable reduction of methanol permeability. For instance the permeability in M_{60} is over one order of magnitude smaller than in the acid-form membrane. This also demonstrates that, while the hydrophobic polymer matrix is comparatively impermeable, methanol diffuses primarily through the hydrophilic domains, as supposed hereinabove. The lower methanol permeability derives also from the reduced diffusivity, as inferred from the time lags observed experimentally. The proton conductivity is depressed to a lesser extent by the presence of cesium ions in the membrane, as expected. It was the intent of this work to develop proton conductive membranes with reduced methanol permeability. The degree to which this task is accomplished is best indicated by the ratio between the hydrogen ion conductivity and the methanol permeability in the membrane, Φ; the higher this ratio, the better the membrane performance. In Fig. 1, Φ is reported for the various membranes investigated here. It is observed that Φ is greater for the cesium doped membranes, indicating that their performance in the DMFC would be superior to that of conventional H^+- form Nafion® membranes. Φ is highest when H^+ is fully exchanged with Cs^+ : about *2.5* times higher than for acid-form Nafion®. Accordingly, Cs^+ - form films with the same proton conductance as in H^+- form Nafion®, afford a 2.5-fold reduction of methanol flux. Similar performance is afforded by M_{60} membranes. That looks attractive from the perspective of the DMFC technology.

It is observed from Fig. 1 that while further Cs^+- doping of M_{60} films affects the transport properties notably, it produces almost no increase of Φ. This apparently anomalous behavior is possibly rationalized on the ground of the methanol transport mechanism. As pointed out in the early discussion, the presence of cesium reduces only the transport rate through the water-rich domains of the membrane. Accordingly, while at low cesium content methanol transport through the hydrophilic clusters is preponderant, at higher contents transport through the hydrophobic perfluorinated matrix may become increasingly relevant. Since methanol diffusion through the perfluorinated matrix is likely to be unaffected by the presence of cesium, further Cs^+- doping produces less remarkable decrease of global methanol permeability than at lower cesium content. This possibly explains the *platoo* attained by Φ as cesium content approaches saturation.

b) 21 °C < T ≤ 60 °C Conductivity data in the temperature range 21 ÷ 60 °C are reported on an Arrhenius plot in Fig. 2 for Nafion® membranes with various cesium content. Each membrane was equilibrated with a solution containing chosen amounts of H_2SO_4 and Cs_2SO_4, after a pre-treatment in de-ionized water at 80 °C for two hours. It can be noted that as the ceium content in the membrane increases, the activation energy E_a for proton conduction also increases. For instance, we found $E_a = 10.6$ KJ/mol for H^+-form membranes. However, for a membrane equilibrated with a solution 10^{-4} M H_2SO_4 and 2×10^{-4} M Cs_2SO_4 the activation energy was 25.6 KJ/mol. This result is not unexpected, since proton migration becomes more hindered as the size of the migration path reduces.

We noticed that the dimensions of a membrane increased irreversibly upon soaking in hot water (80 °C). We found that such physical change produced marginal increase of the proton conductivity at room temperature in all the membranes investigated. However, this thermal pre-treatment seemed to have a dramatic effect on the methanol permeability, depending upon the cesium content in the membrane. It was observed during these preliminary tests that the pre-treatment produces an increase of the permeability at room temperature equal to *0.3* for the for H^+- form membrane, or to about *8* for the Cs^+- form membrane.

Conclusion

This work has shown that methanol permeability at room temperature through polyperfluorosulfonic acid membranes can drastically be reduced by appropriate doping with cesium ions. The doped membranes retain good proton conductivity. Preliminary experiments carried out in the temperature range 21 ÷ 60 °C suggest that the activation energy for proton conductance increases with increasing cesium content. Moreover, thermal treatments on the as-received Nafion® 117 membranes seem to affect dramatically the methanol permeability at high cesium content.

Acknowledgments

The author wishes to thank Professor E.L. Cussler of the University of Minnesota for valuable conversations. Part of the experiments were carried out by Mrs. A.M. Cialdoni. This research was supported by the Italian MURST.

References

(1) K. B. Prater, *J. Power Sources*, **47**, 377 (1994).

(2) S. Surampudi, S. R. Narayanan, E. Vamos, H. Frank, G. Halpert, A. LaConti, J. Kosek, G. K. Surya Prakash and G. A. Olah, *J. Power Sources*, **47**, 377 (1994).

(3) S. R. Narayanan, A. Kindler, B. Jeffries-Nakamura, W. Chun, H. Frank, M. Smart, T. I. Valdez, S. Surampudi, G. Halpert, J. Kosek and C. Cropley, *Annu. Battery Conf. Appl. Adv.*, 11th, 113 (1996).

(4) J. S. Wainright, J-T. Wang, D. Weng, R. F. Savinell and M. Litt, *This Journal*, **142**, L121 (1995).

(5) R. S. Yeo and H. L. Yeager, *Mod. Aspects Electrochem.*, **16**, 437 (1985).

(6) G. Gebel and J. Lambard, *Macromolecules*, **30**, 7914 (1997).

(7) T. D. Gierke, G. E. Munn and F. C. Wilson, *J. Polym. Sci., Polym. Phys. Ed.*, **19**, 1687 (1981).

(8) W. H. Hsu and T. D. Gierke, *J. Membrane Sci.*, **13**, 307 (1982).

(9) J. O'M. Bockris and A. K. N. Reddy, *Modern Electrochemistry*, p. 474, Plenum Press, New York (1970).

(10) F. A. Cotton and G. Wilkinson, *Advanced Inorganic Chemistry*, p. 645, John Wiley, New York (1972).

(11) H. L. Yeager and A. Steck, *This Journal*, **128**, 1880 (1981).

(12) V. Tricoli, *submitted for publication* (1998).

type of membrane	Cs^+	M_{60}	M_{180}	H^+
permeability (cm^2/s)	3.34×10^{-8}	1.04×10^{-7}	2.72×10^{-7}	1.30×10^{-6}
conductivity ($\Omega^{-1}cm^{-1}$)	0.48×10^{-2}	1.47×10^{-2}	1.80×10^{-2}	7.59×10^{-2}

Table 1

Thicknesses, methanol permeabilities, and proton conductivities at 21 °C of the membranes investigated in this work. Thickness values refer to membranes swollen in 8 vol.% methanol in water, unless otherwise specified.

Fig. 1

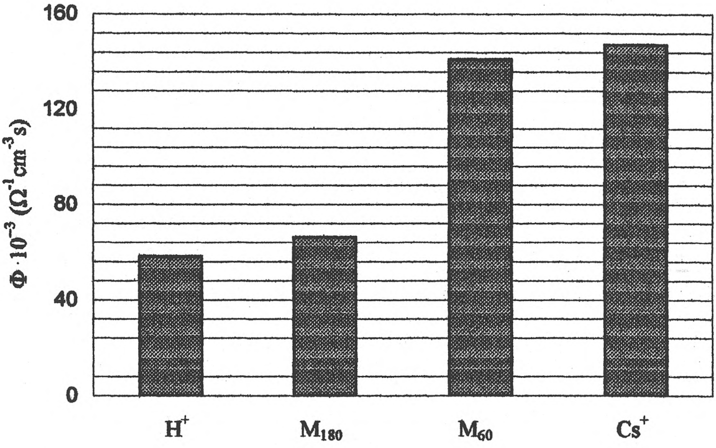

Fig. 1. Proton conductivity / methanol permeability, Φ, reported for Nafion® membranes with various cesium contents.

Fig. 2

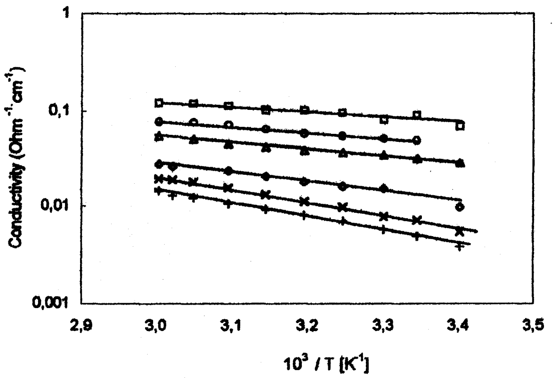

Fig. 2. Proton conductivity vs. temperature for various Cs^+- doped received Nafion® membranes. Membrane in acid form "□", equilibrated with 10^{-3} M H_2SO_4 and 10^{-4} M Cs_2SO_4 "o", 10^{-3} M H_2SO_4 and $2{\cdot}10^{-4}$ M Cs_2SO_4 "Δ", 10^{-3} M H_2SO_4 and 10^{-3} M Cs_2SO_4 "◊", $2{\cdot}10^{-4}$ M H_2SO_4 and 10^{-3} M Cs_2SO_4 "×", 10^{-4} M H_2SO_4 and $2{\cdot}10^{-3}$ M Cs_2SO_4 "+".

Proton_Conducting_Membrane_Fuel_Cells_II, PV 1998-27, 365-379 (1998)
DOI: 10.1149/199827.0365PV © The Electrochemical Society

COMPARISON OF THE CONVERSION EFFICIENCY OF A DIRECT-METHANOL *vs.* A HYDROGEN FUEL CELL

R. M. Moore
University of California
Davis, California, 95616-8762, USA

S. Gottesfeld and P. Zelenay[1]
Los Alamos National Laboratory
Los Alamos, New Mexico 87545, USA

ABSTRACT

This paper first compares the conversion efficiency and power density of a direct-methanol fuel cell (DMFC) with the equivalent parameters of a state-of-the-art direct-hydrogen fuel cell (DHFC) – both for current DMFC data and for projected improvements in DMFC performance. The cell level comparison is then extended to the system level for potential automotive application, and limited comparisons are also made for a system based on methanol reformate fuel. It is concluded that a DMFC-powered vehicle, which apparently can meet the requirements for a general-purpose zero-emission vehicle (ZEV), can become competitive with a DHFC-powered ZEV.

INTRODUCTION

For any application of a fuel cell power system, it is important to maximize fuel utilization and energy conversion efficiency. In the specific case of an automotive fuel cell system, it is particularly critical to maximize the overall conversion efficiency (voltage efficiency × fuel utilization) over as broad a range of cell (and system) power density as possible.

This paper compares the conversion efficiency and power density of a direct-methanol fuel cell (DMFC), which has been optimized for efficiency, with the equivalent parameters of a state-of-the-art direct-hydrogen fuel cell (DHFC). Following a brief outline of the experimental conditions used to generate data reported in this paper, a concept and technique of optimizing the conversion efficiency of a DMFC is introduced. The technique is then applied to DMFC state-of-the-art data, and to two projected data

---

[1] *On leave from the Department of Chemistry, Warsaw University, Warsaw, Poland.*

sets for future DMFC performance. All three of these optimized DMFC characteristics are then compared with the efficiency and power density of the DHFC state-of-the-art.

Next a "system" level comparison is introduced that captures the major differences between the DHFC and DMFC systems for automotive applications. Specifically, it highlights the impact of both the stack (efficiency and power density) and the fuel (energy storage density) on the competitiveness of automotive fuel cell power systems for general-purpose applications. This system level comparison is then used to evaluate the potential of a DMFC-powered vehicle.

Finally, the performance of methanol (and "gasoline") reformate systems is briefly analyzed and discussed. It is noted that a comparison between fuel cell vehicles (FCVs) powered by DHFC or DMFC power systems and by methanol or "gasoline" reformate fueled systems is not an "apples-to-apples" comparison since the former systems are zero-emission while the latter ones are not ZEV (zero emission vehicle) capable. However, since it is common to compare the methanol-reformate FCV with the two types of ZEVs on the limited basis of efficiency and power density, we also present that limited comparison here.

EXPERIMENTAL

DMFC performance considered in the analysis described below is based on fuel cells prepared and tested at LANL. Pretreatment of the Nafion™ 117 membrane in H^+ form, preparation of membrane electrode assemblies (MEAs) for a DMFC using a decal technique, and the single-cell fuel cell hardware have been previously described[1,2] as has the cell testing system used.[3] Two unsupported Pt-Ru blacks of nominal 1:1 atomic ratio were used for DMFC anodes, both supplied by Johnson Matthey. Anode inks were made by dispersing appropriate amounts of the Pt-Ru catalyst in deionized/distilled water and adding 5% Nafion™ solution (1200 in equivalent weight, Solution Technology Inc.). The cathode inks contained unsupported Pt black (30 $m^2 g^{-1}$, Johnson-Matthey), deionized/distilled water and 5% Nafion™ solution (1100 equivalent weight, Solution Technology Inc.). In some cases, the catalyst layers involved direct application of the catalyst inks to PTFE-treated (wet-proofed) carbon cloths. The geometric active area of all the MEAs prepared was 5 cm^2.

Methanol solutions, between 0.25 and 2.0 M in concentration, were pumped through the DMFC anode flow field at precisely controlled rates (0.5-3.0 ml min^{-1}) using a Shimadzu LC-10AS HPLC pump. A back pressure of about 15 psig was imposed upon the anode outlet flow to ensure that the membrane would be in contact with a liquid solution of methanol at the cell operating temperature of 100 °C. The cathode gas feed was air 30 psig pressure and a flow rate 0.5 l min^{-1}. The air was usually pre-humidified at the same or similar temperature as the operating temperature of the cell.

The crossover of methanol as a function of cell current density was recorded with the same cell hardware used for the corresponding cell polarization plot. The determination of crossover was based upon the amount of carbon dioxide present in the cathode exhaust, as measured using a GMM12 Carbon Dioxide IR Sensor (Vaisala Oy, Finland). The IR detector was earlier calibrated with a gaseous mixture of 4% CO_2 and 96% N_2. The CO_2 content in the cathode exhaust was then converted into the corresponding methanol flux through the membrane, expressed as current density of MeOH oxidation at the cathode.

DMFC OPTIMIZATION

It has been shown that it is possible to carry out an optimization of both conversion efficiency and power density for a direct-methanol fuel cell (DMFC) by varying the methanol concentration and solution feed rate at the anode.[4] The result of such an optimization, using experimental data for a state-of-the-art DMFC cell, is shown in **Figure 1** – in the form of an optimized DMFC conversion efficiency curve versus cell power density.

There would be a significant increase in DMFC performance if the crossover current were reduced and the cell voltage increased (in part as a result of a reduced impact on cathode polarization with reduced crossover current). **Figure 2** illustrates the effect on the optimum efficiency curve of these two projected improvements in the characteristics of the DMFC:

(i) reduction of the DMFC methanol crossover flux by 90% (at each cell power),
(ii) combination of that 90% crossover reduction with a decrease in overall cell voltage loss by a uniform 0.1 V.

Figure 2 shows how the crossover reduction improves the conversion efficiency and shifts the peak efficiency to lower power density – with no effect on the maximum power density obtained (*ca.* 0.25 mW cm^{-2}). In contrast, the effect of the decreased voltage loss on the projected performance of the DMFC is twofold, namely:

(i) further increase in the efficiency (especially at higher power density),
(ii) increase in the peak power density which now exceeds 0.3 W cm^{-2}.

As a justification for projecting these potential improvements in the DMFC performance, we note that experimental DMFC membranes have achieved significant crossover reduction while maintaining good protonic conductivity, and decreased DMFC cathode polarization for reduced crossover has been inferred from some experiments.[5]

In **Figure 3**, these three DMFC efficiency curves are compared to a DHFC for the same cathode air pressure and flow. With the combination of both crossover reduction by 90% and overall cell polarization reduction by 0.1 V, the maximum DMFC power density increases to roughly 55% of the direct-hydrogen cell, and the overall conversion efficiency increases to about 75% of the hydrogen cell.

Although a superficial examination of this projected performance might conclude that the DMFC is at an insurmountable disadvantage compared to the DHFC, it is necessary to critically examine the *complete power systems* for the DMFC and DHFC, including fuel storage, before any such conclusion is warranted.

SYSTEM COMPARISONS

The complete automotive power system includes fuel cell stack, system auxiliaries (air supply, water supply, cooling, power control), fuel supply (storage plus reformation, if necessary), and drive train (motor controller, electric motor, reduction gear). In contrast, the efficiency and power density comparisons made in the last section were only at the stack level. In this section, we will establish a basis for the required system level comparison, and extend the comparison at the system level by comparing an automotive DMFC system with a DHFC system as the benchmark.

The use of the DHFC system as a benchmark for evaluating the DMFC may seem somewhat arbitrary. However, if the DMFC is to be positioned as a Zero Emission Vehicle (ZEV) in the automotive marketplace it must compete against the DHFC system[*]. Others have argued that the DMFC system should be compared against the reformed methanol fuel cell (RMFC) system because they both begin from the same "fuel on board". However, we prefer the "ZEV-against-ZEV" evaluation, although it is actually a more difficult benchmark for the DMFC from the viewpoint of fuel conversion efficiency and power density.

In a later section we will discuss similar figures of merit (efficiency, power density) for the RMFC and RGFC (reformed gasoline fuel cell) systems. But, since these reformate systems are clearly not leading to ZEVs, especially in the RGFC case, the reformate-fueled systems are not legitimate "apples-to-apples" comparisons with ZEVs

---

[*] The ZEV regulations in California actually require that a ZEV have zero *exhaust* emissions, not zero *total fuel cycle* emissions but the initials remain the same in both cases – ZEV. Aside from battery powered vehicles, DMFC and DHFC are the only ZEV candidates under the current California regulations.

based on a DMFC or DHFC power system. However, reformate-fueled FCV power systems are actually easier comparisons for efficiency and power density vis-à-vis the DMFC.

All of the system comparisons in the present study are for "load-following" power systems, *i.e.*, the system is not "hybridized" with other energy or power sources. Whenever no realistic or reliable information is available, we will, for the sake of providing a comparison, make several approximations and assumptions. The approximations and assumptions, including their consequences, are:

(i) The DMFC and DHFC fuel cell vehicles will be of the same design and approximately the same weight. (This approximation means that the same total system power is required to provide equivalent acceleration performance for the two FCVs, and the total power systems must fit into the same space, *i.e.*, must have the same overall system power density.)

(ii) Since the same total system power is needed, the drive train components (motor controller, electric motor, and gear train) can be ignored in the comparison, as can the power controller and system controller for the fuel cell power system. (This means that the comparison is reduced to only the stack, auxiliaries, air supply and fuel supply.)

(iii) In the absence of any actual detailed information, we assume that the air supply sub-system for each type of fuel cell system will be roughly equivalent in size and power losses for both types of systems. (One can actually argue in both directions on this point, but, as an assumption, this removes the air supply system from the comparison, leaving only the stack, other auxiliaries, and fuel supply.)

(iv) We assume, again in the absence of any actual detailed information, that the demands, size, and power drain of all of the other auxiliary sub-systems (water, cooling, *etc.*) will be roughly equivalent for both types of systems. This seems over-generous for the DMFC, the RMFC, and especially the RGFC – since there is more rejected heat in the stack for all of these systems. However, some credit should be taken in the case of the DMFC for cooling by liquid feed to the anode.

This finally brings us to the benchmark being a DHFC "system" that consists of the DHFC stack and fuel supply, <u>only</u>.

The chain of reasoning above leads to a fairly simple comparison basis for the DMFC versus the DHFC "system". However, in spite of its relative simplicity, this basis exposes the major differences between the DHFC and DMFC systems, and, in fact, among all of the alternative fuel cell systems for automotive applications. Specifically, it captures the significant impacts of both the stack (efficiency and power density) and the fuel (energy storage density) on the competitiveness of FCVs using alternative fuels.

One final basis of comparison is needed – a criterion related to fuel characteristics. The most obvious choice would simply be fuel efficiency itself. However the experience in the marketplace with battery electric vehicles (BEVs which are the "other ZEVs") has taught us that it is not that simple. Although the BEV has exemplary fuel efficiency (defined with respect to the electricity stored on-board), its characteristic lack of driving range has effectively relegated it to niche applications.

From this real-life experience we suggest that the range of a future general-purpose passenger FCV must be roughly the same as that of current general-purpose passenger vehicles (*ca.* 300-400 miles). This criterion is related to fuel conversion efficiency, but, by using a range requirement, it also establishes the practical need to carry a minimum amount of the "fuel" on-board for a realistic general-purpose FCV.

In turn, this range requirement effectively defines the volume required for fuel storage – through the intermediary of the stack fuel utilization. Finally, this fuel volume is a major determinant of the "system" power density, for the DHFC benchmark, defined here for comparison purposes. This will become clearer for the example that we consider next – the DHFC "system".

DHFC AND DMFC "SYSTEM" COMPARISONS

Based on the foregoing discussion, the DHFC benchmark "system" to be used for our exercise consists of the direct-hydrogen stack plus compressed hydrogen fuel stored in high-pressure tanks. This will be the basis of comparison for the equivalent DMFC "system" which consists of the DMFC stack and the methanol fuel storage tank. The comparison criteria we will use here are the overall "system" power density and, as explained above, an FCV driving range of nominally 350 miles.

Direct-hydrogen fuel cell "system"

We apply these criteria to the DHFC "system" as follows. First we assume that a lightweight FCV design, such as the proposed Ford "P-2000" FCV, is implemented and achieves current PNGV vehicle design goals for vehicle energy efficiency. The combination of a 60 kW peak power DHFC stack (power density of 1 kW l^{-1} per Ballard Power specifications), and a 5000 psi compressed hydrogen supply for this FCV (with a roughly 350 mile range), would require about 240 liters of volume (60 l for the stack and 180 l for the hydrogen at 5000 psig).

Direct-methanol fuel cell "system"

For an equivalent DMFC "system", we would require the same "range" (with our actual calculation being fuel cell stack conversion efficiency times fuel energy on-board). This yields a volume of fuel (to achieve the required range) corresponding to each value of DMFC "system" conversion efficiency used for calculation. Subtracting this fuel volume from the available volume for the DHFC "system' in the FCV (240 l) leaves us with the volume available for the 60 kW DMFC stack – and hence determines the required DMFC stack power density. The final step is then to translate this stack power density into an equivalent *cell* power density (as shown in Figures 2 and 3).

The chemical energy density of methanol (kWh l^{-1}) is approximately five times larger than the energy density of hydrogen compressed at 5000 psi. Thus, if the DMFC stack had the same conversion efficiency *vs.* methanol as the DHFC stack has *vs.* hydrogen, then – for the same FCV range – the methanol fuel required would be 20% of the volume of the hydrogen. Or, at the other extreme, if the DMFC stack has only 50% of the DHFC stack efficiency, the volume of methanol fuel need on-board is 40% of the hydrogen volume.

Using the lower value of 50% of the DHFC stack efficiency as a working assumption (this appears to be attainable based on Figure 3), the methanol fuel volume is 72 l (40% of the 180 l needed for hydrogen), and the allowable DMFC stack volume is approximately 170 l (240 l minus 72 l). For a peak stack power of 60 kW, this leads to a required DMFC stack power density of 0.35 kW l^{-1} (35% of the demonstrated 1 kW l^{-1} power density for a DHFC stack).

Cell vs. stack power density

The final link in our comparison is to relate the *cell* power densities for the DMFC and DHFC technologies (see Figures 2 and 3) to the respective *stack* power densities (computed above in our comparison). As a first approximation, the stack geometry (volume for the cell MEA, electrodes, backing layers, bipolar plates, reactant gases or liquids, cooling channels and plates, humidification cells, etc.) would be expected to be roughly the same for both DHFC and DMFC. At this time there is no clearly compelling argument that the *cell* power density and the *stack* power density should not be in roughly the same ratio for both types of stack when they reach a similar commercialization stage.

In other words, the relative power density performance at the cell level would carry through to the stack – roughly unchanged.

For the calculation above, which assumes a DMFC conversion efficiency of only 50% of the DHFC value, the DMFC power density at the cell level should be at 35% or greater of the DHFC cell power density. This combination of relative values for cell conversion efficiency and power density is roughly met by the state-of-the-art data for the DMFC in Figure 3, and is clearly exceeded by the projected performance levels for reduced crossover and increased cell voltage (the same figure).*

Summary: DMFC versus DHFC "systems"

Overall, the summary of the above calculations is that a DMFC powered FCV could meet the requirements for a general-purpose ZEV and be an effective competitor to a DHFC-based FCV. It would have an equivalent range of 350 miles, and provide the same class of performance (acceleration) as a hydrogen-fueled FCV, if:

(i) the cell/stack power density were at 0.35 $kW l^{-1}$,

(ii) the stack conversion efficiency over the required drive cycle were at 50% of the equivalent DHFC stack efficiency.

These criteria are marginally met for the current state-of-the-art DMFC cell (see Figure 3). If the reductions in methanol crossover and cell polarization assumed in Figures 2 and 3 are achieved, a DMFC power system would exceed these criteria very comfortably. Another factor that could facilitate DMFC stack competitive position is effective cell packaging, a quite likely achievement according to some initial results.

REFORMATE FUEL CELL POWER" SYSTEMS"

As noted earlier, comparisons between FCVs powered by DHFC or DMFC power systems and FCVs fueled by methanol (or "gasoline") reformate is not a valid "apples-to-apples" comparison, because of the non-zero emissions expected from reformate systems. However, the performance of these reformate systems is worth briefly analyzing from the point of view of fuel efficiency and power system density, using the same DHFC benchmark criteria.

---

* A recently LANL-demonstrated short DMFC stack reached packing density of 5 cells per cm, but is still to be tested to confirm repetition of single cell DMFCs at at 100°C, the temperature used in this analysis.

Fuel efficiency of the RMFC "system"

There are several conversion-efficiency and fuel-utilization losses in the methanol reformate "system". These are:

(i) Because of the dilution effects for reformate fuel (about 70% mole fraction hydrogen for methanol steam reformate, and as low as 20% mole fraction for partial oxidation methanol reformate), there is some drop in conversion efficiency in the reformate stack at given power, particularly so at higher dilution and higher power levels. The primary losses are due to increased anode polarization from mass transport limitations in the anode backing and catalyst layer. A loss in maximum power density (relative to a direct-hydrogen fuel cell stack) has been estimated theoretically (and also measured) in the range of 10 to 25% for fuel cell stacks using methanol reformate rather than neat hydrogen.

(ii) There is also an energy loss in the fuel reformer itself, variously estimated at 20-30% for steam and partial oxidation reformers.

(iii) Finally, there is a need to circulate more than the stoichiometric equivalent of hydrogen through the anode of a reformate cell. The dilution of hydrogen in the reformate means that excess hydrogen is needed to provide adequate hydrogen concentration at the anode catalyst layer and reduce anode polarization losses. Since it is not possible to recirculate a reformate fuel – as can be done for pure hydrogen or methanol – this represents a direct loss of fuel for the reformer-based system. For a dynamic automotive system application, this excess hydrogen will be difficult to completely use in the overall system, particularly for a partial oxidation reformer, so it should be counted, at least for the moment, as a loss at the system level. Losses from this effect have been estimated at 15-30% of the reformate hydrogen (depending on the hydrogen mole fraction in the reformate).

The most favorable estimate for a methanol reformer-based system can be calculated from the highest values of the ranges listed above. Using the upper values of 90% relative voltage efficiency (direct hydrogen dilution loss in the stack), 80% reformer efficiency, and 85% fuel utilization (excess fuel stoichiometry) yields a relative efficiency of about 60% for a steam methanol reformate stack vis-à-vis fuel conversion efficiency of a DHFC stack.

Following the process used above for the DMFC "system", this RMFC "system" efficiency estimate can be used to calculate a volume requirement for the methanol storage in the steam reformer RMFC "system". The result is that the RMFC "system" needs about 1/3 of the volume of the hydrogen for the DHFC "system", or 60 l. Subtracting this from the total "system" volume available (240 l for the DHFC "system") leaves 180 l for the remainder of the RMFC "system". However, for the RMFC "system" this added volume must also include the fuel reformer sub-system. The impact of this additional sub-system on the required RMFC stack power density is evaluated next.

Power density of the RMFC "system"

The primary impact on the peak power density of the methanol and "gasoline" reformate fueled stack is the effect of the diluted hydrogen on anode polarization. For the range of dilution expected, *i.e.*, 70% to 20% hydrogen mole fraction, the stack power density would be reduced to the range of 90% to 80% of the DHFC stack, respectively. For steam reformed methanol, the 90% level of power density – compared to the DHFC – is chosen here for comparison.

In addition, for reformate fuel cell systems there is a further loss of power density at the "system" level due to the volume required for the fuel reformer sub-system, *e.g.*, fuel pre-heater, air compressor, main reactor, CO cleanup, expansion and cooling. As with most of the components in reformate systems, there is no accurate information, or common agreement, on the probable volume and weight of such a reformer. For the present discussion, we will – simply as an example for the purposes of providing an estimate – analyze the effect of fuel reformer power density in the range of 0.5 to 1 kW l^{-1}. The latter figure is a commonly stated goal for the complete fuel reformer sub-system, but 0.5 kW l^{-1} is possibly a more realistic expectation.

Using the 1 kW l^{-1} figure to compute the required stack power density for a methanol steam reformate "system", we see that the reformer sub-system requires an additional 60 l from the overall volume available for the RMFC "system". This, plus the 60 l computed for methanol storage (see above), leaves 120 l for the RMFC stack. So, for the required 60 kW "system" power, the required RMFC stack power density is 0.5 kW l^{-1} (if the reformer power density is indeed 1 kW l^{-1}).

If we use the lower value of 0.5 kW l^{-1} for the fuel reformer power density, we find that the reformer sub-system requires an additional 120 l. This, plus the 60 l computed for methanol storage, leaves only 60 l for the RMFC stack. So, at the required 60 kW "system" power, the required RMFC stack power density must be 1 kW l^{-1}, or exactly the same as the DHFC stack (for a reformer power density of 0.5 kW l^{-1}).

For the assumed range of reformer power density – 1.0 to 0.5 kW l^{-1} – the RMFC stack power density must be in the range of 1.0 to 0.5 kW l^{-1}, in inverse relationship. Since we expect the RMFC cell power density to be about 80-90% of the DHFC cell power, this range of 50-100% of the DHFC power density seems reasonable. If the RMFC stack is at 90% of the DHFC stack power density, then the reformer must achieve 0.55 kW l^{-1} for parity.

Summary: RMFC steam reformer "system"

Our conclusion is that it will be possible for the RMFC "system" to achieve the required range and power needed to provide a general purpose FCV with comparable range and performance to that of a DHFC vehicle (based on the PNGV vehicle efficiency goals). This is the result even if the reformer sub-system power density falls to roughly 55% of the goal of 1 kW l^{-1} power density. However, if the steam reformer power density falls below 0.55 kW l^{-1}, the steam reformer RMFC "system" power density will fall commensurately short of the required performance for a general purpose FCV.

In summary, a fuel cell power system based on a methanol steam reformer can be expected to be roughly competitive with a DHFC power system for a general purpose vehicle – but without the "redeeming virtue" of ZEV emissions. The cell power density and power system conversion efficiency will be intermediate between the DHFC and DMFC values, and, without ZEV status, the RMFC powered FCV will not be fully competitive to the DHFC (or DMFC) vehicles.

Comments on partial oxidation reformer "systems"

Although we will not consider the cases of partial oxidation reformer "systems" here in any detail, there are several factors that should be noted. Namely:

(i) The relative efficiency of a partial-oxidation "gasoline" reformer system is lower than that computed above for the methanol steam reformer case. A rough figure for the "gasoline" case can be calculated from the following figures – 80% efficiency due to the dilution loss, 70% reformer efficiency; and 75% fuel utilization of neat oxygen in the stack. The overall efficiency is therefore calculated to be about 40% of that of the DHFC system – i.e.; roughly equivalent to the DMFC state-of-the-art.

(ii) Since the partial oxidation reformation process for both "gasoline" and methanol is exothermic, there is limited opportunity to recover the excess (fuel cell exhaust) hydrogen energy within the overall partial oxidation fuel cell system.

(iii) A partial-oxidation methanol system would have fuel conversion efficiency somewhat higher than the "gasoline" example calculated above (40% of the DHFC benchmark) but lower than the steam reformed methanol case. A figure of about 50% seems reasonable in comparison to the DHFC "system". This is within the range of current to projected DMFC values.

These factors suggest that the partial oxidation systems, particularly for the "gasoline" case, will require reformer power densities closer to the 1.0 kW l^{-1} level than in the methanol steam reformer case.

CONCLUSIONS

A direct-methanol fuel cell powered FCV could meet the requirements for a general-purpose ZEV, and therefore could be an effective competitor to a direct-hydrogen fuel cell powered FCV. In addition to its ZEV status, it could reach an equivalent range of 350 miles, and provide the same class of performance (acceleration) as a hydrogen-fueled FCV, if

- cell/stack power density is at 0.35 kW l^{-1} (35% of the direct-hydrogen value),
- stack conversion efficiency (over the required drive cycle) is at 50% of the DHFC drive cycle stack efficiency.

These criteria are marginally met for the current state-of-the-art DMFC cell (see Figure 3). If the reductions in methanol crossover and cell polarization that are assumed in Figures 2 and 3 are achieved, a DMFC power system would exceed these criteria very comfortably. Another element of DMFC technology that would assist in enhancing power density is high cell packing density in the stack. In addition, the direct-methanol powered vehicle is a ZEV, and can therefore compete with the DHFC on an equal footing in all markets.

Based on a similar comparison, the methanol (steam) reformer fuel cell system can be expected to provide an FCV power system that is also competitive with a DHFC powered general purpose vehicle, in terms of range and performance. However, the reformed-methanol fuel cell system cannot meet the ZEV emissions required for direct competition with the direct-hydrogen (or direct-methanol) systems in every market. Even so, it is frequently compared with the direct-methanol power system, simply because it uses the same fuel.

Finally, the requirements on the reformer power density for a partial oxidation FCV power system (especially the "gasoline" case) are more demanding than those for the reformer in a methanol steam-reformer power system.

ACKNOWLEDGMENTS

This work was supported by the Defense Advanced Research Projects Agency (DARPA) through the Defense Sciences Office, by the U.S. Department of Energy through the Office of Transportation Technology, by the Fuel Cell vehicle Project at the University of California, and by ATA (Advanced Technology Assessment).

REFERENCES

1. X. Ren, M. S. Wilson and S. Gottesfeld, *J. Electrochem. Soc.*, **143**, L12 (1996).
2. X. Ren, W. Henderson and S. Gottesfeld, *J. Electrochem. Soc.*, **144**, L267 (1997).
3. T. E. Springer, M. S. Wilson and S. Gottesfeld, *J. Electrochem. Soc.*, **140**, 3513 (1993).
4. R.M. Moore, S. Gottesfeld and P. Zelenay, *Optimizing the Overall Conversion Efficiency of a Direct-Methanol Fuel Cell*, in *Proton Conducting Membrane Fuel Cells (Second International Symposium)*, S. Gottesfeld, T.F. Fuller and G. Halpert (Eds.), Proceedings Volume 98-27, Electrochemical Society, Pennington, New Jersey, 1998.
5. 5. X. Ren, T.E. Springer, and S. Gottesfeld, *Direct Methanol Fuel Cell: Transport Properties of Polymer Electrolyte Membrane and Cell Performance*, in *Proton Conducting Membrane Fuel Cells (Second International Symposium)*, S. Gottesfeld, T.F. Fuller and G. Halpert (Eds.), Proceedings Volume 98-27, Electrochemical Society, Pennington, New Jersey, 1998.

FIGURES

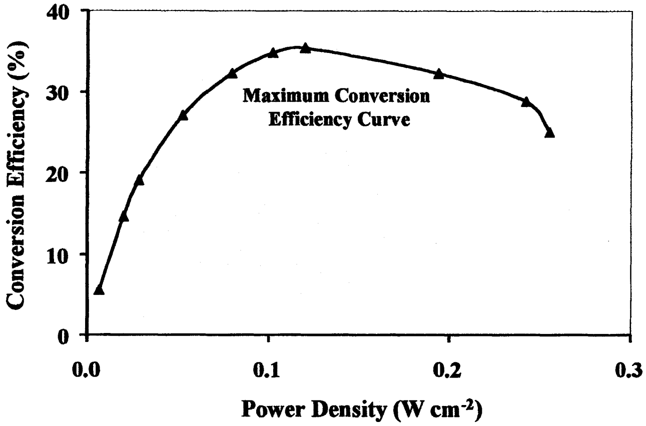

Figure 1. Optimum overall conversion efficiency *vs.* cell power density (voltage efficiency × fuel utilization) for a DMFC, based on experimental data and varying feed conditions with cell power.[4]

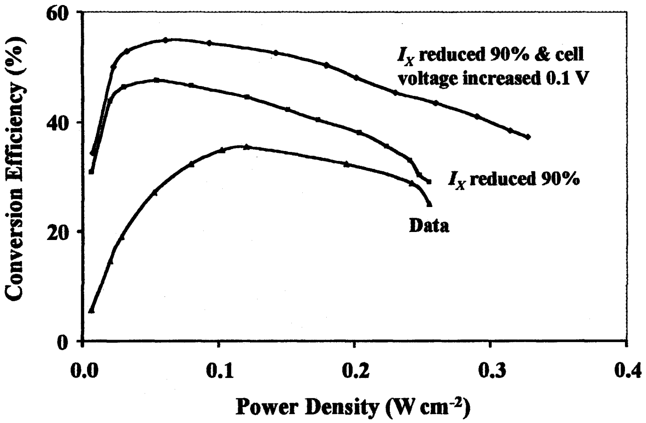

Figure 2. Conversion efficiency of a DMFC with (i) reduced methanol crossover, and (ii) reduced crossover plus decreased voltage loss.

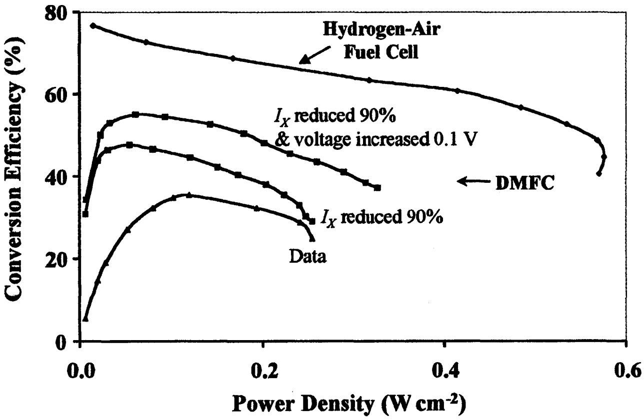

Figure 3. Comparison of overall conversion efficiency of a direct-methanol *vs.* hydrogen fuel cell.

Proton_Conducting_Membrane_Fuel_Cells_II, PV 1998-27, 380-387 (1998)
DOI: 10.1149/199827.0380PV © The Electrochemical Society

RECENT STUDIES ON METHANOL CROSSOVER IN LIQUID-FEED DIRECT METHANOL FUEL CELLS

T. I. Valdez and S.R. Narayanan

Jet Propulsion Laboratory,
California Institute of Technology,
4800 Oak Grove Drive, Pasadena, CA 91109

Abstract

In this work, the effects of methanol crossover and airflow rates on the cathode potential of an operating direct methanol fuel cell are explored. Techniques for quantifying methanol crossover in a fuel cell and for separating the electrical performance of each electrode in a fuel cell are discussed. The Effect of methanol concentration on cathode potential has been determined to be significant. The cathode is found to be mass transfer limited when operating on low airflow rate and high concentrations of methanol. Improvements in cathode structure and low methanol concentrations have been shown to result in improved cell performance.

Introduction

Since the early 90's the Jet Propulsion Laboratory has been pursuing the development of direct methanol fuel cells (DMFCs) under DARPA sponsored programs [1, 2]. The DMFC operates by oxidizing an aqueous solution of methanol to CO_2 and reducing oxygen, from an air stream, to water. The heart of a DMFC is the membrane-electrode assembly (MEA) and it is typically composed of three major components: a Pt-Ru anode, a Pt cathode, and a proton exchange membrane (PEM). Research on DMFCs is currently being pursued at several institutes in the United States and abroad, and various processes in such fuel cells have been investigated [2, 5-6].

The simplicity of the liquid feed direct methanol fuel cell arises from ease of membrane hydration and practical portability of fuel cell reactants. As in all PEM type fuel cells, membrane hydration level is the key to the electrochemical performance of the fuel cell [4]. The ease of membrane hydration allows for the DMFC to be operated over a wide range of environmental conditions. The current state of technology for direct methanol fuel cells is 0.470 V at an applied current density of 150 mA/cm^2 for a cell running at 60 °C, and 5L/min ambient airflow [3].

Under a DARPA-sponsored effort, JPL is currently being developed as a 150-watt DMFC power source for DOD applications. For this application the fuel cell system must be lightweight and capable of operating over a wide range of environmental conditions. The understanding and characterization of the effects of methanol crossover on a DMFC are crucial to the design of practical portable power systems. The following focuses on the electrochemical evaluation of MEAs for implementation in a DARPA 150-watt power source. The study specifically relates to the measurement of methanol crossover rates, evaluation of anode and cathode performance and identification of optimal conditions for fuel cell operation.

Methodology

The electrical performance of DMFCs is characterized by evaluation of methanol crossover, anode and cathode polarization. These processes and the techniques used in understanding them are described as follows.

Methanol Crossover

The crossover reaction at the cathode is given as equation (1).

$$\mathbf{CH_3OH + 3/2\ O_2 \rightarrow CO_2 + 3\ H_2O} \quad \mathbf{(1)}$$

The CO_2 content of the cathode stream is measured using a Horiba VIA 550 gas analyzer. A volume flow rate of CO_2 can then be determined by multiplying the oxidant flow rate by the vol% of CO_2 read from the gas analyzer. Using the ideal gas law this volume can be converted to a flow rate of moles of CO_2/ sec. Faraday's law can now be used to calculate an equivalent current. If **n** represents the number of moles of CO_2 produced per second,

$$\mathbf{I = nFn_e} \quad \mathbf{(2)}$$

Where F is Faraday's constant, and n_e is the number of electrons involved in the reaction. This equivalent current can then be normalized for the electrode area to get an effective crossover current density. This measurement of crossover can be carried out during fuel cell operation and also as a function of the applied load.

Anode and Cathode Polarization

Anode polarization experiments refer to an experiment when hydrogen is introduced into the cathode compartment so as to allow it to behave as a dynamic hydrogen electrode. Under these conditions, the resultant polarization curve will be that of E_a vs. applied current density. After correcting for resistance losses, E_a can now be algebraically added to the cell potential vs. applied current density curve to determine the cathode potential, E_c as such:

$$\mathbf{E_c = E_{cell} + E_a} \quad \mathbf{(3)}$$

In this way one can determine the relative contributions to electrical performance resulting from the anode or the cathode. These polarization results can be combined with crossover rate measurements to determine the effects of crossover on E_c.

The cathode has to provide for both the electrochemical oxidation of the methanol crossing over as well as for the O_2 reduction reaction. In this sense, polarization at the cathode is effectively caused by the applied current density and the crossover current density. The total applied current density is given as equation 4.

$$\mathbf{I_{tot} = I_{app} + I_{cross}} \quad \mathbf{(4)}$$

When E_c is plotted against this total current density, the true polarization behavior of the cathode can be obtained.

Experimental

The MEAs analyzed in this study incorporated an in-house developed process, which allows for the direct deposit of catalyst to a dry Nafion® membrane by various techniques such as spraying, painting, or pouring of the catalyst ink. Both MEAs tested where constructed with the following catalyst loading. The anode and cathode catalyst loading on to the membrane was 4 mg/cm^2 each. Two carbon papers of 25 cm^2 area were coated with Pt and Pt-Ru to make up the current collectors for the cathode and anode respectively. The total catalyst loading is estimated to be between 8-12 mg/cm^2.

The MEAs are first conditioned at 90 °C, 1M methanol, 5 L/min airflow at 20 psig. This step is done to hydrate the MEA and to activate the proton conducting ionomer in the catalyst layer. The high current densities that can be achieved under these testing conditions are required to ensure optimal DMFC performance. MEA characterization is carried out at molarities ranging from 0.25 to 1.5M, with airflow rates ranging from 0.1 to 5 L/min, and temperatures ranging from 20 to 90 °C. Crossover experiments are performed using oxygen as the oxidant. The cathode exhaust gases are then passed through a CO_2 analyzer, which determines the CO_2 volume percent in the exit gas [3]. The final experiments are to determine the electrical performance contributions coming from the cathode and anode separately. To separate the electrode performance it is necessary to introduce hydrogen into the cathode feed of the fuel cells. In this case, the cathode becomes a dynamic hydrogen reference electrode. These test are performed last so that any side effects on the cathode caused by the introduction of hydrogen would not show up in the characterization at the cell level.

Results

Figures 1, 2 and 3 are for crossover experiments performed with methanol concentration of 0.5, 1.0, and 1.5M respectively. In comparing the charts one can ascertain the impact of temperature on the effective crossover current density for a given operating concentration of methanol. At fixed current density of 100 mA/cm^2, the effective methanol crossover rate increases from 35 to 137 mA/cm^2 as the methanol molarity increases from 0.5M to 1.5M at 60 °C.

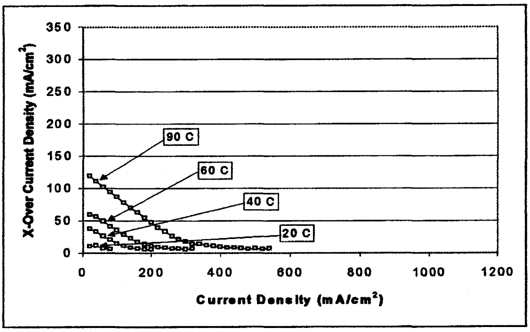

Figure 1. The effects of increasing temperature on crossover rate for a DMFC operating at 0.5M methanol.

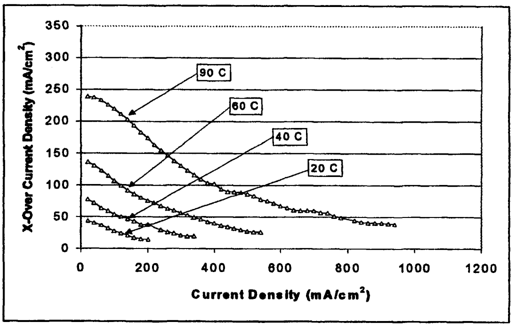

Figure 2. The effects of increasing temperature on crossover rate for a DMFC operating at 0.5M methanol.

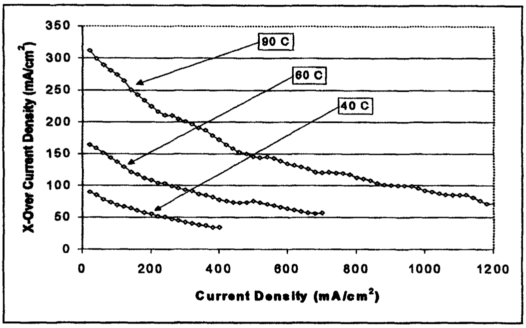

Figure 3. The effects of increasing temperature on crossover rate for a DMFC operating at 0.5M methanol.

The effect of methanol molarity and airflow rate on a DMFC are shown in Figure 4. As the methanol concentration decreases, cell voltages can increase by as much as 50 mV at current densities of 100 mA/cm^2. In Figure 4, the cell voltage is shown as 0.362 V at 100 mA/cm^2, for a cell operating with 60°C, 1M methanol and 0.1 L/min of ambient pressure airflow. With the reduced methanol concentration of 0.5M, the cell voltages for 60°C, and 0.1 L/min ambient airflow rate operation are 0.419 V. The calculated air stoichiometry at a 100 mA/cm^2 for 0.1 L/min, 0.5M methanol corresponds to 1.7 times stoic when the air required to oxidize the methanol that crosses over is also included. A similar increase in DMFC performance can be seen when one increases the airflow rate. At 0.3L/min, the cell voltage is 0.403 V for 60 °C, 1M methanol. The calculated air stoichiometry at a 100 mA/cm^2 for 0.3 L/min, 1.0M methanol corresponds to 3.35 times stoic.

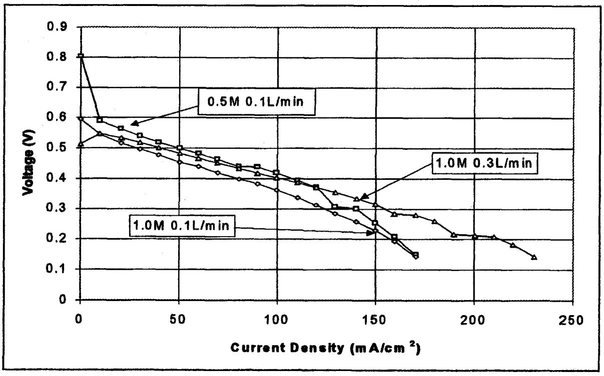

Figure 4. The effect of molarity and ambient airflow rate on the electrochemical performance of a DMFC at 60 °C.

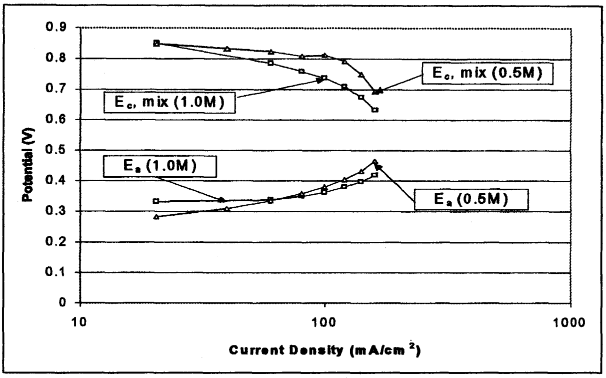

Figure 5. The effect of methanol concentration on the electrochemical performance of the anode and cathode in a DMFC operating at 60 °C, 0.1 L/min ambient airflow rate.

The effect of methanol concentration on the electrochemical performance for both the anode and cathode are shown as a function of current density in Figure 5. The polarization losses at the anode are minimal and there is a marginal improvement in performance of the anode on increasing the concentration from 0.5 to 1.0M at current density of 120 mA/cm^2. The cathode polarization plot obtained is a plot of the mixed potential, $E_{c,mix}$, because of the effects of methanol crossover on that electrode. Increasing the methanol concentration lowers the cathode potential to the extent of 50-100 mV.

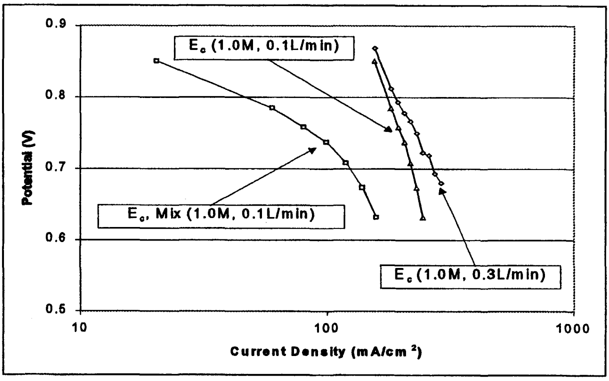

Figure 6. The effects of methanol crossover on the cathode of a fuel cell operating at 1.0M methanol.

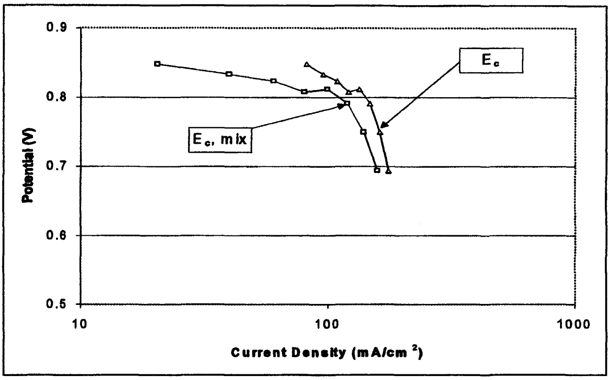

Figure 7. The effects of methanol crossover on the cathode of a fuel cell operating at 0.5M methanol.

The effects of methanol crossover on the cathode potential, $E_{c,mix}$, as a function of applied current density can be seen in Figures 6 and 7. The true cathode potential, E_c, can be determined when one includes the air demand due to crossover as per equation (4). In Figure 6, the 1M methanol case, E_c is always in a mass transfer limited regime regardless of airflow rate. When the methanol molarity is reduced to 0.5M, the overall performance of the cathode is improved as shown in Figure 7. The true cathode potential becomes mass transfer limited only at current densities upwards of 130 mA/cm^2 operating on 0.5M methanol.

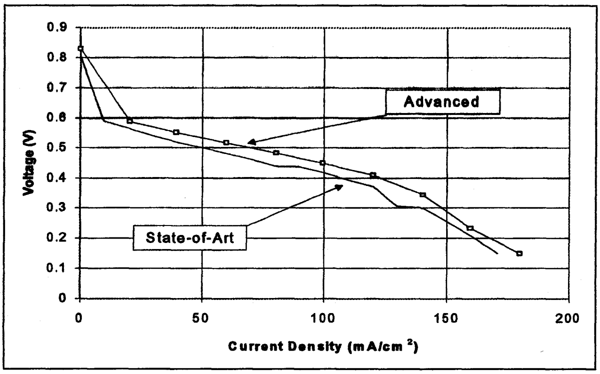

Figure 8. The effect of cathode structure for a DMFC operating at 60 C, 0.5M methanol, and 0.1 L/min ambient airflow.

Thus it is important to reduce the mass transfer barriers at the cathode, and results of such improvements are shown in Figure 8. At an applied current density of 100 mA/cm^2 a 30 mV improvement can be attained with an improved cathode catalyst structure. Cell voltages of 0.449 V at 100 mA/cm^2 are shown for a DMFC operating at 60 °C, 0.5M methanol, and 0.1 L/min of ambient airflow. Under the same conditions the cell is able to perform at voltage as high as 0.410 V at current densities of 120 mA/cm^2. The air stoichiometry at 120 mA/cm^2 corresponds to 1.55 times stoic, when the air required to oxidize the methanol that crosses over to the cathode is included.

Discussion

It has been observed that higher operating voltages at current densities below 150 mA/cm^2 can be obtained when a lower concentration of methanol is used in the operation of a DMFC. A possible reason for this is that the effective crossover rate is less at lower concentrations. The cathode is affected in two ways by crossover; the water produced from the crossover reaction can form a physical barrier to O_2 permeation at the cathode catalyst membrane interface, and the methanol crossing over places an additional demand on the oxygen available at the cathode. When more oxygen is introduced to the cell, in the form of an increased airflow rate, the cell performance is improved. The difference between the 0.1 L/min, 0.5M methanol and 0.3 L/min 1.0M methanol at 60 °C is 16 mV at 100 mA/cm^2 which states that equivalent performances can be obtained under two different operating conditions. The problem is that when one views DMFC performance in light of a total system, the increase from 0.1 to 0.3 liter/min airflow operation translates into increased system weight and complexity.

The results in Figures 1 and 2 demonstrate that methanol molarity has an effect on cell performance. At 1M methanol, the cathode is essentially always mass transfer limited. Even when the airflow rate is tripled, there are significant mass transfer limitations at the cathode. Thus, at 60 °C, the crossover resulting from 1M methanol overwhelms the electrode in such a manner that even increasing the amount of O_2 to the cathode does not make available more O_2 for the reaction. On the other hand, reducing the methanol concentration has the greatest impact on cell performance at 60 °C and at airflow rates less than 2 times stoichiometric. E_c, in the 0.5M case in Figure 7, shows a distinct kinetic region for current densities as high as 120 mA/cm^2.

Conclusions

It has been determined that methanol concentration has a significant effect on the performance of the cathode in a DMFC for current densities below 150 mA/cm^2. This effect has been quantified in three ways: cell electrical performance, apparent polarization, and true cathode polarization. It has been shown that cell voltages can be up to 50 mV higher when operating a DMFC at 0.5M vs. 1.0M, 60 °C methanol, 0.1 L/min ambient airflow, and at 100 mA/cm^2 applied load. When a cathode can be made to be sufficiently water rejecting, we once again see an increase in performance. At 60 °C, 0.5M methanol, 0.1L/min the fuel cell with the improved electrode structure could reach voltages as high as 0.449V. This is a 30 mV improvement over the previous design.

IN summary, the performance of a Nafion-based DMFC is strongly impacted by the methanol crossover, especially at low airflow rates. The mass transfer limited condition of the cathode is considerably worsened by the methanol crossover. While one approach to solving this problem would be to use a membrane with lower methanol crossover, it has been demonstrated here that an improved cathode structure and operation at a lower methanol concentration will result in a significant enhancement of performance.

Acknowledgment

The research described in this presentation was carried out by the Jet Propulsion Laboratory, California Institute of Technology, under contract with the National Aeronautics and Space Administration.

References

1-S.R. Narayanan, E. Vamos, H. Frank, S. Surampudi, and G. Halpert, Presented at Electrochemical Society Meeting, New Orleans, LA, Oct. 10 –15, 1993
2-S.R. Narayanan, H. Frank, B. Jeffreis-Nakamura, M. Smart, W. Chun and G. Halpert, Proceedings of Proton Conducting Membrane Fuel Cells 1, ECS Proceeding Series, Pennington, NJ. 1995 pg. 278 –283
3-S.R. Narayanan, B Jeffreis, T, I. Valdez, W. Chun, and G. Halpert, Presented at The Fuel Cell Seminar, Orlando, FL., Nov. 17 -20, 1996 abstract pg. 525 –528
4-Ren, X., T. A. Zawodzinski Jr., F. Uribe, H. Dai, and S. Gottesfeld, Proceedings of Proton Conducting Membrane Fuel Cells 1, ECS Proceeding Series, Pennington, NJ. 1995 pg. 284 –293
5-Ren, X., W. Henderson, and S. Gottesfeld, J. Electrochemical Society, Vol. 144, No. 9, September 1997 pg. L267 –L270
6-Verbrugge, M.W., J. Electrochemical Society, Vol. 136, No. 2, February 1989 pg. 417 –423

Proton_Conducting_Membrane_Fuel_Cells_II, PV 1998-27, 388-399 (1998)
DOI: 10.1149/199827.0388PV © The Electrochemical Society

OPTIMIZING THE OVERALL CONVERSION EFFICIENCY OF A DIRECT-METHANOL FUEL CELL

R. M. Moore
University of California
Davis, California, 95616-8762, USA

S. Gottesfeld and P. Zelenay[1]
Los Alamos National Laboratory
Los Alamos, New Mexico 87545, USA

ABSTRACT

It is important to be able to maximize the conversion efficiency of a PEM direct-methanol fuel cell (DMFC) over the broadest possible range of cell power density. The research presented here provides conceptual framework for a control strategy that provides such an optimization. This framework leads into a system level optimization of efficiency *vs.* power, and an operational strategy for controlling a direct-methanol fuel cell for maximum efficiency from minimum to maximum power density. Contrary to the conventional wisdom regarding DMFCs, the research reported here shows that, if such operational strategy could be implemented, DMFCs can be considered for highly dynamic applications – including automotive use – without resorting to "hybrid" power systems.

INTRODUCTION

The potential range of application for the direct-methanol fuel cell (DMFC) depends on its conversion efficiency across a broad spectrum of power density levels. Certainly there are potential niche applications for DMFC power systems that can only be operated efficiently at relatively fixed power, or in "hybrid" power systems. However, if the potential use of the DMFC is limited to such niches, this greatly restricts the eventual markets for the DMFC.

The objective of the research reported here is to critically examine the limitations on the efficiency of the DMFC – when operated over a broad power range. The conventional wisdom was that the DMFC could not efficiently operate across the range of

---

[1] *On leave from the Department of Chemistry, Warsaw University, Warsaw, Poland.*

power levels demanded in applications such as automotive power systems. It is shown here that this conclusion may be incorrect.

This paper is organized into four sections, followed by a summary of the results. First, there is an explanation of the experimental conditions used to obtain the DMFC data reported and analyzed here. Next, unique features of the DMFC are discussed – focusing on the methanol crossover phenomenon. This is followed by the presentation of the conceptual framework for the optimization of conversion efficiency, which introduces the idea of the Maximum Conversion Efficiency Curve. Finally there is a discussion of the optimized conversion efficiency in terms of the familiar concepts of voltage efficiency and fuel utilization.

EXPERIMENTAL

Pretreatment of the Nafion™ 117 in the H^+ form, preparation of membrane electrode assemblies (MEAs) for a DMFC using a decal technique, and the single-cell fuel cell hardware have been previously described[1,2] as has the cell testing system used.[3] Two unsupported dispersed Pt-Ru catalysts of nominal 1:1 atomic ratio were used for anode preparation, both supplied by Johnson Matthey. Anode inks were made by dispersing appropriate amounts of the Pt-Ru catalyst in deionized/distilled water and adding 5% Nafion™ solution (1200 in equivalent weight, Solution Technology Inc.). The cathode inks contained unsupported Pt black (30 $m^2 g^{-1}$, Johnson-Matthey), deionized/distilled water and 5% Nafion™ solution (1100 equivalent weight, Solution Technology Inc.). In some cases, the catalyst layers involved direct application of the catalyst inks to PTFE-treated carbon cloths. The geometric active area of all the MEAs prepared was 5 cm^2.

Methanol solutions, between 0.25 and 2.0 M in concentration, were pumped through the DMFC anode flow field at precisely controlled rates (0.5-3.0 ml min^{-1}) using a Shimadzu LC-10AS HPLC pump. A back pressure of about 15 psig was imposed upon the anode outlet flow to ensure that the membrane would be in contact with a liquid solution of methanol at the cell operating temperature of 100°C. The cathode gas feed was air at a pressure of 30 psig and flow rate of 0.5 l min^{-1}. The air was usually pre-humidified at the same or similar temperature as that of the operating cell.

The crossover of methanol as a function of cell current density was recorded together with the corresponding cell polarization (V-I_C) chracteristic. The determination of crossover was based upon the amount of carbon dioxide in the cathode exhaust, as measured using a GMM12 Carbon Dioxide IR Sensor (Vaisala Oy, Finland). The IR detector was earlier pre-calibrated with a gaseous mixture of 4% CO_2 and 96% N_2. The CO_2 content in the cathode exhaust was converted into the corresponding amount of methanol that had crossed through the membrane, expressed as current density of MeOH oxidation on the cathode, I_X (see below).

DMFC CHARACTERISTICS

A unique feature of the direct-methanol PEM fuel cell – when compared to a direct-hydrogen or reformate fuel cell – is the significant crossover of methanol from the anode through the membrane into the cathode. For the purposes of this study, the critical result of the crossover is an efficiency loss due to an unproductive fuel consumption mechanism.

It is possible to treat methanol crossover analytically within the concept of "fuel utilization", while dealing with the cell polarization curve (voltage *vs.* cell current) separately in terms of "voltage efficiency". This is commonly done for reformate PEM fuel cells. However, this disguises the physical interaction between the cell current and crossover current (methanol crossover expressed as equivalent current density of MeOH oxidation to carbon dioxide at the cathode), and obscures the possibilities for optimizing cell current and power density *vs.* crossover losses.

In this paper, we introduce a concept of viewing the crossover current density, together with the cell current density, and voltage – in terms of a "composite" polarization curve. An example of this type of composite polarization curve is shown in **Figure 1**, for a particular set of experimental conditions. The conceptual value of this composite polarization curve is that it explicitly illustrates the interaction between the cell and crossover current densities.

The cell current density (I_C) and crossover current density (I_X) curves in Figure 1 allow to predict the behavior of a direct-methanol cell under variable cell current, illustrating the characteristic impact of increasing the cell current on crossover current losses. When the cell current increases the crossover current decreases and the fuel utilization increases, in this example to almost 90% at about 0.3 V, 0.31 A cm^{-2}. In contrast, where the I_C and I_X curves cross (about 0.6 V in this case) the fuel utilization is 50% and, for the lowest cell current density shown, fuel utilization falls to about 10%.

It is obvious that we would choose to operate a cell with the polarization curve shown in Figure 1 at the highest possible cell current (maximum cell power density), in order to reduce crossover losses. This has led to an argument that direct-methanol cell may have to be a part of a "hybrid" power system – *i.e.*, where the fuel cell is only operated at its highest power density and another electrical energy storage device is used to provide lower power levels.

However, as we will try to show below, there is no fundamental reason to limit the operation of a DMFC power system to a "hybrid" power system configuration. High fuel utilization can be achieved over a complete range of power densities without resorting to additional energy storage devices and without creating the need to control and manage the output from two separate power sources.

The key cognitive step is to realize that the example shown in Figure 1 is for a particular set of anode (and cathode) conditions. However, for a different set of anode conditions, *i.e.*, a different methanol concentration and solution flow rate, the crossover current, cell current, voltage and power density will all change, in a given cell, in a predictable and controllable way. Thus, we will show that it is possible to minimize the crossover losses for a wide range of power densities by manipulating the anode feed conditions. This is illustrated in the next section using data for some direct-methanol fuel cells fabricated and tested at LANL.

EFFICIENCY OPTIMIZATION *vs.* POWER

As shown in the last section, by expressing the methanol crossover flux as a crossover current density, the DMFC performance characteristic can be represented by a set of I_C and I_X curves *vs.* cell voltage. Figure 1 illustrates this for a particular choice of anode and cathode conditions. For a different choice of anode methanol concentration and solution flow rate, there will be a different pair of I_X and I_C curves that characterize the cell.

A set of such curves is shown in **Figure 2** – for the case of a fixed methanol concentration and a variable solution flow rate to the anode. This particular methanol concentration was chosen to illustrate significant impact of anode flow conditions on the crossover current, combined with a fairly minor impact on cell current. Such beneficial effects of anode operation conditions are achieved by appropriate DMFC anode design. It is obvious that, with this set of composite polarization curves, one would choose to operate the cell at the lowest solution flow rate (curve labeled **a**) for this methanol concentration level.

This is further illustrated in **Figure 3**, where the cell power density is plotted *vs.* the cell fuel consumption density (cell plus equivalent crossover current density). In this presentation of the composite data for variable anode solution flow rate at constant anode feed concentration, it becomes even more obvious that one would choose to operate at the lowest solution flow rate (curve **a** for this particular methanol concentration). Curve **a** generates the highest power for every value of fuel consumption density (or fuel rate density).

By following the procedure illustrated above in Figures 2 and 3 for a range of inlet methanol solution concentrations, it is possible to select an optimum flow rate for each concentration value. The result of this optimization procedure is shown in **Figure 4** for three values of methanol concentration: 0.25, 0.5 and 1.0 M (curves **a**, **b**, and **c**, respectively). A 100% conversion efficiency curve is also shown in Figure 4 as reference.

It is obvious from Figure 4 that, assuming one were limited to only these three values of concentration, there is a control strategy that will optimize the power output for a given fuel flow rate or power level. The correct control strategy is: begin with curve **a** for low power levels, transition to curve **b** for moderate power levels, and finally transition to curve *c* for the highest power levels. This control strategy would insure both the highest power density and highest efficiency for every fuel consumption (fuel rate) density.

This result is illustrated in **Figure 5**, where the cell overall conversion efficiency is plotted *vs.* the flow rate for the three sets of conditions in Figure 4, together with an envelope of the discrete curves depicting the limiting case of continuously variable methanol concentration and flow rate. This envelope is referred to as the Maximum Conversion Efficiency Curve. We also refer to it as the "Op Curve" (short for Operating Curve) that maximizes DMFC efficiency for variable methanol feed concentration and flow conditions in the anode.

This Op Curve is displayed in **Figure 6** in a somewhat different format – conversion efficiency *vs.* power density. This format is particularly useful for power system analysis and modeling applications.

DISCUSSION OF RESULTS

It is instructive to translate the results illustrated in Figures 5 and 6, and particularly the resulting Op Curve, into more familiar settings – specifically into the equivalent power density, composite polarization, and fuel utilization curves that correspond to the Op Curve. These composite equivalent curves obtained for the Op Curve control strategy can then be compared with the corresponding curves for fixed anode conditions. This helps us to understand the physical basis for the improved efficiency achieved with the Op Curve control strategy.

Figure 7 shows the Op Curve as cell power density *vs.* cell fuel consumption density. In this representation, it is, of course, simply the envelope of the three discrete curves in Figure 4 – obtained under the condition of continuously variable methanol concentration and solution flow rate.

Figure 8 presents a comparison of both I_C and I_X for (i) the Op Curve control strategy, and (ii) a fixed methanol concentration and solution flow rate case. (The fixed anode condition curves chosen corresponds to the concentration and flow rate for maximum cell power density.) This figure illustrates quite clearly that, while the Op Curve produces somewhat higher voltage at a given cell current density (compared to the cell under fixed anode conditions), the major improvement is a significant reduction in I_X at low current density (power density) values. Thus the primary effect of the Op Curve control strategy is to reduce the crossover losses by up to 50% at low power levels – while also achieving marginally higher voltage efficiency.

Finally, **Figure 9** explicitly shows the impact of the Op Curve control strategy on the crossover losses – using the "fuel utilization" factor (the ratio of the cell current density to the cell plus crossover current density) to evaluate the performance of the DMFC with the Op Curve control strategy. The fuel utilization is plotted *vs.* cell current density (a surrogate for cell power density). This illustrates quite clearly that the primary effect of the Op Curve control strategy is to significantly increase the fuel utilization at low current (power) levels. It is this effect that maintains a relatively high level of cell conversion efficiency across a broad range of power levels, *i.e.*, the result illustrated in Figure 6. There is, of course, also a contribution from the improved voltage efficiency – again primarily at low cell current (power) density.

SUMMARY OF RESULTS

The conceptual framework presented in this paper has established the following:

(i) At a given DMFC fuel consumption density, the DMFC power density is maximized by simultaneously controlling the methanol concentration and solution flow rate to the anode. This is illustrated in Figure 4, where cell power density is plotted *vs.* the sum of the cell and crossover current densities for three particular choices of anode conditions at fixed cathode conditions.

(ii) The envelope of all such points of maximum power density – each for a given fuel consumption – provides the maximum conversion efficiency for the complete range of fuel consumption. This is illustrated in Figure 5, displayed as conversion efficiency versus the fuel rate density.

Finally, the optimized conversion efficiency curve (Op Curve) provides a conceptual basis for an optimum DMFC system control strategy. Figure 6 illustrates the conversion efficiency resulting from this Op Curve control strategy.

A key feature of this optimized curve is its relative flatness versus power density (*e.g.*, greater than 30% efficiency over a range from about 70 to 230 mW cm^{-2}). This is a desirable shape for applications where power demand has a broad dynamic range – such as automotive applications.

The major operational conclusion from the analysis presented in this paper – and particularly illustrated by Figures 5 and 6 – is that it could be possible to optimize the conversion efficiency of a DMFC power system by manipulating the anode feed stream as a function of the system power demand. Such optimum control strategy for direct-methanol fuel cell power systems would be based on following a Maximum Conversion Efficiency Curve (Op Curve) as described in this paper. Needless to say, application of such strategy would depend on defining the system engineering requirements for implementation of a variable concentration, variable flow methanol feed stream.

Comment on cathode optimization

All of the analysis and optimization presented in this paper was illustrated for the case of constant cathode conditions – constant cathode air pressure and flow. This was done for the purpose of clarity in examining the impact of anode conditions. However, for an optimum overall DMFC power system it is necessary to further optimize the operation of the cell by controlling the cathode conditions. The general technique for such an optimization on the cathode side of the DMFC is illustrated in another paper presented in this Symposium (D. J. Friedman and R. M. Moore, *This Symposium*). This optimization for the DMFC is beyond the scope of the current paper, and is highly specific to the particular behavior of the DMFC cathode under the conditions of methanol crossover.

ACKNOWLEDGMENTS

This work was supported by the Defense Advanced Research Projects Agency (DARPA) through the Defense Sciences Office, by the U.S. Department of Energy through the Office of Transportation Technology, by the Fuel Cell Vehicle Project at the University of California, and by ATA (Advanced Technology Assessment).

REFERENCES

1. X. Ren, M. S. Wilson and S. Gottesfeld, *J. Electrochem. Soc.*, **143**, L12 (1996).
2. X. Ren, W. Henderson and S. Gottesfeld, *J. Electrochem. Soc.*, **144**, L267 (1997).
3. T. E. Springer, M. S. Wilson and S. Gottesfeld, *J. Electrochem. Soc.*, **140**, 3513 (1993).

FIGURES

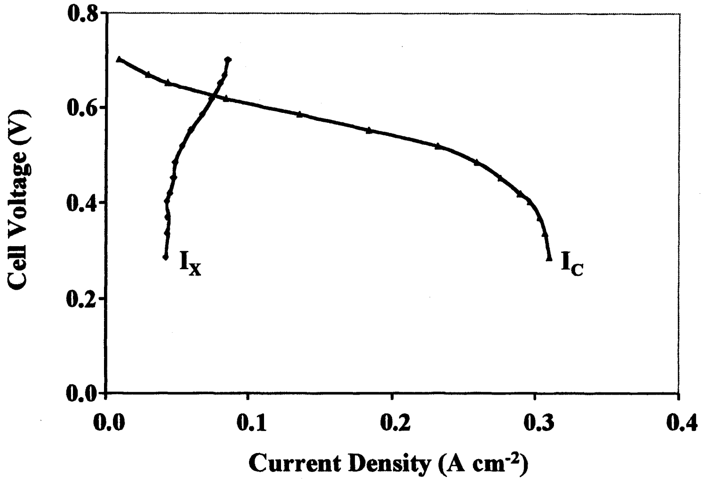

Figure 1. Current density curves for a DMFC, where I_X is methanol crossover current density and I_C is the cell current density (c=0.25 M, f=4 ml min^{-1}, T=100 °C).

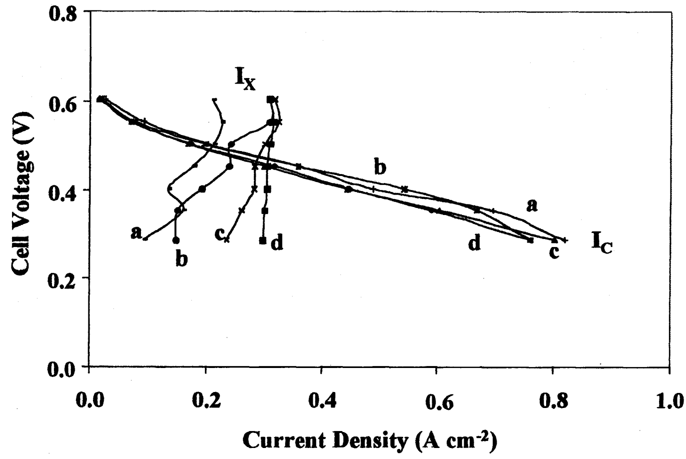

Figure 2. Crossover and cell current density curves for a DMFC; I_X is methanol crossover current density and I_C is the cell current density (c=2.0 M, f= variable; T=100 °C).

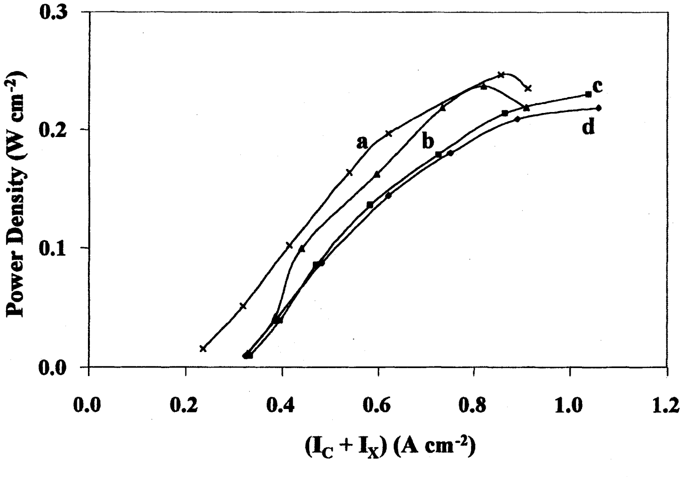

Figure 3. Power density curves for a DMFC *vs.* sum of I_X (methanol crossover current density) and I_C (cell current density); c=2.0 M; T=100 °C; f is (**a**) 0.5 ml min^{-1}, (**b**) 1.0 ml min^{-1}, (**c**) 2.0 ml min^{-1}, and (**d**) 3.0 ml min^{-1}.

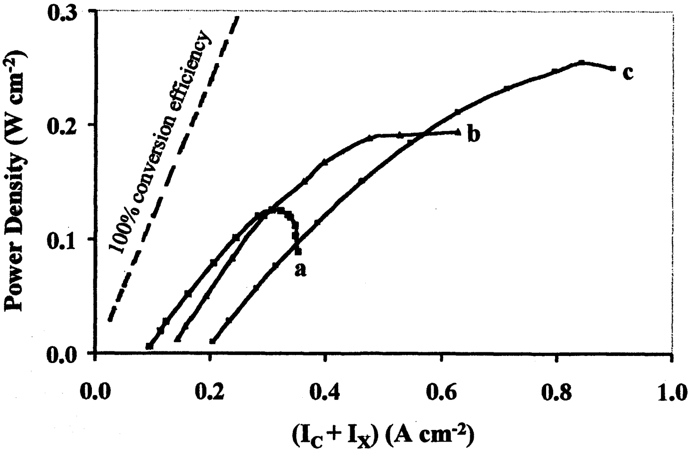

Figure 4. Power density of a DMFC for variable methanol concentration: (**a**) 0.25 M, (**b**) 0.5, (**c**) 1.0 M, as function of overall DMFC fuel consumption density. The reference 100% conversion efficiency plot corresponds to generation of electric power from MeOH at 100% fuel utilization, at the thermodynamically expected cell voltage of 1.21 V.

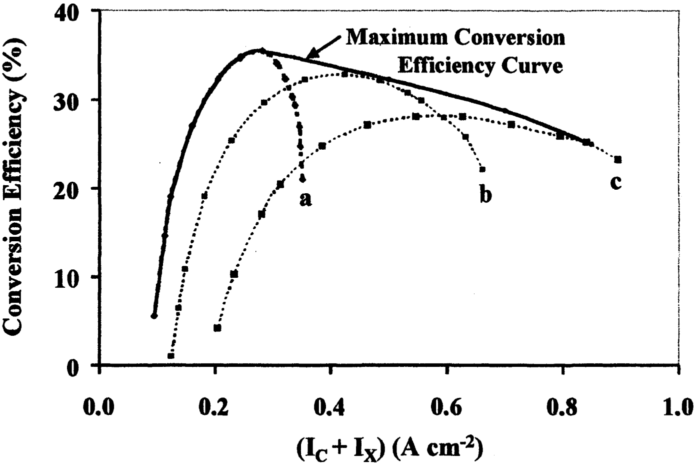

Figure 5. Overall conversion efficiency of a DMFC for variable methanol concentration: (**a**) 0.25 M, (**b**) 0.5 M, (**c**) 1.0 M.

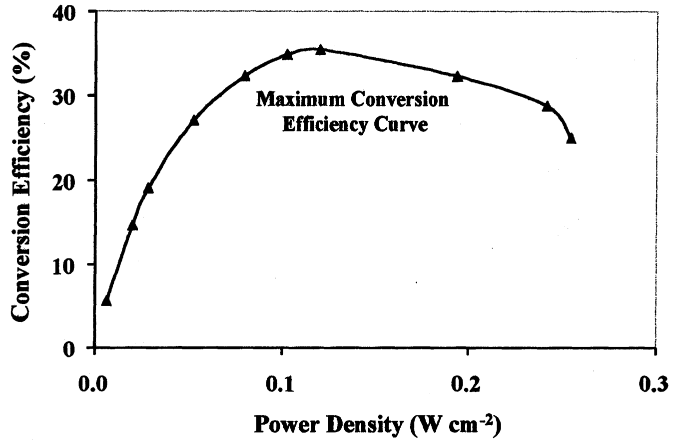

Figure 6. Optimum overall conversion efficiency *vs.* cell power density, plotted against fuel consumption density based on results for the same three feed concentrations of MeOH (0.25, 0.5, 1.0 M) and a variable flow option.

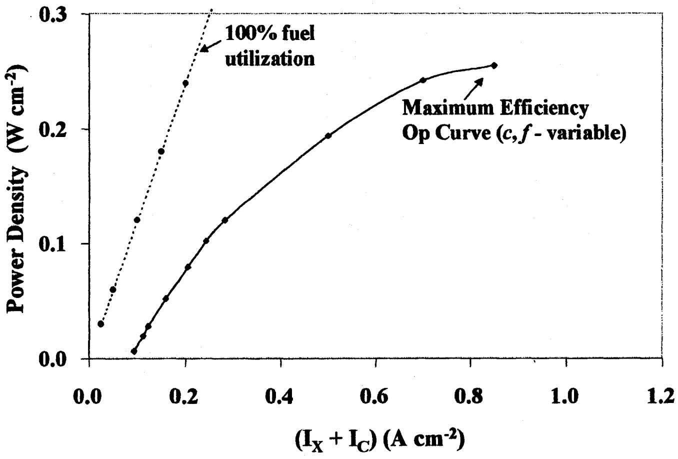

Figure 7. DMFC power density achievable under Maximum Conversion Efficiency conditions ("Op Curve") employing variable methanol concentration and solution flow rate.

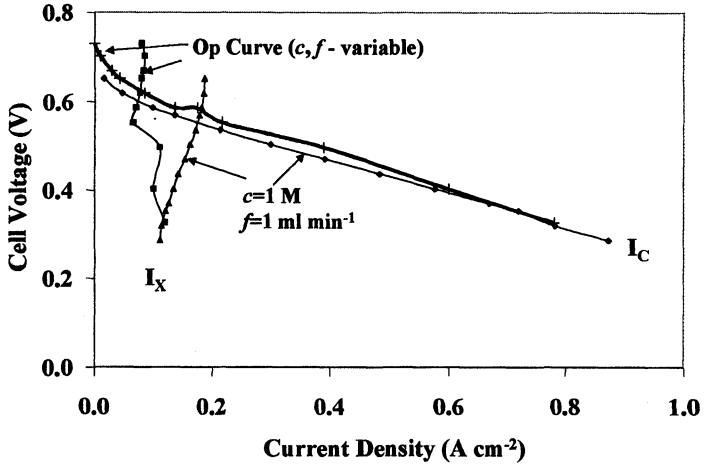

Figure 8. Cell and crossover current density for Op Curve (variable *c* and *f*) and for fixed *c* and *f* (maximum power curve).

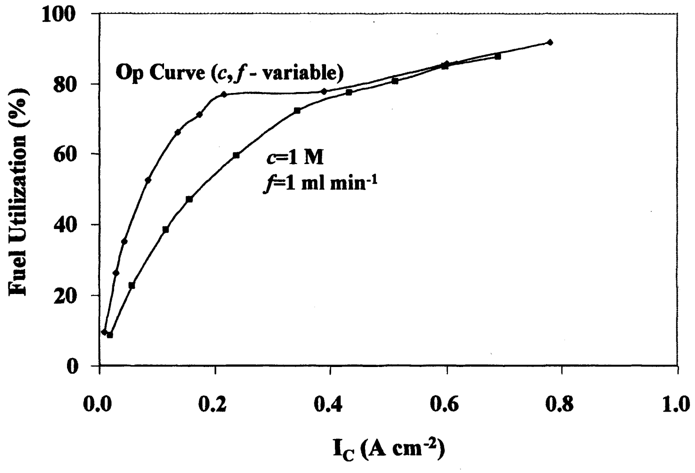

Figure 9. Fuel utilization *vs.* cell current density for Op Curve (*c* and *f* variable) and for fixed *c* and *f* (maximum power curve).

Proton_Conducting_Membrane_Fuel_Cells_II, PV 1998-27, 400-406 (1998)
DOI: 10.1149/199827.0400PV © The Electrochemical Society

Effect of Collector Plate Resistance on Fuel Cell Stack Performance

F. Barbir, J. Braun and J. Neutzler
Energy Partners
1501 Northpoint Pkwy, #102
West Palm Beach, FL 33407

ABSTRACT

The electrical resistance of the collector plate (both bulk and surface resistance) plays a major role in fuel cell stack performance. Energy Partners (EP) has developed molded graphite composite plates with enhanced electrical conductivity, as an alternative to expensive machined graphite. By optimizing collector plate materials, compounding and molding processes, the resistance of the molded collector/backing layer sandwich was reduced by about 12 mΩcm^2. This resulted in an improvement in performance of more than 50 mV per cell at 1 A/cm^2 in a 10-cell stack with 300 cm^2 active area.

INTRODUCTION

Proton Exchange Membrane (PEM) fuel cells can convert chemical energy to electrical energy with high efficiency. They generate electrical power, heat and water, and when operating on hydrogen they generate essentially "zero emissions". PEM fuel cell stacks consist of series connected cells, they are very reliable, have high power density, and are suitable for both transportation and stationary applications. Recently, considerable effort in the fuel cell industry has been directed toward reducing component manufacturing and assembly costs, to allow penetration into automotive markets.

One of the most critical components in the fuel cell stack is the bipolar collector/ separator plate. The first function of the collector plate is to provide series electrical connection between individual cells in a fuel cell stack. The second function is to direct fuel and oxidant gas streams to individual cells, to distribute gas streams within individual cells, and to remove product water from individual cells. The third function is to provide separation of fuel and oxidant gas streams between the series connected cells. The fourth function is to assist in the thermal control (via heat removal) of the fuel cell stack. In addition to these functions, the collector plate must be corrosion resistant in the demanding fuel cell environment (1). Graphite has typically been used as a collector plate material due to excellent corrosion resistance. However, pure graphite is not practical from a cost perspective, since it requires machining of the flow field channels.

To preserve the power density of state-of-the-art fuel cell stacks while reducing cost, the U.S. Department of Energy has specified target bulk resistance of 10 mΩcm or lower for alternative bipolar plate materials (2). Work on graphite composite bipolar plates at Los Alamos National Laboratory (LANL) recently produced materials with bulk resistance of 8.3 mΩcm (3).

Energy Partners has developed graphite composite technology as a means of lowering the manufacturing cost for bipolar collector plates. Since 1991 EP has built several large active area fuel cell stacks (780 cm^2) with molded graphite/composite plates. The use of a polymer binder in the composite plate enables net shape or near net shape molding, but also compels an increase in collector plate resistance. By optimizing material selection, compounding and molding processes we have developed a new generation of molded collector plates with significantly improved electrical properties. This paper investigates the effect of increased collector plate resistance on performance of 10-cell PEM fuel cell stacks.

EXPERIMENTAL

The bulk resistance of the molded composite plate was measured with a 4-point probe method as described by Smits (4). This method allows measurement of bulk resistivity of thin plates by applying a geometry dependent correction factor to the measured value of resistivity. Measurements were performed on thin circular samples (7.62 cm diameter × 3 mm thick).

Total electrical DC resistance (including contact resistance) was also measured with different contact materials and at various contact pressures to simulate conditions in the fuel cell stack. Measurements were performed on the same thin circular samples by pressing the sample between two gold plated copper surfaces (as shown in Figure 1), and measuring the voltage drop while passing a current of 1 A/cm^2. An electrode backing material (ELAT from E-TEK) was then inserted on both sides of the sample and the same DC resistance measurement was performed.

RESULTS/DISCUSSION

The results of bulk resistivity are shown in Table I. The old material had bulk resistivity of 6.8 mΩcm. By optimizing the binder materials, compounding and molding procedure we were able to significantly improve the electrical properties in the new generation molded collector plates. The resulting bulk resistivity is close to that of pure graphite (2.9 and 1.4 mΩcm, respectively).

Bulk resistivity of either material would not make much difference in fuel cell performance. For example, a 3 mm thick collector/separator plate would contribute 0.4

and 2.0 mΩcm^2 to the cell resistance (0.4-2.0 mV drop at 1 A/cm^2), for graphite and graphite/composite respectively. This, of course, would be negligible since the membrane has about two orders of magnitude higher (ionic) resistance.

However, in an actual fuel cell, the hardware (collector plate) resistance is much higher and typically of the same order of magnitude as the ionic resistance in the membrane. This is mainly due to contact resistance. The results of total resistance (contact and bulk) resistance measurements as a function of clamping pressure are shown in Figure 2. The resistance of a 3 mm thick graphite plate is found to be about 5 mΩcm^2 when inserted between two gold plated copper surfaces with a clamping pressure of approx. 1.9 MPa. If an electrode backing material (such as E-TEK's ELAT) is inserted on both sides of the graphite plate the resistance increases to about 20 mΩcm^2. Resistance of the graphite/composite collector plate/ELAT sandwich is much higher (>40 mΩcm^2).

The resistance in an actual fuel cell stack is higher than measured on the samples, as shown in Table I. The resistance in an actual fuel cell stack also includes the ionic resistance in the membrane, and was measured by the current interrupt method. Figure 3 shows that there is a linear relationship between the sample resistance and resistance of operational cells. The intercept on "y"-axis represents the membrane resistance, and the slope is due to reduced surface area of the actual collector plates because of the gas channels embedded on its surface. The total cell ohmic resistance in Energy Partners' fuel cell stacks with "old" material was in excess of 200 mΩcm^2. This created a significant voltage loss, >200 mV per cell at 1 A/cm^2. A new generation 10-cell stack with a 300 cm^2 active area was built with machined graphite collector/separator plates. During operation, an average cell resistance of 125 mΩcm^2 was measured. The resulting polarization curve is shown in Figure 4.

While the graphite collector plates result in very good performance (average cell voltage is about 0.65 V at 1 A/cm^2) the machining process needed to make the gas channels on the surface of the collector plate is prohibitively expensive. On the other side, graphite composite materials are moldable (thus no machining is necessary) but result in much higher resistance – about 100 mΩcm^2 higher than pure graphite (100 mV loss per cell at 1 A/cm^2 or more than 25% power loss at any given stack efficiency).

Significant efforts were applied to reduce those resistive losses, while at the same time preserving or even enhancing the molding properties of the graphite composite materials. By varying the binder materials, compounding and molding procedure we were able to significantly improve the electrical properties in the new generation molded collector plates. Bulk resistance was reduced to 2.9 mΩcm, and total resistance of a 3 mm thick plate was reduced to 28 mΩcm^2 (including the two electrode backing layers). Another identical 10-cell stack with the new generation collector plates was built and tested. The resulting polarization curve is compared with that of the stack with graphite plates in Figure 4. The average cell resistance was found to be about 155 mΩcm^2 which means only about 30 mV per cell loss at 1 A/cm^2 as compared with pure graphite plates, or 50 mV per cell improvement as compared with EP old collector plates.

TABLE I Results of resistivity and resistance measurements

Material	Bulk resistivity[a] (mΩcm)	resistance (mΩcm^2)			
		Bulk[b]	Bulk+ contacts[c]	Bulk+ contacts+ backing[c,d]	operational cell resistance
Ep old	6.8	2.04	40.2	42.3	>200[e,f]
EP new	2.9	0.87	17.1	28.2	155[e,g]
graphite	1.4	0.42	5.7	19.7	125[e,g]

a – measured by 4-point probe
b – calculated for a 3 mm thick flat plate
c – gold contacts, contact pressure 1.9 MPa
d – ELAT backing layer
e – includes both ionic and electronic resistance measured by current interrupt method in an operational multi cell stack with ~0.3 mm thick collector/separator plates
f – 780 cm^2 active area, multi cell stacks
g – ~300 cm^2 active area, 10-cell stack

CONCLUSIONS

The electrical resistance of the collector plate (both bulk and surface resistance) plays a major role in fuel cell stack performance. Energy Partners has developed molded graphite composite plates with enhanced electrical conductivity, as an alternative to expensive machined graphite. The DC resistance of the collector plate material sandwiched between electrode backing layers under suitable clamping pressure correlates with ohmic losses (measured by the current interrupt method) observed during multi-kilowatt fuel cell stack operation. By further optimizing collector plate binder materials, compounding and molding processes, the resistance of the molded collector/backing layer sandwich was reduced by about 12 mΩcm^2. This resulted in an improvement in performance of more than 50 mV per cell at 1 A/cm^2 in a 10-cell stack with 300 cm^2 active area. Current investigations are aimed at further reduction of contact resistance between the layers and improvements in materials properties.

ACKNOWLEDGEMENTS

Additional support for this work was provided under U.S. Department of Energy contract No. DE-FC02-97EE50476.

REFERENCES

1. R.L Borup and N.E. Vanderborgh in Materials for Electrochemical Energy Storage and Conversion – Batteries, Capacitors and Fuel Cells, edited by D. H. Doughty, B. Vyas, T. Takamura, and J.R. Huff, Mater. Res. Soc. Proc. 393, p. 154., Pittsburg, PA, 1995
2. F. M. Smits, *The Bell System Technical Journal*, p. 711-718 (May 1958)
3. Program Research and Development Announcement for Integrated Fuel Cell Systems and Components for Transportation and Buildings, Solicitation No: DE-RA02-97EE 50443, U.S. Department of Energy, Chicago Operations Office, Argonne, IL, 1997
4. M.S. Wilson, DOE Fuel Cells for Transportation Program National Laboratory R&D Meeting, Washington DC, July 22-23 1997

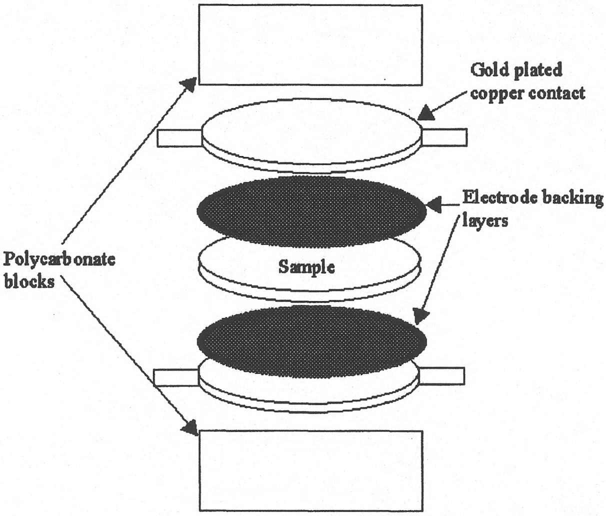

Fig. 1 Schematic diagram of experimental setup for measuring total (contact and bulk) resistance of graphite and molded graphite composite samples, including electrode backing layers.

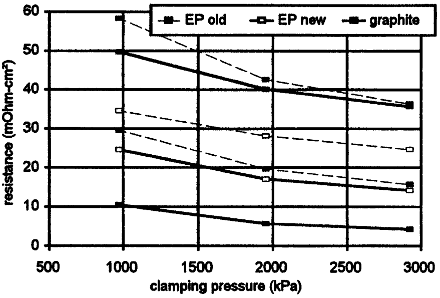

Figure 2 Resistance (bulk and contact) of various collector plate materials (dashed lines include two electrode backing layers)

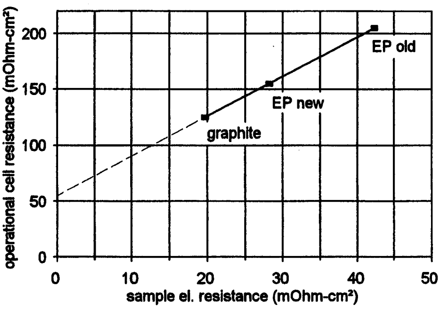

Figure 3 Relationship between sample electrical resistance and operational cell resistance

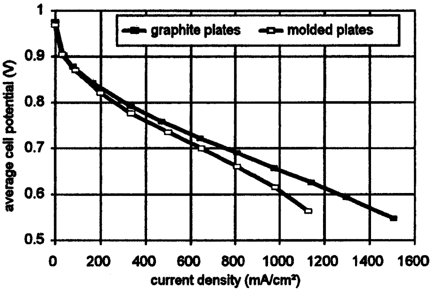

Figure 4 Polarization curves of two 10-cell stacks (H_2/air, 300 cm^2, 300 kPa and 60°C)

Proton_Conducting_Membrane_Fuel_Cells_II, PV 1998-27, 407-423 (1998)
DOI: 10.1149/199827.0407PV © The Electrochemical Society

PEM FUEL CELL SYSTEM OPTIMIZATION

D.J. Friedman and R.M. Moore
Institute of Transportation Studies
University of California
Davis, California, 95616-8762, USA

ABSTRACT

Fuel cells offer the potential of providing clean and efficient energy in a wide variety of applications. This paper presents a methodology for optimizing the fuel conversion efficiency and peak power of a direct-hydrogen proton-exchange-membrane (PEM) automotive fuel cell system over a wide range of power output. It is shown that optimal system operation can provide significant benefits in terms of both increased efficiency (especially in low power operation) and high peak power output from the system.

INTRODUCTION

Fuel cells offer the potential of providing clean and efficient energy in a wide variety of applications. Automotive applications are the most demanding because of the need for high peak power capability (vehicle acceleration and hill climbing performance), high energy conversion efficiency (fuel efficiency and range), and minimum space for the overall fuel cell power system (to provide adequate passenger and luggage). To achieve these simultaneous design requirements it is necessary to carefully optimize the overall fuel cell system.

This paper presents a methodology for optimizing the fuel conversion efficiency and peak power of a direct-hydrogen proton exchange membrane (PEM) automotive fuel cell system over a wide range of power output. The optimization process is based on the trade-off between the stack power and efficiency increases gained from operating at varying air pressures and air stoichiometric ratios, and the power losses required to provide the compressed air flow to the stack. This paper represents the further development and refinement of the concepts introduced by the authors in [1].

Emissions optimization is not included in this paper since a direct hydrogen fuel cell system produces only water and electricity. All of the emissions associated with a direct-hydrogen PEM system are produced in creating the hydrogen, and therefore cannot be minimized through vehicle operation (other than to minimize fuel consumption). The tradeoffs associated with interior space are also not discussed in this paper.

The paper begins with a brief description of the UC Davis fuel cell system simulation and the associated component models that have been developed to analyze automotive fuel cell systems. Next, the optimization of the PEM system is contrasted with optimization of the PEM stack alone – to stress the need for optimizing system rather than stack performance. This highlights the importance of distinguishing between gross stack and net system power output. After the various components associated with the PEM system are briefly described, the emphasis is shifted to the system components that are the most significant for the direct hydrogen system optimization process (the stack and air supply).

Finally, the process of system optimization is described, and examples are provided to illustrate system performance under various operating conditions. The conditions typically used to represent fuel cell stack operation are presented and then contrasted with the system performance that can be achieved through an optimized control strategy. It is shown that optimal system control can provide significant benefits in terms of increased efficiency (especially in low power operation) and high peak power output from the system.

In closing, the limitations of the illustrative optimization curves are discussed. Key effects discussed are:

- Additional practical limitations associated with stack and compressor operation,
- Issues associated with the dynamic response of the air supply system,
- The added difficulties of optimizing a system that includes an expander for energy recovery.
- Complications associated with including a reformer system to supply hydrogen.

FUEL CELL SYSTEM MODEL

A realistic representation of each of the components in a fuel cell system is needed when evaluating the optimal system operating strategy. Through the support of the UC Davis Fuel Cell Modeling Program, a PEM fuel cell system simulation has been developed for automotive applications. The system simulation contains component models for each of the critical fuel cell system components. In turn, this system simulation is embedded in a fuel cell vehicle (FCV) simulation.

The overall FCV simulation is divided into two stages. The first stage models and then applies an optimization procedure for the key components where performance tradeoffs must be made (stack and air supply). The second stage incorporates the information from the first and simulates the performance of a complete fuel cell vehicle (FCV) over a second-by-second driving cycle. This paper focuses on the first stage of the model, the system simulation.

As noted above, the two components simulated and optimized in the first stage of the FCV model are the fuel cell stack and the air supply system. The PEM fuel cell stack model is based on analysis done by the Electronic Materials and Device Research Group at Los Alamos National Laboratory.[2,3,4] The LANL analysis focuses on the mechanisms associated with the cathode (air side) reactions of a well-humidified direct-hydrogen PEM fuel cell.

The LANL cell analysis incorporates a physical understanding of the processes associated with:

- Interfacial kinetics at the interface between the cathode catalyst layer and the PEM membrane,
- Gas-transport and ionic conductivity limitations in the catalyst layer,
- Limitations associated with gas transport through the cathode backing layer.

Because of the physical basis of the model, it can also be used to predict the potential future performance of fuel cell stacks (as the characteristics of the cell and stack improve).

The air supply system model incorporates the ability to model compressors (high pressure and high flow) or blowers (low pressure, high flow). The compressor model used here to illustrate the optimization procedure is based on data supplied by Vairex Corporation for their variable displacement compressor (under development for fuel cell applications).

The simulation program has been developed within the Matlab programming environment, using both the Matlab programming language and Matlab's Simulink visual programming language. The use of Simulink allows for a simple modular design for the program and access to a vast library of mathematical functions and numerical calculation processes.

SYSTEMS VERSUS STACKS

For automotive fuel cell applications, an analysis must incorporate the complete systems that will be required to support the operation of the fuel cell. From the perspective of the fuel cell stack, it is provided with humidified fuel and air while producing electricity and water that are either consumed or reused to continue the process of operating the vehicle.

Figure 1 presents a simplified block diagram of the major components required within an automotive fuel cell system. To provide for the proper operation of the fuel cell stack and to interface with the power requirements of the vehicle, four major subsystem components are integrated together with the fuel cell stack: hydrogen supply, air supply, water and thermal management, and power electronics. Each of these sub-systems are discussed separately below. In addition, the overall system incorporates computer-based control to optimize the interactions within the system. This is, of course, analogous to an electronic control module for an internal combustion engine. Each of these subsystems can interact with one another and with the fuel cell stack to impact the performance of both the stack and the overall system.

Hydrogen Supply

The hydrogen supply subsystem for a direct-hydrogen FCV generally uses high pressure storage tanks for compressed hydrogen gas. From the perspective of the fuel cell stack, the compressed hydrogen gas (CHG) storage is the simplest and most efficient option. The hydrogen is stored at pressures significantly higher than needed for the stack (3000 to 5000 psi), so a simple pressure regulating system and mass flow control are all that are needed to ensure that the stack receives hydrogen at the necessary pressure and flow rate. Further, because the gas is essentially 100% hydrogen there are no performance losses in the anode side of the fuel cell associated with either diluted or CO poisoned input gases. In addition, the purity of the hydrogen allows any excess hydrogen fed through the anode to be recirculated (thereby essentially eliminating any significant losses from exhausting the excess hydrogen). Because of these characteristics, there is no optimization required between the stack and the CHG hydrogen supply – the CHG will essentially always be able to supply the optimal hydrogen input.

Air Supply

The two main choices for the air supply subsystem are either a blower or a compressor, each of which must be powered by an electric motor. The blower supplies near ambient pressure air to the fuel cell stack but can vary the mass flow rate supplied to the stack in order to achieve variable air stoichiometric ratios. In contrast, a compressor can provide either relatively fixed pressure air to the fuel cell stack at varying mass flow rates, or supply both variable air pressure and variable air mass flow.

These two basic types of air supply systems provide highly diluted oxygen (humidified air) to the fuel cell cathode. The strong dilution of the oxygen feed stream dramatically effects the oxygen partial pressure at the cathode catalyst layer, and, in turn, this leads to the need for high overpotentials on the cathode. The interaction of the air supply subsystem with the fuel cell stack is the focus of this paper and is discussed in more detail in the System Optimization section.

Water and Thermal Management

Two extremes that can seriously impact the operation of PEM fuel cell stacks are the flooding of the cathode and anode backing layers due to excess water, and the drying out of the membranes when the water supply is inadequate. Flooding occurs when the combination of the water carried into the anode and cathode by the humidified gases plus the water produced in the reaction between hydrogen and oxygen is not removed efficiently from the respective backing layers.

Flooding impairs the ability of the reactant gases (primarily the oxygen) to diffuse through the backing layers to the catalytic reaction sites. This effect significantly increases the cathode overpotential required to generate high cell current, and ultimately limits the peak power output of the stack. At the other extreme, insufficient supply of water can dry out the anode side of the PEM membrane, causing a significant rise in stack resistance and reduced membrane durability.

To ensure that the stack remains properly humidified and does not flood, a water management system humidifies the incoming feed gasses and removes the excess water from the cathode and anode exhaust streams. This excess water can be re-used for gas humidification.

To ensure operation at the design point temperature, a thermal management system maintains the fuel cell stack operating temperature within a narrow range under widely varying power demands. This thermal management system is also necessary for quick warm-up and safe cool-down of the stack during off-and-on daily operating conditions of the FCV.

Various techniques have been pursued to achieve optimal thermal and water management. These focus on internal stack humidification and cooling along with external water supply pumps, heat exchangers and other ancillary equipment. These systems have to be carefully designed to minimize their power requirements while ensuring that the stack remains at its optimal temperature and humidification levels. The design and optimization of these systems is beyond the scope of this paper.

Power Electronics

The final major subsystem is the power electronics which is the interface of the PEM system with the vehicle drivetrain and vehicle hotel loads (heating, air conditioning and various vehicle accessories). For optimal efficiency, the vehicle electric drive motor will probably operate around 300 volts, while many of the accessories for the fuel cell stack and vehicle may operate around 12 volts.

To accommodate these varying voltage requirements, a power electronics subsystem must be incorporated to either step up or step down the output voltage of the fuel cell stack. This system will have some associated efficiency penalties, but overall does not represent a significant loss in the system.

SYSTEM OPTIMIZATION

Based on the above discussion, it becomes clear that the major optimization for a direct-hydrogen fuel cell system involves the interaction of the stack with the air supply sub-system. The first step in this optimization process is understanding the characteristics of the fuel cell stack and the air supply system. Each of these components must be realistically modeled in order to ensure that the key operating characteristics and associated variables are included. Then the operation of the two components must be integrated to understand in detail where the tradeoffs occur.

PEM Fuel Cell Stack Characteristics

The performance of a direct-hydrogen fuel cell stack is typically illustrated by a polarization curve, which shows the relationship between voltage and current as variable power is drawn from the stack. This curve can vary significantly and depends on a number of factors, including the design and construction of the stack, the design of the membrane-electrode-assembly, and the operating temperature for the stack.

However, once the design of a direct-hydrogen stack, and its operating temperature, are fixed, two key external variables have a major impact on the shape of the polarization curve. These variables are the operating air pressure and the air stoichiometric ratio provided to the stack by the air supply. Together these two inputs control the oxygen partial pressure at the cathode catalyst layer, which in turn determines the cathode polarization (and conversion efficiency) for a specific cathode catalyst layer.

The impacts on the polarization plot of varying the air pressure and air side stoichiometric ratio (SRa) are illustrated in Figure 2 and Figure 3, respectively. To simplify the illustration of the impact of air pressure and stoichiometry, these plots do not include the effects associated with limited gas transport or limited proton conductivity in the catalyst layer. If present, these effects will alter the shape of the curves, but for the purpose of discerning the gross impacts of altering pressure and SRa it is not necessary to include them.

Figure 2 shows that the primary effect of increasing the air pressure in the fuel cell cathode is to raise the cell voltage relatively uniformly for each value of current density. Since raising the voltage directly increases the gross cell efficiency, this is generally viewed as a positive effect. The increased air pressure also produces a marginal increase in the cell limiting current density.

Figure 3 shows that the two primary impacts of increasing SRa are: a slower rate of decrease in cell voltage with increasing current, and an increase in the limiting current density. The slower voltage decrease increases the gross cell efficiency (similar to the effect of increasing pressure, but concentrated at higher current densities). The higher limiting current density allows the cell to reach higher peak power density.

Thus increasing either the air pressure or air flow will increase both the efficiency and the peak power density of a fuel cell. From this result, one might conclude that a direct-hydrogen stack should be operated at the highest pressure and highest SRa possible to achieve maximum efficiency and power density. However, the difficulty with this conclusion is that the energy required to compress and supply high pressure and high mass flow rates of air are substantial, and can overwhelm the gains illustrated in Figure 2 and Figure 3. Thus, the power demand characteristics of the compressor must also be included in the system optimization process.

Air Supply Characteristics

The more flexible of the two air supply options is the compressor, since it can be operated at both varying air pressures and varying air flow. This allows an investigation of the system optimization that is available over the full range from high pressure and high SRa to low pressure and low SRa.

There are many different types of compressors that are being investigated for use in fuel cell vehicles and each has different operating characteristics. Since the purpose of this paper is to present the principle of fuel cell system optimization, the most flexible compressor technology was chosen to demonstrate the trade-off that is available. This is the Vairex variable displacement compressor, a piston compressor that allows relatively independent alterations in the output pressure and mass flow rates.

For the fuel cell vehicle application, air supply system characteristics are best described in terms of the relationship between power demand and mass flow rate at various pressure ratios. Figure 4 presents experimental data (normalized) for the Vairex compressor. The trend towards increasing power requirements with increasing pressure and mass flow indicates that the apparent improvements in performance for the fuel cell stack may not be realized in a system.

At any particular pressure ratio, we can look at the effect of increasing mass flow. It can be seen that small increases from a low level will likely be beneficial to the fuel cell stack – since the power demand does not rise that steeply. But for an increase in air mass flow at higher SRa, the benefits are likely to disappear as the slope of the power curve rises significantly. Although it is difficult to see in Figure 4, the compression power demand increases more sharply with increasing pressure at any specific mass flow rate. This suggests that there may be a point of optimization for the net power from the fuel cell system through a combination of both air pressure and air flow control.

Integrated System Characteristics and Optimization

To begin investigating the interaction between the compressor and the fuel cell stack, a simple case can be investigated based on operation at a single pressure and SRa. Typically, the idealized operation of a fuel cell stack is explained using a single polarization plot at high pressure and high air side stoichiometric ratios, as shown in Figure 5. This figure illustrates that both high stack voltages and high currents can be attained by using both high pressure and high air stoichiometry.

Another context for viewing the performance of a fuel cell stack (that is particularly useful for automotive applications) is the efficiency versus net power plot. Figure 6 illustrates this format for the same conditions as Figure 5. In Figure 6 it can be seen that the fuel cell stack operates at gross efficiencies on the order of 60 to 70 percent over the most of its power range.

However, Figure 6 also indicates that if the power required for high pressure and high air flow is subtracted from the gross stack power, then the operating characteristics of the fuel cell system are not as favorable. In fact both the net efficiency and the net peak power are significantly reduced for these operating conditions. Of course the net efficiency and net power characteristics are the actual determinants of the fuel cell system performance. The critical question is whether the net efficiency and net power characteristics of the fuel cell system can be optimized by operating the fuel cell stack at varying air pressure and/or air stoichiometry.

Varying the air pressure alone corresponds to the polarization plots in Figure 2, where SRa is kept constant and the pressure is varied. Figure 7 shows the impact on net stack efficiency for operation at a SRa of 2.5 with pressure varying from 1.1 to 3.25 atmospheres (assuming a compressor inlet pressure of 1.0 atm). In the low power region the most efficient operation is found at the lower pressures, where the compressor energy requirements are relatively low and very little benefit is achieved in the fuel cell stack from increased pressure. As the pressure increases, higher and higher powers can be maintained at higher efficiency until the extra energy required to compress the air outweighs the benefit of going to a higher stack operating pressure, shown in Figure 7 as occurring between 2.5 atm and 3.25 atm. It can also be seen that the benefit to going from a pressure of 1.5 atm to 2.5 atm is not very large, an increase in net peak power of only about 1 kW.

The location of this crossover point, where additional compression no longer benefits the net characteristics of the fuel cell system, is highly dependent on the SRa. Figure 8 represents a similar case as Figure 7, but at a lower SRa. When the SRa is fixed at 1.5, the increase in pressure from 1.5 to 2.5 atm results in a net peak power increase of over 2 kW, or about eight percent of the net power available at 1.5 atm, and twice the increase as when SRa was 2.5. The increased pressure crossover point is still between 2.5

and 3.25 atm, but in this case it is further from 2.5 than before. Thus, at lower SRa, the stack performance is more sensitive to variations in pressure.

Similar shifts in the stack characteristics can be observed when the pressure is held constant and the air stoichiometric ratio is varied. Figure 9 shows an increase in peak net power with increasing SRa that is similar to that observed for increasing pressures. However, there is not the same increase in stack operating efficiency at lower power (Note: The power scale has been altered in Figure 9 to allow the details at high power to be more visible). This trend is a result of the fact that at these low currents, the air side stoichiometric ratio does not impact the partial pressure of oxygen at the cathode catalyst layer as directly as total pressure does. Under the conditions in Figure 9, the SRa crossover point seems to occur somewhere between 2.5 and 3.0, but closer to a SRa of 2.5. When operating at a lower pressure (not shown), this crossover point shifts out closer to 3.0, indicating that at lower pressures, the stack performance is more sensitive to variations in SRa.

All of this information can be brought together to develop an optimization process for the fuel cell stack and the air supply. In general, it has been shown that low air pressure operation is the best way to improve net system efficiency at low net powers. Further, it was shown that increasing SRa does not have a significant impact on stack efficiency at low powers. Therefore the most efficient low power operation of the fuel cell system will be at low pressure and low SRa.

In the higher power regions, it was shown that both an increased pressure and an increased SRa will improve peak net power achievable in the fuel cell system. Thus, the two should be increased together to achieve the maximum possible benefits. This improvement is eventually terminated by increased power demand for the compression process.

The application of this combination of pressure and flow control is illustrated in Figure 10, where the pressure and flow are both varied depending on the net power drawn from the system. The optimal operating curve for the fuel cell system is the envelope of the curves shown. This can be translated into an optimal operation strategy that achieves high efficiency at low power and also provides a high peak power capability.

This optimal operating strategy can be compared with the high pressure and high SRa operating strategy presented in Figure 6. Figure 11 indicates that the optimal control strategy achieves the same peak net power as that for fixed pressure and SRa, but shows significant efficiency improvement in the low power regions. The peak efficiency is increased by 6 percentage points, for a 15 percent overall improvement in peak efficiency. Further, this increase occurs in the lower power regions where the fuel cell would be expected to operate during normal driving. The efficiencies still do not reach the gross efficiencies as would be expected from compressor energy requirements.

ADDITIONAL CONSIDERATIONS

There are a number of additional stack and compressor limitations that can influence the choice of the optimum operating strategy for a particular direct hydrogen fuel cell system. Examples are:

- Poor Cathode Catalyst Layer Performance: For example because of high resistance to protonic transport, or poor oxygen diffusivity, in the catalyst layer.
- Compressor Limitations: The inability of a particular compressor type or technology to cover the full range of pressure and flow required for the optimization process.
- Dynamic Response of the Air Supply: The inability of the air compressor to follow the required pressure and flow profile during rapid changes in power demand for a vehicle driving cycle.
- Expander Energy Recovery: The need for a relatively high stack air exhaust pressure for energy recovery.

Most of these issues are already incorporated in the model and future work will continue to expand the breadth of complications that can be analyzed. However, even if these effects are present, the system optimization will proceed in the same method as discussed above, only the quantitative details will differ.

Finally, if the optimization of a reformate fueled PEM system is considered, a similar optimization must be carried out for the reformate fuel supply and anode interaction. For reformate, the situation is more complicated because one must deal both with hydrogen dilution effects (analogous to the oxygen dilution in air), and with CO poisoning effects.

SUMMARY

The optimization procedure presented in this paper has been developed to account for the operation of a complete direct-hydrogen PEM fuel cell system. The focus is on the key limiting components, the fuel cell stack and the air supply. The fuel cell stack alone could be optimized by operation at high pressure and high-air side stoichiometric ratio, but in the system context, the power required for compression at low output power significantly reduces the efficiency advantage of the fuel cell system.

The combination of the operating characteristics of the fuel cell stack and air supply leads to an optimal operating strategy where low power operation is achieved using low pressure and low air-side stiochiometry. This allows the power associated with the air supply to be minimized, increasing the overall system efficiency at low power. Under high power conditions, both the pressure and air-side stiochiometry are increased, but limited to the point where diminishing returns set in due to increasing compressor power requirements and minimal stack performance improvements.

Overall, this paper shows that a direct-hydrogen fuel cell system can be optimized to achieve high peak power and high efficiency over a broad range of output powers. The key to achieving this in a practical system is the flexibility of the air supply to provide air at varying pressures and mass flow rates. A balance must be found between the performance characteristics of the stack and the air supply systems. Additional components and practical limitations will alter the results of the optimization process, but the fundamental procedure remains the same and can account for the additional issues.

ACKNOWLEDGMENTS

This work is supported by the Fuel Cell Vehicle Modeling Project at the University of California.

REFERENCES

1. R.M. Moore, D.J. Friedman, A.F. Burke, in *Proceedings of Commercializing FCVs '97,* Frankfurt, Germany, October 20-22, 1997.
2. T. A. Zawodzinski, S. Gottesfeld, *J. Electrochem. Soc.*, **138**, 2334 (1991).
3. T. E. Springer, M. S. Wilson, S. Gottesfeld, *J. Electrochem. Soc.*, **140**, 3513 (1993).
4. T. E. Springer, T.A. Zawodzinski, M. S. Wilson, S. Gottesfeld, *J. Electrochem. Soc.*, **143,** 587 (1996).

FIGURES

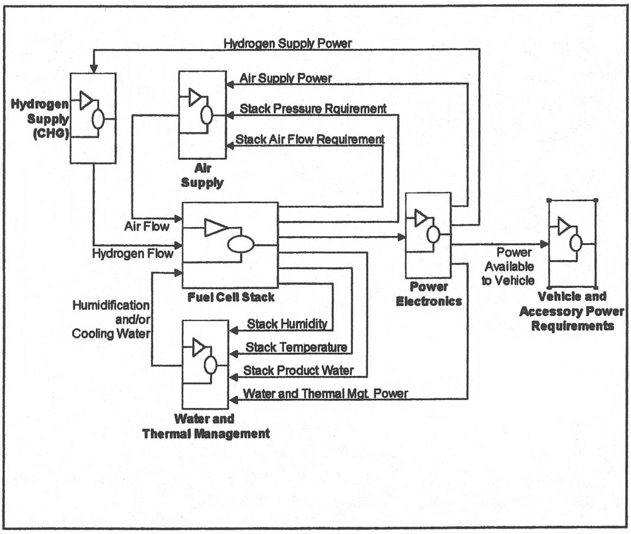

Figure 1. Simplified Schematic of an Automotive Fuel Cell System.

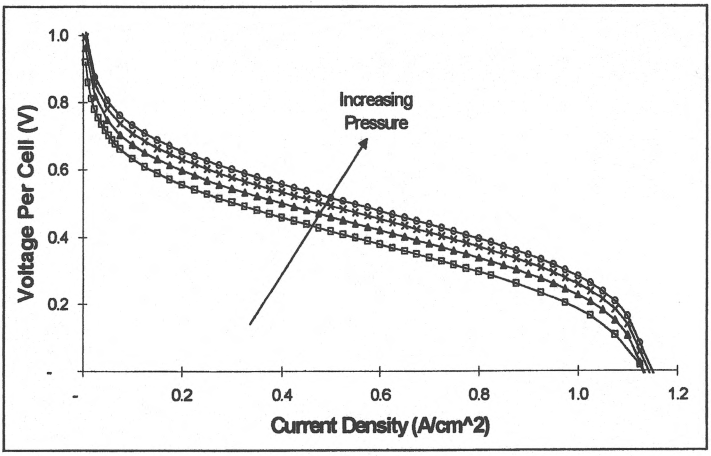

Figure 2. Polarization Plot for Varying Pressure.

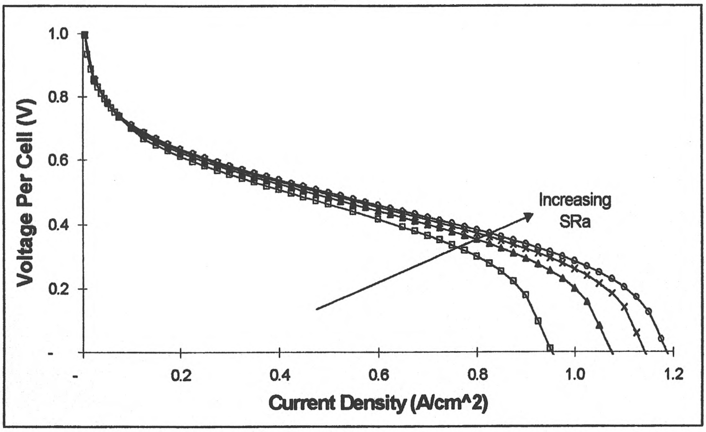

Figure 3. Polarization Plot for Varying Air Side Stoichiometric Ratio (SRa).

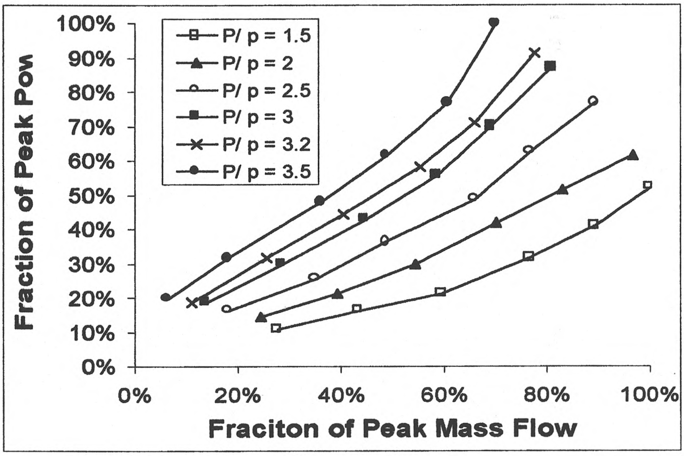

Figure 4. Power Characteristics of the Vairex Variable Displacement Piston Compressor. Source: Vairex Corporation.

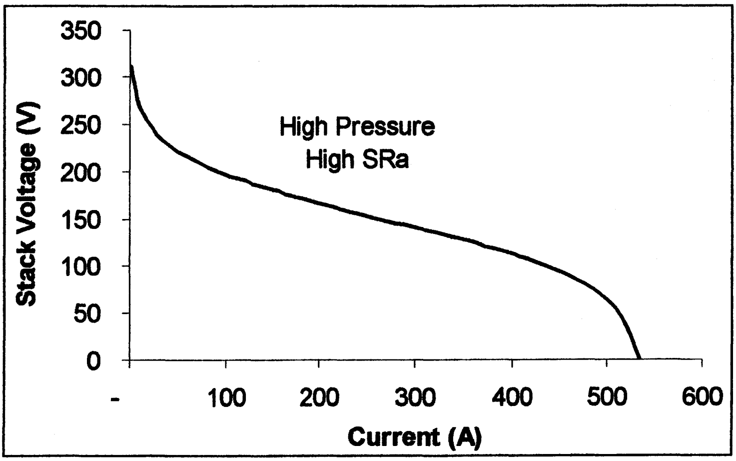

Figure 5. Polarization Plot for a Fuel Cell Operating at High Pressure and High SRa.

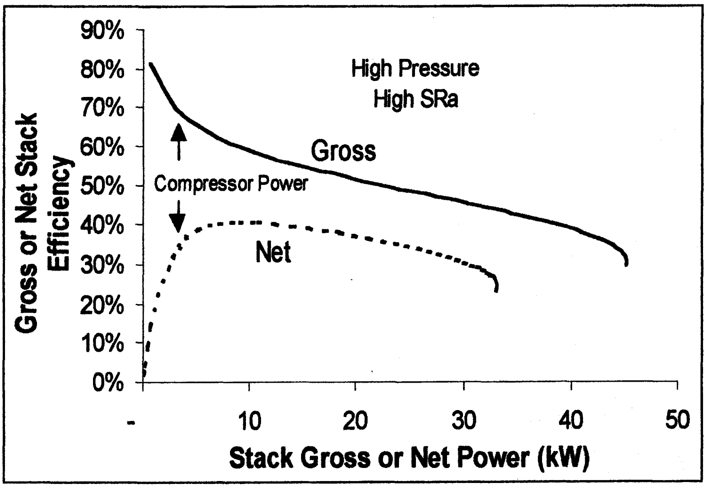

Figure 6. Efficiency Plot for a Fuel Cell Operating at High Pressure and High SRa.

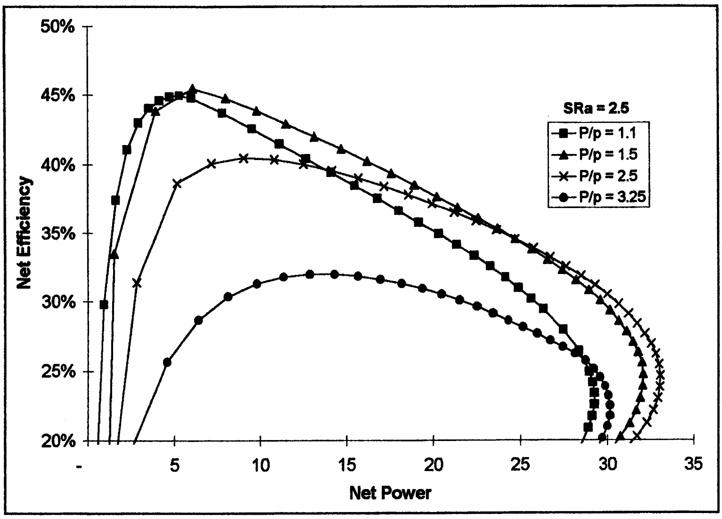

Figure 7. Net Efficiency Plot with SRa at 2.5 and Pressure Varying.

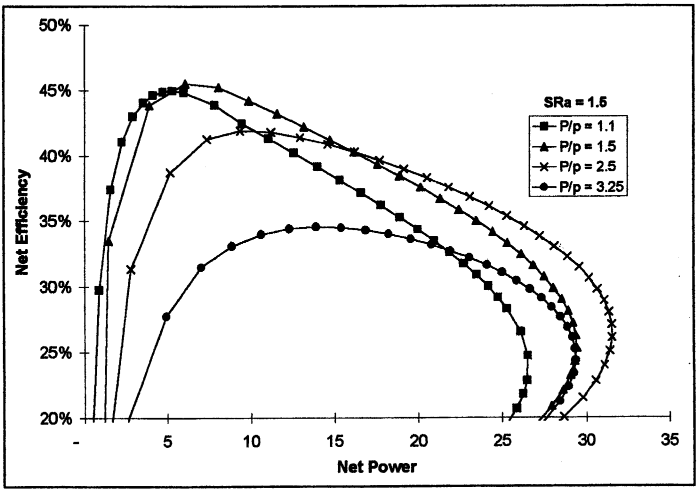

Figure 8. Net Efficiency Plot with SRa at 1.5 and Pressure Varying.

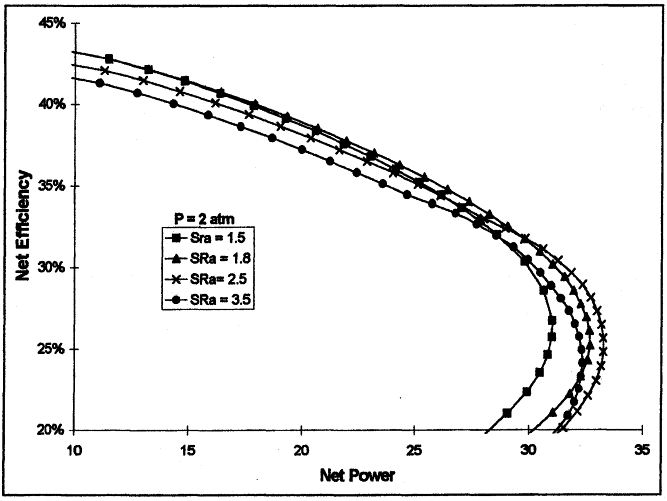

Figure 9. Net Efficiency Plot with P at 2 atm and SRa Varying.

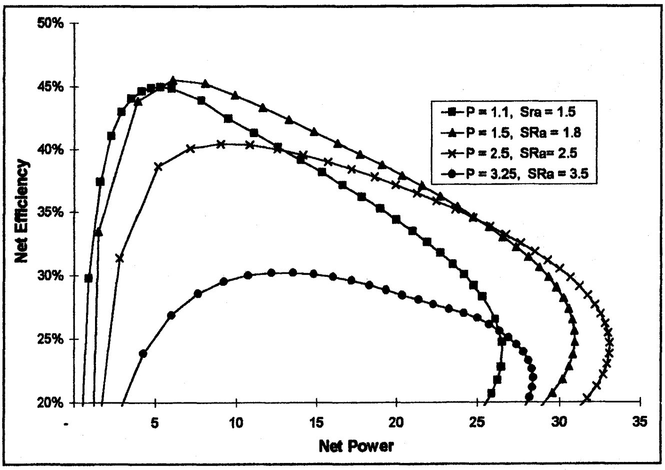

Figure 10. Optimized Net Efficiency Plot with Varying Pressure and SRa.

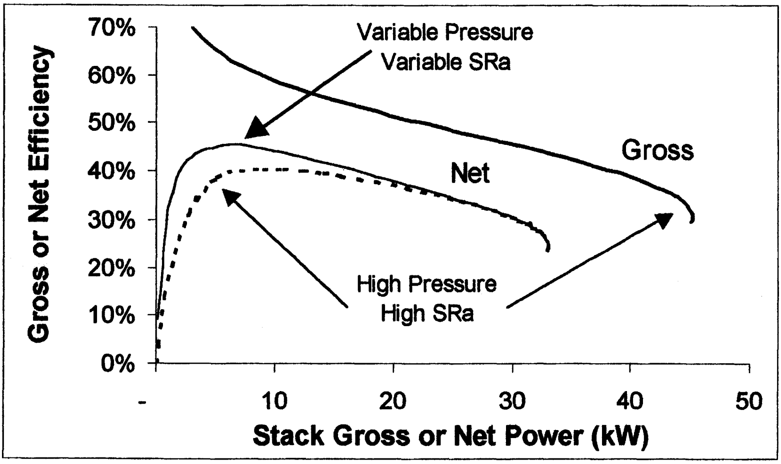

Figure 11. Comparison of Efficiencies Between the Optimized and Non-Optimized Systems.

Proton_Conducting_Membrane_Fuel_Cells_II, PV 1998-27, 424-434 (1998)
DOI: 10.1149/199827.0424PV © The Electrochemical Society

DIRECT LIQUID WATER HYDRATION OF FUEL CELL MEMBRANES

Mahlon S. Wilson, Christine Zawodzinski, and Shimshon Gottesfeld
Materials Science and Technology Division, MS D429
Los Alamos National Laboratory, Los Alamos, N. M. 87545

Direct liquid water hydration of polymer electrolyte fuel cell membranes improves cell performance and has system advantages over conventional reactant humidification schemes. The liquid hydration of the membrane is accomplished in our case by wicking water from a supply in the anode flow-field through the otherwise hydrophobic anode gas diffusion backing directly to the membrane/electrode assembly. The liquid water can be provided to the anode plenum either by injecting droplets into the hydrogen cell inlet or by integrating water channels into the anode flow-field. Conventional carbon-cloth gas diffusion backings are modified to provide the anode wicking backing by sewing in fine multifilament wicking threads using a conventional sewing machine. This simple scheme is demonstrated to provide improved performance and good stability.

INTRODUCTION

One of the primary challenges in attaining the optimal performance of polymer electrolyte fuel cells (PEFCs) is in attaining effective hydration of the ionomeric structure. Less than full hydration results in a decrease in the ionomer protonic conductivity. In addition, the kinetics of the oxygen reduction reaction (ORR) at the cathode are also adversely affected by a decrease in water content. Maintaining a high hydration level at all times throughout the membrane/electrode assembly (MEA) is difficult in fuel cells for a number of reasons. For example, at low current densities or at open circuit, when little liquid water is produced by the ORR, the MEA hydration level will tend to drop even when the reactant gases are at saturated water vapor conditions because the water uptake of perfluorosulfonate membranes is less when vapor-equilibrated as opposed to liquid-equilibrated (1). On the other hand, at higher current densities, the electro-osmotic drag of water with the protonic flux from the anode to the cathode tends to dry out the anode. An additional problem is that the cathode side also then tends to flood because of the ORR generated water as well as the water dragged across. In general, it is difficult to maintain optimum hydration levels under all operating conditions.

Certainly, the simplest PEFC system would be one where no auxiliary humidification system is required. In principle, the water produced in the ORR reaction is sufficient to maintain adequate hydration of the fuel cell under certain conditions (2). Relatively high fuel cell performances have been demonstrated at near ambient pressures with no external humidification using thin ionomeric membranes at fairly low cell temperatures of around 50°C (3, 4). Another approach uses catalysts and hydrophilic fillers within the membrane to generate and retain water generated by the recombination of the reactants (5, 6). While attractive, these self-humidifying approaches may have some operational limitations. For example, the combination of low current density (i.e., high voltage efficiency), typical operating temperatures (e.g., 80°C), and near ambient reactant pressures is of much practical interest but would be quite difficult to maintain sufficiently hydrated.

In most PEFC systems, water is provided to the polymer electrolyte membrane in the vapor form by humidification of the reactants. A general approach to simplify reactant humidification entails some means of introducing humidification plates within the individual cells. In one particular approach, International Fuel Cells (South Windsor, CT) uses water permeable bipolar plates to both recover liquid water from the cathode plenum (7) and directly humidify the anode and cathode flow-streams within the cells (8).

In most other humidified reactant technologies, the reactant gas streams are humidified before entering the cell using either heated sparger bottles or humidification modules. In some stacks, the gas streams are humidified by flowing the reactants through a humidity exchanger integrated into one end of the stack. Accommodating the exchanger tends to increase stack size and system complexity. Control of the stack is also complicated if the cells are humidified via the reactant streams because the two systems then become coupled. Often, the optimal hydration level may not match the most effective reactant flowrate, and it may be difficult, for example, to switch-off the cathode humidification if the cell starts to flood, or to increase the humidification level at low current densities as the cell starts to dry out as less water is produced by the ORR. As mentioned above, this lack of water is further exacerbated by the membrane's tendency to take up less water when only vapor-humidified. For such reasons, it is difficult to provide optimal (and not excessive) hydration over all current densities with a particular set-up.

In general, the best way of decoupling hydration from the other subsystems and assure a liquid-equilibrated hydration level of the membrane is to introduce liquid water directly to the MEA, as has been done previously both by wicking from the periphery of the electrode through the ionomeric membrane and by injecting water from the periphery through miniature tubes formed in the membrane. In the former case, Watanabe et al. introduced liquid water to the membrane from a supply reservoir around the periphery of the membrane (9). Since the standard perfluorosulfonate membranes do not wick water particularly well, a composite layer component was added to the anode side of a conventional perfluorosulfonate membrane that consisted of recast ionomer for ionic conductivity and a wicking material to facilitate the transport of the water through the x-y plane of the membrane. Performance improvements over reactant humidification were demonstrated in small cells. In the other liquid hydration approach, researchers at Lynntech, Inc. formed miniature channels in perfluoroionomer membranes and injected water from the edge through the tubes thus formed (10, 11). In these configurations, it may be difficult to wick or pump the water a substantial distance, the membranes need to be relatively thick, and currently off-the-shelf membranes and MEAs can not be directly utilized. As a result, we are developing an approach to introduce liquid water directly through the anode gas diffusion backing from a water supply in the anode flow-field region. In this way, sufficient water should be readily available throughout the active area of a large cell.

EXPERIMENTAL

Anode Wicking Backing

The direct liquid hydration approach that we have adopted is a wicking configuration in which the liquid water is delivered to the MEA through the otherwise hydrophobic backing from a liquid water source in the anode plenum. In this manner, a near unlimited supply of water can be provided over the entire active area because there are no water transport limitations as in the case of the membrane serving as the water conduit. In order to convey the water from the anode plenum to the membrane, the concept utilizes a two-part hydrophilic/hydrophobic backing structure. The simplest means that we have found to realize the two-part structure is to use a wicking thread sewn through a conventional hydrophobic gas diffusion backing to supply the hydrophilic wicking component as is shown in the exploded cross-section depicted in Figure 1 (not to scale). A number of materials could conceivably be used for the backing such as fluorocarbon/carbon black treated carbon paper (12), but we prefer to use a carbon black/PTFE filled carbon cloth gas-diffusion electrode such as non-catalyzed ELAT, from E-TEK, Inc. (Natick, MA). With a serpentine thread pattern with each stitch about 2 mm long and the rows separated by about 2 to 3 mm, about forty segments of the thread convey water in the z-direction for each square centimeter of electrode area. The actual region that is in contact with wicking thread is even greater because of the portion of the stitches that overlie the backing on both sides. This allows take-up and delivery of the liquid water over a greater area. The liquid water could be supplied from droplets in the gas channels or from separate water-filled channels in the anode plate that could be arrayed in a number of configurations. At less than 80 μm in diameter, the wicking thread is readily impressed into the originally 350 μm thick backing. Upon compression of the cell during assembly, the backings deform sufficiently to close the needle holes and accommodate the wicks to provide good interfacial contacts of the various materials.

In principle, the wicking thread can be sewn into conventional, catalyzed gas diffusion carbon cloth electrodes that are then impregnated with ionomer and hot-pressed to the membrane (13), although thin-film catalyzed membranes (or MEAs) are used in the experiments described here (14). As such, the platinum catalyst loadings of the membranes are in the neighborhood of 0.12 mg Pt/cm^2/electrode. While loadings as low as 0.03 mg Pt/cm^2 are shown to be effective on the anode side, MEAs with symmetrical loadings are used in this case. If a catalyzed membrane or MEA is used, as here, the water supplied from the anode wick must traverse the catalyst layer to access the membrane. Even though the thin-film catalyst layers are not particularly hydrophilic structures, no special effort has been made to modify the anode catalyst structure for interfacing with the wicking backing.

The first cells used for comparing the anode wicking technique to conventional reactant humidification both used standard E-TEK gas-diffusion backings in conventional hardware. The only difference between the baseline comparison cells and the anode wicking cells is that wicking thread is sewn into the anode backing. The wick material we used is a 200 m/g continuous multifilament polyester thread that is less than 80 μm in diameter available as U151 from Güntermann of America. The wicking backing is used only on the anode side because of the tendency of this side to dry out and the preponderance of water at the cathode side (due to the ORR) at higher current densities.

A membrane/electrode/gasket (MEG) assembly was used in the comparison cells that prevents condensate from contacting the membrane around the periphery of the electrode. If the MEG is not used, a certain amount of direct liquid hydration is achieved from the periphery in the small (5 cm^2) laboratory cells. The use of the MEG thus provides a more relevant comparison between the humidification techniques and the direct water injection is found to have a much clearer advantage over the humidified reactants than in comparisons without the MEG assemblies.

RESULTS AND DISCUSSION

5 cm^2 Cells Operated with Water Injection

In the initial 5 cm^2 cell experiments, the water for the anode wicking backing was provided by injecting a droplet of water each second into the anode reactant inlet of the cell at a rather generous 1.5 ml/min. The water droplets were carried by the hydrogen flow through the conventional 5 cm^2 active area single-channel serpentine flow-field to provide contact with the anode wicking thread over the active area. No external humidification of the reactants was used with the water injection. Humidifier bottles, heated above cell temperature, were used for reactant humidification on the conventional comparison cells.

Figure 2 depicts polarization curves for two Nafion 115 membrane (DuPont) based fuel cells; one configured with an anode wicking backing using water injection and the other a standard cell with conventional reactant humidification. The cell with the wicking backing outperforms the conventional cell over the entire current density range even though the latter is using relatively aggressive humidification conditions (anode and cathode humidifiers at 110 and 90°C, respectively). Not only is the performance higher at the low current densities where it might be expected that the enhanced hydration conditions improves the ORR, but it is also greater at the higher ranges where the relatively dry cathode gases probably improve the mass transport situation within the cathode backing and flow-field.

The most dramatic difference in the two humidification techniques is shown in Figure 3, which depicts the high frequency (8 kHz) cell resistances for the two cells in Figure 2. As commonly observed, the resistance of the conventionally humidified cell is much greater at the higher current densities where the anode side of the MEA tends to dry out due to the electro-osmotic drag of water away from this side. The use of a relatively thick membrane such as Nafion 115 amplifies this effect compared to higher performance membranes which tend to allow a more effective back-diffusion of water. The run with water injection shows much more constant, and ultimately much lower, cell resistances. It appears that the droplets of injected water are contacting the plenum side of the wicking thread, where it is carried across the backing to supply the membrane directly with liquid water.

One of the difficulties with the off-the-shelf polyester thread used above was that it lost hydrophilicity with time in the cell. When examined afterwards under the microscope, the thread fibers appeared intact, as no damage or degradation was apparent. In all likelihood, the surface of the inherently hydrophobic polyester annealed, resulting in a loss of whatever surface functionality provided its original hydrophilic nature. The hydrophilicity of the polyester thread can be maintained by first passing the thread through 5% Nafion solution (Solution Technology, Inc., Mendenhall, PA). While Nafion is chosen for its chemical stability, other approaches, such as using other types of threads (e.g. cotton/polyester blends, rayon, etc.) or other coatings can result in more hydrophilic surfaces with greater wicking capacities. However, the products that are available and strong enough to provide very thin threads are limited and also would need to be tested for their long-term stabilities.

Additional cells were prepared using anode wicking backings with the Nafion solution treated threads. The 500 h life test performance of one such cell operated continuously at 0.5 V using a higher performance, developmental membrane from Dow is shown in Figure 4. Initially, the cell was operated using aggressive anode humidification (the use of humidifier temperatures substantially higher than cell temperatures delivers considerable amounts of condensate to the cell) which was sufficient to maintain good hydration with the wicking backing. Direct water injection at 0.37 ml/min was eventually started at about 175 h whereupon the cell resistance, shown in Figure 5, did drop slightly. Less water injection appeared to be necessary to assure hydration using the higher performance membranes. After about 500 h, the life test was terminated due to difficulties with the hydrogen supply. As seen in Figure 4, a slight loss in current density was observed over the 500 hours. However, it was probably not due to cell humidification as Figure 5 demonstrates that the high frequency cell resistance only improved over this time, so the membrane appears to have been well hydrated throughout the run.

Carbon monoxide levels as low as 10 ppm in the hydrogen supply can have a detrimental effect on fuel cell performance because of CO's tendency to occupy the catalytically active sites at the anode. One strategy for improving the anode tolerance to CO is to increase the cell operating temperature considerably higher than the typical 80° C, whereupon the CO sticking coefficient (and surface coverage) is decreased, which frees up sites for the desired hydrogen oxidation reaction. With reactant humidification, however, the membrane tends to operate drier at elevated temperatures and the cell resistances are thus higher and the membrane more susceptible to failure. The performance obtained with a cell using the anode wicking backing and a developmental Dow membrane operating with direct water injection at 115° C is close to that of cells operating at 80° C, and the cell resistance remains likewise similar to the 80° C case (i.e., the roughly 0.08 Ω cm^2 as depicted in Figure 5), a result not normally attained with vapor-humidified cells at these higher cell temperatures.

Cells with Hydrogen / Water Anode Flow-Fields

The water injection experiments demonstrate the concept of providing direct liquid hydration of the membrane using a "hydrophilic/phobic" anode wicking backing. While the water injection technique might be viable in some situations, it would be difficult to implement in a stack and still assure uniform water distribution to each cell. The inability to do so would eventually lead to some cells becoming flooded and others drying out. Even within the individual cells, we assure a uniform distribution of water within the 5 cm^2 cells using water injection by the use of a single-channel serpentine flow-field. The use of multi-path flow-fields that are suitable for large active areas would invariably result in a poor distribution of the water droplets.

The general approach we then pursued for supplying a stable reservoir of water for anode wicking was to provide separate channels for the liquid water and for the anode gases, which can be done a number of different ways. Initially, sets of channels were formed into both sides of a thick, porous, electronically conductive carbon paper (Spectracarb from Spectracorp, Ltd., Lawrence, MA). The structure thus formed was somewhat similar to the porous channeled flow-fields used by IFC (8). The anode gases (i.e., hydrogen) and liquid water were manifolded to the opposing faces of the channeled paper, and the porous material was rendered either hydrophilic (if the water channels were on the current collector side) or hydrophobic (if the water channels were against the wicking backing). As such, the water was supplied to the anode wicking threads either through the hydrophilic paper flow-field ribs in the first case or through the water channels against the face of the wicking backing in the latter (where the hydrogen then accesses the electrode via the hydrophobic porous ribs). The former configuration tended to collect water in the hydrogen channels, which led to erratic performance whereas the hydrophobic paper configuration provided results that were basically similar to those depicted for the anode wicking backing in Figures 2 and 3. For the former to have worked stably, it would probably have been necessary to control the paper pore size and the water/hydrogen pressure differential, as done by IFC in their scheme, to keep the two separated.

In any case, the two H_2/H_2O flow-field configurations described above resulted in awkward manifolding configurations and required a separate porous element in addition to the impermeable graphite composite component of the "bipolar" plate. A much simpler configuration that eliminates the porous element is to manifold separate hydrogen and liquid water channels within a conventional flow-field configuration. This also decreases the amount of space required for the anode flow structure, which decreases the pitch of the unit cell and increases the power density of the stack. Because it is difficult to provide the necessary channels on a 5 cm^2 scale and a demonstration using a larger active area was of interest, a graphite composite plate for a 50 cm^2 active area was machined with an H_2/H_2O anode flow-field that accommodates both reactant gas and water flow-channels as shown in Figure 6. Here, three channels are formed in a conventional serpentine arrangement, however, the middle channel is manifolded to carry water and the outer two to carry reactant gas. Flanking the water channel on both sides with hydrogen channels prevents the water channel from doubling back on itself. As such, the furthest diffusion pathway for the hydrogen to access the MEA is through the backing across a flow-field rib and halfway across a water-filled channel, a distance of slightly more than a millimeter.

In contrast to the water injection approach, the 50 cm^2 cell has a separate water manifold. In operation, a separate recirculation loop is thus provided for the water as is shown in Figure 7. A small pump is used as before to inject water into the cell, albeit to the separate H_2O manifold rather than into the hydrogen inlet. A needle valve (or a second back pressure regulator) is used on the stack effluent side of the water loop in order to slightly pressurize the water stream compared to the hydrogen reactant gas. This discourages the hydrogen from infiltrating into the higher pressure water channel in order to assure that the water channel remains continuously filled with liquid throughout. The water and hydrogen effluents both pass though a common back-pressure regulator to maintain the pressure within the cell at 3 atm. The water is collected in a combination trap and reservoir for reintroduction within the cell. In a practical system, the trap would be at cell pressure to minimize the water pump head and facilitate the recycle of hydrogen.

The polarization curves for two Nafion 115 based 50 cm^2 active area cells are compared in Figure 8. One is a standard cell with conventional reactant humidification, the other utilizes the separate water channel in the anode flow-field described in conjunction with an anode wicking backing. More realistic operating conditions are used in the 50 cm^2 cell compared to the 5 cm^2. For example, the cathode pressures are considerably lower (3 instead of 5 atm) and the stoichiometric airflows are more carefully controlled (about 2 X at 1 A/cm^2 instead of 4 X or more). However, as in the case of the smaller cells (Figure 2), the scheme that delivers liquid water directly to the MEA in the 50 cm^2 comparison (Figure 8) outperforms the otherwise similar conventional cell over the entire current density range. With the continuously filled water channel, it was necessary to pump only about 3 ml/min into the special plate, and even less would have sufficed if a fair amount of the water had not wicked over the ribs separating the water from the hydrogen channels. This can in principle be alleviated by selectively introducing the plenum side of the wicking threads only in those areas overlying the water channels (the wicking on the membrane side can conceivably still span the hydrogen channels to supply the liquid water in these areas). As the sewing piece is currently positioned by hand, it is too difficult to attain the required accuracy. However, computer-controlled embroidery machines are available that could provide the desired wicking thread pattern (with accuracies close to 0.1 mm).

CONCLUSIONS

A very simple means is provided to maintain the polymer electrolyte membrane in direct contact with liquid water to assure optimal hydration over all types of conditions and current densities. It demonstrates effectiveness at higher operating temperatures and is probably beneficial under ambient pressure conditions. This approach results in a fuel cell hydration system that is low-cost, compact, simple, versatile (applicable to a variety of off-the-shelf membrane products and electrode technologies), and enhances performance.

Possibly more important than the increase in performance is the demonstration of a much simpler hydration approach from a system perspective. De-coupling the water and gas supply subsystems in principle simplifies the optimization of stack performance. Eliminating humidifier modules decreases system volume and improves response. This potentially low-cost, compact hydration system essentially requires only a pump and a water reservoir, which are required for most hydration schemes anyway. Conceivably, a stack system could be even further simplified by combining the stack cooling with the hydration system by pumping a sufficient amount of cooled water through the hydration channels in the anode plate to remove the excess heat generated by the fuel cell stack.

ACKNOWLEDGMENTS

This work was supported by the U. S. Department of Energy, Office of Advanced Automotive Technology.

REFERENCES

1. T. A. Zawodizinski, S. Gottesfeld, S. Shoichet and T. J. McCarthy, *J. Appl. Electrochem.*, **23**, 86 (1993).
2. D. M. Bernardi and M. W. Verbrugge, *J. Electrochem. Soc.*, **139**, 2477 (1992).
3. H. P. Dhar, *U. S. Patent No. 5 242 764*, Sept. 7 (1993).
4. H. P. Dhar, *U. S. Patent No. 5 318 863*, June 7 (1994).
5. M. Watanabe, H. Uchida, Y. Seki, M. Emori, and P. Stonehart *J. Electrochem. Soc.*, **143**, 3847 (1996).
6. M. Watanabe, H. Uchida and M. Emori, *J. Electrochem. Soc.*, **145**, 1137 (1998).
7. A. P. Meyer, G. W. Scheffler and P. R. Margiott, *U. S. Patent No. 5 503 944*, April 2 (1996)
8. C. Reiser, *U. S. Patent No. 5 700 595*, Dec. 23 (1997).
9. M. Watanabe, Y. Satoh and C. Shimura *J. Electrochem. Soc.*, **140**, 3190 (1993).
10. A. J. Cisar, A. Gonzalez-Martin, G. D. Hitchens and O. J. Murphy, *U. S. Patent No. 5 635 039*, June 3 (1997).
11. A. J. Cisar, A. Gonzalez-Martin and O. J. Murphy in *Proceedings of the 1st International Symposium on New Materials for Fuel Cell Systems*, O. Savadago, P. R. Roberge and T. N. Veziroglu, Eds., p. 104, Montreal, Canada, July 9-13, (1995).
12. R. D. Mussell, S. P. Webb, C. L. Scortichini and K. R. Plowman, *U. S. Patent No. 5 620 807*, April 15 (1997).

13. I. D. Raistrick, *U.S. Patent No. 4 876 115*, Oct. 24 (1989).
14. M. S. Wilson, J. A Valerio, and S. Gottesfeld, *Electrochim. Acta*, **40**, 355 (1995).

FIGURES

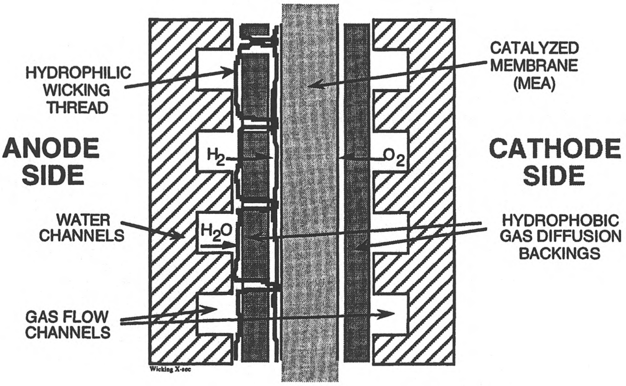

Figure 1. Cross-section of a fuel cell incorporating an anode wicking backing.

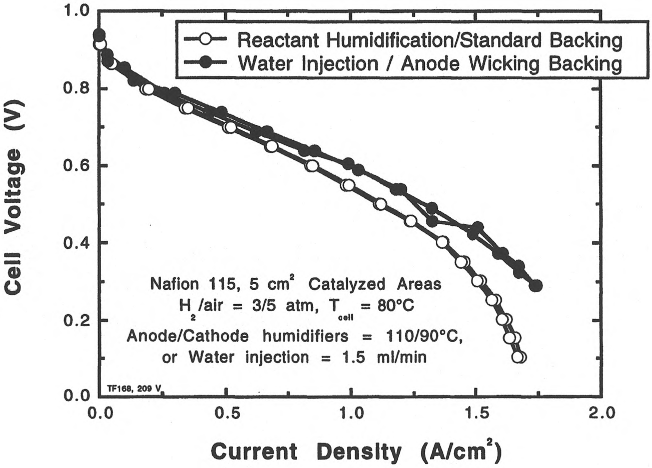

Figure 2. Polarization curves for 5 cm^2 Nafion 115 cells comparing the performance of humidified reactant and anode wicking backing hydration schemes.

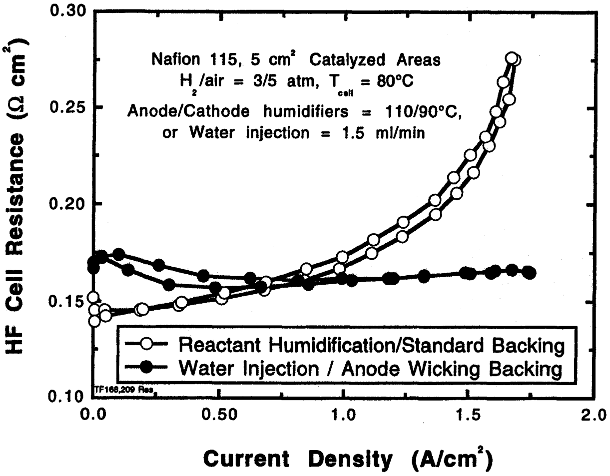

Figure 3. High frequency resistance curves for the cells portrayed in Figure 2.

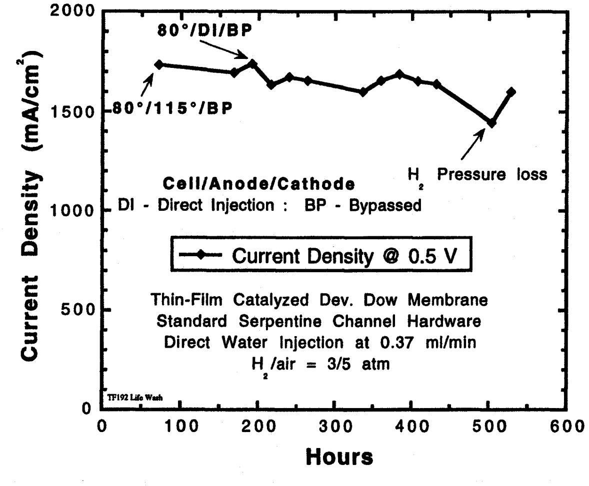

Figure 4. Current density of a 500 h life test for an anode wicking backing cell using developmental Dow membrane.

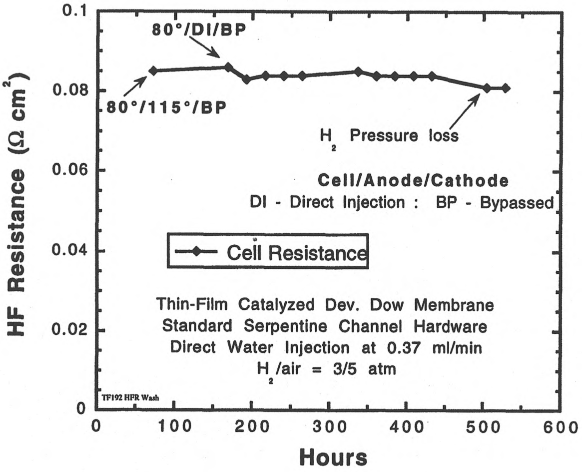

Figure 5. High frequency cell resistance for the life test of the cell shown in Figure 4.

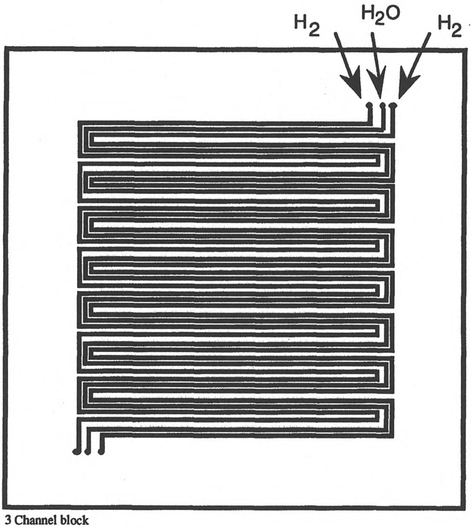

Figure 6. Anode block depicting the layout and manifolding of the serpentine H_2/H_2O flow-field channels.

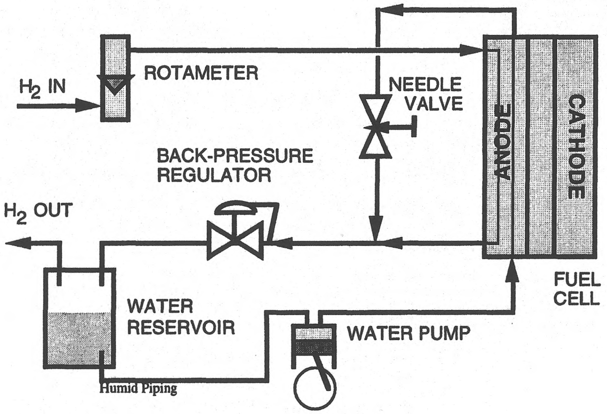

Figure 7. Schematic of the hydration and anode flow scheme for the 50 cm² cell using the H_2/H_2O anode flow-field.

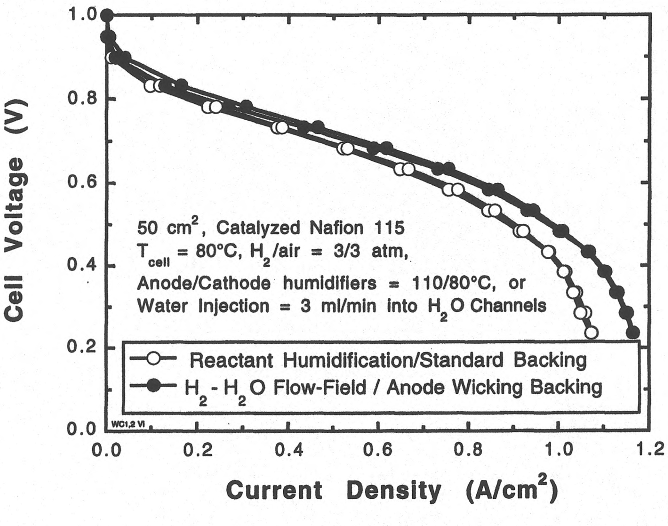

Figure 8. Polarization curves for 50 cm² Nafion 115 cells comparing the performance of humidified reactant and anode wicking backing hydration schemes.

Proton_Conducting_Membrane_Fuel_Cells_II, PV 1998-27, 435-445 (1998)
DOI: 10.1149/199827.0435PV © The Electrochemical Society

LOW-COST COMPOSITE BIPOLAR PLATES FOR PEFC STACKS

Deanna N. Busick and Mahlon S. Wilson
Materials Science and Technology Division
MS D429, Los Alamos National Laboratory
Los Alamos, NM 87545

ABSTRACT

With the current emphasis on more economical PEFC stacks, fuel cell developers are focusing on new technologies that offer high performance as well as low cost. One component whose cost can be considerably reduced is the bipolar plate. Besides meeting economic constraints, bipolar plates must satisfy a host of other requirements, including high electronic conductivity, low gas permeability, corrosion resistance, low weight, high strength, and manufacturability. To achieve this demanding combination of properties, we are developing new material formulations for composite bipolar plates. Commercially available, corrosion resistant thermosetting resins are combined with graphite powder to produce relatively inexpensive composite materials that satisfy current performance objectives. Traditional and non-traditional fiber reinforcements and other additives further improve the properties of the material without substantially increasing cost. Some significant advantages of these composites over existing bipolar plate materials are described, particularly in the critical areas of weight, cost, and ease of manufacture.

INTRODUCTION

Background

Polymer electrolyte fuel cells (PEFCs) are under widespread development to produce electrical power for a variety of stationary and transportation applications (1). To produce useful currents and voltages, individual fuel cells are connected in series to form stacks of cells. Adjacent cells in a stack are typically separated by bipolar plates, which serve as the anode for one fuel cell and the cathode for the adjacent cell. Thus the bipolar plate must function as a current collector as well as an impermeable barrier between the gases on either side of the plate. In addition, many stack designs incorporate gas flow channels into the bipolar plate. These flow fields ideally provide uniform distribution of reactant gases over the entire area of a catalyzed proton exchange membrane. Flow fields are commonly molded or machined into both sides of a bipolar plate, with an anode flow field on one side and a cathode flow field on the other side.

To date, the bipolar plate remains the most problematic and costly component of PEFC stacks (2). The most commonly used material for single cell testing is machined graphite, which is expensive and costly to machine. The brittle nature of graphite also prevents the use of thin components for reducing stack size and weight, which is particularly important for transportation applications. Other stack designs consider the use of metal hardware such as stainless steel (2-4). But a number of disadvantages are associated with stainless steel, including high density, high cost of machining, and possible corrosion in the fuel cell environment. In light of these difficulties, much of the recent work on fuel cell bipolar plate materials has been centered around graphite/polymer composites (5-8). Composite materials offer the potential advantages of lower cost, lower weight, and greater ease of manufacture over traditional graphite and metal plates. For instance, flow fields can be molded directly into these composites, thereby eliminating the machining or forming steps required for graphite or metal hardware.

Development of Novel Composite Bipolar Plates

Although polyethylene and polypropylene have also been used as matrices, most of the thermoplastic composite materials used in fuel cell bipolar plates are composed of graphite powder in poly(vinylidene fluoride) (PVDF), with or without short carbon fibers for reinforcement (5,6). Unfortunately, PVDF is relatively expensive, and any thermoplastic composite must be cooled before being removed from the mold. Thermosetting resins such as phenolics, epoxies, and polyesters generally offer shorter process cycle times than thermoplastics because, once cured, they can be removed from the mold while still hot. However, most of the documented methods of production of graphite/thermoset bipolar plates include difficult and costly steps such as extensive heat treatments and resin or metal coatings, and for phenolic resins in particular some concerns remain regarding porosity and corrosion issues (7-9).

Thus, the major challenge in developing a suitable composite bipolar plate material is to simultaneously meet cost, performance, and manufacturability objectives. To this end, the primary merit properties required of bipolar plate materials for PEFC stacks are listed in Table I.

Table I. Desired Attributes of Bipolar Plate Materials

Merit Property	*Target Value*
Good electrical conductivity	> 100 S/cm bulk and/or > 200 S/cm^2 areal
Low permeability	<< 1mA/cm^2 H_2 equivalent with $\Delta P = 2$ atm
Low production cost	< $10/kg including materials and processing
Good mechanical properties	Sufficient strength and elasticity to allow thin plates to tolerate assembly and stack conditions
Corrosion resistance	Chemical and physical stability during stack operation
Low weight	> 1 kW/kg for transportation; not as critical for stationary power

Existing composite bipolar plate technologies are adequate in most respects, but require major improvements in cost and ease of manufacture to become feasible for consumer applications. For both thermoplastic and thermoset matrix composites, compression molding is favored over injection or transfer molding due to the high solids content required to attain high electrical conductivity. High solids loading (> 50%) results in a thixotropic compound with poor rheology; injection molding of such a compound would be nearly impossible due to the exceedingly high pressures that would be required to achieve adequate fill in the mold.

If compression molding is used, cost-effective mass production appears to be more readily achievable with thermosets than with thermoplastics based on cycle time. One particular family of thermoset resins seems especially well-suited to bipolar plates; vinyl esters are methacrylated epoxy difunctional polyesters, and as such are often described as a cross between polyester and epoxy resins. These resins are highly corrosion resistant, lightweight, strong, tough, and commercially available at low cost, making them nearly ideal matrix material candidates for composite bipolar plates. Regardless of matrix material, the most widely used conductive filler in composite bipolar plates is graphite powder. It is employed in the vinyl ester composites described here as well, although the relationship between electrical conductivity and graphite volume fraction has been found to depend somewhat on particle size distribution. Thus we have identified a particular type of graphite powder that offers relatively high conductivity for a given volume fraction and is reasonably easy to combine with the liquid resin to form a homogeneous mixture. Graphite/vinyl ester composites are very promising candidates for bipolar plates, even with baseline formulations, but certain types of fiber reinforcement could offer even further advantages in mechanical properties.

Selection of Reinforcing Fibers

Composite materials, including bipolar plates, are often reinforced with fibers to provide additional strength. Traditional fiber reinforcements for structural composites include graphite, glass, Kevlar or metal. The fibers are typically used as-is but may have surface treatments designed to improve fiber-resin adhesion. "Sized" glass fibers, for example, possess functional groups at the surface that improve adhesion or provide chemical bonds to the resin. In general, these high-strength traditional fibers impart vastly improved mechanical properties in structural composites where long fibers or fabric rovings are used and the volume fractions of resin are typically quite high (e.g., 60% or more). In the case of electrically conductive composites for electrochemical applications, any fiber reinforcements that are used need to be relatively short to attain good fill, avoid hand lay-up, and provide a relatively homogenous structure. As a result, short "microfibers" (<1 mm) are utilized. On the other hand, the volume fractions of resin and fiber in the conductive composite must be considerably lower than in structural composites to accommodate sufficient graphite powder for conductivity. As such, it is difficult for a resin to sufficiently encapsulate or adhere to the fibers to effectively utilize their superior mechanical properties.

Improving the fiber/resin adhesion in such composites is required to adequately capitalize upon the fiber reinforcement. One approach is to use a fiber of similar nature as the resin such that a more compatible interface is obtained. Short polymer microfibers, commonly referred to as "flock", could conceivably provide enhanced fiber/resin interfaces and are readily available.

A novel method of improving the "adhesion" of the resin to the fiber is to utilize a porous microfiber that imbibes the resin such that the resin/fiber interface is effectively continuous. Porous, hollow fibers are widely utilized for separations, etc., but are not readily available on a microfiber scale. Activated carbon microfibers and porous ceramic whiskers are commonly available but adequate inclusion of the resin and cost are issues. We have found an alternative porous fiber for this purpose that is readily available and very low-cost. These fibers readily swell with resin and the cured structures thus formed effectively become micro-composite fibers that are integrally linked with the remainder of the resin matrix. At only 40,000 - 120,000 psi, these fibers do not have the tensile strength of graphite (520,000 psi) or glass (200,000 - 300,000 psi), but the direct link with the resin allows a more effective use of the fiber component.

EXPERIMENTAL

Material Components

The baseline composite material studied here comprises graphite powder encapsulated in a low-cost, corrosion resistant vinyl ester resin matrix. Catalysts and promoters/accelerators (in the present case methyl ethyl ketone peroxide and cobalt naphthenate) are added to the liquid resin solution to facilitate curing. Other liquid additives, such as antifoam agents and surface-functional additives, may be incorporated into the resin as desired to improve particle wet-out or composite surface tension. Synthetic graphite powder of a fairly narrow particle size distribution constitutes the major conductive component of the composite; other types of graphite or carbon powder may also be added to increase conductivity. Short (< 1 mm) fibers are often added to the material to provide reinforcement. These may include traditional fibers such as graphite and glass, or nontraditional, porous and/or polymeric fibers.

Composite Compounding and Molding

To prepare the molding compound for laboratory-scale samples, all liquid additives (accelerators, promoters, catalysts, surfactants, etc.) are thoroughly mixed into the resin solution with a hand mixer. The pre-blended solids (powders and/or fibers) are then gradually added to the formulated resin and the mixture is blended to form a stiff paste with a friable consistency. The mold is filled with a weighed charge of paste and pressed at ca. 100°C and 1000-2000 psi for 15 minutes. The hardened part is removed from the mold while hot and postcured in an 80-90°C oven, generally for 1-2 hours. Laboratory-scale molded parts take the form of either a 6 x 6 x 0.1 in. plaque or a 1 in. diameter disk (thickness dependent on charge).

Property Characterization

Various techniques are employed to measure the merit properties of these composite materials. Hydrogen gas permeability is measured using a filter-type permeation cell with an upstream H_2 pressure of 30 psig ($\Delta P_{hydrogen} = 2$ atm) in which the volume of water in a column displaced by hydrogen permeation is measured. Bulk electrical conductivity is measured with a linear 4-point probe; to eliminate offset errors, the slope of the V/I scan is used to calculate resistance. Resin cure characteristics are evaluated through differential scanning calorimetry (DSC) to investigate the effects of material composition and processing conditions on gel time, cure time, and cure rate. The surface tension of the molded material is characterized using measurements of water droplet contact angles. Mechanical properties are evaluated by using an Instron materials testing system to conduct tensile tests and 3-point-bend (flexural) tests. Corrosion resistance is assessed by measuring the weight loss of samples submerged in sulfuric acid solutions of varying pH at 80°C for 1000 hours. To examine reactant gas effects, the solutions were continuously sparged with either 6% hydrogen/argon or air.

RESULTS

Preliminary Results for Small Samples

Initial development of a baseline composition with the required values of conductivity, permeability, strength, and cure rate was performed using 1 in. diameter compression molded disks. Cure profiles generated using DSC showed that, for the same catalyst concentration, raising the cure temperature from 100°C to 110°C effectively cuts cure time in half. Cure profiles for neat resin and a resin/47 wt% graphite mixture were nearly identical, providing no evidence of any effect of graphite on cure time. Hydrogen permeabilities of disks containing 40-75 wt% graphite were below the detection threshold of the apparatus (ca. 0.01 mA/cm^2) and therefore well below the target maximum of 1 mA/cm^2.

Tests with small samples also revealed that the choice of graphite powder influences the conductivity of the molded disks. This effect appears to arise from differences in particle size and particle size distribution. 3-point bend tests were performed on samples containing about 40 wt% of the graphite which gave the best electrical conductivity for a given filler loading. Flexural strengths obtained from these tests ranged from 4200-4500 psi for samples with bulk conductivities of 50-120 S/cm. These results were quite promising in light of a target value of 4000 psi suggested elsewhere (9). The same graphite powder was incorporated into several subsequent samples to generate an empirical percolation curve, given in Figure 1. This curve shows that although a percolated conductive network is formed at less than 5 vol% graphite, 50-55 vol% (65-70 wt%) graphite is the threshold at which samples consistently have bulk conductivities greater than or equal to 100 S/cm. High resin content is desirable, since a continuous matrix lends structural integrity to the composite. With only 50-55 vol% graphite powder, short reinforcing fibers may be incorporated into the composite while maintaining a reasonably high resin content. Additionally, since flexural strengths for composites without fibers are already very close to a reasonable target value such as 4000 psi, a wise choice of reinforcement could provide sufficient improvements in strength at very low loading. Graphite and glass fibers are obvious candidates; porous and polymeric fibers are also strong possibilities. While graphite and glass fibers are not particularly susceptible to corrosion in a fuel cell environment, corrosion was a valid concern for the non-traditional fibers. Corrosion testing was performed on castings of both neat resin and resin containing a few wt% of either the porous or polymeric fibers. Samples containing fibers sustained slightly more weight loss than the neat resins, and the effect was more pronounced for the porous fibers than for the polymeric ones. Despite the measured weight loss, after 1000 hours no visible corrosion or pitting was present on the samples and the sulfuric acid solutions in which they were immersed remained clear. Therefore, it was suspected that a great deal of the weight loss could be attributed to escape of residual unreacted styrene from the resin, and that very little corrosion of the samples actually occurred. Additional corrosion and in-cell tests are planned to investigate this possibility.

Scale-up to Large Samples

To better address manufacturability issues, and to obtain standard-size mechanical test coupons, sample size was scaled up from 1 in. disks to 6 x 6 in. plates. Even though previous experience suggested that larger plates do not always reproduce the properties of smaller samples, the compositions and processing conditions of large samples were developed based on information gained from the smaller samples. One particular type of graphite powder with a "tailored" particle size distribution was used for all of the large samples based on conductivity results for the smaller samples. Processing was similar to the small sample case, and 68 wt% graphite was selected as a baseline composition for the composite based on the percolation curve shown in Figure 1. For a 3 mm thick plate, a bulk conductivity of 60 S/cm corresponds to the target value of 200 S/cm^2 areal conductivity; plates containing 68% graphite consistently exhibited bulk conductivities of 60 S/cm or higher.

With 6 x 6 in. plates, it was possible to generate some basic comparisons between the graphite/vinyl ester composites and other composite bipolar plate materials. Some measured mechanical properties of an unreinforced vinyl ester composite containing 68% graphite and a commercially available graphite/thermoplastic composite are listed in Table II. As shown in the table, the graphite/vinyl ester material outperformed the commercial material in each category.

Table II. Baseline Mechanical Property Comparison

	Commerical Graphite/Thermoplastic Composite	LANL Graphite/Vinyl Ester Composite
Percent strain at break	0.24	0.34
Tensile strength (psi)	2800	3400
Flexural Strength (psi)	3000	4300

In-Cell Testing

As part of a collaboration, Plug Power, LLC, designed and successfully used a 4 x 4 x 0.375 in. tool to mold bipolar plates with and without integral flow fields. A set of these molded plates which had machined flow fields were demonstrated in fuel cells at Plug Power and performed nearly as well as machined graphite. A thinner, more conductive set of the 6 x 6 plates molded at LANL and described above were also tested at Plug Power after being cut and machined to their specifications. These plates exhibited improved performance comparable to current baseline bipolar plate materials. Polarization curves for these plates along with similar data for stainless steel are shown in Figure 2 for comparison.

Mechanical Properties with Fiber Reinforcement

In addition to making baseline comparisons using unreinforced formulations, another objective of producing and studying large plate samples was to investigate the effects of different fiber additives on composite mechanical properties. Four types of fibers were used to generate preliminary comparisons: graphite, sized glass, polymeric fibers, and porous fibers. The tensile and flexural strengths of these four fiber reinforced materials relative to an unreinforced sample are shown in Figure 3. The data are normalized to the unreinforced material since the results from this figure and Table II were obtained at two different facilities.

Electrical conductivities were reduced for most of the fiber reinforced plates, but this is primarily because graphite powder loading was reduced slightly to accommodate the fibers. The conductivity of the graphite fiber reinforced composite was surprisingly low since graphite fibers are electrically conductive, but this phenomenon has also occurred in small samples and in other composite systems. It was assumed that the conductivity of any one of these composites could be brought up to acceptable levels by sacrificing resin rather than graphite powder to incorporate the fibers, so the relative improvements in mechanical properties offered by the various fibers were the real focus of the comparison in Figure 3. Despite the sizing of the glass fibers and the chemical compatibility of the polymeric fiber with the matrix, neither of these two reinforcements offered significant improvements in composite strength. Both graphite and porous fibers offered substantial improvements in strength -- over 50% increases in flexure -- at only 5 wt% loading. The porous fibers offered the greatest improvement in both tensile strength and flexural strength, despite the fact that this fiber has only 10-20% of the tensile strength of the graphite fibers. Presumably, this is because adhesion and wetting between the resin and graphite fibers is relatively poor, while the resin actually penetrates the porous fibers, effectively creating a continuous interphase region. The strength improvements offered by this porous fiber coupled with its low cost (a fraction of the cost of graphite fibers) rendered it the most intriguing of the four candidates, provided that adequate electrical conductivity could be achieved.

To further examine the relationship between mechanical properties and electrical conductivity in composites containing the porous fibers, an additional group of plates containing the porous fiber was fabricated. These plates were of various compositions within the range of 2-6 wt% fibers and 64-71 wt% graphite. With the exception of two plates with very high resin content, all of the new group of porous fiber reinforced plates met or exceeded the target of 200 S/cm^2 when conductivity was normalized to plate thickness, and all exhibited improved flexural strength over unreinforced samples. The flexural strengths and conductivities of these plates are shown in Figure 4, where the flexural strength values have again been normalized to the unreinforced formulation of Figure 3 to account for different testing equipment. A more complete characterization of the mechanical properties and corrosion resistance of the porous fiber reinforced samples is planned.

Potential Benefits of Surface Property Additives

Depending upon the approach adopted by the stack designer, hydrophobic channel walls are often desirable for effective water transport and removal within the flow fields of the bipolar plate. Surface-functional additives may be added to the resin to enhance the surface properties of the composite. Certain fluorochemical intermediates tend to migrate to the surface of the molded part, such that additions to the resin of only a few volume percent can substantially lower the surface energy and discourage the accumulation of water in the channels. For a sample with 1.5% of a particular surface additive incorporated into the resin, water droplet contact angles increased by about 10° relative to an otherwise identical sample without the additive. These additives are expensive, however, so their relative merit continues to be evaluated.

Cost Analysis

Bulk material costs for composite bipolar plates can be readily estimated from the baseline composition, with allowances for any fiber reinforcements and/or additives that may be desired. For 1 kg of material, the projected costs are as follows:

Resin:	$ 1.25
Graphite powder:	$ 1.00
"Expensive" fiber reinforcements (e.g., graphite):	$ 0.75
"Inexpensive" fiber reinforcements (e.g., glass, polymeric, porous):	$ 0.10
Additives (e.g., catalysts, promoters):	$ 0.40
	$2.75-3.40/kg

With a target total cost of $10/kg, this leaves about two-thirds of the target cost available for processing. We are currently working with compounders and molders to develop efficient and cost-effective processing methods to meet this goal.

ONGOING EFFORTS

Although bipolar plates must be sufficiently physically robust to withstand stack assembly and operation, specific required values of strength parameters are difficult to quantify. Bipolar plates must be able to support clamping forces of hundreds of pounds per square inch. But the plates are often subjected to additional stresses during handling and assembly. While high strength is desirable, a certain amount of flexibility/elasticity is also required, for example, for plates to tolerate slight misalignment during assembly. As such, in addition to further mechanical testing of the composite materials, we plan to more fully examine the mechanical property requirements of the plates. Creep is less problematic with thermoset resins than with thermoplastics, but the long-term effects of elevated temperature on mechanical properties of these composites also deserves some investigation.

A better understanding of the use and relevance of surface property additives is required, and could possibly be accomplished with in-cell testing. In-cell testing is also needed for fiber reinforced plates, along with corrosion testing and post-corrosion mechanical testing.

In cooperation with compounders and molding houses, we anticipate improvements in mixing and cycle time. Additionally, we are exploring the possibilities of other vinyl ester resin and/or additive systems. Alternative resin systems may offer advantages in mechanical properties or corrosion resistance, while changes in additives may offer processing improvements. The catalyst system for the results described here produces molding compounds with a shelf life of a few hours; we are exploring different catalyst systems that offer shelf lives of several weeks while maintaining short cycle times. The effects of certain additives on the corrosion susceptibility of the composites also need to be evaluated. Some of these additives possibly contain metal/organic salts. Therefore, we need to ascertain if metal ions can leach out of the composite plate and promote corrosion or accumulate in the proton exchange membrane.

CONCLUSIONS

Using commercially available vinyl ester resins and "tailored" graphite powder, we have developed a composite material that appears to meet the property requirements for PEFC bipolar plates, including high conductivity, low permeability, low weight, low cost, corrosion resistance, high strength, and good flexibility. The performance of these plates in fuel cells is comparable to that of machined graphite or stainless steel. Incorporating low-cost porous microfibers into the material significantly improves its mechanical properties, and other additives show promise for enhancing surface properties. Bulk raw material costs remain at about $3/kg, and forthcoming improvements in processing should keep the total materials and manufacturing cost below the $10/kg target. Hence, this material possibly offers considerable advantages over other composite bipolar plate technologies not only in cost and processing, but in performance as well.

ACKNOWLEDGMENTS

This work was funded by the U.S. Department of Energy's Office of Advanced Automotive Technologies through the Propulsion System Materials Program. Plug Power, LLC, contributed significantly to this effort.

REFERENCES

1. S.J.C. Cleghorn, X. Ren, T.E. Springer, M.S. Wilson, C. Zawodzinski, T.A. Zawodzinski, and S. Gottesfeld, *Int. J. Hydrogen Energy*, 22, 1137 (1997).

2. R.L. Borup and N.E. Vanderborgh, in *Materials for Electrochemical Energy Storage and Conversion -- Batteries, Capacitors and Fuel Cells*, D.H. Doughty, B. Vyas, T. Takamura and J.R. Huff, Editors, PV 393, p. 151, *Materials Research Society Symposium Proceedings Series*, Pittsburgh, PA (1995).

3. K.B. Prater, *J. Power Sources*, 61, 105 (1996).

4. R. Hornung and G. Kappelt, *J. Power Sources*, 72, 20 (1998).

5. R.J. Lawrance, *U.S. Patent No. 4 214 969* (July 29, 1980).

6. E.N. Balko and R.J. Lawrance, *U.S. Patent No. 4 339 322* (July 13, 1982).

7. A. Pellegri and P.M. Spaziante, *U.S. Patent No. 4 197 178* (April 8, 1980).

8. D.A. Beckley, *U.S. Patent No. 4 265 727* (May 5, 1981).

9. R.C. Emanuelson, W.L. Luoma, and W.A. Taylor, *U.S. Patent No. 4 301 222* (November 17, 1981).

FIGURES

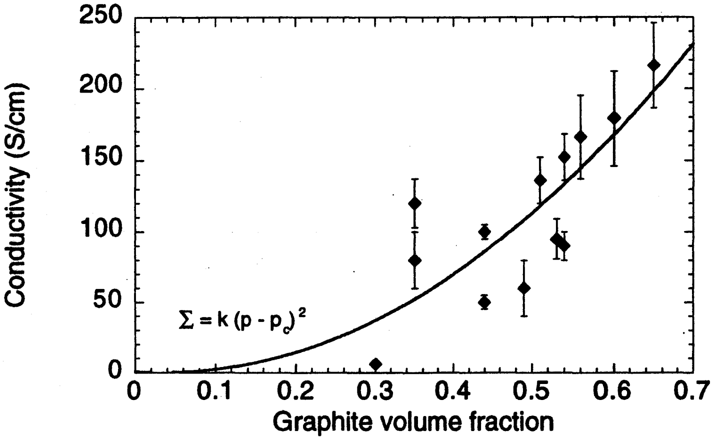

Figure 1. Empirical percolation curve for 1 in. diameter graphite/vinyl ester composites.

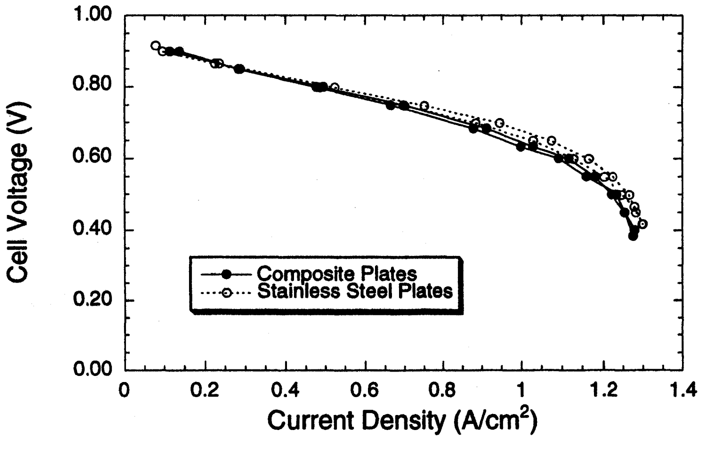

Figure 2. Polarization curves for composite and stainless steel bipolar plates. In-cell testing was performed as part of a collaboration with Plug Power, LLC.

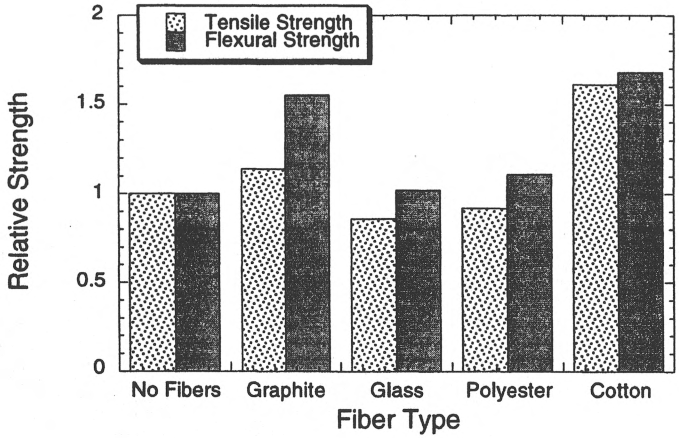

Figure 3. Effects of different types of fiber reinforcement on composite strength.

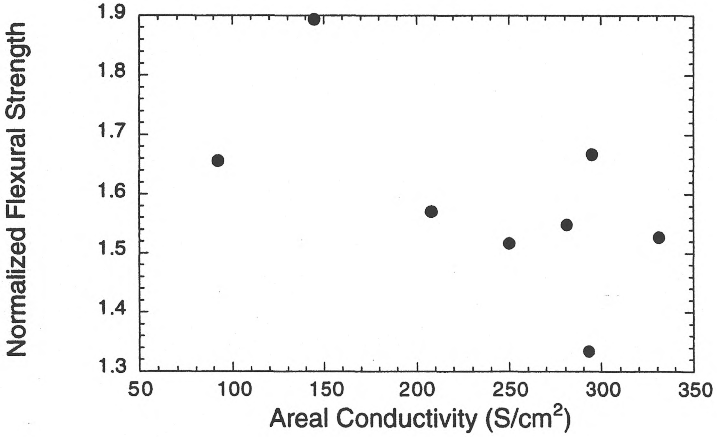

Figure 4. Flexural strength vs. conductivity for porous-fiber reinforced composites.

Proton_Conducting_Membrane_Fuel_Cells_II, PV 1998-27, 446-456 (1998)
DOI: 10.1149/199827.0446PV © The Electrochemical Society

METAL SCREEN AND FOIL HARDWARE FOR POLYMER ELECTROLYTE FUEL CELLS

Christine Zawodzinski, Mahlon S. Wilson
and Shimshon Gottesfeld
Materials Science and Technology Division, MS D429
Los Alamos National Laboratory, Los Alamos, NM 87545

Stainless steel wire mesh screens and foils are employed as bipolar/flow-field plates in polymer electrolyte fuel cells as a low-cost alternative to machined graphite or titanium plates. Hardware performance in 100 cm^2 single cells and small stacks as well as corrosion resistance of 316 stainless steel have been evaluated.

INTRODUCTION

Polymer electrolyte fuel cell (PEFC) technology has been attracting ever increasing attention as a potential means to provide near zero-emission electric vehicles as well as efficient home-based stationary power systems. Many industrial efforts are underway to commercialize PEFCs, however, widespread adaptation of the technology will strongly depend on reaching demanding cost goals.

A major contributor to the cost is the fuel cell hardware, which typically consists of intricately machined graphite or metal bipolar plates. The challenge with bipolar plates is in attaining low-cost, durable, highly conductive, corrosion resistant structures that provide an effective flow-field configuration. A conventional flow-field design consists of a number of channels machined into a plate, configured to provide uniform reactant distribution combined with effective water removal. Achieving an effective flow-field design often comes at the expense of high material and machining costs.

Historically, the most commonly used bipolar plate material, solid graphite, is conductive and corrosion resistant, but is expensive and relatively brittle. Titanium, considered a possible alternative, is extremely hard and can be treated (e.g. nitrided) to provide adequate conductivity and corrosion resistance, but is expensive and difficult to machine. A number of options are being considered to replace these materials, as well as provide an alternative to machining in an effort to lower costs. Two approaches along these lines are 1) the use of composites such as the commercially available Kynar^{TM}/graphite molded plates, and 2) relatively conventional flow-field/bipolar plate designs produced using metal fabrication techniques.

In the case of graphite composite plates, it has been difficult to attain adequate conductivity in combination with physical strength and flexibility to allow the use of thin unit cells. Ingredients such as Kynar that tend to promote a less brittle, tougher structure (as compared to solid graphite plates) also tend to decrease the plate's conductivity. Significant work is being done in this area to marry the two attributes into a low-cost effective formulation (1). Commercial fuel cells of the future will probably utilize both graphite/composite and metal bipolar plates depending on the particular application.

Metal hardware is attractive because it can provide thin, strong, flexible plates that are also very conductive. To date, metal hardware has been implemented in a variety of ways that range from simple applications such as a separator plate between graphite flow-fields (2) or as an intricate flow-field/bipolar plate consisting of several etched sheets of Ti bonded together to form a single unit (3). Flow-field/bipolar plates based on more conventional designs such as serpentine channel plates made of Ti and stainless steel have been demonstrated as well (4, 5). However, the high cost of machining or forming materials such as titanium or stainless steel has been a major obstacle to establishing an approach to inexpensive mass production. Additionally, long-term corrosion resistance is a problem that must be addressed for metal hardware to be utilized in commercial units.

Eventually, alternative fabrication techniques such as lithography or stamping may provide a low-cost means to produce metal bipolar plates. Yet a different option is to eliminate the need to machine or fabricate patterns into plates altogether. This is the approach we have taken at LANL through the use of inexpensive, off-the-shelf metal wire screens and foils (6). Metal screens were originally implemented in PEFCs to provide better water removal between a gas-diffusion backing and flow-field (7), and more recently, have been incorporated as reactant distributors within a metal bipolar plate/cooling structure (8). In our configuration, simple woven wire-mesh screens serve as flow-fields, which can be sandwiched together with a thin metal foil of the same material to create a flow-field/bipolar plate for use in a stack.

An immediate advantage of this design is the elimination of expensive machining costs, yet other benefits are gained as well. If a material that is readily available, such as stainless steel, is used, materials costs are also significantly reduced. Because the metal screens and foils are strong without being brittle, thin units can be utilized, resulting in a flow-field/bipolar plate that is relatively light-weight in comparison to thick graphite or solid metal plates, making it possible to increase stack power density with the same number of cells. Thus, if corrosion resistance can be attained, this type of hardware could provide the means to produce a low-cost, high performance PEFC stack. This paper will describe such hardware based on 316 stainless steel (SS) and its performance in fuel cell and corrosion tests.

EXPERIMENTAL

Wire Screen Flow-Field Design

In order to provide an effective flow-field, it is essential that the reactant and effluent flow through a simple screen flow-field be uniform. This was achieved using "corner-to-corner" flow across the screen. In this configuration, a wire-screen flow-field is oriented such that the wires of the weave are parallel to the edges of the screen, which is sealed around the periphery except for the opposing manifolded corners. Reactant flow is introduced to one corner and the effluent is discharged at the diagonally opposing corner. The flow pattern through the screen is defined by the nature of the mesh itself. For example, in the over-and-under weave of a simple square mesh wire screen, flow between the small box regions defined by the interwoven wires can only be between elements with common sides. The two wires stacked upon one another that define a corner of an element prevent flow between diagonal elements in the interweave sections. Thus, if one considers the simple schematic in Figure 1, the flow can only be in the (x) or (y) directions through the weaves of the screen. Two possible flow-paths are shown in the figure, path a) proceeds straight in the (-y) direction and then straight in the (+x) to the exit while closely passing by the distant lower-left corner. Path b) proceeds along the diagonal, but because of the x-y flow preference, the flow follows a staircase-like path. Once the total length of all the individual segments in the staircase are summed, the lengths of paths a) and b) are identical. Therefore, the flowrate along each path should be equivalent, and hence, the flow should be uniformly distributed throughout the entire flow-field; with no dead spots in the far corners as may be intuitively expected.

This flow configuration was confirmed experimentally by the use of a wire screen flow-field mock-up in a transparent plastic housing to observe the reactant flow distribution and water accumulation in a simulated cathode flow-field. Air was introduced at 3 atm pressure at a flowrate equivalent to 1 A/cm^2 at 50% oxygen utilization and humidified above the saturation point within the cell to replicate two-phase flow conditions. As the humidified air passed through the flow-field, water vapor would fog the cool surface of the Plexiglas housing. Condensed water droplets passing through the flow-field would wet the wall and clear the surface until it had a chance to fog again. It was thus possible to observe the condensed water streamlines, whose patterns demonstrated that the flow did follow a staircase path and was well distributed, even to the distant corners. Additionally, water removal was effective and there were minimal and only temporary accumulations within the flow-field.

Fuel Cell Design Based on 100 cm^2 Active Area with Metal Screen Flow-fields

One challenge to implementing the corner-to-corner flow scheme with wire screens was fixturing the screens within a cell while sealing the periphery. This was achieved through the use of a structure we call a "picture frame MEA". The assembly of this structure is illustrated in Figure 2. Two thin polysulfone frames (0.035" thick), which have been die-cut to form penetrations for the manifolds and the window for the active area of the cell, are adhered directly to the membrane/electrode assembly (MEA), hence the name. Channels cut into opposing manifold corners direct reactants from the manifold openings of the frames to the flow-fields, which sit inside the windows defined by the frames.

Besides fixturing the screens within the cell and providing a simple manifolding scheme, the picture frame structure provides other benefits. The finished product of an MEA encased within a rigid frame is easily handled and does not change dimensions, assuring proper alignment of the MEA within the cell and enhancing sealing. The picture frame assembly can be pretested to check the integrity of the MEA (e.g., no gas cross-over). Additionally, the rigidity of the structure serves to control compression within the cell, which is especially important in stack assembly. The MEAs used in these structures consist of catalyzed Nafion™ 112 (0.14 mg Pt/cm^2/electrode) (5) and ELAT carbon cloth backings (0.018" thick, E-TEK), which are cold-pressed to the membrane before final assembly.

A unit cell is then built around a picture frame MEA (Figure 3). Relatively coarse screens (24 x 24 mesh, 0.014" diameter wire) serve as the main gas flow-fields and directly contact the metal foil separator plates (0.010" thick). Originally, a fine mesh screen (60 x 60 mesh, 0.0075" diameter wire) was introduced between the flow-field screen and the carbon cloth backing to prevent the backing from "falling" into the open weave of the coarse screen, while still allowing reactant and water vapor to reach the MEA. If a relatively soft backing material is used without a barrier, it becomes deeply embedded into the coarse screen, resulting in relatively high pressure drops (0.4 atm/6 psi at an air flow rate of two times stoichiometric at 1 A/cm^2) and cell resistances (> 0.5 Ω-cm^2). With the fine screen in place, the pressure drops and cell resistances were significantly improved (0.13 atm/2 psi, 0.15 Ω-cm^2, respectively). However, the fine mesh screen collected water over time. The square openings formed by the tight weave acted as hydrophilic "cages", trapping water and decreasing reactant access to the MEA. It therefore became necessary to hydrophobize the fine screens prior to use to prevent water from collecting in the openings.

For simplicity (i.e., no pretreatment), thin, flattened expanded metal mesh and perforated plates were utilized in place of the fine screen. Perforated plates in particular appear to provide an advantage to fine screens in terms of water management within the cell. By design, a perforated plate can have larger "openings" and "islands" that more nearly replicate the configuration obtained with conventional channeled flow-fields and still provide adequate reactant access to the MEA, protect the backing from blocking the coarse screen, and yet be very thin. Because a thin perforated plate with large openings does not tend to trap water, it is not necessary to hydrophobize the structure. We have employed 0.005" thick acid-etched perforated plates made of 316 SS that have 0.040" penetrations on a 0.060" stagger.

The unit cell is approximately 3 mm thick, providing for a thin, compact design in which the active area comprises 59% of the total area encompassed by the metal foils and frames. Because the individual cell components are adhered together between metal foil plates, the resulting structure is a one-piece unit that we refer to as a "cartridge". A cartridge can contain one or several cells sharing separator plates as well as cooling plates. However, there are advantages to retaining the cooling plate as a separate structure. Cooling plates are provided by sandwiching two cartridges around a cooling plate flow-field (Figure 4). Our cartridges typically contain two cells each, thus, except for the cells against the current collector plates, each cell will be adjacent a cooling plate in this configuration. As with the reactant flows, a channel is formed in the frame to connect the manifold to the coolant flow-field. This flow-field may be a wire screen or a serpentine channel cut into a compressible, electronically conductive material such as graphite gaskets (e.g. Grafoil from Union Carbide).

100 cm^2 Single Cell and Stack Testing

Single cells and 2 - 4 cell stacks based on a 100 cm^2 active area were assembled as described above. The cell cartridges (and cooling plates when used) were fixtured between gold-coated copper current collector plates, which in turn were placed between and electrically isolated from manifolded, iridized aluminum endplates. All of the metal hardware components were made of 316 SS, which was not pretreated except for degreasing to remove surface oils and residues. In general, testing was conducted at constant voltage (0.5 V for single cells, equivalent voltages for stacks) with the cell temperature maintained at 80°C. The pressures, flowrates and humidification temperatures for hydrogen and air were, respectively: 3/3 atm, 2x/2x stoich flow at 1 A/cm^2, 105/80°C. With single cells, it was possible to operate continuously and one life test of 2000 hours was completed. The stacks, however, were operated only during working hours for safety reasons.

Corrosion Testing

To assess the corrosion resistance of 316 SS, two types of tests were conducted. These tests were designed to subject the metal for limited periods to much harsher environments than exist in a typical fuel cell environment. The first test, long-term immersion of foil samples, involved submerging pieces of 316 SS (1 in^2, 0.002" thick) in sulfuric acid solutions of various pH values, maintained at 80°C and continuously sparged with either H_2 or air for 250 - 500 hours. At the end of the test period, corrosion rates were determined based on gravimetric measurements and the solutions were analyzed by ICP-MS and ICP-ES for metal ions such as Mo and Cr. The second type of corrosion test involved assembling a fuel cell with the metal hardware in direct contact with uncatalyzed Nafion 112 (no backings were used), supplying it with hydrogen and air, and holding it at open-circuit voltage (0.94 V) for approximately 120 hours. The membrane was intentionally left uncatalyzed to maximize stainless steel to membrane contact and was analyzed by EDAX and XRF for corrosion products. Parts of the metal hardware were analyzed by EDAX as well.

RESULTS / DISCUSSION

Corner-to-Corner Flow-field Design / Thin Fuel Cell Cartridges

Based on the results of the mock-up flow-field studies and testing in fuel cells, the corner-to-corner flow-field design appears to provide effective reactant and effluent distribution throughout the area of the screen. This design offers an advantage in that the shape of the flow-field is not limited to a square; rectangular meshes will also provide equidistant flow-paths with corner-to-corner flow. Another, more subtle advantage may lie in the nature of the flow dynamics. With corner-to-corner flow in the wire-screen, the relative space velocity of the reactants is probably much greater at the entrance and exit. When operating the cathode on air (or the anode on a dilute hydrogen stream), this may increase the uniformity of the current distribution over the electrode compared to a more conventional set-up with a relatively constant space velocity in all areas. Additionally, the design allows for a simple manifold to flow-field transition. Since the two different sets of opposing corners can be used for the anode and cathode reactant flows, a simple channel connecting a manifold penetration to each corner is all that is necessary. Large distribution channels, as typically used with numerous small, parallel channels or with "porous" flow-fields, are not required, which simplifies the configuration and allows more of the footprint to be active electrode area.

Along with simpler manifolding, the overall metal hardware design allows for thin unit cells to be produced. In a conventional fuel cell, the bipolar plate is generally a thick one-piece structure that serves multiple functions as the gas flow-field, separator plate, and even as a means to cool the cell (8). Separating these functions, particularly with respect to cooling the cell, allows each component to be optimized for its own specific function. Thus, thin screens can serve as flow-fields in combination with thin foils, whose only purpose is to separate adjoining cells. In our current configuration, a typical one cell cartridge is about 3 mm thick. Because the cartridges are thin, it may be possible to provide high power density stacks that are relatively small, compact, and light-weight. Additionally, the overall packaging of the hardware into cartridges enables the quick and easy assembly of stacks and also makes it possible to remove and replace problem cells within a stack without compromising the remaining cells.

100 cm^2 Single Cell and Stack Performance

In general, single cells based on a 100 cm^2 active area and 316 SS metal screen hardware performed as well as 5 cm^2 LANL test cells based on conventional serpentine channel graphite hardware. One such cell was operated continuously at 0.5 V for 2000 hours to assess the long-term performance of the 316 SS hardware (9). Over the course of the first 1700 hours, the cell maintained an average power density of 0.45-0.5 W/cm^2, however, in the last few hundred hours, the cell exhibited some loss of performance due to flooding associated with the fine screen. In later testing, replacing the fine screen with a perforated plate ultimately solved the problem and subsequent single cells and stacks utilized the new configuration. Despite the flooding, the cell performed quite well and upon disassembly, there was no visible evidence of corrosion of the hardware.

Figure 5 shows polarization curves for a single cell, a 2-cell stack and a 4-cell stack. The stacks performed as well as the single cell in the kinetic region of the curves, suggesting that reactant access to the MEAs was adequate in all of the cartridges. Likewise, the high frequency resistance (not depicted) was about 0.15 Ω-cm^2 in all cases, confirming that sufficient compression was attained within the stacks. The main losses in cell performance between the stacks and the single cell, occurring in the intermediate current regions of the curves, were primarily due to reactant maldistribution in the hand-made assemblies. An additional factor affecting the stack performance was the method of cooling used for these stacks. For single cell testing, a small fan suffices to keep the cell at 80°C, whereas stacks generate enough heat that only internal cooling will maintain the proper temperature. In this case, cooling plate flow-fields are added between cartridges (as depicted in figure 4) and ambient temperature water is circulated through each cooling plate via a peristaltic pump that is activated when the cell temperature rises 3° above its setpoint. The problem encountered was that the stack temperature fluctuated by several degrees each time the pump sent water through the cooling plate, causing erratic cell performance at lower voltages in particular. A more effective coolant system and plate needs further development. One approach may be to circulate warmer water (closer to the stack temperature of 80°C) at a slower continuous flowrate to minimize the temperature fluctuations.

Overall, it appears that the hardware design works relatively well for single cells, but needs further optimization to attain equal performance characteristics in stacks. Yet based on the thinness of the structures and the initial power densities demonstrated, it may indeed be possible to produce inexpensive, high power density, compact PEFC stacks utilizing this hardware configuration once further optimized.

Corrosion Testing

Corrosion rates were determined based on the weight loss of the 316 SS samples used in the immersion tests, and were consistently <0.34 µm/yr, regardless of the pH of the test solution or nature of the sparge gas. However, analysis of the test solutions revealed a strong pH dependence of the concentrations of leached metals found in solution. Figures 6 and 7 illustrate this effect for the hydrogen and air sparged solutions, respectively. As might be expected, the lower the pH of the test solution, the higher the concentrations of Ni, Fe, Cr, and Mo ions that were detected. Additionally, the data show some dependence on the sparge gas as well. Though the pH appears to be the predominant factor influencing corrosion of the metal, the presence of hydrogen enhances the process. In general, these data suggest that 316 SS should be corrosion-resistant in a fuel cell if the cell water can be maintained above pH 5.

Analyses of water samples collected from the 2000 h life-test cell, as well as from a 4-cell stack and other cells were in the range of pH 6 - 7. In comparison with the water supplied through the test stations (used for humidification), the 2000 h cell water effluent was virtually identical, whereas the water from the 4-cell stack contained somewhat elevated levels of Fe and Cr. The humidifier system is a potential source of contamination because it contains components made of 304 SS. Thus, the presence of Mo is of prime interest because it is unique to 316 SS. Essentially no Mo was detected in either the 2000 h test cell water or the stack water. Though the stack hardware showed no visible signs of corrosion, the elevated ion levels may be an indication of corrosion due to shunt currents in the manifold region of the cell. Corrosion can occur in this area if water ionically shorts across several cells, which is further exacerbated in a stack due to higher voltages. Even with this effect, however, the overall content of metal ions in the effluents was quite low, if not at the detection limit.

Another concern has been that metal ions may be taken up by the membrane and adversely affect cell performance. Thus, a variety of MEAs were analyzed for Ca, Fe, Ni, Cr, Mn, Mo, Cu, and Zn by EDAX and later by XRF, a more sensitive technique. Samples were obtained from the 2000 h metal hardware test-cell, a metal hardware 4-cell stack, the membrane that was in direct contact with metal hardware at open-circuit, and a 500 h graphite hardware test-cell. In addition, an unused protonated MEA was analyzed to determine if our materials or preparation process might be a possible source of contamination. Only the Pt catalyst was detected in this case, thus the pretreatment process does not appear to adversely affect the MEA. Analyses by XRF showed that Ca, Fe, and Ni were the predominant contaminants detected in all of the used MEAs, while Mn, Cu, and Zn were generally present in much lesser amounts or were not detected. None of the MEAs contained detectable quantities of Cr or Mo, where the detection limit was approximately 10 ppm. Estimates of the percentage of sulfonic acid sites "tied up" by Ca and Fe were significant and at a maximum in the 2000 h test-cell MEA. In two separate samples of the MEA, the Fe content, vis-à-vis active sites, was calculated to be in the range of 11-20% whereas the Ca was 0.5-8%. Some effort is still required to determine the correlation between replacement of protons by Fe ions in an MEA and the consequences on both high frequency resistance (HFR) and electrocatalytic activity, depending on level and spatial distribution within the MEA. As described above, in spite of the significant levels of Fe and Ca ions detected in the membrane, the HFR under these circumstances did not increase significantly and some effects on cathode performance could have originated from water transport limitations.

Overall, the most critical factor affecting corrosion appears to be water quality and its pH. If very pure water is used and direct metal to membrane contact is avoided, 316 SS may be corrosion-resistant, although the manifold design would need to be designed to minimize shunt currents.

CONCLUSIONS

We have developed potentially low-cost, high performance metal hardware for PEFCs based on 316 SS screens and foils. In this hardware, woven wire mesh screens serve as flow-fields, which are sandwiched around thin foils to form a bipolar plate. Reactants are introduced at one corner of the screen and exit at the opposing diagonal corner. Though one might expect that this configuration would lead to an uneven distribution of reactants, the "corner-to-corner" flow scheme effectively distributes reactants across the entire active area of the cell and prevents water accumulation and flooding. Additionally, the design allows for very thin cell components to be used, making it possible to have thin unit cells and stacks with a high cell pitch and power density. The unit cells are adhered together into 2-cell "cartridges" and can be combined with cooling plates in between to make large stacks. The cartridges offer advantages in that stack assembly is made easier and problem cells can be removed without compromising the rest of the stack.

Fuel cells based on 316 SS metal screen hardware have been tested on an individual basis as well as in 2 - 4 cell stacks, showing performances equal or close to those obtained with conventional serpentine-channel graphite blocks. Operating on pressurized and humidified H_2/air, power densities of 0.45 - 0.5 W/cm^2 at 0.5 V have been achieved for as long as 2000 h of continuous operation, with no visible signs of corrosion to the hardware. Cell effluents and MEAs from a number of cells were analyzed by ICP-MS and XRF, respectively. Additional corrosion tests have been conducted involving immersion testing of 316 SS foil samples in acidified, gas-sparged water, and fuel cell testing of metal hardware at open circuit, where the metal hardware directly contacted an uncatalyzed membrane. The results of these tests suggest that under typical operating conditions for a PEFC, 316 SS appears to be corrosion-resistant if high water purity can be maintained, and the metal hardware does not directly contact the MEA. Thus, if shunt currents within stacks can be minimized or eliminated, 316 SS hardware can conceivably provide the means for low-cost, high performance PEFCs.

ACKNOWLEDGMENTS

This work was funded by the Hydrogen Program of the U. S. Department of Energy, Office of Utility Technology. We would also like to thank Dr. Fernando Garzon of Los Alamos National Laboratory for his assistance with the XRF analyses.

REFERENCES

1. R. J. Lawrance, U. S. Patent 4214969, 1980.
2. D. P. Wilkinson, G. J. Lamont, H. H. Voss, C. Schwab, U. S. Patent 5527363, 1996.
3. R. G. Spear, H. H. Mueggenburg, R. Hodge, U. S. Patent 5683828, 1997.
4. R. K. A. M. Mallant, F. G. H. Koene, C. W. G. Verhoeve and R. Ruiter, Program and Abstracts of the Fuel Cell Seminar, San Diego, CA, p. 503 (1994).
5. C. Zawodzinski, M. S. Wilson and S. Gottesfeld, in 1st International Symposium on Proton-conducting Membrane Fuel Cells/1995, S. Gottesfeld, G. Halpert, and A. Landgrebe, Editors, PV 95-23, p. 57, The Electrochemical Society Proceedings Series, Pennington, NJ (1995).
6. M. S. Wilson, C. Zawodzinski, U. S. Patent 5798187, 1998.
7. J. F. McElroy, U. S. Patent 4855193, 1989.
8. G. Faita, C. Mantegazza, U. S. Patent 5482792, 1996.
9. C. Zawodzinski, M. S. Wilson and S. Gottesfeld, in Program and Abstracts of the Fuel Cell Seminar, Orlando, FL, p. 659 (1996).

FIGURES

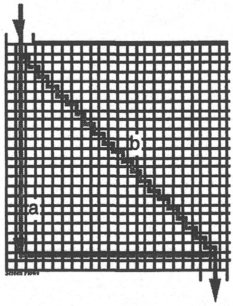

Figure 1. Schematic illustrating that flow-paths a) and b) of the reactant along the surface of a woven metal screen are the same net distance, given that flow can only progress in the x or y directions.

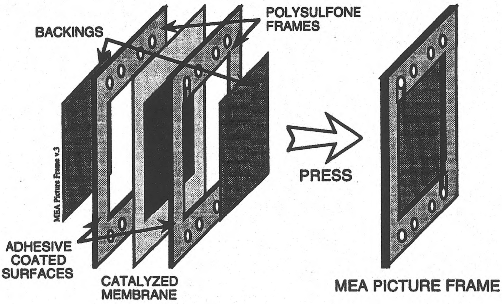

Figure 2. Schematic depicting the assembly of a Picture Frame MEA.

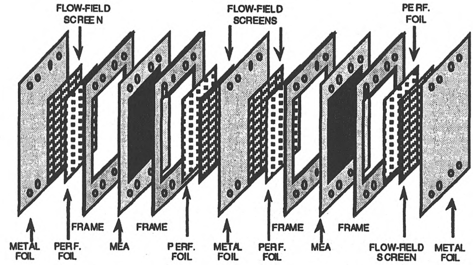

Figure 3. Components of a two-cell cartridge utilizing wire-screen flow-fields, metal foil separators, and picture frame MEAs.

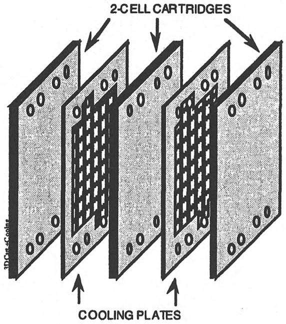

Figure 4. A stack containing 3 two-cell cartridges separated by removable cooling plates.

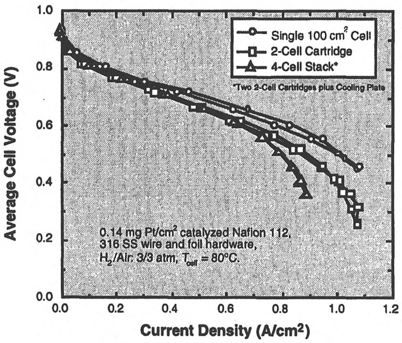

Figure 5. Polarization curves of single cells, and 2-4 cell stacks based on 100 cm^2 metal screen hardware.

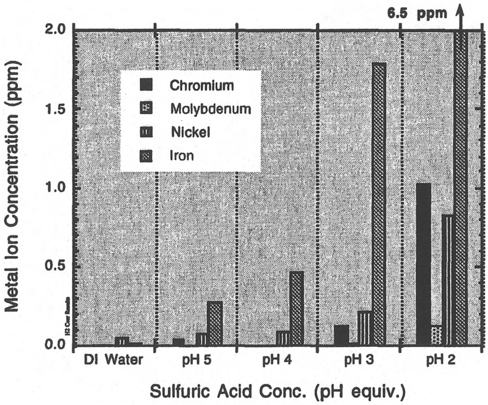

Figure 6. Metal ion concentration versus pH of test solution for H_2-sparged samples.

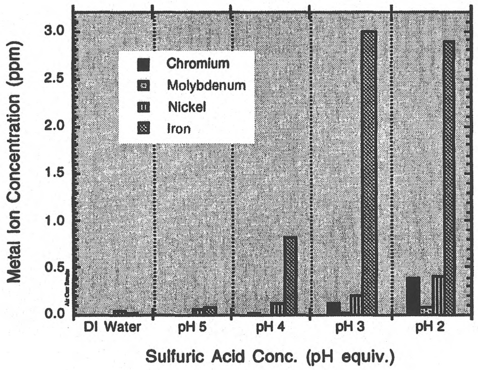

Figure 7. Metal ion concentration versus pH of test solution for air-sparged samples.

Proton_Conducting_Membrane_Fuel_Cells_II, PV 1998-27, 457-461 (1998)
DOI: 10.1149/199827.0457PV © The Electrochemical Society

ADVANCED METHOD TO MEASURE CURRENT GRADIENTS IN POLYMER ELECTROLYTE FUEL CELLS

CHRISTIAN WIESER, AXEL HELMBOLD, WERNER SCHNURNBERGER
INSTITUT FÜR TECHNISCHE THERMODYNAMIK,
DEUTSCHES ZENTRUM FÜR LUFT- UND RAUMFAHRT,
PFAFFENWALDRING 38-40, 70569 STUTTGART, GERMANY

Polymer electrolyte fuel cells (PEFC) comprise extended areal electrodes where the electrochemical reactions take place. These reactions lead to material conversion and are represented by an electric current. Due to the individual design of electrochemical cells and especially to the type of the flow field an inhomogeneous mass transport of the reactants across the electrode area occurs affecting the performance of the cell as a whole. Measuring the current distribution along the electrode area the design of fuel cell components and the operation modes can be suited to the requirements. Such a technique for measuring lateral current gradients in electrochemical cells working independently from the dynamic cell operation has been developped and applied in a PEFC.

Introduction

Fuel cells are electrochemical devices in which the storage of the chemical energy is separated from the location of the conversion reaction. Consequently, gaseous or liquid reactands have to be supplied adequately to the electrodes and reaction products as well as inert constituents have to be removed from the cell. At the latest this is a problem if the electrode areas increase to commercially relevant dimensions and the thickness of the bipolar plates is reduced. The configuration of inlet and outlet channels and especially the design of the flow-field considerably influence the occurence of local concentration gradients which strongly affect the local electrochemical reaction rate. Furthermore, the local performance from inlet to outlet is depending on the operating conditions, e. g. reaction gas flow rate or humidification strategy. During operation such inhomogeneities in electrochemical cells cannot be recognized because usually only integral measured values like cell voltage, current and impedances are obtained. In order to resolve the measurement locally a modification of the fuel cell is necessary. This modified cell must ensure sufficient resolution at reasonable expenditure. Furthermore, the steady-state and dynamic operation must not be affected and the design should allow the integration in a fuel cell stack. Existing approaches do not fullfill the entirety of these requirements (1). Therefore an advanced technique of current mapping measurements has been developped by applying a new approach using a magnetic loop array based on a technique similar to a DC current clamp. In the following first results are being presented.

Experimental

In order to observe distinct effects, a large fuel cell with an active area of 578 cm^2 (papersize A4 as being considered commercially relevant) has been designed. Disregarding lateral currents in the electrode membrane assembly (EMA) only one flow-field is divided in an array of 5×8 equal area squares. The segmented flow-field comprises straight channels of 1×1 mm^2 cross section with a spacing of 4, 8 mm. First investigations were undertaken with the same flow-field at the counter electrode side. Each segment of the measuring frame has a cylindrical end on the current collector side around which a ferrite ring is placed. The rings are manufactured with a gap where a magnetic field sensor (Hall sensor) is positioned. For insulating and sealing reasons the individual segments are separated by a silicon cast. A schematic cross section of the measuring frame is shown in Fig. 1. Measuring the magnetic fields of the electric currents the Hall sensors generate a voltage output which is proportional to the electric currents crossing the individual segments. Independent of the fuel cell operation the output voltages of the 40 segments are scanned by a multiplexer and measured by a microvoltmeter. Automatic calibration of the Hall voltage offset and online visualization of the current density distribution is done by a PC. Because all sensor wires are connected through the side of the 10 mm thick measuring frame the integration in a fuel cell stack is possible and the temperature control of the cell by water flow could be implemented on the reverse side. Eventually, the whole cell is clamped between two pairs of brackets in the lower and upper third and installed in the test rack.

To simplify the exchange of the air flow field the measuring frame was installed on the hydrogen side of the cell. The EMA with an active area of 578 cm^2 was produced by hot-pressing two ELAT gas diffusion electrodes with 20 wt.% Pt on Vulcan XC-72 and 4 g Pt/m^2 on a Nafion® 117-membrane for three minutes at 160 °C and 80 bar pressure.

Results

First measurements demonstrate that the measurement technique is suited to resolve local effects such as dehumidification, changes of partial pressure or contact resistances. Exemplary, a series of measurement with operation under different air flow rates at constant pressure (2 bar$_{abs}$ on both sides), cell potential of 535 mV and 60 °C temperature has been performed. The gases were fed unhumidified and hydrogen flow was dead ended. The cell was held at constant operation conditions for more than twelve hours to achieve steady-state before the air flow rate variation. The total current output during operation is shown in Fig. 2. The main information one can extract from this figure is that the subsequent increase of the air flow rate at first leads to a moderately higher total current output and later on to a decrease at high flow rates. The moderate effect might lead to the assumption of slight changes in the relative spacial conditions of the cell. However, the locally resolved measurements presented in Fig. 3 demonstrate that dramatic changes occur.

In the following we assume that the influence of the hydrogen side on the current distribution can be neglected. With regard to the chosen experimental conditions two distinct phenomena can be observed at low air flow rates which is shown in map (a) of Fig. 3 where each point of intersection represents a measured data point. At first, the depletion of oxygen leads to the decrease of local cell performance toward the air outlet. Furthermore, the special design of the air inlet in combination with the low pressure drop resulting from the low air flow rate might be the reason for a preferential gas flow in the channels on the right side of the cell diminishing the current density on the left side.

The significant decrease of the performance in the upper part of the cell as shown in map (b) of Fig. 3 can be explained by dehumidification of the membrane with increasing flow rate of the dry air. The higher flow rate diminishes the problem of oxygen depletion in the lower part of the cell. Trying to interpret the local peaks in the upper half we cannot exclude differences in the contact pressure due to variing segment thicknesses resulting from manufacturing tolerances. To exclude this influence in future investigations the surface of the mounted segments has been carefully grinded over meanwhile to reduce contact resistance deviation.

With preceeding operation time and further increase of the air flow rate the tendency of membrane dehumidification in combination with the shift of the electrochemical activity towards the outlet as shown in map (c) of Fig. 3 becomes more obvious. Although the total current just starts to decrease remarkably (Fig. 2) the locally resolved measurement shows that already about half of the cell area is electrochemically inactive.

Outlook

The presented results demonstrate the feasibility of current distribution measurements using the magnetic loop array technique. Future investigations will concentrate on systematic study of different flow field designs under variing operation conditions in the PEFC and DMFC, e.g. flow rates and water management. Another interesting topic for this kind of measurement will be the consideration of effects on the anode with the focus on catalyst poisoning and regeneration for example by carbon monoxide. Besides these relatively slow phenomena fast transients such as load changes and sudden flushing of the cell will be considered.

References

1. S.J.C.Cleghorn, C.R. Derouin, M.S. Wilson and S. Gottesfeld, J. Appl. Electrochem., 28,1 (1998) and references therein

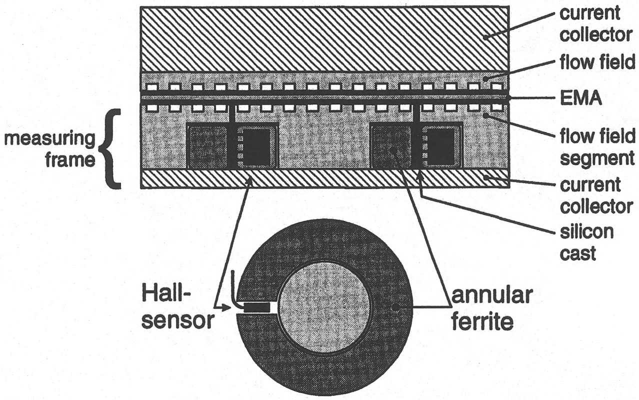

Figure 1: Schematic cross section of the fuel cell assembly including a segment of the measuring frame. Beneath the elements of the magnetic loop are shown separately in the top view (not to scale).

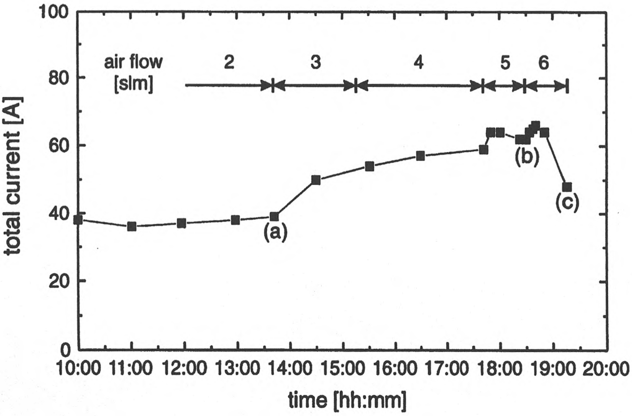

Figure 2: Total current depending on gas flow rate with time including the points in time of flow rate changes.

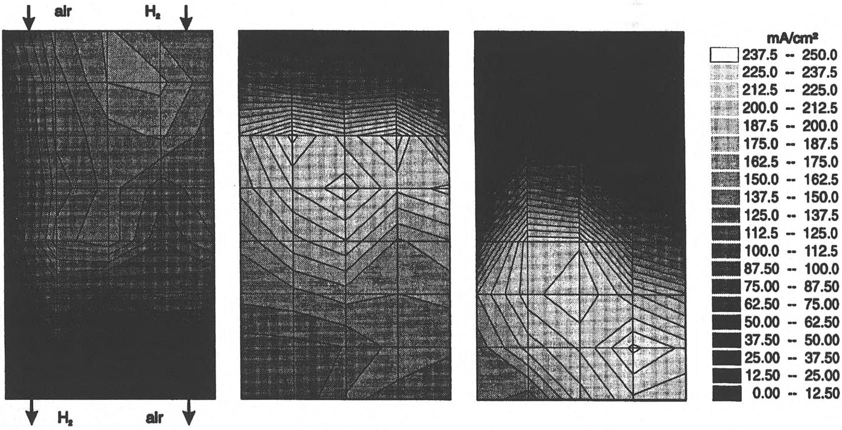

(a) 13:42 (b) 18:34 (c) 19:16

Figure 3: Current mapping at three selected times (points a, b, c of Fig. 2) normalized to segment area of 14.5 cm^2 in a non-humidified hydrogen/air PEFC.

Proton_Conducting_Membrane_Fuel_Cells_II, PV 1998-27, 462-469 (1998)
DOI: 10.1149/199827.0462PV © The Electrochemical Society

TRANSIENT FINITE ELEMENT SIMULATIONS OF POLYMER-ELECTROLYTE FUEL CELLS

I-Ming Hsing and Peter M. Futerko
The Hong Kong University of Science and Technology
Department of Chemical Engineering
Clear Water Bay, Kowloon, Hong Kong

The transient behavior of the cell polarization and transport phenomena of polymer-electrolyte fuel cells (PEFCs) has been investigated using the Galerkin Finite Element Method (GFEM). The effects of a linear ramp in current density on cell potential, temperature, water concentration, and the flux of water leaving the cell are reported. Simulations indicate that the time constant for the fuel cell to reach steady state after a sudden change in load or current density is on the order of an hour. Model predictions further indicate that steady state is reached more quickly during a ramp up in current density; considerably longer times are needed to reach steady state during a ramp down.

INTRODUCTION

Polymer electrolyte fuel cells provide a means to obtain high power density at low operating temperature with clean and efficient conversion of energy. Such characteristics are desirable for power sources to be used in future vehicles. However, several factors are known to impact the performance of PEFCs, including dehydration of the membrane and flooding of the pores of the gas diffusion electrodes. Several modeling studies (1-4) of PEFCs have described water management and operating characteristics in steady state. More recent studies (5-7) have addressed some of the transient characteristics of water management in fuel cells, which is of particular concern because operating current densities and loads of fuel cells used in transportation applications can be unsteady. Furthermore, the time constants for the fuels cells to reach steady-state operating conditions can be as long as two hours (8).

In this work we have attempted to formulate a detailed model of the underlying physics governing the transient behavior of PEFCs. Simulations have been conducted to characterize the effect of unsteady current density operation on cell potential, membrane water content, flux of water leaving the fuel cell, and cell temperature.

MODELING APPROACH

Our model incorporates the one-dimensional, isothermal, steady-state analysis of Bernardi et al. (2,3) plus unsteady heat and water balance equations and temperature-dependent physical properties. The residual equations are discretized onto an exponentially spaced mesh. To capture the sharp gradients of dissolved oxygen concentration near the interface between the catalyst and gas diffuser, element sizes on the order of 10^{-8} cm are required. The nonlinear differential/algebraic equations are solved using DASPK (9) in combination with a frontal solver. The Jacobian is computed analytically. The model is calibrated to data following a procedure similar to one described by Bernardi et al. In figure 1 computed cell polarization characteristics are compared with data from Ticianelli et al. (10) over a range of current densities and operating temperatures.

The following variables are solved in one dimension: membrane potential, electrode potential, water velocity, gas phase concentrations, dissolved oxygen and hydrogen concentrations, liquid water concentration, and temperature. The model equations will be discussed in detail in future work. For the present work, we will only discuss the evaporation model, which has a strong influence on the simulation results. The evaporation rate of liquid within the gas diffusion electrodes is modeled as a homogeneous process described by the rate expression:

$$R_w = A \exp(-\Delta H_{vap}/RT)\, C_w\, (P^* - P_w) \qquad [1]$$

in which A is the pre-exponential factor, the activation energy is taken as the heat of vaporization of water ΔH_{vap}, C_w is the concentration of liquid water in the electrode, P^* is the vapor pressure, and P_w is the partial pressure of water. Equation [1] gives the following limiting characteristics: (i) the evaporation rate approaches zero as the electrode becomes dry; (ii) net evaporation occurs when P^* is greater than P_w; (iii) net condensation occurs when P^* is less than P_w; (iv) the temperature dependence of the rate constant follows the Arrhenius expression. We have not tested equation [1] against experiments.

The initial point for a transient simulation is obtained by solving the steady-state model at a specified current density. Temperature is determined by a heat balance over the fuel cell, which includes terms for heat generated by electrode reactions, Joule heating of the electrodes, heat exchange with the ambient, latent heat of evaporation, and conduction within the cell. The time integration is accomplished using DASPK (9), which first computes self-consistent values for the derivatives of the solution components at time zero, and then integrates the differential/algebraic system of equations using a combination of backward differentiation formula methods. Because of the strong coupling between temperature and liquid water concentration in equation [1], the model is stiff and very small times steps are needed to obtain an accurate solution.

RESULTS AND DISCUSSION

Profile of Water Concentration

The distribution of water in the membrane and electrode regions of the fuel cell is dependent on several factors including the humidity of the fuel streams, membrane and electrode characteristics, temperature, pressure, and current density. A typical water concentration profile computed by the present model is shown in figure 2. The humidity and pressure of the anode fuel stream are 69.6% and 3 atm, and the corresponding values for the cathode are 28.7% and 5.0 atm. The temperature of the fuel cell is 86 °C. Water concentration is at the highest level in the active catalyst region of the cathode gas diffuser, where water is produced by the reduction of oxygen. Water moves through the membrane by three mechanisms including osmotic drag, concentration diffusion, and pressure driven transport. Evaporation occurs in the gas diffusers provided that the gas phase has not reached saturation. The overall mechanism for water removal is evaporation followed by gas-phase diffusion out of the fuel cell. In the present modeling effort, we do not consider flooding of the fuel cell, which tends to occur at low temperature and high fuel-stream humidity. Under such conditions water will exit the fuel cell in the liquid phase.

Transient Response of Cell Temperature

Fuel cell temperature behavior is shown in figures 3 and 4 for cases of linear changes in current density in the 0.65 to 0.90 A/cm^2 range. The duration of the ramp in each case is 60 seconds. During the ramp up in current density, increasing heat generation by the electrode reactions causes an increase in cell temperature from 69 °C to about 74 °C. After the ramp, cell temperature increases to 86 °C while the water balance reestablishes equilibrium. Steady state is reached after about half an hour. In figure 4, we show the transient response of fuel cell temperature as current density is ramped down from 0.90 to 0.65 A/cm^2 in 60 seconds. Temperature decreases because of less heat is produced by electrode reactions. For the case of decreasing current density, steady state is achieved after about three hours. This is considerably longer than the time needed to reach steady state for the case of ramping up current density.

Transient Response of Cell Potential

Figure 3 shows cell potential as a function of time as current density is increased. Initially, the evaporation rate of water is low because the cell temperature is low. As current density increases, the evaporation rate increases, and as water leaves the fuel cell, the membrane becomes dehydrated. This results in a decrease in the conductivity of the membrane, and the cell potential drops abruptly.

Transient Response Water Concentration

Figure 4 shows water concentration at the membrane/cathode interface as a function of time as current density is decreased. Water content is nearly constant on the time scale of the ramp down. However, as cell temperature changes the water balance within the electrodes must reestablish equilibrium resulting in a higher water level in the final state. It is interesting to examine the time scales for changes in cell temperature and membrane water content. In figure 4 there appears to be two time scales for change of the cell temperature. On the short time scale, the cell temperature is closely coupled to the current density. On the long time scale, there seems to be a strong coupling between cell temperature and membrane water content.

Transient Response of Water Flux

Figure 5 shows the time-dependent behavior of water leaving both the anode and cathode sections of the fuel cell. The temperature of the humidifier for the cathode fuel stream is 47 °C and total pressure is 5 atm. The corresponding values for the anode fuel stream are 67 °C and 3 atm. The initial cell temperature is 69.1 °C. The high humidity of the anode fuel stream results in a low flux of water leaving the anode side of the fuel cell. At the initial cell temperature, the water concentration is high and the membrane is nearly saturated. At the final temperature 86°C, the membrane is partially dehydrated and the water concentration level is significantly lower. A sudden increase in the water flux is needed to realize the lower water concentration at the final state. This adjustment of the water balance responding to an increase of the cell temperature can be seen in figure 5.

CONCLUSIONS

The transient operation of PEFCs during a ramp-up or ramp-down in current density have been simulated using detailed models which capture the underlying physics. Simulations indicate that the time required for fuel cells to reach steady state after a sudden change in current density can be longer than an hour. A large contributing factor to the time constant is the time needed for the water balance to reestablish equilibrium in the gas diffusion electrodes. During the transient phase, dehydration of the membrane or flooding of the pores of the electrodes can occur.

REFERENCES

1. T. E. Springer, T. A. Zawodzinski and S. Gottesfeld, J. Electrochem. Soc., 138, 2335 (1991).
2. D. M. Bernardi and M. W. Verbrugge, AIChE J., 37, 1151 (1991).
3. D. M. Bernardi and M. W. Verbrugge, J. Electrochem. Soc., 139, 2477 (1992).
4. T. F. Fuller and J. Newman, J. Electrochem. Soc., 140, 1218 (1993).
5. T. F. Fuller, Ph.D. Thesis, University of California, Berkeley, CA (1992).
6. T. Okada, G. Xie and Y. Tanabe, J. Electroanal. Chem., 413, 49 (1996).
7. M. Wohr, K. Bolwin, W. Schnurnberger, M. Fischer, W. Neubrand and G. Eigenberger, Int. J. Hydrogen Energy, 23, 213 (1998).
8. T. R. Ralph, G.A. Hards, J. E. Keating, S. A. Campbell, D. P. Wilkinson, M. Davis, J. St-Pierre and M. C. Johnson, J. Electrochem. Soc., 144, 3845 (1997).
9. P. N. Brown, A. C. Hindmarsh, and L. R. Petzold, SIAM J. Sci. Comp., 19, 1495 (1998).
10. E. A. Ticianelli, C. R.Derouin, A. Redondo, and S. Srinivasan, J. Electrochem. Soc., 135, 2209 (1988).

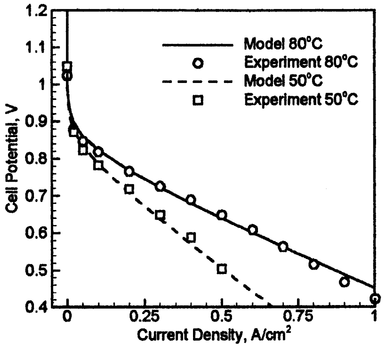

Figure 1. Comparison of measured fuel-cell potentials with simulations for varying current density and temperature. Experimental data is from the work of Ticianelli et al. (10)

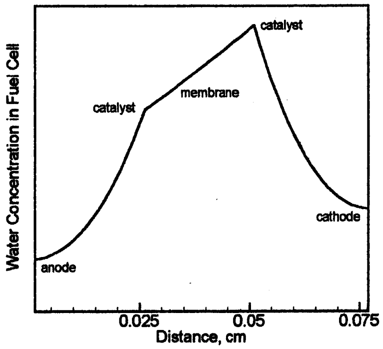

Figure 2. Simulated water concentration profile at the end of a ramp-up in current density from 0.65 to 0.90 A/cm^2 in 60 s.

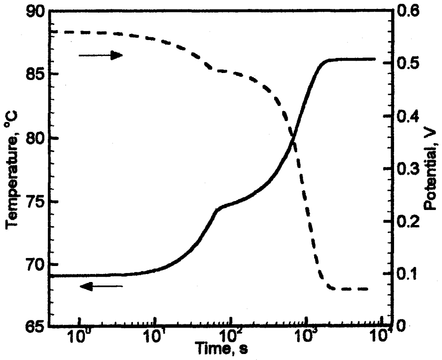

Figure 3. Simulation of fuel-cell potential and temperature during a ramp-up in current density from 0.65 to 0.90 A/cm^2 in 60 s.

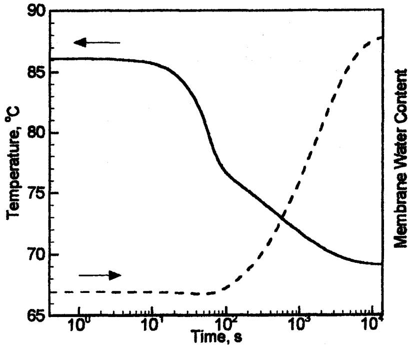

Figure 4. Simulation of fuel-cell temperature and membrane water content during a ramp-down in current density from 0.90 to 0.65 A/cm^2 in 60 s.

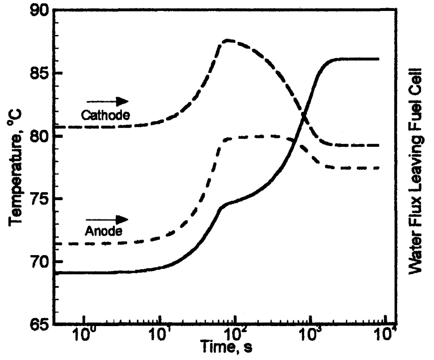

Figure 5. Simulation of fuel-cell temperature and water flux during a ramp-up in current density from 0.65 to 0.90 A/cm^2 in 60 s.

Proton_Conducting_Membrane_Fuel_Cells_II, PV 1998-27, 470-478 (1998)
DOI: 10.1149/199827.0470PV © The Electrochemical Society

PERFORMANCE OF POLYMER ELECTROLYTE MEMBRANE FUEL CELL STACK

Deryn Chu and Rongzhong Jiang

U.S. Army Research Laboratory
Sensors and Electron Devices Directorate
Adelphi, MD 20783-1197

ABSTRACT

The performance of an air-breathing polymer electrolyte membrane fuel cell (PEMFC) stack is evaluated under different conditions. These different conditions include humidity, temperature and H_2 flow rate. When the humidity is less than 10 percent relative humidity (RH) at 35°C, the stack does not work properly. Self-humidifying by the product of water in the stack is observed at below 30 percent RH. It is suggested that the appropriate humidity for operating the stack is at least 30 percent RH or higher. The best operational temperature for the stack ranges from 20 to 40°C. The rate of H_2 flow does not have any apparent effect on the stack power output. Rather only determines the maximum operating current.

INTRODUCTION

Steadily increasing portable electric power requirements have created the need to develop more efficient and energetic power sources. The polymer electrolyte membrane fuel cell (PEMFC) is one of the best candidates for a portable power supply device for commercial applications primarily because of its lightweight and high-power density. PEMFCs have received much attention since the 1980s. Their development was helped by the invention of Nafion by DuPont in the 1960s [1]. Nafion is a perfluorinated cation exchange polymer membrane that has shown good conductivity and stability up to 100°C in fuel cell environmental operating conditions. Early research concentrated mainly on membrane electrolytes and their properties. Later research has focused on the PEMFC's components. More recently, there have been numerous reports in the literature describing the performance of single-cell PEMFCs [2-10]. It appears that PEMFCs will be going through a commercialization and demonstration stage soon. PEMFC stacks having a variety of types and functions have been emerging from many developers [11-13], but there have been no detailed on systematic investigations evaluating their performance, which varies from one design to another.

Understanding the performance characteristics of PEMFC stacks is important for arriving at optimum cost/weight/performance ratios. The objective of this study is to bridge the gap between the development and application of PEMFC stacks for military and civilian applications. The air-breathing PEMFC stack is a two-dimensional fuel cell stack with individual cells in the same plane [11]. This allows all of the cells to access the same reservoir of hydrogen, and the opposite face to be openly exposed to air. This design has a lightweight, simple feature for portable electric power sources. In this research we investigate a class of air-breathing PEMFC stacks in which air is provided by spontaneous convection from the environment.

EXPERIMENT

The air-breathing PEMFC stack was composed of 6 bi-cells connected in series. The area of each electrode is approximately 32 cm^2. The open circuit voltage was approximately 6V. The oxygen supply to the cathode was obtained by convection from the air. High-purity hydrogen (99.99%) was used. The experiments used dry hydrogen and wet hydrogen (saturated with water). A Matheson TF601 rotameter was used for measuring the hydrogen flow rate. The temperature and humidity were controlled with a Tenney environment chamber (model BTRC) and heatless Dryer (model No. HF 200A). A Hewlett-Packard electronic load (model No. 6050B) and a Hewlett-Packard multimeter were used for measuring the stack's current and voltage, respectively. The Tenney environment chamber was controlled through a computer using Linktenn II software.

RESULTS AND DISCUSSION

It is well known that the performance of a PEMFC is a function of temperature and pressure. However, operating temperature increases will cause thermal management and membrane dry-out problems. Operating pressure increases will result in system complications. Therefore, our emphasis here is on the evaluation of ambient pressure, normal environmental temperatures, and humidity for a PEMFC stack that can be carried by one person. The air-breathing PEMFC stack was designed to use oxygen from the surrounding air. This makes it lighter, simpler and cheaper than other types of stacks because no auxiliaries for providing oxygen or air are required. The reaction product of water at the cathode electrode was automatically exhausted to the environment. The disadvantage of air-breathing PEMFC stack is that many factors present in the surrounding environment may affect stack performance. The first factor considered is humidity.

I. Humidity:

Figure 1A shows the effect of relative humidity (%RH) on stack performance at 35°C and constant H_2 flow rate. The polarization curve with 85 percent RH has the highest value of voltage at the same current. This means that the highest power output is at 85 percent RH. The performance of the stack degrades with decreasing percent RH. Between an RH of 85 and 30 percent, the voltage decreases steadily with increasing current. However, at 20 percent RH, the decrease stops. Surprisingly, when the operating current increases past 1.0 A, the voltage increases instead of decreasing. This is because of the stack's self-humidifying effect due to water production at the cathode. When the RH value is less than 10 percent the stack's voltage decreases considerably with increasing current. Figure 1B shows the calculated stack power from the data shown in Fig. 1A. The stack's power increases with increasing current until reaching the highest current value. If it goes above the highest current, the voltage drops to zero because the amount of hydrogen supplied is completely consumed. The stack's performance completely deteriorates for percent RH level equal to or less than 10 percent at 35°C. The voltage and power versus current plots for different percent RHs at 10°C are shown in Fig. 2. A comparison of Figs. 1 and 2 shows that the effect of humidity on stack performance at 10°C is less than that at 35°C.

Figure 3 shows the polarization curves for the same flow rate of the hydrogen, both saturated with water and not saturated with water, that is fed into the anode at 40°C and 20 percent RH. As expected the stack performance for the hydrogen saturated with water, which is fed into the anode compartment, is better than that for the hydrogen not saturated with water.

The effect of humidity on Nafion's ionic conductivity at different temperatures was reported by Sone et al [14]. The temperature range was from 20 to 50°C. They reported that Nafion's ionic conductivity is significantly affected by humidity. Their results are in agreement with the experimental results shown in Fig. 1.

II Temperature:

Figure 4 shows a series of polarization curves for the PEMFC stack at constant humidity (50 percent RH) as a function of temperature. With increasing current, the voltage decreases and the power increases. The stack performance improves with increasing temperatures. In order to understand the performance of the stack in more detail, the data from Fig. 4 were used to construct a plot of voltage versus temperature at different currents shown in Fig. 5. Within the range of temperatures tested, stack performance seems to be linearly proportional to temperature at constant current applied. At lower currents, the curves show a small deviation from linearity and a smaller slope.

This indicates that the electrochemical process is controlled mainly by a charge transfer reaction or activation of the electrodes. At the higher currents, the curves show a large deviation from linearity and a larger slope, which implies that the electrochemical process is controlled mainly by ohmic polarization. Nafion's impedance becomes more appreciable at higher currents, causing a larger IR drop when the H^+ ions pass through the membrane.

III. H_2 Flow Rate:

The air-breathing PEMFC stack was designed to work at low H_2 pressure. Therefore, the H_2 flow rate is one of the critical parameters that determine the performance of the stack. The H_2 flow rates were varied at constant temperature and humidity. Figure 6 shows a series of polarization curves for the stack at different H_2 flow rates. Surprisingly, the H_2 flow rate has no appreciable effect on the performance of the stack until the current increases to a maximum value. This is because the air-breathing PEMFC stack is still maintaining approximately the same H_2 pressure even at different H_2 flow rates. The voltage does drop to zero when the current is greater than a maximum value because the hydrogen at the anode compartment is completely consumed. The stack cannot be operated at a value equal to or greater than the maximum value. If it did, this value would probably damage the stack. Figure 7 shows the plot of the maximum current versus H_2 flow rate. As expected, it is a straight line and passes through the origin. If a high H_2 flow rate is applied, this may cause a waste of fuel or may also damage the stack. According to Fig. 7, a properly operating stack needs to use an appropriate H_2 flow rate. Because oxygen is provided from the air, the maximum performance of the air-breathing PEMFC stack is limited by the natural convection of the surrounding air. Even if an excess amount of H_2 is supplied, the stack's performance is still determined by the amount of oxygen supplied from the air.

IV. System Optimization and Stability:

After optimization of temperature, humidity, and hydrogen flow rate, the best performance of the air-breathing stack was obtained. Figure 8 shows the highest possible power output. It is approximately 22.5 W at operating conditions of 7.5 A, 3 V, 35°C and 85 percent RH humidity. The long-term performance of the air-breathing PEMFC stack was also evaluated at 35°C, and 50 percent RH for 4.05 A and 5.04 A. The result is shown in Fig. 9 which depicts the stack operation voltage versus time. After a 30-hour test, it was still stable at constant of 4 A and 5 A, respectively.

CONCLUSION

The humidity in the surrounding air significantly affects the performance of the air-breathing PEMFC stack. When humidity is less then 10 percent RH, the stack does not operate properly. A phenomenon of self-humidifying by the product of water in the stack is observed at an operating current higher than 1.0 A for a humidity level of a 20 percent RH. It is suggested that the appropriate humidity level for operating the stack is 30 percent RH or higher. The proper operational temperatures for the air-breathing PEMFC stack range from 20 to 40°C. Operating at temperatures lower than 5°C results in poor performance. The rate of H_2 flow does not have any apparent effect on the power output. It determines only the maximum current point at which the voltage drops to zero.

ACKNOWLEDGEMENTS

The authors wish to thank the Army Material Command for its financial support of this project.

REFERENCES

1. T. F. Fuller, The Electrochemical Society Interface, Fall 1997, p 26.
2. E. A. Ticianelli, C. R. Derouin, and S. Srinivasan, J. Electroanal. Chem. 251, 175(1988).
3. I. D. Raistrick, U.S. Patent # 4,876,115 (1990).
4. M. S. Wilson and S. Gottesfeld, J. Appl. Electrochem., Vol 22, pp. 1-7, 1992.
5. J. Kim, S. M. Lee, Srinivason and C.E. Chamberlin, J. Electrochem. Soc., 142 (1995) 2670.
6. Y.W. Rho, O. A. Velev, S. Srinivason and Y. T. Kho, J. Electrochem. Soc., 141 (1994) 2084.
7. H. F. OetJen, V.M. Schmidt, U. Stimming and F. Trila, J. Electrochem. Soc., 143 (1996) 3838.
8. M. Uchida, Y. Aoyama, N. Eda and A. Ohta, J. Electrochem. Soc., 142 (1995) 4143.
9. F. N. Buchi, B. Gupta, O. Haas and G.G. Scherer, J. Electrochem. Soc., 142 (1995) 3044.
10. M. Uchida, Y. Aoyama, N. Eda and A. Ohta, J. Electrochem. Soc., 142 (1995) 463.
11. J. B. Lakeman and J. Cruickshank, Proceedings of the 38 Power Sources Conference, at Cherry Hill, NJ, June 1998, p. 420.
12. A. C. Oliver and E. Clarke, Proceedings of the 38 Power Sources Conference, at the Cherry Hill, NJ, June 1998, p. 424.

13. L. P. Jarvice and D. Chu, Proceedings of the 38 Power Sources Conference, at the Cherry Hill, NJ, June 1998, p. 428.
14. Y. Sone, P. Ekdunge and D. Simonsson, J. Electrochem. Soc., 143 (1996) 1254.

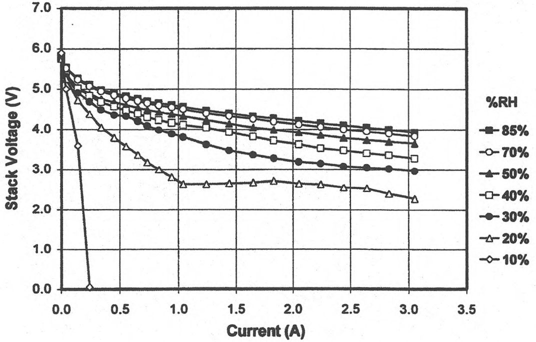

Figure 1A. Effect of %RH on stack voltage. T = 35 °C, H_2 flow = 68 ml/min.

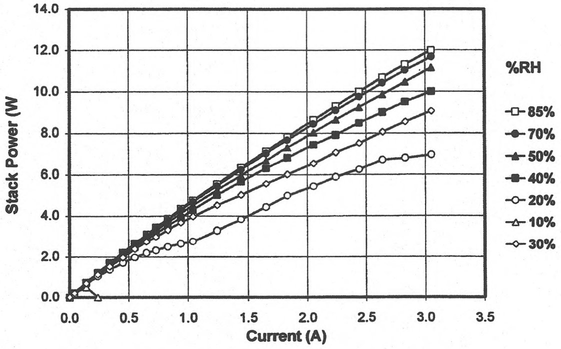

Figure 1B. Effect of %RH on stack power. T = 35 °C, H_2 flow = 68 ml/min.

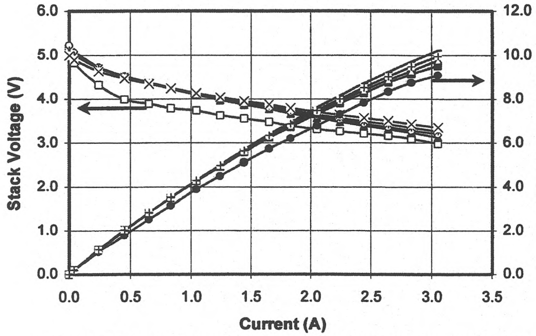

Figure 2. Effect of %RH on stack power and voltage at low temperature (10 °C). H_2 flow = 68 ml/min. Lines from bottom to top for the humidity (%RH) are 22%, 30%, 40%, 60% and 90%, respectively.

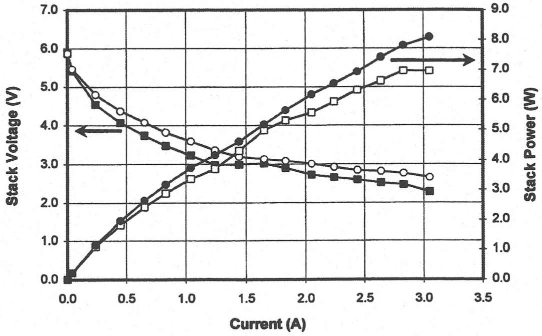

Figure 3. Effect of wet H_2 fill on stack power and voltage. T = 40 °C, RH as 20%, H_2 Flow = 68 ml/min. Lines from top to bottom are wet and dry H_2 fill, respectively.

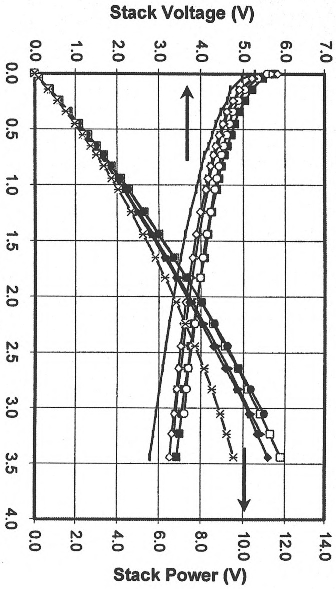

Figure 4. Effect of temperature on stack voltage and power. RH = 50%, H_2 flow = 68 ml/min. Lines from bottom to top temperature (°C) are 5, 20, 30, 35, and 40, respectively.

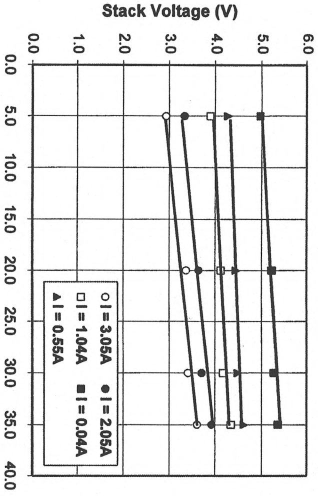

Figure 5. Stack voltage vs. temperature with variety of current values.

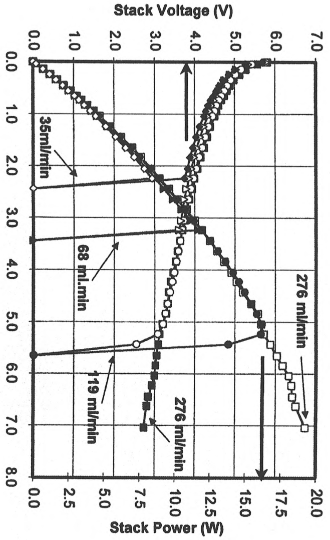

Figure 6. Effect of H_2 flowrate on stack power and voltage. T = 35 °C, RH as 50%.

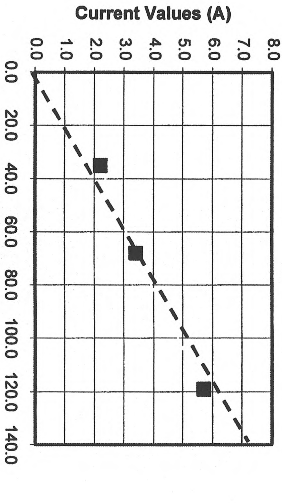

Figure 7. H_2 flow rate vs. the current values at which voltage dropping rapidly . T = 35 °C and RH = 50%.

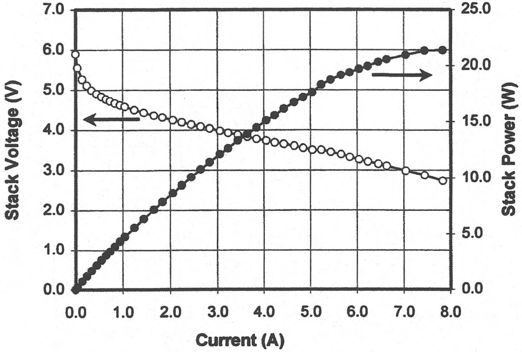

Figure 8. Optimized performance of the air-breath PEMFC stack. RH = 85%, H_2 flow = 276 ml/min and T = 35 °C.

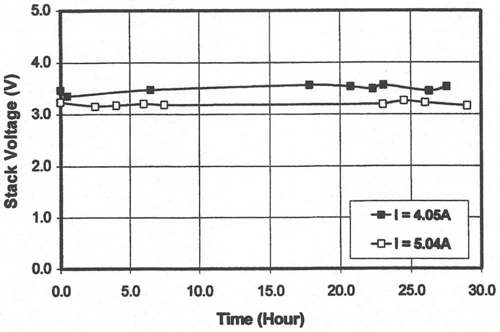

Figure 9. Stack performance at constant current operation. The T = 35 °C, RH = 50%. H_2 flow rates were 110 ml/min and 134 ml/min for I = 4.05A and I = 5.04A, respecitvely.

Proton_Conducting_Membrane_Fuel_Cells_II, PV 1998-27, 479-503 (1998)
DOI: 10.1149/199827.0479PV © The Electrochemical Society

TWO-DIMENSIONAL MODEL FOR THE ENTIRE SANDWICH OF A PEM FUEL CELL

Vladimir Gurau[†][*] Frano Barbir[†] Hongtan Liu[‡]

[†] Energy Partners, 1501 Northpoint Parkway, Suite 102, Technology Center, West Palm Beach, Florida 33407

[‡] University of Miami, Mechanical Engineering Department, Coral Gables, Florida 33124

ABSTRACT

A two dimensional, non-isothermal mathematical model for the entire sandwich of a proton exchange membrane (PEM) fuel cell including the gas channels has been developed. In order to take into consideration the real concentration distributions along the interface between the gas diffuser and catalyst layer, transport equations are solved simultaneously for the domain consisting of the coupled gas channel, gas diffuser, catalyst layer and membrane. The selfconsistent schematical model for porous media is used for the equations describing transport phenomena in the membrane, catalyst layers and gas diffusers, while standard Navier-Stokes, energy transport, continuity and species concentration equations are solved in the gas channels. A special handling of the transport equations enabled us to use the same numerical method to solve them, and therefore to treat the gas channel-gas diffuser-catalyst layer domains as an entirety, avoiding arbitrary boundary conditions at their interfaces. The oxygen mole fraction distribution in the coupled cathode gas channel-gas diffuser is studied for different values of the operating current density. Influences of the inlet conditions at the gas channel entries and of the gas diffuser porosity on the cell performance are also analyzed.

INTRODUCTION

One of the most challenging problems in fuel cells modeling seems to have been the possibility to simulate, rather than prescribe or guess the concentration variations along the interface between the gas diffusers and catalyst layers. This is a major problem, since the distribution of the reactant concentrations along the electrodes is needed to calculate the transfer currents in electrochemical cells. In the particular case of a PEM fuel cell, this phenomenon is related to the gas transport in the coupled domain of a gas channel-gas

---

[*] Corresponding author: phone: (561) 688-0500; fax: (561) 688-9610; e-mail: vgurau@gate.net

diffuser-catalyst layer, and the ability to solve the transport equations in this heterogeneous domain apparently has been the main draw-back in simulating reactant distributions. A mathematical model together with a numerical procedure featuring this ability, would represent a significant step in simulating transport phenomena and performance of PEM fuel cells.

In their study, Ridge and White (1), Verbrugge and Hill (2), (3), Bernardi and Verbrugge (4), (5), Springer *et al.* (6) treated 1-D models of the same problem which provided useful information for further development of the 2-D models.

The 2-D models published so far, are mostly concerned with the transport phenomena in the domains consisting of the membrane, catalyst layers and gas diffusers, while the concentrations/partial pressures in the gas channels are assumed more or less arbitrarily, or averaged values are used as boundary conditions at the interface with the gas diffusers. The work of Singh *et al.* (7) assumed linear variations of the chemical species at the gas channel-gas diffuser interfaces, and the developed model describes phenomena exclusively in the membrane-catalyst layers-gas diffusers. Fuller and Newman (8) solved for the transport across the fuel cell sandwich at certain locations along the gas channel and thereafter integrated in the second direction, while the gas outside the gas diffusers was assumed to be of uniform composition in the direction across the cell. Nguyen and White (9) used algebraic expressions for the concentrations along the electrodes, while Amphlett *et al.* (10), in their modeling of the Ballard IV fuel cell, assumed averaged partial pressures along the gas channels.

In real life, the concentrations along the gas channels-gas diffusers-catalyst layers will vary due to diffusion-convection transport and electrokinetics in the catalyst layers. These distributions will depend therefore on the gas/medium properties, as well as on the reaction rates. These latter ones are in turn functions of the reactant concentrations and an iterative procedure would be required to predict them. A proper description of the species concentration distribution would involve the use of the 2-D momentum equations in the coupled gas channel-gas diffuser-catalyst layer domain. Together with the continuity and species concentration equations (Stefan-Maxwell), equations describing the electrochemical reactions have to be also part of the system. These latter ones are coupled with the transport equations in membrane *via* electro-osmotic terms. The only independent variables for constant geometry and material properties are the mass flow rates, temperatures, humidities and the pressures of the gas mixtures at the gas channel inlets, the external circuit resistance and the temperature of the heating (cooling) agent, the last one having influence on the electrochemical reactions *via* Arrhenius type terms. These are actually the only parameters that can be controlled in laboratory experiments or other fuel cell applications.

MODEL DESCRIPTION AND ASSUMPTRIONS

The model used here is two dimensional, and is presented in Fig. 1. It represents a cross-section along one of the cathode channels and contains all fuel cell elements, from one collector plate to the other. It is assumed here that the design of the collector plates is such, that the anode and cathode gas channels have the same orientation and appear in the same cross-section.

The following assumptions are used in our mathematical formulation:

- The gas mixtures are considered to be perfect gases.
- The volume occupied by liquid water in the gas channels, coming from the gas diffusers is negligible (in gas channels, only gas mixtures are present).
- The flow is laminar everywhere.
- The gas mixture flows are incompressible.
- Only the steady state case is taken into account.
- The gas diffusers, catalyst layers and the PEM are considered each as isotropic porous media.
- Dilation or contraction of the porous media is neglected.
- The contact electrical losses at the interfaces between different fuel cell elements are neglected.
- The catalyst layers are considered to have vanishingly small thicknesses when the transport equations are solved, but the real values are taken into account when the membrane phase potential and current density are calculated.
- The dispersion of the fluids in the porous media is disregarded at this stage. Anyhow, it can be taken into account if the general diffusion coefficients are properly corrected.
- The heat generated under reversible conditions is neglected in this work.

Our mathematical model uses nondimensional transport equations. Three different domains are considered, corresponding to the phase of the fluid taken into account (Fig 2): the cathode gas channel-gas diffuser-catalyst layer for the air mixture; the cathode gas diffuser-catalyst layer-membrane-anode catalyst layer-gas diffuser for liquid water; the anode gas channel-gas diffuser-catalyst layer for hydrogen.

In order to take into consideration the real concentration distributions along the interface between the gas diffuser and catalyst layer, transport equations are solved simultaneously for the domain consisting of the coupled gas channel, gas diffuser, catalyst layer and membrane. The selfconsistent schematical model for porous media is used for the equations describing transport phenomena in the membrane, catalyst layers and gas diffusers, while standard Navier-Stokes, energy transport, continuity and species concentration equations are solved in the gas channels. A special handling of the transport equations enabled us to use the same numerical method to solve them, and therefore to treat the gas channel-gas diffuser-catalyst layer domains as an entirety, avoiding arbitrary boundary conditions at their interfaces.

The fuel cell parameters and the fluid properties for the base case condition are presented in Tables 1 and 2.

Table 1
The Physical Parameters of the Fuel Cell Elements

gas channel length, $7.62 \times 10^{-2}\ m$
gas channel width, $D = 7.62 \times 10^{-4}\ m$
gas diffuser width, $2.54 \times 10^{-4}\ m$
catalyst layer width, $D_{cl} = 0.287 \times 10^{-4} m$
membrane width, $L = 2.3 \times 10^{-4}\ m$ (1)
gas diffuser porosity, $\varepsilon = 0.4$
membrane porosity, $\varepsilon_m = 0.28$ (1)
volume fraction membrane in catalyst layer, $\varepsilon_{mc} = 0.5$ (1)
permeability to air of the gas diffuser, $k = 1.76 \times 10^{-11}\ m^2$
thermal conductivity of the graphite matrix of the gas diffuser, $k_{gr} = 150.6\ W.m^{-1}.K^{-1}$
hydraulic permeability of the membrane, $k_p = 1.58 \times 10^{-18}\ m^2$ (1)
electrokinetic permeability of the membrane, $k_\Phi = 1.13 \times 10^{-19}\ m^2$ (1)
thermal conductivity of the dry membrane, $k_{m,\, dry} = 100\ W.m^{-1}.K^{-1}$
fixed charged site concentration in membrane, $c_f = 1.2 \times 10^3\ mol.m^{-3}$ (1)
charge of sulfonate site in membrane, $z_f = -1$
reference exchange current density times area, $a\, j_0^{ref} = 5 \times 10^2\ A.m^{-3}$ (1)
cathodic transfer coefficient for cathode, $\alpha_c = 2$ (1)

Table 2
The Physical Parameters of the Fluids (Base Case Condition)

air inlet temperature, $T_i = 353\ K$
air inlet pressure, $p_i = 3\ atm$
air inlet velocity, $U_i = 0.35\ m.s^{-1}$
air viscosity, $\mu = 1.85 \times 10^{-5}\ kg.m^{-1}.s^{-1}$
air thermal conductivity, $k = 2.5 \times 10^{-2}\ W.m^{-1}.K^{-1}$
molecular mass of air, $29 \times 10^{-3}\ kg.mol^{-1}$
molecular mass of oxygen, $32 \times 10^{-3}\ kg.mol^{-1}$

molecular mass of nitrogen, $28 \times 10^{-3}\ kg.mol^{-1}$
molecular mass of water, $18 \times 10^{-3}\ kg.mol^{-1}$
air specific heat at constant pressure, $c_p = 1008\ J.kg^{-1}.K^{-1}$
air relative humidity at inlet, *100 %*
oxygen/nitrogen ratio in air at inlet, *0.21/0.79*
hydrogen inlet pressure, $p_i = 1\ atm$
water density, $\rho = 971.1\ kg.m^{-3}$
water viscosity, $\mu = 8.91 \times 10^{-4}\ kg.m^{-1}.s^{-1}$
water thermal conductivity, $k = 0.6\ W.m^{-1}.K^{-1}$
water specific heat at constant pressure, $c_p = 4190\ J.kg^{-1}.K^{-1}$
proton diffusivity in water, $D_{H+} = 4.5 \times 10^{-9}\ atm\ m^2.s^{-1}$ (1)
critical temperature for oxygen, $T_{cr} = 154.4\ K$
critical pressure for oxygen, $p_{cr} = 49.7\ atm$
critical temperature for nitrogen, $T_{cr} = 126.2\ K$
critical pressure for nitrogen, $p_{cr} = 33.5\ atm$
critical temperature for water, $T_{cr} = 647.3\ K$
critical pressure for oxygen, $p_{cr} = 221.2\ atm$

RESULTS AND DISSCUSION

The mathematical model and the solution technique have been validated by comparing the characteristics of the fuel cell determined numerically with the experimental results of Ticianelli *et al.* (11) and have been discussed by Gurau (12). The behavior of the mathematical model in predicting the values of the velocity and the scalar variables at the interface between a gas channel and the adjacent porous gas diffuser has been presented in the same work.

Cell Performance

Effect of the Gas Diffuser Porosity on the Cell Performance. Figure 3 shows the cell voltage versus the operating current density for different values of the gas diffuser porosity ε, assuming the isothermal case with the temperature $T = 353\ K$, an inlet air velocities $U_i = 0.35\ m/s$ and the water vapor mole fraction at the gas channel inlet, $X^{sat}_{w,i} = 0.1579$ (*100 %* humidity).

For lower values of ε, lower values of the limiting current density are found. This phenomenon is due to the limited possibilities of the reactant in the cathode side gas mixture (oxygen) to be transported towards the catalyst layer. Bernardi and Verbrugge (5) present limiting current density as a function of porosity for three different catalyst layer thicknesses, obtained for their 1-D model. Extrapolating these curves for the catalyst layer thickness used in our model, one may find close values for the limiting current. The slope of the curve is in good agreement with their results as well. Unlike other numerical methods, where the program fails to give results when the limiting current is achieved, the present one is able to predict phenomena even in the region where the concentration overpotentials are predominant.

Effect of the Inlet Air Velocity on the Cell Performance. Figure 4 presents the current density for different values of the air velocity at the cathode gas channel entrance, considering the gas diffuser porosity $\varepsilon = 0.4$, a constant temperature $T = 353\ K$ (isothermal case) and the water vapor mole fraction at the cathode gas channel inlet, $X_{w,i}^{sat} = 0.1579$ (*100 %* humidity). For higher inlet air velocities (higher air mass flow rates), more oxygen is fed and therefore more oxygen is likely to arrive at the catalyst layer, with the result of a higher limiting current density. This is explained by the fact that for the same pressure field, for higher velocities, the axial momentum transfer across the gas channel-gas diffuser interface becomes more important, with a consequence of more "fresh" air arriving to the catalyst layer. For inlet air velocities higher than approx *2 m/s*, the limiting current becomes constant, which shows that there is a limit effect of the momentum transfer across the gas channel-gas diffuser interface.

Effect of Temperature on the Cell Performance. Figure 5 presents the effect of the cell temperature on the voltage-current density characteristic for an inlet air velocity $U_i = 0.35$ *m/s*, gas diffuser porosity $\varepsilon = 0.4$, and *100 %* air humidity. Content of water vapor in air at the cathode channel inlet is taken as a function of temperature from available data. Water vapor concentration at the cathode gas diffuser-catalyst layer interface will determine the liquid water content in the membrane and therefore the membrane ionic conductivity, with the final effect of better cell performances (higher current densities) at higher temperatures. At higher temperatures, the open circuit potential is higher as well.

The Oxygen Mole Fraction Field in the Cathode Gas Channel-Gas Diffuser Coupled Domain. Figure 6 shows the oxygen mole fraction field in the coupled cathode gas channel-gas diffuser domain for the base case conditions (isothermal case) and the limiting current density. The oxygen is consumed in the catalyst layer. Although the rate of oxygen depletion is higher at the left side of the catalyst layer-gas diffuser interface, the oxygen concentration is lower in the right side. This phenomenon is explained by the convective transport in gas diffuser. The corresponding stoichiometric ratios are calculated as the ratio between the average oxygen mole fraction at the inlet and the average oxygen mole fraction difference between exit and inlet.

The Oxygen Mole Fraction Distribution as a Function of the Fuel Cell Operating Current Density. Most of the mathematical models for PEM fuel cells use oxygen mole fraction or partial pressure distributions along the cathode gas channel-gas diffuser interface as input data. These "guessed" or *a priori* prescribed distributions may eventually affect the computed values of the operating current density. The present mathematical model enables us to solve the transport equations in the coupled gas channel-gas diffuser domain, therefore the oxygen mole fraction is *calculated*, not *prescribed*. Figure 7 presents the computed oxygen mole fraction distributions at the interface between the cathode gas channel and gas diffuser for the base case conditions and different operating current densities. For higher operating current densities, these distributions are clearly non linear, as assumed in other models. For the base case conditions and operating current densities higher than $3.17+04\ A/m^2$, the oxygen mole fraction distribution remains almost unchanged at this interface, which shows that limiting current density is approached.

The Current Density Distribution at the Membrane-Cathode Catalyst Layer as a Function of the Fuel Cell Operating Current Density. If the operating current density was an input data and the distribution of the oxygen mole fraction at the cathode gas channel-gas diffuser was not prescribed before performing the computations, it would be unclear how the current density distribution could be found. Even though the operating current density is the average of the current density distribution at the membrane-cathode catalyst layer interface, the knowledge of the former one is not sufficient to determine the latter one. Therefore, in the present formulation we used the total electrode overpotential as an input data to find the operating current density, the current density distribution and the oxygen mole fraction distribution. This was possible, since there is a bijective relationship between the cell overpotential and the cell voltage. It is true that for a certain regime, the total electrode overpotential is not known *a priori*. Therefore one has to calculate the operating current density-cell voltage curve for different regimes, from zero current density until the limiting current density is achieved, and after that to interpolate for the desired regime. Figure 8 shows the current density distribution at the membrane-cathode catalyst layer interface, for the base case and the oxygen mole fraction distributions in Fig. 7.

CONCLUDING REMARKS

The mathematical model presented here enabled us to predict the phenomena in the entire fuel cell sandwich, including the gas channels. The input data are only those parameters that can be controlled in the real life fuel cell operation. No assumptions are necessary for the distribution of the species concentrations or current density, as they are assumed in other fuel cell models available in the literature. The computed oxygen mole fraction along the gas channel-gas diffuser interface and the current density along the membrane-catalyst layer interface do not present linear distributions, as are assumed in other works. The oxygen mole fraction field is also presented in the coupled gas channel-gas diffuser domain. The computed fuel cell performances are realistic. They are compared only to other computed results, obtained using simpler fuel cell models, therefore actual validation of this 2-D model with experimental results remain to be done. The present mathematical model will be used in conjunction with laboratory experiments for optimization of the fuel cell structure and performance.

REFERENCES

1. S. J. Ridge, R. E. White, Y. Tsou, R. N. Beaver, G. A. Eisman, J. Electrochem. Soc., 136, 1902 (1989).
2. M. W. Verbrugge, R. F. Hill, J. Electrochem. Soc., 137, 886 (1990).
3. M. W. Verbrugge, R. F. Hill, J. Electrochem. Soc., 137, 3770 (1990).
4. D. M. Bernardi, M. W. Verbrugge, AIChE J., 37, 1151 (1991).
5. D. M. Bernardi, M. W. Verbrugge, J Electrochem Soc, 139, 2477 (1992).
6. T. E. Springer, T. A. Zawodinski, S. Gottesfeld, J. Electrochem. Soc., 136, 2334 (1991)
7. D. Singh, D. M. Lu, N. Djilali in Proceedings of the First International Energy and Environment Symposium, Karadeniz Technical University, Trabzon, Turkey, 615 (1996)
8. T. F. Fuller, J. Newman, J. Electrochem. Soc., 5, 1218 (1993)
9. T. V. Nguyen, R. E. White, J. Electroch. Soc., 140, 2178 (1993)
10. J. C. Amphlett, R. M. Baumert, R. F. Mann, B. A. Peppley, and P. R. Roberge, J. Electrochem. Soc., 142, 1 (1995)
11. E. A. Ticianelli, C. R. Derouin, S. Srinivasan, J. Electroanal. Chem., 251, 275 (1988)
12. V. Gurau, Ph.D. Thesis, University of Miami, Coral Gables, FL (1998)

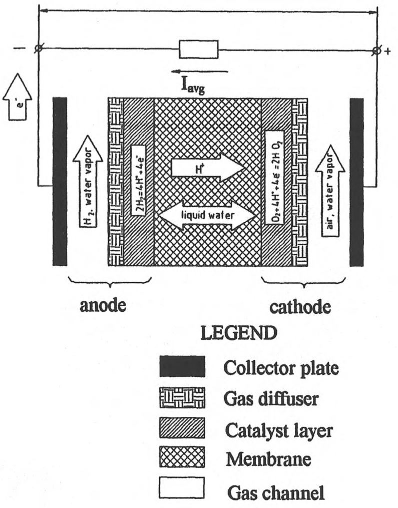

Figure 1
Two dimensional representation of a PEM fuel cell

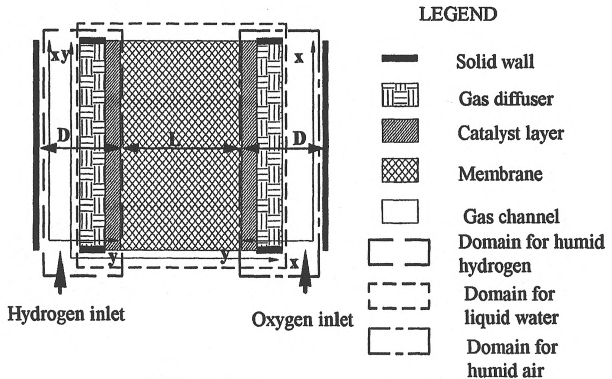

Figure 2
The geometry, the coordinate axes, the boundary types and the characteristic dimensions of the three domains

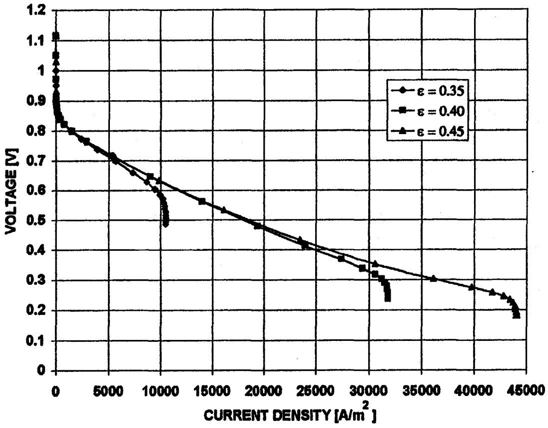

Figure 3
Effect of the gas diffuser porosity on the voltage-current density characteristic; $U_i = 0.35$ m/s, $T = 353$ K, (isothermal case), $X_{w,i} = 0.1579$ (100% humidity)

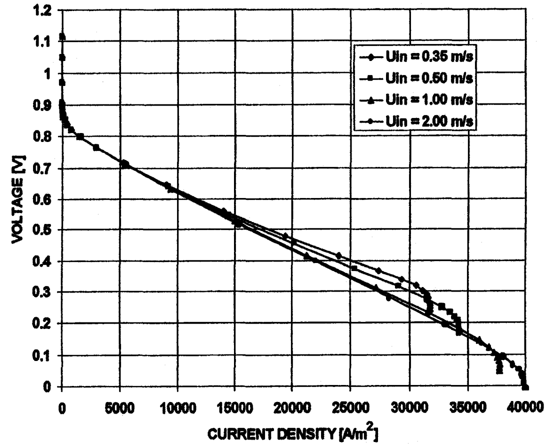

Figure 4
Effect of the air inlet velocity on the voltage-current density characteristic; $T = 353$ K (isothermal case), $X_w = 0.1579$ (100% humidity), $\varepsilon = 0.40$

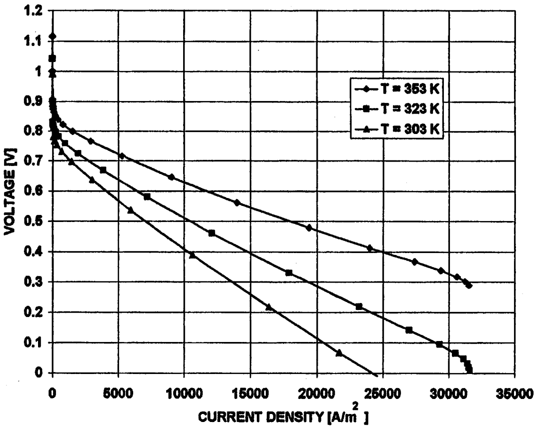

Figure 5
Effect of the cell temperature on the voltage-current density characteristic;
$U_i = 0.35\ m/s$, $\varepsilon = 0.40$, *100%* humidity

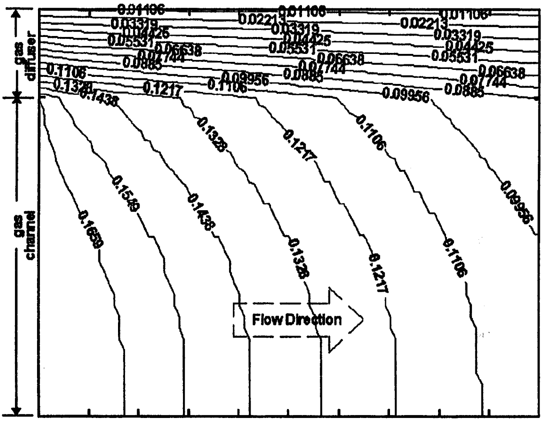

Figure 6
The oxygen mole fraction in the cathode gas channel-gas diffuser domain, for
$I_{avg} = 3.18\ 10^4\ A/m^2$ (limiting current), $U_i = 0.35\ m/s$, $T = 353\ K$, (isothermal case),
$X_{w,i} = 0.1579$ (100% humidity), $\varepsilon = 0.40$. Resulting stoichiometric ratio: $\xi_+ = 2.28$

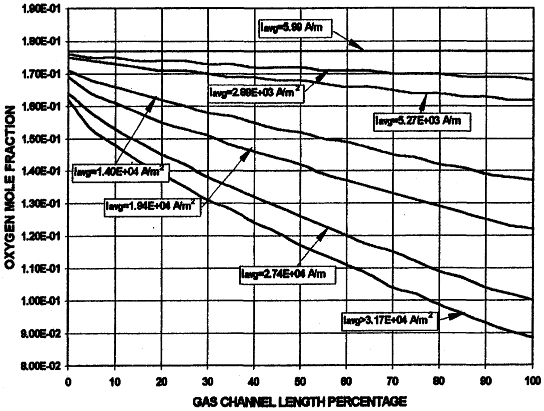

Figure 7
The oxygen mole fraction distribution along the gas channel-gas diffuser interface, for different cell operating current densities; U_i=*0.35 m/s*, *T* = *353 K* (isothermal case), $X_{O2,i}$ = *0.1579* (100%humidity), ε = *0.40*

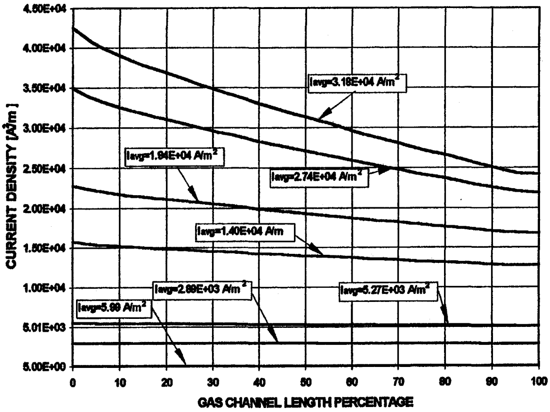

Figure 8
The current density distribution along the membrane-catalyst layer interface, for different cell operating current densities; U_i = *0.35 m/s*, *T* = *353 K* (isothermal case), $X_{O2,i}$ = *0.1579* (100% humidity), ε = *0.40*

APPENDIX

MATHEMATICAL MODEL

In Gas Channels

The fluid mechanics in the gas channel are described by the continuity and Navier-Stokes equations, which in non-dimensional form and under the assumptions mentioned in the previous section become (13):

$$\frac{\partial \bar{u}}{\partial \bar{x}}+\frac{\partial \bar{v}}{\partial \bar{y}}=0 \qquad [1]$$

$$\bar{u}\frac{\partial \bar{u}}{\partial \bar{x}}+\bar{v}\frac{\partial \bar{u}}{\partial \bar{y}}=-\frac{\partial \bar{p}}{\partial \bar{x}}+\frac{1}{\mathrm{Re}}\left(\frac{\partial^2 \bar{u}}{\partial \bar{x}^2}+\frac{\partial^2 \bar{u}}{\partial \bar{y}^2}\right) \qquad [2]$$

$$\bar{u}\frac{\partial \bar{v}}{\partial \bar{x}}+\bar{v}\frac{\partial \bar{v}}{\partial \bar{y}}=-\frac{\partial \bar{p}}{\partial \bar{y}}+\frac{1}{\mathrm{Re}}\left(\frac{\partial^2 \bar{v}}{\partial \bar{x}^2}+\frac{\partial^2 \bar{v}}{\partial \bar{y}^2}\right) \qquad [3]$$

where the non-dimensional parameters are defined as:

$$\bar{u}=\frac{u}{U_i},\ \bar{\mathrm{v}}=\frac{v}{U_i},\ \bar{\mathrm{x}}=\frac{x}{D},\ \bar{\mathrm{y}}=\frac{y}{D},\ \bar{\mathrm{p}}=\frac{p-p_e}{\rho_i U^2{}_i},\ \mathrm{Re}=\frac{\rho_i U_i D}{\mu}$$

Similarly, the energy equation becomes:

$$\bar{u}\frac{\partial \bar{T}}{\partial \bar{x}}+\bar{v}\frac{\partial \bar{T}}{\partial \bar{y}}=\frac{1}{\mathrm{Re}\,\mathrm{Pr}}\left(\frac{\partial^2 \bar{T}}{\partial \bar{x}^2}+\frac{\partial^2 \bar{T}}{\partial \bar{y}^2}\right) \qquad [4]$$

where

$$\bar{T} = \frac{T - T_w}{T_i - T_w} \text{ and } \Pr = \frac{\mu c_p}{k}$$

The equation for the species mole fraction is:

$$\bar{u}\frac{\partial X_k}{\partial \bar{x}} + \bar{v}\frac{\partial X_k}{\partial \bar{y}} = \frac{1}{\mathrm{Re}\, Sc_k}\left(\frac{\partial^2 X_k}{\partial \bar{x}^2} + \frac{\partial^2 X_k}{\partial \bar{y}^2}\right) \qquad [5]$$

where X_k stands for the mole fraction of the k'th component, and the Schmidt number: $Sc_k = \mu / \rho D_k$. The diffusion coefficients can be expressed in terms of binary diffusion coefficients as:

$$D_k = \frac{1 - \frac{\rho_k}{\rho}}{\sum\limits_{m \neq k} \frac{c}{c_m}\frac{1}{D_{k,m}}} \qquad [6]$$

Equation [5] may be solved only for n-1 components (water vapor and oxygen in the cathode), the last one for nitrogen coming out from the relation:

$$X_n = 1 - \sum_{i=1}^{n-1} X_i \qquad [7]$$

In Gas Diffusers

The gas diffusers in our virtual fuel cell are made from carbon cloth of *E-Tek* fabrication.

Particular forms of the transport equations [1]-[5] may be derived for the gas diffusers if their porous nature is taken into account. This is possible if the macroscopic, instead of the microscopic variables are used, and by ensemble or space averaging the terms in the transport equations.

In terms of macroscopic variables, the continuity equation in the porous gas diffuser reads:

$$\frac{\partial \overline{q_x}}{\partial \bar{x}} + \frac{\partial \overline{q_y}}{\partial \bar{y}} = 0 \qquad [8]$$

where q_x and q_y are the components of the specific discharge.

The macroscopic velocity field in the porous medium is provided by expressions obtained by space averaging the Navier-Stokes equations. The resulting equations are a generalized form of Darcy's law (14), which in non-dimensional form read as:

$$\bar{q}_x \frac{\partial \bar{q}_x}{\partial \bar{x}} + \bar{q}_y \frac{\partial \bar{q}_x}{\partial \bar{y}} = -\varepsilon \frac{\partial \bar{P}}{\partial \bar{x}} + \frac{1}{\mathrm{Re}} r^{(2)} \left(\frac{\partial^2 \overline{q_x}}{\partial \bar{x}^2} + \frac{\partial^2 \overline{q_x}}{\partial \bar{y}^2} \right) - \varepsilon \frac{\mu}{k} \cdot \bar{q}_x \frac{D}{\rho_i U_i} \qquad [9]$$

$$\bar{q}_x \frac{\partial \bar{q}_y}{\partial \bar{x}} + \bar{q}_y \frac{\partial \bar{q}_y}{\partial \bar{y}} = -\varepsilon \frac{\partial \bar{P}}{\partial \bar{y}} + \frac{1}{\mathrm{Re}} r^{(2)} \left(\frac{\partial^2 \overline{q_y}}{\partial \bar{x}^2} + \frac{\partial^2 \overline{q_y}}{\partial \bar{y}^2} \right) - \varepsilon \frac{\mu}{k} \cdot \bar{q}_y \frac{D}{\rho_i U_i} \qquad [10]$$

When $r^{(2)} = 1$, equations [9] and [10] turn into Brinkman's equations. Dagan (15) showed that $r^{(2)} >> 1$, and the relationship for $r^{(2)}$ can be estimated as:

$$r^{(2)} = 2.25 \frac{(1-\varepsilon)^2}{\varepsilon^2} \qquad [11]$$

At this stage it is clear to see the similarity between equations [2], [3] and [9], [10]. This enables us to consider the whole domain (channel + gas diffuser) as an entire, if in the numerical program the extra body forces are taken into account for the gas diffuser sub-domain. When the flow field is obtained numerically, one has to remember that the values of the velocities in the porous gas diffuser stand for the specific discharge.

In the gas diffuser layers, energy is transported by diffusion and locally by convection in the fluid phase, and by conduction in the solid matrix of the porous graphite cloth. For such a porous medium, the energy equation can be obtained by ensemble averaging the microscopic energy equations in the fluid and solid phase respectively, neglecting the heat generation by viscous dissipation and adding them up. To define the resulting effective, macroscopic heat conductivity, different schematical models of porous media are available in the literature (14). In this work, we have chosen the self-consistent approximation:

$$k_{eff} = -2k_{gr} + \frac{1}{\dfrac{\varepsilon}{2k_{gr} + k_{gas}} + \dfrac{1-\varepsilon}{3k_{gr}}} \qquad [12]$$

where k_{gr} and k_{gas} are the thermal conductivities of the graphite solid matrix and of the gas mixture, respectively. The energy transport equation for the gas diffusers, in non-dimensional form will be therefore (14):

$$\overline{q}_x \frac{\partial \overline{T}}{\partial \overline{x}} + \overline{q}_y \frac{\partial \overline{T}}{\partial \overline{y}} = \frac{1}{\mathrm{Re}\,\mathrm{Pr}} \left(\frac{\partial^2 \overline{T}}{\partial \overline{x}^2} + \frac{\partial^2 \overline{T}}{\partial \overline{y}^2} \right) \qquad [13]$$

where

$$\mathrm{Pr} = \frac{c_p \mu}{k_{eff}}$$

c_p standing for the specific heat of the gas mixture at constant pressure. The variables in equation [13] have been non-dimensionalised in the same manner like equation [4] and is similar to it..

The chemical species in the gas mixtures will be transported by diffusion and locally by convection. The effective macroscopic diffusion coefficient for the *k'* th component in the frame of the adopted schematical porous medium model will be (14):

$$\begin{aligned} D_{eff,k} &= \frac{3\varepsilon - 1}{2\varepsilon} D_k \quad \text{if} \quad \varepsilon > 1/3 \\ D_{eff,k} &= 0. \qquad\qquad \text{if} \quad \varepsilon \leq 1/3 \end{aligned} \qquad [14]$$

where D_k is the microscopic diffusion coefficient for the k' th species, defined by equation [6]. The transport equation for the chemical species in nondimensional form will become:

$$\overline{q}_x \frac{\partial X_k}{\partial \overline{x}} + \overline{q}_y \frac{\partial X_k}{\partial \overline{y}} = \frac{\varepsilon}{\mathrm{Re}\, Sc_k} \left(\frac{\partial^2 X_k}{\partial \overline{x}^2} + \frac{\partial^2 X_k}{\partial \overline{y}^2} \right) \qquad [15]$$

where Schmidt number is defined in terms of the effective macroscopic diffusion coefficient given by equation [14]:

$$Sc_k = \frac{\mu}{\rho D_{eff,k}}$$

Equation [15] is non-dimensionalised in the same manner like equation [5] and is similar to it.

In Membrane

The subject of the transport equations in the porous membrane are variables related to the water flow; therefore, similar equations like the ones developed for the gas diffusers may apply, if the proper parameters for water are plugged in. A different form of the momentum transport equations, containing source terms accounting for electro-osmotic forces has to be used here. In non-dimensional form, these equations read:

$$\begin{aligned} \overline{q}_x \frac{\partial \overline{q}_x}{\partial \overline{x}} + \overline{q}_y \frac{\partial \overline{q}_x}{\partial \overline{y}} = -\varepsilon_m \frac{\partial \overline{P}}{\partial \overline{x}} + \frac{1}{\mathrm{Re}} r^{(2)} \left(\frac{\partial^2 \overline{q_x}}{\partial \overline{x}^2} + \frac{\partial^2 \overline{q_x}}{\partial \overline{y}^2} \right) - \varepsilon_m \frac{\mu}{k_p} \cdot \overline{q_x} \frac{D}{\rho_i U_i} + \\ + \frac{k_\phi}{k_p} z_f c_f F \frac{\partial \phi}{\partial \overline{x}} \frac{1}{\rho U_i^2 L} \end{aligned} \qquad [16]$$

$$\bar{q}_x \frac{\partial \bar{q}_y}{\partial \bar{x}} + \bar{q}_y \frac{\partial \bar{q}_y}{\partial \bar{y}} = -\varepsilon_m \frac{\partial \bar{P}}{\partial \bar{y}} + \frac{1}{\mathrm{Re}} r^{(2)} \left(\frac{\partial^2 \overline{q_y}}{\partial \bar{x}^2} + \frac{\partial^2 \overline{q_y}}{\partial \bar{y}^2} \right) - \varepsilon_m \frac{\mu}{k_p} \cdot \overline{q_y} \frac{D}{\rho_i U_i} + \\ + \frac{k_\phi}{k_p} z_f c_f F \frac{\partial \phi}{\partial \bar{y}} \frac{1}{\rho U_i^2 L} \qquad [17]$$

Equations [16] and [17] represent a generalized form of the Schlögl's equations.

The transport of the dissolved protons is governed by an equation similar to equation [15], with an extra term accounting for migration:

$$\overline{q_x} \frac{\partial X_{H^+}}{\partial \bar{x}} + \overline{q_y} \frac{\partial X_{H^+}}{\partial \bar{y}} = \frac{\varepsilon_m}{\mathrm{Re}\, Sc_{H^+}} \left(\frac{\partial^2 X_{H^+}}{\partial \bar{x}^2} + \frac{\partial^2 X_{H^+}}{\partial \bar{y}^2} \right) + \\ \varepsilon_m z_{H^+} X_{H^+} \frac{F}{RT} D_{eff,H^+} \left(\frac{\partial^2 \phi}{\partial x^2} + \frac{\partial^2 \phi}{\partial y^2} \right) \frac{1}{U_i L} \qquad [18]$$

The energy equation is similar to equation [13]with a new ohmic source term:

$$\overline{q_x} \frac{\partial \bar{T}}{\partial \bar{x}} + \overline{q_y} \frac{\partial \bar{T}}{\partial \bar{y}} = \frac{1}{\mathrm{Re}\,\mathrm{Pr}} \left(\frac{\partial^2 \bar{T}}{\partial \bar{x}^2} + \frac{\partial^2 \bar{T}}{\partial \bar{y}^2} \right) + \frac{i^2}{\sigma_m} \frac{L}{U_i \rho_i c_P T_i} \qquad [19]$$

and the effective conductivity given by equation [14], with k_{gr} replaced by $k_{m,\,dry}$ and k_{gas} by $k_{w,\,l}$. In equation [19], i is the modules of the membrane phase current density vector and σ_m is the ionic conductivity.

For the membrane phase potential the following equation applies:

$$\frac{\partial}{\partial x}\left(\sigma_m \frac{\partial \Phi}{\partial x} \right) + \frac{\partial}{\partial y}\left(\sigma_m \frac{\partial \Phi}{\partial y} \right) = 0. \qquad [20]$$

and the membrane phase current density satisfies:

$$i_x = -\sigma_m \frac{\partial \phi}{\partial x} - F z_f c_f u$$
$$i_y = -\sigma_m \frac{\partial \phi}{\partial y} - F z_f c_f v \qquad [21]$$

In Catalyst Layers

Continuity and equations [16] and [17] apply in these regions with the porosity ε_m replaced by $\varepsilon_m \varepsilon_{mc}$, where ε_{mc} is the membrane volume fraction in the catalyst layer. Equations like [15] will apply, with the following source terms:

- at the anode, the source term for the hydrogen molecules and hydrogen protons are:

$$-\frac{1}{2F} j_a \frac{D}{U_i c} \text{ and } \frac{1}{F} j_a \frac{L}{U_i c} \qquad [22]$$

- At the cathode side, the source terms for the oxygen, water and hydrogen protons are:

$$-\frac{1}{4F} j_c \frac{D}{U_i c},\ \frac{1}{2F} j_c \frac{L}{U_i c} \text{ and } -\frac{1}{F} j_c \frac{L}{U_i c} \qquad [23]$$

where the transfer current j_a and j_c are defined by the Butler-Volmer expressions:

$$j_a = a j_0^{ref} \left(\frac{X_{H_2}}{X_{H_2 ref}} \right)^{\frac{1}{2}} \left[e^{\frac{\alpha_a F}{RT}\eta} - \frac{1}{e^{\frac{\alpha_c F}{RT}\eta}} \right] \qquad [24]$$

$$j_c = a j_0^{ref} \left(\frac{X_{O_2}}{X_{O_2 ref}} \right) \left[e^{\frac{\alpha_a F}{RT}\eta} - \frac{1}{e^{\frac{\alpha_c F}{RT}\eta}} \right] \qquad [25]$$

Equation [13] applies with the a new source term:

$$\overline{q}_x \frac{\partial \overline{T}}{\partial \overline{x}} + \overline{q}_y \frac{\partial \overline{T}}{\partial \overline{y}} = \frac{1}{\mathrm{Re}\,\mathrm{Pr}}\left(\frac{\partial^2 \overline{T}}{\partial \overline{x}^2} + \frac{\partial^2 \overline{T}}{\partial \overline{y}^2}\right) + i\eta \frac{D}{U_i \rho_i c_p T_i D_{cl}} \qquad [26]$$

The membrane phase potential satisfies equation:

$$\begin{aligned} &\frac{\partial}{\partial x}\left(\sigma_m \frac{\partial \Phi}{\partial x}\right) + \frac{\partial}{\partial y}\left(\sigma_m \frac{\partial \Phi}{\partial y}\right) = -j_a \quad \text{at anode} \\ &\frac{\partial}{\partial x}\left(\sigma_m \frac{\partial \Phi}{\partial x}\right) + \frac{\partial}{\partial y}\left(\sigma_m \frac{\partial \Phi}{\partial y}\right) = -j_c \quad \text{at cathode} \end{aligned} \qquad [27]$$

The membrane phase current density satisfies:

$$\begin{aligned} &\frac{\partial i_x}{\partial x} + \frac{\partial i_y}{\partial y} = j_a \quad \text{at anode} \\ &\frac{\partial i_x}{\partial x} + \frac{\partial i_y}{\partial y} = j_c \quad \text{at cathode} \end{aligned} \qquad [28]$$

The next additional equations have to be as well part of the system:

- the equation of state for the perfect gasses apply in the first and third domains of Fig. 2:

$$\frac{p}{\rho} = RT \qquad [29]$$

- the ionic conductivity of the membrane has the following expression:

$$\sigma_m = \frac{F^2}{RT} D_{eff,H^+} c_{H^+} z_{H^+} \qquad [30]$$

It has been shown anyhow that the membrane ionic conductivity is not only a function of temperature, but it features a strong dependence on the membrane water content. Springer *et al.* (6) present the following empirical expressions to determine the ionic conductivity in a 117 Nafion® proton exchange membrane:

$$\sigma_m^{ref} = 0.005139\lambda - 0.00326 \quad \text{if } \lambda \geq 1 \qquad [31]$$

where σ_m^{ref} is the reference ionic conductivity at a temperature of *303 K*. For values of the membrane water content with λ less than one, the reference ionic conductivity is assumed constant. At other temperatures, it is given by:

$$k(T) = \sigma_m^{ref} \exp\left[1268\left(\frac{1}{303} - \frac{1}{T}\right)\right] \qquad [32]$$

where temperature is expressed in *K*. The membrane water content in equation [31] is given by the following empirical formula (6):

$$\begin{aligned} \lambda &= 0.043 + 17.81a - 39.85a^2 + 36.0a^3 && \text{for } 0 < a \leq 1 \\ \lambda &= 14 + 1.4(a-1) && \text{for } 1 \leq \text{a} \leq 3 \end{aligned} \qquad [33]$$

a being the water vapor activity at the cathode gas diffuser-catalyst layer interface assuming equilibrium, given by:

$$a = \frac{X_w p}{p^{sat}} \qquad [34]$$

The saturated water partial pressure is expressed by the following empirical equation that fits the tabulated values (6):

$$\log_{10} p^{sat} = -2.1794 + 0.02953T - 9.1837 \cdot 10^{-5} T^2 + 1.4454 \cdot 10^{-7} T^3 \qquad [35]$$

- the temperature dependence of the binary diffusion coefficients is given by Slattery and Bird (16):

$$pD_{A,B} = a\left(\frac{T}{\sqrt{T_{crA}T_{crB}}}\right)^{b}\left(p_{crA}p_{crB}\right)^{\frac{1}{3}}\left(T_{crA}T_{crB}\right)^{\frac{5}{12}}\left(\frac{1}{M_A}+\frac{1}{M_B}\right)^{\frac{1}{2}} \qquad [36]$$

where *a* and *b* are constants, the pressure is in *bar*, and the binary diffusion coefficient in $cm^2.s^{-1}$.

- the thermodynamic open circuit potential for the overall reaction is given by (5):

$$E = 1.23 - 0.9\cdot 10^{-3}(T-298) + 2.3\frac{RT}{4F}\log\left(p_{H_2}^2 p_{O_2}\right) \qquad [37]$$

Examination of equation [37] shows a decrease of the open circuit potential with temperature. Experimental results show an opposite effect. This is due to higher exchange current density for oxygen reduction at higher temperatures (17). At the time being, we are not aware of any mathematical model to describe this dependency, therefore we used the empirical results of Parthasarathy *et al.* (17) in our formulation. They tabulated values for the open circuit potential as a function of temperature, which can be fitted in the following equation:

$$E = 0.0025T + 0.2329 \qquad [38]$$

temperature being in *K*.

The special treatment of the boundary conditions and the solution technique are presented in detail elsewhere (12).

NOMENCLATURE

a	water vapor activity
aj_o^{ref}	reference exchange current density times area, $A.m^{-3}$
c	molar concentration, $mol.m^{-3}$
c_f	concentration of the sulfonic ions, $mol.m^{-3}$
c_p	specific heat, $J.kg^{-1}K^{-1}$
D	gas channel width, m
D_{cl}	catalyst layer thickness, m
D_k	diffusion coefficient of the k'th component, $m^2.s^{-1}$
F	Faraday constant, 96.487 C/mol
E	Thermodynamic open circuit potential, V
i	current density, $A.m^{-2}$
I_{avg}	operating cell current density, $A.m^{-2}$
j	transfer current, $A.m^{-3}$
k	permeability of gas in the porous layer, m^2
k	thermal conductivity, $W.m^{-1}.K^{-1}$
k_p	hydraulic permeability of the porous layer, m^2
k_Φ	electrokinetic permeability, m^2
L	membrane width, m
M	molecular mass, $kg.kmol^{-1}$
n	number of electrons participating in reaction
p	pressure, Pa
Pr	Prandtl number
q	specific discharge, $m.s^{-1}$
Q	heat source, $W.m^{-2}$
R	resistance, Ω
R	universal gas constant, 8,314 $J.mol^{-1}.K^{-1}$
$r^{(2)}$	coefficient.
Re	Reynolds number
S	entropy, $J.kg^{-1}.K^{-1}$
S	source term of the generalised transport equation
Sc	Schmidt number
T	temperature, K
u, v	velocity components, $m.s^{-1}$
U_i	inlet velocity, $m.s^{-1}$
x, y	coordinates, m
X	mole fraction
z_f	charge number of the sulfonic ions

Greek Symbols

α	transfer coefficient
Γ	diffusion coefficient of the generalised transport equation
ε	porosity
η	total electrode overpotential, V
λ	membrane water content, $mol\,H_2O/mol\,SO_3^-$
ρ	density, $kg.m^{-3}$
μ	viscosity, $kg.m^{-1}.s^{-1}$
Φ	membrane phase potential, V
σ_m	membrane ionic conductivity, $\Omega^{1}.m^{1}$
ξ	stoichiometric ratio

Superscripts

$\bar{}$	nondimensionalised variable
$\rightarrow$	vector
ref	reference

Subscripts

a	anode
A, B	components
avg	average
c	cathode
ch	channel
cl	catalyst layer
cr	critic
e	exit
eff	effective
f	related to the sulfonic acid ions
gas	related to the gas mixture
gr	related to the graphite
H^+	related to the hydrogen protons
H_2	related to the hydrogen molecule
i	inlet
k	k'th component
l	liquid
m	related to the membrane
mc	membrane volume in catalyst layer
O_2	related to the oxygen molecule
pm	porous medium

w	wall or related to water
x, y	directions
+	cathode

REFERENCES

13. S. Kakac, Y. Yener, Convective Heat Transfer. Second edition, CRC Press (1994)
14. G. Dagan, Flow and Transport in Porous Formations, Springer-Verlag (1989)
15. G. Dagan, Water Resources Research, 15, 1 (1979)
16. J. C. Slattery, R. B. Bird, AIChE J., 137 (1958)
17. A. Parthasarathy, S. Srinivasan, A. J. Appleby, J. Electrochem. Soc., 139, 2530 (1992)

SUBJECT INDEX